

# **Microreactor Technology and Process Intensification**



ACS SYMPOSIUM SERIES **914**

# **Microreactor Technology and Process Intensification**

**Yong Wang**, Editor  
*Pacific Northwest National Laboratory*

**Jamelyn D. Holladay**, Editor  
*Pacific Northwest National Laboratory*

**Sponsored by the  
ACS Divisions of Fuel Chemistry, Industrial and  
Engineering Chemistry, Inc., and Petroleum  
Chemistry, Inc.**



American Chemical Society, Washington, DC



**Library of Congress Cataloging-in-Publication Data**

**Microreactor technology and process intensification / Yong Wang, editor, Jamie Holliday, editor.**

p. cm.—(ACS symposium series ; 914)

“Developed from a symposium sponsored by the Divisions of Fuel Chemistry, Industrial and Engineering Chemistry, Inc. and Petroleum Chemistry, Inc. at the 226<sup>th</sup> National Meeting of the American Chemical Society, New York, New York, September 7–11, 2003.”

Includes bibliographical references and index.

ISBN 0-8412-3923-1 (alk. paper)

1. Microreactors—Congresses. 2. Bioreactors—Congresses. 3. Microchemistry—Congresses. 4. Chemical reactors—Congresses

I. Wang, Yong, 1964 Mar. 31- II. Holladay, Jamie. III. American Chemical Society. Meeting. (226<sup>th</sup> : 2003 : New York, N.Y.) IV. American Chemical Society. Division of Fuel Chemistry. V. American Chemical Society. Division of Industrial and Engineering Chemistry, Inc. VI. American Chemical Society. Division of Petroleum Chemistry, Inc. VII. Series.

TP248.25.B55M53 2005  
660'.2832—dc22

2005040997

The paper used in this publication meets the minimum requirements of American National Standard for Information Sciences—Permanence of Paper for Printed Library Materials, ANSI Z39.48-1984.

Copyright © 2005 American Chemical Society

Distributed by Oxford University Press

**Cover design by Nathan Johnson.**

All Rights Reserved. Reprographic copying beyond that permitted by Sections 107 or 108 of the U.S. Copyright Act is allowed for internal use only, provided that a per-chapter fee of \$30.00 plus \$0.75 per page is paid to the Copyright Clearance Center, Inc., 222 Rosewood Drive, Danvers, MA 01923, USA. Republication or reproduction for sale of pages in this book is permitted only under license from ACS. Direct these and other permission requests to ACS Copyright Office, Publications Division, 1155 16th Street, N.W., Washington, DC 20036.

The citation of trade names and/or names of manufacturers in this publication is not to be construed as an endorsement or as approval by ACS of the commercial products or services referenced herein; nor should the mere reference herein to any drawing, specification, chemical process, or other data be regarded as a license or as a conveyance of any right or permission to the holder, reader, or any other person or corporation, to manufacture, reproduce, use, or sell any patented invention or copyrighted work that may in any way be related thereto. Registered names, trademarks, etc., used in this publication, even without specific indication thereof, are not to be considered unprotected by law.

PRINTED IN THE UNITED STATES OF AMERICA

# Foreword

The ACS Symposium Series was first published in 1974 to provide a mechanism for publishing symposia quickly in book form. The purpose of the series is to publish timely, comprehensive books developed from ACS sponsored symposia based on current scientific research. Occasionally, books are developed from symposia sponsored by other organizations when the topic is of keen interest to the chemistry audience.

Before agreeing to publish a book, the proposed table of contents is reviewed for appropriate and comprehensive coverage and for interest to the audience. Some papers may be excluded to better focus the book; others may be added to provide comprehensiveness. When appropriate, overview or introductory chapters are added. Drafts of chapters are peer-reviewed prior to final acceptance or rejection, and manuscripts are prepared in camera-ready format.

As a rule, only original research papers and original review papers are included in the volumes. Verbatim reproductions of previously published papers are not accepted.

**ACS Books Department**

# **Chapter 1**

## **Silicon-Based Microreactors**

**Klavs F. Jensen**

**Departments of Chemical Engineering and Materials Science and  
Engineering, Massachusetts Institute of Technology, 77 Massachusetts  
Avenue, Cambridge, MA 02139**

The microscale revolution in chemistry promises to transform classical batch wise laboratory procedures into integrated systems capable of providing new understanding of fundamental chemical processes as well as rapid, continuous discovery and development of new products with less use of resources and waste generation. Applications of silicon based microreactors are illustrated with a broad range of cases studies, including high throughput experimentation in organic synthesis, integration of ultraviolet (UV), visible and infrared (IR) spectroscopy; investigations of high temperature heterogeneous catalytic reactions, obtaining high mass transfer rates in gas-liquid reactions over solid catalysts, enabling difficult to perform reactions, synthesis of solid nanoparticles, and high temperature conversion of hydrocarbons to hydrogen.

## Introduction

The term “microreactor” originally referred to small tubular reactors used in catalysis research, but with advances in microreaction technology it has become synonymous with microfabricated systems consisting of multiple sub-millimeter channels in which fluid flows continuously and chemical reactions take place (1-12). These microreactors have the potential for less waste, fewer utilities, higher throughput experimentation, and safety advantages compared to conventional reaction system. The small reaction volumes of microsystems combined with the high heat and mass transfer rates enable reactions to be performed under more aggressive conditions with higher yields than can typically be achieved with conventional reactors. Moreover, new reaction pathways deemed too difficult to control in conventional macroscopic equipment can be conducted safely because of the high heat transfer and ease of confining small volume. The latter feature becomes particularly important when chemical transformations involve highly reactive intermediates. In that case, large exotherms can lead to thermal runaway with potentially catastrophic consequences. These inherent safety characteristics of microreactors also imply that systems of multiple microreactors could be deployed in distributed point-of-use synthesis of small volume chemicals with storage and shipping limitations, such as highly reactive and toxic intermediates.

Microreaction technology is closely related to integration of analytical tools as in the field of micro Total Analysis ( $\mu$ TAS) systems (13-16). In fact, when microreactors are integrated with chemical analysis, such as optical spectroscopy, they become powerful tools for determining chemical kinetics and optimal conditions for chemical reactions. Microreactors with larger sized channels (~mm) become useful in process intensification (17)—a field that often employs ceramics monoliths as “multichannel microreactors”.

A microreactor based process can, in principle, be scaled to meet demands for product testing by multiplying the numbers of reaction chips and running the reaction for longer times. This “scale-out” strategy, as opposed to the traditional “scale-up,” makes it feasible to go from microgram to kilogram quantities without additional chemistry modifications or reactor engineering. Furthermore, the use of a continuous processing technology instead of batch wise synthesis eliminates batch-to-batch variation and enables tight control of product specifications. Microreactors can also be used to accelerate conventional scale-up by more rapidly providing essential chemical mechanics and kinetic information than conventional pilot plant experimental facilities. The ultimate choice between scale-up and scale-out depends on the chemical kinetics, heat transfer characteristics, and production levels of the process.

The choice of design and construction material for a microreactor depends on the intended application. Classical chemical reaction engineering principles (18,19) apply to microreactor design and prediction of performance. A large number of microreactor designs have been realized in stainless steel (1-3,8,20), glass (9,10), silicon (7), and polymers (21) Additional examples of microreactor studies appear in this volume.

Stainless steel microreactors have typically been used in microreactor

applications relevant to chemical production, whereas glass reactors have been attractive for laboratory applications, in part because of the chemist's traditional use of glass equipment. Microreactors realized by rapid prototyping in poly(dimethylsiloxane) (PDMS) (21) have been used extensively in biochemical studies because of the rapid turn-around from design to experiment offered by this platform. However, limited chemical compatibility, low mechanical strength, and low thermal conductivity typically restrict applications of the technique for non-aqueous and elevated pressure/temperature systems.

Silicon is also a useful material for realizing microreactor designs. The large fabrication infrastructure developed for microelectromechanical systems (MEMS) (22) provides a series of integrated fabrication platforms for producing complex, three-dimensional microchannel networks. Well established wet and drying etching procedures (23,24) enable fabrication of microchannels with controlled sidewall shape and channel dimensions from nm to mm. Moreover, advances in silicon microsensors, *e.g.*, flow, pressure, and temperature sensors, can readily be integrated with the microreactors. Silicon has excellent mechanical strength and temperature characteristics, and it has good chemical compatibility characteristics. Oxidation of silicon leads to the formation of a glass layer on the surface so that an oxidized silicon microreactor becomes functionally equivalent to a glass reactor. For cases where silicon or glass lacks the necessary chemical resistance, such as for fluorination reactions, it is possible to deposit protective coatings (25).

In this contribution, we illustrate the use of silicon based microreactors for (i) high throughput experimentation of homogeneous organic synthesis, (ii) integration of ultraviolet (UV), visible and infrared (IR) spectroscopy; (iii) investigations of high temperature heterogeneous catalytic reactions, (iv) obtaining high mass transfer rates in gas-liquid reactions over solid catalysts, (v) enabling difficult to perform reactions, (vi) synthesis of solid nanoparticles, and (vii) high temperature conversion of hydrocarbons to hydrogen. The need for integration of reaction units with fluid control, separation, and analytical techniques is also briefly discussed.

### High Throughput Experiments

The glycosylation reaction shown in Figure 1a serves as an example of probing the reaction space with microreactors (26). When combined with a suitable analytical technique, in this case high performance liquid chromatography (HPLC) with an auto-sampler, microreactors can be used to scan through reaction space to optimize reaction conditions and to gain understanding of reaction mechanisms and rates. Characteristic of complex organic transformations, glycosylation is often a difficult synthesis, which depends on the chemical nature of the reaction partners as well as reaction variables such as composition, temperature, reaction time, and activator (27,28). Much effort in organic synthesis is spent on searching for optimal reaction conditions to achieve a particular transformation. Moreover, method optimization can ultimately require significant time and large quantities of valuable starting materials. Thus, microreactor based techniques for efficiently

identifying optimal reaction conditions could have major impact on research and development in organic chemistry.

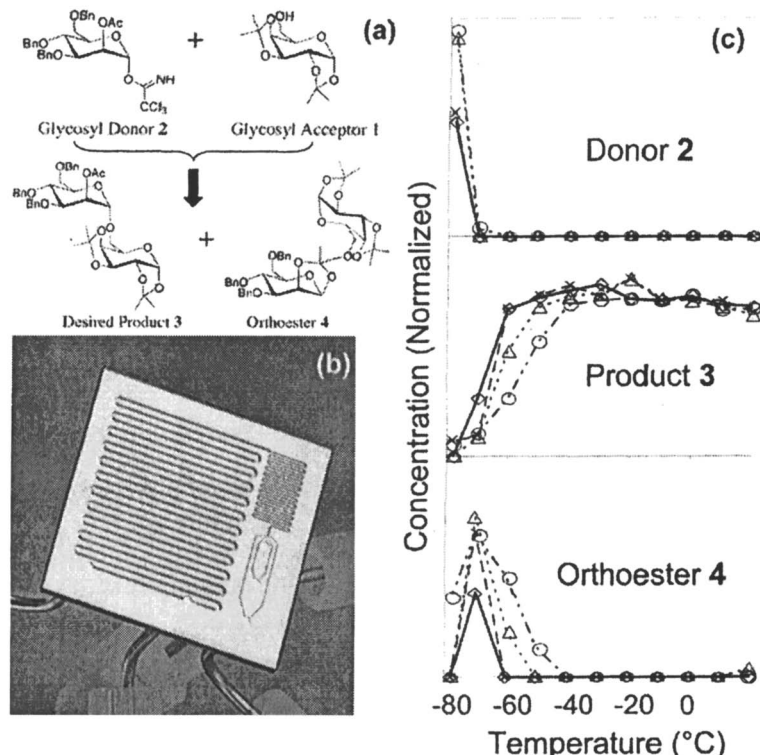


Figure 1. Example of glycosylation reaction, (a) microreactor designed to perform the glycosylation reaction (b), and results (c) (26)

The five-port silicon microreactor (Figure 1b) exemplifies microreactor design components typically needed to realize a particular organic transformation. It has a mixing region providing controlled contact of the reactants – in this case, glycosylating agent, nucleophile (acceptor), and activator – in such a manner that side reactions are minimized. Lamination of reaction streams by narrow channels is sufficient for the present case. Increased mixing could be achieved by incorporating one of the many microfluidic mixing schemes demonstrated over the past decade (29), *e.g.* chaotic advection through patterned channel walls (30). In general, the mixer should be designed to have a mixing time significantly shorter than the reaction time. Once mixed, the reactants enter the reaction zone which provides sufficient residence time for the reaction to proceed. A simple channel typically suffices for homogenous reactions, whereas flow obstacles in the channel (“packaging”) is useful to increase interfacial area in heterogeneous reactions (see below). If the Peclet number (defined as  $UL/D$ ,

where  $U$  is the average velocity of the liquid,  $L$  is a characteristic dimension and  $D$  is the diffusion coefficient) is high, advection dominates over diffusion and the time a flow segment spends traveling through the channel will equal the reaction time.

A quench port is included near the outlet, so that the reaction can be quenched before the reaction stream exits the reactor for collection and analysis. This port is important in quantitative work with microreactors, since the outlet tubing otherwise adds a significant volume and uncertainty as to whether the reaction was completed in the device or the reactor interface to the macroscopic fluid handling environment.

Results from the microreactor-HPLC case study show a clear relationship between reaction temperature, reaction time and formation of product (Figure 1c). For a given reaction time, the yield of product increases with temperature until maximum conversion is achieved. At temperatures lower than the optimum, yield increases with increasing reaction time (i.e., decreasing flow rate). Moreover, the formation of orthoester, a major side product, is observed at lower temperatures. The example demonstrates the ability of the microreactor system to rapidly obtain comprehensive information about a given transformation. With a single preparation of reagents, 44 reactions were completed in less than a day at varying temperatures and reaction times requiring just over 2 mg of glycosylating agent for each reaction. Conventional batch reaction procedures would have been limited to ~3 experiments/day and have required significantly larger quantities of starting material.

### Integration of IR Spectroscopy and Microreactors

Integration of chemical analysis methods and physical sensors (e.g., temperature and pressure) enhances the utility of microreactors for optimization as well as studies of reaction mechanisms and kinetics. Integrated chemical sensors offer the potential for computer control optimization of reaction conditions, which reduces the time and materials costs in identifying optimal operating conditions. Miniaturized chemical analysis systems have been developed for the most macroscopic counterparts (14-16). Specific techniques for monitoring species concentration include fluorescence, electrochemical, optical absorption (UV-vis and IR), and nuclear magnetic resonance (NMR) methods. The availability of excellent optical fibers, light sources, and detectors in the UV-vis to near IR makes it possible to integrate these techniques in microreactors (31,32). If absorption bands are easily distinguished, these techniques can be useful for monitoring species, but the broad nature of the absorption bands means that it is difficult to obtain sufficient information for detailed chemical studies.

Fourier transform infrared spectroscopy (FTIR) methods are efficient, broadly applicable techniques for determining chemical structure and quantifying species concentrations. As a result, FTIR has been implemented in microsystems by a variety of approaches, including capping microchannel structures with IR transparent materials and integrating microreactors with off-chip FTIR detection (33-35). Silicon is transparent to IR radiation in most of the

wavelength region of interest ( $4000\text{-}800\text{ cm}^{-1}$ ). The thin  $\text{SiO}_2$  that could be formed by oxidation to increase chemical compatibility is still sufficiently thin ( $\sim 500\text{ nm}$ ) to not impact the IR transmission characteristics of the device. In fact, for transmission studies, dielectric coatings of silicon oxide and nitride can be used to reduce reflections and improve transmission through the reactor (36). Figure 2 shows a silicon based microreactor combining micro mixing, a reaction channel, an IR detection region, and temperature control along with measured  $\text{NaOH}$  absorbance at different levels of concentrations (36). As an example of the utility of monitor concentrations, the reactor was used to determine the rate constant for alkaline hydrolysis of methyl formate.

The strong IR absorption of many solvents, especially water and suspensions, limits the path length in solution through which the incident IR radiation can travel. In that case, sampling by the evince wave at the interface

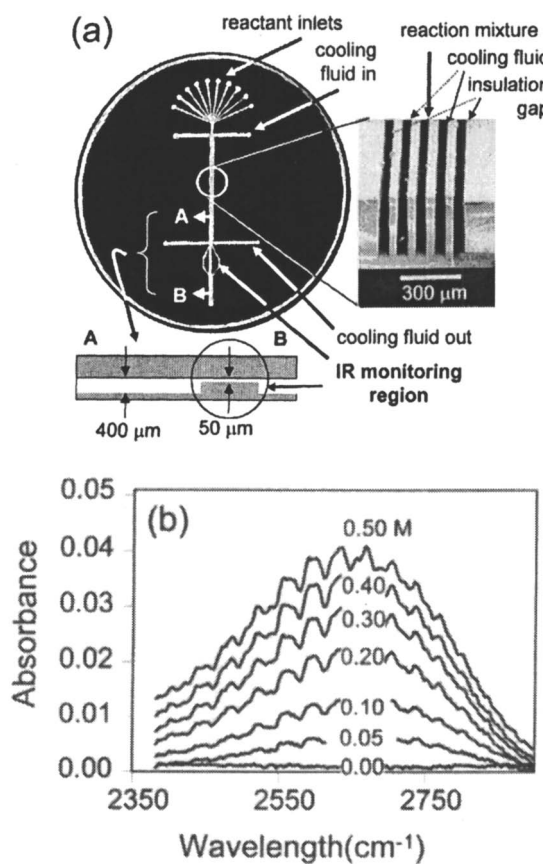


Figure 2. Microreactor with mixer, heat exchanger, and transmission FTIR section (a). Data obtained monitoring hydroxide, small contributions from interference patterns are apparent in the absorption peaks (b) (36).

between the solution and an Attenuated Total Reflection (ATR) (also called Multiple Internal Reflection, or MIR) crystal (Figure 3a) becomes an attractive method for FTIR spectroscopy (37). Anisotropic etching of silicon provides a simple alternative to commercial crystals produced by individually polishing crystals, which makes them expensive and difficult to integrate. Moreover the microfabricated crystal can be integrated into microreactors to produce integrated systems for monitoring the progress of a particular reaction, as exemplified in Figure 3b for the model reaction system, hydrolysis of ethyl acetate.

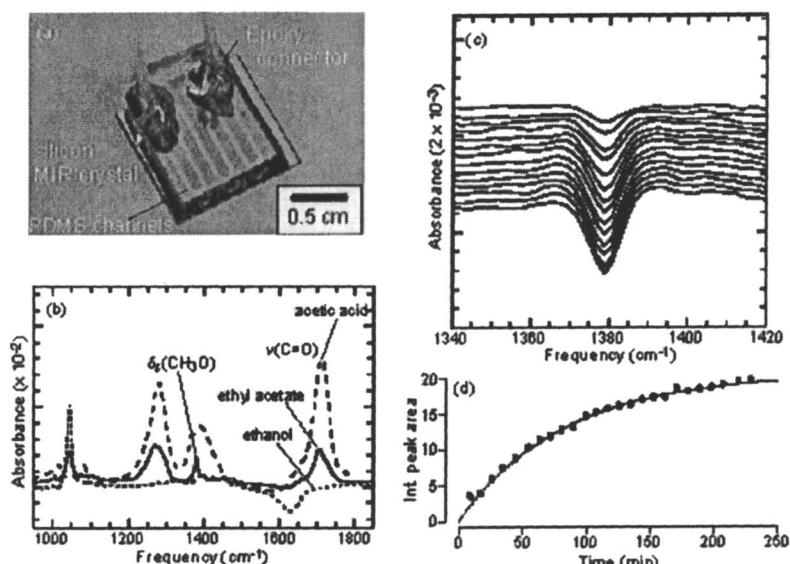


Figure 3. a) Photograph of a PDMS microreactor attached to a microfabricated MIR silicon crystal (a). Infrared spectra of reactants and products of ethyl acetate hydrolysis (b). Sample kinetic data from ethyl acetate hydrolysis -growth of the ethyl acetate depletion peak as a function of time from top to bottom (from 6 to 112 minutes) (c and d). (37)

For gas phase reactions, the short path lengths in microreactors and low optical densities of gases typically render IR absorption spectroscopy impracticable in gas-phase microreactors. Photoacoustic spectroscopy (PAS) is a potential alternative optical method for gas-phase detection (38,39). In this technique, incident light is modulated at an acoustic frequency and if the optical wavelength couples to an energy transition in the gas, the gas absorbs the light resulting in a periodic gas expansion. The small thermal mass of microreactors,

especially membrane based systems (40), and the ability to measure pressure fluctuations (as in hearing aids) implies that the techniques could be implemented in microreactors. PAS applies to many chemical compounds and its sensitivity scales inversely with dimensions. The microreactors with integrated gas sensing have been demonstrated, but several technical issues have to be solved to make the technique generally applicable (39).

### **Microreactors for Heterogeneous Catalytic Reactions**

The interest in faster development of new catalysts has led to significant advances in high-throughput screening and combinatorial methods in which large arrays of catalysts are rapidly screened. Detailed characterization of catalyst performance, such as kinetics, selectivity, and deactivation, is necessary for translation of promising candidates into process environments. These studies are simplified by the use of a reactor in which mass, thermal, and pressure gradients are minimal, but the realization of such conditions can be a challenge with traditional reactor technology. Microfabrication of chemical reactors, such as micro packed-beds, provide unique advantages for the efficient testing of catalysts, including reduced transport limitations and increased surface area-to-volume ratio for enhanced heat transfer. Microfabrication also gives flexible control over reactor geometry enabling configurations difficult to realize in macroscopic testing systems.

Conventional catalyst testing is typically performed with small tubular reactors. A corresponding, microfabricated packed-bed channel reactor (Figure 4a) with 60  $\mu\text{m}$  catalyst particles demonstrates the potential for using microfabricated reactors to obtain chemical kinetics (41). However, this configuration has significant pressure drop due to the small catalyst particle size. In general, low pressure drops and small conversions (differential operation) facilitates obtaining chemical kinetics for catalyst testing experiments. On the other hand, it is desirable to have as much catalyst as possible for subsequent analysis of the catalyst (42). Microfabrication enables a solution to these apparent contradicting demands in the form of a silicon-based, cross-flow packed-bed, microreactor for catalyst testing (Figure 4b) (43). This design integrates short parallel beds into a continuous wide packed-bed, providing for short contact time with sufficient catalyst to allow characterization of reaction performance and catalyst post-reaction structure. Even flow distribution across the wide bed is accomplished by 256 shallow channels that provide a pressure drop much larger than the pressure drop through the catalyst bed. In this way, differences in catalyst packing density have negligible effect on the overall flow distribution. The cross-flow geometry renders the bed isothermal and isobaric. Moreover, the cross-flow geometry enables the use of practical flow rates and catalyst quantities while minimizing pressure drop.

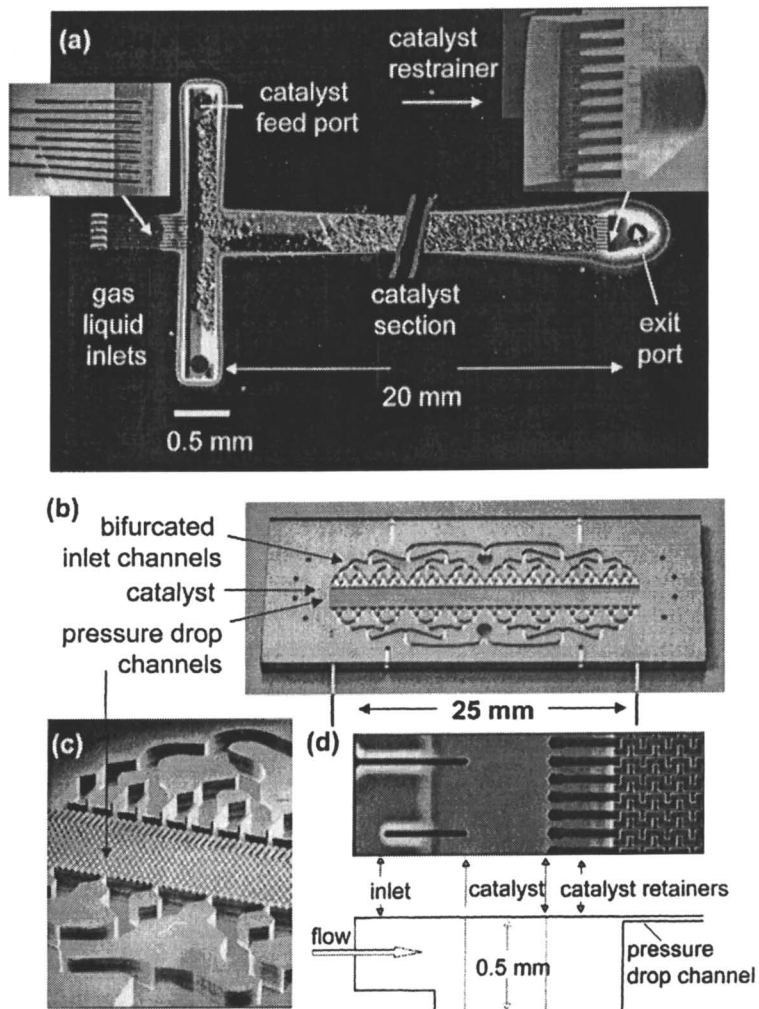


*Figure 4. Catalyst packed bed microreactor with active carbon catalyst. The image has been edited to remove the long midsection of the catalyst to allow greater magnification of inlet and outlet sections (a) (41,44). Microfabricated silicon cross-flow reactor – photograph microreactor chip (b), scanning electron micrographs of channel and press drop details (c), cross-section in the flow direction (d) (43)*

The operation of the cross-flow microreactor was characterized through finite element simulations and experiments with model catalytic reactions—CO oxidation and ethyne hydrogenation on supported catalysts (43,45). The consistency of kinetic parameters (turnover frequency and activation energy) and mechanistic information (reaction order) obtained in the microreactor with previously reported values across different catalysts, demonstrated the potential of microfabricated cross-flow reactors as laboratory tools for heterogeneous catalyst testing. A quantitative analysis of the transport effects in the microreactor showed that the small catalyst particle size and reactor geometry eliminate mass and thermal gradients both internal and external to the catalyst particles. By reducing thermal, mass, and pressure gradients and ensuring even flow distribution over the catalyst bed, the cross-flow microreactor provides a useful platform for the determination of kinetic parameters.

### High Mass Transfer Rate Multiphase Microreactors

For fast multiphase reactions, the rate and selectivity of the chemical process can be greatly influenced by the transport of reagents within and across phases. Using silicon microfabrication, it is possible to construct packed-bed microreactors (Figure 5) that provide a hundredfold or more improvement in mass transfer for gas–liquid heterogeneously catalyzed processes, such as hydrogenation of unsaturated hydrocarbons (44). In these devices, standard catalyst particles (50–75  $\mu\text{m}$  diameters) are retained in silicon channels by an integrated microfabricated filter unit. A specially designed gas–liquid inlet section with narrow channels provides rapid contact of the gas and liquid reagents. In order to achieve uniform flow, pressure drops in the inlet gas and liquid sections exceed those in the individual reactor channels.

The small particles provide the high surface areas for improved gas–liquid mixing, but they also represent a challenge in terms of pressure drop and fluid distribution among the ten parallel channels. The pressure drop can be reduced by replacing the catalysts bed by a microfabricated support structure, such as illustrated in Figure 5b (46). In this case, the catalyst support consists of arrays of columns, 50  $\mu\text{m}$  in diameter, 300  $\mu\text{m}$  tall, with nearly 20,000 columns per device. As a result of the extreme uniformity of the structured packing arrangement, control over fluid flow is greatly enhanced relative to the micro packed-beds. The columns are microfabricated by using deep reactive ion etch (DRIE) technology (23) and the challenge becomes to incorporate the catalyst in such a manner that the activity is comparable to that of the standard catalysts. The activity is greatly enhanced if the catalytic component is supported upon a porous layer, formed by making the silicon posts porous (46,47), or by forming a porous alumina wash coat (48). The resulting surfaces can be impregnated with noble metal catalyst by standard catalyst preparation techniques, or homogeneous catalysts could be immobilized on the surfaces by using linking techniques recently demonstrated for glass channel reactors (49).

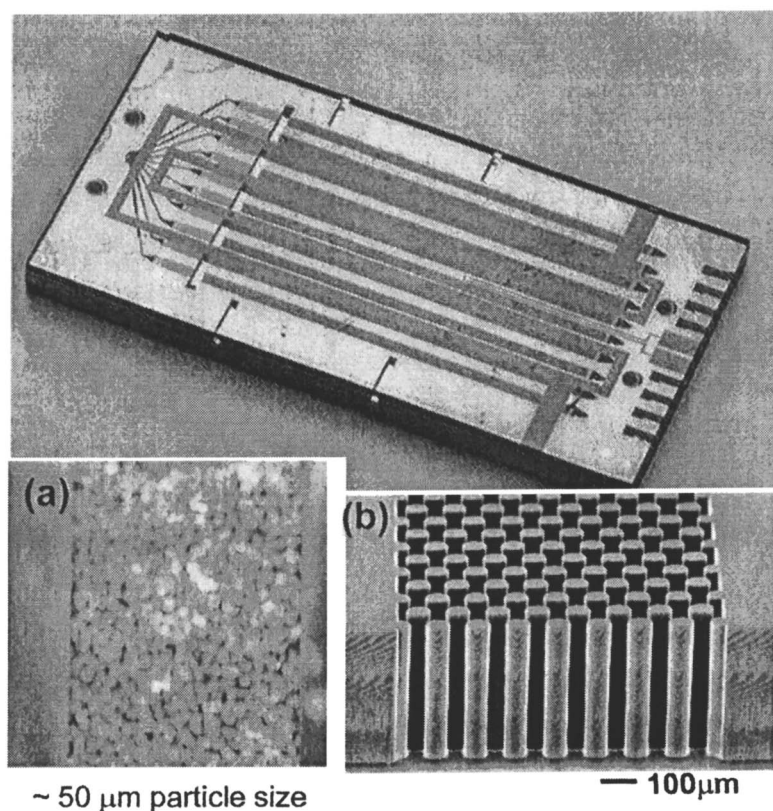


Figure 5. Multiphase-multichannel microreactor - with porous catalyst particles (a) or microstructured packing (b) (44,46).

## Microreactors for Difficult to Perform Reactions

The high heat transfer rates and small reactor hold-up volumes associated with microreactors, make it possible to perform reactions that are difficult to perform in large conventional reactors. As an example, Figure 6a (50) shows data from direct synthesis of hydrogen peroxide from hydrogen and oxygen in a dilute sulfuric acid/phosphoric acid/ sodium bromide solution flowing over palladium catalysts at 30 atm pressure in a multiphase microreactor similar to that shown in Figure 5. By keeping the bubble size small and having excellent gas-liquid contact with the solid catalysts, the heterogeneous reactions are preferred over homogeneous reactions that could lead to chain branching free radical reactions and ultimately, explosion. Thus, it becomes feasible to directly synthesize hydrogen peroxide from mixtures of hydrogen and oxygen in the explosive regime.

Oxidation of olefins by ozone is another example of a useful reaction (51) that can be difficult to run in conventional reactors because of the high heat of reaction and the potential for highly reactive side product formations, e.g., peroxy-polymers (52,53). However, it has the advantages of high selectivity and generation of oxygen as the only side product. The high-surface-to volume ratio in microreactors increases the gas-liquid interface area enhancing mass flux of ozone through the interface, and facilitates removal of heat generated by the chemical reactions. Including microfabricated post structures in the channel (Figure 6b) increases further interfacial area and mixing in the reactor. Ozonolysis of olefins and amines at room temperature led to very high conversion (>98%) and selectivity, even at short contact times <1s (54).

The direct fluorination of organic reagents is yet another example of a transformation rarely practiced on a preparative scale because of the difficulties in controlling the large heat of reaction and the selectivity of the process (25). Moreover, because of the low solubility of fluorine in commonly used solvents, reactions tend to proceed at the gas-liquid interface and form localized hot spots. Thus, direct fluorination forms an excellent case for microreaction technology, and it has consequently been demonstrated in several different reactor types(55,56), including silicon-based microreactors (25). In order to make the latter reactors chemically compatible, a nickel surface coating was included. Direct fluorination has also served as an inspiration for development of flow distribution, allowing controlled scaling of gas-liquid reactions from a few channels to a large number of channels (~100) with uniform flow distribution (57,58). This flow distribution can be measured by integrated flow sensors (Figure 7), which use multiple optical waveguides to monitor flow regimes and detect the speed of liquid segments (plugs) moving through different channels (59).

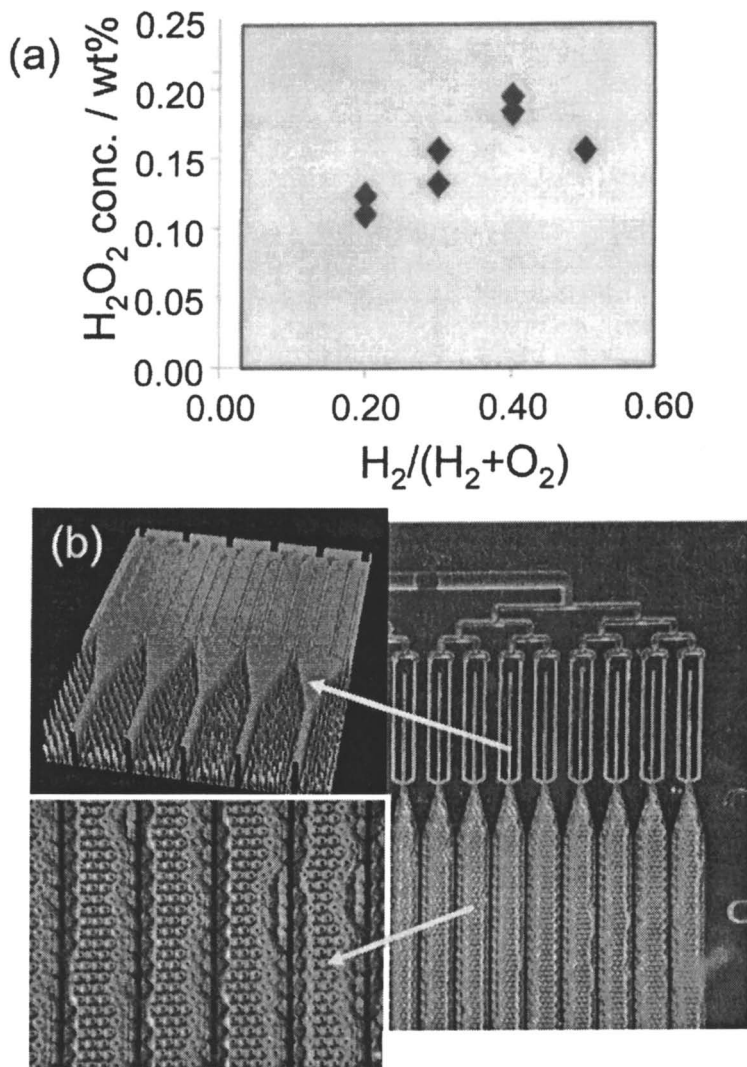


Figure 6. Data from direct formation of hydrogen peroxide from hydrogen and oxygen reacting at 30 atm over a carbon supported palladium catalyst in a microreactor similar to Figure 5 (a) (50,54). Multiphase multichannel microreactor with posts used in ozonolysis, panels show details (b) (54).

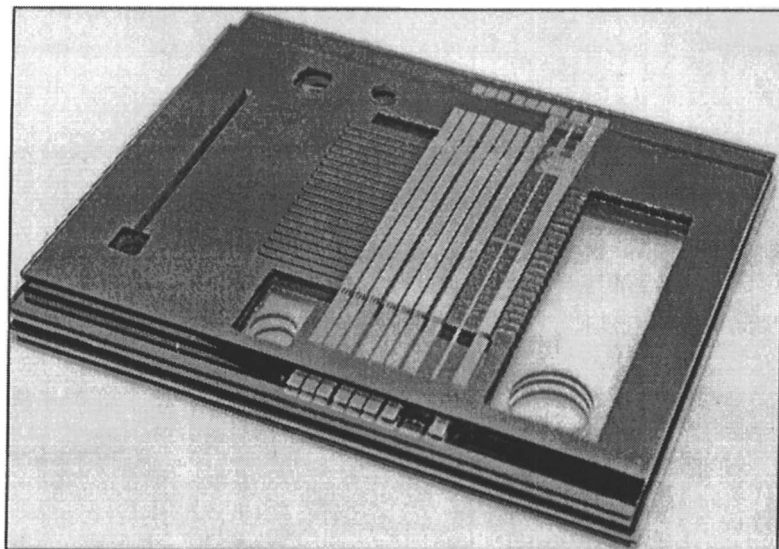


Figure 7. Photograph of a multichannel, multilayer ("numbered-up") microreactor for gas-liquid reactions, specifically direct fluorination. The metal lines form optical wave guides for the flow sensor (57-59).

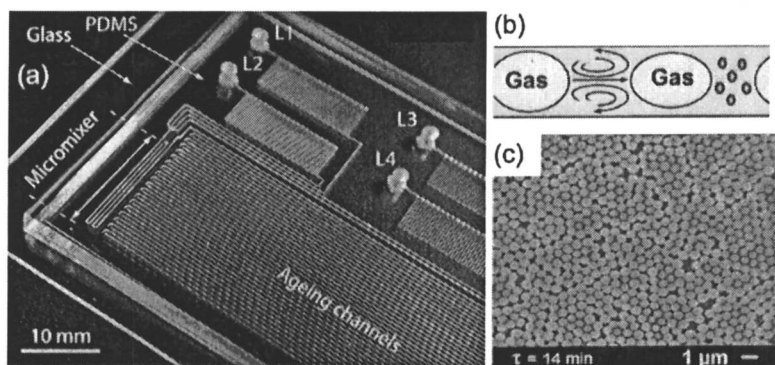


Figure 8. Microreactor for synthesis of colloidal silica particles (a), schematic of a gas-liquid segmented flow (b), and representative sample of silica particles synthesized in the microreactor (c) (60).

## Synthesis of Solid Particles in Microreactors

Generation of solid particles is generally thought to be a problem for microreactors in terms of agglomeration and plugging of channels. Nevertheless, with carefully control of nucleation and growth, microreactors can be an excellent tool for continuous synthesis of particles with well-controlled properties. This is particularly the case for nano-sized particles requiring multiple synthetic steps, such as synthesis of colloid particles and subsequent surface modifications for biological assays and optics (60,61).

Scaling down dimensions to sub-millimeter in a microreactor provides opportunities for improved size and composition control of colloidal synthesis. Microfabrication also affords increased flexibility in reactor design; specifically, reactant-contacting schemes difficult to achieve in macroscale units can be realized. Simple homogeneous flow is not usually desirable for particle synthesis in microreactors because of broadening of the size distribution by axial dispersion—the variation in residence times caused by the fluid moving slower near the tube wall than in the center. The dispersion effect can be reduced and a narrow particle size obtained by using a segmented flow in which the synthesis fluid is divided into separate fluid segments (plugs) moving through the channel as small individual batch reactors. The segmenting fluid, aside from dividing the synthesis liquid into small batches, also serves to accelerate micromixing by recirculation within each segment. Gas-liquid segmented microreactors are attractive by the ease with which the gas can be separated from the liquid by using capillary forces (62).

Synthesis of colloidal silica by the Stöber method (63), an extensively studied system, serves as a model system. Figure 8a illustrates a microreactor, fabricated in PDMS, which has sufficient chemical compatibility to handle the water-ethanol -tetraethoxy silane mixtures used in this case. The synthesis of silica is characterized by rapid initial growth followed by slow growth, which implies that synthesis in a single phase flow will be particularly sensitive to residence time effects at short times. Particles near the wall move slower than those near the center of the channel, and thus spend more time in the reactor. On the other hand, in the segmented flow the synthesis fluid is divided into a series of well mixed batch reactors (Figure 8b), which produce a narrow size distribution (Figure 8c). These results illustrate the importance of being able to quantify, the residence time distribution (RTD) of each fluid element in the microreactor. Measurement of the RTD is readily accomplished in microreactors, by introducing a means for injecting a fluorescent tracer (e.g., by using an integrated piezoelectric bending disk element) and then following the spatial spread of the fluorescence as the tracer plug flows through the channel (64).

The synthesis of nanocrystalline, semiconductor quantum dots (QDs) (2-10

nm diameter), specifically CdSe, constitutes a second example of microreactor facilitated particle synthesis (61). The optical properties and average size of QDs synthesized in conventional batch processes are influenced by factors that are difficult to control such as injection process, local temperature and concentration fluctuations, rate of stirring, and rate of cooling. A gas-liquid segmented flow microreactor allows for rapid and controlled mixing of precursors. Moreover, as in the case of colloidal silica, the segmented flow narrows the RTD and thus, the size distribution of QDs produced. Silicon is used as the material of construction to allow nucleation and growth at temperatures up to ~300°C, which are needed to achieve good luminescence properties of the QDs. The silicon is again oxidized to provide the glass surface preferred in many chemical applications.

### **Microreactors for High Temperature Fuel Conversion**

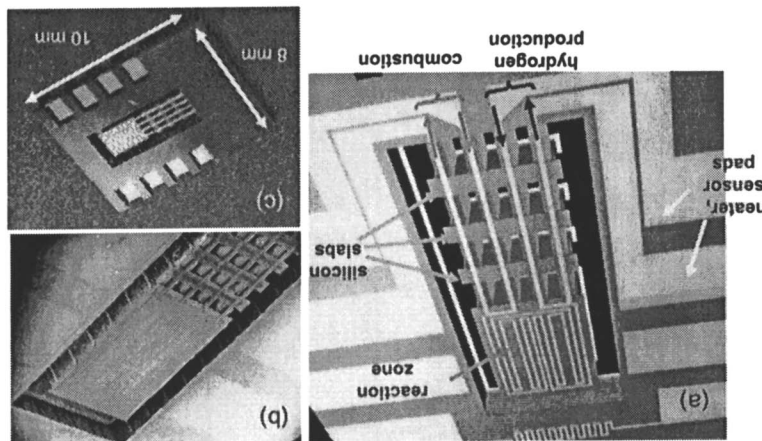
Microreactors for high temperature conversions of hydrocarbon fuels to thermal energy and hydrogen constitutes the last illustration of the advantages afforded by silicon technology in realizing microreactors designed for specific applications. There is considerable interest in miniaturizing conversion of hydrocarbon fuels to electric power generation for portable applications since combustible fuels store up to a hundred times more energy per unit weight than batteries. However, fuel conversion systems have proven difficult to miniaturize because of a number of challenges, perhaps most importantly, thermal losses. Thermal loss to the environment caused by the rapid heat transfer across small devices is a major problem for any miniaturized system involving one or more high-temperature steps, such as combustion engines, thermoelectric (TE) and thermophotovoltaic (TPV) generators, and fuel cell systems based on high-temperature fuel processors for hydrogen production.

Figure 9 shows a suspended-tube reactor that directly addresses the thermal management issues in small fuel processors (48). This microfuel processor consists of four thin-walled (~2  $\mu\text{m}$ ) silicon nitride tubes (~300 $\mu\text{m}$  hydraulic diameter), comprising two separate U-shaped fluid channels. On one end, the tubes are fixed into a silicon substrate containing fluidic channels and ports; on the other end, the channels form a free-standing structure. This free end (hot zone) is partially encased in silicon to form a thermally isolated silicon region in which the chemical reactions take place. Heat conduction along the length of the tubes is very small due to the high aspect ratio (2  $\mu\text{m}$  wall thickness, 3 mm length) and low thermal conductivity of the silicon nitride tubes. The tubes contain silicon slabs that permit heat transfer between fluid streams (for heat recuperation) without significantly adding to heat loss down the length of the tubes. In the case of hydrogen production (e.g., ammonia cracking or hydrocarbon reforming), combustion in one stream provides the energy required for endothermic reforming in the other stream. The high thermal conductivity of the silicon in the reaction zone improves the heat transfer between the two process streams. In TPV applications, the thermally isolated silicon zone would serve as a nearly isothermal fuel combustor that radiates to a photovoltaic cell (TPV) (65). The microcombustor could also have applications in high temperature, short contact chemistry.

The above examples selected from the MIT effort represent a small fraction of the variety of designs for microrreactors being pursued at many academic institutions and company research laboratories. Examples of those efforts are given elsewhere in the volume and in the referenced literature. Examples of microrreactors to enable multi-step syntheses made in microreactors to enable multi-step syntheses. Progress has been made in microfluidic systems for both gas-liquid separation (62) and liquid-liquid extraction (67), but general multi-step synthesis procedures remain a challenge.

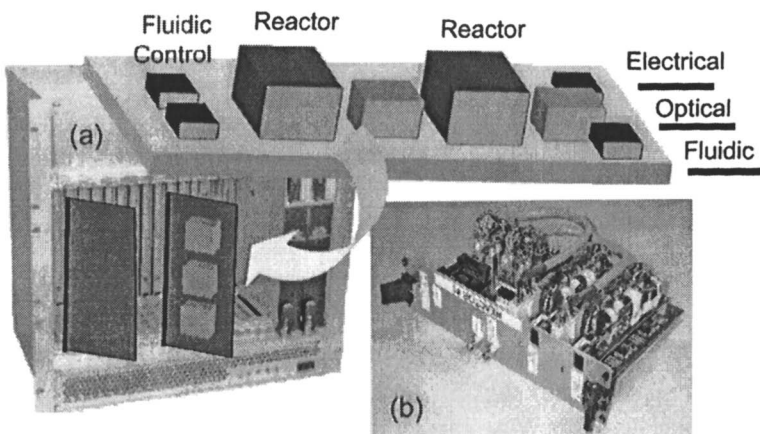
## Conclusion

Figure 9 Schematic (a), scanning electron micrograph (b), and photorograph (c) of suspended-tube reactor showing four suspended silicon nitride tubes connecting to the silicon reaction zone as well as silicon slabs thermally linking the four tubes and a Ti/Pt resistive heater/temperature sensor (48).



The necessity of synthesizing sufficient quantities for subsequent evaluation dictates that microchemical systems are operated as continuous systems. Such systems will need fluid controls for adjusting reagent volumes and isolating defective units. Integration of sensors will enable optimization of reaction conditions, as well as the extraction of mechanistic and kinetic information. Early implementation of integrated microchemical systems is likely to involve modular systems with microreactors, separation units, and analytic components mounted on electrical, fluidic, and optical "circuit boards" (68) (see Figure 10).

The realization of integrated microchemical systems ultimately will revolutionize research by providing flexible tools for rapid screening of reaction pathways, catalysts, and materials synthesis procedures, as well faster routes to new products and optimal operating conditions. Moreover, such microsystems for chemical will clearly require less space, use fewer resources, produce less waste, and offer safety advantages. Progress towards integrated systems will require continued development and characterization of microreactors, separation units, and integrated analytical methods, as well as new, innovative approaches for connecting modular microfluidic components into flexible fluidic networks allowing active control and providing potential for matching components to a particular application.



*Figure 10. Conceptual picture of integrated microreactor system (a). Example of early stage microreactor "Circuit board" (68,69)*

### Acknowledgements

The author thanks Professor Martin A. Schmidt and members of the microreactor research group for joint work forming the basis for this summary, as well as DARPA-MTO, ARO-MURI and the members of the MicroChemical Systems Technology Center for funding.

**References:**

1. Ehrfeld, W.; Hessel, V.; Lowe, H. *Microreactors: New Technology for Modern Chemistry*; Wiley-VCH.: Weinheim, Germany, 2000.
2. Hessel, V.; Lowe, H. *Chemie Ingenieur Technik* **2004**, *76*, 535-554.
3. Hessel, V.; Hardt, S.; Lowe, H. *Chemical Micro Process Engineering : Fundamentals, Modelling and Reactions*; Wiley-VCH: Weinheim, Germany, 2004.
4. Fletcher, P. D. I.; Haswell, S. J.; Pombo-Villar, E.; Warrington, B. H.; Watts, P.; Wong, S. Y. F.; Zhang, X. *Tetrahedron* **2002**, *58*, 4735-4757.
5. Haswell, S. J.; Watts, P. *Green Chemistry* **2003**, *5*, 240-249.
6. Pennemann, H.; Watts, P.; Haswell, S. J.; Hessel, V.; Loewe, H. *Organic Process Research & Development* **2004**, *8*, 422-439.
7. Jensen, K. F. *Chemical Engineering Science* **2001**, *56*, 293-303.
8. Jahnisch, K.; Hessel, V.; Lowe, H.; Baerns, M. *Angewandte Chemie-International Edition* **2004**, *43*, 406-446.
9. Fletcher, P. D. I.; Haswell, S. J.; Pombo-Villar, E.; Warrington, B. H.; Watts, P.; Wong, S. Y. F.; Zhang, X. L. *Tetrahedron* **2002**, *58*, 4735-4757.
10. Chow, A. W. *Aiche Journal* **2002**, *48*, 1590-1595.
11. Tonkovich, A. Y.; Zilka, J. L.; LaMont, M. J.; Wang, Y.; Wegeng, R. S. *Chemical Engineering Science* **1999**, *54*, 2947-2951.
12. Hu, J. L.; Wang, Y.; VanderWiel, D.; Chin, C.; Palo, D.; Rozmiarek, R.; Dagle, R.; Cao, J.; Holladay, J.; Baker, E. *Chemical Engineering Journal* **2003**, *93*, 55-60.
13. Laurell, T.; Nilsson, J.; Jensen, K. F.; Harrison, D. J.; Kutter, J. P., Eds. *Proceedings of the 8th International Conference on Miniaturized System in Chemistry and Life Sciences*; Royal Society of Chemistry.: London, 2004.
14. Vilkner, T.; Janasek, D.; Manz, A. *Analytical Chemistry* **2004**, *76*, 3373-3385.
15. Reyes, D. R.; Iossifidis, D.; Auroux, P. A.; Manz, A. *Analytical Chemistry* **2002**, *74*, 2623-2636.
16. Auroux, P. A.; Iossifidis, D.; Reyes, D. R.; Manz, A. *Analytical Chemistry* **2002**, *74*, 2637-2652.
17. Stankiewicz, A. I.; J.A. Moulijn *Chem. Eng. Prog.* **2000**, 22-34.
18. Fogler, H. S. *Elements of Chemical Reaction Engineering*; 3rd ed.; Prentice Hall: Upper Saddle River, NJ, 2000.
19. Doraiswamy, L. K. *Organic Synthesis Engineering*; Oxford University Press: New York, 2000.
20. Schwalbe, T.; Autze, V.; Hohmann, M.; Stirner, W. *Organic Process Research & Development* **2004**, *8*, 440-454.
21. Xia, Y. N.; Whitesides, G. M. *Angewandte Chemie-International Edition in English* **1998**, *37*, 551-575.
22. Wise, K. D. *Proc. IEEE* **1998**, *86*, 1531-1533.
23. Ayon, A. A.; Braff, R.; Lin, C. C.; Sawin, H. H.; Schmidt, M. A. *Journal of the Electrochemical Society* **1999**, *146*, 339-349.
24. Madou, M. J. *Fundamentals of Microfabrication: The Science of Miniaturization*; 2nd ed.; CRC Press, 2002.

25. de Mas, N.; Gunther, A.; Schmidt, M. A.; Jensen, K. F. *Industrial & Engineering Chemistry Research* **2003**, *42*, 698-710.
26. Ratner, D. M.; Murphy, E. R.; Jhunjhunwala, M.; Snyder, D. A.; Jensen, K. F.; P. H. Seeberger *Chem. Commun.* **2005**.
27. Toshima, K.; Tatsuta, K. *Chemical Reviews* **1993**, *93*, 1503-1531.
28. Nukada, T.; Berces, A.; Zgierski, M. Z.; Whitfield, D. M. *Journal of the American Chemical Society* **1998**, *120*, 13291-13295.
29. Ottino, J. M.; Wiggins, S. *Philosophical Transactions of the Royal Society of London Series a-Mathematical Physical and Engineering Sciences* **2004**, *362*, 923-935.
30. Stroock, A. D.; Dertinger, S. K. W.; Ajdari, A.; Mezic, I.; Stone, H. A.; Whitesides, G. M. *Science* **2002**, *295*, 647-651.
31. Jackman, R. J.; Floyd, T. M.; Ghodssi, R.; Schmidt, M. A.; Jensen, K. F. *Journal of Micromechanics and Microengineering* **2001**, *11*, 263-269.
32. Lu, H.; Schmidt, M. A.; Jensen, K. F. *Lab on a Chip* **2001**, *1*, 22-28.
33. Kakuta, M.; Hinsmann, P.; Manz, A.; Lendl, B. *Lab on a Chip* **2003**, *3*, 82-85.
34. Hinsmann, P.; Frank, J.; Svasek, P.; Harasek, M.; Lendl, B. *Lab on a Chip* **2001**, *1*, 16-21.
35. Lendl, B.; Schindler, R.; Frank, J.; Kellner, R.; Drott, J.; Laurell, T. *Analytical Chemistry* **1997**, *69*, 2877-2881.
36. Floyd, T. M.; Schmidt, M. A.; Jensen, K. F. *Ind. Eng. Chem. Res.* **2005**, *44*, xxx.
37. Herzig-Marx, R.; Queeney, K. T.; Jackman, R. J.; Schmidt, M. A.; Jensen, K. F. *Analytical Chemistry* **2004**, *76*, 6476-6483.
38. Firebaugh, S. L.; Jensen, K. F.; Schmidt, M. A. *Journal of Microelectromechanical Systems* **2001**, *10*, 232-237.
39. Firebaugh, S. L.; Jensen, K. F.; Schmidt, M. A. *Journal of Applied Physics* **2002**, *92*, 1555-1563.
40. Quiram, D. J.; Hsing, I. M.; Franz, A. J.; Jensen, K. F.; Schmidt, M. A. *Chemical Engineering Science* **2000**, *55*, 3065-3075.
41. Ajmera, S. K.; Losey, M. W.; Jensen, K. F.; Schmidt, M. A. *Aiche Journal* **2001**, *47*, 1639-1647.
42. Baertsch, C. D.; Schmidt, M. A.; Jensen, K. F. *Chemical Communications* **2004**, 2610-2611.
43. Ajmera, S. K.; Delattre, C.; Schmidt, M. A.; Jensen, K. F. *Journal of Catalysis* **2002**, *209*, 401-412.
44. Losey, M. W.; Schmidt, M. A.; Jensen, K. F. *Industrial & Engineering Chemistry Research* **2001**, *40*, 2555-2562.
45. Ajmera, S. K.; Delattre, C.; Schmidt, M. A.; Jensen, K. F. In *Science and Technology in Catalysis* **2002**, **2003**; Vol. 145, pp 97-102.
46. Losey, M. W.; Jackman, R. J.; Firebaugh, S. L.; Schmidt, M. A.; Jensen, K. F. *Journal of Microelectromechanical Systems* **2002**, *11*, 709-717.
47. Drott, J.; Lindstrom, K.; Rosengren, L.; Laurell, T. *Journal of Micromechanics and Microengineering* **1997**, *7*, 14-23.
48. Arana, L. R.; Schaevitz, S. B.; Franz, A. J.; Schmidt, M. A.; Jensen, K. F. *Journal of Microelectromechanical Systems* **2003**, *12*, 600-612.

49. Kobayashi, J.; Mori, Y.; Okamoto, K.; Akiyama, R.; Ueno, M.; Kitamori, T.; Kobayashi, S. *Science* **2004**, *304*, 1305-1308.
50. Inoue, T.; Murphy, E. R.; Schmidt, M. A.; Jensen, K. F. In *Seventh International Conference on Microreaction Technology*: Lausanne, Switzerland, 2003.
51. Haines, A. H. *Methods for the Oxidation of Organic Compounds*; Academic Press: Washington DC, 1985.
52. Urben, P. G. *Handbook of reactive Chemical Hazards*; Butterworth Heinemann: Oxford, 1990.
53. Kula, J. *Chemical Health & Safety* **1999**, *21*-22.
54. Wada, Y.; Schmidt, M. A.; Jensen, K. F. In *Seventh International Conference on Microreaction Technology*: Lausanne, Switzerland, 2003.
55. Chambers, R. D.; Spink, R. C. H. *Chem. Commun.* **1999**, 883-884.
56. Jaehnisch, K.; Baerns, M.; Hessel, V.; Ehrfeld, W.; Haverkamp, V.; Lowe, H.; Wille, C.; Guber, A. *Journal of Fluorine Chemistry* **2000**, *105*, 117-128.
57. de Mas, N.; Guenther, A.; Schmidt, M. A.; Jensen, K. F. In *Transducers - 12th International Conference on Solid-State Sensors, Actuators and Microsystems*; Transducers Research Foundation: Boston MA, 2003; Vol. 1, pp 655 - 658.
58. Mas, N. d. *Ph.D. thesis, Massachusetts Institute of Technology, Cambridge 2004*.
59. Kraus, T.; Gunther, A.; de Mas, N.; Schmidt, M. A.; Jensen, K. F. *Experiments in Fluids* **2004**, *36*, 819-832.
60. Khan, S. A.; Gunther, A.; Schmidt, M. A.; Jensen, K. F. *Langmuir* **2004**, *20*, 8604-8611.
61. Yen, B. K.; Günther, A.; Thalmann, M.; Bawendi, M. G.; Jensen, K. F. In *8th International Conference on Miniaturized System in Chemistry and Life Sciences (mTAS2004)*; Royal Society of Chemistry.: Malmoe, Sweden, 2004.
62. Gunther, A.; Jhunjhunwala, M.; Thalmann, M.; Schmidt, M. A.; Jensen, K. F. *Langmuir* **2005**, xxx.
63. Stöber, W.; Fink, A.; Bohn, E. *Journal of Colloid and Interface Science* **1968**, *26*, 62-69.
64. Gunther, A.; Khan, S. A.; Thalmann, M.; Trachsel, F.; Jensen, K. F. *Lab on a Chip* **2004**, *4*, 278-286.
65. Nielsen, O. M.; Arana, L. R.; Baertsch, C. D.; Schmidt, M. A.; Jensen, K. F. In *Transducers - 12th International Conference on Solid-State Sensors, Actuators and Microsystems*; Transducers Research Foundation: Boston MA, 2003; Vol. 1, pp 714-717.
66. Wilhite, B. A.; Schmidt, M. A.; Jensen, K. F. *Industrial & Engineering Chemistry Research* **2004**, *43*, 7083-7091.
67. Tokeshi, M.; Minagawa, T.; Uchiyama, K.; Hibara, A.; Sato, K.; Hisamoto, H.; Kitamori, T. *Analytical Chemistry* **2002**, *74*, 1565-1571.
68. Quiram, D. J.; Jensen, K. F.; M. A. Schmidt; J. F. Ryley; Mills, P. L.; Wetzel, M. D.; Ashmead, J. W.; Bryson, R. D.; Kraus, D. J.; A. P. Stamford In *2000 Solid-State Sensor and Actuator Workshop*; Transducers Research Foundation: Hilton Head, SC, 2000, pp pp.166-169.
69. Quiram, D. J. *PhD Thesis Massachusetts Institute of Technology 2002*.

## Chapter 2

# Chemical Microprocess Engineering: Current Trends and Issues To Be Resolved

Volker Hessel\* and Holger Löwe

Institut für Mikrotechnik Mainz GmbH, Carl-Zeiss-Str. 18–20,  
D–55129 Mainz, Germany

\*Corresponding author: [hessel@imm-mainz.de](mailto:hessel@imm-mainz.de)

The use of microstructured devices or, more general, microfluidics for performing chemistry and chemical engineering tasks has become a widely investigated matter in the laboratory. Considerable scientific advances on a device level (e.g. for micro mixers) were pointed out; the most relevant current trends among these are listed within this article. In the focus of many current works come now technical issues needed to install the technology for chemical production such as suitable manifolding solutions, large capacity devices, and plant concepts. In near term, the technology will thus be mature for industrial field tests. The question then is whether industry will – and actually can – implement this technology for commercial business. The most relevant trends of the latest works towards this issue will be given. On a device level, there is a need for more detailed information, benchmarking and generic evaluation to compare the new technology to existing conventional and novel alternative process intensification solutions. The micro-reactor devices have to be considered as part of a multi-scale toolbox and, thus, to supplement, rather than to replace conventional technology. To fulfil production demands on a system / plant level, large-

capacity apparatus are needed and plant engineering has to address their integration. In particular, several types of docking platforms, bus concepts and interfaces are currently developed to facilitate the erection of plants. To control the novel microstructured reactors, concepts for sensorics and process control are being validated and complemented, where necessary. At a process level, the recent investigations are considering much more the whole process development, rather than characterizing unit operations only. Economic calculations for the whole process will be demanded based on such information. Finally, it is necessary to look for novel processes and routes which are tailored for micro-reactor operation.

## Introduction

About 400 peer-reviewed papers and conference presentations of at least of the same magnitude, complemented by still more proceedings contributions, give us now a clear, accurate and also comprehensive picture of what chemical micro process engineering can do (1-8). Micro process engineering is the exploitation of microfluidic phenomena by engineering routine. This may be used for many purposes, including food, home or personal care, energy, and chemistry. Concerning the latter, the term chemical micro process engineering is used in this text, since it is just one among the other applications based on the same engineering (and microfabrication) background, namely micro process engineering. So far, the chemical exploitation is the most visible scientific and industrial activity; however, this may change in future. Energy research with microstructured tools, e.g. fuel processors and fuel cells, is gaining increasing importance.

Many reviews cover the subject of summing up the major achievements made in the past, often either from a chemist's or chemical engineer's view (1-8). A few give an outlook what next steps might be taken. The present activities, including the presentations held at IMRET 7 in Lausanne, bridge between the efforts taken in the past and the resolution of the future issues. Slightly, but constantly the research topics orient more towards applications and exploitation. System approaches outpace the simple device characterizations. In Germany, a three-year program was announced in June 2004 by the federal ministry for education and science (BMBF), explicitly and exclusively heading for chemical production. In Japan, the MCPT (Micro chemical process technology) consortium, guided by the respective ministry (METI) and a development organization (NEDO), is doing a similar job. In the U.S., we see some private initiatives to found companies active in the energy sector and corresponding huge activities funded by the energy (DOE) and defense (DARPA) ministeries.

Thus, a change in the chemical micro process engineering activities is noticeable, albeit still vague in all its nuances. This chapter tries to give some of the most visible and probably relevant trends and aims to point at the issues which still need to be resolved.

### Trends at a Device Level

#### More Detailed Information and Benchmarking

Having a glance at the awareness of the scientific community for chemical micro process engineering, it becomes evident that there is great openness for the new technology (2, 4); however, many experts comment on that they want to see more in-depth investigations following the routes traditionally taken.

Peer-reviewed papers of the past, especially in the fields of mixing, organic chemistry and catalysis, have mainly documented the means to achieve a target and provide only a first result as proof of feasibility. Often not a proper comparison to the state of the art is given; usually owing to insufficient data base.

As a consequence, only a few experts have changed their habits in the last years, i.e. to apply microstructured tools for their studies. They remain still in a wait-and-see position which eventually means they are not fully convinced.

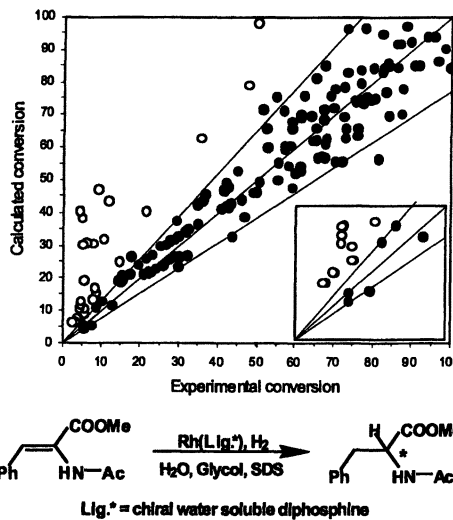


Fig. 1 Kinetic study for the hydrogenation of a cinnamonic acid derivative: Parity plot comparing experimental and modeling data (reproduced from (15); Copyright: Elsevier). Open and closed circles correspond to data outside or within a match of experiments and modeling.

Just recently we see that this situation is changing. Triggered by the acceptance of presentations of the topic at expert conferences (e.g. ISMIP for mixing, ISCRE for reaction engineering or ICC for catalysis), more in-depth works with micro reactors are documented in scientific literature. Detailed investigations on the droplet forming in a split-and-recombine micro mixer depending on the wall material, the number of stages, flow rate, oil concentration, and benchmarking to other micro mixers are given in the literature (9). In-depth catalytic studies on the propane reforming to hydrogen (10) and the carbon monoxide oxidation (11, 12) were undertaken; the latter studies also applied criteria established in catalysis engineering for judging mass and heat transport in micro channels (see a broader description of using the Anderson and Mears criteria as well as the Weisz modulus in (13)). In the field of homogeneous catalysis, complete libraries are being tested and kinetic data are extracted (see Fig. 1) (14, 15).

#### Generic and Systematic Evaluation

An increase in information does not necessarily and automatically push the technology forward. If information is too diverse and addresses too many application fields, especially the non-specialist, albeit acknowledging the prospects, loses orientation what actually can be done for his specific problem. Therefore, generic approaches and at best systematic models are needed. A technology that will always require a long evaluation phase will probably not be accepted, if not some empirical correlations can be made ad hoc or at least within short time; like this is done conventionally, e.g. that a Rushton impeller may be an adequate tool for gas dispersion operations.

Albeit the large number of publications (400 when accounting only for the peer-reviewed), we still are lacking of some generic and systematic approaches. When we face a new engineering problem, it seems that we are still groping in the dark, i.e. the knowledge gathered does not really help. Among the very few first systematic approaches known, a systematic means for judging the flow splitting quality of manifolds on microstructured plates was proposed based on dimensionless parameters already some years ago (16). By the same group, a systematic and fundamental analysis on the interplay of mass and heat transport with reaction was made assuming a first simple reaction scheme (17) (see also a respective chapter in (3)).

This has been recently extended to more complex reaction scenarios, for the first time considering the fluidics as well. The effectiveness of lamination segments as a feed provision on the product distribution for multiple reactions is described in (18). In this study, e.g., the simulation reveals that the lamination width greatly affects the yield for the desired product (see Fig. 2) (18). In most cases, when the conversion of the reactant is the same, the yield of the desired product for perfect mixing is higher when reactants are fed with lamination segments. An exception is that the rate constant of the reaction producing the

desired product is much smaller than that consuming the desired product, and the order of the former reaction is less than the latter.

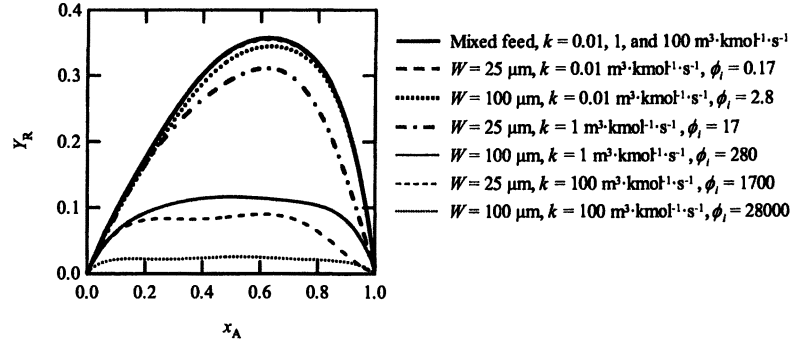


*Fig. 2 Relation between yield of R and conversion of A with different rate constants and lamination widths for a specific reaction type ( $A + B \rightarrow R; B + R \rightarrow S$ ). (reproduced from (18); Copyright: Elsevier). W: lamellae width; k: rate constant;  $\phi$ : ratio of reaction rate to diffusion rate.*

Knowing this in advance and having access to kinetic data, a costly and maybe disappointing scouting study can be stopped at an early level. Contrariwise, the studies can be fine tuned to achieve the most promising benefits.

#### Multi-scale Toolbox

Some studies show benefits of continuous processing in channels with a hydraulic diameter which one would not term “micro” anymore (see e.g. (19, 20)). In some cases, even conventional equipment such as small mixing tees does the same job (21). In contrast, in other applications the superior processing by means of micro mixers as compared to mixing tees is demonstrated (22).

Altogether this triggers current research to explore mini- and meso-scale devices besides microstructured reactors to finally have a toolbox which offers a portfolio of processing facilities that ideally match the demands of a reaction. Today’s practice is otherwise; the reactions are adapted to the equipment (often under loss of performance). Thus, the new methodology is termed “multi-scale technology”, i.e. a toolbox with different processing functions and different internal scales to match mass and heat transport. This toolbox comprises micro-channel reactors ‘enlarged’ in internal dimensions to mini- and meso-scale and process intensification equipment (23, 24) such as spinning-disk reactors (25), besides ‘standard’ micro reactors.

In the framework of a Clariant process development of a pigment production process by diazo chemistry, four micro and mini reactors with differently sized internal were compared for their performance (26). Following a

pre-evaluation for their mixing properties, two selected devices with differently sized internals were characterized for their optical properties (see Fig. 3). The CPC micro reactor is equipped with internal cooling functions, while the IMM caterpillar mixer is not. Thus, their differences may be explained in terms of isothermal and adiabatic processing, respectively. Increased mixing performance in both reactors leads to the generation of smaller particles, giving better coloristic properties, e.g. a higher color strength.

Coloristic property	CPC-microreactor	IMM caterpillar mixer
Color dC	0.73	0.68
Color strength	143%	143%
Color shade dH	5.21	5.82
Color lightness dL	1.48	1.64

*Fig. 3 Coloristic properties of a yellow pigment yielded under isothermal and adiabatic reaction conditions in a CPCmicroreactor and IMM's standard caterpillar mixer, respectively. Data are compared to an internal standard. (reproduced from (26); Copyright: Elsevier).*

#### Microfluidic Devices Beyond Microfabrication

There are other ways to create thin liquid or gaseous layers, which give good mass and heat transport, besides using microfabricated devices. The reasons to search for such alternatives may be due to equipment cost reduction, higher flexibility, more robustness, and more ease in cleaning. An early concept was the catalytic filament reactor exploiting micro-flow phenomena (27). Not microfabricated channels are needed, but a superstructure of the micron-sized filaments forms interstices, virtually like a micro channel.

It is logical to employ these alternative microfluidic approaches, where microstructured devices tend to fail in operation. When, e.g., carrying out precipitations for powder generation in micro devices, problems with clogging often have to be encountered. Thus, alternative fluidic approaches for providing micro spaces are being tested here. One example refers to a reactor consisting of same axle dual pipes (see Fig. 4) (28). This assembly gives a micro space by an annular laminar flow of two immiscible liquids. Titania particles were produced by supplying tetraisopropoxide (TTIP) solutes to the inner tube and an isopropanol/water mixture to the outer tube. Mono-modal spherical particles of titania with narrow size distribution were successfully produced without precipitation of the particles at the wall. The particle size could be controlled in the range from 40 nm to 150 nm simply by changing the diameter of the inner tube at a low TTIP concentration.

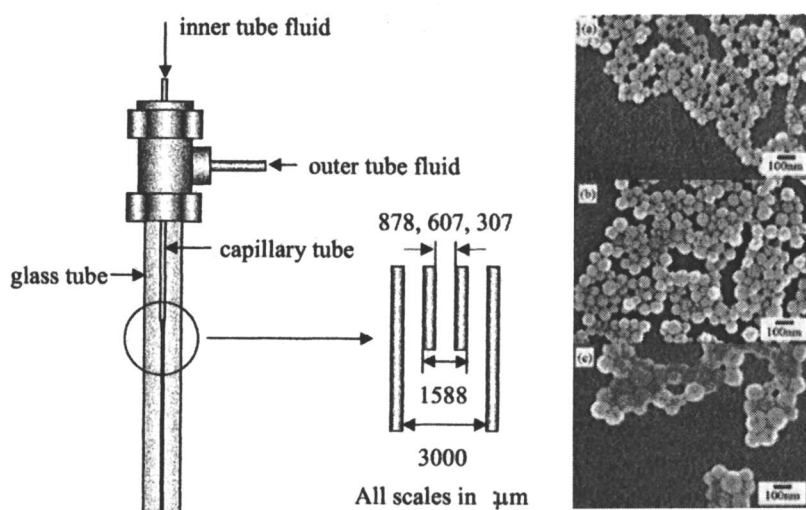


*Fig. 4 Scheme of the dual-pipe reactor and SEM photographs of the titania particles, produced with different inner tube diameter, (a) 307  $\mu\text{m}$ -I.D., (b) 607  $\mu\text{m}$ -I.D., (c) 877  $\mu\text{m}$ -I.D. (reproduced from (28); Copyright: Elsevier).*

### Smarter Microfluidics

Apart from a better understanding of the impact of the microfluidics, we need a better control of the microfluidics itself. Just recently, advanced microfluidic processing – besides simple bi- or multi-lamination – has been utilized for reaction purposes such as slug (Taylor) flow (29, 30), electroosmotic flow (5, 31, 32), or falling-film concepts (33, 34).

Slug flow, for example, benefits from defined recirculation patterns giving efficient mass transfer. Residence time distributions are similar to plug-flow operation (unlike the parabolic profiles typically found under laminar-flow conditions). In addition, a sort of digital reaction technology can be proposed, if smart merging and splitting of slugs is exerted (30). In this way, a multitude of reaction pairs can be generated within one channel, which is equivalent to a multitude of information. Thus, such concepts may further stimulate screening techniques used in catalysis or drug discovery.

### Large-Capacity Microstructured Apparatus

The applicability towards production is seen by many experts as the key step to be taken for a commercial exploitation of the technology. First of all, large-capacity tools are needed for this purpose.

Since mid of the 90s large-capacity microstructured heat exchangers and, somewhat later, mixers of similar design were tested; liquid flows being up to the  $\text{m}^3/\text{h}$  range (35). Starting from 2002, a larger variety of production-type micro mixers was introduced, including multi-laminating interdigital (SuperFocus (36-38)), turbulent interdigital (StarLam (39)), and split-and-recombine (Caterpillar (40)) mixers. The gap from earlier microstructured mixers, operating in the  $\text{l/h}$  range at maximum, up to static mixers, reaching much beyond  $10 \text{ m}^3/\text{h}$ , essentially has been closed (41). Today's micro mixers have liquid capacities up to about  $5 \text{ m}^3/\text{h}$  at pressure drops below 10 bar (39). This is one contribution to the so-called multi-scale technology, as expressed in the IMPULSE proposal a project submitted to the EU 6<sup>th</sup> framework programme ([www.cefic-sustech.org](http://www.cefic-sustech.org) see IMPULSE under "research consortia" (42).

It seems that industry is still not able to use such offer yet. Funding programmes are required to cover the extensive costs for testing such equipment under field conditions. Even more important, the R&D character of these programmes sidesteps the risk management of a completely new process technology. No one in industry can cope with that at the moment when facing commercial production; the industry internal organization of process development is headed by a few decision makers only, which have to guarantee for commissioning, often under severe time pressure. To break this conservative scheme, co-operative actions are hence required and, first of all, flag-ship projects with successful proof of production have to be known. In the latter context, the German DEMIS project with the chemical company Degussa and the large-scale plant engineering company Uhde should be mentioned, building a microstructured reactor, about 6 m high (see Fig. 5). (43, 44). Just recently, UOP and IMM have announced that they are heading for a production process up to 150,000 t/a for the direct synthesis of hydrogen peroxide from the elements (45, 46).

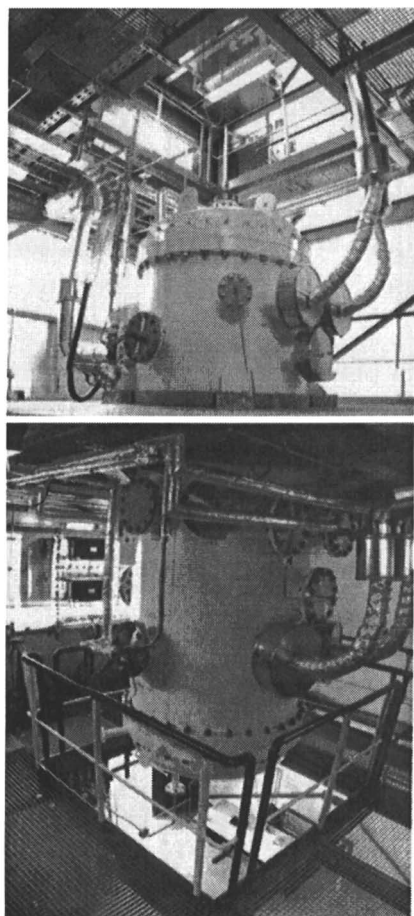


*Fig. 5 Heavy-pilot test reactor at Degussa site, two storeys high; developed with Uhde Company (reproduced from (2); Copyright: Wiley-VCH).*

### Trends at a System / Plant Level

#### Docking Platforms, Bus Concepts and Interfaces

In future there will be a demand for professional docking of microfluidic devices to a system and for combining many such devices within one system. Obviously there are devices from different manufacturers and still a lot home-made ones. Integrating them within a plant would need insertion of a number of fluidic fittings or even individual, self-made connectors, which can lead to a reduction in performance (e.g. because of large dead volumes). Viewing at all world-wide efforts, it becomes clear that it is worth establishing a fluidic platform that is satisfying most needs and is widely accepted.

In Germany, there is a federal initiative, organized by Dechema and steered by a committee (industrial platform IP $\mu$ VT), to design a modular fluidic system with standardized interfaces (47, 48) ([www.microchemtec.de](http://www.microchemtec.de)). The goal is to connect virtually all available microstructured devices without changing - too much - their interfaces, which are different, and their other construction. For this purpose, a fluidic backbone was developed, containing small tubing as fluidic bus similar to large-scale plant concepts (see Fig. 6). Standardized cube-like hollow elements give a frame for the tubing and may carry an electric bus as well. The elements can be connected in 3-D to give frames of various lengths and connectivity. In this way, a flexible 3-D arrangement of existing micro devices was achieved, as demonstrated by a small micro plant for allyl borane synthesis which combines up to 10 unit operations at small foot print (see Fig. 6). The system is designed for fully integrated process investigation at the micro scale and may be applicable to preparative pilot synthesis as well.

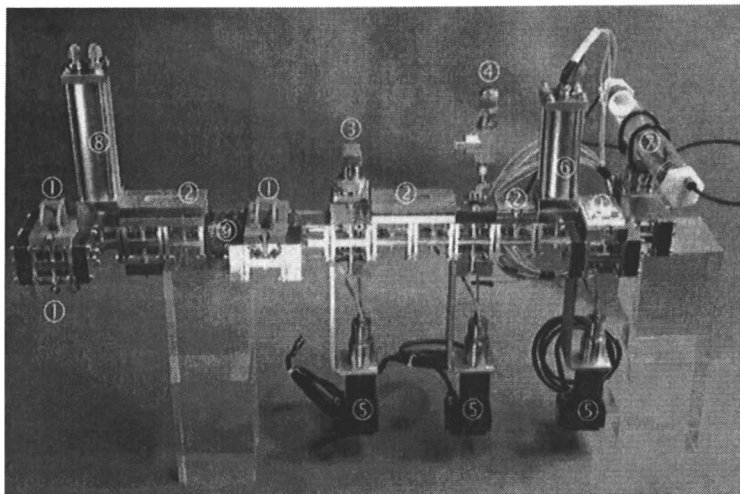


*Fig. 6 Micro plant with fluidic backbone: 1) Micro heat exchanger; 2) Micro mixer; 3) Valve; 4) Safety valve; 5) Mini pump; 6) Heated delay loop; 7) Mixer-settler extractor; 8) Heated micro mixer-tube reactor; 9) Thermal insulation module (47); Copyright: Elsevier).*

The Fraunhofer Organisation, also in Germany, has proposed the so-called FAMOS toolkit ([www.microreaction-technology.info](http://www.microreaction-technology.info)) (see Fig. 7) which allows to set-up microreaction processes on a functionalised base-plate with suitable fluidic and electronic interfaces for the interconnection of toolkit modules, recording of measurement data and connection to the macroscopic periphery (pumps, analytics, sample handling, etc.). Thus, this platform serves for fast and flexible exchange of microstructured plates (not devices at first instance, different from the backbone mentioned above) (49, 50). Since the FAMOS toolkit integrates separate microfluidic components in one multifunctional unit, the dead volumes through additional fluidic couplings like tubes and pipes is avoided and better tempering conditions of the whole unit are achieved. Further, it enables to integrate temperature sensors allowing an active thermal management of the chemical reactions as it is often required. Finally, the platform makes the adaptation of infrared spectroscopy possible, thus enabling the performance of online analysis of the chemical reaction inside the microreaction unit. This may be used e.g. for tuning of the reaction and metering of the process parameters. Therefore, screening of microstructured designs for a specific application may be one strength of this system and more generally, any analytical investigation.

The so-called NeSSI system is a US developed backbone system, initially designated for analytical purposes ([www.cpac.washington.edu/NeSSI/NeSSI.htm](http://www.cpac.washington.edu/NeSSI/NeSSI.htm)). NeSSI is a non-affiliated international ad hoc group composed of over 250 people (and growing) including end-users such as Dow and ExxonMobil, etc. as well as manufacturers such as A+, ABB analytical, Siemens, Fisher-Rosemount, Swagelok, Tescom, Parker-Hannifin, Circo and many others who are looking to modularize and miniaturize process analyzer sample system components. NeSSI operates under the sponsorship and umbrella of CPAC (Center for Process Analytical Chemistry) at the University of Washington in Seattle. The task of the manufacturers is to supply parts and components for the initiative. End-users contribute by "in house" testing. Meanwhile, several NeSSI sampling manifold designs were developed which conform approximately to the SEMI 1.5" manifold. In addition, an ISA standard is being concurrently drafted called SP76. NeSSI's driver is to simplify and standardize sample system design. It is envisaged to adapt the emerging class of Lab-on-a-Chip sensors to a miniature/modular smart manifold order to change the way industry does process analysis.

#### **Numbering-up**

We meanwhile know that for some fine-chemical syntheses at production scale one or a few micro mixers may be just enough. This is owing to the fact that in these cases some 'internal scale-up' was made, i.e. enlarging the channel diameter from micro- to mini-scale, with significant loss of performance. Thus, not all numbering-up issues are as critical as they have been seen in the early literature (see e.g. (51)).

When dealing with higher exothermic reactions, such simple concepts cannot be used anymore rather integrated mixer-reactor systems with multiple channels are needed. In a similar way, gas phase processing reactors described

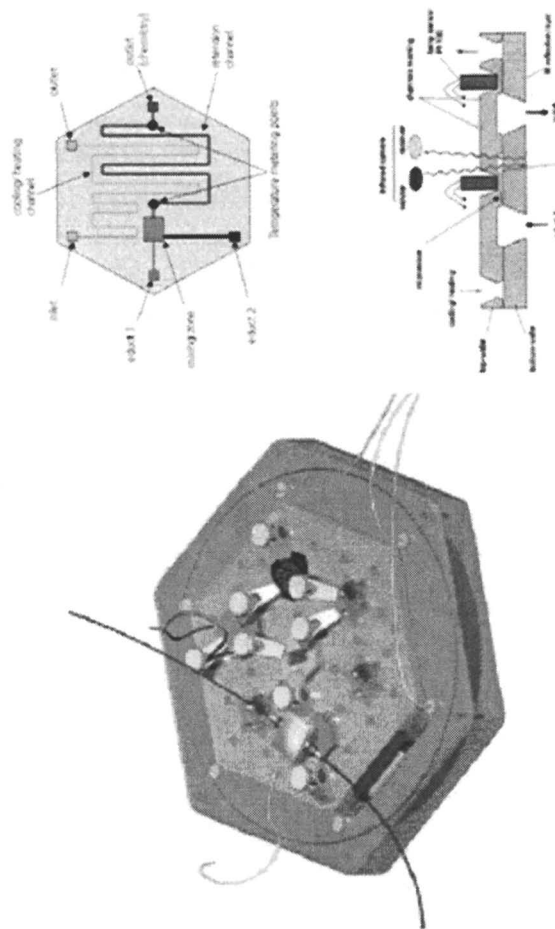


Fig. 7 FAMOS toolkit with functionalised base-plate with fluidic and electronic interfaces for the interconnection of toolkit modules (reproduced from (49); Copyright: Elsevier).

for pilot operations contain a multitude of channels, owing to the short contact times and heat management control. 5 or 10 kW reactors used for fuel processing typically have thousands of micro channels (52).

Thus, there are manifolding issues which demand for theoretical and experimental investigations. For connection at a device level, i.e. the external numbering-up, a flow-splitting unit for liquid-phase operation was described (53, 54). For connection at an element (i.e. micro channel) level, a heat exchanger with nearly 7000 micro channels was realised (52); older work has shown similar achievements (35). This is named internal numbering-up or equaling-up (53, 54).

Modelling of flow distribution in such and similar structures has so far been done at a sub-device (i.e. platelet) level using generic designs (16, 55). In one recent work, an analytical model based on resistance networks has been developed for the study of two manifold structures, considering consecutive and bifurcation designs with different channel geometries (55). This model allows manufacturing variations to be generated randomly within specified tolerances as well as blockages at any part of the structure (see Fig. 8). This allowed to quantify parametric dependencies of flow maldistribution for manufacturing tolerances of the micro channel. Known tolerances of  $\mu$ EDM, milling and etching were implemented and their effect was demonstrated. Further, the effect of worst-case scenarios such as channel blocking was quantified.

For future, modelling of real designs at a device level (flow distribution between channels on one platelet + between various platelets) is needed. Also, experimentation has to validate the predictions made by the simulations.

### Plant Engineering

Plant engineering is one of the most important topics of the future developments, i.e. the integration of microstructured reactors in plants at industrial field site.

This is essentially the topic of the recently announced new German funding programme of BMBF. However, presently there is not much to be said about this topic in the context of a scientific description; there has not much been documented yet and one would not expect this situation to change notably. Since production field tests will be performed at industrial site, for approval and installation reasons, this will remain proprietary know-how.

Nonetheless, several pilots are now running at institutes and experience for their construction and operation is gained in the framework of government projects (see Fig. 9). There is a hope that such knowledge may be distributed to a larger share in the next years.

Engineering companies need to be involved more during future developments and will need specific data for the basic and detailed engineering.

### Sensorics and Process Control

Many experts believe that more information about the processes in micro channels is needed for a better understanding. Already at a laboratory level, in-line temperature profiles could give valuable hints similar to a calorimetric analysis. However, the use of thermocouples has limits and hardly gives useful

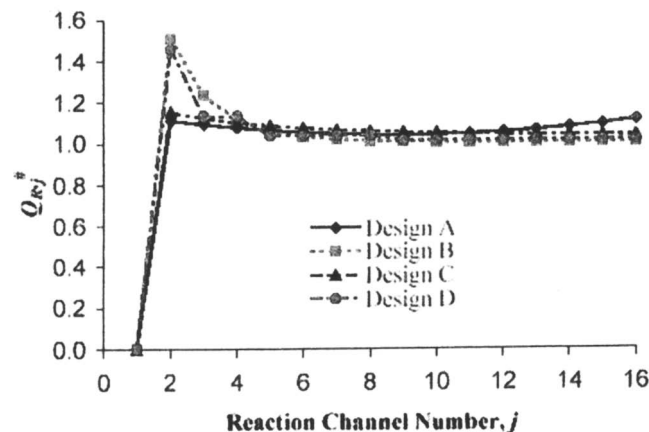


Fig. 8 Flow distribution in the reaction channels of various designs (for design specification refer to (55)), when one channel is blocked.  $Q$  is a normalised flow rate, as defined in (55). (reproduced from (55); Copyright: Elsevier).

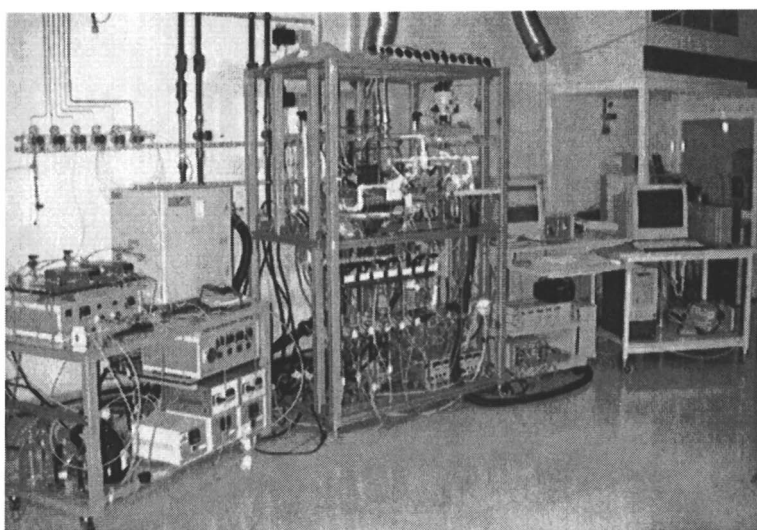


Fig. 9 Pilot fuel processing plant for single reactor and complete (non-integrated) system testing at the 5 kW level (Copyright: IMM).

reactor (e.g. following the Redox potential, see Fig. 11 (26)). A flow outlets as well as process-specific concentration monitoring outside the micro-mechanical pressure hold valves and temperature determination at the in- and today. Usually this is done in a rather conventional fashion, e.g. using commodity/institutes/universities and industry where process control is exerted already have to be conform to the CE regulation.

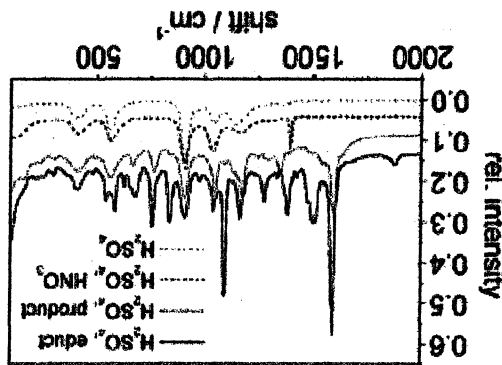
here are regulatory demands during commissioning, e.g. in Europe the sensors calculation and some of these issues can be taken as granted. On the other side, moreover, be asked if it is needed at all. There are, e.g., means for flow since it may have to deal with large numbers (of micro channels). It may, be questioned if such complex sensing will once be feasible and practicable, demands arise here such as flow equipartition and pressure monitoring. It has to monitor and control processes at a production level. Additional monitoring Besides for data gathering, the same miniature sensors may be used to kinetic model for scale-out studies which has not been made yet.

If available now, so far only the functioning of such sensors has been demonstrated. How to use such information during process development has only been pointed out so far. Such data needs to be implemented in a kinetic model for residue time monitoring have been developed as well (63).

It is not clear whether sensors for other parameters are of major importance. If available now, so far only the functioning of such sensors has been demonstrated. How to use such information during process development has only been pointed out so far. Such data needs to be implemented in a kinetic model for scale-out studies which has not been made yet.

Accordingly, the insertion of in-line sensors, as initially already made (37, 38), reduce thermal insulation and thus give wrong temperature profiles. data. Thermographic imaging (see (56)), if accessible at all, may require to is required.

Fig. 10 Raman spectroscopic monitoring of the nitration of chlorobenzene with  $HNO_3$ . Copyright: Elsevier.



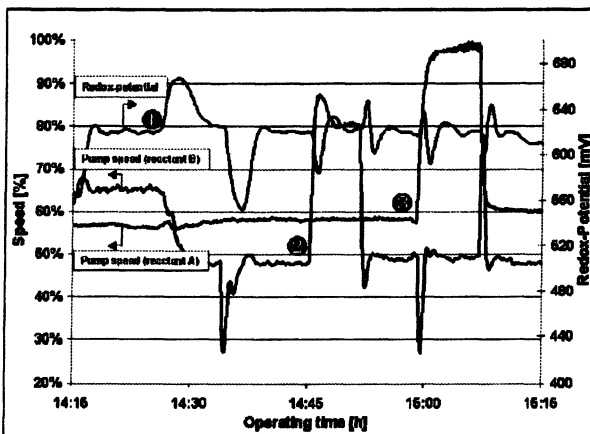


Fig. 11 Process control for a Clariant pilot process: Redox-potential plot of continuous fully automated diazotation (reproduced from (26); Copyright: Elsevier).

manifolding issue is not always given, as sometimes just one channel is fed (see use of split-and-recombine mixers (20) and (26)). Thus, tomorrow's miniature sensors have to fill the niches which conventional control equipment is not able to.

To sum up, process control is currently available; some commercial providers even offer labprocessing software together with their fluidic package. Whether other sensorics are required will be answered by the users in near future; regulatory and commissioning issues will influence this to an extent. For scientific investigations, in-line sensorics can contribute a lot. However, the efforts of a few single groups (59, 60, 64-68) need continuation and more penetration.

### Trends at a Process Level

#### Process Development instead of Operations only

The majority of today's efforts are dedicated to characterization of reactions or related unit operations such as mixing or heat exchange (1). Downstream processing such as product purification is often not investigated; analytical analysis (e.g. FTIR, GC, HPLC) is usually performed and no preparative product isolation is carried out. For conventional processing it is known that the capex (capital) and opex (operating) costs for purification often are much higher than for the reaction step itself; thus they dominate the process costs and for any optimization of the process by micro-reaction processing this has to be considered first.

This was outlined for the synthesis of phenyl boronic acid with a micro-reactor plant (20). Although the reaction engineering benefits, e.g. a 23% higher yield, were impressive, other process specs were even more important. First, the

reaction step could be carried out at ambient temperature, reducing energy costs considerably. Secondly, an about 10% higher purity of the raw product was achieved, which allowed one to omit the costly distillation step from the process and to perform separation simply by extraction or precipitation (see Fig. 12).

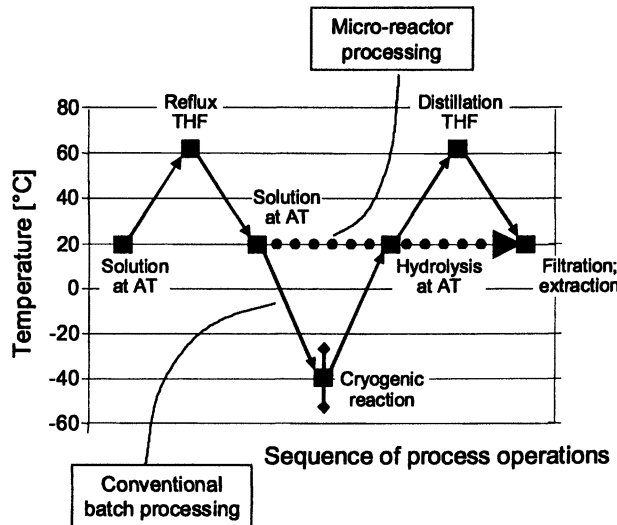
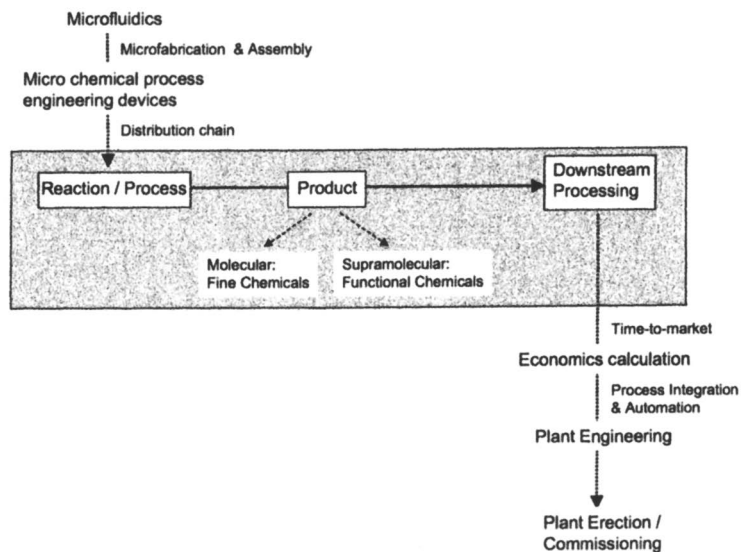


Fig. 12 Temperature profile for the whole process in the phenyl boronic acid synthesis, indicating energy costs (reproduced from (20); Copyright: ACS).

Again, energy costs were saved and also equipment expenditure. Therefore, this example proves that for an industrially convincing implementation strategy the whole process has to be considered.

Accordingly, there is by far too little information about micro-reactor studies at a process level, at least in open literature. We need a comprehensive analysis of all process steps, finally including an economic balancing (see Fig. 13) (1). Expert tools or at least design correlations are required that determine process capital and operational costs. However, care has here to be taken considering the data base. It is daily experience that we change our way to assemble and control micro devices up to the choice of the micro devices themselves. There are practically no open-literature experiences with production of micro devices. When undergoing an economic calculation, one has to be aware of all these options. The phenyl-boronic acid case study shows that unforeseen effects, e.g. a higher product purity, may result in a totally different view on the economics of the process.



*Fig. 13 Process development by steps: the grey shaded area is currently largely addressed by research works, while the other steps need to be explored (reproduced from (1); Copyright: ACS).*

### Novel Processes and Routes

Existing processes are very advanced; often they look back on decades of experience. Even if the micro-reactor processing is better, we cannot be sure that industry will really use it, for a number of reasons such as reliability and costs. However, if there is practically no alternative, the situation may change. Thus, micro-reactor processing has to orient on developing novel processes (3).

Novel processes are not a simple modification of existing processes or adaptation thereof to new products (3); they should provide a breakthrough in processes ('game changing'), e.g. going from cryogenic to ambient conditions, from high pressure to atmospheric, from dilute dissolved to pure reactant and so on.

There is a further reason to develop novel processes. Micro reactors have completely different heat and mass transfer characteristics than conventional stirred batch equipment. This means that we have to change existing protocols to more harsh conditions (3). One should, however, not only look for the few known 'uncontrollable' reactions, but rather intentionally explore more such new routes to use the full potential of micro reactors. For this reason expert simulation tools are needed predicting the potential benefits of chemical micro processing engineering (a first step is described in (18)).

Novel processes can rely on the direct synthesis from the elements under harsh conditions. Examples are here the direct fluorination from elemental fluorine (33, 69-72) and the hydrogen peroxide synthesis from a detonating oxygen/hydrogen gas mixture (46) (see also (73)). Existing multi-step routes can be replaced that way.

Novel processes can achieve the elimination of additives, catalysts and other auxiliary agents, since processing in a micro reactor changes. Thus a simplification of the whole process can be given. One example is the production of soap-free emulsions (9). Even more surprising at first sight, former catalytic processes can be carried out without catalyst or co-additive in micro channels, because the respective species can be generated directly at the large specific interface by surface reactions. Examples are the base-free Suzuki coupling (5, 74) and the acid-free esterification of a pyrene butyric acid (75).

Novel processes can also include a change from cryogenic to ambient temperature processing, involving a temperature change of more than 70 K, like for the synthesis of phenyl boronic acid (20). On the contrary, if there are good arguments, a former low-temperature operation can be tuned into a 'hot' process. At the example of brominations, this was combined with a change from dilute to pure reactant processing. The normal slow addition of bromine into a solvent – drop by drop – under reflux, was changed to a 200°C processing under pressure with pure bromine as one fluid and the pure organic substrate as the other. Sluggish reacting molecules like 4-nitro toluene were converted at reasonable conversion and selectivity in this way (see Fig. 14) (71). Most important, space-time yields were set high thereby.

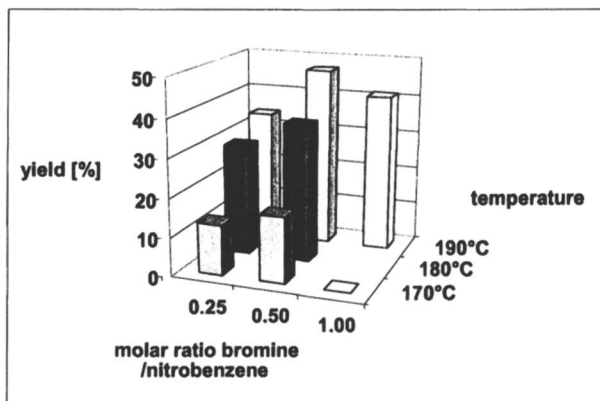


Fig. 14 Enhancement of yield by bromination of 4-nitro benzene at unusually high temperatures using undiluted bromine (reproduced from (71); Copyright: Elsevier

### Conclusions

Major advancements were made for laboratory developments with micro reactors in the past. This was dedicated mainly to investigations on a device level, giving information of the functioning of the micro-reactor devices with regard to several chemical operations. The paramount issue now is to group such information for better benchmarking and to allow one to draw generic conclusions. This will lead to placing the microstructured reactors as parts of a multi-scale toolbox used for modern industrial chemical processing. However, the investigations should not stick solely to the device level, but must address issues of plant and process engineering. Accordingly, the current efforts heading for chemical production set new trends concerning the development of large-capacity apparatus, docking platforms, bus concepts and interfaces as well as the integration of sensorics for process control and economic calculations. The whole process – including both micro-reactor and conventional operation – has to be considered, instead of the micro-reactor operation only. Thus, we go from micro-reactor design to a micro-reactor-plant engineering. This has to be supplemented by changes on a process level, meaning the tailoring of the chemistry itself for optimal use in a microstructured reactor, which is termed novel processes and routes. There is a considerably larger need to have interdisciplinary skills. Now, plant engineers, process control specialists, and economists, just to name a few, have to work together. Also, R&D experts have to deal with commercial manufacturers, both at the chemical and microstructured equipment level. Simple and robust routes have to be identified to replace batch equipment that has been used for decades. Finally, the micro-reactor implementation is not solely a technical issue. As outlined above, it involves personnel and organizational changes which need to be addressed as well, albeit today's chemical companies get more and more used to face such interdisciplinary developments.

1. Pennemann, H.; Watts, P.; Haswell, S.; Hessel, V.; Löwe, H. *Org. Proc. Res. Dev.* 2004, 8 422-439.
2. Jähnisch, K.; Hessel, V.; Löwe, H.; Baerns, M. *Angewandte Chemie International Edition* 2004, 43 (4) 406-446.
3. Hessel, V.; Hardt, S.; Löwe, H. *Chemical Micro Process Engineering - Fundamentals, Modelling and Reactions*, Wiley-VCH: Weinheim 2004.
4. Hessel, V.; Löwe, H. *Chem. Eng. Technol.* 2003, 26 (1) 13-24.
5. Fletcher, P. D. I.; Haswell, S. J.; Pombo-Villar, E.; Warrington, B. H.; Watts, P.; Wong, S. Y. F.; Zhang, X. *Tetrahedron* 2002, 58 (24) 4735-4757.
6. Haswell, S. T.; Watts, P. *Green Chemistry* 2003, 5 240-249.
7. Jensen, K. F. *Chem. Eng. J. Sci.* 2001, 56 293-303.
8. Gavriilidis, A.; Angelis, P.; Cao, E.; Yeong, K. K.; Wan, Y. S. S. *Trans. IChemE.* 2002, 80/A (1) 3-30.

9. Mae, K.; Maki, T.; Hasegawa, I.; Eto, U.; Mizutani, Y. *Chem. Eng. J.* **2004**, 101 (1-3) 31-38.
10. Aartun, I.; Gjervan, T.; Venvik, H.; Görke, O.; Pfeifer, P.; Fathi, M.; Holmen, A.; Schubert, K. *Chem. Eng. J.* **2004**, 101 (1-3) 93-99.
11. Ajmera, S. K.; Delattre, C.; Schmidt, M. A.; Jensen, K. F. *Sensor Actuat.* **2002**, 82 (2-3) 297-306.
12. Ajmera, S. K.; Delattre, C.; Schmidt, M. A.; Jensen, K. F. *J. Catal.* **2002**, 209 401-412.
13. Kolb, G.; Hessel, V. *Chem. Eng. J.* **2004**, 98 (1-2) 1-38.
14. de Bellefon, C.; Abdallah, R.; Ireland, T. *Chem. Ing. Tech.* **2004**, 76 (5) 633-637.
15. de Bellefon, C.; Pestre, N.; Lamouille, T.; Grenouillet, P. *Advances in Synthesis and Catalysis* **2003**, 345 (1+2) 190-193.
16. Commenge, J. M.; Falk, L.; Corriou, J. P.; Matlosz, M. *AIChE J.* **2000**, 48 (2) 345-358.
17. Commenge, J.-M. PhD thesis, Institut National Polytechnique de Lorraine, Nancy, France, 2001.
18. Aoki, N.; Hasebe, S.; Mae, K. *Chem. Eng. J.* **2004**, 101 (1-3) 323-331.
19. Krummradt, H.; Kopp, U.; Stoldt, J. In *Microreaction Technology: 3rd International Conference on Microreaction Technology, Proc. of IMRET 3*; Ehrfeld, W., Ed. Springer-Verlag: Berlin 2000; pp 181-186.
20. Hessel, V.; Löwe, H.; Hofmann, C.; Meudt, A.; Scheurer, S.; Schönfeld, F.; Werner, B. *Org. Proc. Res. Dev.* **2004**, 8 511-523.
21. Burns, J. R.; Ramshaw, C. *Trans. Inst. Chem. Eng.* **1999**, 77 (5/A) 206-211.
22. Suga, S.; Nagaki, A.; Tsutsui, J.-I.; Yoshida, J.-I. . *Book of Abstracts, IMRET 7*, Lausanne, September 7-10, 2003 **2003**, 208-210.
23. Ramshaw, C.; *Proceedings of 1<sup>st</sup> Int. Conf. Process Intensification for Chem Ind.*, London, UK, 1995; BHR- Group: p 1.
24. Stankiewicz, A. I.; Moulijn, J. A. *Chemical Engineering Progress* **2000**, (1) 22-34.
25. Oxley, P.; Brechtelsbauer, C.; Ricard, F.; Lewis, N.; Ramshaw, C. *Ind. Chem. Res.* **2000**, 39 2175-2182.
26. Wille, C.; Gabski, H.-P.; Haller, T.; Kim, H.; Unverdorben, L.; Winter, R. *Chem. Eng. J.* **2004**, 101 (1-3) 179-185.
27. Wolfrath, O.; Kiwi-Minsker, L.; Renken, A. In *Microreaction Technology - IMRET 5: Proc. of the 5th International Conference on Microreaction Technology*; Matlosz, M.; Ehrfeld, W.; Baselt, J. P., Eds. Springer-Verlag: Berlin 2001; pp 192-201.
28. Tagaki, M.; Maki, T.; Miyahara, M.; Mae, K. *Chem. Eng. J.* **2004**, 101 (1-3) 269-276.
29. Burns, J. R.; Ramshaw, C. *Lab Chip* **2001**, 1 10-15.
30. Köhler, J. M.; Henkel, T.; Grodrian, A.; Kirner, T.; Roth, M.; Martin, K.; Metze, J. *Chem. Eng. J. J.* **2004**, 101 (1-3) 201-216.
31. Skeilton, V.; Grenway, G. M.; Haswell, S. J.; Styring, P.; Morgan, D. O.; Warrington, B. H.; Wong, S. Y. F. *Analyst* **2001**, 126 11-13.
32. Fletcher, P. D. I.; Haswell, S. J.; Paunow, V. N. *Analyst* **1999**, 124 1273-1282.

33. Jähnisch, K.; Baerns, M.; Hessel, V.; Ehrfeld, W.; Haverkamp, W.; Löwe, H.; Wille, C.; Guber, A. *J. Fluorine Chem.* **2000**, 105 (1) 117-128.
34. Yeong, K. K.; Gavriilidis, A.; Zapf, R.; Hessel, V. *Catal. Today* **2003**, 81 (4) 641-651.
35. Schubert, K.; Brandner, J.; Fichtner, M.; Linder, G.; Schygulla, U.; Wenka, A. *Microscale Therm. Eng.* **2001**, 5 17-39.
36. Löb, P.; Dresc, K. S.; Hessel, V.; Hardt, S.; Hofmann, C.; Löwe, H.; Schenk, R.; Schönfeld, F.; Werner, B. *Chem. Eng. Technol.* **2003**, 27 (3) 340-345.
37. Hessel, V.; Hardt, S.; Löwe, H.; Schönfeld, F. *AIChE J.* **2003**, 49 (3) 566-577.
38. Hardt, S.; Schönfeld, F. *AIChE J.* **2003**, 49 (3) 578-584.
39. Werner, B.; Hessel, V.; Löb, P. *Chem. Ing. Tech.* **2004**, 76 (5) 567-574.
40. Schönfeld, F.; Hessel, V.; Hofmann, C. *Lab Chip* **2004**, 4 65-69.
41. Bayer, T.; Himmller, K.; Hessel, V. *Chemical Engineering* **2003**, (5) 2-9.
42. Bayer, T.; Matłosz, M.; Jenck, J. *Chem. Ing. Tech.* **2004**, 76 (5) 528-533.
43. Schirrmeister, S.; Markowz, G. *27th International Exhibition-Congress on Chemical Engineering, Environmental Protection and Biotechnology, Achema*, Frankfurt, Germany., 19 - 24 May 2003, 2003; DECHEMA: p 3.
44. Markowz, G.; Schirrmeister, S.; Albrecht, J.; Becker, F.; Schütte, R.; Caspary, K. J.; Klemm, E. *Chem. Ing. Tech.* **2004**, 76 (5) 620-625.
45. Löwe, H.; Hessel, V. *International Symposium on Chemical Reaction Engineering, ISCRE*, Chicago, USA, 6 - 9 June, 2004.
46. Pennemann, P.; Hessel, V.; Löwe, H. *Chemical Engineering Science* (special issue for ISCRE, Chicago, June 2004) **2004**, accepted.
47. Müller, A.; Cominos, V.; Hessel, V.; Horn, B.; Schürer, J.; Ziogas, A.; Jähnisch, K.; Hillmann, V.; Großer, V.; Jam, K. A.; Bazzanella, A.; Rinke, G.; Kraut, M. *Chem. Ing. Tech.* **2004**, 76 (5) 641-651.
48. Müller, A.; Cominos, V.; Horn, B.; Ziogas, A.; Jähnisch, K.; Grosser, V.; Hillmann, V.; Jam, K. A.; Bazzanella, A.; Rinke, G.; Kraut, M. *Chem. Eng. J.* (special issue for CHEMREACTOR XVI, Berlin, 1 - 4 Dec, 2003); in print.
49. Koeschkerjan, R.; Richter, M.; Boskovic, D.; Schnürer, F.; Loebbecke, S. *Chem. Eng. J. J.* **2004**, 101 (1-3) 469-475.
50. Loebbecke, S. *Chem. Ing. Tech.* **2004**, 76 (5) 581-583.
51. Lerou, J. J.; Harold, M. P.; Ryley, J.; Ashmead, J.; O'Brien, T. C.; Johnson, M.; Perotto, J.; Blaisdell, C. T.; Rensi, T. A.; Nyquist, J. In *Microsystem Technology for Chemical and Biological Microreactors; DECHEMA Monographs*; Ehrfeld, W., Ed. Vol. 132, Verlag Chemie: Weinheim 1996; pp 51-69.
52. IMM Institut für Mikrotechnik Mainz GmbH: unpublished results.
53. Schenk, R.; Hessel, V.; Hofmann, C.; Kiss, J.; Löwe, H.; Ziogas, A. *Chem. Eng. J.* **2004**, 101 (1-3) 421-429.
54. Schenk, R.; Hessel, V.; Hofmann, C.; Kiss, J.; Löwe, H.; Schönfeld, F. *Chem. Eng. Technol.* **2003**, 26 (12) 1271-1280.
55. Amador, C.; Gavriilidis, A.; Angelis, P. *Chem. Eng. J.* **2004**, 101 (1-3) 379-390.

56. Wille, C.; Ehrfeld, W.; Herweck, T.; Haverkamp, V.; Hessel, V.; Löwe, H.; Lutz, N.; Möllmann, K.-P.; Pinno, F. *VDE World Microtechnologies Congress, MICRO.tec 2000*, EXPO Hannover, Germany, 25 -27 September, 2000; VDE Verlag, Berlin: pp 349-354.
57. Srinivasan, R.; Hsing, I.-M.; Berger, P. E.; Jensen, K. F.; Firebaugh, S. L.; Schmidt, M. A.; Harold, M. P.; Lerou, J. J.; Ryley, J. F. *AIChE J.* **1997**, *43* (11) 3059-3069.
58. Jensen, K. F.; Hsing, I.-M.; Srinivasan, R.; Schmidt, M. A.; Harold, M. P.; Lerou, J. J.; Ryley, J. F. In *Microreaction Technology - Proc. of the 1st International Conference on Microreaction Technology; IMRET 1*; Ehrfeld, W., Ed. Springer-Verlag: Berlin 1997; pp 2-9.
59. Ferstl, W.; Loebbecke, S.; Antes, J.; Krause, H.; Haeberl, M.; Schmalz, D.; Muntermann, H.; Grund, M.; Steckenborn, A.; Lohf, A.; Hassel, S.; Bayer, T.; Leipprand, I. *Chem. Eng. J.* **2004**, *101* (1-3) 431-438.
60. Loebbecke, S.; Antes, J.; Tuercke, T.; Boskovich, D.; Schweikert, W.; Marioth, E.; Schnuerer, F.; Krause, H. H. *6th International Conference on Microreaction Technology, IMRET 6*, New Orleans, USA, 11 -14 March, 2002; AIChE Pub. No. 164: pp 37-38.
61. Antes, J.; Tuercke, T.; Marioth, E.; Lechner, F.; Scholz, M.; Schnürer, F.; Krause, H. H.; Loebbecke, S. In *Microreaction Technology - IMRET 5: Proc. of the 5th International Conference on Microreaction Technology*; Matlosz, M.; Ehrfeld, W.; Baselt, J. P., Eds. Springer-Verlag: Berlin 2001; pp 446-454.
62. Tuercke, T.; Schweikert, W.; Lechner, F.; Antes, J.; Krause, H. H.; Loebbecke, S. In *Microreaction Technology - IMRET 5: Proc. of the 5th International Conference on Microreaction Technology*; Matlosz, M.; Ehrfeld, W.; Baselt, J. P., Eds. Springer-Verlag: Berlin 2001; pp 479-488.
63. Günther, M.; Schneider, S.; Wagner, J.; Georges, R.; Henkel, T.; Kielinski, M.; Albert, J.; Bierbaum, R.; Köhler, J. M. *Chem. Eng. J.* **2004**, *101* (1-3) 373-378.
64. Lu, H.; Schmidt, M. A.; Jensen, K. F. In *Microreaction Technology - IMRET 5: Proc. of the 5th International Conference on Microreaction Technology*; Matlosz, M.; Ehrfeld, W.; Baselt, J. P., Eds. Springer-Verlag: Berlin 2001; pp 175-184.
65. Firebaugh, S. L.; Jensen, K. F.; Schmidt, M. A. *Microelectromechanical Systems* **2001**, *10* (2) 232-237.
66. Jackman, R. J.; Floyd, T. M.; Ghodssi, R.; Schmidt, M. A.; Jensen, K. F. *J. Micromech. Microeng.* **2001**, *(11)* 263-269.
67. Lu, H.; Schmidt, M. A.; Jensen, K. F. *Lab Chip* **2001**, *1* 22-28.
68. Loebbecke, S.; Ferstl, W.; Lohf, A.; Steckenborn, A.; Hassel, J.; Häberl, M.; Schmalz, D.; Muntermann, H.; Bayer, T.; Kinzl, M.; Leipprand, I. *Chem. Ing. Tech.* **2004**, *76* (5) 637-640.
69. de Mas, N.; Günther, A.; Schmidt, M. A.; Jensen, K. F. *Ind. Eng. Chem. Res.* **2003**, *42* (4) 698-710.
70. Chambers, R. D.; Holling, D.; Spink, R. C. H.; Sandford, G. *Lab Chip* **2001**, *1* 132-137.
71. Löb, P.; Löwe, H.; Hessel, V. *J. Fluorine Chem.* **2004**, accepted for publication.
72. Hessel, V.; Löb, P.; Löwe, H. *chimica oggi - Chemistry Today* **2004**, *(5)* 32-36.

73. Görke, O.; Pfeifer, P.; Schubert, K. *6th International Conference on Microreaction Technology, IMRET 6*, New Orleans, USA, 11 -14 March, 2002; AIChE Pub. No. 164: pp 262-274.
74. Skelton, V.; Greenway, G. M.; Haswell, S. J.; Styring, P.; Morgan, D. O. In *Microreaction Technology: 3rd International Conference on Microreaction Technology, Proc. of IMRET 3*; Ehrfeld, W., Ed. Springer-Verlag: Berlin 2000; pp 235-242.
75. Brivio, M.; Oosterbroek, R. E.; Verboom, W.; Goedbloed, M. H.; van den Berg, A.; Reinhoudt, D. N. *Chem. Comm.* **2003**, 1924-1925.

## **Chapter 3**

### **Overview of Early-Stage Microchannel Reactor Development at Pacific Northwest National Laboratory**

**Anna Lee Y. Tonkovich<sup>1</sup> and Yong Wang<sup>2</sup>**

**<sup>1</sup>Velocys, 7950 Corporate Boulevard, Plain City, OH 43064**

**<sup>2</sup>Pacific Northwest National Laboratory, Richland, WA 99301**

Investigation of microchannel reactors at Pacific Northwest National Laboratory (PNNL) began in the mid 1990s. During the half decade leading to 2000, many concurrent challenges were faced involving device design, catalyst development, and fabrication methods. Microchannel reactor development efforts at PNNL were focused on solving applied problems, including vaporization of hydrocarbon fuels and their steam reforming for fuel processing. Efforts at PNNL also focused on the development of engineered catalysts based on structured metal substrates and device fabrication using diffusion-bonded metal sheets.

Development of microchannel reactors at Pacific Northwest National Laboratory (PNNL) focused on applied problems related primarily to fuel processing at scales ranging from small portable (10 watt) to automotive full-scale (50 kilowatt). Challenges involving reactor design, engineered catalysts specifically designed for microchannel reactors, and methods of fabrication resulted in technical insights and innovations that spurred future development. The approach to reactor design evolved with the development of innovative catalysts and fabrication methods. Initial catalyst investigations in 1996 revealed that direct washcoating of microchannel walls presented significant hurdles to rapid development. While these problems were later solved, the challenge of catalyst development was decoupled from hardware design and fabrication through the development of innovative insertable engineered forms of catalysts. The resulting new forms of catalysts created opportunities in diverse fields. The PNNL fabrication innovation was to develop complex microchannel designs through diffusion bonding of thin metal sheets to form hermetically sealed devices, thus overcoming the sealing challenges of gasketed reactors. Many of the significant breakthroughs in microchannel reactor design resulted from developing designs for specific commercial applications.

## Background

Concurrent with the work at PNNL (1, 2), several other groups were investigating microchannel reactors, including the Institut for Microtechnology Mainz (3-7), BASF (7, 8), DuPont (9-11), Massachusetts Institute of Technology (12, 13), University of Newcastle (14), University College London (15), University of Frankfurt (16), Bayer and the University of Chemnitz (17), and Forschungszentrum Karlsruhe GmbH (Karlsruhe) (16, 18). The early work of microreaction engineering researchers focused on challenges similar to those observed at PNNL, namely catalyst integration, fabrication, and hardware design for the application of interest. The methods for solving these problems varied, in part based on the catalysis, fabrication, and design tools available to the researchers at the time.

In the early stages of microreactor development, typical fabrication techniques included etched channels in silicon, deep channels formed with LIGA, and stacked structured sheets. Catalysts were also under development and included 1) packing of catalyst particles in channels, 2) direct washcoating of catalyst slurry, 3) washcoating of high surface area catalyst supports followed by impregnation of catalyst precursor solution, 4) forming high surface area catalyst supports directly from the reactor wall material via anodization, 5) forming reactors directly from the catalytic metals, and 6) line-of-sight vapor deposition techniques. The applications varied and included fuel processing, hydrogen oxidation, specialty chemical production, and other gas and liquid phase reactions.

## Microchannel Reactor Design

Microchannel reactor design efforts at PNNL focused on developing fuel processors for large- and small-scale applications. The research ranged from demonstrating full-scale automotive fuel vaporization to developing portable fuel processors.

### **Automotive Fuel Processing Applications**

The ongoing PNNL automotive fuel processor project (funded by the U.S. Department of Energy's Department of Transportation Technology) began in the fall of 1996. The first year of the program focused on the full-scale demonstration of on-board methanol vaporization to support a 50-kilowatt electric equivalent (kWe) fuel cell. In the second year, the focus shifted to gasoline vaporization. From late 1998 to mid 1999, the program demonstrated isoctane steam reformation, a fuel simulant for gasoline, in a microchannel reactor with heat supplied by an external combustor. Since 1999, work has focused on refining the reformer design with lower pressure drop, better heat integration, fast start-up, and more fuel flexibility.

#### *Methanol Vaporization*

The intent of methanol vaporization was to capture the waste energy present in fuel cell anode effluent (in the form of dilute hydrogen: 8% by volume) to vaporize methanol fuel. Initial catalyst screening tests quickly showed that palladium (Pd) was an excellent active metal for low-temperature hydrogen combustion. Pd catalyst powders were tested in quartz tubes for efficacy. The powders were subsequently tested in a plate microchannel reactor, and the generated heat was used to fully vaporize methanol.

Several surprising operational characteristics were observed from these initial tests. When the catalyst was packed within the reactor's microchannels and lit off at room temperature, heat was quickly dissipated, and temperatures sufficient for vaporization could not be sustained. When the catalyst was packed in the header and upstream of the microchannels, the reaction lit off at room temperature, and a high catalyst and gas temperature ( $>200^{\circ}\text{C}$ ) was sustained—sufficient to vaporize water or methanol in an opposing array of microchannels. However, the tests revealed a high gas pressure drop ( $>10$  pounds per square inch [psi] gauge for a few liters per minute of flow).

The high pressure drop of the powders made it necessary to investigate new catalyst forms such as open foam structures with high void fractions (see Engineered Catalysts below). Nickel foams were readily available and provided an excellent catalyst support, both with and without an extra high surface area layer catalyst coating. Further advances were made by adding buffer layers to both passivate the surface from corrosive attack and to improve adhesion of the catalyst layers (19).

Because the foam catalyst structure did not fit well within either the microchannels or the headers, the original reactor design was improved to create a near adiabatic pocket for the foam catalyst. The dilute hydrogen stream from the fuel cell anode effluent (or simulated stream) was pre-mixed with stoichiometric amounts of air and fed to the foam catalyst. The resulting hot-gas stream was routed to an array of parallel microchannels that were opposed to an adjacent array of microchannels for fuel vaporization. To reduce thermal losses and increase device compactness, the layers were stacked on top of each other.

The advances achieved in improving catalyst form were matched by fabrication advances. To increase the throughput and heat duty, microchannels with a larger aspect ratio were required. Forming channels in stainless steel with fabrication methods available at the time created a maximum 4:1 aspect ratio (channel height to width ratio). To increase the aspect ratio, aluminum was used instead of stainless steel so that slitting saws could form deep microchannels. The initial microchannel reactors were made in four layers: a top plate, a pocket plate for the engineered foam catalyst, a plate with flue gas microchannels on one side and fuel vaporization microchannels on the back, and a bottom plate to seal the device. The resulting single cell (defined as one parallel array of microchannels with a common header and footer) successfully demonstrated methanol vaporization by capturing heat from the combustion of a dilute hydrogen stream (20).

Scaling up the reactor was far more challenging. A multi-cell reactor (having multiple cells, each with distinct headers and/or footers) was designed and fabricated using layered sheets with channels formed with a slitting saw. The reactor was designed to match half capacity for a full-scale methanol fuel processor or to vaporize sufficient methanol for a 25-kWe fuel cell. Two parallel devices, each with four cells (shown in Figure 1), provided an operating turn-down ratio of 8:1. It was envisioned to individually operate one or more vaporization cells to enable both idle (low power draw) and acceleration (high power draw requiring the concurrent operation of many or all cells) in the fuel cell vehicle.

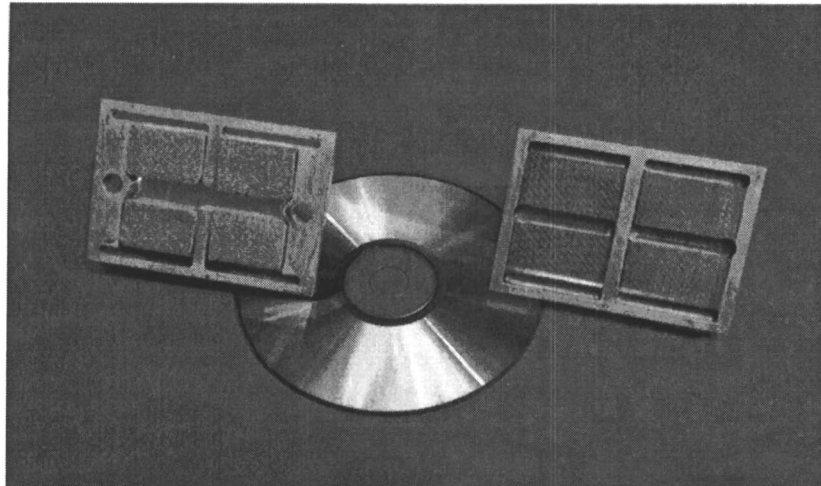


Figure 1. Full-scale methanol reactor

Initially, there were many operational challenges to scaling up. The large gaseous flow rates (> 500 standard liters per minute [SLPM]) necessary to simulate the fuel cell anode flows required testing facilities and an infrastructure well beyond the standard bench-scale facility. The small four-cell reactor weighed less than four pounds, but required a high-bay pilot plant facility for testing. A tube trailer feed source also had to be integrated for the gas supply.

Early experiments revealed several other practical challenges. The initially selected silicone gasket material proved insufficient for the four-cell reactor because the interior temperature between the foam catalysts exceeded the allowable temperature. This problem was not observed in the single-cell experiments as a result of higher heat losses. Flow distribution of the liquid methanol was unstable in the original header design. Flow distribution of the feed gases based on using passive manifolding between the four cells also was unreliable depending on how the catalysts were loaded.

To solve the gasket-material problem, all the silicone gaskets were replaced with graphite gaskets, which proved reliable for testing. Overcoming the flow-distribution challenges required both design and installation changes. The instability of the liquid flow distribution resulted from vaporization in the microchannels that created a feedback mechanism, causing the liquid to preferentially travel to the lowest pressure drop channels where vaporization was not occurring. In the initial runs, liquid methanol moved *en masse* from side to side or from cell to cell. One side of the device would receive an estimated 90% of the flow and then would receive an estimated 10% moments later with an irregular time constant. The chaotic nature of the flow would not support

operation. To overcome this problem, a small amount of pressure drop was added to the inlet of each array of microchannels. An insert was placed in the header that occluded the opening into the microchannels except for the top 0.001 inch across the 0.01-inch opening that directed flow to the array of microchannels. The small amount of extra pressure drop (a few psi) that resulted from an orifice effect stabilized the flow and damped the oscillations.

The pressure drop of a few psi through the inserted foam catalysts should have been sufficient to create nearly uniform flow, but the method of catalyst insertion created a non-uniformity in the pressure-drop profile. Because the foams were slightly oversized after catalyst application and somewhat malleable, two methods of insertion were tried. In one method, the catalyst was compressed to tightly fit within the microchannel. In the second method, the catalyst structure was cut to fit within the microchannel. The compression method, albeit slight, created a higher pressure drop through some of the catalysts—sufficient to maldistribute flow by more than 25%. All catalysts before insertion, therefore, were standardized, whereby edge material was carefully ground away without compressing the catalyst structure. The first successful multi-cell microchannel reactor (Figure 1) was demonstrated in the early fall of 1997 (19,33).

#### *Gasoline Vaporization*

In the second year of the automotive fuel processing program, emphasis shifted from methanol to gasoline vaporization. Stainless steel rather than aluminum was used to create a robust product and minimize potential corrosion concerns. In addition, sealing challenges with the gaskets necessitated a new approach. Concurrent with this development effort, other researchers at PNNL had used laminate formation and diffusion bonding to create two-stream heat exchangers. This concept was extended to a multi-layered reactor device. Sheets were procured in thicknesses that matched the desired microchannel gap (nominal 0.01 inch), and features were fully etched from the material to create flowpaths, headers, footers, and channels (see Fabrication Advances below).

Devices were made and tested at both bench-scale (one cell equals one-quarter of full scale) and full-scale (four-cell device). Figure 2a shows the finished device, and Figure 2b shows the interior microchannels used for the full-scale gasoline reactor (21).

The challenges in developing a gasoline fuel vaporizer became more apparent later in the development and were less about catalyst (Pd/SiO<sub>2</sub>/stainless steel/foam) and design (channel dimensions determined during the previous year) and more about fabrication and implementation. The diffusion bonding process required much iteration to find conditions (temperature, pressure, and time) that produced the desired material properties.

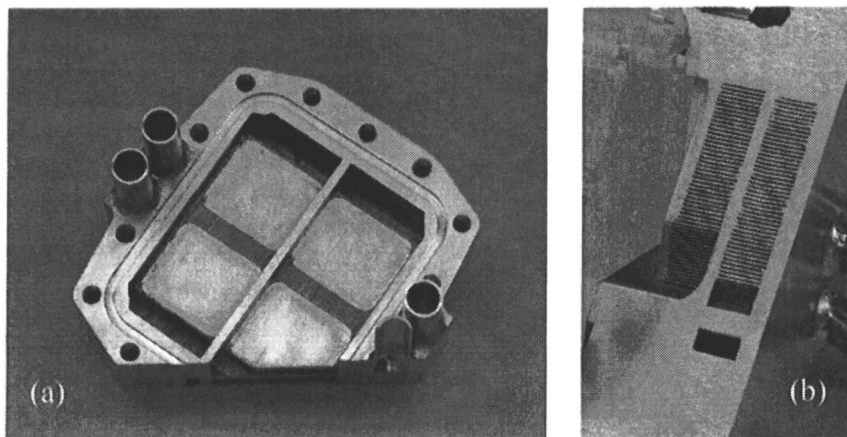


*Figure 2. Full-scale gasoline reactor formed from bonded sheets*

Two full-scale gasoline vaporizers ( $3 \times 4 \times 2$  inches) were demonstrated at roughly 300 milliliters (mL) per minute of gasoline. The total flue gas flow rate was nearly 1400 SLPM of combined nitrogen, hydrogen, and oxygen (21, 22). The measured rate of heat transfer through the wall intervening between the heat transfer microchannels approached  $100 \text{ W/cm}^2$ . Comparable gasoline vaporization in conventional hardware required heat-transfer rates more than an order of magnitude lower.

Successful demonstration of the full-scale automotive fuel vaporizer created the opportunity to evaluate additional fuel processing applications—including steam reforming.

#### *Steam Reforming*

Steam reforming of transportation fuels provides the highest system efficiency for an on-board automotive fuel processor. PNNL initially evaluated steam reforming of iso-octane as a simulant of gasoline. Highly active catalysts had been identified with powder catalyst screening tests where contact times of 25 milliseconds (ms) to achieve over 90% conversion were routinely observed using a rhodium (Rh)/ $\text{Al}_2\text{O}_3$  catalyst (23). To add high rates of heat to the endothermic reaction without facing either mass transfer or pressure drop limitations, a new engineered catalyst (a thick porous catalyst held against a microchannel wall) was developed (see Engineered Catalysts below). The engineered catalyst demonstrated superior results with contact times below 5 ms compared to 25 ms or greater in a powder.

The engineered catalysts (0.01-inch thick) were placed on both sides of a 0.03-inch microchannel to create a center gap (0.01 inch) for process flow. Adjacent heat-transfer channels were interleaved between reforming channels. A 10-process channel device was about 2 in.<sup>3</sup> and produced sufficient hydrogen for 1-kWe fuel cell. With contact times in the range of 1 to 5 ms at 600 to 700°C for steam to carbon ratios between 3:1 and 6:1, isoctane feed conversions greater than 90% were measured with hydrogen selectivity greater than 90% (24).

In the isoctane reformer shown in Figures 3 and 4, four devices were connected to create the functionality of a steam reforming system. An external catalytic combustor was used, where a mixture of hydrogen, methane, and air were burned to create a high-temperature gas stream (between 700 and 900°C). The combustion stream flowed to the heat-exchange channels of the microchannel steam reformer to provide heat to drive the endothermic reaction. The mixture of isoctane and steam was preheated in a separate heat exchanger by pulling waste heat from the effluent combustion stream exiting the steam reformer. The fourth and final component was a vaporizer for water and isoctane. Vaporization heat was reclaimed from the hot exhaust leaving the preheater.

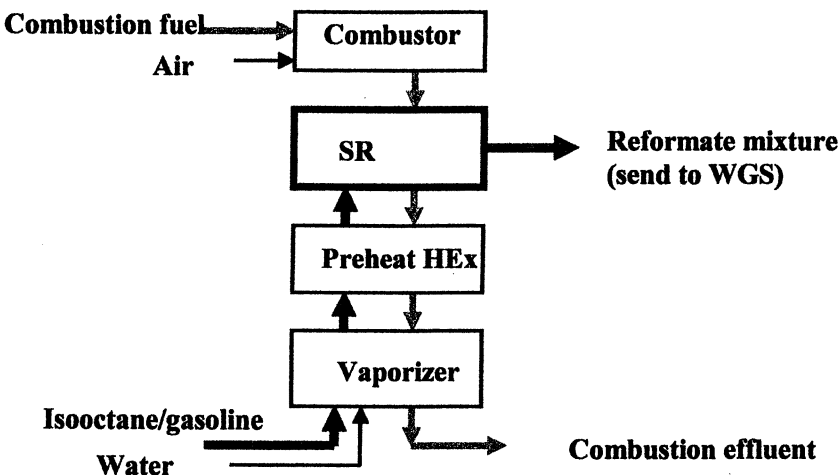


Figure 3. Isooctane reformer schematic

SR = Steam reforming

WGS = Water gas shift

HEX = Heat exchanger

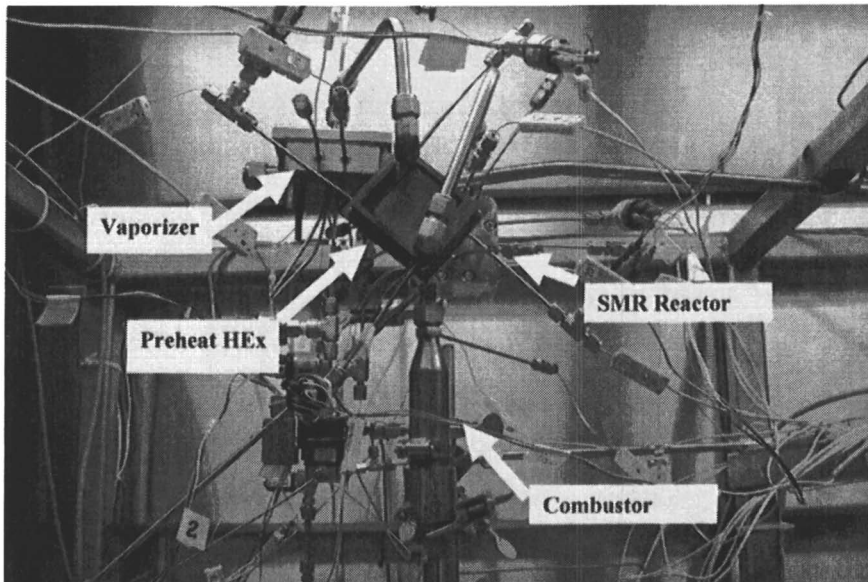
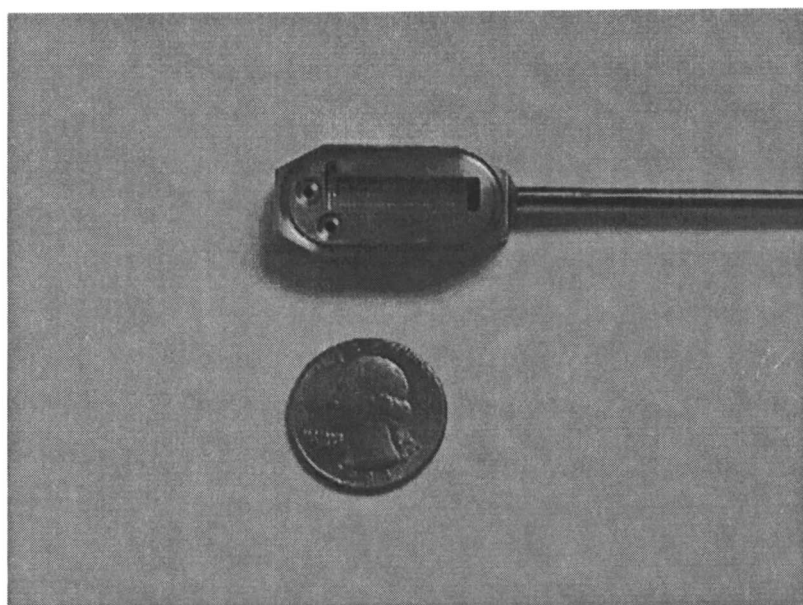


Figure 4. Isooctane reformer hardware photograph

### Other Fuel-Processing Applications

Other government-funded programs at PNNL exploited microchannel technology for portable and small-scale fuel processing. To create a small-scale reactor that would support a 10-W fuel processor (Figure 5), a small device was fabricated with a chamber in which to hold an engineered catalyst and several layers (not shown) to supply reaction heat and to quench the product stream (25). The small reactor was demonstrated for both the butane steam reforming and water gas shift reactions. While reactor sealing problems with the tiny gaskets around the inserted catalyst created challenges in getting reproducible data for the higher temperature butane reforming (600°C), the water gas shift reaction was successfully demonstrated at short contact times (10 to 100 ms) and lower temperatures (250 to 350°C). Additional microchannel reactor demonstrations using water-gas shifts were performed at larger scales (26).

Several fuels were evaluated on an exploratory basis for use in fuel processing applications. In summary, it was found that, given the right temperature and steam-to-carbon ratio, every low-sulfur transportation fuel reformed to high yields of synthesis gas using a Rh-based catalyst (5% Rh/Al<sub>2</sub>O<sub>3</sub> powder) at short contact times. The fuels were evaluated near 1-atm operating pressure and included gasoline, diesel, kerosene, and methane (27, 28). Commercial methane steam reformers (with Ni-based catalysts) require more than 1-second residence time. Results were also collected with a conventional



*Figure 5. Microchannel reactor for 10-W fuel cell*

Ni-based reforming catalyst placed within a microchannel test reactor where the performance was less than half that reported for Rh-based catalysts.

The most interesting result of these screening tests (Table I) was the lack of coke formation—even at very low steam-to-carbon ratios—with steam-to-carbon ratios as low as 1:1 for methane steam reforming at 800°C and 25 ms; no coke was detected on the catalyst surface (23, 28).

**Table I. Multi-Fuel Reforming in a Microchannel Reactor**

<i>Feed (steam:carbon/ reaction temperature)</i>	<i>Residence time (ms)</i>	<i>Conversion (%)</i>	<i>Selectivity (%)</i>
Gasoline (6:1/800°C)	50	95	95 (H <sub>2</sub> )
Diesel (6:1/600°C)	50	100	88 (H <sub>2</sub> )
Methane (1:1/800°C)	25	60	80 (CO)
Kerosene (6:1/600°C)	50	95	95 (H <sub>2</sub> )

### Engineered Catalysts

Engineered catalysts were integral to the evolution of microchannel reactors. Initial work involved evaluating direct washcoating of catalyst onto microchannel walls, but this approach resulted in significant hurdles for rapid development. Therefore, insertable forms of catalysts were explored to decouple the challenges of catalyst development from hardware design and fabrication.

Washcoating catalysts directly onto channel walls in 1996 resulted in poor catalyst adhesion and metal surface passivation, which promoted coke formation. Catalysts were coated onto stainless steel with a gap of less than 500 microns, and partial oxidation reactions of butane, methanol, and methane to form synthesis gas were tested. Catalyst washcoating problems were abated by placing active powders within arrays of microchannels. Immediate performance improvements were observed, including high conversion at relatively short contact times (from 25 to 250 ms).

The first performance breakthrough came from decoupling the problems with washcoating catalysts on the reactor walls from reactor design and operation. In mid 1996, synthesis-gas formation from butane was successfully demonstrated using powder catalysts packed in microchannels at less than 100 ms. At modest reaction temperatures, 400 to 600°C, minimal coke was observed over the run duration (several days).

Further development with powders to produce synthesis gas from the partial oxidation of methane demonstrated high conversion at contact times less than 25 ms. The results also demonstrated non-equilibrium product selectivity (29).

By late 1996, a need for improved engineered catalyst forms emerged to reduce pressure drop and further reduce mass-transport limitations to improve performance. Packed catalyst powders had a relatively low void fraction, less than 40%, and, when placed in microchannels, gave pressure drops from a few psi to many tens of psi per inch as contact time decreased.

An improved engineered structure, an open pore metal foam with a higher void fraction (>80%), was evaluated in 1997 to reduce pressure drop. The foams included porous nickel and stainless steel foams. Ceramic foams also were evaluated, but were found to have lower net porosity than metal foams, giving a higher pressure drop per unit length. The ceramic foams also were more difficult to machine and integrate within microchannels because they had less intimate contact with the channel walls, creating both reactant by-pass and higher contact resistance for heat transfer.

Two approaches to catalyst deployment on engineered foams were pursued: direct active metal washcoating on the porous foam and an initial washcoating of a high surface area support followed by impregnating the active catalyst metal precursor solution to increase the loading of active catalyst metal. The foams were passivated and coated *ex situ* with catalyst before being placed within the microchannel reactor (19).

The engineered foams (Figure 6) were tested for many applications (19). The primary use of foams was a catalyst substrate for the fuel vaporizer project where a dilute hydrogen stream was oxidized to generate a hot gas stream for subsequent fuel vaporization. For this reaction, rapid heat transfer to the wall was not required. The foam structures also were tested with applied catalysts for reforming reactions of methane, butane, and methanol and evaluated for the water-gas shift reaction. The performance results were less dramatic for reforming reactions. The high rate of heat transfer required to drive the endothermic reforming reactions at a few ms was not satisfactory in the engineered foams. The high void fraction desirable for low pressure drop limited the heat-transfer rate through the porous foam.

Additional forms of engineered catalysts for use in microchannel reactors were evaluated in 1997, including aerogels filling the channels, anodizing aluminum walls to form porous layers, and high-surface-area mesoporous silica fibers (> 1,500 m<sup>2</sup>/gm) placed in channels.

A new engineered catalyst form was developed in 1998 with improved thermal characteristics to drive more heat into the endothermic reforming reactions while further reducing pressure drop (27) and are shown in Figure 7. Porous metal fibers or felts were held adjacent to the heat-transfer wall, with a gap for flow above the catalyst form. Metal felts were one example of the new catalyst substrate and contained, on average, less than 20% void and a much higher thermal conductivity to facilitate adding heat to the endothermic reforming reactions. As a further advantage, the thin felt (nominally 0.01 inch thick) structures had sufficient internal large-pore porosity to easily facilitate

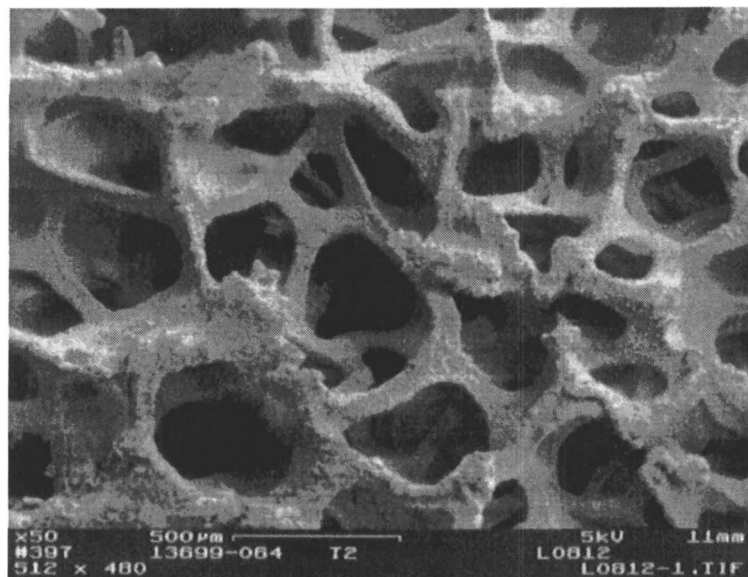


Figure 6. Foam catalyst structure

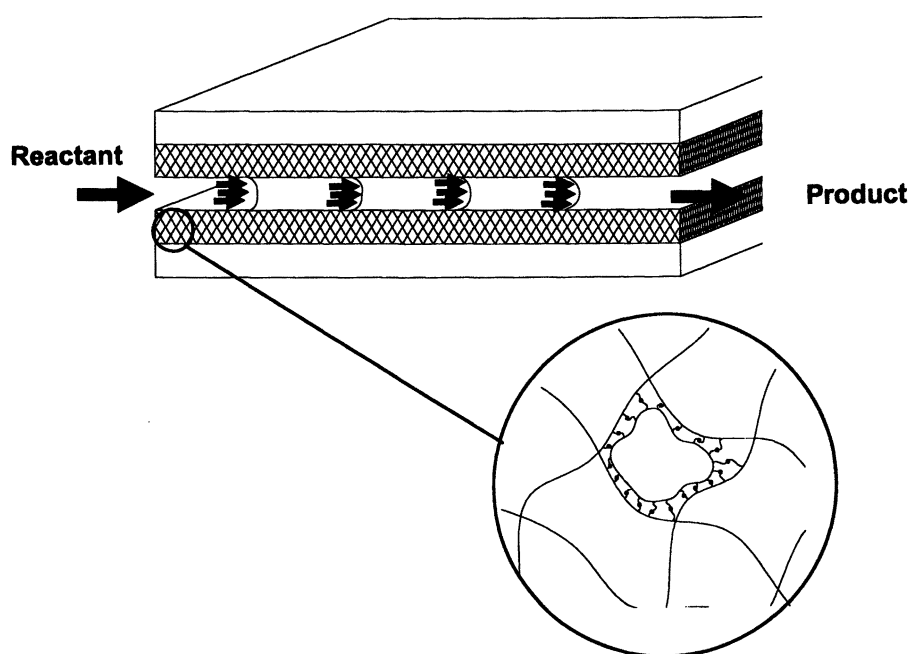


Figure 7. Engineered felt catalysts (0.01 inch thick) held against a microchannel wall with a 0.01-inch open gap for reactant flow

reactant and product diffusion such that the reactants could easily access the internal coated microporous catalyst. A gap was maintained above the felts to create an open laminar flow path for low pressure drop where reactants diffused across stream lines to the surface of the felt catalyst. The reactants further diffused within the macropores of the felt before entering the micropores of the washcoated catalyst. The open channel for flow gave superior pressure drop per length while maintaining sufficient contact with the catalyst. The felts were coated *ex situ* and inserted within the microchannels.

## Fabrication Advances

The design and development of microchannel reactors were driven in large part by fabrication constraints and innovations to overcome those fabrication constraints. Initial reactors were fabricated by machining low-aspect-ratio microchannels in metal plates (where aspect ratio is defined as a microchannel height to width). Plates were bolted together with gaskets to form operational hardware. Electrodischarge machining created a maximum aspect ratio of 4:1 for a 250-micron microchannel (width) in stainless steel. Initial heat-transfer experiments for reactor applications were conducted with the low-aspect-ratio stainless steel channels in 1995 (30). Many gasket materials were used for various applications, including silicone rubber, graphite, and metallic C-rings and O-rings; but, with all gasketed microreactors, leaks were inevitable.

In 1997 and 1998, efforts were underway at PNNL to develop low-cost manufacturing techniques. Features were formed in thin metal sheets that were subsequently diffusion bonded to form microchannel arrays. The small microchannels were no longer machined or formed from plates, but were created from the thickness of the thin sheets themselves. Large or small features could be removed from the thin sheet material, avoiding the need for micromachining. The initial work in making heat exchangers was extended to form multi-layer microchannel reactors that included reactant pre-heat and product quench. In 1998, a microchannel partial oxidation reactor was fabricated from stainless steel. The etched sheets and finished bonded reactor are shown in Figure 8 (31-33).

Fabricating microreactors from metal sheets was a breakthrough on many fronts. Eliminating gaskets represented an opportunity to create robust reactors capable of leak-free high-pressure and long-duration operation. Further, this method of manufacturing created design flexibility. Channel connections and flow paths could be easily added to tailor the reactors to the desired application.

The original stacking and assembly of sheets created heat exchangers and reactors with high-aspect-ratio fins for heat transfer. This style was not optimal because fin efficiency decreased with increasing aspect ratio. With the ability to partially etch sheets, hardware could now be made with interleaved channels

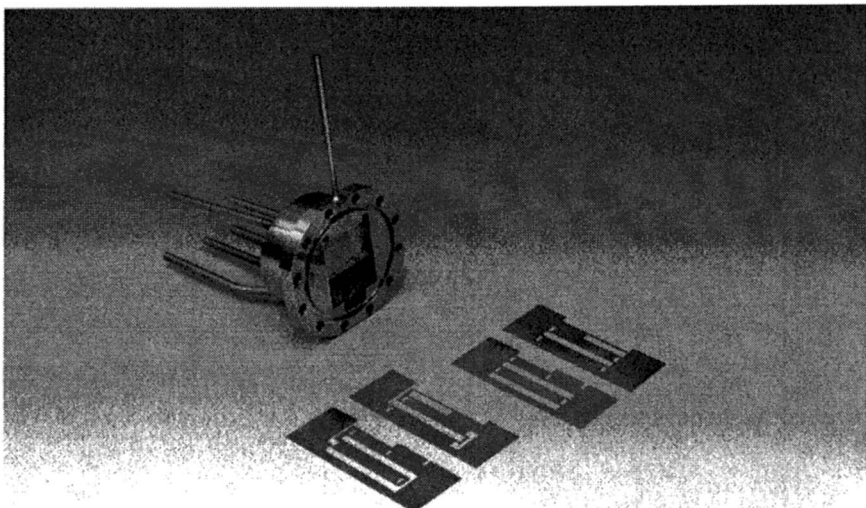


*Figure 8. Stainless steel microreactor for partial oxidation reactions*

where most of the heat-transfer area was on the intervening walls between channels—thus eliminating low fin efficiencies with nickel alloys. Sheets were partially etched to create flow paths, flow-distribution features, and pressure-support structures.

Sheets were formed by etching, cutting, or stamping features in metals. Photochemical machining, which could easily create a partial etch or groove within a thin metal sheet, was commonly used. Diffusion bonding of the metal sheets formed devices with material properties near the parent material. Typical bonding temperatures were nearly two-thirds the metal melting point in absolute temperature. Bonding times and pressures were empirically determined for specific design geometries.

### **Commercial Development at PNNL**

Concurrent with the development of fuel-processing applications, work was initiated on developing commercial systems. Methane steam reforming was

advanced from concept to practical hardware for hydrogen generation to support Fischer-Tropsch chemistry. Reactors were developed for a compact gas-to-liquids process demonstration in 2000 that converted methane to Fischer-Tropsch liquids in a series of microchannel unit operations, including reactors, heat exchangers, and vaporizers. Also in 2000, the development nexus shifted toward scale-up requirements with industrial partners. The development efforts at PNNL bifurcated with some team members moving exclusively to industrial systems and others continuing to develop systems for government clients. More than 15 patents have resulted from the early development work at PNNL.

## Summary

The initial microchannel reactor investigations at PNNL in the 1990s identified and addressed a number of critical issues, including device design, catalyst development, and fabrication methods. The prevailing design methodology evolved to interleaving reaction and heat-exchange microchannels to maximize heat transfer. The interleaved design methodology was enabled by fabrication advancements that enabled hermetically-sealed diffusion bonded devices. Development of catalysts for microchannel reactors evolved with process requirements. Insertable engineered catalyst forms allowed for *ex situ* application and were successfully demonstrated in a number of microchannel reactors.

## Acknowledgments

Development of microchannel technology at PNNL required the hard work, patience, inspiration, and dedication of many staff members, managers, and funding agents. Funding was gratefully received from the U.S. Department of Energy, Office of Transportation Technology, where Steve Chalk and JoAnn Milliken were especially instrumental in promoting microtechnology. Other instrumental funding sources included the Defense Advanced Research Projects Agency, the Army Research Institute, internal lab-directed research and development (R&D) funding from PNNL, internal R&D funding from Battelle, and funding from several private industrial clients.

The development of microchannel technology at PNNL would not have been initiated without the driving efforts of Bob Wegeng and Kevin Drost, who created the vision and inspired an army. The transformation of microtechnology from investigative R&D into a practical commercial reality was a direct result of the confidence, influence, and inspiration of Wayne Simmons, Ben Maiden, and Laura Silva. Developing solutions to the challenging problems described in this chapter was particularly supported by the ingenuity and perspiration of the following staff members: Gary Roberts, Jennifer Zilka-Marco, Sean Fitzgerald, Yufei Gao, Dave VanderWiel, Harley Freeman, Mike LaMont, Steve Perry, Jianli Hu, Cathy Chin, Chunshe Cao, Eric Daymo, and Jeff Marco.

Additional staff members are gratefully acknowledged for their contributions to microchannel reactor development activities at PNNL, including Jamie Holladay, Wayne Wilcox, Max Phelps, Rick Orth, George Deverman, Gary Neuenschwander, Todd Hart, Matt Covert, Dave Brenchley, Lynette Jagoda, Eric Alderson, Dan Palo, Ward TeGrotenhuis, Kriston Brooks, Mike White, Greg Whyatt, Karen Schielke, and Vish Viswanathan. Many others at PNNL were actively involved in developing microtechnology for non-reactive applications and are also acknowledged for creating a collaborative collegial environment that was ripe for innovation. The fabrication breakthroughs and advances at PNNL resulted from the efforts of Pete Martin, Don Stewart, Dean Matson, Wendy Bennett, Daryl Hurley, and others. Other former PNNL staff members who contributed to the evolution of this technology at PNNL and at related technology companies include Chuck Call, Mike Powell, Joe Birmingham, Christine Martin, and Jerry Martin.

The development efforts were enabled by the active support of PNNL management; several are acknowledged for their extraordinary efforts to keep this technology funded, including Eddie Baker, Evan Jones, Eugene Morrey, Jim Buelt, John Sealock, Jack White, Russ Rhodes, Don Boyd, and Mark Morgan. Technology development was assisted by the talents of many interns and students, including Dan Jimenez, Ryan Boger, Bob Rozmiarek, Rob Dagle, Jeremy Dixon, Monesh Kapadia, Dave Lamont, Collin May, Clyde Washington, Kim Priest, Jason Gymerk, and Chrissy Tsemos.

## References

1. Wegeng, R.S.; Call, C.J. ; Drost, M.K. *AIChE*. 1996. New Orleans, LA: AIChE.
2. Wegeng, R.S.; Birmingham, J. C.; Call, J.; Drost, K. ; Friedrich, M.; Kurath, D.; Martin, P. ; TeGrotenhuis, W.; Tonkovich, A. *Proceedings of the First International Conference on Microreaction Technology*. 1997.
3. Ehrfeld, W.; Hessel, V.; Möbius, H. ; Richter, T.; Russow, K. "Potentials and Realization of Microreactors." *Workshop on Microsystem Technology*

*for Chemical and Biological Microreactors.* 1996. Frankfurt, Germany: VCH Verlagsgesellschaft.

4. Lowe, H.; Ehrfeld, W.; Gebauer, K.; Goldbig, K.; Hausner, O.; Haverkamp, V.; Hessel, V.; Richter, T. *Proceedings of the Second International Conference on Microreaction Technology.* 1998.
5. Ehrfeld, W.; Hessel, V.; Lowe, H. *Microreactors: New Technology for Modern Chemistry.* 1st ed. 2000: Wiley, VCH.
6. Ehrfeld, W. *Proceedings of the First International Conference on Microreaction Technology.* 1998.
7. Worz, O.; Jackel, K.P.; Richter, T.; Wolf, T. *Proceedings of the Second International Conference on Microreaction Technology.* 1998.
8. Jackel, K.P. "Microtechnology: Application Opportunities in the Chemical Industry." *Workshop on Microsystem Technology for Chemical and Biological Microreactors.* 1996. Frankfurt em Main, Germany: VCH Verlagsgesellschaft.
9. Ashmead, J.; Blaisdell, C.; Johnson, M.; Nyquist, J.; Perrotto, J.; Ryley, J. US Patent 5,534,328, 1996.
10. Lerou, J.J.; Ng, K.M. "Chemical reaction engineering: a multiscale approach to a multiobjective task." *Chemical Engineering Science,* 1996, 51, 1595-1614.
11. Lerou, J.J.; Harold, M.P.; Ashmead, J. T.; O'Brien, C.; Johnson, M.; Perrotto, J.; Blaisdell, C.T.; Rensi, T.A.; Nyquist, J. *DECHEMA Monographs.* 1996. Frankfurt am Main, Germany.
12. Srinivasan, R.; Hsing, I.M.; Riley, J.; Harold, M.P.; Jensen, K.F.; Schmidt, M.A. *Proceedings of the 1996 Solid-State Sensor and Actuator Workshop.* 1996.
13. Srinivasan, R.; Hsing, I.-M.; Berger, P.E.; Jensen, K.F.; Firebaugh, S.L.; Schmidt, M.A.; Harold, M.P.; Lerou, J.J.; Ryley, J.F. *AIChE Journal,* 1997, 43, 3059-3069.
14. Burns, J.R.; Ramshaw, C.; Bull, A.J.; Harston, P. *Proceedings of the First International Conference on Microreaction Technology.* 1997.
15. Gavrilidis, A.; Konstandinidis, S.; Gobby, D. *Proceedings of the Second International Conference on Microreaction Technology.* 1998.
16. Hagendorf, U.; Janicke, M.; Schuth, F.; Schubert, K.; Fichtner, M. *Proceedings of the Second International Conference on Microreaction Technology.* 1998.
17. Weissmeier, G.; Honicke, D. *Proceedings of the Second International Conference on Microreaction Technology.* 1998.
18. Schubert, K.; Bier, W.; Brandner, J.; Fichtner, M.; Franz, C.; Linder, G. *Proceedings of the 2nd International Conference on Microreaction Technology,* 1998: p. 88-95.
19. Tonkovich, A.Y.; Wang, Y.; Gao, Y. US Patent 6,440,895. 2002.

20. Tonkovich, A.Y.; Roberts, G.; Wegeng, R.; Call, C.; Wang, Y. US Patent 6,2000,536. 2001.
21. Tonkovich, A.Y.; Fitzgerald, S.; Zilka, J.L.; Lamont, M.J.; Wang, Y.; Vanderwiel, D.; Wegeng, R.S. *Proceedings of the Third International Conference on Microreaction Technology: Industrial Prospects*. 2000.
22. Zilka-Marco, J.L.; Tonkovich, A. L.Y.; Michael,J. ; LaMont,S. ; Fitzgerald, P.; Vanderwiel, D.P.; Wang, Y.; Wegeng, R.S. *Proceedings of the Fourth International Conference on Microreaction Technology*. 2000.
23. Wang, Y.; Chin, Y.; Rozmiarek, R.; Johnson, B.; Gao, Y.; Watson, J.; Tonkovich, A.; VanderWiel, D. *Catal. Today*, 2004, 98, 575-581.
24. Fitzgerald, S.P.; Wegeng, R.S.; Tonkovich, A.Y.; Wang, Y.; Freeman, H.; Marco, J.L.; Roberts, G.L.; VanderWiel, D.P. *Proceedings of the Fourth International Conference on Microreaction Technology*. 2000.
25. Daymo, E. ; VanderWiel, D. "Microchannel Fuel Processing for Man Portable Power." *Proceedings of the Fourth International Conference on Microreaction Technology*. 2000.
26. Tonkovich, A.Y.; Zilka, J.L.; LaMont, M.J.; Wang, Y.; Wegeng, R.S. *Chemical Engineering Science*, 1999, 54, 364-371.
27. Tonkovich, A.Y.; Wang, Y.; Fitzgerald, S.P.; Marco, J.L.; Roberts, G.L.; Vanderwiel, D.P.; Wegeng, R.S. US Patent 6,680,044. 2004.
28. Wang, Y.; Tonkovich, A.Y.; VanderWiel, D.P. US Patent 6,607,678. 2003.
29. Tonkovich, A.Y.; Call, C.J.; Zilka, J.L. *Proceedings of the Second International Conference on Microreaction Technology*. 1998.
30. Tonkovich, A.Y.; Call, C.J.; Jimenez, D.; Wegeng, R.S.; Drost, M.K. *AIChE Symposium Series 310*. 1996.
31. Matson, D.; Martin, P.; Stewart, D.; Tonkovich, A.Y.; White, M.; Zilka, J.L.; Roberts, G. *Proceedings of the Third International Conference on Microreaction Technology: Industrial Prospects*. 1999.
32. Martin, P.M.; Matson, D.W.; Bennett, W.D. *Chemical Engineering Communications*, 1999, 173, 245-254.
33. Matson, D.W.; Martin, P.M.; Tonkovich, A.Y.; Roberts, G. *SPIE Proceedings 3514*. 1998.

## Chapter 4

### Parallel Heterogeneous Reactor Systems for Catalyst Screening

**A. Karlsson<sup>1</sup>, D. E. Akporiaye<sup>1</sup>, M. Plassen<sup>1</sup>, Ralph Gillespie<sup>2</sup>,  
and J. S. Holmgren<sup>2,\*</sup>**

**<sup>1</sup>SINTEF Materials and Chemistry, P.O. Box 124, Blindern, N-0314,  
Norway**

**<sup>2</sup>UOP LLC, 25 East Algonquin Road, Des Plaines, IL 60017**

Parallel approaches (Combinatorial / High Throughput) for testing of heterogeneous catalysts provides significant opportunities for more rapidly evaluating complex catalyst systems. An overview of a number of reported systems for parallel screening has been considered in terms of the extent to which such units approximate the capabilities of conventional reactor set-ups. This has highlighted the challenges of screening large arrays of catalyst samples while maximising the degree and detail to which the performance of the samples can be evaluated.

The development, optimization and improvement of catalysts for use in commercially viable processes provides major challenges for scientific research, both with respect to the complexities of the systems being investigated and the practical challenges of the research effort. Commercial catalysts, particularly heterogeneous systems, are often complex multi-elemental, multi-component systems that are usually prepared via multi-step procedures with the conditions under which each intermediate step is performed often impacting performance.

The advent of Combinatorial Chemistry in drug discovery, driven by the need to synthesise and screen a large number of candidates for a variety of applications, has provided a new opportunity for catalyst development and screening. These new parallel approaches (Combinatorial / High Throughput) aim to address the fundamental need to more effectively and efficiently evaluate complex systems to a degree that still provides useful results. The concepts and successes of parallelization of the experimental effort is clearly illustrated in the application of the fully automated synthesizers to unraveling the sequence of the Human Genome:

- Through the use of these systems, the goal of mapping and investigating large complex multi-parameter systems becomes attainable within an accessible timescale, without the need for astronomical expenditure.
- If correctly designed, these parallel systems can be valuable tools that do not compromise in terms of the quality of the information that can be generated.
- The use of these fully automated systems provides unique opportunities for validating and cross-checking the integrity of the results as part of the routine operation.

The goal of the development and application of Parallel Approaches to catalyst development is thus to provide equivalent tools and techniques that significantly expand the ability to explore the large and complex parameter space addressed, while still generating results of an adequate quality in terms of resolution and accuracy. The achievement of this goal is dependent on a good understanding of how to integrate the Parallel Approach into the target activities. An illustration of this is to consider the implementation of such approaches to the development of catalysts for commercialization. As shown in Figure 1, parallel preparation and screening can link to an established workflow, in which bench-scale testing already provides the basis for the careful selection of candidates from a target parameter space, for scale-up to the significantly more costly pilot plant tests.

In a similar manner, screening of arrays of samples can be the basis for selection of candidates from a significantly expanded parameter space for



Figure 1, Integration of parallel screening within established development work flows.

validation at the bench-scale level. The impact of the parallel approach will thus be determined by the degree to which the results obtained from evaluating the performance of arrays of samples aligns with the results obtained from the conventional bench-scale testing. The challenges of addressing this key issue is determined by a variety of factors and will very often be linked to the application being studied.

It is evident that the simultaneous handling of many samples and large amounts of data imposes a need for the development of workflows and associated toolsets that minimise bottlenecks. This applies to all levels of operation, from advanced informatics tools allowing efficient planning of multiple-experiments to such mundane steps as handling and moving sets of samples between stations. A high level overview of typical workflows involved

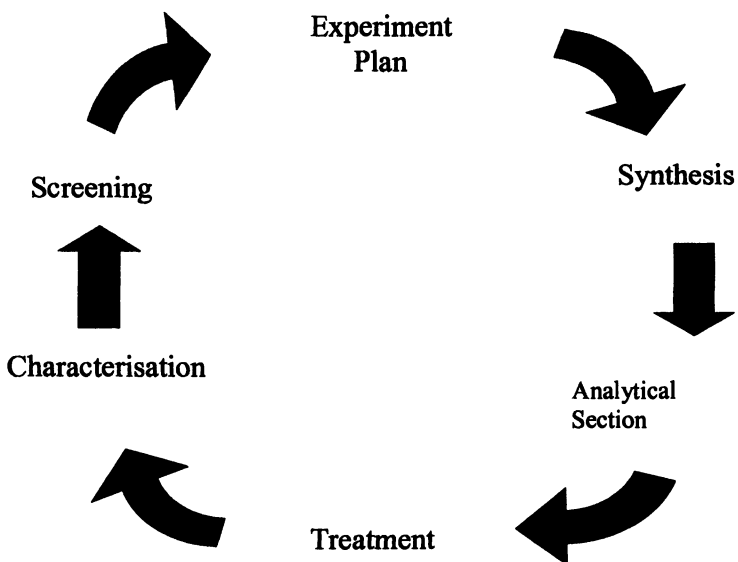


Figure 2. Typical workflow cycle involved in catalyst development, showing some key steps.

in catalyst development is shown in Figure 2. The key components of the workflows are:

- **Informatics systems:** Providing tools for handling information and data flow between the various operations, both in terms of the real-time data flow as well as the historical data.
- **Characterisation systems:** Providing techniques that allow parallel characterization of key properties of the sample arrays being investigated
- **Preparation systems:** Providing tools for the synthesis, formulation and treatment of arrays of samples for evaluation.
- **Reactor systems:** Providing tools for evaluating the performance of sample arrays for particular target applications.

### Parallel Reactor Systems Strategies

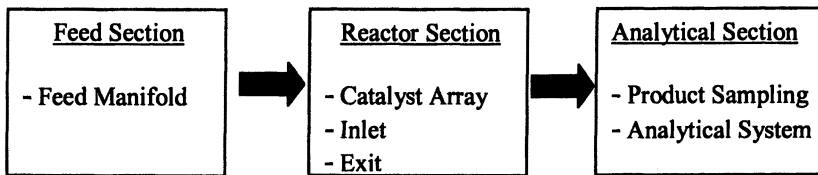


Figure 3. Key sections in a combinatorial test system for catalyst screening

Conventional catalyst test systems are usually configured to be flexible enough to screen catalyst activity as well as control and optimise process parameters (temperature, pressure, WHSV). Such systems normally provide for a well-defined flow pattern across the samples, well-defined interaction between the feed and the catalyst sample, representative sampling of products and appropriate analytical systems with high degree of accuracy and precision to differentiate between components in the products. An idealised case for the implementation of parallel approaches in catalyst screening would be the ability to cost-effectively test thousands of samples within the same timescales, under the same conditions and evaluating relevant properties as obtained under such

conventional bench scale tests. This presents the challenge of providing effective parallel solutions to the key sections of typical reactors system. As shown in Figure 3 these sections can be summarised as been related to a) the parallel feed system for delivering the feed to the catalyst, b) a parallel reactor section containing catalysts that can be efficiently loaded and unloaded, with the feed interacting with the catalysts in a controlled manner to generate an effluent and, c) a parallel sampling / analytical system that analyses the effluent product for evaluation of the activity and selectivity to the relevant product components.

Technical and costs constraints have in general limited how effectively the major reactor sections can be parallelized and for most groups has resulted in a staged approach to the implementation of parallel methodologies to catalyst screening. As shown in Figure 4, with expanding degree of parallelization an increasing level of compromise is made with respect to how each individual catalyst sample is handled. Typically, the highest level of parallelization functions as a primary screening tool, providing a limited degree of individual control of each sample's environment and only a rough assessment of the relative performance of the catalysts in the array. At the opposite end of the scale, the secondary screening tools aim to provide almost the same level of individual control of conditions and detailed assessment of catalyst performance as a bench scale system.

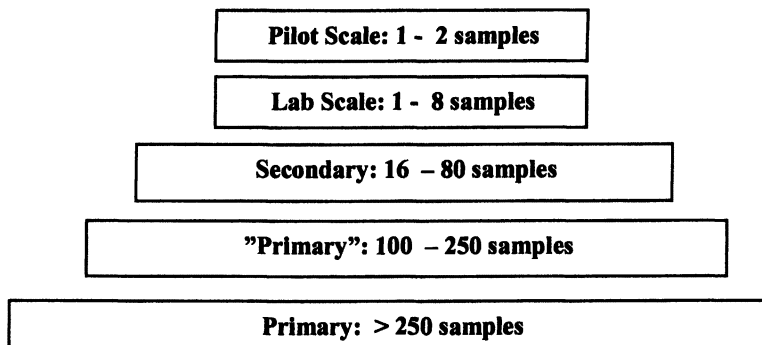


Figure 4. Schematic representation of different levels of parallelisation each step-change involves equivalent compromise in data quality.

Within the published literature, a variety of reactor systems have been presented each in their own way providing technical solutions that are the

product of some form of compromise with respect to the degree of parallelization and the degree of control of test conditions and amount of information obtained for each catalyst. Table 1 provides a systematic overview over the different approaches to screening found in the literature, described in terms of the choices or compromises made for the feed section, reactor section and the sampling/analytical section. In general, the division between primary and secondary screening has been based on a combination of the inherent quality of the data obtained for a chosen configuration rather than the number of samples or the speed of the screening process. In published versions of primary screening it often appears, that the efficient preparation of catalyst libraries has been prioritized, and the “infrastructure” needed to screen performance in an efficient way is adjusted to the constraints of the library.

In one example, a common feed atmosphere is contacted with all samples at the same time, and the products generated mix with the feed atmosphere applied (1). The result is a preliminary screening of large libraries, but without catalyst evaluation in the conventional sense since, space velocity and interaction between the feed and the catalysts are undefined, the feed mixes with the products, and there is potential for cross-talk between different sample positions. In this case the system for analyzing the catalyst performance focuses instead on the heat of reaction as measured in parallel for all samples using IR thermography (1,3).

In an attempt to have a more controlled delivery of feed and analysis of products, an alternative approach tests arrays of samples using a probe which sequentially deliver a flow of feed gas close to each individual sample position (5,6). The same probe at the same time samples through a capillary to a rapid analytical such as an mass spectrometer, which provides detailed analysis of selected components. The speed of this sequential process is sufficiently high to allow screening of relatively large libraries of up to 256 samples. The space velocity, flow pattern and feed/catalyst interaction are still not well-defined in the conventional sense, and therefore the results are qualitative, even though the analytical system is both quantitative and selective. An additional drawback is that catalyst activation or deactivation can not be easily studied.

A means of solving this problem has been by interfacing the sample libraries to feed distribution systems (8,11) allowing a fairly controlled stream of feed to flow over each sample position. After the streams have passed the catalyst samples, one example of a parallel analysis method has involved the use of dyes (11) providing colour changes specific for a particular component. In this case involving the implementation of an offline quantification of the degree of colour change, after completion of the test. Using a sequential configuration (8) the product streams have also been sampled sequentially using a probe that is

**Table 1, Overview of typical configurations of Primary Reactor Units**

<i>Feed delivery section</i>	<i>Sample/reactor section</i>	<i>Sampling/analytical section</i>	<i>Reference</i>
Parallel feed system with individual feed control to each sample. No restriction on feed compositions	Samples in well-controlled environment with ideal flow pattern for interaction of feed and catalyst	Isolation of effluents from each reactor. Parallel analytical system. Analytical system selective and accurate	Idealised System
Common feed to all samples	Arrays of samples or pellets in open flat configuration. Single temperature oven system	Parallel analysis of secondary properties from sample activity (heat of reaction). No analysis of product components.	1, 2, 3, 4
Sequential delivery of feed to each individual sample via a single feed line feed.	Arrays of samples or pellets in open flat configuration. Single temperature oven system.	Sequential sampling and analysis of product from individual sample positions.	5, 6, 7
Parallel feed distribution systems with similar flows to each sample	Arrays of samples or pellets in open flat configuration. Single temperature oven system	Sequential sampling and analysis of product from individual sample positions.	8, 9
Parallel feed distribution systems with similar flows to each sample	Arrays of reactor tubes interfaced to feed delivery system. Open reactor "exit" configuration. Single temperature oven system.	Isolation of effluents from each reactor. Parallel detection system. Simple detection and quantification of selected components	10, 11, 12

positioned close to each sample position. A capillary inside the probe samples to a mass spectrometer as an analytical device. The samples are semi-separated by well-shaped or tubular environments to reduce cross-talk between neighboring sample positions. The samples are present as pellets of tablets, and by-pass of the samples is expected, however, quite reproducible ranking have been reported for libraries of up to 80 samples.

With respect to published systems for secondary screening, examples in Table 1 show that priority has been given to designs that approximate much more closely, the conditions in conventional lab-scale test systems for interaction between the feed and the catalyst, and to maintain close control on process variables. As a consequence, the sample arrays are not easily interfaced to the test systems in a simple manner, and “loading” of samples into environments which approximate conventional plug-flow reactors is the common approach. The compromises made allow more control over the flow of feed and interaction between the feed and catalysts, the sampling is representative with no cross-talk between different streams and the analytical techniques are often the same as in conventional set-ups. The major differences between the examples reported have related to the degree in which individual and independent control of process conditions for each reactor has been implemented, and the extent to which the analytical solutions are parallel but providing more detailed information than achievable in primary screening configurations or involve the sequential sampling of the reactor arrays.

For full flexibility in experimental design, independent control of space velocity, feed composition, temperature and pressure for each individual sample, with sample/analysis at the same time on stream for all samples in order to be able capture activation deactivation differences. One example reports a 49-parallel reactor in which a common feed stream is split equally to each individual reactor using restrictor elements (14). The reactors are of plug-flow type, and the product streams are sequentially analyzed by chromatographic techniques. With a reduced number of reactors, reports of 16 reactor (19,16) and 6 reactor (18) parallel system have been able to provide a greater degree of control. In these cases measurement and/or control of temperature, pressure, flow of gas feed and liquid feed is carried out individually for each reactor

### **Parallel Screening system interfacing with scale-up**

Our strategy for secondary screening systems has been to establish a parallel reactor unit that allows the screening of a significant number of samples, combined with the flexibility and freedom for control and optimization of key process conditions. Thus the design is able to operate with 48 samples in parallel, while still maintaining accuracy close to conventional bench scale test units. A schematic overview of the overall unit, shown in Figure 5, illustrates the major sections of the reactor, which is constructed of separate modules allowing a

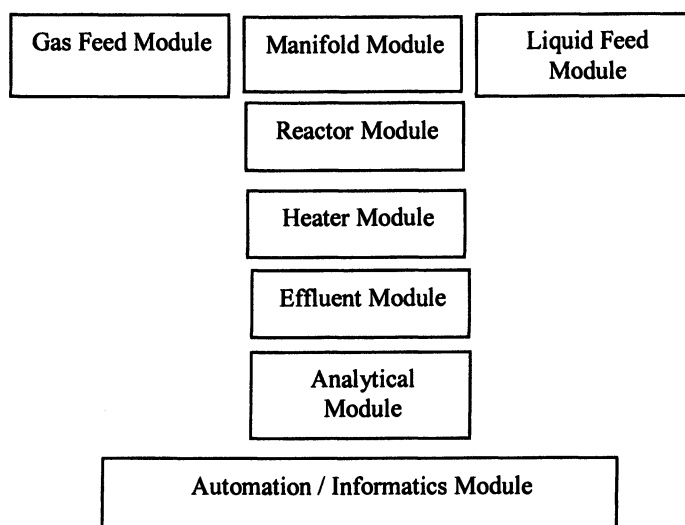


Figure 5. Schematic overview of the modular structure of the test system. A variety of test systems can be configured combining different options or sub-sets from the schematic presentation.

Table 2, Overview of typical configurations of Secondary Reactor Units

<i>Secondary System</i>	<i>Feed delivery section</i>	<i>Sample/reactor section</i>	<i>Sampling/analytical section</i>	<i>Reference</i>
Idealised system	Parallel feed with individual control of flow to each sample. No restriction on feed compositions	Arrays of reactor tubes with ideal flow pattern through sample. Individual temperature	Isolation of effluents from each reactor, sampled to parallel analytical system. Analytical system selective and accurate	Idealised System
A	Parallel feed distribution systems with similar flows to each sample	Arrays of reactor tubes with ideal flow pattern through each sample. Single temperature oven system	Sequential sampling and analysis from isolated effluent streams.	10, 13, 14, 15
B	Parallel feed with individual control of flow to each sample. No restriction on feed compositions	Arrays of reactor tubes with ideal flow pattern through each sample. Single temperature oven system	Sequential sampling and analysis from isolated effluent streams.	16, 17, 18
C	Parallel feed with individual control of flow to each sample. No restriction on feed compositions	Arrays of reactor tubes with ideal flow pattern through each sample. Single temperature oven system	Isolation of effluents from each reactor, sampled to parallel analytical system. Detection and quantification of selected components	19

variety of alternative configurations or solutions to be implemented, dependent on the needs of the particular application or process. The reactors are arranged in a standardised 6x8 matrix and carefully designed for plug-flow operation with temperature measurement in the catalyst bed of each reactor and allowing catalyst loadings in the range of 70-200 microliters.

The flexibility of this modular structure allows operation over a range of pressures and temperatures, while still maintaining parallel operations such as opening, loading and closing of all 48 reactors. In one modification, reactor pressures can be controlled independently for six subsections comprising 8-reactors and this can be linked to a feed manifold that can provide different feed mixtures to each of the six subsections. The flexibility of operation has also been implemented to allow different sampling / analysis strategies including a range of sampling sequences for selecting reactor effluent for analysis at predetermined times. This allows a variety of analytical options to be implemented, for example, using GC to obtain detailed analysis relatively light components from all 48 samples in less than 20 minutes or more complex higher boiling effluent streams in under 30 mins, or combination of methods such as mass spectrometer and gas chromatography.

To control and monitor all aspects of catalytic test runs, the hardware is interfaced to automation / informatics modules providing fully unattended operation of the reactor unit. The LabView based automation has been implemented with the same modular structure as the hardware, with the philosophy of making all functionality under automated control accessible to a sophisticated Run Protocol. Thus, within each step of a multi-step test protocol changes can be made to among other aspects, temperatures, flows, pressures, sampling sequences, analytical methods and even safety alarm triggers. The status of the test and test conditions for each of the 48 reactors may also be monitored in real-time, with the opportunity to pause, make adjustments and restart the test protocol as needed.

The test systems described above have been used on a routine basis for a number of years and have been applied to a variety of applications. One example that illustrates the success of integrating such parallel screening units as part of catalyst development is the discovery and optimisation of a new catalyst for C5 and C6 isomerisation of naphtha to high octane products (20). High octane products are favored by low reaction temperatures, however, current low temperature processes using chlorinated alumina catalyst are sensitive to certain impurities and require purification of the feed. The more robust zeolite based catalysts, however, are not as active and thus require a higher operating temperature, with the associated penalties in lower product octane. Using the development of a new catalyst as the target, a discovery program was initiated generating a library of materials based on variation of the composition and the intermediate treatment steps, as shown in Figure 6. This catalyst library

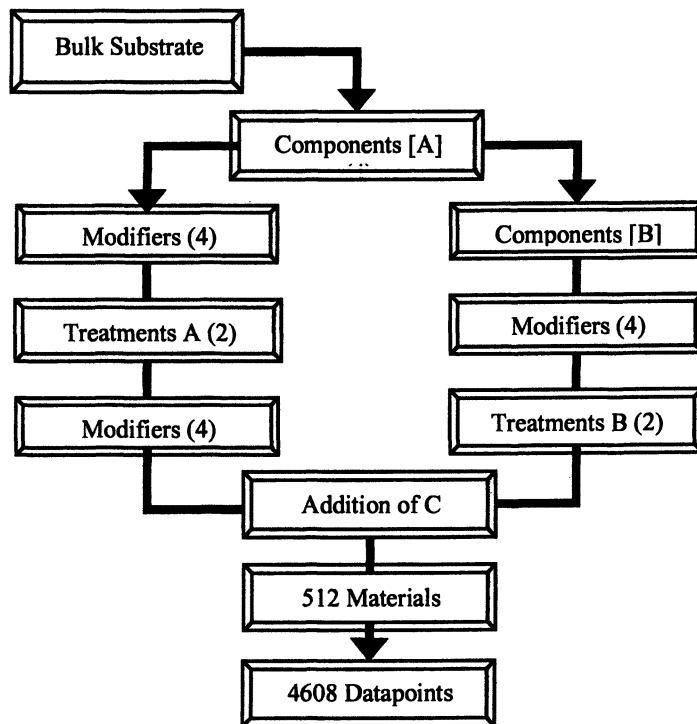


Figure 6. Schematic presentation of the generation of the 512 membered library using different components and treatment procedures. Additional, testing under varying process conditions leads to mapping of “compositional and conditional” parameter space.

consisted of a total of 512 different catalyst materials. Systematic screening of the library included varying process parameters and resulted in a total program generating more than 4500 data points within “compositional and process conditions” parameter space.

The ability to rapidly and extensively map composition and test conditions revealed a number of materials with superior performance as shown in Figure 7. Three leads were isolated, all showing a significant improvement relative to the reference system and subsequent Pilot plant testing confirmed the results.

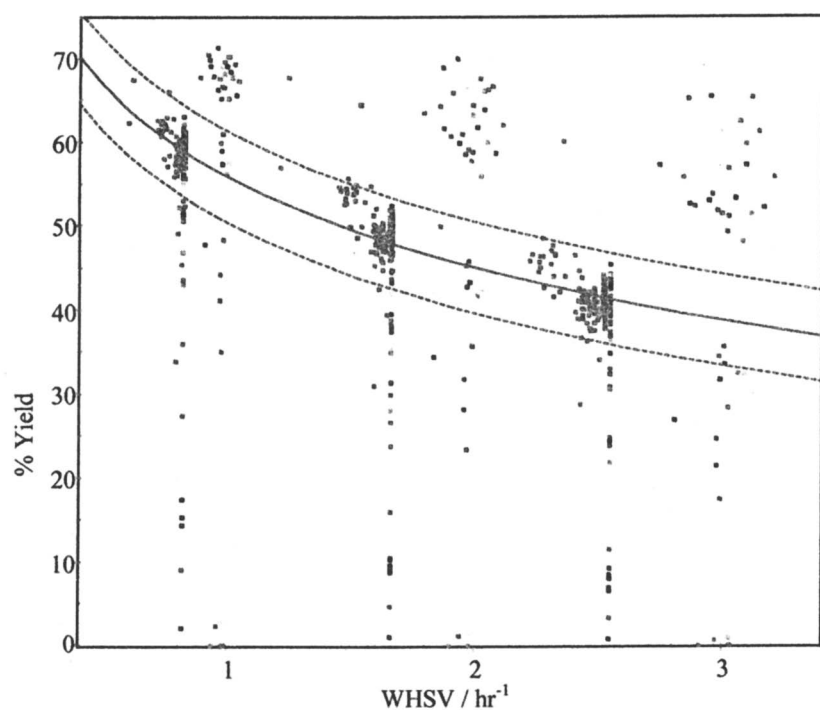


Figure 7, Overview from parallel screening of library of catalysts for C5 isomerisation. Data represent variation in catalyst composition, treatment and test conditions. Dashed lines outline reference zone from reference catalyst system included in all test runs.

The data obtained in the detailed study of modifier elements were used in to build fundamental understanding and were the basis of the discovery of catalysts that have a substantial performance advantage relative to the zeolite based catalysts in octane number (3 times RONC number), improved selectivity to 22DMB and higher conversion of naphthenes to paraffins. An additional advantage was that one of the catalysts was a “drop-in” into existing low capital reactors.

It is evident from such studies that a Parallel test system can operate quite efficiently even in the discovery phase of a research program. This provides the advantage of allowing subsequent optimization to take place in the same test system and infrastructure using the same informatics and software for handling the data. Since all data obtained are of a sufficient quality for more detailed interpretation, all historical data from a research program can be used in subsequent modeling work to build theoretical understanding. Further, optimization experiments which were earlier associated with bench-scale experiments can be performed, and speed up the way to the marketplace.

## Conclusion

Parallel approaches are increasingly being applied to the testing of heterogeneous catalysts as a means of more rapidly evaluating complex catalyst systems. These approaches have in general been categorized into “primary” and “secondary” screening systems. The latter aim to provide detailed information on defined arrays of catalyst samples, in a testing mode that approaches that of conventional catalyst testing units. The former aim to evaluate significantly larger arrays of catalyst samples with a range of solutions compromising significantly on the degree to which they approximate conventional systems. Several research groups appear to have targeted working on limited size of sample arrays, though there is a great variation in the extent to which these systems approximate the mode of conventional systems, with some cases applying essentially primary screening “solutions” to a rather limited number of samples.

Our approach to parallel catalyst screening has been to have the flexibility allowing optimisation of process conditions with an accuracy equivalent to conventional units, but applied to an array of 48 samples. This strategy of integrating detailed catalyst screening and flexible process control within a large parallel array has shown success in the discovery of new commercial catalysts, the results of which have been successfully validated at all levels from the miniaturised parallel scale to final commercial operation.

## References

1. Saalfrank, JW; Maier, WF, *Comptes Rendus Chimie*, **2004**, 7, 483- 494
2. Gracia, F; Li, W; Wolf, EE, *Catalysis Letters*, **2003**, 91, 235-242
3. Reichenbach, HM; McGinn, PJ, *Applied Catalysis A-General*, **2003**, 244, 101-114
4. Su, H; Yeung, ES, *Applied Spectroscopy*, **2002**, 56, 1044-1047
5. Yaccato, K; Hagemeyer, A; Lesik, A; Volpe, A; Weinberg, H, *Topics in Catalysis*, **2004**, 30&31, 127-132
6. Paul, JS; Urschey, J; Jacobs, PA; Maier, WF; Verpoort, F, *Journal of Catalysis*, **2003**, 216, 110-119
7. Lucas, M; Claus, P, *Applied Catalysis A-General* **2003**, 254, 35-43
8. Senkan, S; Ozturk, S; Krantz, K; Onal, I, *Applied Catalysis A-General*, **2003**, 254, 97-106
9. Miyazaki, T; Ozturk, S; Onal, I; Senkan, S, *Catalysis Today*, **2003**, 81, 473-484
10. Guram, A; Hagemeyer, A; Lugmair, CG; Turner, HW; Volpe, AF; Weinberg, WH; Yaccato, K, *Advanced Synthesis & Catalysis*, **2004**, 346, 215-230
11. Busch, OM; Hoffmann, C; Johann, TRF; Schmidt, HW; Strehlau, W; Schuth, F, *JACS*, **2002**, 124, 13527-13532
12. Watanabe, Y; Umegaki, T; Hashimoto, M; Omata, K; Yamada, M, *Catalysis Today*, **2004**, 89, 455-464
13. Wang, H; Liu, ZM; Shen, JH, *Journal of Combinatorial Chemistry*, **2003**, 5, 802-808
14. Kiener, C; Kurtz, M; Wilmer, H; Hoffmann, C; Schmidt, HW; Grunwaldt, JD; Muhler, M; Schuth, F, *Journal of Catalysis*, **2003**, 216, 110-119
15. Hahndorf, I; Buyevskaya, O; Langpape, M; Grubert, G; Kolf, S; Guillon, E; Baerns, M, *Chemical Engineering Journal*, **2002**, 89, 119-125
16. Serra, JM; Corma, A; Farrusseng, D; Baumes, L; Mirodatos, C; Flego, C; Perego, C, *Catalysis Today*, **2003**, 81, 425-436

17. Potyrailo, RA; May, RJ, *Review of Scientific Instruments*, **2002**, 73, 1277-1283
18. Pérez-Ramirez, J; Rob J. Berger, RJ; Mul, G; Kapteijn, F; Moulijn, JA, *Catalysis Today*, **2003**, 81, 425-436
19. Hendershot, RJ; Lasko, SS; Fellmann, MF; Oskarsdottir, G; Delgass, WN; Snively, CM; Lauterbach, J, *Applied Catalysis A-General*, **2003**, 254, 107-120
20. Spring 2004 NPRA and Spring 2004 AIChE and 2004 ARTC

## Chapter 5

### Microreactor Research and Development at Louisiana Tech University

#### Fabrication of Silicon Microchannel Reactors for Catalyst Studies on Conversion of Cyclohexene and Syngas to Alkanes

S. Zhao<sup>1</sup>, V. S. Nagineni<sup>1,2</sup>, Y. Liang<sup>1</sup>, J. Hu<sup>1</sup>, K. R. Aithal<sup>1</sup>,  
N. V. Seetala<sup>3</sup>, J. Fang<sup>1</sup>, U. Siriwardane<sup>2</sup>, R. S. Besser<sup>1</sup>,  
K. Varahramyan<sup>1</sup>, J. Palmer<sup>1</sup>, R. Nassar<sup>1</sup>, and D. Kuila<sup>1,2,\*</sup>

<sup>1</sup>Institute for Micromanufacturing and <sup>2</sup>Chemistry Program, Louisiana  
Tech University, Ruston, LA 71272

<sup>3</sup>Department of Physics, Grambling State University, Grambling, LA 71245

Design and fabrication of microreactors and catalyst development of two reactions are described. A prototype reaction - gas phase conversion of cyclohexene to cyclohexane and benzene - has been studied extensively. The conversion is significantly improved (>90%) using silica sol-gel impregnated catalyst. An industrially relevant reaction on syngas conversion (CO+H<sub>2</sub>) to alkanes using mixed metal catalysts encapsulated in alumina or silica sol-gel has also been investigated. A high conversion of CO (~73 %) in the presence of a catalyst promoter with high selectivity to propane (~80%) has been achieved. Characterization of the catalysts, design of experiments on syngas conversion, and development of a parallel array microreactor system for fast and effective screening of catalysts are discussed in this chapter.

## Introduction

Process miniaturization and microreaction technology provide opportunities for improving process capability and control in chemical/biochemical synthesis allowing safer and more efficient chemical/biochemical kinetic investigations. Compared to normal scale reactors, microreactors have the following advantages: decrease of linear dimensions, increase of surface to volume ratio, fast and efficient process development, decreased potential of environmental impact, and increased safety. The large surface-to-volume ratios of the micro channels inhibit gas-phase free-radical reactions and improve heat transfer for exothermic reactions. Microreactors' narrow channels and thin walls also make them suitable candidates for studying potentially explosive reactions with minimum risks.

Microreactors, "Lab-on-a-chip" device (Figure 1), in general, consist of micro channels, with lateral dimensions on the order of micrometers, etched on metal, glass, silicon, or other substrates *via* photolithography or other techniques [1-3]. The physical design of the device can be the size of a dime containing ~ 200 or more channels depending on their width (Figure 2). Silicon is usually a material of choice because of well developed photolithography and etching techniques used in microelectronics industry [2].

Microreactor technology is relatively new but has a significant industrial interest as judged by the number of issued patents (<100). It provides relatively simple and quick means towards commercialization of a process [4-8]. The economic production of large numbers of microreactors enables the shift from the present production paradigm of batch process and "scaling up" to a new paradigm of continuous process and "numbering up", i.e., running numerous microreactors in parallel for mass production [9] and catalyst screening [10, 11]. This would lead to short lead times from laboratory catalyst development to industrial production as well as the ability to produce chemicals on demand on-site. The potential exists for every chemical process to be miniaturized to increase process safety as well as overall efficiency and productivity...

At the Institute for Micromanufacturing (IfM) of Louisiana Tech University, we have been doing microreactor research for ~ 10 years including simulation, design and microfabrication of the reactors. The conversion of cyclohexene to benzene and cyclohexane has been chosen as a model reaction [12-14]. In addition, two reactions of industrial significance are being investigated: Fischer-Tropsch synthesis to higher alkanes [15, 16] and preferential oxidation for CO amelioration in hydrogen fuel cell feeds. While the former is part of this paper, the latter is presented in another chapter of this book [17].

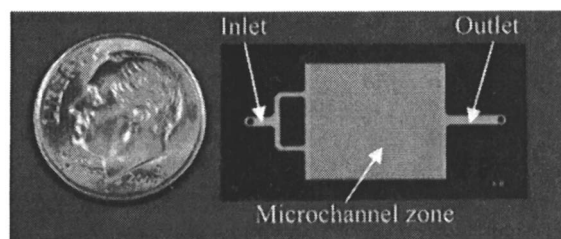


**Figure 1.** Top view of a silicon microreactor fabricated at Institute for Micromanufacturing, Louisiana Tech University.

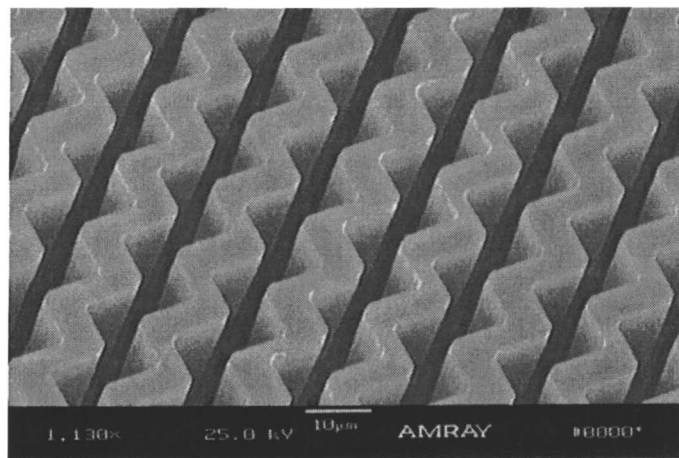


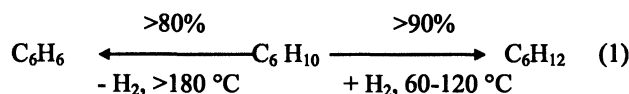
**Figure 2.** SEM image of 5  $\mu\text{m}$  channel Si-microreactor fabricated using Inductively Coupled Plasma (ICP) dry etching.

### History of Microreactors Developed at IfM

Microreactors were initially fabricated at IfM using a <110> silicon wafer by anisotropic wet etching and comprised of a system of 10 channels - 10  $\mu\text{m}$  deep, 500  $\mu\text{m}$  wide, and 50 mm long [18]. Platinum was sputtered on the channels to catalyze the gas-liquid heterogeneous reaction with a minimal conversion (9%) of cyclohexane to benzene. A finite difference model was developed to determine the conversion for a given length, depth, and pressure drop by taking into account flow regime through Knudsen number, the reaction probability, and the number of collisions. Simulation results suggest that channel depth has a profound effect on conversion of cyclohexane to benzene [18].

Dehydrogenation of cyclohexane to benzene is an endothermic reversible reaction with an equilibrium conversion of 18.9% at 200°C. However, the conversion can be driven beyond equilibrium to 99%, if the hydrogen is selectively removed from the system using a palladium membrane (Figure 3) [19]. This structure allowed for 50% exposure of the palladium membrane (3 to 6  $\mu\text{m}$  thick) with the rest being supported by silicon braces. The model, mentioned above [18], showed that the efficacy of the membrane was also sensitive to channel depth, operating pressures and catalyst activity.

After successful fabrication of 500 $\mu\text{m}$  wide channels, 100  $\mu\text{m}$  and 5 $\mu\text{m}$  wide channels with 100 $\mu\text{m}$  depth were subsequently developed using ICP (Inductively Coupled Plasma) dry etching (Figure 2). The high resolution and anisotropy of ICP etching have produced microchannels with high surface-to-volume ratio and vertical channel walls [20]. Using these reactors, hydrogenation and dehydrogenation of cyclohexene (see below), as a prototype reaction, have been investigated. Conversion of cyclohexene with sputtered Pt is over 95% with high selectivity to cyclohexane and benzene as shown in equation (1) [21,22].



### Microreactor Design and Fabrication

We have developed microreactors with different dimensions and geometry, with a very high depth to width (aspect) ratio over the years [15, 16]. Besides straight and zigzag channels, column and novel sine-wave channels have also been fabricated. Recently, we have performed microfluidic modeling studies in different micro channels using CoventorWare software to understand the effect

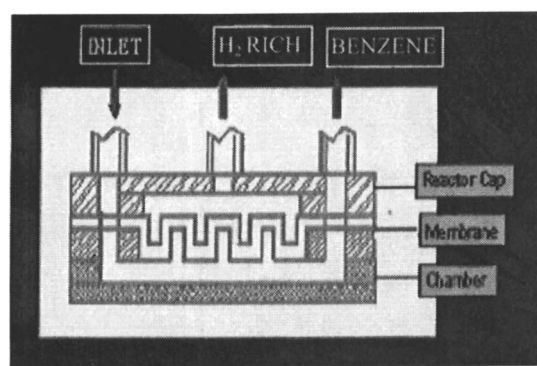


Figure 3. A palladium membrane microreactor for dehydrogenation of cyclohexane.

of surface area on catalysis and the residence time of reactants in the micro channels. Figure 4 shows the effect of channel geometry on fluid flow in 5  $\mu\text{m}$  straight and zigzag channels. Under similar inlet flow rates, the flow velocity in straight channels is much greater than in the zigzag channels, yielding a lower residence time. Also, the velocity vector in Y direction is much higher in zigzag channels producing higher surface fluid interaction.

Fabrication follows simulation of a desired design. Currently, the microreactors are made from a four-inch diameter, 500  $\mu\text{m}$  thick, double side polished silicon wafer using two main processes: photo-lithography and ICP etching. The lithography process used to make the microreactor is similar to the one used in the integrated circuit (IC) industry [23]. The details of this procedure is described elsewhere [24].

A typical fabricated microreactor is 3.1 cm x 1.6 cm, with a reaction area of 1.3 cm x 1.2 cm and consists of vias (the holes through the wafer) for feed inlet, and product outlet and numerous micro channels of 5-50  $\mu\text{m}$  width and 100  $\mu\text{m}$  depth (Figure 1). After the channels are coated with the catalyst (described later), the reactor is covered with a Pyrex glass 7740 by anodic bonding [25-27].

### Experimental Apparatus

For a typical reaction in a microreactor, additional peripheral equipment are needed to control flow, temperature, and pressure, and for the acquisition of product distribution in the effluent stream (Figure 5). The silicon reactor chip interfaces to a steel holding block fitted with an O-ring sealed gas connector to the inlet and outlet openings on the bottom side of the chip. The block also has resistive heating elements and a thermocouple for temperature control of the reactor. Gases are fed to the block by mass flow controllers. Digital pressure sensors are situated in the inlet and outlet streams to monitor pressure drops. Experiments with liquid reactants, such as cyclohexene, were conducted by bubbling a carrier gas, such as argon. The flow and reactor temperature settings were monitored and controlled by a PC with LabView software.

The reactant gases flow through the *via* into the inlet area and the microchannels with the effluent leaving the reactor through another *via* where it is diluted with helium (He) gas. The effluent is then analyzed using a Stanford Research Systems mass spectrometer where the progress of the reaction is monitored.

### Catalyst Study

The development of a catalyst and its support is an important area of our research [15]. Higher surface area materials such as sol-gel increase the catalyst

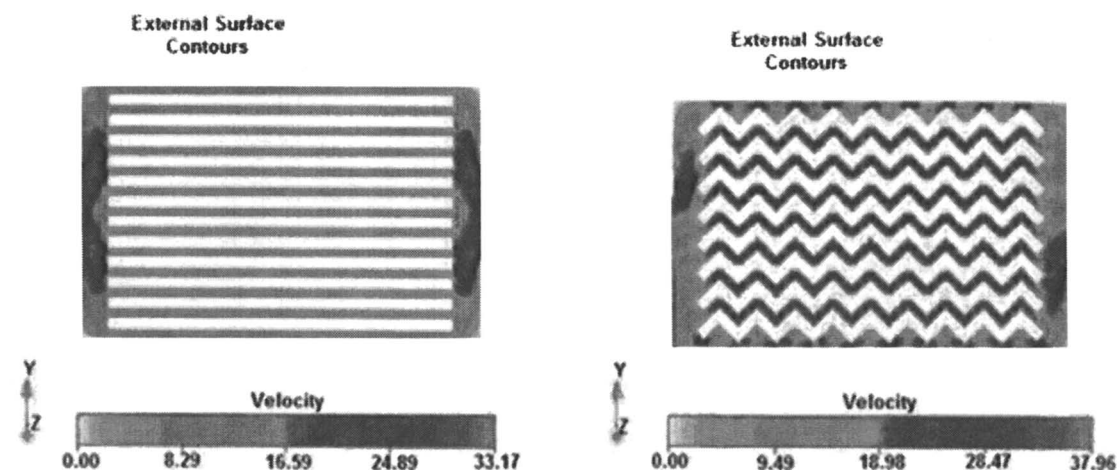


Figure 4. Numerical modeling of fluid flow in  $5\mu\text{m}$  straight channels (left) and zigzag channels (right) using CoventorWare software.

activity by increasing the number of active sites located on the surface of pure metal.

General: We have used both physical and chemical methods for the preparation of the catalysts/catalyst supports. While the physical method involved sputtering, the chemical procedure included sol-gel and ion impregnation techniques. The chemical methods are preferred as they increase the surface area of the catalyst and lower the deposition cost compared to that of sputtering. The catalyst supports were prepared using alumina and silica sol-gel precursors.

Three sol-gel methods - dip coating, spin coating, and drop coating - have been used for the preparation of catalyst and its support inside microreactor channels [24]. Lithography techniques can be used to perform selective deposition of sol-gel to the desired regions of the microreactor [22]. In general, the catalyst/support is deposited in the microchannels either by mixing the support with catalyst precursors or by sol-gel coating followed by catalyst deposition (sputtering or impregnation). The properties of sol-gel matrices are significantly affected by the experimental conditions such as calcination temperature and the time of aging.

### Cyclohexene Conversion Reaction

The prototype reaction on conversion of cyclohexene was studied in the presence of a platinum catalyst at different reaction conditions to compare the efficiency of two types of catalyst preparations. For sol-gel impregnation, tetraethoxysilane ( $\text{Si}(\text{OC}_2\text{H}_5)_4$ ) was chosen as the precursor of silica due to its ease of preparation and compatibility to microfabrication [28-31]. The silica sol-gel was prepared in an acidic medium as the surface area is expected to be approximately ten times higher than that obtained in a basic environment [30]. Platinum was then deposited on the catalyst support in the form of  $\text{Pt}^{+2}$  by ion impregnation followed by reduction in an hydrogen atmosphere to  $\text{Pt}^0$  [23, 33].

The specific surface area of silica supported Pt catalyst using BET (Brunauer-Emmett-Teller) method is  $\sim 292 \text{ m}^2/\text{g}$ . The high surface area is due to porous structure of the silica sol-gel particles with an average size of 50-80 nm in diameter as observed using Atomic Force Microscopy (AFM). Also, the X-ray Photoelectron Spectroscopy (XPS) sputter depth profiling of the catalyst/support film indicates uniform Pt concentration to a depth of at least 5  $\mu\text{m}$  thickness of the film.

A series of experiments were designed and performed in 100  $\mu\text{m}$  wide channel reactors to compare the efficiency of sputtered catalyst with that of impregnated catalyst in sol-gel matrix. The temperatures and flow rates for reactants were varied as shown in Table 1. Cyclohexene conversion on impregnated Pt remains around  $\sim 90\%$  at all flow and temperature settings,

whereas it is less than 70% for sputtered Pt catalyst (Figure 6). This is presumably due to the porous structure of sol-gel catalyst supports, which increases reactant-catalyst interaction surface significantly. In contrast, for sputtered Pt, the only reaction interface is the flat surface of microchannels which causes lower conversion of cyclohexene. Cyclohexene is converted to cyclohexane or benzene depending on the reaction conditions. While sol-gel supported Pt at temperature below 120°C produces cyclohexane, benzene is exclusively formed at temperatures higher than 150 °C (not shown here) [24]. These results show that catalyst screening and desired product distribution can be achieved easily using microreactors.

**Table 1. Different Reaction Conditions for Testing Platinum Catalyst Using Cyclohexene Conversion Reaction.**

\* Standard cubic centimeters per minute (sccm)

Design point	Temp (°C)	H <sub>2</sub> (sccm)*	Ar with cyclohexene (sccm)	Contact time (sec)
1	62.5	0.82	0.28	5.659
2	62.5	0.82	0.82	3.795
3	62.5	0.28	0.82	5.659
4	125	0.55	0.55	5.659
5	187.5	0.28	0.28	11.115
6	187.5	0.82	0.28	5.659
7	187.5	0.82	0.82	3.795

#### Syngas to Alkanes (Fischer-Tropsch Synthesis)

After a thorough investigation of the prototype reaction of cyclohexene to cyclohexane and benzene, we have started catalyst studies on the Fischer-Tropsch synthesis of higher alkanes from syngas (CO+H<sub>2</sub>).



*Catalyst used : Fe, Co; Catalyst support: Alumina or Silica sol-gel*

As the sol-gel support improves cyclohexene conversion ( shown above) , our current studies have focused on sol-gel medium for catalyst deposition . For syn-gas reaction, aluminum tri-sec butoxide and tetraethylorthosilicate are used as the precursors for the preparation of alumina and silica sol-gel, respectively. The basic step involves acid hydrolysis followed by polycondensation to form a highly porous sol-gel network [34]. Iron (II) nitrate and cobalt (II) nitrate were incorporated into alumina or silica sol- gel solution to obtain the desired

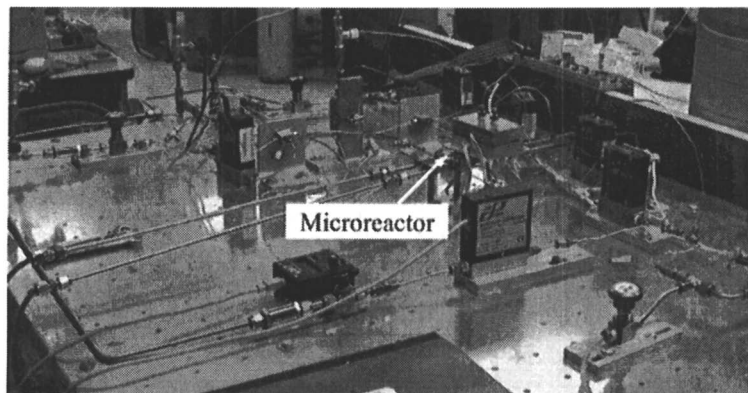


Figure 5. Microreaction setup system at Institute for Micromanufacturing, Louisiana Tech University.

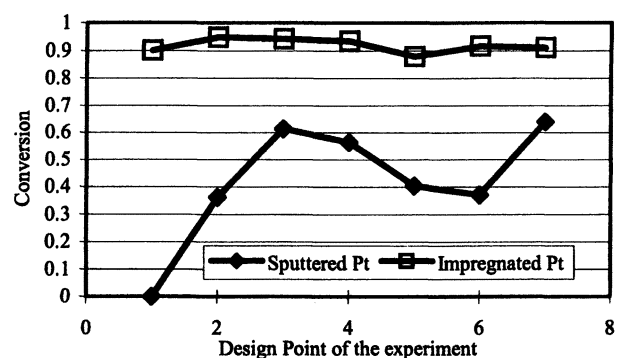


Figure 6. Conversion of cyclohexene as a function of different reaction conditions (see Table 1).

composition. The mixture of sol-gel and catalyst is deposited into the microchannels of the reactor by wash coating and reduced to the metallic form in an atmosphere of H<sub>2</sub>.

*Characterization of the Catalyst and its Support*

The BET surface area measurements were performed for sol-gel encapsulated Fe/Co catalyst as described above for cyclohexene reactions. The sol-gel encapsulated catalysts yield an average specific surface area of 285 m<sup>2</sup>/g for alumina and ~ 300 m<sup>2</sup>/g for silica. This high surface area is due to high porosity of alumina and silica sol-gel supports observed in their AFM images (Figure 7 and Figure 4 of the other chapter in this book). It can also be inferred from Figure 7 that the diameter of the alumina sol-gel granules is ~ 50- 100 nm. It is expected that the diameter of encapsulated metallic Fe and Co particles would be less than 50 nm.

In order to optimize the solgel preparation and deposition processes in the microchannels of the reactor, SEM studies were carried out as shown in Figure 8. We have noticed that sol-gel can be deposited evenly in the 25  $\mu$ m channel reactors compared to that in the narrow 5  $\mu$ m channels (not shown). An Energy Dispersive X-ray (EDX) spectrometer coupled with the SEM was used to study the elemental composition of sol-gel encapsulated catalyst (Fe and Co) deposited in the reactor. Although the intended metal composition of Fe and Co in the reaction is 24 % (12% each), the EDX results indicate that only 5-7 % of total metal catalyst is loaded onto sol-gel prepared from metal nitrate solution. However, the metal loading can be improved significantly to around 16-18% using commercially available nanoparticles of iron oxide (10-40 nm) and synthesized cobalt oxide (15-30 nm) as the catalyst precursors [15]. The EDX data suggest that the metal loading using nitrates is quite less compared to the direct use of oxide nanoparticles.

*Conversion of CO to Alkanes*

Conversion of CO to alkanes has been studied both in alumina and silica sol-gel coated in 5  $\mu$ m and 25  $\mu$ m channel reactors. As the alumina sol-gel deposition in the 5  $\mu$ m channel reactors is not uniform, we have done most of our studies in 25  $\mu$ m channel reactors [35]. The conversion of CO is ~ 53 % in 25  $\mu$ m channel reactors containing Fe-Co-Al<sub>2</sub>O<sub>3</sub> at 230°C, H<sub>2</sub>: CO ratio of 3:1, total flow rate of 0.8 sccm and contact time of 0.994 second. Similar studies were done with silica sol-gel encapsulated in 25  $\mu$ m channel reactors in the presence of Ru-promoter to yield ~62 % conversion (Figure 9). We have achieved CO conversion of ~ 73 % using ruthenium promoter under different reaction conditions that will be reported elsewhere [35]. However, the selectivity for alkanes is not affected by the channel geometry or the type of

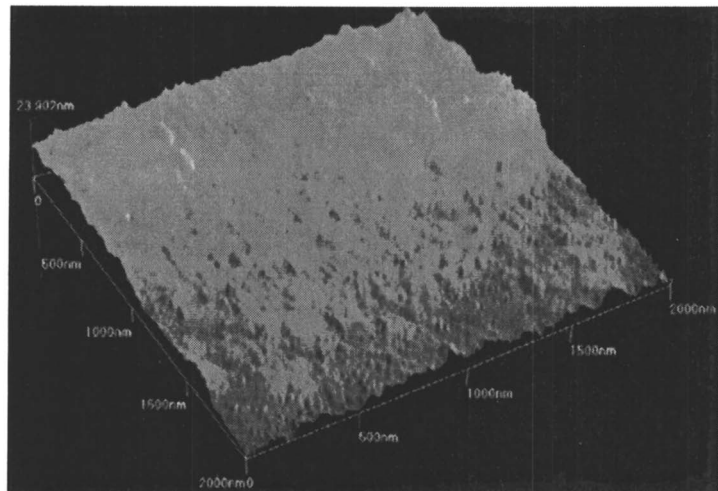


Figure 7. AFM image of alumina sol-gel encapsulated Fe/Co catalyst (on glass) for syngas conversion to alkanes.

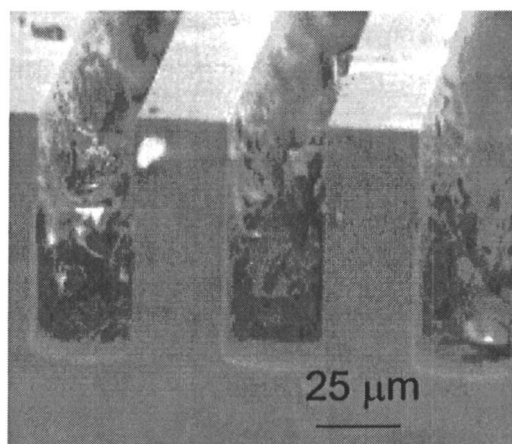


Figure 8. SEM image of silica sol-gel deposited in 25  $\mu\text{m}$  channel reactors.

catalyst support. Propane has been the major product with a selectivity of ~ 80% under all reaction conditions.

To determine the nature and activity of the catalyst at different stages, magnetization studies were performed using Vibrating Sample Magnetometer (VSM). The magnetic behaviors of the sol- gel encapsulated Fe-Co catalyst coated microreactors after calcination, after reduction with hydrogen and after syngas (CO+H<sub>2</sub>) reaction are shown in Figure 10. The catalyst in as-deposited reactor shows paramagnetic behavior mostly coming from the iron and cobalt oxides. As Fe and Co oxides are reduced to pure metals, ferromagnetic behavior is observed. The saturation magnetization of the ferromagnetic component can be used to estimate a lower limit of ~ 40 % for the reduction efficiency at higher temperatures. The ferromagnetic behavior, however, diminishes in the post catalytic reaction sample, as Fe and Co are forming inactive compounds. The magnetic data indicate that about 85% of the catalyst has become inactive after 25 hrs of catalytic reaction.

#### *Comparison to Macroscale Reactions*

In parallel to the microreactor research at the IfM, Chemistry Program is also involved in the macroscale synthesis of higher alkanes from syngas. The process involves a modified sol-gel/oil drop method [36] to prepare Co/Fe/Cu nanoparticles that are incorporated into mesoporous  $\gamma$ -alumina and silica granules [37]. The efficacy of CO/H<sub>2</sub> conversion was investigated with the Co/Fe (12%) metal loaded  $\gamma$ -alumina granules in both gas and slurry phase reactors. The conversion of CO after 15 hrs is higher in the slurry phase (~80 %) compared to that observed in the gas phase (~30%) at a lower rate (0.67 sccm) compared to flow rate of 0.8 sccm for microreactors. In the gas phase, we have observed a variety of hydrocarbons such as CH<sub>4</sub>, C<sub>2</sub>H<sub>6</sub>, C<sub>3</sub>H<sub>8</sub>, isoC<sub>4</sub>H<sub>10</sub>, C<sub>4</sub>H<sub>10</sub>, isoC<sub>5</sub>H<sub>12</sub>, C<sub>5</sub>H<sub>12</sub> with very little benzene. This is in contrast to the alkanes observed in microreactors. It is not clear, at this stage, why alkanes higher than propane are not observed in our reactions in the microreactors coated with sol-gel coated Fe/Co catalyst. It is possible that the lower flow rates through the granules increase the residence times in the macroscale reaction and may have a significant effect on the formation of higher alkanes.

In contrast to reaction in the gas phase reactor, the ratio of CO/H<sub>2</sub> seems to affect the alkane distribution in the slurry phase reactor. At low CO/H<sub>2</sub> ratio, the major product is methane. With an increase in CO/H<sub>2</sub> ratio, higher alkanes are produced. We have not yet observed hexane in the product mixture and speculate that it is converted to benzene. We also notice that CO/H<sub>2</sub> ratio of 1:1 produces wider distribution of alkanes and may be suitable for fuel production with nanoparticles of Co/Fe encapsulated in alumina [38]. Currently we are

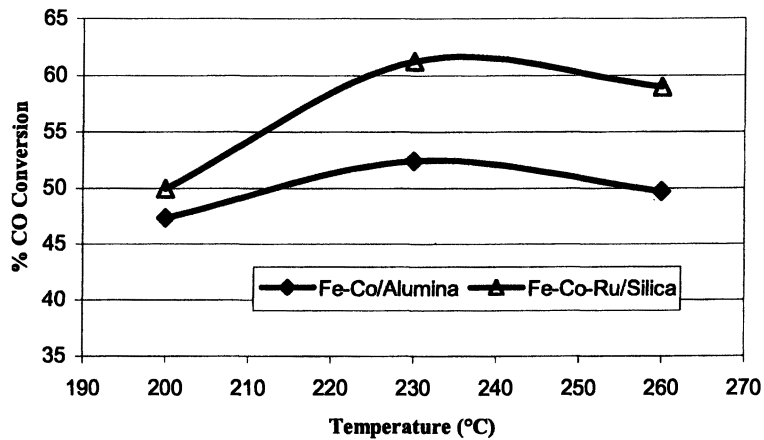


Figure 9. CO conversion in 25  $\mu\text{m}$  channel reactors using alumina and silica as catalyst supports.

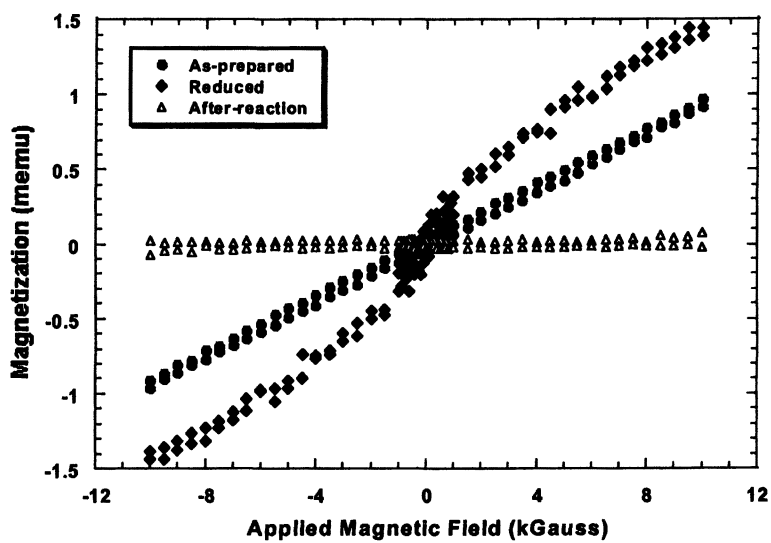


Figure 10. Magnetization studies of sol-gel encapsulated Fe/Co catalyst before and after the syngas reaction.

investigating alkane distribution when alumina is gradually replaced by silica in the granules.

*Empirical Modeling and Statistical Analysis for Syngas Conversion in a Microreactor*

In order to have a better understanding of surface catalysis and to optimize conversion of CO in microreactors, we have considered design of experiments using response surface methodology developed by Box and Wilson in 1951 [39,40]. The main goal of the Fischer-Tropsch (F-T) synthesis experiment, based on the central composite design, [41] is to obtain higher CO conversion with greater propane ( $C_3H_8$ ) selectivity.

Three independent variables or factors were considered important for this reaction: the total flow rate ( $x_1$ ) in sccm,  $H_2 : CO$  ratio ( $x_2$ ), and temperature ( $x_3$ ) in C. Here, total flow rate relates to residence time and the  $H_2 : CO$  ratio relates to the stoichiometry of the chemical reaction. The conversion of CO ( $Y_1$ ), and the selectivity to  $C_3H_8$  ( $Y_2$ ) were considered as the dependent variables. The purpose of using experimental design is to find the treatment combination  $\mathbf{x} = (x_1, x_2, x_3)$  for which the conversion of CO and the selectivity of  $C_3H_8$  are maximized.

First order regression models were fitted to conversion and selectivity of experimental data based on the cube portion of the central composite design. Results of the analysis showed no quadratic lack-of-fit of the linear model for CO conversion, but did show a quadratic lack-of-fit for propane selectivity. This indicates that the surface of CO conversion is planar, but the surface of selectivity for propane ( $C_3H_8$ ) is not. As a result, a second-order regression for propane selectivity was fitted to the full second-order central composite design (shown below). It shows that  $H_2 : CO$  ratio ( $x_2$ ) has the largest effect on propane selectivity. Canonical analysis on the second-order regression model of propane selectivity showed that the total flow rate,  $H_2 : CO$  ratio, and temperature combination at the point (0.60, 4.51, and 218.16) gave a maximum selectivity of propane ( $C_3H_8$ ) equal to 88.25%. Additional experiments are underway to verify this prediction.

$$Y_4 = 0.841 + 0.035BL_1 - 0.014BL_2 - 0.014x_1 + 0.04x_2 + 0.011x_3 - 0.005x_1^2 \\ - 0.013x_2^2 - 0.028x_3^2 + 0.004x_1x_2 - 0.005x_1x_3 - 0.011x_2x_3$$

### Parallel Array of Micro-reactors

We have described all reactions using a single microreactor in the sections above. We are currently developing a parallel array of reactors to screen catalysts simultaneously as well as scale up microreactions [42]. Precise process control, flexible experiment operations and low operation/maintenance cost can provide distinct advantages of this system. This procedure can hasten catalyst development with automatic control and data acquisition.

### Conclusions

Microreactor technology based on silicon has been successfully developed at IfM of Louisiana Tech University over past ~ 10 years. Microreactors with different geometries and channel structures have been microfabricated using general photolithography, wet/dry etching (ICP etching) and anodic bonding. A micro reaction system has been built with flexibility and compatibility to different microscale reactions. A prototype reaction, catalytic hydrogenation and dehydrogenation of cyclohexene, has been studied extensively with different preparation of the catalyst and its deposition in the microchannels. An industrially significant reaction such as syngas conversion to higher alkanes has been realized with ~70% conversion of CO and ~80% selectivity to propane using microreactors. Other commercialization opportunities using microreactor technology are currently being explored.

**Acknowledgement:** We thank Drs. F. Jones and T. Cui, Mr. S. Ouyang, Mr. A. Potluri, and Ms. A. Zheng for their help in this work. This research was supported by Board of Regents ( to R. S. Besser), NSF-EPSCoR, and DOE ( DE-FG26-00NT40836).

### References

1. Ehrfeld W.; Hessel V.; Lowe H. *Microreactors: New Technology for Modern Chemistry*, WILEY-VCH, Weinheim, Germany, 2000 ISBN3-527-29590-9.
2. Madou M. *Fundamentals of Microfabrication: The Science of Miniaturization*, Second Edition CRC Press, 1997 ISBN 0-8493-9451-1.
3. Lowe H.; Hessel V.; Mueller A. *Pure and Applied Chemistry* (2002), 74(12), 2271-2276.
4. VanderWiel D. P.; Zilka-Marco J. L.; Wang Y.; Tonkovich A. Y.; Wegeng R. S. *AIChE 2000 Spring National Meeting*, Atlanta, GA.
5. Tonkovich A. Y.; Zilka J. L.; Lamont M. J.; Wang Y.; Wegeng R. S. *Chemical Engineering Science* 1998.

6. TeGrotenhuis W. E.; Wegeng R. S.; Vanderwiel D. P.; Whyatt G. A.; Viswanathan V. V.; Schielke K. P. *AICHE 2000 Spring National Meeting*, Atlanta, GA.
7. Pattekar, A. V.; Kothare, M. V. *Journal of Microelectromechanical Systems* (2004), 13(1), 7-18.
8. Mukherjee S.; Hatalis M. K.; Kothare M. V. *Annual Meeting Archive - American Institute of Chemical Engineers*, Indianapolis, IN, United States, Nov. 3-8, 2002 (2002).
9. Quiram, D. J.; Ryley J. F.; Ashmead J. W.; Bryson R. D.; Kraus D. J.; Mills P. L.; Mitchell R. E.; Wetzel M. D.; Schmidt M. A.; Jensen K. F. *Micro Total Analysis Systems 2001, Proceedings □TAS 2001 Symposium, 5th*, Monterey, CA, United States, Oct. 21-25, 2001 (2001).
10. Ajmera S. K.; Delattre C.; Schmidt M. A.; Jensen K. F. *Studies in Surface Science and Catalysis* (2003), 145(Science and Technology in Catalysis 2002), 97-102.
11. Ajmera, S. K.; Delattre C.; Schmidt M. A.; Jensen K. F. *Journal of Catalysis* (2002), 209(2), 401-412.
12. Roberts J. T.; Madix R. J. *Surface Science* (1990), 226(3), L71-L78.
13. Hunka D. E.; Land D. P. *Book of Abstracts, 214<sup>th</sup> ACS National Meeting*, Las Vegas, NV, 1997 September 7-11.
14. Hassan S. A.; Sadek S. A.; *Studies in Surface Science and Catalysis* (1996), 100(Catalysts in Petroleum Refining and Petrochemical Industries 1995), 407-18.
15. Kuila D.; Nagineni V.S.; Zhao S.; Induduri H.; Liang Y.; Potluri A.; Siriwardane U.; Seetala N.; Fang J. *Proceeding of Materials Research Society (MRS) Annual Spring Meeting* (2004), April 25-16, 2004, San Francisco, CA.
16. Nagineni V. S.; Zhao S.; Liang Y.; Siriwardane U.; Seetala N. V.; Fang J.; Palmer J.; Kuiila D. Manuscript submitted.
17. Zhao S.; Hu J.; Kuila D.; Besser R. S.; Nassar R.; Palmer J. *another chapter in this book* 2004.
18. Francis J.; Qing D.; Fang J.; Cui T. *Proceedings of the 4th International Conference on Microreaction Technology (IMRET IV)*, Atlanta, GA, AIChE, 2000.
19. Zheng A.; Francis J.; Fang J.; Cui T. *Proceedings of the 4th International Conference on Microreaction Technology (IMRET IV)*, Atlanta, GA, AIChE, 2000.
20. Shin W.C. McDonald J.A.; Zhao S.; Besser R.S. *Proceedings of the 6th International Conference on Microreaction Technology (IMRET VI)*, New Orleans, LA, ed. I. Renard, AIChE, 2002.
21. Surangalikar H.; Besser R. S. *Proceedings of the 6th International Conference on Microreaction Technology (IMRET VI)*, New Orleans, LA, ed. I. Renard, AIChE, 2002.

22. Zhao S.; Besser R. S. *Proceedings of the 6th International Conference on Microreaction Technology (IMRET VI)*, New Orleans, LA, ed. I. Renard, AIChE, 2002.
23. Okuzaki S.; Okude K.; Ohishi T. *Journal of Non-crystalline Solids*, vol. 265, pg 61-67.
24. Zhao S. PhD Dissertation, Louisiana Tech University, Ruston, LA 2003.
25. Fung C. D.; Cheung P. W.; Ko W. H.; Fleming D. G. *Micromachining and Micropackaging of Transducers* (Amsterdam: Elsevier Science) p 41
26. Holloway P. H.; Sebastain J.; Trottier T.; Swartand H.; Petersen R. O. *Solid State Technol.* August 47
27. Kovacs G. T. A. *Micromachined Transducers Sourcebook*, McGraw-Hill Press, ISBN 0-07-290722-3.
28. Siriwardane U.; Seetala N. V.; Vegesna N. S.; Satyendra V.; Goduguchinta R.; Luurtsema K.; Jones C.; Leonard J. J. *Catal.*, 2004 submitted.
29. Golemme, G.; Facchini, G.; Gleria, M.; Guarino, L.; Drioli, E. *Phosphorus Research Bulletin* (1999), 10 736-741.
30. Lobnik, A.; Wolfbeis, O. S.; Majcen L.; Mechal A. *Zbornik Referatov s Posvetovanja Slovenski Kemijski Dnevi, Maribor, Slovenia*, Sept. 18-19, 1997 (1997), 621-626.
31. Kurauchi, Y.; Ukeguchi, S.; Egashira N.; Ohga K. *Kichin, Kitosan Kenkyu* (1996), 2(2), 144-145.
32. Pazzuconi G.; Bassi G.; Millini R.; Perego C.; Perego G. *Eur. Pat. Appl.* (1996), 27 pp.
33. Lopez T.; Bosch P.; Moran M.; Gomez R. *React. Kinet. Catal. Lett.*, 52 (1), 65-71, 1994.
34. Pecchi G.; Morales M.; Reyes P.; *React. Kinet. Catal. Lett.*, 61 (2), 237-244, 1997.
35. Haas-Santo K.; Fichtner M.; Schubert K. *Forschungszentrum Karlsruhe*, Postfach 3640, 76021 Karlsruhe, Germany.
36. Nagineni V. S.; Zhao S.; Siriwardane U.; Seetala N. V.; Fang J.; kuila D. Manuscript in preparation.
37. Wang Z.; Lin Y. S. *Journal of Catalysis* 174, 43-51 (1998)
38. Tong B.; Siriwardane U.; Seetala, N. V.; Akundi M. N.; Zhong Z. *MRS Annual Fall Meeting* (2001), November 25 - December 1, 2001, Boston, MA.
39. Siriwardane U.; Barnett B. G.; Satyendra V.; Radersl S.; Seetala N. V. *Division of Inorganic Chemistry, Nanoscience , ACS National meetings*, Anaheim CA March 2004.
40. Siriwardane U.; Seetala N. V.; Barnett B.G.; Vudarapu S.; Anderson S.; Jones C.; Leonard J. J. *Catal.* Manuscript in preparation.
41. Box G.E.P.; Draper N.R. *Empirical Model-Building and Response Surfaces*, John Wiley & Sons, New York, 1987.
42. Box G. E. P.; Wilson K. B. *Journal of the Royal Statistical Society*, 1951 Series B 13, 1-45.
43. Hu J. PhD Dissertation, Louisiana Tech University, Ruston, LA 2004.
44. Fang J.; Cao W. U.S.Patent filed, 2003.

## **Chapter 6**

### **Engineered Catalysts for Microchannel Reactor Applications**

**Yong Wang<sup>1</sup>, Bradley R. Johnson<sup>1</sup>, James Cao<sup>1</sup>, Ya-Huei Chin<sup>1</sup>,  
Robert T. Rozmiarek<sup>1</sup>, Yufei Gao<sup>1</sup>, and Anna Lee Tonkovich<sup>2</sup>**

**<sup>1</sup>Pacific Northwest National Laboratory, P.O. Box 999,  
Richland, WA 99352**

**<sup>2</sup>Velocys, 7950 Corporate Boulevard, Plain City, OH 43064**

Porous metal substrates with improved mass and heat transfer characteristics were used to design engineered catalyst structures for microchannel reactor applications. Metal substrates have advantages such as high thermal conductivity, but are difficult to integrate with refractory metal oxides often used as catalyst supports. This problem can be mitigated by incorporating an interfacial layer between the porous metal substrate surface and the catalyst layer which improves the catalyst adhesion, prevents metal surface corrosion, and minimizes the undesired side reactions catalyzed by the underlying metal substrate. The interfacial layer can be either directly grown as a native oxide layer on Al containing alloys and/or coated as a metal oxide layer using chemical vapor deposition (CVD). The described interfacial design provides a flexible method to develop engineered catalysts for a variety of microchannel reactor applications, particularly for highly endothermic or exothermic reactions under corrosive reaction conditions. Here, methane steam reforming is used as an example to demonstrate potential advantages of this approach.

Microchannel reactors have a sandwich-like multi-layer structure consisting of a large number of closely spaced channels with a gap of less than 1mm. The narrow gap reduces heat and mass transport distance and greatly enhance heat and mass transfer efficiency. Heat transfer coefficients in microchannel reactors are as high as 10,000-35,000 W/m<sup>2</sup>K (1,2) compared to 100-700 W/m<sup>2</sup>K (3,4,5) in conventional reactors. Such high heat transfer coefficients coupled with the high surface-to-volume ratio achievable in microchannel reactors permit the process intensification and unprecedented temperature control, particularly for highly endothermic or exothermic reactions (6,7,8,9,10,11). To achieve advanced performances of microchannel reactors, novel reactor designs (10,12), development of catalysts specifically for microchannel reactor applications (13,14) and the optimization of the catalyst structures to provide synergistic mass and heat transfer improvement (15) are key. Conventional catalysts are either in the forms of extrudates or pellets to reduce the pressure drop (Figure 1a). The internal transport distances range from several milimeters to centimeter range. It is not surprising to obtain low catalyst effectiveness factors for highly endothermic reactions such as methane steam reforming (16) or to not be able to fully take advantages of highly active catalysts for exothermic reactions.

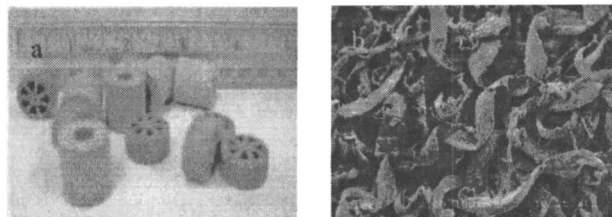


*Figure 1. a) Conventional catalyst pellets b) Scanning electron micrographs of FeCrAlY felt substrate used in microchannel reactor. (See page 1 of color insert.)*

Structured catalyst supports such as foams and monoliths have been widely used for gas-phase reactions, such as catalytic converters, due to their low pressure drop and high catalyst utilization efficiency. Metal-based structured supports, as shown in the scanning electron micrograph in Figure 1b, have additional advantages which are desired for microchannel reactor applications. First, a metal-based device typically have a higher thermal conductivity (Table 1) and their superior strength and toughness permit the use of thinner pieces, thus realizing an overall better heat transfer. Secondly, the sponge-like mechanical properties of a metal-based support structure allow convenient sealing of catalysts in a reaction channel via mechanical contact. Thirdly, the closely matched thermal expansion between the structured metal supports and the

housing reaction channel minimizes cracking of the structured supports which, in turn, minimizes gas channeling around the structured supports at higher reaction temperatures. Additionally, catalyst utilization is high due to a thin layer coating of catalyst (typically less than 20 $\mu$ m) on metal substrate as opposed to internal transport distances of up to centimeter range in conventional catalysts. Metal based structured substrates have thus attracted research interest. Pestryakov *et al* prepared metal foam supported transition metal oxide catalysts for the oxidation of n-butane (17,18). Kosak (19) examined several approaches to disperse precious metals on various metal foams where the surface was pre-etched with HCl solution, and reported that electroless deposition provides the best adhesion of precious metals to the foam supports. Podyacheva *et al* (20) also synthesized foam metal supported LaCoO<sub>3</sub> perovskite catalyst for methane oxidation.

**Table I. Thermal conductivities for selected materials at specific temperatures.**

Material	Thermal Conductivity	Temperature
FeCrAlY foam	1.1 W/m K	400 K (21)
FeCrAlY bulk	16 W/m K	298 K (22)
304 Stainless Steel	15 W/m K	298 K (23)
Inconel	15 W/m K	298 K (23)
Copper	393 W/m K	400 K (23)
Nickel	90.7 W/m K	300 K (23)
Silver	425 W/m K	400 K (23)
Gold	311 W/m K	400 K (23)
Aluminum	240 W/m K	400 K (23)
Alumina	30 W/m K	373 K (23)
Fused Quartz	1.5 W/m K	373 K (23)

Metal based structured supports have their own challenges when compared to ceramic based structured supports for catalyst applications. The principle challenges are related to catalyst adhesion, metal support corrosion, and metal support catalyzed side reactions. For example, conventional catalysts are typically prepared on high surface area refractory metal oxides which have lower thermal expansion coefficients than the metal alloy substrates. When integrated inside a microchannel reactor, thermal expansion mismatch between substrate and catalyst can lead to delamination of the ceramic catalyst supports at high temperatures, or after thermal cycling. Additionally, more aggressive conditions such as high temperatures are often exploited in microchannel reactors to take advantage of their enhanced heat and mass transfer so that increased space time yields can be achieved. Such aggressive reaction conditions often accelerate the oxidation or corrosion rate of metal-based structured supports, thus reducing

their useful lifespan. And finally, metal surfaces are not necessarily inert, and can often catalyze undesired reactions under reaction conditions. One example is methanation catalyzed by Ni based alloy/metal surfaces in the presence of CO and hydrogen.

The ideal engineered catalytic structure incorporates the superior thermal conductivity and toughness properties of a metallic substrate combined with the superior refractory, corrosion and oxidation resistances of ceramics. This can be accomplished by applying ceramic coatings to metallic substrates. This paradigm is often used for such diverse applications as thermal barrier coatings on engine parts, low friction coatings on bearing surfaces, and wear resistant coatings on cutting tools. Success in these coatings is achieved by design and control of the metal-ceramic interface. For catalytical applications, the requirement for the ceramic coating is that it must be firmly adherent to the metal substrate, accommodate the thermal expansion of the substrate, increase the adhesion of the ceramic catalyst support washcoat, sufficiently cover the metal substrate to eliminate undesired side reactions, and minimize the metal corrosion under severe reaction conditions.

Previous research in overcoming these technical hurdles has been sparse. For example, growing native oxide layers using aluminum containing alloys<sup>24</sup> or caging catalyst particles inside the metal mesh (25) have been attempted to overcome the problem of catalyst adhesion on metal substrate surfaces. The objectives of the present study were to systematically develop interfacial design strategies to integrate the catalyst on the metal substrates, mitigate the metal surface corrosion, and eliminate the metal substrate catalyzed side reactions.

In our research we have chosen to control and engineer the metal-ceramic interface using several distinct processes. First, a super alloy that forms a highly adherent native oxide layer was selected as the metallic substrate. The alloy called “fecraloy” (FeCrAlY) which contains the elements iron (Fe, ~ 74 wt%), chromium (Cr, ~ 20 wt%), aluminum (Al, ~4.5 wt%), and yttrium (Y<sub>2</sub>O<sub>3</sub>, ~ 0.5 wt%), was primarily chosen for the development effort. Under appropriate conditions, this alloy forms an adherent, thermodynamically stable, and native aluminum oxide scale. Secondly, we developed CVD methods to provide additional oxide layers (on top of the native oxide layer) to further reduce oxidation of the FeCrAlY substrate. This CVD method can also provide an interfacial layer to integrate catalysts on non-aluminum containing metals such as nickel and copper which have higher thermal conductivity than FeCrAlY alloy. And finally, supported metal catalyst can be applied onto the structured metal substrates using a conventional washcoat approach.

## Experimental

The formation of an adherent and passivating native oxide layer on FeCrAlY felt (Technetics, Orlando, Florida) was studied by oxidizing the material under varying conditions. The key control parameters were oxidation temperature, atmosphere, and exposure duration. The quality of the native oxide layer was microstructurally evaluated using scanning electron microscopy (SEM). Its ability to impede subsequent oxidation and corrosion of the underlying metal was studied using thermogravimetric analysis (TGA) and by testing the material in a reaction vessel under hydrothermal conditions. Five different oxidation protocols were tested (Table II), and the subsequent microstructures were evaluated.

Stainless steel (type 316) and nickel foams with 80 ppi (pores per inch) were purchased from Astomet (Cincinnati, Ohio). Chemical vapor deposition was used to apply a  $\text{TiO}_2$  coating approximately 1000 Å thick. Ti isopropoxide (Strem Chemical, Newburyport, Mass.) was used as the precursor vapor and deposited at a temperature range from 200 to 800°C and at chamber pressure from 0.1 to 100 torr. Superior  $\text{TiO}_2$  films with excellent adhesion to the metal foams were obtained at a deposition temperature of 600°C and reactor pressure of 3 torr. A layer of 5-10%  $\text{SiO}_2$  doped  $\text{Al}_2\text{O}_3$  was then coated on the  $\text{TiO}_2$  layer also using CVD. After the CVD coatings, the substrate was wash-coated with porous alumina (PQ alumina, Nyacol Products, Ashland, Mass.) to act as a support for subsequent precious metal impregnation. The wash-coat slurry was made by using a colloidal dispersion of the alumina powder, and after dipping the pieces into the slurry they were dried in a vacuum oven overnight and calcined at 500°C for 2 hours.

Engineered catalysts were prepared based on FeCrAlY felts. As previously shown (26,27), heat treatment at high temperature under an oxidizing environment facilitates the migration of Al species from the alloy to the surface, which is subsequently oxidized to form a native aluminum oxide layer. A 10wt% Rh/MgO- $\text{Al}_2\text{O}_3$  powder catalyst was first prepared using the method described elsewhere (28), and then ball-milled into aqueous catalyst slurry (water to catalyst powder weight ratio of 8:1) for 24 hours. The catalyst particles in the slurry, as measured by particle size analysis, was 1-3  $\mu\text{m}$ . About 14 mg/cm<sup>2</sup> of catalyst was wash-coated by dip-coating onto FeCrAlY felt with a thickness of 0.25mm, followed by drying and calcination at 500 °C for 2 hours. The catalyst activities were evaluated in a microchannel configuration with dimensions of 0.75mm x 9mm x 51mm heated using a Thermcraft clam-shell furnace. Methane steam reforming was used as a model reaction. The microchannel was placed within a tube furnace to provide the required endothermic reaction heat. A mixture of methane and water (varying steam to carbon molar ratios) was introduced at contact times varying from 1 to 25 m-sec. Here, contact time is

defined as the catalyst bed volume divided by the volumetric inlet gas flowrate at standard temperature and pressure. Methane was controlled via Matheson 8272 or Brooks 5850E mass flow controllers. Water was introduced using a Cole-parmer 74900 series syringe pump for ambient experiments and by an Acuflow Series III HPLC pump for pressurized testing. Inconel sheathed type K thermocouples were utilized for temperature measurement in the catalyst bed, preheating zone, vaporizer and outlet. No-shok pressure transducers were used at both the upstream and downstream positions for pressure measurement. On-line analysis of product gases were performed by an Agilent Quad Micro GC which utilizes a 5A PLOT (MS-5A), PoraPLOTQ, PoraPLOTU, and OV-1 columns equipped with thermal conductivity detectors.

**Table II. Matrix of experimental test conditions used to grow native aluminum oxide coatings on FeCrAlY felt substrates.**

Sample ID	Thermal treatment	Atmosphere during heating	Atmosphere at $T_{max}$
S1	16.7°C/min to 900°C, 20min	3 Torr N <sub>2</sub>	Flowing air, 100 sccm
S2	16.7°C/min to 900°C, 2h	3 Torr N <sub>2</sub>	Flowing air, 100 sccm
S3	16.7°C/min to 900°C, 2h	3 Torr N <sub>2</sub> , w/ ~400ppm air	3 Torr N <sub>2</sub> , w/ 400ppm air
S4	20°C/min to 900°C, 30min	In air	In air
S5	20°C/min to 900°C, 2h	In air	In air

Two types of engineered forms were evaluated. The catalyst "DF" consists of two single felts. Both felt catalysts had the identical dimensions (0.25mm x 9mm x 51mm), and were evaluated in a single channel device (0.75mm x 9mm x 51mm). Two felts with a gap of about 0.25mm were placed in the single channel device so that both felts were in close contact with the walls. The catalyst chamber volume is defined as the single channel volume (0.75mm x 9mm x 51mm). The catalyst "C" was configured as follows. Felt with a thickness of 0.25mm was crimped into a corrugated form, and is called a "ruffle". Ruffles studied in this work have a fixed wavelength of 3mm and a fixed amplitude of 1.3mm. The dimensions of ruffle are 9mm in width and 51mm in length. Reactants flow in the direction perpendicular to the waves. A single ruffle was snug-fitted into a single channel device (0.75mm x 9mm x 51mm), which confines the catalyst chamber volume.

## Results and Discussions

**Native  $\text{Al}_2\text{O}_3$  growth on FeCrAlY** Owing to their excellent mechanical and corrosion resistance properties, oxide dispersion strengthened (ODS) aluminium alloys have widely been used as materials for high temperature applications such as gas turbines and combustion engines. One of the desired features of aluminium containing intermetallic alloys is that, upon heating at elevated temperatures in an oxidizing atmosphere, a layer of thermally grown oxide (TGO) forms on the alloy surface by outward diffusion of cations (29) and/or inward diffusion of anions (30,31). More specifically, when exposed to an oxidizing atmosphere at elevated temperatures the Al at the surface of the FeCrAlY alloy reacts with oxygen to form  $\text{Al}_2\text{O}_3$ . This results in a near-surface depletion layer of Al metal which creates a concentration gradient within the alloy and consequently provides the thermodynamic driving force for Al metal from within the bulk of the alloy to diffuse to the surface. As more Al diffuses to the surface, it continues to react with oxygen forming  $\text{Al}_2\text{O}_3$  scale on the alloy surface. The oxide layer that forms is adherent to the metal substrate, and has a passivating effect that slows down (but does not eliminate) subsequent oxidation. If further oxidation is allowed to occur, all of the Al metal in the alloy eventually oxidizes. At that point, the Cr in the alloy begins to react with oxygen to form  $\text{Cr}_2\text{O}_3$ , creating a concentration gradient that drives diffusion from the bulk to the surface analogous to Al. The experimentally observed precedence of oxidation (Al, Cr, and finally Fe) is consistent with thermodynamic activities, as presented in such references as Ellingham diagrams (32). Under a controlled growth atmosphere, however, the physical and chemical properties of this thermally grown oxide layer can be tailored such that a dense layer of  $\alpha$ -alumina may be formed that covers the alloy surface. This feature provides two significant advantages in terms of properties as a catalyst substrate. First, the dense  $\text{Al}_2\text{O}_3$  scale uniformly adheres to the substrate and provides protection to the underlying ODS alloy substrate from corrosion and embrittlement. Secondly, the native oxide improves the adhesion of subsequently applied (e.g. wash-coat) porous catalyst support layers because it is both firmly adherent to the metal substrate yet also chemically and mechanically similar to the catalyst support material. Consequently, problems typically associated with spallation and poor adhesion between a ceramic washcoat layer and metallic substrates are mitigated because of this interfacial TGO layer.

The primary focus of our research was to optimize the formation of the native oxide layer by controlling the atmosphere under which the heat treatment was performed. Consequently, five different conditions were designed as summarized in Table 2. The resulting microstructures for specimens S1, S2, and S3 are shown in Fig. 2. Specimen S1 had the least exposure to oxygen, being heated under a nitrogen atmosphere and subjected to 100 sccm air for only 20

min. The microstructure of the native oxide coating (Fig. 2 A & D) consisted of discontinuous, sub-micron (~780 nm) tabular crystals of alumina that were approximately 610 nm thick. This microstructure was considered inadequate due to the discontinuous nature of the oxide layer. Specimen S2 was subjected to 100 sccm air for 2 h at 900°C. This treatment resulted in a more continuous, thicker oxide layer (Fig 2. B & E), however, the tabular morphology was still considered unsuitable for optimum performance as a protective, bonding, interfacial layer. Specimen S3 (Fig. 2 C & F) was heat treated in an atmosphere with a very dilute concentration of oxygen. This resulted in a much thinner native oxide layer, however, it appeared discontinuous, which would not provide adequate protection to subsequent oxidizing exposures. XRD analysis of all three samples after heat treatment, not shown here, confirmed that the native oxide layer was  $\alpha$ -Al<sub>2</sub>O<sub>3</sub>.

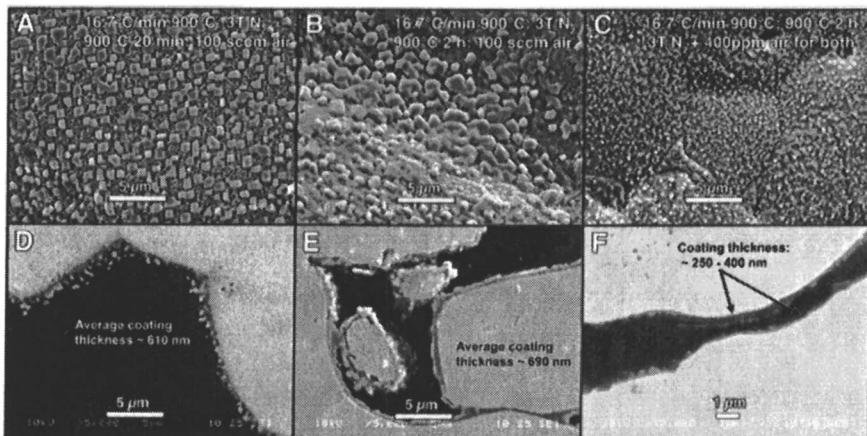


*Figure 2. SEM micrographs comparing the surface and cross-sections of FeCrAlY felts with native oxide coatings created under different conditions. "A & D" correspond to specimen S1; "B & E" correspond to specimen S2, and "C & F" correspond to S3 in Table 1*

The conclusion from the heat treatment of specimens S1 through S3 was that exposure to dilute concentrations of oxygen during the initial heating ramp resulted in the nucleation of a smaller number of aluminum oxide crystals at the FeCrAlY surface, which therefore allowed them individually to grow into larger crystals that eventually coalesced. However, there was concern that a lower density of larger crystals might consume all of the aluminum in the alloy before achieving complete coverage. This concern was evidenced by the fact that the coating on S2 was only 15% thicker than on S1 although it had 6 times the exposure to oxygen. This may indicate that most of the aluminum in the alloy had diffused to the surface and had oxidized under heat treatment conditions for S1. Since complete surface coverage of the fiber surface was required to

accomplish the objectives for the native oxide layer, further optimization on the heat treatment was needed.

Heat treatments under atmospheric conditions were also tested. The objective was to nucleate a very high density of aluminum oxide crystals that would laterally impinge and coalesce to form a continuous passivating layer before all of the aluminum in the alloy had diffused to the surface and oxidized. The heat treatment conditions for specimens S4 and S5 were chosen to evaluate this approach. The resulting microstructures are shown in Fig. 3. After only a

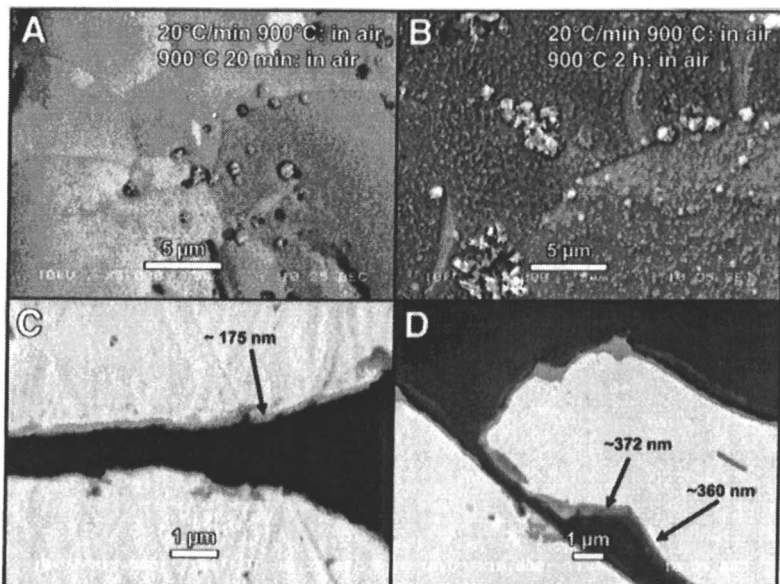


*Figure 3. SEM micrographs comparing the surface and cross-sections of FeCrAlY felts with native oxide coatings created under different conditions: "A & D" correspond to specimen S4; "B & E" correspond to specimen S5 in Table I*

20 min hold at 900°C, a continuous and essentially smooth native oxide layer had formed on specimen S4 that was approximately 175 nm thick (Fig. 3, A & C). Sustained exposure at 900°C for 2 h resulted in a continuous coating that was approximately 370 nm thick. Again, XRD analysis of the samples after heat treatment (not shown) confirmed that the native oxide layer was  $\alpha$ -Al<sub>2</sub>O<sub>3</sub>. A number of important conclusions were drawn from these results. First, thermal treatment in air at 900°C for 20 min produced a continuous, thin, passivating, native oxide layer. Second, there was evidence that there was residual aluminum in the FeCrAlY alloy since the native oxide layer was much thinner for S4 and S5 than for specimens S1 or S2, and also because the native oxide layer doubled in size from S4 to S5. Thirdly, since the native oxide coating continued to grow from S4 to S5 (doubled in thickness after six times the exposure), it was

concluded that additional oxidative protection was necessary for sustained exposure to oxidizing conditions at elevated temperatures. This prompted the application of CVD coatings on top of the native oxide layer. The CVD coating approach also provides the potential to apply CVD coatings directly on non-alumina containing metal/alloys such as stainless steel and nickel foams.

**Coating of interfacial metal oxides** Under hydrothermal conditions at high temperatures ( $>800^{\circ}\text{C}$ ), such as those for methane steam reforming, a single layer of thermally grown oxide alone might not be effective in preventing the corrosion of the metal substrate by steam. It was known that diffusion of reactants such as steam and hydrogen into the alloy or outward diffusion of metallic cations proceeded at high rates over the grain boundaries and dislocations on substrates, which served as short circuit diffusion pathways. Previous studies on alumina suggested that the grain boundary self diffusion coefficient is more than two orders of magnitude greater than the lattice diffusion coefficient (33,34). Grain boundary transport could be suppressed by coating the TGO layer with an additional oxide layer using a CVD approach. CVD proceeds via a nucleation and growth process, which is favored at high-energy sites such as at defects and/or grain boundaries. Consequently, a CVD deposited layer could seal the “short-circuit” diffusion pathways in the TGO layer to further impede oxidative corrosion of the base metal. The key to the success of this strategy was the formation of a dense, pin-hole-free, CVD layer firmly bonded to the TGO layer.

The CVD methods demonstrated here involved reaction of isopropoxide precursors of Al, Ti, Zr, or TEOS on the TGO surfaces with oxygen, to decompose and form an adherent oxide layer. Among the metal oxides studied ( $\text{Al}_2\text{O}_3$ ,  $\text{TiO}_2$ ,  $\text{SiO}_2$ , and  $\text{ZrO}_2$  or combinations thereof),  $\text{TiO}_2$  exhibited the best adhesion to the TGO layer and served as an excellent candidate for the first interfacial sub-layer. Because of its excellent resistance to oxygen diffusion, a second CVD sublayer of  $\alpha\text{-Al}_2\text{O}_3$  (approximately 1  $\mu\text{m}$  thick) was coated on top of the  $\text{TiO}_2$  sublayer (also approximately 1  $\mu\text{m}$  thick). The  $\alpha\text{-Al}_2\text{O}_3$  sublayer was a dense layer that provided excellent protection of the underlying metal surface.

To demonstrate the effectiveness of the  $\text{TiO}_2$  and  $\alpha\text{-Al}_2\text{O}_3$  sublayers against high temperature oxidation, Nickel foams with and without the interfacial coating layers were evaluated in a TGA with air. Nickel was chosen since it can be readily oxidized in air without protection. Fig. 4a shows the SEM micrograph of the nickel foams coated with the  $\text{TiO}_2$  and  $\alpha\text{-Al}_2\text{O}_3$  sublayers. As shown in Fig. 4b, the uncoated nickel foam rapidly oxidized (as shown by the weight gain versus temperature) while the  $\text{TiO}_2$  and  $\alpha\text{-Al}_2\text{O}_3$  coated nickel exhibits negligible oxidation due to excellent resistance to oxygen diffusion. Since the interfacial layer was resistant to the diffusion of gas molecules such as

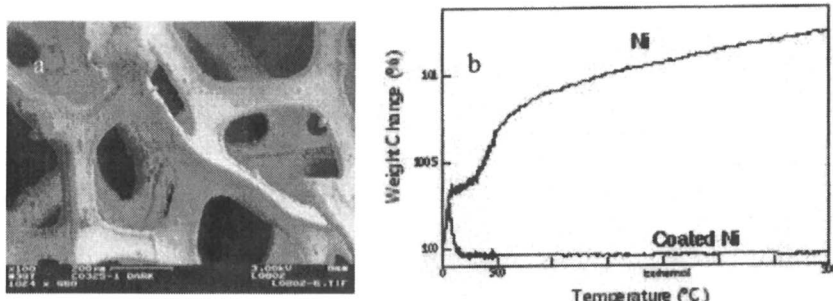


Figure 4. a) SEM micrograph of coated Ni foam, and b) thermogravimetric analysis (TGA) results of bare Ni and coated Ni foams (in air, heating rate of 10°C/min to 500°C, hold isothermally at 500°C for 12hrs )

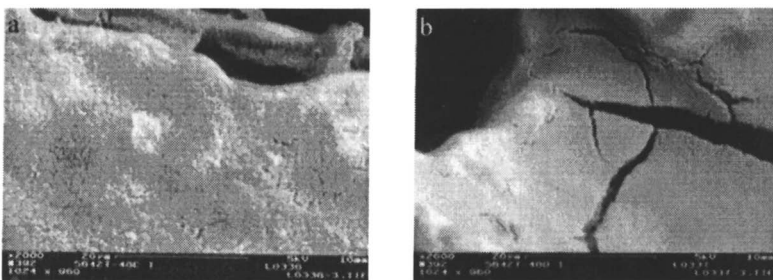


Figure 5. SEM micrographs of wash coated alumina layer on stainless steel foam a) with interfacial layer oxide coating by CVD of Ti, and b) without interfacial layer Ti coating after thermal cycling to 600°C

oxygen, it is anticipated to be resistant to most reactant/product molecules, which can subsequently minimize the metal substrate catalyzed side reactions.

The effectiveness of the  $\text{TiO}_2$  interfacial layer against the spalling of the catalyst coating layer was also demonstrated using a stainless steel (type 316) foam. Stainless steel (type 316) foam was first coated with a layer of  $\text{TiO}_2$  (about 1 $\mu\text{m}$  thickness) using CVD, followed by wash coating a layer of PQ alumina sol. As shown in Fig 5a, SEM analysis showed that supported gamma-alumina wash-coated on stainless steel foam with a  $\text{TiO}_2$  interfacial layer did not show spalling after three thermal cycles from room temperature to 600 °C. In a control experiment with a stainless steel foam support coated with gamma-alumina without the  $\text{TiO}_2$  interfacial layer (Fig 5b), severe flaking or spalling of the gamma alumina under the identical testing conditions was observed.

**Catalytic activities** Methane steam reforming at 850°C was used as a model reaction to evaluate the activities of engineered catalysts. Figure 6 shows methane steam reforming conversion as a function of pressure at 850°C on two types of engineered catalysts based on the FeCrAlY felts. Equilibrium data is also included for comparison purposes. The configurations of both types of engineered catalysts, namely "DF" and "C", were described in the Experimental section. In general, methane conversion decreases with decreasing contact time and increasing pressure, as expected. Also shown in Figure 6, the "DF" configuration was more active than the "C" geometry over the entire range of pressure studied. For example, even at a shorter contact time of 3.8 m-sec, catalyst "DF" outperforms catalyst "C" at a longer contact time of 7.5 m-sec over the entire range of pressure studied. Numerical modeling of the two different types of engineered catalysts was performed to provide the insight about the differences in activity.

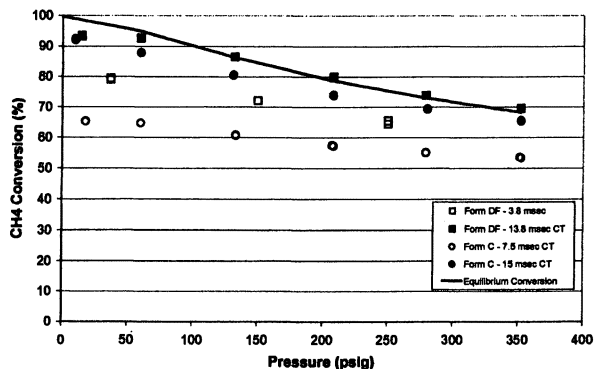


Figure 6. Pressure dependence of methane steam reforming reaction performed in microchannel reactor. (850°C, steam/C=2)

A three-dimensional heterogeneous reactor model (35) was developed to describe the mass/heat transport and reaction in the microchannel catalytic system. A major assumption of the model is a uniform catalyst distribution in the structured forms. Empirical kinetic rate constant and apparent activation energy were used to express the first order reaction with respect to methane. Simulation revealed the local temperature and methane conversion profiles in the microchannel reactor with structured catalysts. Figure 7 shows the temperature profiles in a cross-section of microchannel at an axial position  $z = 2.54\text{mm}$ . The scale on the graph is in millimeters representing the actual dimensions of the reactor channels and the structured catalysts. It can be seen that the catalyst "DF" structures gave more uniform temperature profiles within the cross-section of

catalyst at about 72% methane conversion (850°C, 20atm, steam/C ratio=2, 13.8 msec contact time). In contrast, catalyst "C" showed larger temperature gradient across the engineered catalyst, where numerous cold spots occurred and the maximum temperature difference was about 13 °C. Apparently, the average temperature on catalyst structure "C" is lower than that on catalyst structure "DF", which, in part, results in the lower overall methane conversion on catalyst structure "C". Another possible reason for lower activity in catalyst "DF" is due to lower total catalyst volume in catalyst "C" than in "DF" (0.15cm<sup>3</sup> versus 0.22cm<sup>3</sup>).

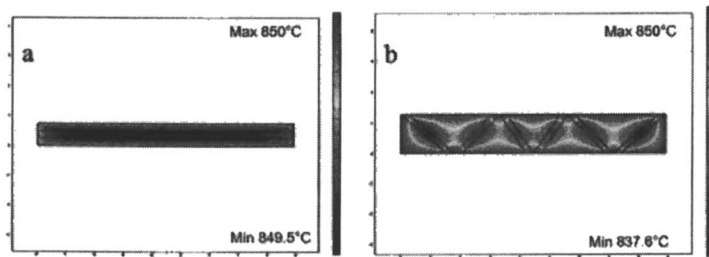


Figure 7. Temperature distribution in a cross-section of methane steam reforming microchannel reactor ( $z=2.54$  mm, 13.8 msec contact time, 850°C, 20 atm, steam/C=2) for a) catalyst "DF", and b) catalyst "C". (See page 1 of color insert.)

In addition to temperature profiles, conversion profiles were also modeled for both types of catalysts. Figure 8 shows the local methane concentration profiles at a fixed distance from the reactor inlet in the axial direction. The methane partial pressure was illustrated on the surface plots in concentration form with a unit of mol/mm<sup>3</sup>. It can be seen that the conversion distribution is not uniform in both gas and solid phases. The concentration gradient is caused predominantly by the increased Knudsen diffusion resistance in the catalyst layers with an average pore radius of 50Å. The integral value of the local concentration gives average conversion at the particular axial position. The overall conversion is subsequently the integrated value at the reactor exit. Figure 9 shows such conversion profiles along the reactor length (axial  $z$ - direction). The numerical analysis quantitatively indicates that catalyst "DF" would yield much higher total conversion (70%) than catalyst "C" (42%). The results agree with the experimental data from a test at 13.8 msec contact time with catalyst "DF", but appear to underestimate the experimental data with catalyst "C".

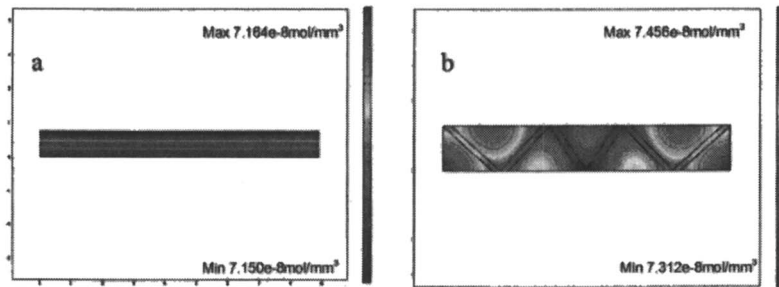


Figure 8. Local methane concentration profile in a methane steam reforming microchannel reactor ( $z=2.54$  mm, 13.8 msec contact time, 850°C, 20 atm, steam/C=2) for a) catalyst "DF", and b) catalyst "C". (See page 1 of color insert.)

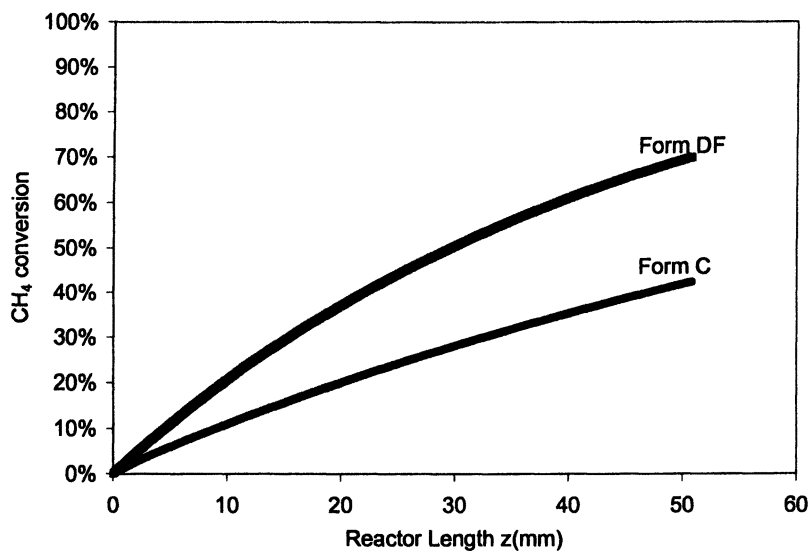


Figure 9. Methane conversion along reactor length (850°C, 20atm, steam/C=2, 13.8msec contact time)

## Conclusions

Engineered catalysts based on porous metal substrates were developed for microchannel reactor applications. Porous metal substrates have the advantages of high thermal conductivity, low pressure drop, and high utilization of catalyst due to thin layer of catalyst coating. However, metal substrates have a thermal coefficient of expansion different from that of the high surface area catalyst carrier, and metal substrate surfaces can either be corroded under severe reaction conditions and/or catalyze undesired reactions. We have accordingly developed an engineered, layered, interfacial coating approach to mitigate these potential problems. Interfacial layers were developed by either growing a native oxide layer from Al containing alloys and/or by using CVD to coat the porous metal substrates with multiple oxides layers. The interfacial layers developed were effective in minimizing corrosion of the metal substrate. They also improved adhesion of ceramic catalytic support powders, and are projected to also minimize deleterious side reactions. Catalytic performance of these engineered supports under methane steam reforming conditions were evaluated and engineered catalysts with an interfacial layer provides flexibility in configuration of catalyst structures, which is important to catalyst activity and stability.

## Acknowledgements

This work was performed in the Environmental Molecular Science Laboratory, a national scientific user facility sponsored by the U.S. Department of Energy's Office of Biological and Environmental Research and located at Pacific Northwest National Laboratory in Richland, WA. Pacific Northwest National Laboratory is operated by Battelle for the Department of Energy under contract DE-AC06-76RLO 1830.

## References

- 1 Tonkovich, A.L.Y.; Call, C.J.; Jimenez, D.M.; Wegeng, R.S.; Drost, M.K. *AIChE Symp.Ser.*, 1996, 92 (310), 119-128, AIChE, New York.
- 2 Thonon, B.; Mercier, P. *Proc. 2<sup>nd</sup> Int'l. Conf. Proc. Intensif. in Pract.*, BHR Group, London, 1997, vol 28, 49-62.

3 Bock, H.J.; Molerus, O. in *Fluidization*, Grace, J.R.; Matsen, J.M. eds, Plenum, New York, 1980, p217.; *German Chem. Eng.*, **1983**, 5, 57.

4 Seko, H.; Tone, S.; Otake, T. in *Fluidization*, D.Kunii and R. Toei, eds, Engineering Foundation, New York, 1983, p331.,

5 Froment,G. F.; Bischoff, K. B. in *Chemical Reactor Analysis and Design*, 2<sup>nd</sup> edition, John Wiley & Sons, Inc. 1990.

6 *Microreactor*; Ehrfeld, W.; Hessel, V.; Lowe, H. eds.; Wiley-VCH Verlag GmbH, D-69469 Weinheim (Federal Republic of Germany), 2000.

7 Jensen, K.F. *AIChE J.*, **1999**, 45(10), 2051-2054; *Chem.Eng.Sci.*, **2001**, 56, 293-303.

8 Schubert, K.; Brandner, J.; Fichtner, M.; Linder, G.; Schyhulla, U.; Wenka, A. *Microscale Thermophysical Engineering*, **2001**, 5, 17.

9 Lerou, J.J.; Ng, K.M. *Chem.Eng.Sci.*, **1996**, 51 (10), 1595-1614.

10 Wegeng,R.S.; Drost, M.K.; Call,C.J.; Birmingham, J.G.; McDonald, C.E.; Kurath, D.E.; Friedrich, M. U.S.Patent 5,811,062, 1998.

11 Holladay, J.D.; Wang, Y.; Jones, E.O. *Chem.Rev.*, **2004**, 104(10), 4767-4790.

12 Tonkovich,A. L.Y.; Perry, S.; Wang, Y.; Rogers, W.A.; Qiu, D.; Peng, Y. "Microchannel Process Technology for Compact Methane Steam Reforming", *Chem.Eng.Sci.* **2004**, 59(22&23), 4819-4824.

13 Chin,Y-H.; Dagle, R.A.; Dohnalkova, A.; Hu, J.; Wang,Y. *Catal. Today* **2002**, 77, 79-88.

14 Wang,Y.; Chin, Y-H.; Rozmiarek, R.T.; Watson, J.; Tonkovich, A.L.Y. *Catal.Today*, **2004**, 98, 575-581.

15 Tonkovich, A.L.Y.; Wang, Y.; Gao, Y. U.S. Patent 6,479,428, 2002.

16 Adris, A.M.; Pruden, B.B.; Lim, C.J.; Grace, J.R. *The Canadian J.Chem.Eng.*, **1996**, 74 (4), 177.

17 Pestyakov, A.N.; Fyodorov, A.A.; Shurov, V.A.; Gisinovich, M.S.; Fyodorova, I.V. *React.Kinet.Catal.Lett.*, **1994**, 53(2), 347.

18 Pestyakov, A.N.; Fyodorov, A.A.; Gaisinovich, M.S.; Shurov, V.P.; Fyodorova, I.V.; Gubaykulina, T.A. *React.Kinet.Catal.Lett.*, **1995**, 54(1), 167.

19 Kosak, J.R. A in *Novel Fixed Bed Catalyst for the Direct Combination of H<sub>2</sub> and O<sub>2</sub> to H<sub>2</sub>O<sub>2</sub>*, Scaros, M.G.; Prunier, M.L. Eds., *Catalysis of Organic Reactions*, Marcel Dekker, Inc. 1995, p115-124.

20 Podyacheva,O.Y.; Ketov,A.A.; Ismagilov, Z.R.; Ushakov, V.A.; Bos A.; Veringa, H.J. *React.Kinet.Catal.Lett.*, **1997**, 60(2), 243.

21 Zhao, C. Y.; Lu,T. J.; Hodson, H. P.; Jackson, J. D. *Material Science and Engineering A*, **2004**, 367 (1-2), 123-131.

22. Fuller, A. J.; Kim, T.; Hodson, H. P.; Lu, T. J. *Measurement and interpretation of the heat transfer coefficients of metal foams*, Cambridge University, 2003. URL: [aif28@eng.cam.ac.uk](mailto:aif28@eng.cam.ac.uk); *Automation Creations*, I, “Fecralloy™ 134 Electrical Resistance Steel”, Matweb.com, 2004.
23. *CRC Handbook of Chemistry and Physics*. D. R. Linde, G. Baysinger, L. I. Berger, R. N. Goldberg, H. V. Kehiaian, K. K. Uchitsu, C. C. Lin, R. Gosenblatt, A. L. Smith, Eds. CRC Press, LLC: 2004; Vol. 84.
24. Twigg M.V.; Webster, D.E. in *Metal and Coated-Metal Catalysts*, Cybulski, A.; Moulijn, J.A. Eds., Structured Catalysts and Reactors, Marcel Dekker, Inc. 1998, p59-90.
25. Trubac, R.E.; Dautzenberg, F.M.; Griffin, T.A.; Paikert, B.; Schmidt, V.R.; Overbeek, R.A. *Catal. Today*, 2001, 69, 17-24.
26. Wang, Y.; Chin, Y.-H.; Gao, Y. U.S. Patent 6,713,519, 2004.
27. C. Badini and F. Laurella, *Surface & Coatings Tech.* 135 (2001) 291-298.
28. Wang, Y.; Tonkovich, A.L.Y.; VanderWiel, D.P. U.S. Patent 6,607,678, 2003.
29. Golightly, F. A.; Stott, F.H.; Wood, G.C. *J. Electrochem. Soc* 1979, 126, 1035.
30. Mennicke, C.; Schumann, F.; Ruhle, M.; Hussey, R.J.; Sproule, G.I.; Graham, M.J. *Oxid Metals* 1998, 49, 455.
31. Quaddakkers, W.J.; Elschner, A.; Speier, W.; Nickel, H. *Appl. Surf Sci*, 1991, 52, 271-287.
32. Gaskell, D. R. *Introduction to Metallurgical Thermodynamics*. 2<sup>nd</sup> ed.; Hemisphere Publishing Corp., New York, 1981.
33. Le Gall, M.; Huntz, A. M.; Lesage, B.; Monty, C.; Bernardini, J. J. *Mater. Sci.* 1995, 30, 201-211.
34. Messaoudi, K.; Huntz, A.M.; Lesage, B. *Mater. Sci. Eng.* 1998, A 247, 248-262.
35. Cao, C.; Rozmiarek, R.T.; Wang, Y. “Heterogeneous Reactor Model for Steam Reforming of Methane with Microstructured Catalysts”, manuscript in preparation.

## Chapter 7

### Fuel Reformation: Catalyst Requirements in Microchannel Architectures

**D. L. King, K. Brooks, C. Fischer, L. Pederson, G. Rawlings,  
V. S. Stenkamp, W. TeGrotenhuis, R. Wegeng, and G. Whyatt**

**Pacific Northwest National Laboratory, P.O. Box 999, Richland, WA 99352**

Microchannel reactors have unique capabilities for onboard hydrocarbon fuel processing, due to their ability to provide process intensification through high heat and mass transfer, leading to smaller and more efficient reactors. The catalyst requirements in microchannel devices are demanding, requiring high activity, very low deactivation rates, and strong adherence to engineered substrate. Each unit operation benefits from microchannel architecture: the steam reforming reactor removes heat transfer limitations, allowing the catalyst to operate at elevated temperatures at the kinetic limit; the water gas shift reactor uses unique temperature control to reduce catalyst volume requirements; the PROX reactor provides high CO conversion and minimizes H<sub>2</sub> oxidation through effective control of reactor temperature.

### **Introduction: The Case for Microchannel Reactors in Onboard Fuel Processing**

There are a number of reasons for the implementation of microchannel reactors for onboard hydrocarbon fuel processing via steam reforming. These include:

- Compactness. Microchannel reactors have high surface to volume ratios, reducing or removing the limitations arising from heat or mass transfer. This allows the catalyst to operate at its kinetic limit. In the case of steam reforming, the kinetic activity of steam reforming catalysts, especially precious metal catalysts, is substantial. For example, turnover numbers for methane steam reforming exceed  $10 \text{ sec}^{-1}$  at 873K for supported platinum [1]. Conventional wisdom that steam reforming is an inherently slow process is incorrect and is based on the assumption that, for larger scale systems, it is difficult to get heat into the catalyst at a rapid enough rate to sustain the endothermic reaction. This is not a limitation with microchannel reactors. As a result of the high activity that can be realized, reactor volume can be substantially reduced.
- Efficiency. Improved thermal management provides high heat transfer effectiveness in heat exchangers and reactors for maximum heat utilization and high fuel efficiency in microchannel systems. Laminar flow results in very low pressure drop. In typical operation of the PEM fuel cell, hydrogen-containing anode tail gas is produced as consumption of hydrogen is incomplete. A benefit of steam reforming is that the anode tail gas can be burned, providing heat to sustain the endothermic steam reforming reaction. This increases the efficiency in comparison with autothermal reforming or catalytic partial oxidation, where the nitrogen-diluted tail has minimal utility. Moreover, efficiency is gained by producing higher  $\text{H}_2$  partial pressure in the reformate with no  $\text{N}_2$  dilution, in comparison with autothermal or partial oxidation approaches.
- Temperature control. Close and responsive temperature is possible with microchannel devices, providing rapid response to load demands. Temperature control provides benefits in onboard fuel processing, for example for the water gas shift and PROX reactions. For example, it is possible to control or minimize reaction exotherms, allowing close to isothermal operation or, in some instances, control of the reaction temperature along the axis of flow. This is important for the PROX reaction. For water gas shift, where there is a significant tradeoff between kinetics and thermodynamics of CO conversion, the ability to decrease the temperature along the flow path in a controllable fashion can lead to higher CO conversion than is available through adiabatic or isothermal operation for the same reactor volume [2].

### Catalyst Challenges

Operation of microchannel reactors is demanding in terms of the performance of the catalyst. Because of the limited volume available in a microchannel reactor, high catalyst activity is required. This requires control of both the chemical formulation of the catalyst and its textural properties on the engineered substrate or support. The operation of the catalyst at or near the kinetic limit implies that there is no excess catalyst for the process to fall back on if deactivation occurs, thus highly stable catalysts are required. The design of microchannel reactors may require sealing the catalyst in hardware, so that it is difficult to remove and replace the catalyst if deactivation does occur. Therefore, the catalyst must be long-lived or easily regenerable *in situ*. Operation in microchannels typically leads to short residence times and high flow rates. Strong adherence of the catalyst to the engineered substrate under high flow conditions is necessary, as catalyst spalling could lead to both loss of activity and possible channel plugging. In our work to date, catalysts have typically been coated onto felts, foams, or monoliths that are then inserted into the microchannel reactor, therefore means to assure good adhesion of the catalyst to the substrate is required. An alternative method of employing the catalyst is to coat it onto the walls of the reactor. This provides even better heat transfer to the catalyst, however the methods to assure adequate and uniform coating of the catalyst to the reactor walls, especially after the primary assembly of the device, is challenging and has not been pursued thus far in our studies.

### Catalyst Preparation Methods

We have used engineered catalyst supports, based on either metal felts or foams. Examples are shown in Figure 1. The majority of the testing in the single channel reactor employed FeCrAlY metallic felts (Technetics; 24% dense). In our single channel test reactor (Figure 2), the strips were cut from sheets of the FeCrAl felt, with dimensions typically 1x8x.025 cm.

Calcination of the felts at 890°C in air for 6-10 hours facilitates migration of the aluminum to the external surface of the felt, providing a surface of polycrystalline aluminum oxide to which the catalyst readily adheres, as seen in the SEM photographs provided in Figure 3.

As-received catalysts were ball milled to facilitate producing a high solids content suspension in isopropanol solvent and a more uniform particle size

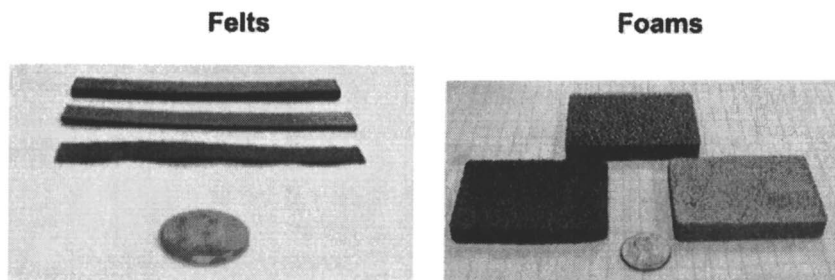


*Figure 1. Engineered Catalyst Supports*

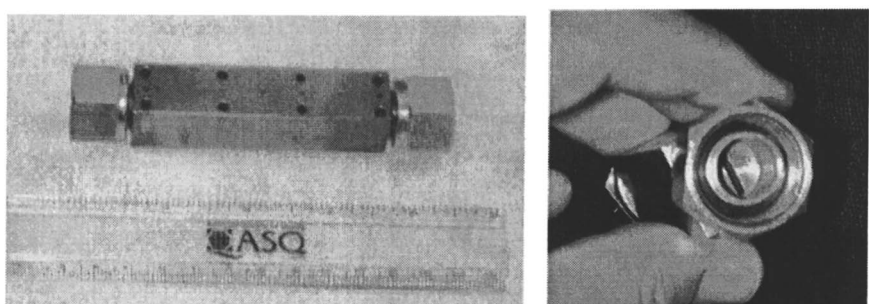


*Figure 2. Single Channel Test Reactor*

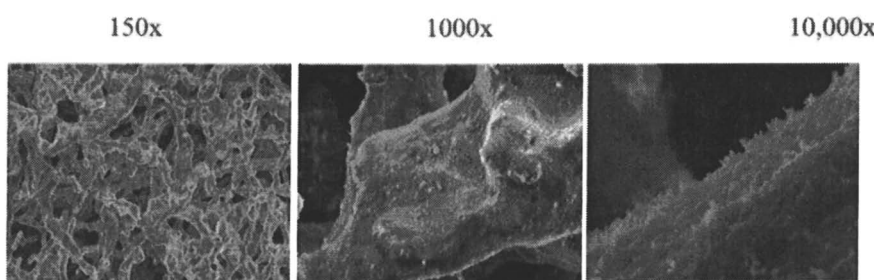


*Figure 3. SEM of Aluminum Oxide Surface Layer on FeCrAlY Felts at Different Magnification.*

distribution. Ball milling was for a period of 10 minutes and achieved a submicron particle size. The catalyst was added to the support without a binder by several dip-and-dry cycles in the stirred suspension, with drying provided with flowing nitrogen to remove any catalyst particles that were not strongly adhering to the support. The final catalyst loading varied between 40-250 mg per felt strip. A cross section of the felt coated with catalyst at high and low loadings is shown in Figure 4. The lighter regions are the metallic felt filaments, the darker regions contain the catalyst. Electrophoretic deposition of the catalyst onto the support was also evaluated as a means to replace the tedious dip-and dry approach. However, we found evidence of catalyst spalling with the electrophoretic method, and did not pursue methods to optimize this latter approach.

### Catalysts

Catalysts were predominantly obtained from vendors, in order to assure that any high performing catalysts could be obtained at significant scale. Since many of the catalysts obtained were "developmental", a non-analysis agreement was typically required, so that characterization of catalyst post reaction was only possible by working with the vendor. This is the tradeoff under which we chose to operate. In most cases, we obtained catalyst powders from the vendor, allowing us to control the amount of catalyst deposited on the support. In other cases the vendor carried out the coating onto our felt supports, somewhat limiting flexibility.

For the steam reforming reaction, a proprietary precious metal catalyst from Battelle was utilized. For the water gas shift reaction, we evaluated both copper-based and precious metal-based catalysts provided by Süd Chemie Inc. For our purposes, the superior activity of the precious metal catalysts was determined to be critical to the operation of our unit, in order to minimize catalyst requirements. For the PROX reaction, we employed a combination of non-precious metal catalyst from Süd Chemie and precious metal catalyst from Engelhard Corporation.

### Microchannel Reactor Testing

Many of the details of the microchannel hardware employed for fuel reforming are provided in a paper by K.P. Brooks, et. al., included in this monograph [3].

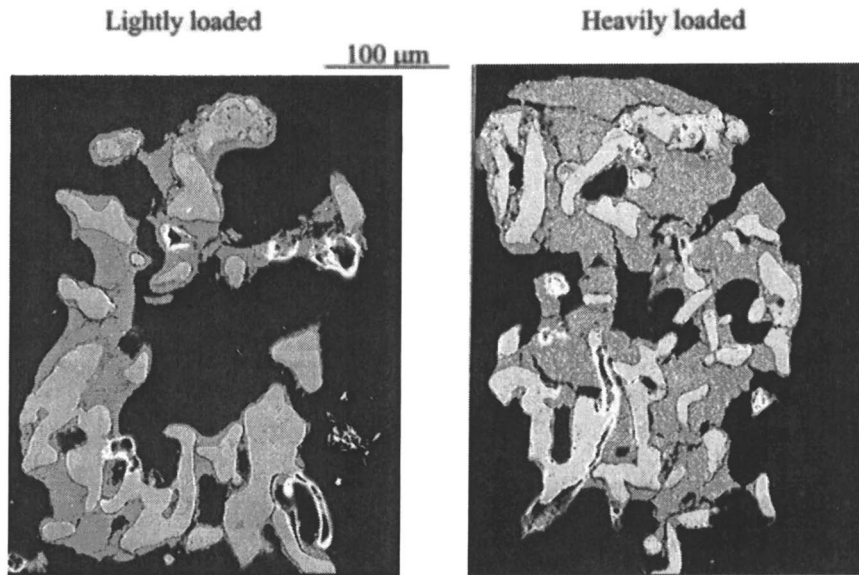
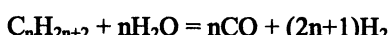


*Figure 4. Cross Section of Ball Milled Catalyst on FeCrAlY Felt at Two Different Loadings.*

#### Steam Reforming

The steam reforming reaction stoichiometry for alkane feedstock can be summarized:

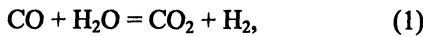


The reaction is endothermic, and heat is provided by flowing fuel through a combustor and then into a separate set of interleaved channels (no catalyst within the channels). The efficient microchannel heat exchange provides heat necessary to support the steam reforming reaction. An important goal is to minimize hydrocarbon slip (unconverted hydrocarbon). Table 1 shows the operating temperature, space velocity (on catalyst), and calculated reactor core volume necessary to provide reformate for a 50kWe fuel cell with no more than 0.1% hydrocarbon slip. These data were obtained using benchmark fuel as feedstock (74% isoctane, 20% xylenes, 5% methyl cyclohexane, 1% 1-pentene) and a S/C ratio of 3. High temperature operation is clearly beneficial in reducing reformer volume.

*Table 1: Microchannel Steam Reformer Performance With Precious Metal Catalyst*

Temperature	650°C	850°C
Gas Hourly Space Velocity, hr <sup>-1</sup>	83,000	257,000
Reformer volume, liter	12.7	4.1

The water gas shift reaction also occurs over this catalyst,



and generally reaches equilibrium (CO concentration in the range of 10-14 vol%) under the conditions of operation.

#### Water Gas Shift

In this unit operation, CO is converted to less than 1 vol% (H<sub>2</sub>O-free basis) according to reaction (1). The reaction is mildly exothermic, ~9.5 kcal/mole. Typically water gas shift is carried out in two stages [4]. The first stage operates at 370-400°C with iron-chrome catalysts, producing CO in the range of 2-4 vol %. The second stage, based on copper-zinc catalyst formulations, reduces CO to as low as 0.1-0.3 vol % operating at or below 250°C. In an onboard fuel processor, this combination of catalysts results in large catalyst beds. Moreover, copper-based catalysts are sensitive to elevated temperatures, unstable in the presence of liquid water (which may collect during shutdown) and pyrophoric (air leakage into the catalyst bed may also occur during frequent startup and shutdown). For this reason, we chose to employ precious metal water gas shift catalysts. These catalysts operate over a wide temperature range, and have acceptable activity for a compact fuel processor. Potential concerns regarding these catalysts are their cost and their long term stability in the microchannel environment under frequent startup and shutdown. We are continuing to investigate the latter issue.

#### Preferential CO Oxidation (PROX)

The preferential CO oxidation reaction,



is employed to convert the CO exiting the water gas shift reactor to a concentration of less than ~10ppm. Low CO concentration is required as CO

poisons the anode of the PEM fuel cell. The reaction is exothermic,  $\Delta H = -67.8$  kcal/mole. The challenge is to reduce CO to these low levels without oxidizing the H<sub>2</sub>, present in the reformate at much higher concentrations, to H<sub>2</sub>O. Reaction exothermicity exacerbates the challenge, as with increasing temperature the PROX catalyst becomes much less selective toward CO. For this reason, the PROX is typically a series of staged adiabatic beds with interstage cooling. Microchannel hardware with excellent heat transfer has the potential to operate the first stage reactor at near isothermal conditions, leading to low CO exit concentration and minimizing the load on the second stage reactor. The CO output from the second stage reactor is sensitive to temperature and again can benefit from the temperature control provided by the microchannel architecture. Our testing in the single channel reactor identified both precious metal and non-precious metal catalysts that successfully converted CO to CO<sub>2</sub> to below 0.1 vol% with approximately 50% selectivity (50% selectivity means as many moles of H<sub>2</sub> were oxidized as were CO, a tolerable amount when initial CO concentration is low). The conditions for the test were: 190-200°C; O<sub>2</sub>:CO = 1; gas hourly space velocity (GHSV) = 100,000, see Figure 5. In order to achieve the final 10 ppm CO, the second stage PROX reactor operated with a precious metal catalyst at a lower space velocity of 50,000 hr<sup>-1</sup> and lower temperature of 120°C and required slightly higher O<sub>2</sub>:CO ratio of 1.4 to achieve the necessary level of CO conversion, as shown in Figure 6. Further details are provided in the paper by Brooks et. al. in this same monograph [3].

### Summary and Conclusions

Microchannel reactors have unique capabilities for onboard hydrocarbon fuel processing, due to their ability to provide process intensification through high heat and mass transfer, leading to smaller and more efficient reactors. The catalyst requirements in microchannel devices are demanding, requiring high activity, very low deactivation rates, and strong adherence to engineered substrate.

Each unit operation benefits from microchannel architecture. The steam reforming reactor achieves high catalyst activity realized by removing heat transfer limitations, allowing the catalyst to operate at elevated temperatures at the kinetic limit. The water gas shift reactor takes advantage of the high activity of the precious metal water gas shift catalyst and unique temperature control to reduces catalyst volume requirements by trading off kinetics and thermodynamics. The two stage PROX reactor provides high CO conversion and minimizes H<sub>2</sub> oxidation through effective control of reactor temperature.

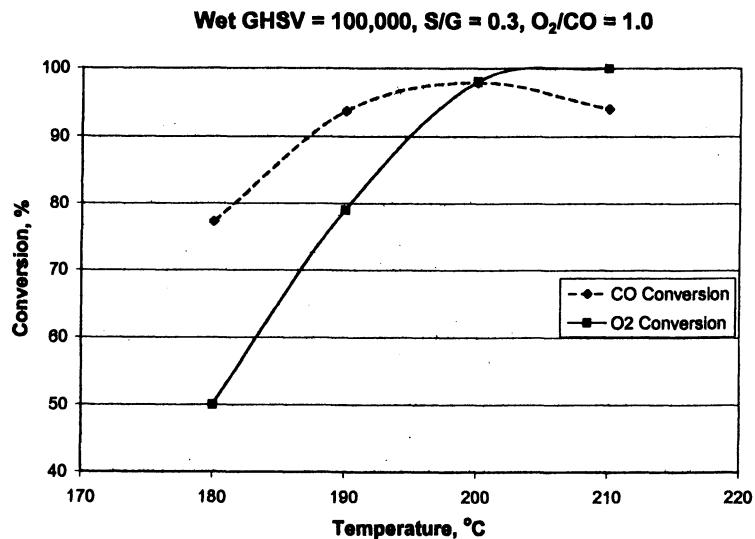


Figure 5. First Stage PROX Reaction With Non-precious Metal Catalyst

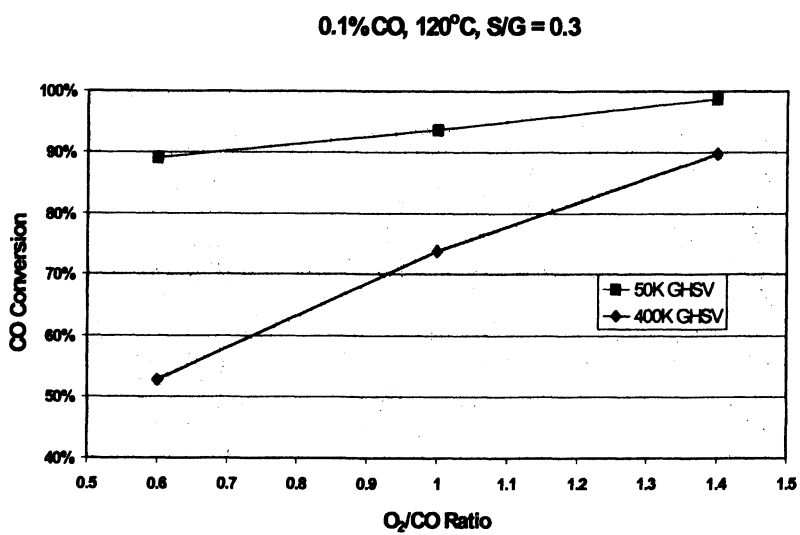


Figure 6. Second Stage PROX Reaction With Precious Metal Catalyst:  
Effect of O<sub>2</sub>/CO Ratio

### Acknowledgments

Support from the U.S. Department of Energy, Office of FreedomCAR & Vehicle Technologies Program, with direction from Dr. Nancy Garland, is gratefully acknowledged.

### References

- [1] J. Wei, and E. Iglesia. Mechanism and Site Requirement for Activation and Chemical Conversion of Methane on Supported Pt clusters and Turnover Rate Comparisons Among Noble Metals. *J. Phys. Chem. B* 2004, 108, 4094-4103.
- [2] W.E. TeGrotenhuis, K.P. Brooks, R.A. Dagle, B.F. Davis, J.M. Davis, J. Holladay, M.J. Kapadia, D.L. King, L.R. Pederson, V.S. Stenkamp, R.S. Wegeng. Microchannel Reformate Cleanup: Water Gas Shift and Preferential Oxidation. *2004 DOE Hydrogen, Fuel Cells & Infrastructure Technologies Program Review*, Poster Presentation, May 2004.
- [3] K.P. Brooks, J.M. Davis, C.M. Fischer, D.L. King, L.R. Pederson, G.C. Rawlings, V.S. Stenkamp, W. Tegrotenhuis, R.S. Wegeng, G.A. Whyatt. Fuel Reformation: Microchannel Reactor Design. *Microreaction Technology and Process Intensification*, ACS National Meeting, New York, September 8, 2003.
- [4] L. Lloyd, D.E. Ridler, and M.V. Twigg. The Water Gas Shift Reaction. *Catalyst Handbook*, 2<sup>nd</sup> ed., Chapter 6. M.V. Twigg, ed.

## Chapter 8

### **Nanoscale Platinum Catalyst in Microreactors for Preferential Oxidation of CO for Hydrogen Fuel Cell Feeds**

**S. Zhao, J. Hu, D. Kuila, R. S. Besser, R. Nassar, and J. D. Palmer\***

**Chemical Engineering Program, Louisiana Tech University,  
Ruston, LA 71272**

Oxidative removal of a small quantity of CO from a hydrogen atmosphere has been attempted by using nano-scale impregnated platinum coated silicon based sol-gel in a microreactor. The microreactor with 25  $\mu\text{m}$  wide channels was fabricated by general photolithography and Inductively Coupled Plasma (ICP) dry etching. The catalytic preferential oxidation of CO was observed over a temperature range from 393 to 493 K. Air or pure O<sub>2</sub> was the oxidizer. The effects of temperature, total flow rate and ratio of O<sub>2</sub>/CO on the conversion and selectivity are presented. A statistical design of experiment approach was implemented to minimize the experiments necessary for the study. The conversion of CO reaches 91% at 160 °C, O<sub>2</sub>/CO ratio of 0.5 and a WHSV of 13 h<sup>-1</sup>, while the highest selectivity to CO<sub>2</sub> is 90%. At higher temperatures, the oxidation of H<sub>2</sub> increases and the selectivity to CO oxidation decreases. Deactivation of the platinum catalyst was observed over a period of 50 hours of reaction time.

## Introduction

Fuel cells hold substantial promise in reducing the environmental impact of transportation. A fuel cell is a battery in which a fuel - normally hydrogen or methanol - reacts at the anode and oxygen reacts at the cathode. However, unlike in a normal battery, fuel cell electrodes are not consumed - only the fuel is consumed [1]. In most cases, hydrogen is the preferred fuel for use in the present generation of fuel cells being developed for commercial applications [2]. When generating hydrogen from natural gas, methane, or methanol, one of the by-products is carbon monoxide. The presence of carbon monoxide in the hydrogen rich feed gas to fuel cells can poison the platinum anode electrode and dramatically reduce the power output [3]. Therefore, carbon monoxide clean-up and amelioration is very important for fuel cell technology development. Various CO-removal technologies have been developed: 1) water-gas shift, 2) preferential oxidation, 3) methanation, 4) hydrogen separation, and 5) CO-adsorption [4].

Oxidative removal of a small quantity of CO from a hydrogen atmosphere has been examined using different catalysts containing 3D transition metal oxides. Currently, the predominate catalysts used world-wide are platinum [5-12] and ruthenium [13-17]. In the U.S., Manaslip presented the results of selective CO oxidation, in macro-scale, in simulated reformate gas over single-step sol-gel prepared Pt/alumina catalysts [7]. The effects of water vapor, carbon dioxide, CO and oxygen concentrations, temperature, and Pt loading on the activity and selectivity were presented. Their results showed that a 2% Pt/alumina sol-gel catalyst can selectively oxidize CO down to a few ppm with constant selectivity and high space velocity. The presence of water vapor in the feed increases the activity of the catalysts dramatically and in the absence of water vapor, CO<sub>2</sub> in the feed stream decreases the activity of the catalysts significantly. Ajmera determined the reaction rates and activation energy of Rh, Pt, and Pd on an Al<sub>2</sub>O<sub>3</sub> substrate in a microreactor [18]. In 1998, Tonkovich presented results of preferential oxidation of CO in a microreactor [19].

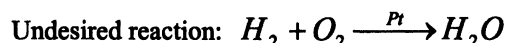
The preferential oxidation of CO on Ru/ $\gamma$ -Al<sub>2</sub>O<sub>3</sub> in a reformer gas (1% CO, 75% H<sub>2</sub> and rest N<sub>2</sub>) was investigated by Han in Germany. The results show that ~150°C is the optimum temperature for PROX of CO, and Ru/ $\gamma$ -Al<sub>2</sub>O<sub>3</sub> catalyst has a higher activity and selectivity than the conventionally used Pt/ $\gamma$ -Al<sub>2</sub>O<sub>3</sub> catalyst [13]. Echigo, in Japan, utilized a novel Ru catalyst in a single-stage CO preferential oxidation reactor for polymer electrolyte fuel cell (PEFC) cogeneration systems to obtain less than 1ppm of CO concentration at [O<sub>2</sub>]/[CO]

= 1.5. Moreover, the durability of the Ru catalyst has been confirmed for more than 16,000h in a microreactor [14]. The combined Pt-Ru electrocatalysts supported on a high-surface area carbon powder has been investigated by Dudfield in Italy to study the oxidation kinetics of H<sub>2</sub> and H<sub>2</sub> + 100 ppm CO [20]. Best performances, both in H<sub>2</sub> and H<sub>2</sub> + CO, were achieved by the catalyst with the ratio of Pt/Ru = 1.

In addition to Pt and Ru catalyst, other catalysts, like Co, Mn, Ag, can also be used for PROX of CO for fuel cell feed gas. In Turkey, Guldur reported the synthesis of 1:1 molar ratio of the silver cobalt and silver manganese composite oxide catalysts to remove CO from hydrogen-rich fuels in a microreactor. Ag/Co composite oxide catalyst calcined at 200°C has good activity and 90% of CO conversion was achieved at 180°C [21].

In our current study, we have focused on preferential oxidation of CO using a microreactor for portable power device application. Process miniaturization and process intensification were reasons for applying chemical microreactor technology to this particular reaction. Process miniaturization is important, as smaller and lighter devices are necessary for fuel cells to supplant batteries as a source of energy for a number of applications. Process intensification through the increase in surface area to volume ratio of miniaturized devices can enhance both heat and mass transfer.

The reactions of preferential oxidation of CO are shown below:



Platinum was chosen as the catalyst, and a sol-gel support was utilized to maximize the surface area. High conversion is required to reduce the CO concentration to a level that is not detrimental to a Proton Exchange Membrane (PEM)-based fuel cell. High selectivity to CO<sub>2</sub> is desired because hydrogen is used to generate electricity in the fuel cell. Oxidation of hydrogen to water reduces energy available for the fuel cell.

## Experimental

### Microreactor design and fabrication

The microreactor was 3.1 cm long and 1.6 cm wide with 119 microchannels 25  $\mu\text{m}$  in width and 100  $\mu\text{m}$  in depth (Figure 1). It was made from a four-inch diameter, 500  $\mu\text{m}$  thick, single side polished  $<100>$  silicon wafer. The reactant gases were premixed before entering the microreactor. An inlet manifold was designed to promote a uniform distribution of flow among the reaction microchannels. The inlet manifold consisted of two channels symmetrically off axis from the single outlet.

The microreactor fabrication includes two main processes: photolithography and Inductive Coupling Plasma (ICP) etching. The microreactor mask layout was designed using AutoCAD 2000 software. The masks were produced on chromium plated glass. The lithography process used to make the microreactor is much like the one used in the integrated circuit (IC) industry. The wafer was pre-baked to 165 °C for 90 seconds in a nitrogen environment. Hexamethydisiloxane (HMDS) was spun on to dehydrate the surface of the wafer to improve the adhesion of the photoresist. Microposit 1813 positive photoresist was spun on to create a film thickness of 1-2  $\mu\text{m}$ . The wafer was then etched using an Alcatel 601E ICP to achieve highly anisotropic side walls.

### Catalyst/support preparation and coating

Silica support for catalysts can be prepared from either tetraethoxysilane ( $\text{Si}(\text{OC}_2\text{H}_5)_4$ ) or tetramethoxysilane ( $\text{Si}(\text{OCH}_3)_4$ ). Tetraethoxysilane ( $\text{Si}(\text{OC}_2\text{H}_5)_4$ ) was chosen as the precursor of silica since a previous study showed that silica produced from  $\text{Si}(\text{OC}_2\text{H}_5)_4$  resulted in a higher surface area than silica produced from  $\text{Si}(\text{OCH}_3)_4$ . The silica sol-gel solution was prepared by mixing tetraethoxysilane ( $\text{Si}(\text{OC}_2\text{H}_5)_4$ ), water, ethanol, and nitric acid in the molar ratio of 1:12:45:0.26 [22]. The silica precursor was added to water/ethanol solution, and was followed by a subsequent addition of nitric acid. The resultant solution was then stirred vigorously at 40 °C for 30 minutes.

After the silica sol-gel mixture was aged for two weeks, lithography technology was used to coat the desired regions of the microreactor with the sol-gel [23]. A negative photoresist (NR1500-P) was chosen as the mask for selective deposition because the unexposed channel part of the negative photoresist can be completely removed by the developer, minimizing residual photoresist. A window was opened in the channel region of the microreactor for

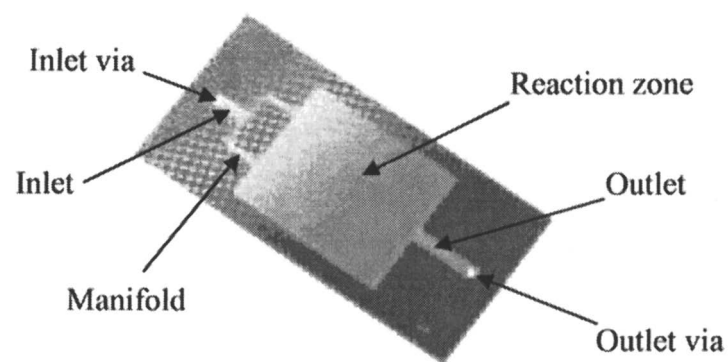


Figure 1 Top view of the microreactor

silica coating, and droplets of sol was dispensed into the microchannels, allowing the sol to permeate by capillary action, thus forming the silica film in the microreactor. A 200 °C, 20-minute baking step in air was required to dry the sol-gel coating for good adhesion between the silicon channel and the silica gel.

Then, platinum was deposited on above silica support in the form of Pt<sup>+2</sup> by ion impregnation. Platinum (II) 2,4 Pentanedionate (Pt (C<sub>5</sub>H<sub>7</sub>O<sub>2</sub>)<sub>2</sub>) was first dissolved completely in a toluene solution. The solution was dropped into the channel area of the microreactor to obtain a Pt/SiO<sub>2</sub> loading ratio of 1:2. A reduction process [24] was completed in order to convert the deposited Pt<sup>+2</sup> to metallic Pt<sup>0</sup>. After microreactor fabrication and catalyst/support coating, the reactor was sealed with a pyrex glass top to prevent air and moisture from degrading the reduced catalyst.

### **Microreaction setup**

In addition to the microreactor, peripheral equipment was needed for control of flow, temperature, and pressure, and for the acquisition of the product distribution of the effluent stream. The reactor chip interfaces to a steel block fitted with silicone o-rings to seal the inlet and outlet vias on the bottom side of the microreactor. The block interface has resistive heating elements and a thermocouple touching the backside of the microreactor through a hole drilled in the heater block to maintain a desired temperature. Although the reaction of this study is exothermic, the top surface temperature of the silicon microreactor was not higher than the control temperature. Gases are fed to the block by Cole-Parmer 32915-24 mass flow controllers. Cole-Parmer 68023-02 digital pressure sensors are situated in the inlet and outlet streams to monitor the pressure drop across the microreactor. The gas flow and reactor temperature settings were monitored and controlled by a PC running LabView software.

Reactor effluent was monitored for composition using a Stanford Research Systems mass spectrometer (QMS 200) with PC data acquisition and control. The effluent stream was diluted with helium prior to the mass spectrometer sampling point to prevent the spectrometer's vacuum system from affecting the reactor operating pressure.

70% hydrogen, 2% carbon monoxide, and 28% argon was obtained premixed from NextAIR. The composition of carbon monoxide and hydrogen is similar with that of a commercial fuel cell feed gas. Ultra High Purity (UHP) oxygen and air (from NextAIR) was used to oxidize carbon monoxide.

### Characterization of the microreactor with catalyst/support

A Scanning Electron Microscope (SEM) picture of the microchannels in the microreactor is shown in Figure 2. Wave-line channels were utilized to increase the mass transfer in the microreactor. One hundred and nineteen 25  $\mu\text{m}$ -wide channels were fabricated in this design.

SEM analysis was also performed on the silica coated channels to examine the catalyst support and to verify the thickness of the silica film. (Figure 3) The gel covers the bottom and concave surface of the channel walls well but has poor coverage on the convex surface of the channel walls due to stress cracking during drying and curing of the catalyst.

AFM images of the microchannels were taken to study the presence of the sol-gel encapsulated catalysts in the microreactor. Figure 4 shows the surface of the coated silica sol-gel catalyst support on the 25  $\mu\text{m}$  channels of the reactor. It is evident from Figure 4, the average size of the sol-gel particle is 50-80 nm in diameter, which contribute to a specific surface area of  $\sim 285 \text{ m}^2/\text{g}$  and a surface area of  $\sim 4.5 \text{ m}^2$  in one microreactor measured using a Quantachrome NOVA 2000 instrument and Brunauer-Emmett-Teller (BET) method respectively.

X-Ray Photoelectron Spectroscopy (XPS) results of sol-gel impregnated with platinum before and after reduction by hydrogen treatment are shown in Figure 5. The Pt 2s core level peaks shift from 73.125 eV to 71 eV. In each curve, the distance between the two peaks is 3.3 eV, which is in agreement with the separation between  $\text{Pt}^0$  and  $\text{Pt}^{+2}$  peaks [25]. Moreover, the sputter depth profiling of the catalyst film indicates uniform Pt concentration to a depth of at least 5  $\mu\text{m}$  thickness of the film.

### Results and discussion

The reaction was initiated after one hour of vacuum, followed by two hours of  $\text{H}_2$  treatment at a flow rate of 1 sccm and room temperature to activate the catalyst. A mixed gas of  $\text{CO}/\text{H}_2/\text{Ar}$  and oxidizer were then fed into the microreactor. The  $\text{Pt}/\text{SiO}_2$  loading ratio was 1:2 for the initial screening experiments of  $\text{O}_2/\text{CO}$  ratio and was increased to 1:1 for all subsequent experiments. The oxidizer for the experimental results depicted in Figure 6 and 7 was air. The oxidizer was then changed to oxygen to increase the resolution of CO by the mass spectrometer by reducing interference from  $\text{N}_2$ . Therefore, the experimental results depicted in Figures 8, 9, and 10 were conducted using pure oxygen as the oxidizer.

In the first screening experiments, the ratio of  $\text{O}_2/\text{CO}$  was varied between 0.3 and 10 by keeping the mixed gas at 1 sccm and changing the air flow rate from 0.02 to 0.4 sccm. The temperature of the experiments was held constant at

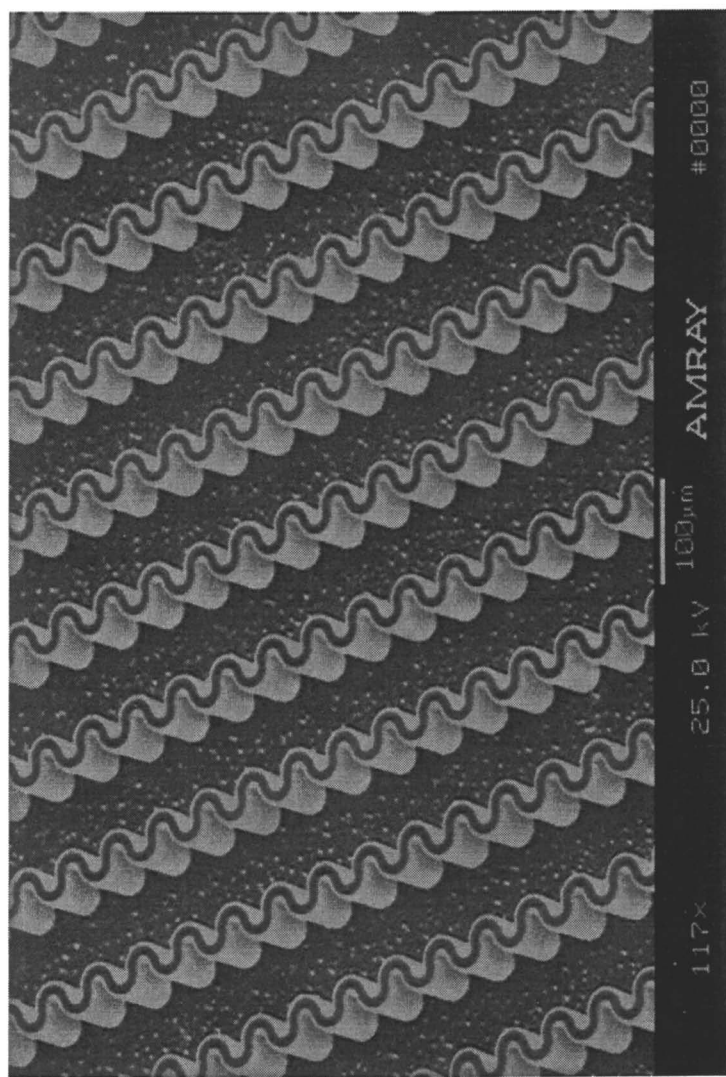


*Figure 2. The SEM image of the microreactor channel*

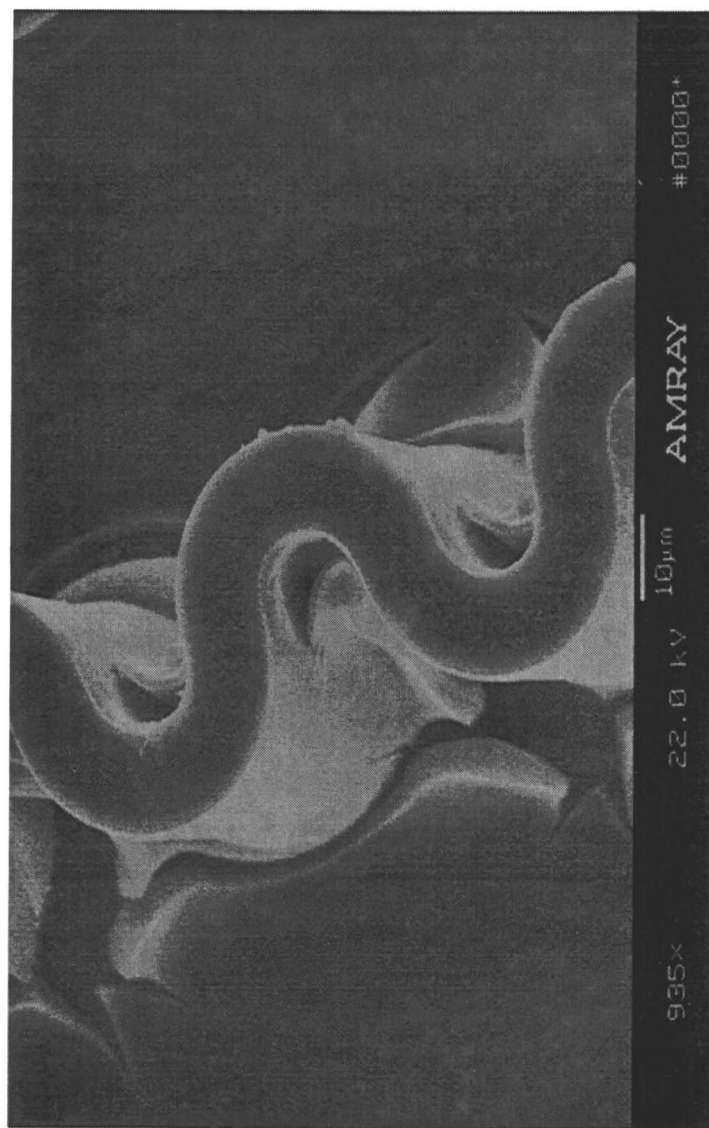


*Figure 3. The silica sol-gel covering the microchannels*

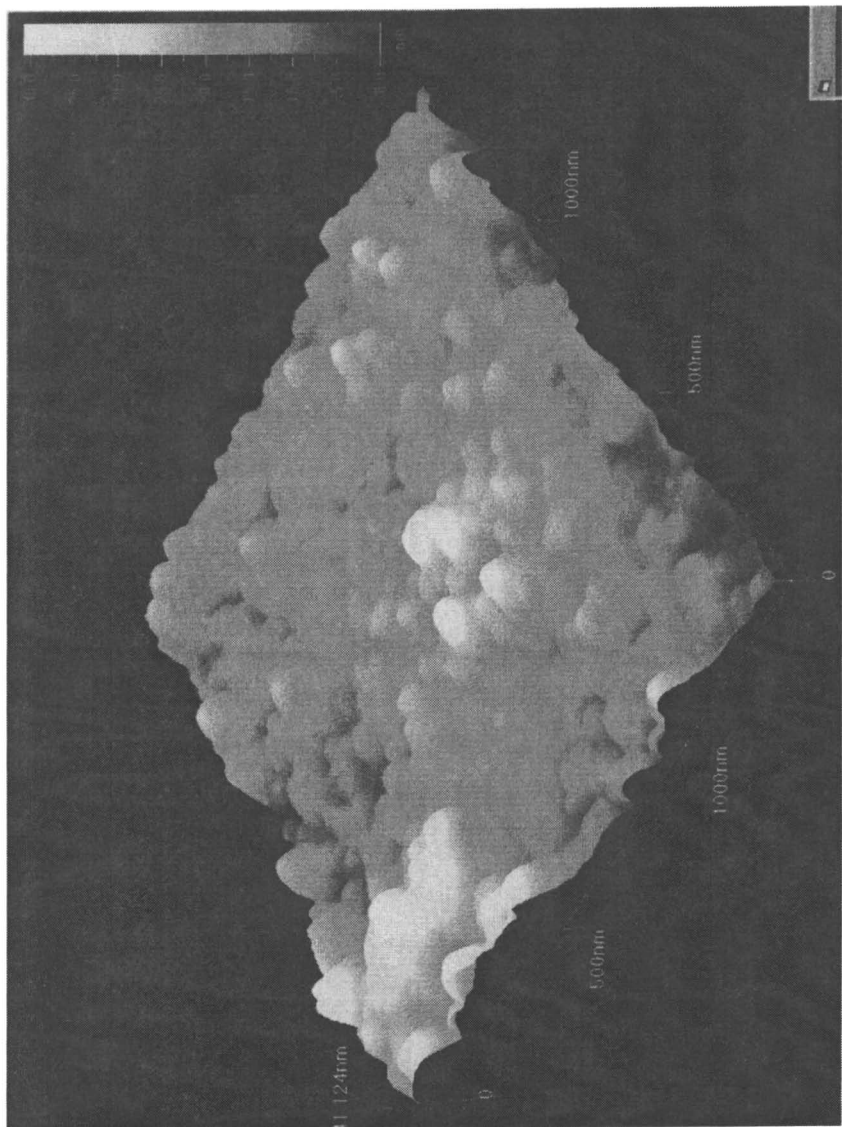


Figure 4. Surface of the coated *succa succa* sol-gel catalyst support

**XPS for platinum reduction**

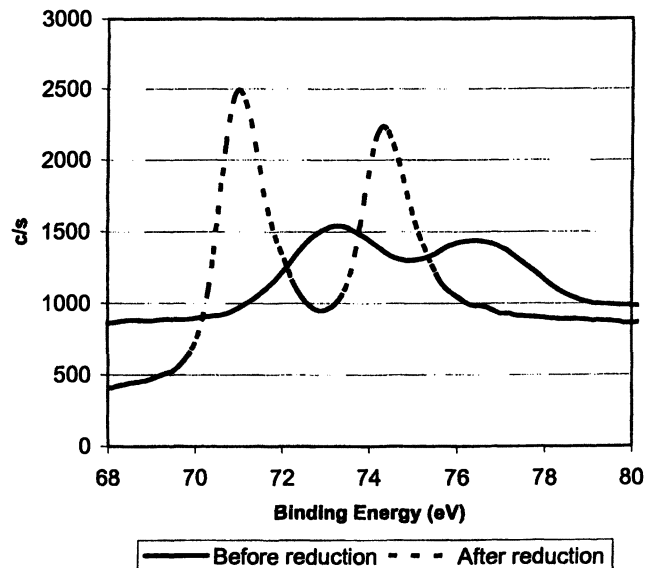


Figure 5. Binding energy of platinum before and after reduction

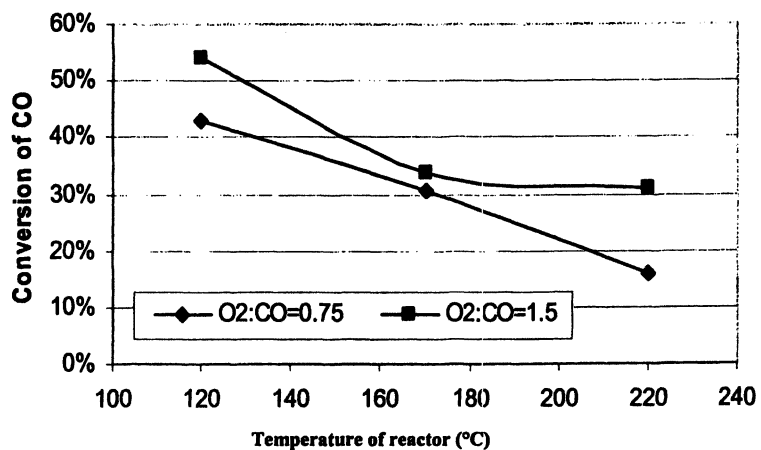


Figure 6. Temperature effect on conversion of CO (113 h<sup>-1</sup> WHSV)

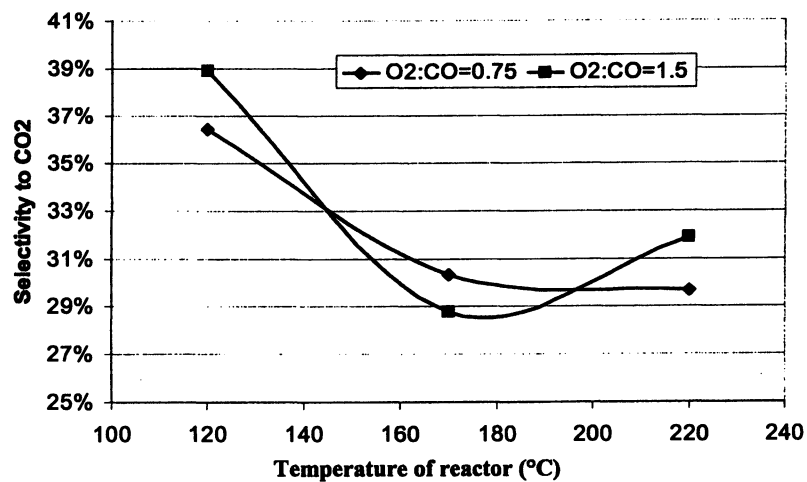


Figure 7. Temperature effect on selectivity to  $\text{CO}_2$  ( $113 \text{ h}^{-1}$  WHSV)

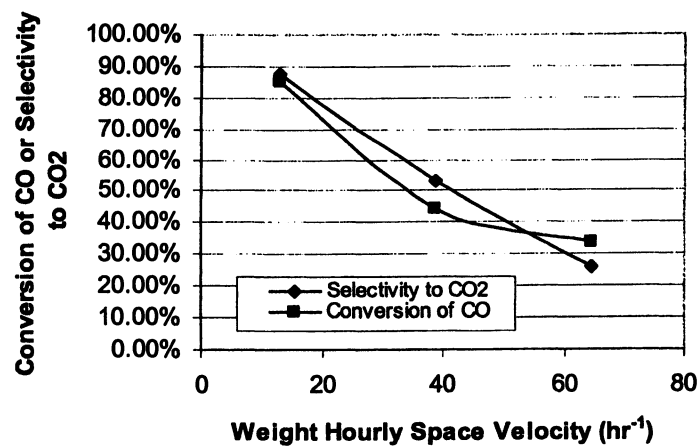


Figure 8. Residence time effect on conversion of CO and selectivity to  $\text{CO}_2$  ( $\text{O}_2/\text{CO}$  ratio of 0.5;  $170^{\circ}\text{C}$ )

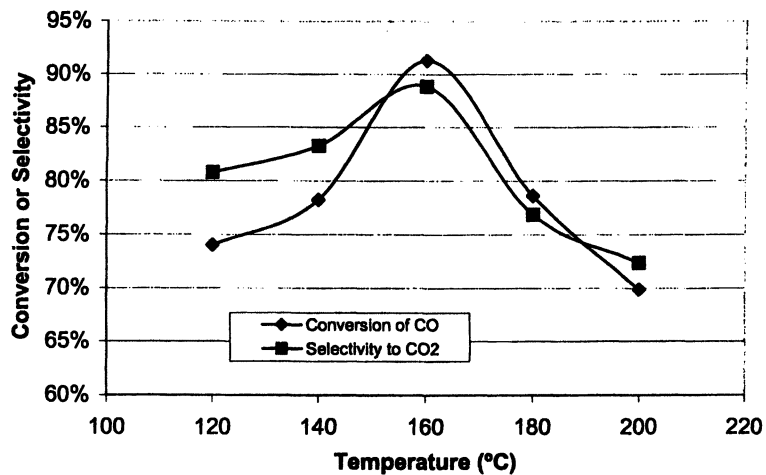


Figure 9. Temperature effect on the conversion of CO and selectivity to CO<sub>2</sub> at low space velocities (13 h<sup>-1</sup> WHSV; O<sub>2</sub>/CO ratio of 0.5)

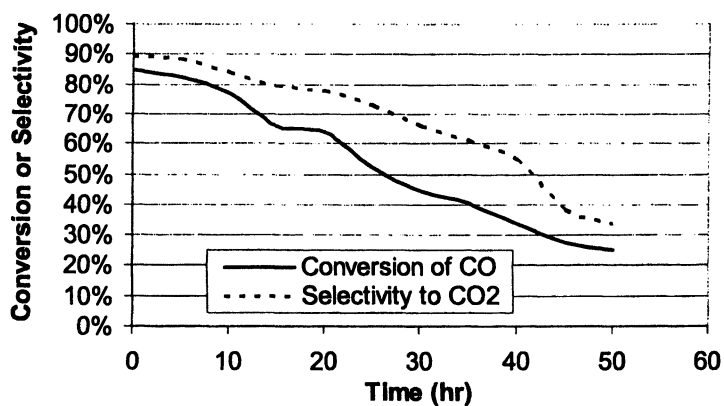


Figure 10. Deactivation effect of platinum catalyst on CO and selectivity to CO<sub>2</sub> (13 h<sup>-1</sup> WHSV; O<sub>2</sub>/CO ratio of 0.5; 170 °C)

200 °C. As expected, the selectivity of oxidation of CO decreased as the O<sub>2</sub> ratio to CO was increased above 2. Surprisingly, the conversion of CO did not appear to significantly increase as the ratio of O<sub>2</sub> to CO was increased above 2. Based on these results, subsequent experiments focused on O<sub>2</sub>/CO ratios lower than 2.

A statistical design of experiment approach was then implemented for the remainder of the study. The variables manipulated were O<sub>2</sub>/CO ratio, total reactant flow (residence time), and temperature. The three points depicted on the figures resulted from coded values from a central composite design. Details of the design of experiment will be published at a latter date.

Figure 6 and Figure 7 depict the effect of temperature on conversion and selectivity respectively. For these experiments, the total flow rate was maintained at 1.75 sccm, corresponding to a weight hourly space velocity (WHSV – gram gas/hr gram catalyst) of 113 h<sup>-1</sup>. An O<sub>2</sub>/CO ratio of 0.75 and 1.5 were tested. Conversion and selectivity were both maximized at the minimum temperature tested, 120 °C. The lower stoichiometric excess of O<sub>2</sub> displayed a higher sensitivity of conversion with respect to increases in temperature.

The sensitivity of conversion and selectivity on reactor residence time was then tested. These tests were conducted at 170 °C with an O<sub>2</sub>/CO ratio of 0.5. This particular catalyst and reactor combination favored the lowest space velocity that could be achieved, 13 h<sup>-1</sup>. Figure 8 depicts the decrease in conversion and selectivity as the space velocity was decreased.

Additional experiments were then conducted at WHSV of 13 h<sup>-1</sup> to finalize the optimal temperature of operation. The ratio of O<sub>2</sub>/CO was held constant at a stoichiometric ratio of 0.5. Figure 9 shows that 160 °C is optimal temperature of operation at these conditions.

A study was performed to test the stability of the catalyst over time. The test was operated at 170 °C, an O<sub>2</sub>/CO ratio of 0.5, and a WHSV of 13 h<sup>-1</sup>. Figure 10 depicts the drop in conversion and selectivity over time. After 50 hours of reaction, the conversion of CO dropped from over 85% to almost 25%, and selectivity to CO<sub>2</sub> dropped below 35%. Two likely mechanisms for catalyst deactivation are oxidation of the platinum and sintering of the platinum nanoclusters into larger particles [26]. Limited recovery of catalyst activity through repeated reduction treatments suggest the former has some contribution. The irreversible reduction in exposed surface area through sintering of the platinum nanoclusters at the temperatures of operation is the likely cause for the remaining drop in activity. Carbon deposition is not thought to be a major contributor due to the lack of a possible mechanism as predicted by Chemkin simulations [26]. Improvement of the catalyst activity and efficiency will be a significant issue for future research and commercialization of this technology.

## Conclusions

The platinum impregnated silica sol-gel catalyst did result in preferential oxidation of CO and offers another possible candidate for study in addition to the alumina support described in the literature. The particle size of the catalyst with support is 50-80 nm in diameter. Long residence times are required to yield a high conversion of CO and a high selectivity to CO<sub>2</sub>. The conversion of CO reaches to 91% at 160 °C, O<sub>2</sub>/CO ratio of 0.5, and WHSV of 13 h<sup>-1</sup>, while the highest selectivity to CO<sub>2</sub> is 90%. The conversion of CO and selectivity to CO<sub>2</sub> decreases with increase of the O<sub>2</sub> concentration above the stoichiometric amount for the desired reaction. Deactivation of Pt catalyst was observed during 50 hours of reaction time.

## References

1. Burstein, G.T. *Materials World*, v 6, n 7, Jul, 1998, p 412-413
2. Dicks, Andrew L. *Journal of Power Sources*, v 61, n 1-2, Jul-Aug, 1996, *Proceedings of the 1995 4th Grove Fuel Cell Symposium Opportunities, Progress and Challenges*, Sep 19-22 1995, London, UK.
3. Manasilp. Akkarat; Gulari. Erdogan *Applied Catalysis B: Environmental*, v 37, n 1, Apr 8 , 2002, p 17-25
4. Ito. Takashi *Nihon Enerugi Gakkaishi/Journal of the Japan Institute of Energy*, v78, n11, 1999, p 911-920
5. Denis, M.C.; Lalande, G.; Guay, D.; Dodelet, J.P.; Schulz, R. *Journal of Applied Electrochemistry*, v 29, n 8, 1999, p 951-960.
6. Korotkikh Olga; Farrauto Robert *Catalysis Today* 62(2000) 249254.
7. Manasilp, Akkarat; Gulari, Erdogan *Applied Catalysis, B: Environmental* (2002), 37(1), 17-25.
8. Son, I.H.; Shamsuzzoha, M.; Lane, A.M. *Journal of Catalysis* (2002), 210(2), 460-465.
9. Bednarova, L.; Ouyang, X.; Chen, H.; Lee, W.Y.; Besser, R.S. *Preprints of Symposia – American Chemical Society, Division of Fuel Chemistry* (2003), 48(2),846-847.
10. Chang, Bong-Kyu; Tatarchuk, Bruce J. *Preprints of Symposia – American Chemical Society, Division of Fuel Chemistry* (2003), 48(2),843-845.
11. Rodrigues, Aida; Amphlett, John C.; Mann, Ronald F.; Peppley, Brant A.; Roberge, Pierre R. *Proceedings of the Intersociety Energy Conversion Engineering Conference* (1997), 32<sup>nd</sup> 768-773.
12. Son, In Hyuk; Lane, Alan M. *Catalysis Letters* (2001), 76(3-4), 151-154.

13. Han, Y.-F.; Kahlich, M.J.; Kinne, M.; Behm, R.J. *Physical Chemistry Chemical Physics* (2002), 4(2), 389-397.
14. Echgo, Mitsuaki; Shinke, Norihsa; Takami, Susumu; Higashiguchi, Seisaku; Hirai, Kazuhiro; Tabata, Takeshi *Catalysis Today* (2003), 84(3-4), 209-215.
15. Finnerty, C.; Tompsett, G.A.; Kendall, K.; Ormerod, R.M. *Journal of Power Sources* (2000), 86(1-2), 459-463.
16. Newson, E.; Truong, T.B.; De Silva, N.; Fleury, A.; Ijpelaar, R. *Studies in Surface Science and Catalysis* (2003), 145(Science and Technology in Catalysis 2002), 391-394.
17. Echgo, Mitsuaki; Tabata, Takeshi *Applied Catalysis, A: General* (2003), 251(1), 157-166.
18. Ajmera, S. K.; Delattera, C.; Schmidt, M.A.; Jensen, K.F. *Journal of Catalysis* (2002), 209, 401-412.
19. Tonkovich, A.Y.; Zilka, J.L.; Powell, M.R.; Call, C.J. *Proceedings from 2<sup>nd</sup> International Conference on Microreaction Technology*, New Orleans, LA, 1998.
20. Dudfield, C.D.; Chen, R.; Adcock, P.L. *International Journal of Hydrogen Energy*, v 26, n 7, July , 2001, p 763-775.
21. Guldur, Cigdem; Balikci, Filiz. *International Journal of Hydrogen Energy* (2001), volume date 2002, 27(2),219-224.
22. Okuzaki S.; Okude K.; Ohishi T. *Journal of Non-crystalline Solids*, vol. 265, pg 61-67.
23. Zhao, S.; Besser, R. S. *Proceedings from 6<sup>th</sup> International Conference on Microreaction Technology*, New Orleans, LA, 2002, p 289-296.
24. Pecchi G.; Morales M.; Reyes P. *React. Kinet. Catal. Lett.*, 61 (2), 237-244, 1997.
25. Moulder, J. F.; Stickle, W. F.; Sobol, P. E.; Bomben, K. D. *Handbook of X-ray photoelectron spectroscopy*, Physical Electronics, Eden Prairie, MN, 1995.
26. Ouyang, X.; Bednarova, L.; Ho, P.; Besser, R. S. accepted for publication in *AIChE Journal*, 2004.

## Chapter 9

# Process Intensification through Heat-Integration for High-Temperature Catalysis

Götz Veser<sup>1,2</sup>

<sup>1</sup>Department of Chemical Engineering, University of Pittsburgh,  
Pittsburgh, PA 15261

<sup>2</sup>Max-Planck-Institut für Kohlenforschung, 45470 Mülheim an der Ruhr,  
Germany

## Introduction

Process intensification denotes a current trend in the chemical industry towards more efficient and sustainable processes (1,2). Even though no universally accepted definition of 'process intensification' seems to exist, increased process efficiency – i.e. reduced energy consumption and/or reduced byproduct formation – as well as decreased equipment size are usually emphasized. Process intensification is therefore also often discussed in the context of microreaction technology, since here the achievement of highly efficient processes in equipment with often drastically reduced size is typically the main objective.

A closely related concept are so-called 'multifunctional' reactors which integrate more than one unit operation in a single – and hence multifunctional – reactor unit (2-5). Since this integration results in fewer and more compact units with increased process efficiency, multifunctional reactors can be regarded as prime examples of process intensification. To date, mainly three basic concepts of multifunctional reactors have been discussed in the literature: the integration of mixing and reaction, such as in spinning disk reactors (6,7); the integration of reaction and (product) separation in membrane reactors (8), reactive distillation (9) or simulated moving-bed reactors (10,11); and the integration of reaction and heat-exchange in recuperative and regenerative heat-exchange reactors (12). In the present contribution, the application of such heat-integrated reactor concepts to high-temperature catalysis will be discussed, using catalytic partial oxidation of methane as example.

Catalytic partial oxidation of methane (CPOM) to synthesis gas has been studied as a potentially attractive alternative to the steam reforming route since the 1940s (13). However, while the homogeneous partial oxidation of methane quickly developed into a commercial process, the development of CPOM ran into repeated road blocks and technological problems and appears to have been essentially dormant until it was 'rediscovered' in the 1990s by a number of groups around the world, most notably in the work from Schmidt and coworkers (14,15). They demonstrated that it is indeed possible to convert methane with air or oxygen to synthesis gas in a very fast catalytic reaction over noble metal catalysts. Due to the high reaction rates at the very high process temperatures ( $> 1200$  K), catalyst contact times are in the order of 10 – 100 ms, i.e. about one to two orders of magnitude below the contact times in a typical steam reforming process. As a consequence, CPOM can be conducted in a reactor with a size reduced by at least one order of magnitude, and this reaction itself can thus already be regarded as an example of 'process intensification' (although by some definitions, improvements based on a change in reaction route rather than on reactor engineering aspects are not categorized as 'process intensification').

However, while CPOM constitutes in principle a highly efficient reaction route, in a conventional fixed-bed reactor CPOM is subject to significant auto-thermal equilibrium limitations as the heat of reaction of the mildly exothermic partial oxidation reaction is not sufficient to achieve the very high temperatures ( $T > 900^\circ\text{C}$ ) required for selective partial oxidation (16-18). Consequently, part of the methane feed is internally combusted at the fixed-bed entrance, raising reaction temperatures and allowing the partial oxidation reaction to proceed. This combustion is thus a necessity for the partial oxidation reaction in a fixed-bed reactor but also puts an intrinsic limit on the attainable syngas yield.

In this contribution, we demonstrate further evidence that these auto-thermal limitations can be overcome by the use of heat-integrated reactors. Recuperative heat-integration in a counter-current heat-exchange reactor is compared to regenerative heat-integration in a reverse-flow reactor. The performance of the reverse-flow reactor is further evaluated, and a general definition of efficiency for heat-integrated reactor concepts is proposed.

## Experimental

The experimental set-up is presented in detail in previous reports and is therefore only briefly described here (17,18). A simple counter-current heat-exchange reactor (HXR) and a reverse-flow reactor (RFR) were studied. The two reactor set-ups are shown schematically in figure 1.

The catalysts used in all experiments reported here are either alumina foam or extruded monoliths which are coated with a thin layer of a noble metal (Pt or

Rh) via conventional wet impregnation from a salt solution. This catalyst is positioned between two extruded cordierite monoliths. In case of the heat-exchange reactor, the inert extruded monoliths have a length of 10 mm and serve as radiation shields to minimize radiative heat losses. In this reactor, heat integration is achieved through recuperative heat-exchange between the hot product gases and the cold feed gases by flowing the product gases back through an outer tube which surrounds the feed tube (see figure 1 a).

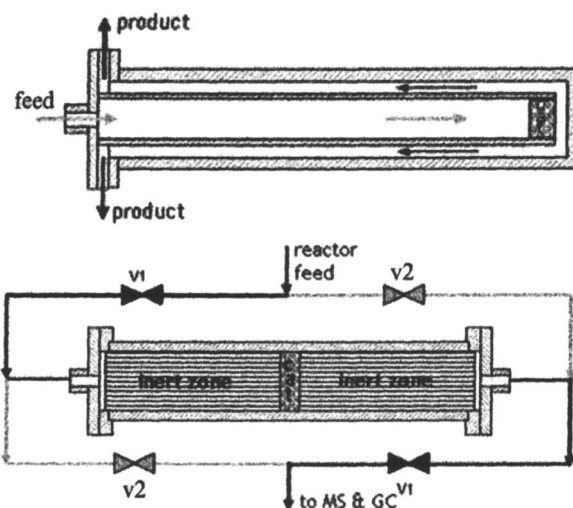


**Figure 1:** Schematic of the heat-integrated reactors used for CPOM: counter-current heat-exchange reactor (top) and reverse-flow reactor (bottom).

In the case of the reverse-flow reactor, the extruded monoliths have a length of 110 mm and, in addition to being radiation shields, serve as heat reservoirs. This configuration thus allows regenerative heat-integration as follows: cold reactants enter the catalyst bed, react, and the heat of reaction leads to increasing temperatures in the catalyst zone and the inert zone downstream of the catalyst. When the gas flow through the reactor is reversed, the cold reactor feed now flows through the pre-heated inert zone, increasing the feed gas temperature while cooling the inert zone. The reactants thus enter the catalyst zone at an elevated temperature, which is further increased by the reaction heat. Upon exiting

the catalyst zone, the hot product gases then exchange heat again with the ('new') downstream inert zone. If this flow reversal is repeated at an appropriate cycling frequency, a "periodic steady state" is eventually reached, which is characterized by a symmetric temperature profile with very high temperatures in the reaction zone and comparatively cold reactor ends. In the laboratory reactor, flow reversal is accomplished via four magnetically operated valves which are synchronized in pairs. Reactor operation and data acquisition are fully computer-controlled (PC with DA/AD-boards and LabView software).

In both reactors, moveable thermocouples allow the measurement of temperature profiles along the reactor axis in the inert zones. The irregular structure of the foam monoliths precludes temperature measurements inside the catalyst zone itself. Therefore, in some experiments the foam monolith is replaced by an extruded alumina monolith which thus allows measurement of temperature profiles inside the catalyst zone at operating conditions. Product concentrations are measured with gas chromatography and C-, O- and H-atom balances close in a typical experiment to better than 3%. All results reported in the following were obtained during reactor operation with air (rather than pure oxygen).

For a direct comparison of the performance of a reverse-flow reactor with a conventional stationary reactor, the same reactor setup is used for steady state experiments without switching of the flow direction. In this way, it is assured that all differences between steady state results and results at reverse-flow operation are due to differences in reactor operation rather than differences in the experimental setup. For the heat-exchange reactor, however, no such direct comparison is possible.

## Results and Discussion

### Comparison between Heat-Integrated Reactor Concepts

Figure 2 shows results for catalytic partial oxidation of methane with air in the conventional flow-tube reactor (SS, open symbols and dotted lines), the counter-current heat-exchange reactor (HXR, half-filled symbols and dashed lines) and the reverse-flow reactor (RFR, filled symbols and solid lines) for a total volumetric inlet flow rate of 3 slm (standard liters per minute). CO and hydrogen yields (squares and circles, respectively) are shown versus the molar methane-to-oxygen ratio in the inlet flow.

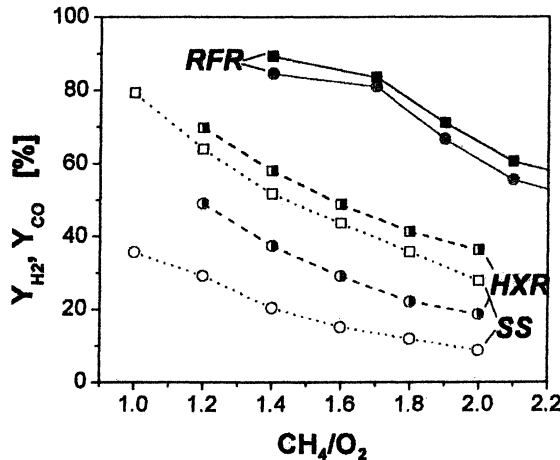


**Figure 2:** CO (squares) and H<sub>2</sub> yields (circles) for CPOM in a reactor without heat integration (SS, open symbols and dotted lines), a counter-current heat-exchange reactor (HXR, half-open symbols and dashed lines) and a reverse-flow reactor (RFR, filled symbols and solid lines) with varying CH<sub>4</sub>/O<sub>2</sub> ratio (O<sub>2</sub>/N<sub>2</sub> = 1/4). Experimental conditions: V = 3 slm,  $\tau/2$  = 15 s (RFR), Pt.

One can see that heat-integration leads to an improvement in the yields of both syngas components. While the recuperative heat-integration in the HXR leads to improvements of about 5-10% for CO and 10-20% for H<sub>2</sub>, the regenerative heat-integration in the RFR results in rather drastic improvements of 20-30% for CO and up to 60% for H<sub>2</sub>. The strong differences between the HXR and the RFR are due in part to an undesired blind activity of the stainless steel reactor housing in the HXR (17), which has been avoided in the RFR by inserting the catalyst and inert zones into an inner quartz-glass tube (18,19). However, while this improvement in reactor design is responsible for some of the observed yield increase, the main differences stem from the significantly improved heat-exchange in the regenerative reactor as apparent from the temperature profiles in the reactor shown below.

Figure 3 shows the temperature profiles upstream of the catalyst in the conventional flow-tube reactor (SS, circles) in comparison with the counter-current heat-exchange reactor (HXR, squares) and the reverse-flow reactor (RFR, triangles). In both reactor configurations, heat integration leads to significantly increased catalyst entrance temperatures: while radiative and conductive heat transport raises the temperature at the catalyst entrance in the simple flow-tube reactor (SS) to about 500°C, this temperature increases to about 800°C in the

counter-current heat-exchange reactor (HXR) and to 950°C in the reverse-flow reactor (RFR). These increased catalyst entrance temperatures as well as the steeper slope for the RFR in comparison with the HXR indicate that heat is more efficiently transferred from the hot product gases to the cold feed gases, i.e. that the regenerative heat-integration is more efficient than the recuperative design.

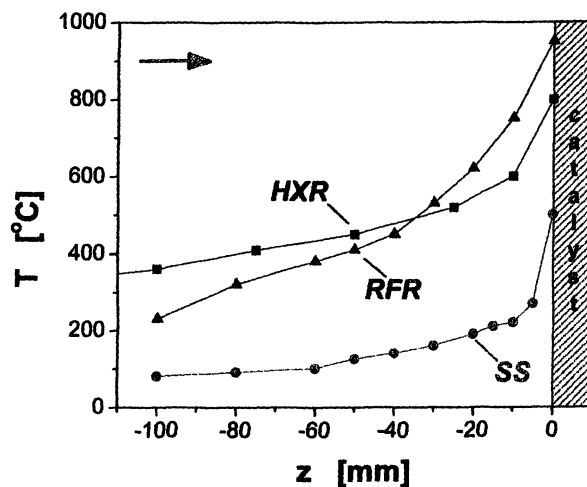


*Figure 3: Upstream temperature  $s$  in a reactor without heat integration (SS, circles), the counter-current heat-exchange reactor (HXR, squares) and the reverse-flow reactor (RFR, triangles). The catalyst position is indicated by the shaded area and flow direction of the gases is from left to right. Experimental conditions:  $CH_4:O_2:N_2 = 1.8:1:4$ ,  $V = 3 \text{ slm}$ ,  $\tau/2 = 15 \text{ s}$  (RFR), Pt catalyst.*

This brief comparison between the two integrated reactor concepts demonstrates that the regenerative heat-integration in the dynamically operated reverse-flow reactor is a particularly efficient and appropriate reactor concept for the present high-temperature reactions. This reactor concept is therefore investigated in more detail in the following.

#### Regenerative Heat-Integration in a Reverse-Flow Reactor

One of the main characteristics of high-temperature catalysis are the unusually short contact times which are in the order of only about 10 - 100 milliseconds due to the extremely fast reaction rates at such high temperatures. It is therefore of particular interest to investigate how a reactor concept affects process yields as the reactor throughout hence catalyst contact times is varied.

Results from a test with a Rh-coated foam monolith in a reverse-flow reactor configuration are shown in figure 4. The flow rate was varied between 1 and 9 slm (corresponding to estimated contact times at the respective reaction temperatures of about 100ms to 8ms). The left graph shows CO and H<sub>2</sub> yields (squares and circles, respectively) for conventional steady-state operation ('SS', open symbols and dashed lines) and reverse-flow reactor operation ('RFR', filled symbols and solid line), while the right graph shows the corresponding catalyst temperatures (entrance and exit temperatures at SS, and maximum and mean temperatures at RFR).

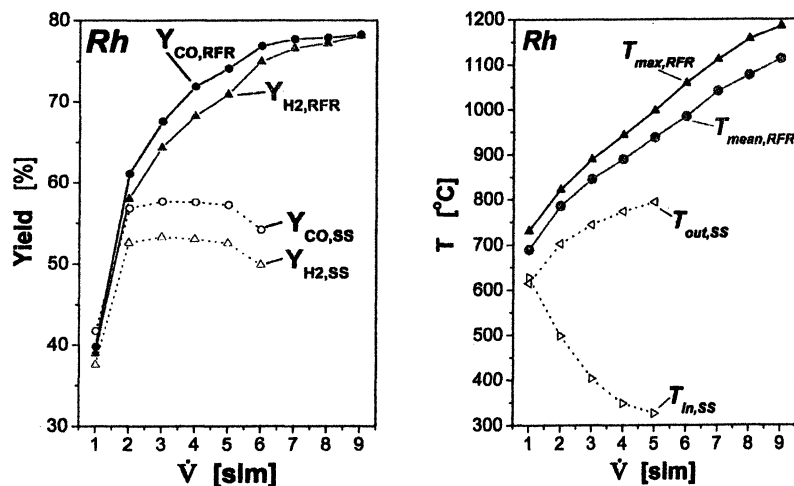


Figure 4: Left graph: CO (squares) and H<sub>2</sub> yields (circles) in a conventional 'steady-state' reactor (SS, open symbols and dotted lines) and a reverse-flow reactor (RFR, filled symbols and solid line) vs feed flow rate. Right graph: corresponding catalyst inlet and outlet temperatures at SS (right- and left-pointing triangles, respectively) and maximum and mean temperatures at RFR (upward triangles and circles, respectively). Experimental conditions: CH<sub>4</sub>:O<sub>2</sub>:N<sub>2</sub> = 2:1:4,  $\tau/2 = 15$  s (RFR), Rh/Al<sub>2</sub>O<sub>3</sub> catalyst.

Syngas yields at SS operation show a rather flat plateau for inlet flows between 2 and 4 slm, with a steep drop-off towards lower flow rates and a more gradual decrease towards higher flow rates. The steep drop towards low flow rates is due to insufficient heat production to attain the high reaction temperatures necessary for selective partial oxidation as reflected in the low catalyst temperatures of  $\sim 630^\circ\text{C}$ . The more gradual decrease towards higher flow rates, on the other hand, is due to a cooling of the catalyst front edge with increasing

flow of (cold) feed gases as apparent from the strong divergence of the catalyst entrance and exit temperatures in the right-hand graph. Clearly, a cold catalyst entrance zone leads to total oxidation and hence to decreasing reaction selectivity and conversion (20).

The curves for RFR operation show a quite different behaviour: At the lowest flow rate, no improvement over the SS curves is observed, in agreement with the above explanation that not sufficient heat is produced by the reaction to sustain a highly selective partial oxidation. Hence, not enough heat is available either for efficient heat integration. Furthermore, the flushing-back of unconverted reactants in the pre-catalytic reactor zone leads to intrinsic losses in the reactor performance for very low flow rates and short switching frequencies and thus puts a limit on the attainable yields in the RFR (19).

However, as the flow rate increases syngas yields at RFR operation increase significantly over the SS values and this improvement is further enhanced with increasing flow rate. The increase in syngas yields continues over the whole range of feed gas flows investigated up to maximum syngas yields of about 78% for catalytic partial oxidation of methane with *air*! (Higher flow rates were not investigated since our experimental set-up was limited to a maximum total flow of 9 slm). These strong improvements in syngas yields are also reflected in continuously increasing catalyst temperatures with increasing flow rates in the RFR. It seems interesting to note that despite drastically increased yields, catalyst temperatures are only increased by about 100-250°C in comparison to SS reactor operation, and maximum temperatures at the catalyst ends also remain within 100°C of the mean catalyst temperatures even for the highest flow rates. Thus, RFR operation not only leads to strong improvements in syngas yields, but also allows at least a three-fold increase over the already unusually high reactor throughput in high-temperature millisecond contact-time catalysis.

The above explanations are further corroborated by another set of experiments, in which we replaced the foam monoliths by extruded monoliths. In this way, we were able to measure temperature profiles during reactor operation not only in the inert zones surrounding the catalyst, but also throughout the catalyst zone. Results for SS reactor operation with a Pt-coated extruded alumina monolith are shown in figure 5. Temperature profiles inside the upstream inert zone and throughout the catalyst (indicated by the shaded box) are shown for feed gas flows between 1 and 4 slm.

One can clearly observe how the increasing gas flow leads to increasing temperatures inside the catalyst due to more heat generation. At the same time, however, the front end of the catalyst is continuously cooled down and the maximum in the temperature profile is shifted further into the catalyst: while at 1 slm the maximum temperature of ~800°C is observed about 2mm inside the catalyst, this maximum shifts to ~950°C at  $z \approx 4$  mm with an increase in the flow rate to 4 slm while front end temperatures drop to ~500°C. This demonstrates how in-

creasing flow rates lead to decreasing syngas yields: Thermodynamic calculations show that temperatures of at least 900°C are necessary for optimal syngas selectivities. At the lowest flow rate, these temperatures are never reached inside the catalyst, thus limiting the attainable syngas yields. With increasing flow rates, however, the catalyst entrance zone cools down and a zone with temperatures well below 800°C extends over several mm. This 'cold zone' leads to increasing amounts of total oxidation near the catalyst front edge and hence to decreasing syngas yields. The measured temperature profiles furthermore demonstrate the extremely steep temperature gradients which can be achieved in millisecond contact-time reactions: at a flow rate of 4slm, temperature gradients as high as 200K/mm or  $2 \times 10^5$  K/m are obtained in these experiments!

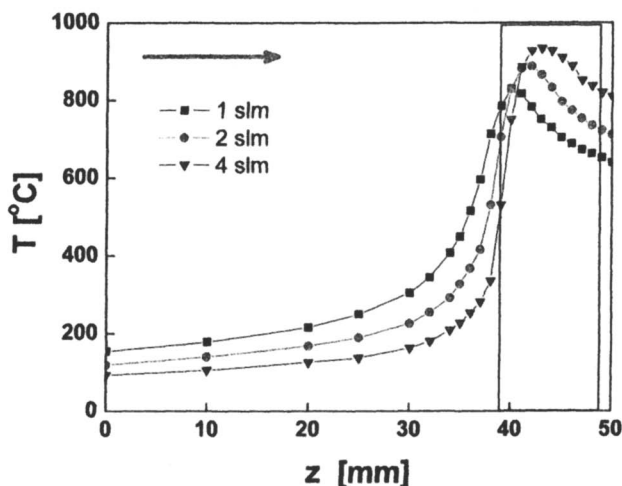
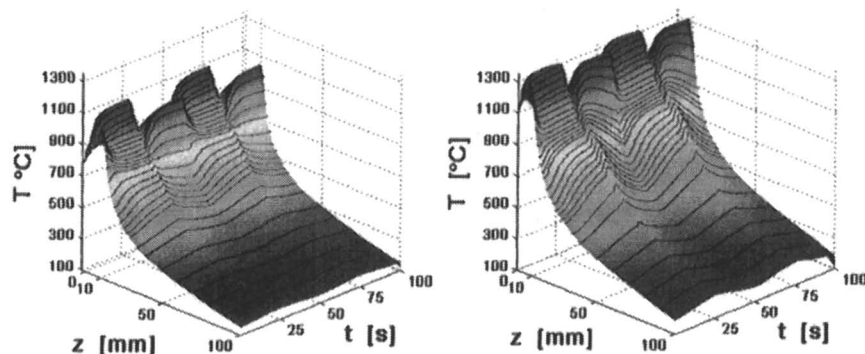


Figure 5: Temperature profiles in the upstream inert and the catalyst bed (shaded area) for different feed gas flows in a standard fixed-bed reactor with a Pt/Al<sub>2</sub>O<sub>3</sub> catalyst and CH<sub>4</sub>:O<sub>2</sub>:N<sub>2</sub> = 2:1:4.

The corresponding temperature profiles at RFR operation are shown in figure 6. Temperatures are shown for the catalyst zone (which is located between  $z=0$  and 10 mm) as well as one of the inert zones for a half-period of 25s and feed gas flow rates of 1 and 2 slm, respectively. One can see that the maximum temperatures inside the catalyst are increased by about 200-300°C in comparison with SS operation. However, while very high maximum temperatures of up to 1300°C with amplitudes of up to 250°C are achieved inside the catalyst, the temperatures at the reactor end remain well below 300°C with amplitudes of less than 50°C. Clearly, maximum temperatures can be very efficiently contained in the reaction zone via reverse-flow reactor operation.



**Figure 6:** Temperature profiles in one inert zone and 5 the catalyst bed for feed gas flows of 1 slm (left graph) and 2 slm (right graph) in a RFR. The  $\text{Pt}/\text{Al}_2\text{O}_3$  catalyst is an extruded monolith and is located between  $z = 0$  and 10 mm. Experimental conditions  $\text{CH}_4:\text{O}_2:\text{N}_2 = 2:1:4$ ,  $\tau/2 = 25\text{s}$ .

Most importantly, these measurements explain the continuous yield improvements observed with increasing feed gas flow rate in the RFR: As indicated by the strongly decreasing amplitude of local temperature oscillations in the inert zone at a gas flow of 1 slm, the heat capacity of the inert zones, and hence the capacity for heat-integration of this reactor, is not utilized efficiently at such low flow rates. Upon doubling the flow rate from 1 to 2 slm, one can already observe a significant increase in the amplitude of the temperature oscillations and hence also the spatial extent of these oscillations. Clearly, the regenerative heat-integration is more efficiently exploited at higher flow rates, and this increase in efficiency can be expected to continue further until the heat capacity of the inert zones is essentially completely exhausted over the entire length of the reactor, or until optimal equilibrium yields are achieved.

#### Heat-Integration and Catalyst Stability

A significant problem of high-temperature catalysis is catalyst stability. Due to the extreme temperatures, the catalyst choice is essentially restricted to noble metals, but even among those stability remains a concern as sintering and volatilization lead to a loss of catalytic activity and selectivity for many catalyst systems (21,22). It can be expected that due to the further increased reaction temperatures as well as the continuous ignition-extinction processes at both catalyst ends, this loss of activity is significantly enhanced at reverse-flow operation.

To test this hypothesis, we operated a Pt-coated alumina foam monolith at reverse-flow conditions for up to 36 hours, and during this RFR operation

switched repeatedly back to steady-state operation to evaluate the catalyst performance in 'conventional' reactor mode. Results from such a test are shown in figure 7, where hydrogen and CO yields (circles and squares, respectively) are shown for RFR ('RFR', filled symbols and solid lines) and conventional steady-state operation ('SS', open symbols and dashed lines) versus catalyst time-on-stream. One can see that already over the course of 20 hours reactor operation, significant catalyst deactivation is observed both at RFR as well as SS conditions. However, while both CO and H<sub>2</sub> yields drop by about 20% at SS (from ~59% to 40%, and from ~48% to 19%, respectively), this loss of catalyst activity is reduced to 12% for CO yields (from 77% to 65%) and to 8% for CO yields (from 82% to 74%). Clearly, RFR operation not only yields strongly improved syngas yields, but it also compensates for catalyst deactivation!

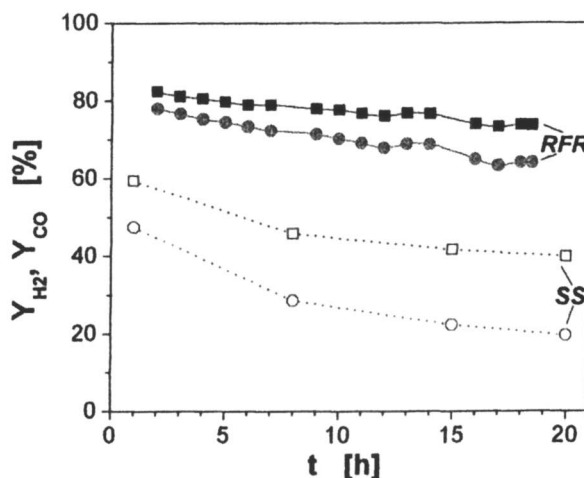


**Figure 7:** Catalyst deactivation at high-temperature conditions: CO (squares) and H<sub>2</sub> yields (circles) for catalytic partial oxidation of methane in a reactor without heat integration (SS, open symbols and dotted lines) and a reverse-flow reactor (RFR, filled symbols and solid lines) versus time-on-stream. Experimental conditions: CH<sub>4</sub>:O<sub>2</sub>:N<sub>2</sub> = 1.6:1:4, V = 4 slm,  $\tau/2 = 15$  s (RFR), Pt/Al<sub>2</sub>O<sub>3</sub> catalyst.

This is an interesting and unexpected additional benefit of the regenerative heat-integration in the RFR and can be explained as follows: The dominant effect of catalyst deactivation in the present system is the loss of hydrogen selectivity. Therefore, despite the loss of methane conversion, reaction temperatures

increase with increasing catalyst deactivation, resulting in hotter product gases. At steady-state reactor operation, this heat is simply lost with the reactor effluent, while at RFR operation at least part of this heat is re-integrated into the reactor, further increasing the catalyst inlet temperatures and thus again improving reaction yields as explained above. In this way, the integrated heat-regeneration in the RFR leads to an *intrinsic* compensation of catalyst deactivation.

### Quantifying ‘Process Intensification’

While an increasing number of studies on ‘process intensification’ and ‘integrated/multifunctional reactor concepts’ has been published over the past two decades (3-5, 12, 23), hardly any attempts to quantify the ‘intensification’ achieved with these reactor concepts can be found in the literature. While different definitions are needed depending on the target of the ‘intensification’ (reaction yield, waste minimization, reactor cost, efficiency or cost of product separation, etc), it seems nevertheless important to define quantifiable measures of the improvement achieved by the change in reactor design or concept.

We have previously suggested a definition of an efficiency for heat-integrated reactors (18). Figure 8 shows a schematic plot of (standard) enthalpy versus temperature to illustrate the idea behind this definition: The enthalpy of a gas can be separated into the “latent heat”,  $H^\theta$ , and the “sensible heat”,  $C_p \Delta T$  (where  $\Delta T = T - T^\theta$ ). In a steady-state process, products exit the catalyst bed at high temperature ( $T_{catalyst-exit,SS}$ ) and relatively low standard enthalpy ( $H_{SS}^\theta$ ). In comparison, the products of heat-integrated process exit the reactor at a lower temperature ( $T_{reactor-exit,RFR}$ ) and higher enthalpy due to increased reaction yields ( $H_{RFR}^\theta$ ). The difference between  $T_{catalyst-exit,SS}$  and  $T_{reactor-exit,RFR}$  is then proportional to the amount of sensible heat which is available for heat-integration in the RFR (with the proportionality factor being the mixture-averaged heat-capacity of the gases). On the other hand, the difference between the enthalpies of the steady state and the RFR process at temperature  $T_{reactor-exit,RFR}$  is equal to the difference in latent heat of the product gases (i.e. the difference in chemical energy).

The enthalpy flow (of sensible heat) is thus calculated via:

$$\dot{H}_{sh} = \sum_i \dot{n}_{i,SS} \cdot (c_{p,i} T_{catalyst-exit,SS} - c_{p,i} T_{reactor-exit,RFR}) \quad (1)$$

Where  $\dot{H}_{sh}$  is the flow of sensible heat,  $\dot{n}_{i,SS}$  is the molar flow of component  $i$  in the steady state process,  $c_{p,i}$  the temperature dependent heat capacity of species  $i$ ,  $T_{catalyst-exit,SS}$  the temperature at the catalyst exit in the steady state process, and  $T_{reactor-exit,RFR}$  is the temperature at the reactor exit in the RFR.  $\dot{H}_{sh}$  thus

represents the maximum amount of heat per unit time which can be integrated in the heat-integrated reactor.

Differences in latent heat between product gases of the RFR and the steady state process are calculated with the respective product gas compositions at the RFR exit temperature. This difference therefore represents the amount of heat converted into 'chemical energy' via heat-integration:

$$\Delta\dot{H}_{RFR-SS} = \sum_i \dot{n}_{i,RFR} H_i(T_{reactor-exit,RFR}) - \sum_i \dot{n}_{i,SS} H_i(T_{reactor-exit,RFR}) \quad (2)$$

where  $\Delta\dot{H}_{RFR-SS}$  is the difference in enthalpy flow between RFR and steady state operation,  $\dot{n}_{i,RFR}$  is the molar flow of the RFR product gas component  $i$ ,  $H_i$  is the enthalpy of species  $i$  at temperature  $T$ .

The efficiency  $\eta$  with which sensible heat is converted into chemical energy through regenerative heat-exchange is then defined by the ratio of these two enthalpy flows:

$$\eta = \frac{\Delta\dot{H}_{RFR-SS}}{\dot{H}_{sh}} \quad (3)$$

Using this definition, we had previously calculated the efficiency of the RFR reactor concept as a function of  $\text{CH}_4/\text{O}_2$  ratio and feed gas flow rate and found that the efficiency was not significantly affected by the  $\text{CH}_4/\text{O}_2$  ratio but increased strongly with increasing gas flow rate, which is in agreement with our qualitative observation above that increasing flow rates lead to improved heat integration and hence improved syngas yields (18).

Here, we apply this definition of heat-integration to the above discussed experiments with a deactivating catalyst. Results are shown in figure 8. We obtain an efficiency of about 50% at the conditions of this experiment, i.e. about 50% of the difference in sensible heat between the RFR and the conventional reactor have effectively been converted into 'chemical energy', i.e. into improvements in syngas yield. Interestingly, this efficiency does not change over time, i.e. the deactivation of the catalyst does not affect the calculated efficiency. This may seem surprising, since we saw that heat-integration very efficiently compensates for the ongoing deactivation of the catalyst and hence relative improvements in syngas yield increase with time. However, our definition of efficiency is rather conservative in that increasing catalyst exit temperatures are taking into account as a 'credit' in sensible heat of the products, i.e. it is implied in our definition that the sensible heat of the effluent gases will be used further downstream (such as through external heat-exchangers and subsequent utilization of the heat in other processes), and hence represents an 'asset' for the process. Therefore, the

calculated efficiency only increases if the change in reactor operation (or in the catalyst state) results in an improvement in heat-integration, i.e. if a larger proportion of the heat of the effluent gases is re-integrated into the process (rather than the same proportion of an increasing heat flow, as is the case here). Obviously, if the heat of the reactor effluent can not be utilized in some way (as often the case in decentralized processes), this definition of efficiency is too conservative and needs adjustment or redefinition. Furthermore, further increases in the already very high temperature of the exit gases will be undesirable in many practical applications, and the immediate, internal re-integration of this heat in an integrated reactor concept is thus not only more efficient but typically also advantageous with respect to the downstream handling of the product gases.

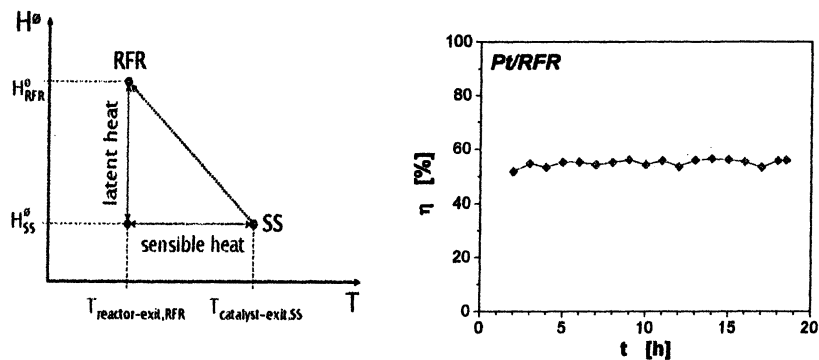


**Figure 8:** Left graph: Schematic diagram of standard enthalpy  $H^0$  vs. temperature  $T$ , illustrating the definition of 'energy efficiency'  $\eta$  in a heat-integrated reactor. Right graph:  $\eta$  versus time-on-stream in a RFR with deactivating catalyst (cp. fig. 7). Experimental conditions:  $\text{CH}_4:\text{O}_2:\text{N}_2 = 1.6:1:4$ ,  $V = 4 \text{ slm}$ ,  $\tau/2 = 15 \text{ s}$ ,  $\text{Pt}/\text{Al}_2\text{O}_3$  catalyst.

## Summary and Conclusions

We presented a brief overview of an on-going study into the use of heat-integrated reactor concepts for high-temperature, millisecond contact-time catalysis. The reaction system discussed here is the catalytic partial oxidation of methane to synthesis gas over noble metal coated monoliths. We demonstrated that this reaction system can profit from heat-integration in many ways: Heat-integration allows to overcome intrinsic limitations of reaction yields at auto-thermal reactor operation. While a simple thermodynamic equilibrium calcula-

tion shows that autothermal syngas yields are limited (at a stoichiometric ratio of  $\text{CH}_4/\text{O}_2=2$ ) to 64% and 68% for CO and  $\text{H}_2$ , respectively, we demonstrated that these yields can be pushed to at least 78% via heat-integration, with additional improvements possible via further optimization of reactor design and operation<sup>19</sup>. As these yield improvements are based on an effective conversion of thermal energy into chemical energy, heat integration has the additional advantage of keeping the effluent gases (as well as the reactor ends) relatively cool, thus greatly facilitating downstream handling of the product gases. Finally, heat-integration also resulted in a very efficient compensation of catalyst deactivation again based on the re-integration of the heat of reaction which increases with progressing deactivation.

We also demonstrated that regenerative heat-integration in a reverse-flow reactor (RFR) is superior to recuperative heat-integration in a counter-current heat-exchange reactor (HXR). While particularly the efficiency of the latter reactor concept could be improved via more advanced reactor designs, the superior efficiency of the dynamically operated RFR has also been found previously (12,24-26). Additionally, the RFR represents the more compact reactor design and thus perfectly complements the compactness of short contact-time reactors. While this compactness and efficiency is achieved at the expense of complexity in reactor operation, we found in all our experiments that despite the dynamic reactor operation mode, control of CPOM in an RFR was entirely unproblematic, with all aspects of reactor operation (start-up, shut-down, change in operating conditions) comparable to a simple steady-state flow-tube reactor.

It is interesting to compare this application of heat-integrated reactors with previous studies: heat-integration has typically been applied either for combustion of highly diluted off-gases, where the heat of reaction is not sufficient to sustain an autothermal reaction (25,27) (and, in a closely related, though more complex case, for the coupling of endothermal and exothermal reactions (28)), or alternatively for highly exothermal reactions which are subject to severe equilibrium limitations (24,29). Catalytic partial oxidation is an interesting “hybrid” between these two cases: while the reaction evolves sufficient heat in a simple fixed-bed configuration to sustain itself, this is not based on the exothermicity of the desired partial oxidation route, but rather on (undesired) total oxidation (18). This leads to an effective equilibrium limitation at steady-state autothermal reactor operation, although the desired reaction path itself shows no equilibrium limitations at stoichiometric composition and sufficiently high reaction temperatures. The reaction thus represents neither a ‘conventional’ equilibrium-limited system nor a conventional ‘heat-limited’ system. Nevertheless, we demonstrated that it is in fact ideally suited to the use of heat-integrated reactor concepts.

Finally, we proposed a general definition of an efficiency of heat-integration. This efficiency is based on the amount of sensible heat of the steady-state product gases that is converted into ‘chemical energy’, i.e. yield improve-

ments, in the heat-integrated reactor. This, our definition of efficiency could in fact be seen as a energy-based equivalent to the concept of 'atom efficiency' which has found widespread application in the context of Green Chemistry and sustainability: Just as 'atom efficiency' introduced the idea that simple reaction selectivity is not a sufficient criterion for an efficient chemical reaction, but that one needs to consider the number of atoms in the initial reactants which are eventually incorporated into the desired products, our definition of 'energy efficiency' considers the amount of heat that is directly converted into 'chemical energy' in the form of desired reaction products rather than a broad distribution of heat onto the sensible heat of all reactor effluent gases.

We suggest that such definitions of the efficiency of 'process intensification' are needed for an unbiased and quantifiable comparison between reactor concepts. In particular, general use of such efficiency would enable a direct comparison between different reactor concepts and reactor designs in the published literature and thus put 'process intensification' on a more rigorous scientific basis. Clearly, our proposed definition of efficiency is only applicable to heat-integrated reactor concepts and only takes the thermal efficiency of the reactor design into account. Additional, application-specific considerations (such as cost of equipment, operating cost, and similar) will need to be taken into account on the route towards more wide-spread application of integrated reactor concepts.

Overall, we have shown that heat-integrated reactor concepts yield highly efficient, small and simple reactors for high-temperature catalysis, and thus could help to lead the way to an industrial realization of these reactions. Furthermore, by integrating the large amount of heat necessary to achieve high-temperature conditions into the process rather than utilizing the heat downstream, integrated reactor concepts render this (and similar) reactions independent of other processes in which this heat would need to be utilized to make this reaction route economically viable. This reduction of the interdependence of chemical plants and processes as a result of multifunctional reactor design could lead to an increased flexibility of the chemical process industry and thus an increased willingness to adapt new reactor concepts or novel, more efficient reaction pathways for a more sustainable future.

### References:

- 1) Tsuris, C.; Porcelli, J. V. *Chem. Eng. Progress* **2003**, Oct., 50-55.
- 2) Dautzenberg, F.; Mukherjee, M. *Chem. Eng. Sci.* **2001**, 56, 251-267.
- 3) Agar, D. W.; Ruppel, W. *Chem. Ing. Tech.* **1988**, 60, 731-741.
- 4) Westerterp, K. R. *Chem. Eng. Sci.* **1992**, 47, 9-11.
- 5) Agar, D. W. *Chem. Eng. Sci.* **1999**, 54, 1299-1305.

- 6) Trent, D.; Tirtowidjojo, D. In *Commercial Operation of a Rotating Packed Bed (RPB) and Other Applications of RPB Technology*; 4th Int'l Conf. on Proc. Intensification in Practice; BHR Group Conf. Series: London, 2001; pp 11-19.
- 7) Oxley, P.; Brechtelsbauer, C.; Ricard, F.; Lewi, N.; Ramshaw, C. *Ind. & Eng. Chem. Res.* **2000**, 39, 2175-2182.
- 8) Saracco, G.; Specchia, V. *Catal. Rev.-Sci. Eng.* **1994**, 36, 304-383.
- 9) Gilbert, G. R.; Rock, K.; McGuirk, T. In *Advances in Proc. Technol. through Catalytic Distillation*; 10<sup>th</sup> Int'l Symp. on Large Chemical Plants, Antwerpen, 1998; pp 103-113.
- 10) Tonkovich, A. L. Y.; Carr, R. W. *AICHE J.* **1996**, 42, 683-690.
- 11) Tonkovich, A. L.; Carr, R. W.; Aris, R. *Science* **1993**, 262, 221-223.
- 12) Kolios, G.; Eigenberger, G. *Chem. Eng. Sci.* **2000**, 55, 5945-5967.
- 13) Prettre, M.; Eichner, C.; Perrin, M. *Trans. Faraday Soc.* **1946**, 43, 335-339.
- 14) Hickman, D. A.; Schmidt, L. D. *Science* **1993**, 259, 343-346.
- 15) Hickman, D.; Haupfear, E.; Schmidt, L. *Catal. Lett.* **1993**, 17, 223-237.
- 16) Veser, G.; Frauhammer, J.; Friedle, U. *Catal. Today* **2000**, 61, 55-64.
- 17) Friedle, U.; Veser, G. *Chem. Eng. Sci.* **1999**, 54, 1325-1332.
- 18) Neumann, D.; Veser, G. *AICHE J.* **2004**, in print.
- 19) Neumann, D.; Gepert, V.; Veser, G. *Ind. & Eng. Chem. Res.* **2004**, in print.
- 20) Veser, G.; Frauhammer, J. *Chem. Eng. Sci.* **2000**, 55, 2271-2286.
- 21) Bartholomew, C. H. *Appl. Catal. A* **2001**, 212, 17-60.
- 22) Mitri, A.; Liu, T.; Veser, G. *Chem. Eng. Sci.* **2004**, accepted.
- 23) Salden, A.; Eigenberger, G. *Chem. Eng. Sci.* **2001**, 56, 1605-1611.
- 24) Eigenberger, G., Fixed Bed Reactors. In: *Ullmann's Encyclopedia*; Schulz, B. E. (Ed.) 1992; Vol. B4.
- 25) Eigenberger, G.; Nieken, U. *Intl Chemical Engineering* **1994**, 34, 4-16.
- 26) Matros, Y. S.; Bunimovic, G. K. *Catal.-Rev. Sci. Eng.* **1996**, 38, 1-68.
- 27) Eigenberger, G.; Nieken, U. *Chem. Eng. Sci.* **1988**, 43, 2109-2115.
- 28) Glockler, B.; Gritsch, A.; Morillo, A.; Kolios, G.; Eigenberger, G. *Chem. Eng. Res. & Des.* **2004**, 82, 148-159.
- 29) van den Bussche, K. M.; Neophytides, S. N.; Zolotarskii, I. A.; Froment, G. F. *Chem. Eng. Sci.* **1993**, 48, 3335-3345.

## Chapter 10

### Miniaturization of a Hydrogen Plant

**J. D. Holladay, E. O. Jones, R. A. Dagle, G. G. Xia, C. Cao,  
and Y. Wang**

**Battelle, Pacific Northwest Division, P. O. Box 999, MS K6-24,  
Richland, WA 99352**

The development of a miniaturized hydrogen plant is discussed. The micro-scale system is capable of producing 1-5 sccm hydrogen that could be used as a fuel supply in a small fuel cell to produce <1 W power. The paper describes the developmental approach, significant unit operations, material selection, and reactor design. The final microscale fuel processing system is composed of a catalytic combustor, catalytic methanol reformer, selective methanation reactor, and the necessary vaporizers and heat exchangers. The fuel processing system is less than 0.3 cm<sup>3</sup> and less than 1 gram mass. Thermal efficiencies as high as 33% for hydrogen production were achieved. When a methanation reactor was incorporated into the system, a carbon monoxide level of less than 100 ppm was reached, but at a reduced system efficiency. Further development work includes increasing efficiency through improved system integration.

## Introduction

Over the last 50 years, technical advancements have reduced the size of many chemical processes now commonly used in electronics, manufacturing, and fuel production(*1*). These advancements have led to smaller and more efficient systems, including energy-saving and energy-producing micro-devices. In the work reported here, a micro-scale fuel processor was developed that reproduces the major unit operations of a commercial hydrogen production plant, but at perhaps as little as one billionth the processing flow and approximately one billionth the volume. The resulting miniaturized fuel processor, which is less than 0.3 cm<sup>3</sup> in volume and less than 1 gram mass, fits on a dime.

In recent years, there has been considerable interest in the development of miniature sub-watt electric power generation using hydrocarbon fuels (*2-10*). The hydrogen produced from the new processor could be used in a micro-scale power supply to produce <1 W of power from a fuel cell. The work to develop the micro fuel processor mainly focused on creating a power supply with greater energy density than the secondary batteries currently in microelectronic devices, such as microelectromechanical systems (MEMS) and microsensors. Due to the high energy density of hydrocarbons (e.g., methanol ~5.6 kWh/kg compared to lithium-ion batteries ~0.12 kWh/kg), even a very inefficient chemical to electrical energy conversion device could be a significant improvement over the available secondary battery technology (*10,11*). This paper discusses the research, considerations, and design development and testing involved in minimizing conventional-scale unit operations and packaging them into an efficient micro fuel processor.

## Approach

Successfully miniaturizing major unit operations requires that the functions at both the conventional scale and the micro scale be considered.

### Significant Operations

The primary unit operations considered in developing this technology included: desulfurization, reforming reactors, heat exchangers, heat source, and hydrogen purifiers. Vaporization, proper mixing, flow distribution, and other process parameters were included in the unit operation design.

Desulfurization involves organic sulfur removal and hydrogen sulfide removal. Typically, the organics are removed by hydrodesulfurization, and the

hydrogen sulfide is removed by adsorbents (12). Compact, ultra-deep sulfur removal is a serious issue for microreactors, because the sulfur poisons both the reforming catalysts and the fuel cell catalysts (12,13). Although there have been great advances in the development of sulfur adsorbents (14), the technology is still not feasible for the <1 W size range over an extended period of time. A simple solution, then, is to use a sulfur-free fuel, such as methanol.

Steam reforming (SR) is commonly used in industrial hydrogen and syngas production (15). Steam reforming was selected for the micro fuel processor to avoid coking and other problems associated with processing techniques such as partial oxidation (POx) and autothermal reforming (ATR) (12,13).

Several recent articles (12,16,17) provide in-depth reviews of hydrocarbon reforming for fuel cells. The hydrocarbon steam reforming reactions can be written as follows:



These reactions are endothermic. For example, the enthalpy change for methane is  $206 \text{ kJmol}^{-1}$ . The highly endothermic nature of the reactions typically causes heat transfer limitations to be the limiting mechanism. To overcome this limitation, for higher hydrocarbons, the reaction generally occurs between  $750^\circ\text{C}$  and  $1000^\circ\text{C}$  with excess water, typically 3 moles of water for every mole of carbon present, to prevent coking (12,13,15). Since the reactions are limited by heat transfer, a low-activity, inexpensive catalyst, such as nickel, is commonly used (12,13,15). The advantages of SR also include its high hydrogen concentration (>65%) and high efficiency, since some of the hydrogen is obtained from the water present. For hydrogen production, SR is often combined with water-gas shift (WGS) reactors to maximize the hydrogen production and decrease the carbon monoxide from as high as 10% or 15% to <1% on dry gas basis. The WGS reaction is (12,13):



The significant issues for conventional SR reactors include low heat and mass transfer, slow kinetics, high-temperature operation, and multiple unit operations to maximize the hydrogen production. Microchannel architecture has been shown to increase the heat and mass transfer rates, making the use of highly active catalysts desirable (17,18). The temperature can be reduced from  $750\text{-}1000^\circ\text{C}$  to  $250\text{-}350^\circ\text{C}$  by using methanol as the fuel (13,17,18). Processing methanol has the added advantage of being less endothermic than higher hydrocarbons ( $\Delta\text{H} = 49 \text{ kJmol}^{-1}$  for methanol compared to  $\Delta\text{H} = 206 \text{ kJmol}^{-1}$  for methane) (13). In addition to lowering the reaction temperature, methanol requires less water (1.2-2.0 moles water per mole carbon) than higher

hydrocarbons (17,18). For a miniature power supply, such as discussed in this paper, all the water needed for the reforming would likely be carried on the system, as water recovery would be a difficult task and would greatly increase the size and complexity of the system. The water weight should therefore be included in the energy calculation of the hydrocarbons, as depicted in Table 1. For comparison purposes, the ideal minimum amount of water required for the hydrocarbon conversion was used in these calculations. In practical reactors, higher steam-to-carbon ratios are used. When water is included, the methanol/water mixture has an energy density greater than that of the other hydrocarbon/water mixtures. The water/methanol mixture energy density also compares favorably with the energy density of fuels used in directly fueled fuel cells such as the direct methanol fuel cell (0.55 kW<sub>i</sub>-hr/kg for 3M methanol) and the direct formic acid fuel cell (0.55 kW<sub>i</sub>-hr/kg for 10M formic acid).

**Table 1. Fuel Processor Feed Energy Density (hydrocarbon + water)**

<i>Fuel</i>	<i>Water- to- Carbon Ratio</i>	<i>Pure Fuel Energy Density kW<sub>i</sub>-hr/kg</i>	<i>Mixed Fuel Energy Density kW<sub>i</sub>-hr/L</i>	<i>Mixed Fuel Specific Energy kW<sub>i</sub>-hr/kg</i>	<i>Reforming Temp. (°C)</i>
<i>Methanol</i>	1	5.6	2.81	3.29	300-400
<i>n-Butane</i>	2	12.6	2.57	3.11	450-650
<i>n-Octane (gasoline)</i>	2	12.3	2.67	2.99	550-750

Finally, through the lower-temperature fuel processing and the use of a methanol-specific catalyst, the amount of carbon monoxide in the product stream is typically less than 1%, thus eliminating the need for WGS reactors (13,17-20). In this work, a palladium zinc oxide (Pd/ZnO) catalyst was chosen for methanol reforming. The catalytic activity operating at atmospheric pressure and at various weight hourly space velocity is shown in Figure 1. The water-to-carbon ratio was 1.78:1 (molar). The typical dry product gas composition was 72-74% hydrogen, 24-26% carbon dioxide, and less than 1% carbon monoxide (18,19). The carbon monoxide levels were maintained at 1% or lower even when the catalyst was operated at higher temperatures up to 350°C. The Pd/ZnO catalyst was tested for over 1000 hours with no signs of deactivation and appeared to remain stable during shutdown and startup in air. Further information about this catalyst can be found in references (18-20).

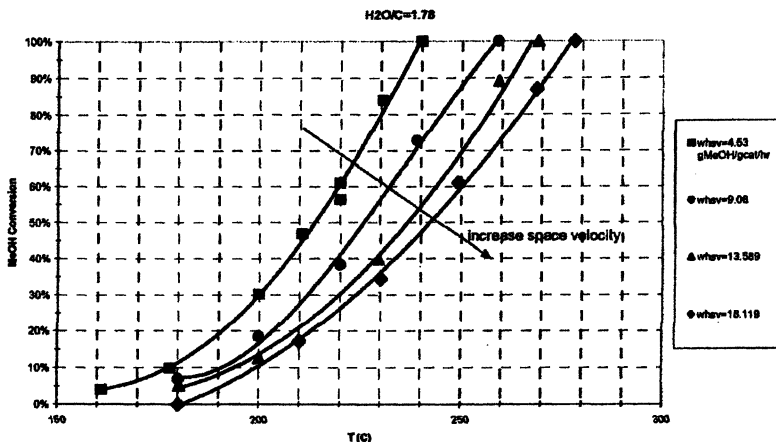


**Figure 1. Catalytic Performance of Pd/ZnO Catalyst in a Microchannel Reactor**  
(Reproduced with permission from reference 18. Copyright 2004 Elsevier.)

For conventional reactors, efficient heat exchangers are required to compensate for heat loss through the exhaust streams. The heat exchangers are used to vaporize water or fuel, and transfer heat from the hot combustion streams to the reactor and reactants, and to control the reactor temperature. Heat exchangers are also used to remove heat from the product streams (21). In order for high thermal efficiency to be achieved, microreactors will need to minimize heat loss, control reactor temperature, and vaporize fuels. Arana et al. (5) have shown that the mechanism for heat loss is not through the exhaust as in larger systems, but via conduction and, at higher temperatures, radiation. The heat loss via conduction and radiation can be addressed through fuel choice, material selection, and integrated system design.

Thermal energy for the conventional steam reforming reactor is provided by homogeneous combustion. During homogeneous combustion, the radicals that propagate the flame absorb onto the walls of the combustor and, consequently, may actually limit the propagation (22). This wall quenching effect depends on the diameter of the furnace, the wall material, and the temperature (22). The effect becomes particularly important in microreactors where the gap between the microchannel walls is often too small for homogeneous combustion to occur, particularly during startup when the walls are cool. Additionally, for methanol reforming, the extremely high temperatures from a homogeneous flame are not needed, and in fact make material selection difficult and temperature control complicated. An alternative approach is catalytic combustion, which is controllable even at low temperatures, and, since no flame is used, quenching is not an issue (10,23). However, startup using catalytic combustion can be difficult. The fuel needs to be in the vapor phase and may, depending on the type

of hydrocarbon, need elevated temperatures for the oxidation reaction to initiate on the catalyst surface (10,23). However, methanol ignites in the vapor phase at low temperatures, which makes it a suitable fuel (10,23).

After the hydrogen is produced, it needs to be purified for use in most applications. Hydrogen purification in industrial applications often involves pressure swing adsorption (PSA) (24-26). PSA operates by preferential hydrogen adsorption from the reformer product gas into an adsorbent bed. Multiple beds are used in this process, where one is adsorbing the hydrogen and the other(s) are releasing the hydrogen. The adsorption usually occurs at elevated pressures; for example, Iyuke et al. operated at 17 atmospheres (24). The desorption occurs at significantly lower pressures, and often the bed requires heating to desorb the maximum amount of hydrogen (24,25). In this type of purification, the high operating pressure, the use of multiple beds, and the required controls (valves, etc.) present challenges. Furthermore, to employ this technology for fuel cells to enable the use of diluted hydrogen, the carbon monoxide must be reduced to below 100 ppm (12,13).

Other purification technologies include metal membrane purifiers, preferential oxidation reactors (PrOx), and selective methanation reactors. Metal membranes, typically composed of palladium alloy, operate at elevated temperatures 300-400°C and pressures 100-400 psi (12,13,26,27). The hydrogen from metal membranes is often >99.999% pure, thus no further purification is required. The high pressure requirements make this technology difficult to integrate in some microreactor systems. Additionally, in some cases, the membranes are not stable for multiple (>100) thermal cycles (10,28,29).

The PrOx and methanation reactors are catalytic reactors. Note that although PrOx reactors are sometimes called selective oxidation reactors, selective oxidation actually refers to carbon monoxide reduction reactions occurring inside the fuel cell (13). The PrOx reactor increases the system complexity, because carefully measured concentrations of air must be added (12,13,30,31). However these reactors are compact and, if excessive air is introduced, some hydrogen is burned. Selective methanation reactors are simpler in that no air is required; however, for every molecule of carbon monoxide reacted, three hydrogen molecules are consumed. Also, as the temperature increases, the carbon monoxide selectivity decreases, and carbon dioxide may react with hydrogen. Careful control of the reactor conditions is important to maintain the selectivity. The catalysts for both these systems are typically noble metals such as platinum, ruthenium, or rhodium supported on  $\text{Al}_2\text{O}_3$  (12,13,30,31). Researchers at the Stevens Institute for Technology have had some success at fabricating a microscale PrOx reactor for a 0.5-W<sub>e</sub> fuel cell (30-31). However, to simplify the reactor, a selective methanation step was used in the work discussed here.

### Material Selection

Materials selection takes into account chemically compatible materials, thermal properties, and manufacturing complexities (e.g., feature fabrication and sealing). Table 2 lists the benefits and drawbacks of metals, silicon (which includes materials containing silicon or that are processed with semiconductor fabrication techniques), low-temperature co-fired ceramics (LTCC) (33,34), and plastics (polymers). Of particular importance to microreactors is the requirement

**Table 2. Common Materials for Microreactors: Benefits and Challenges<sup>1</sup>**

<i>Substrate</i>	<i>Benefits</i>	<i>Challenges</i>
<i>Metal</i>	Standard fabrication techniques Durable Low to modest costs No clean room required	High thermal conductivity Poor compatibility with ceramics and glass
<i>Silicon</i>	Well characterized silicon fabrication techniques High precision Low cost	Modest thermal conductivity Fragile Requires a clean room
<i>LTCC</i>	Flexible fabrication Refractory and durable Low cost No clean room required	Non-standard fabrication Low thermal conductivity Sealing
<i>Polymers</i>	Low cost Flexible fabrication Low thermal conductivity	Chemical compatibility Thermal compatibility Sealing

Source: Adapted with permission from references 33 and 34. Copyright 2003 Elsevier.

that the materials have a low thermal conductivity (5,10) and that joining and sealing of dissimilar materials can easily be achieved (5,33,34). Table 3 lists the thermal conductivity and coefficient of thermal expansion for materials that can be considered for microreactors. Polyimide is an interesting material that is thermally stable at high temperatures (>400°C) and has a low thermal conductivity (36). However, it may not be compatible with methanol, steam, and the other components at elevated temperatures. Furthermore, sealing it is difficult. The other materials, which were chemically compatible, were considered in the micro processor design development.

**Table 3. Thermal Conductivity and Coefficient of Thermal Expansion for Some Common Materials**

<i>Substrate</i>	<i>Thermal Conductivity (W/m*K at 600K)</i>	<i>CTE (1/C)</i>
<i>Silicon (35)</i>	62	$2.6 \times 10^{-6}$
<i>SiO<sub>x</sub> (35)</i>	5	$5.0 \times 10^{-7}$
<i>Silicon Nitride (35)</i>	11	$3.6 \times 10^{-6}$
<i>Alumina (35)</i>	16	$8.8 \times 10^{-6}$
<i>Zirconia (35)</i>	~3	$1.0 \times 10^{-6}$
<i>316 Stainless Steel (35)</i>	18	$16.0 \times 10^{-6}$
<i>Polyimide (36)</i>	0.12 (at 296K)	$20.0 \times 10^{-6}$

### Reactor Design Considerations

The strategy in this work was to identify feasible reforming reactor designs and then engineer a system that would thermally integrate the other unit operations. The steam reforming reactor incorporated a structured catalyst. In a structured catalyst, a catalyst powder is supported on a foam or felt. By supporting the catalyst on structured substrates, plugging can be avoided and pressure drop can be reduced due to the large opening pores in the foams or felt (typically 100 to 300  $\mu\text{m}$  in diameter). Additionally, conventional catalysts typically used in packed-bed reactors can be used. Plugging and pressure drop can be minimized by the design. The reactor is fabricated with an open side or port for loading the supported catalysts. This port requires sealing for practical use and can cause problems in the design and material selection. The reactor design must also minimize reactant bypass or “channeling” (1).

A radial flow system design (Figure 2) was used to incorporate all the unit operations into the fuel processing system. It was desired to have all the unit operations located close together to minimize the volume (especially the surface area) of the system in order to increase the efficiency. With the dimensions so small and the flow rates so low, the processing system would be designed to localize the heat to where it was needed the most (the reformer) and allow it to conduct to the other unit operations (primarily the vaporizers and preheaters).

### Results and Discussion

The first microscale fuel processor design involved using an engineered catalyst, if possible, and low temperature co-fired zirconia, with its low thermal conductivity. All of the fuel processing systems were fabricated in house. The

system was designed with two vaporizers/preheaters, a catalytic combustor, catalytic methanol steam reformer, and a heat exchanger. The reactor walls varied in thickness, depending on where additional strength was needed, but ranged from 0.1 to 0.25 mm thick. The reactor channels were slightly larger, ranging from 0.1 to 0.5 mm thick, depending on the unit operation. The catalyst was engineered onto a felt that was inserted into the reformer section.

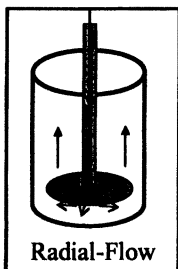


Figure 2. System Design.

The reforming reactor was sized to be approximately  $5 \text{ mm}^3$  for about 200 mW<sub>t</sub> hydrogen production with the gas flow rates at 1-2 sccm. Also, at such low flow rates, less than 0.01 W<sub>t</sub> was being carried in the gases. The combustor volume, also less than  $5 \text{ mm}^3$ , had a capacity of up to 3 W<sub>t</sub>. The oversized combustor capacity allowed a wide range of operating conditions to be examined. By keeping the design simple and using thin walls to minimize thermal conductivity, a small device could be designed. The premixed liquid methanol and water was fed and vaporized in the center of the processor. The reactant gaseous mixture was then distributed by a porous disk and flows through the catalyst bed counter-currently against the feed, whereby conversion takes place. The heat required for the reaction is supplied by the combustion chamber below the disk.

The fabrication of the device was extremely difficult due to sealing issues and to the fragile nature of the zirconia. By increasing the wall thicknesses (from 0.25 mm to less than 0.5 mm), a more structurally sound device could be built, but this would significantly increase the size of the device and also eliminate the low thermal conductivity advantage of the zirconia. In addition, connecting the input and outlet lines was difficult, and no acceptable seals were achieved. Ultimately, 316 stainless steel was chosen for the fuel processor system (Figure 3), which provided a stronger reactor, while maintaining compactness.

The combustor fuel consisted of hydrogen or methanol. The hydrogen feed during startup was less than 5 sccm, and the methanol feed to the combustor was from 0.1 to  $0.4 \text{ cm}^3 \cdot \text{hr}^{-1}$  to maintain the reactor temperatures at 300-450°C. In addition, 8-20 sccm air was fed to the combustor. A thermocouple was inserted

into the combustor to monitor the device temperature. The processor could be started without the use of electric heating, by initially feeding hydrogen gas to the combustor and then, once above 70°C, decreasing the flow of the hydrogen while slowly increasing the flow of methanol. The reformer fuel consisted of distilled de-ionized water/methanol mixture (1.8:1 steam-to-carbon molar ratio) for the first-generation reactor. The maximum flow rate was 0.05 cm<sup>3</sup>·hr<sup>-1</sup>. The methanol was Aldrich reagent grade (>99% purity). Gaseous product samples were analyzed with a microgas chromatograph (Agilent Quad G2891A). A combustion temperature of over 400°C was required to achieve >99% conversion of the methanol. This temperature was higher than anticipated, and the resultant product stream (reformate) contained higher amounts of carbon monoxide than desired. The reformate composition on a dry gas basis was 72-74% hydrogen, 24-26% carbon dioxide, and 1-2% carbon monoxide (10).

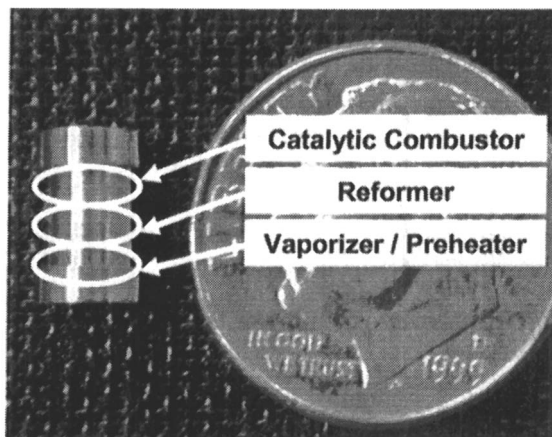


*Figure 3. Microscale Fuel Processing System. (Reproduced with permission from reference 39. Copyright 2004 Elsevier.)*

The thermal efficiency ( $\eta_t$ ) was calculated by dividing the lower heating value of the hydrogen in the reformate stream by the heating value of the methanol fed to the reformer plus the heating value of the fuel fed to the combustor:

$$\eta_t = \frac{\Delta H_c \text{hydrogen}}{\Delta H_c \text{methanol(reformed)} + \Delta H_c \text{combustion} \cdot \text{fuel}} \quad (3)$$

Where  $\Delta H_c$  is the lower heating value of hydrogen or methanol as indicated. Using equation 10, the maximum efficiency was found to be 13% (10).

From these initial tests, it was apparent that the vaporizers and preheaters were over designed. Therefore, a new design was developed that decreased the size of the vaporizer and preheater units and increased the reactor volume by approximately a factor of three. The package size did not significantly change ( $<0.2\text{ cm}^3$ ). In addition, the steam-to-carbon ratio of the reformer fuel was decreased from 1.8:1 to 1.2:1 (molar) (39).

The second-generation reactor was operated similarly to the first, except that the reformer fuel flow range increased to a maximum of  $0.2\text{ cm}^3\text{-hr}^{-1}$ . This reactor showed significant improvement. There was a substantial decrease in carbon monoxide production (0.5% compared to over 1.5% at the same reactant feed rate) with a significant increase in capacity and efficiency (Figure 4). The higher efficiency was attributed to the lower steam-to-carbon ratio of the reformer feed and the lower operational temperatures (255-320°C) (39).

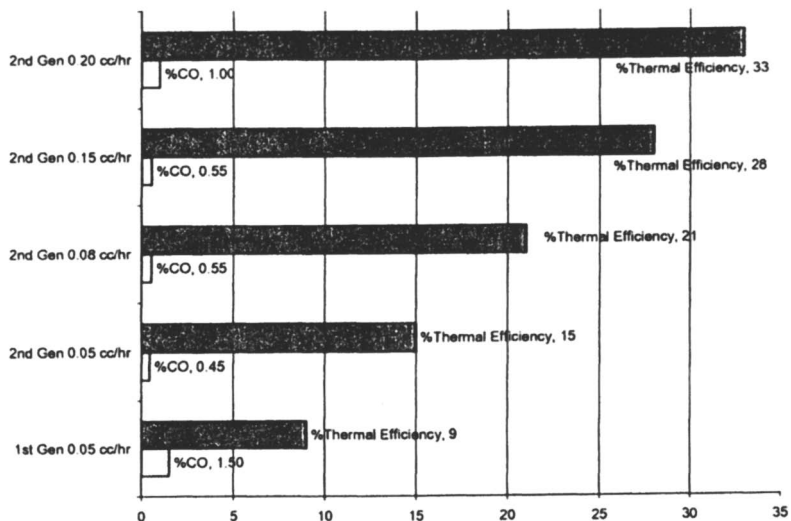


Figure 4. Second-Generation Performance.

Understanding the temperature distribution within the catalytic reactor helps to optimize the reactor design and choose operating conditions. In particular, there are three major heat sinks in this system: 1) the endothermic catalytic steam reforming reaction; 2) the premixed liquid methanol/water latent heat of vaporization in the center of the reactor, which will also affect the reactor temperature; and 3) heat transfer to the environment due to convection and conduction. The possible local cold spots in the reforming section reduced the reaction rate significantly and forces the system running at longer residence time or higher temperature to achieve high conversion level. However, high-temperature operation can affect catalyst performance, such as high carbon

monoxide selectivity and shortened catalyst life, and also can cause more heat loss to the environment. A model was developed from the mass and energy continuity equations, including the heat of reaction. Specific details are reported elsewhere (40).

The next step was to include a selective methanation reactor to reduce the carbon monoxide to below 100 ppm. From other experiments, the methanation reactor was determined to prefer operating at 220-270°C for selective methanation of carbon monoxide compared to carbon dioxide. As the temperature increased, the selectivity to carbon dioxide also increased. The model indicated that the selective methanation reactor could be added to the system; therefore, the proposed design was built and tested (Figure 5). The total volume was less than 0.3 cm<sup>3</sup>. The methanation reactor was designed to operate at 0.05 cm<sup>3</sup>·hr<sup>-1</sup> reformer methanol/water feed. It was operated from 0.05 to 0.15 cm<sup>3</sup>·hr<sup>-1</sup>. The carbon monoxide composition was determined using an infrared gas analyzer (ZRH, California Analytic Instruments).

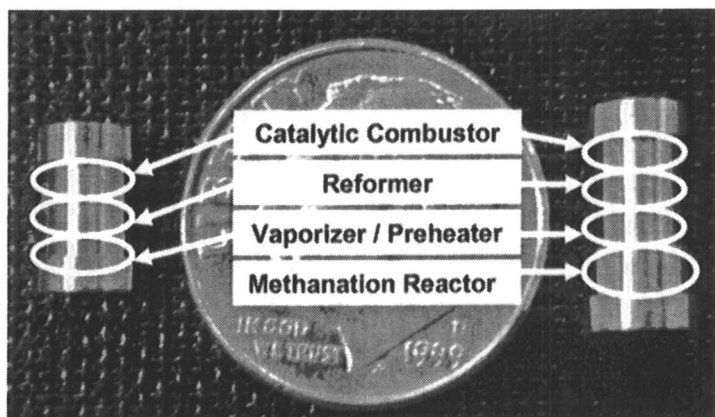
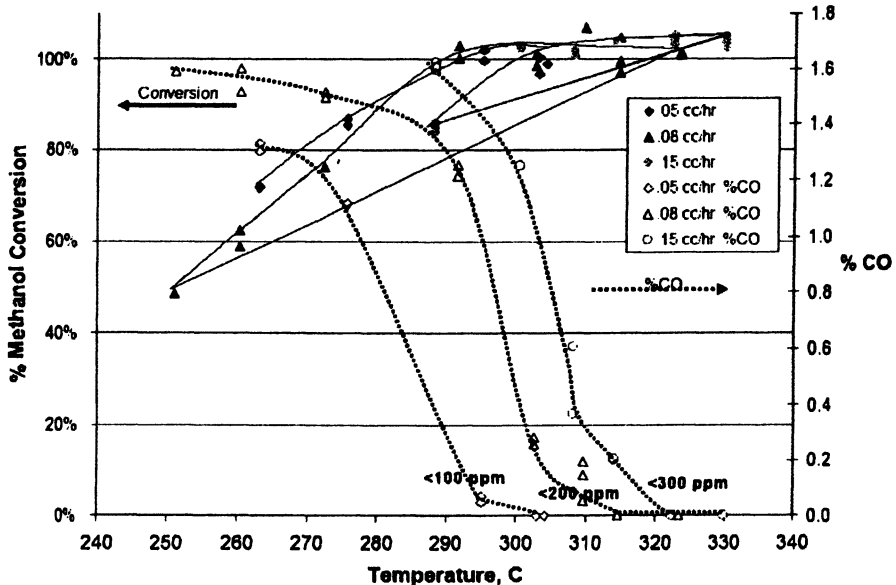


Figure 5. Micro-scale Reactor System and Micro-scale Reactor System with Selective Methanation Reactor. (Reproduced with permission from reference 39. Copyright 2004 Elsevier.)

The integrated fuel processor/methanation system was operated the same as the previous reactors, although slightly higher operation temperatures were required (304-345°C) for >99% methanol conversions and for low carbon monoxide production (Table 4). Significant reduction in the carbon monoxide levels did not occur until >99% of the methanol was reacted (Figure 6). The unreacted methanol decomposed in the methanation reactor, decreasing the effectiveness of the reactor. The carbon monoxide levels were reduced to below 300 ppm and, in some cases, below 100 ppm. There was also a significant reduction in the efficiency caused by the higher operating temperatures and loss of hydrogen to methane and water production. It was estimated that 13-15% of the hydrogen produced in the reformer was consumed in the methanation reactor.

**Table 4. Micro-scale Fuel Processor Performance Summary (adapted from references 10 and 39)**

Feed Rate (cm <sup>3</sup> -hr <sup>-1</sup> )	T(°C)	Reformate flow (sccm)	H <sub>2</sub> (%)	CO (%)	CO <sub>2</sub> (%)	CH <sub>4</sub> (%)	Thermal Efficiency (%)
<b>1<sup>st</sup> Generation</b>							
0.05	400	1.1	73-74	1-2	25-26	----	9
<b>2<sup>nd</sup> Generation</b>							
0.05	255	1.2	73-74	0.4-0.6	25-26	----	15
0.08	263	2.0	73-74	0.5-0.8	25-26	----	21
0.15	270	3.0	72-73	0.6-0.7	25-26	----	28
0.2	280	3.8	72-73	1.0-1.1	25-26	----	33
<b>2<sup>nd</sup> Generation + Methanation</b>							
0.05	304	1.0	69-70	<0.01	25-25.5	5-5.5	9.5
0.08	323	1.65	69-70	<0.02	25-25.5	6-6.2	14
0.10	330	2.1	69-70	<0.02	25-25.5	6-6.2	17
0.15	345	3.2	68-69	<0.03	25-26	5.3-6	19



*Figure 6. Low Carbon Monoxide Fuel Processor Performance<sup>1</sup>.*

<sup>1</sup> Conversion >100% was sometimes calculated when carbon did not balance. This was attributed to experimental error and slight variations (pulsing) in flow from the pumps, which was observed.

This consumption was higher than the anticipated 10%, and believed to be caused by higher-than-ideal temperatures in the methanation reactor for selective methanation of the carbon monoxide (i.e., some carbon dioxide was reacting in addition to the carbon monoxide). The next steps in further developing this system include: greater efficiency through improvements in the system integration, development of better insulation and thermal isolation methods, and development of the balance-of-plant components (e.g., pumps, fans, valves, and controls). Integrating this reactor with a microscale fuel cell is being explored. An efficient high-temperature fuel cell being developed at Case Western Reserve University (41) for this application.

## Conclusions

The method of miniaturization of a hydrogen production process was presented. The general philosophy was to identify the significant unit operations and their controlling mechanisms; identify how microreactors can be developed to perform the same operations; and finally to build, test, and model the reactors. Significant unit operations were miniaturized and then thermally integrated into a single unit. A radial reactor design using engineered catalysts was selected in this work. The compact unit was built of 316 stainless steel and contained two vaporizers/preheaters, a catalytic combustor, a catalytic methanol reformer, and, in one variation, a methanation reactor. The highest thermal efficiency attained was 33% with carbon monoxide levels being approximately 1%. A model was used to understand the reactor performance and to develop the methanol processor/selective methanation system. When a methanation reactor was integrated with the system, the carbon monoxide levels were reduced to less than 300 ppm and in one case less than 100 ppm, but at cost of substantial reduction in efficiency (9.5-19%). In addition to improving the reactor design, the next steps will be to develop improved packaging and identify or develop the necessary balance-of-plant components.

## References:

1. Ehrfeld, W.; Ehrfeld, U., In *Microreaction Technology IMRET 5: Proceedings of the Fifth International Conference on Microreaction Technology*; Matlosz M.; Ehrfeld, W.; Baselt, J.P., Eds.; Springer: New York, 2002; pp 3-12.

2. Savinell, R.F., Microfabricated Miniature Fuel Cells, In *Gordon Research Conference on Electrochemistry*, California, January 2001.
3. Wainright, J.S.; Savinell, R.F., A Microfabricated Hydrogen-Air Fuel Cell Incorporating a Novel Polymer Electrolyte, presented at the *Fall Meeting of the Electrochemical Society*, October 2000, Phoenix, AZ.
4. Matta, L.M.; Nan, M.; Davis, S.P.; McAllister, D.V.; Zinn, B.T.; Allen, M.G., Miniature Excess Enthalpy Combustor For Microscale Power Generation, In *American Institute of Aeronautics and Astronautics (AIAA) Paper 2001-0978*, AIAA, Aerospace Sciences Meeting and Exhibit, 39th, Reno, NV, January 8-11, 2001.
5. Arana, L.R.; Schaevitz, S.B.; Franz, A.J.; Schmidt, M.A.; Jensen K.F., *J.MEMS*, 2003, 12, 600-611.
6. Fu, K.; Knobloch, A.; Martinez, F.; Walther, D.C.; Fernandez-Pello, C.; Pisano, A.P.; Liepmann, D.; Miyaska K.; Maruta, K., Design and Experimental Results of Small-Scale Rotary Engines, In: *Proc. 2001 International Mechanical Engineering Congress and Exposition (IMECE)*, 2001.
7. Fu, K.; Knobloch, A.; Martinez, F.; Walther, D.C.; Fernandez-Pello, C.; Pisano, A.P.; Liepmann, D., Design and Fabrication of a Silicon-Based MEMS Rotary Engine, In: *Proc. 2001 International Mechanical Engineering Congress and Exposition (IMECE)*, 2001.
8. Maruta, K.; Koichi Takeda, K.; Sitzki, L.; Borer, K.; Ronney, P.D.; Wussow S.; Deutschmann, O., Catalytic Combustion in Microchannel for MEMS Power Generation, In *Third Asia-Pacific Conference on Combustion*, Seoul, Korea, June 24-27, 2001.
9. Richards, C.D.; Bahr, D.F.; Xu C-G; Richards, R.F., MEMS Power: the P<sup>3</sup> System, In *Proceedings of IECEC 2001, 36<sup>th</sup> Intersociety Energy Conversion Engineering Conference*, Savannah, GA, July-August 2001.
10. Holladay, J.D.; Jones, E.O.; Phelps, M.; Hu. J., *J. Power Sources*, 2002, 108, 21-27.
11. Koeneman, P.B.; Busch-Vishniac, I.J.; Wood, K.L., *J. MEMS*, 1997, 6, 355-362.
12. Song, C., *Cat. Today*, 2002, 77, 17-49.
13. Hoogers, G. In *Fuel Cell Technology Handbook*; Hoogers, G. Ed.; CRC Press: New York, 2003, pp 5-1 -5-23.
14. Hernández-Maldonado, A.J.; Yang, R.T.; *Ind. Eng. Chem. Res.*; 2003, 42, 3103-3110.
15. Krummenacher, J.K.; West, K.N.; Schmidt, L.D., *J. Catal.*, 2003, 215, 332-343.

16. Moon, D.J.; Sreekumar, K.; Lee, S.D.; Lee, B.G.; Kim, H.S.; *Appl. Cat. A.* **2001**, 215, 1-9.
17. Hu, J.; Wang, Y.; VanderWeil, D.; Chin, C.; Palo, D.; Rozmiarek, R.; Dagle, R.; Cao, J.; Holladay, J.; Baker, E., *Chem. Eng. J.*, **2003**, 93, 55-60.
18. Cao, C.; Xia, G.; Holladay, J.; Jones, E.; Wang, Y., *App. Catal. A.*, **2004**, 262, 19-29.
19. Chin, Y.H.; Dagle, R.; Hu, J.; Dohnalkova, A.C.; Wang, Y.; *Cat. Today.*, **2002**, 77, 79-88.
20. Iwasa, N.; Masuda, S.; Ogawa, N.; Takezawa, N.; *App. Catal. A*, **1995**, 125, 145-157.
21. Whyatt, G.A.; TeGrotenhuis, W.E.; Geeting, J.G.H.; Davis, J.M.; Wegeng, R.S., In *Microreaction Technology IMRET 5: Proceedings of the Fifth International Conference on Microreaction Technology*; Matlosz M.; Ehrfeld, W.; Baselt, J.P., Eds.; Springer: New York, 2002; pp 303-312.
22. Strahle, W.C., *An Introduction to Combustion*; Gordon and Breach Science Publishers: Langhorne, PA, 1993; Vol. 1, pp 78-80.
23. Jones, E.O.; Holladay, J.; Perry, S.; Orth, R.; Rozmiarek, B.; Hu, J.; Phelps, M.; Guzman, C.; In *Microreaction Technology IMRET 5: Proceedings of the Fifth International Conference on Microreaction Technology*; Matlosz M.; Ehrfeld, W.; Baselt, J.P., Eds.; Springer: New York, 2002; pp 277-285.
24. Iyuke, S.E.; Daud, W.R.W.; Mohamad, A.B.; Kadhum, A.A.H.; Fisal, Z.; Shariff, A.M.; *Chem. Eng. Sci.*, **2000**, 55, 4745-4755.
25. Mohamad, A.B.; Iyuke, S.E.; Daud, W.R.W.; Kadhum, A.A.H.; Fisal, Z.; Al-Khatib, M.F.; Shariff, A.M.; *J. Mol. Struct.*, **2000**, 550-551, 511-519.
26. Appleby, A.J.; In *Fuel Cell Systems*; Blomen, L.J.M.J.; Mugerwa, M.N. Eds.; Plenum Press, New York, 1993, pp. 157-199.
27. Ward, T.L.; Dao, T.; *J. Mem. Sci.*; **1999**, 153, 211-231.
28. Buxbaum, R.E.; Kinney, A.B.; *Ind. Eng. Chem. Res.*; **1996**, 35, 530-537.
29. Kusakabe, K.; Takahashi, M.; Maeda, H.; Morooka, S.; In *Microreaction Technology IMRET 5: Proceedings of the Fifth International Conference on Microreaction Technology*; Matlosz M.; Ehrfeld, W.; Baselt, J.P., Eds.; Springer: New York, 2002; pp 78-85.
30. Karnik, S.V.; Hatalis, M.K.; Kothare, M.V.; In *Microreaction Technology IMRET 5: Proceedings of the Fifth International Conference on Microreaction Technology*; Matlosz M.; Ehrfeld, W.; Baselt, J.P., Eds.; Springer: New York, 2002; pp 295-302.
31. Bednarova, L.; Ouyang, X.; Chen, H.; Besser, R.S.; Microreactors with Thin-Film Catalyst for Preferential Oxidation of CO; In *226th ACS National Meeting*, New York, September 7-11, 2003.
32. Besser, R.S.; Shin, W.C.; *J. Vac. Sci. Tech.B.*, **2003**, 21, 912-915.
33. Thompson, L.T.; Novel Fuel Processing Catalysts and Reactors; In *226th ACS National Meeting*, New York, September 7-11, 2003.

34. Johnson, W.L.; Phillips, C.B.; Chen, Z.; Ransom, T.S.; Thompson, L.T.; Novel, heat integrated, Low Temperature Co-fired, Ceramic (LTCC) Methanol Reformer for Hydrogen Generation; In *226th ACS National Meeting*, New York, September 7-11, 2003.
35. Incropera, F.P.; DeWitt, D.P.; *Fundamentals of Heat and Mass Transfer 3rd Edition*; John Wiley & Sons, New York, 1990, A1-A30.
36. *Kapton® Polyimide Film Summary of Properties*; Dupont High Performance Films; Dupont: Circleville, OH, 2000, pp 1-4.
37. Tonkovich, A.Y.; Zilka, J.L.; LaMont, M.J.; Wang, Y.; Wegeng, R.S.; *Chem. Eng. Sci.*, **1999**, 54, 2947-2951.
38. Ahn, J.; Eastwood, C.; Sitzki, L.; Ronney, P.D.; "Gas Phase and Catalytic Combustion in Heat Recirculating Burners", *Proceedings of the Combustion Institute*, Vol. 30. 2003.
39. Holladay, J.D.; Jones, E.O.; Dagle, R.A.; Xia, G.G.; Cao, C.; Wang, Y.; *J. Power Sources.*, **2004**, 131, 69-72.
40. Cao, C.; Holladay J.D.; Wang, Y.; Xia, G.; Jones, E.O.; submitted to J. AIChE.
41. Holladay, J.D.; Wainright, J.S.; Jones, E.O.; Gano, S.R.; *J. Power Sources.* **2004**, 130, 111-118.

## Chapter 11

### Downsizing Chemical Processes for Portable Hydrogen Production

D. G. Norton<sup>1</sup>, S. R. Deshmukh<sup>1</sup>, E. D. Wetzel<sup>2</sup>, and D. G. Vlachos<sup>1,\*</sup>

<sup>1</sup>Department of Chemical Engineering and Center for Catalytic Science and Technology (CCST), University of Delaware, Newark, DE 19716

<sup>2</sup>Army Research Laboratory, Aberdeen Proving Ground, MD 21005-5069

#### Abstract

Various exothermic and endothermic components of a portable hydrogen production system are explored through modeling and experiments. Gas phase combustion in a microburner to generate energy needed for hydrogen generation by endothermic reactions is first studied. An elliptic computational fluid dynamics model of a microburner is used to determine the effects of wall conductivity, external heat losses, choice of fuel, and operating conditions on the steady state, self-sustained gaseous flame stability of propane/air and methane/air mixtures. Experimental prototype catalytic microburners are subsequently evaluated to determine the range of operating conditions for stabilized catalytic combustion of propane/air mixtures. It appears that the dimensions of microburners have a strong effect on performance. Finally, catalytic, post microreactors for the production of hydrogen from ammonia decomposition over ruthenium catalyst are modeled using a hierarchy of models. Good agreement of simulation predictions with experimental data is observed. Important issues in the design of the above components are identified.

The use of portable electronic devices, including cellular phones, laptop computers, global positioning devices, and electrically powered vehicles, continues to grow. This growth necessitates the exploration of lightweight, efficient, and portable power generation devices.

Here we give an overview of our research group's recent progress on the portable production of hydrogen needed for proton exchange membrane fuel cells along with some new results. The focus of this work is on downsizing commercial processes that (1) create heat, i.e., microburners, and (2) use it to generate H<sub>2</sub>, i.e., microreactors.

### Downsizing Large Scale Gaseous Flames

When designing miniaturized power/heat generation devices, an intuitive proposal is to downsize plant scale processes, i.e., gaseous hydrocarbon flames. However, in 1817 Davy showed that gaseous flames extinguish when confined between gaps of sub-millimeter range (1), and these results were confirmed numerous times since. The two primary causes for lack of flame stabilization are thermal and radical quenching at walls (2-4). Increased surface area to volume ratios, resulting from miniaturization, exacerbate chemical and thermal quenching. Despite general belief to the contrary, self-sustained, stabilized gas-phase combustion at the microscale is possible in microburners with gaps smaller than 1 mm (5). These microburners were constructed to combat the quenching mechanisms discussed earlier.

In order to better understand gaseous flame stability in confined geometries, two dimensional (2D) computational fluid dynamics (CFD) simulations were conducted. Details of these calculations can be found in (6). A major finding of these simulations is that in microcombustors, upstream heat transfer is integral to igniting and stabilizing flames with non-preheated feeds but at the same time heat losses through the walls are responsible for loss of flame stability. The thermal conductivity of the walls is generally several orders of magnitude greater than that of the fluid and the fluid volume is relatively small. This disparity in conductivities results in the majority of heat being transferred upstream mainly through the reactor walls, instead of through the fluid phase.

The wall thermal conductivity and external heat loss coefficient were modified parametrically to determine the critical points at which flame stability is lost for methane/air and propane/air flames, as shown in Figure 1. Note that the resistances to heat transfer within the microburner and its wall are explicitly taken into account via solving the governing energy balances in the gas-phase and the wall, respectively, and only the external heat loss coefficient is modeled in a lumped way (using Newton's law of cooling). The shaded area below each curve and the horizontal axis represents the regime where stabilized flames are possible for a microburner with a 600  $\mu\text{m}$  gap, a stoichiometric feed, and an inlet

velocity of 0.5 m/s. The lines in this figure are just guides to the eye. There appear to be two primary ways for flame stability loss. The first stems from excessive heat losses to the surroundings, resulting in too much energy leaving the system tangential to the direction of flow. The second stems from sufficiently low wall thermal conductivity that chokes the upstream heat transfer through the walls. As a result, the upstream preheating is delayed and blowout occurs.

Methane's operation window is a subset of that of propane (7). Propane can operate in burners of materials with a smaller thermal conductivity and withstand higher heat loss coefficients. A sensitivity analysis elucidated the cause of the differences between methane and propane's stability. The analysis showed that the lower ignition temperature of propane compared to that of methane is the main reason for propane's enhanced stability. A reduced ignition temperature requires less preheating. Consequently, the ignition distance is shorter and stabilization further upstream occurs.

The inlet flow rate also plays a key role in determining the location of the flame in a microburner. When the flow rate is sufficiently high, the residence time is short to allow for preheating of the feed by the walls. On the other hand, when the flow rate is sufficiently low, the external heat losses dominate over the low power generated, and the system is thermally quenched. Figure 2 shows the critical velocity versus the wall thermal conductivity for a microburner with a 600  $\mu\text{m}$  gap, a stoichiometric propane/air feed, and an external heat loss coefficient of 10  $\text{W}/\text{m}^2/\text{K}$ . The shaded area between the curves represents conditions that allow for stabilized microcombustion whereas the areas on either side denote non self-sustained combustion. The lines are just guides to the eye. Low power systems, which require low flow rates, need materials with low wall thermal conductivity. Conversely, high power systems require materials of higher wall thermal conductivity for self-sustained operation.

## Catalytic Microburners

As discussed above, stabilizing homogeneous microcombustion is difficult. The allowable heat loss coefficients are typically in the range of free convection, the permitted range of flow rates is restrictive, and the materials of construction must be carefully prepared to eliminate radical quenching. Catalytic combustion typically requires lower ignition temperatures, operates at lower temperatures that eliminate thermal NO<sub>x</sub> and ensure materials' mechanical stability, and could sustain fuel leaner mixtures than homogeneous combustion. Typically, catalytic combustion is mass transfer limited. However, the high surface area to volume ratio, inherent to microscale devices, increases the transport rates, making catalytic combustion at the microscale an attractive energy production route. The lower temperatures of catalytic combustion make it a more suitable path of

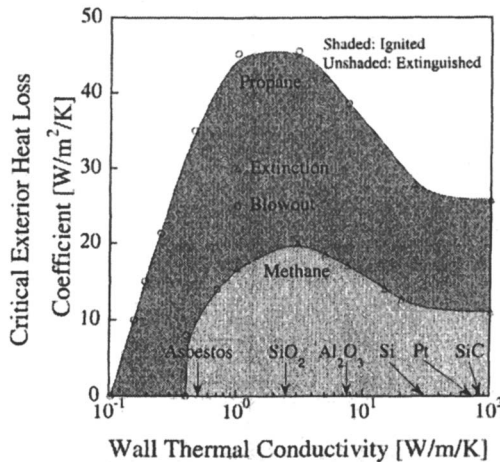


*Figure 1 Critical external heat loss coefficient vs. wall thermal conductivity. Typical ceramics allow maximum external heat loss coefficients. Materials with lower wall thermal conductivities limit the upstream heat transfer. Materials with higher wall thermal conductivities result in enhanced heat transfer to the surroundings. Propane allows self-sustained combustion for higher external heat loss coefficients and more insulating materials than methane. The rest of the parameters are denoted in the text. Heat transfer inside the burner and its wall are explicitly accounted for through the governing equations.*

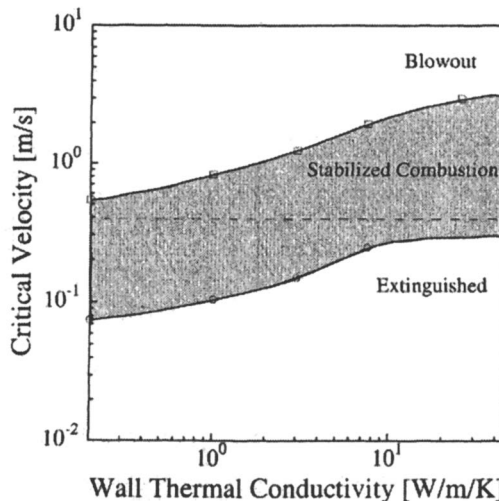


*Figure 2 Critical velocity vs. wall thermal conductivity. The lower curve (-o-) represents stability loss due to insufficient heat generation. The upper curve (-□-) represents blowout. The shaded region allows for stabilized combustion. The experimentally determined laminar flame speed (22) is plotted as a dashed line. Higher wall thermal conductivity allows for higher energy devices whereas more insulating materials for low heat production devices. The parameters are denoted in the text.*

chemical energy conversion to electricity for some applications. This advantage stems from the relatively low temperatures that simplify critical packaging and thermal management issues in terms of available insulation methods (e.g., vacuum packaging could be an option up to 200-400 °C), bulkiness of insulation materials, and personal safety (avoid flames).

Prototype ceramic microburners were fabricated to test the feasibility of this concept. They consisted of a ceramic cylinder with a rectangular channel in the center. A diagram of the reactor parts is shown in Figure 3. The channel dimensions were 5 cm long by 1 cm wide by a small channel gap height. The channel gap height can easily be modified in the fabrication. Typical heights studied varied from 250  $\mu\text{m}$  to 1000  $\mu\text{m}$ , resulting in reactor volumes ranging from 125  $\mu\text{L}$  to 500  $\mu\text{L}$ . About 44 mg of Pt catalyst was deposited onto the reactor walls via wet deposition. Near the inlet, staggered posts were included to ensure uniform flow within the channel. Integrated thermocouples were placed flush with the channel walls to obtain axial and transverse temperature profiles. Details of the fabrication protocol are given elsewhere (8).

Figure 4 shows typical ignition/extinction behavior of propane/air mixtures. The temperature at 1.6 cm from the inlet is plotted versus the power supplied electrically to 250 and 1000  $\mu\text{m}$  gap size burners for an equivalence ratio of  $\phi = 0.77$ . Starting from an unignited state, there is a linear ramping of the temperature with the power supplied. Once the temperature reaches the ignition temperature, the temperature jumps to a high value. Upon ignition, as the power supplied is decreased, there is a linear ramping of the temperature down to zero power input in the 250  $\mu\text{m}$  gap size burner where self-sustained (autothermal) combustion occurs. The multiple autothermal data points shown for the 250  $\mu\text{m}$  gap size indicate the variation in measurements over the period of days. In contrast to the smaller gap size, in the 1000  $\mu\text{m}$  gap size burner, as the power supplied is reduced from high values to  $< 12$  W, the system extinguishes. This ignition/extinction or ignition/autothermal hysteresis-type behavior is characteristic of catalytic combustion systems seen previously over foils and wires e.g. (9-11).

While in the unignited state, both burners exhibit the same linear ramping of temperature vs. power supplied. However, the 250  $\mu\text{m}$  gap size burner ignites at a lower ignition temperature (~150 °C) and power (~30 W) compared to the 1 mm gap size burner (~235 °C at ~50 W). In a stagnation point foil burner, where the boundary layer is in the order of a few mm for these flows, the ignition temperature observed for a similar composition is ~250 °C (10), in close agreement with the 1 mm gap size burner measurement.

Figure 5 shows the temperature at 1.6 cm from the inlet versus  $\phi$  for the 250 and 1000  $\mu\text{m}$  gap size burners. Leaner mixtures exhibit lower temperatures as expected due to decreased heat generation. In the 250  $\mu\text{m}$  gap size burner, in all fuel lean self-sustained cases, the propane conversion is  $> 97\%$  and the

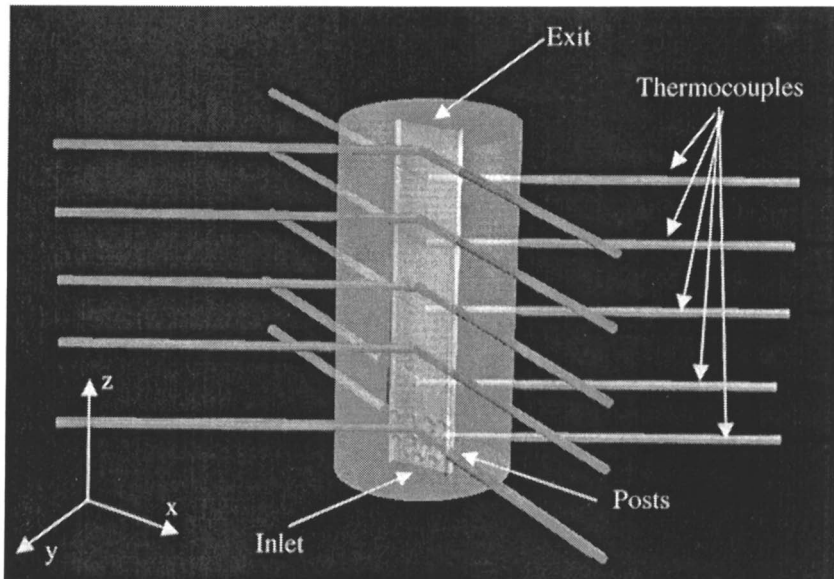


Figure 3 Schematic showing the placement of the embedded microburner components.

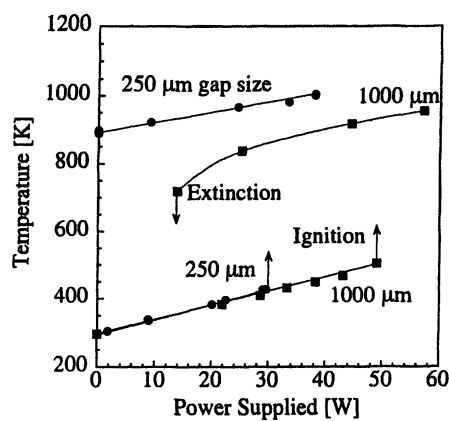


Figure 4 Temperature at 1.6 cm from the inlet versus the power supplied for propane/air at  $\phi = 0.77$  in the 250  $\mu\text{m}$  and 1000  $\mu\text{m}$  microburners. Ignition is easier and extinction more difficult in smaller gap sizes.

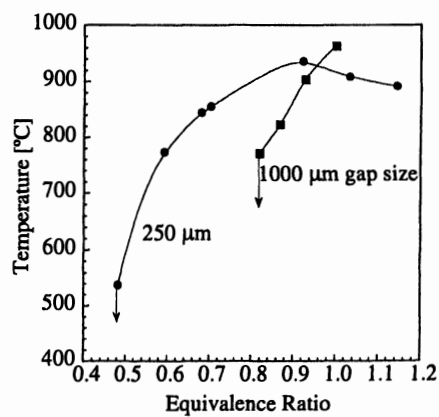


Figure 5 Temperature at 1.6 cm from the inlet versus equivalence ratio in the 250  $\mu\text{m}$  and 1000  $\mu\text{m}$  microburners. A sharp falloff in temperature is seen, near  $\phi = 0.48$  for the 250  $\mu\text{m}$  and  $\phi = 0.80$  for the 1000  $\mu\text{m}$  microburner, below which combustion cannot be self-sustained.

selectivity to carbon dioxide and water is  $> 99\%$ . The minimum equivalence ratio for stabilized combustion is  $\sim 0.48$ . In the  $1000 \mu\text{m}$  gap size burner the behavior is less robust. For stoichiometric mixtures, the temperature is near that of the smaller gap size burner. However, as the equivalence ratio decreases, the temperature drops significantly, and extinction is observed at  $\phi < \sim 0.8$ . In all cases in the  $1 \text{ mm}$  gap size burner, the conversion of propane is incomplete. For example, at stoichiometric, the conversion is only  $86\%$  and at  $\phi = 0.87$  the conversion is  $76\%$ , indicating transport limitations with increased gap size.

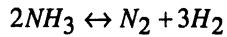
From these results, it appears that smaller gap sizes render the ignition temperature lower, increase temperatures and conversion, and expand the regime of self-sustained combustion, features that are consistent with enhanced transport rates. Another important outcome of smaller dimension is the possibility for autothermal operation at much lower temperatures, while still getting relatively high conversions. From a practical standpoint, this feature implies that the microcombustor is much easier to incorporate into consumer devices, personal power supplies, etc. While the two burners are made the same way, they are not exactly identical, for example in terms of catalyst amount and dispersion and ceramic porosity. So the observed differences may not be solely attributed to size. Future work is needed to delineate the mechanism causing these differences.

The considerable lower fuel lean composition with decreasing device size (Figure 5) differs substantially from the way gaseous microburners behave. Decreasing length scales in homogeneous microburners increases the rate of heat and radical loss from the gas to the walls and causes flame quenching. These catalytic microsystems enable stabilized combustion under fuel-leaner conditions than homogeneous microburners of similar dimensions. For example, our previous modeling work has shown that the fuel-lean limit in a  $600 \mu\text{m}$  gap size single-channel homogeneous microburner is  $\sim 0.80$  (7) compared with the  $\sim 0.48$  in  $250 \mu\text{m}$  gap size catalytic microburner. Thus, the reduction in device size disfavors gas-phase chemistry while promoting surface chemistry, rendering the catalytic route more robust even for single channels.

Ronney et al. observed a minimum equivalence ratio of  $\sim 0.5$  at similar Reynolds numbers in a 3.5 turn, mesoscale, spiral, counter-flow swiss roll burner with a characteristic gap size of  $3.5 \text{ mm}$  (12). The swiss roll design inherently recycles heat from the hot combustion products to the incoming reactants, and yet does not allow combustion of significantly leaner feeds than the  $250 \mu\text{m}$  gap single channel burner used here. The increase in transport rates between the gas and the walls compensate for the lack of preheating in our single channel design. Clearly, it is entirely possible to combine the benefits of confinement and the swiss roll heat recycling to expand the operation window of catalytic microburners.

## Chemistry for Hydrogen Production

Hydrogen can be produced via multiple routes. In our work, ammonia decomposition



has been selected over alternative routes, such as the commercial steam reforming and the promising partial oxidation, mainly due to the elimination of downstream processes (i.e., water gas shift and preferential oxidation of CO) needed to prevent poisoning of the fuel cell catalyst.

Modeling of microreactors for H<sub>2</sub> production requires first a good understanding of the underlying chemistry. Despite ammonia synthesis being a well-studied reaction, ammonia decomposition is not as well understood. In previous work, we have found that available surface science based rate expressions are inadequate to describe microreactor data (13). To overcome this problem, we have used the multi-step methodology described in (14) to develop a detailed ammonia decomposition mechanism on Ru. Six elementary, reversible steps involving the adsorption/desorption of NH<sub>3</sub>, N<sub>2</sub> and H<sub>2</sub> and H-abstraction from NH<sub>x</sub> intermediates were postulated. Order of magnitude estimates of the pre-exponential factors were obtained from transition state theory and the activation energies from the semi-empirical unity bond index quadratic exponential potential theory (15, 16) with heats of chemisorption from surface science experiments and adsorbate-adsorbate interactions from density functional theory calculations. Details can be found in (13). An important finding is that adsorbate-adsorbate lateral interactions (in particular N-N interactions) strongly affect model prediction and need to be accounted for (17).

CFD simulations using this detailed kinetic model are computationally intensive. A one-step reduced chemistry model was developed starting from the full kinetic model using a novel computer-aided chemistry reduction methodology described in (13). The reduced chemistry model can then be employed in CFD simulations to gain insight into the interplay of chemistry, flow, and transport within microreactors, as described below.

## CFD Simulations of a Post Microreactor

Microreactors for portable applications must meet certain design characteristics including low-pressure drop, non-movable parts, high conversion, fast heat transfer, and good mixing. To meet these characteristics, several designs have recently been proposed (18, 19). Here we focus on the experimental post microreactor of (18), which is an anodized framework of Al with about 275 posts (diamonds in Figure 6) impregnated with Ru each being 300 μm x 300 μm x 3mm in size. The posts occupy a length of 1 cm in a 2.1cm

long reactor. Initial 3D studies (20) indicate that 2D simulations are adequate, and thus we present here only 2D results. CFD modeling details are presented in (13).

Figures 6a and 6b shows typical ammonia mass fraction and flow contours in the post microreactor. The flow pattern is complex with an overall parabolic velocity profile developing downstream that is locally perturbed by posts. Back diffusion is observed at low flow rates, but is negligible at moderate and high flow rates such as the one shown in Figure 6a. Figure 6c compares experimental data with CFD simulation results. Overall, good agreement is found.

The ammonia contours in Figure 6b and comparison using various reactor models (continuously stirred tank reactor (CSTR), plug flow reactor (PFR), tubular, diffusion-convection-reaction) (13, 20) indicate that mass transfer in the transverse direction is fast and thus, the post microreactor behaves effectively like a PFR, especially at faster flows where back diffusion is negligible.

An important question in designing microreactors then is how close these posts should be to get the benefits of fast mass transfer without further increasing pressure drop. We provide insight into this question using dimensional analysis arguments. In particular, simulations in a geometry consisting of two parallel plates of distance  $L$  apart and of length 1.5 cm, depicted in Figure 7a, have been performed. The primary mechanism for mass transfer in the transverse direction that is responsible for transport of reactants and products between the catalyst surface and the bulk is diffusion. Hence, comparison of time scales of diffusion,  $\tau_d$ , and of surface reaction,  $\tau_r$ , in terms of the second Damkhöler number (21),  $Da = \tau_d / \tau_r = (L^2 / D) / (1/k_r)$ , provides an estimate of the rate-determining step. In particular, when  $Da < 0.1$  diffusion is considerably faster than surface reaction, implying a kinetics limiting situation where further reduction in post distance is unnecessary. On the other hand, when  $Da > 10$ , severe mass transfer limitations occur. Between these two bounds a transition regime exists.

Here, the pseudo-first-order reaction rate constant is estimated from  $k_r' = \sigma \underline{a} / C$ , where  $\sigma$  is the rate of ammonia decomposition,  $\underline{a} = 2/L$  is the catalyst area per unit volume, and  $C$  is the concentration of ammonia. Since the rate expression is complex and depends on all gaseous species, the pseudo-first-order reaction rate constant depends implicitly on transport/flow and location within the reactor that determine local concentrations. However, to a first approximation one can compute the intrinsic reaction time scale,  $\tau_r$ , using a PFR model (or from the rate vs. conversion expression) where transverse mass transfer is assumed to be infinitely fast. Since for our chemistry  $k_r'$  decreases with length,  $Da$  also decreases along the reactor as shown in Figure 7b. Below,  $Da$  is calculated near the entrance (at 10% of the length, i.e., at 1.5 mm from the entrance) to give an upper bound and thus to ensure no diffusion limitations in the entire channel.

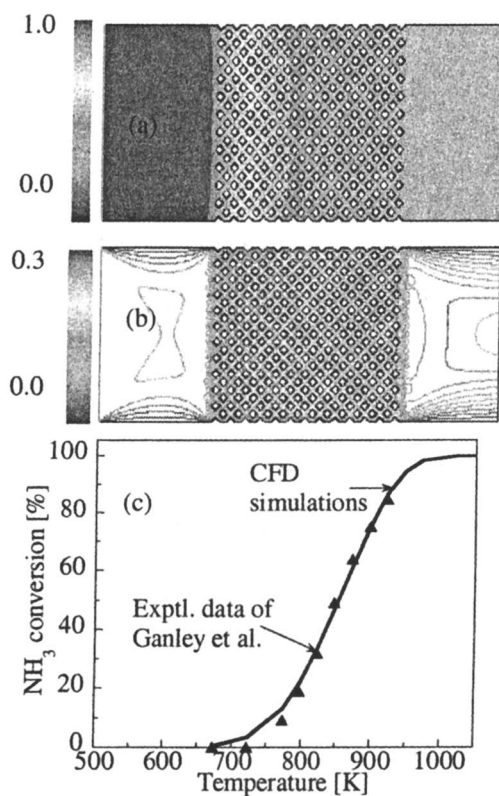


*Figure 6 (a) Mass fraction contours of ammonia and (b) velocity magnitude contours in the post microreactor at 923 K and 30 sccm flow rate. (c) Comparison of CFD predictions with experimental data vs. temperature at 15 sccm inlet ammonia flow.*

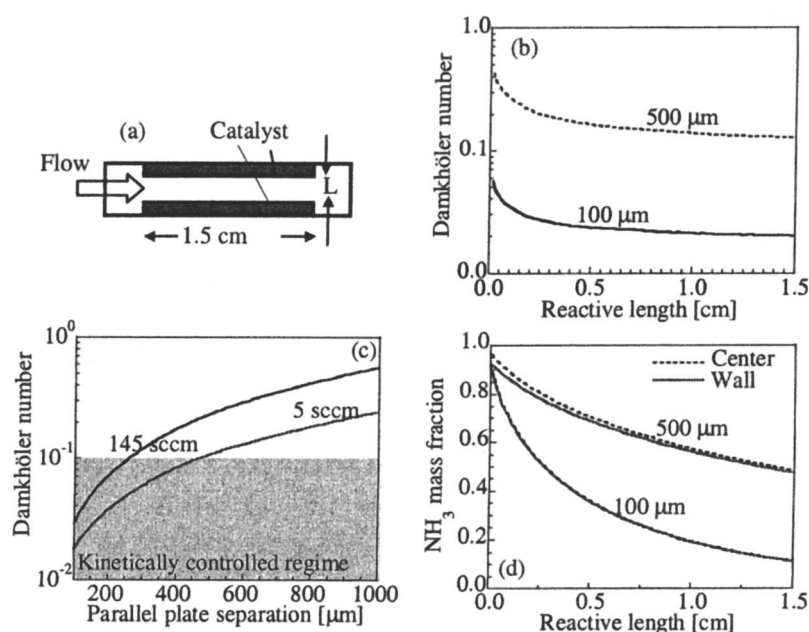


*Figure 7 (a) Schematic of parallel plate microreactor geometry used in CFD simulations. (b)  $Da$  along the reactor for two separation distances indicated for the ammonia decomposition chemistry at a flow rate of 145 sccm. (c)  $Da$  at 1.5 mm from the entrance as a function of the parallel plate separation. (d) Mass fraction contours of ammonia at the center and wall from CFD parallel plate microreactor simulations at a flow rate of 145 sccm. Differences in profiles at the larger separation indicate the onset of diffusion limitations. The temperature is 923 K.*

Figure 7c is an operation diagram in terms of the Da vs. parallel plate separation, constructed based on the aforementioned assumptions, for two extreme experimental flow rates. The shaded region indicates the reaction-limited regime within which the plates or posts are sufficiently close. For our conditions, Da is relatively low, i.e., operation typically happens in the kinetically limiting or transition regimes.

In order to validate the PFR operation diagram Figure 7c, the ammonia mass fractions at the wall and the center of the channel obtained from CFD simulations are plotted in Figure 7d. The slight difference between bulk and surface mass fractions at the larger separation of 500  $\mu\text{m}$  indicates the onset of diffusion limitations. On the other hand, for a separation of 100  $\mu\text{m}$ , there are practically no gradients in species mass fractions. CFD predictions in Figure 7d are qualitatively consistent with the PFR operation diagram Figure 7c. The simple PFR operation diagram can thus provide approximate channel size or post distance that is necessary for operating in the kinetically limiting regime.

## Conclusions

The characteristics of premixed propane/air and methane/air gaseous microcombustion obtained using CFD were first reviewed. It was shown that homogeneous microcombustion is possible but requires careful materials design, e.g., proper choice of wall thermal conductivity to allow adequate upstream preheating while minimizing external heat losses. Materials with low wall thermal conductivities are suitable for lower power devices, whereas those with higher wall thermal conductivities are suitable for higher power devices. Furthermore, microburner dimensions are also important.

Experimental prototype catalytic microburners were then tested to determine their suitability for portable power generation. Propane/air mixtures were found to be self-sustained and the microburners were shown to be very robust. It appears that the microchannel size controls transport rates and can be tuned to affect ignition and extinction characteristics as well as microburner efficiency (in terms of conversion).

Finally, 2D CFD simulations of a post microreactor were performed as an example for hydrogen generation, with ammonia decomposition on Ru as the chosen chemical route. Simulation results are in good agreement with the experimental data. It was found that the post microreactor behaves effectively like a PFR at higher flow rates but exhibits back diffusion at low flow rates. An operation diagram, which provides estimates of sizes ensuring kinetically controlled operation, was finally proposed. Future work will focus on integrations of various components discussed in this paper.

### Acknowledgements

This work has been funded through the Army Research Laboratory Composite Materials Research program at the University of Delaware Center for Composite Materials and by the Army Research Office under contract DAAD19-01-0582. Any findings, opinions, and conclusions or recommendations expressed here are those of the authors and do not necessarily reflect the views of the Army Research Laboratory or the Army Research Office.

### References

1. Davy, H., Some researches on flame. *Trans. Roy. Soc. London* 1817, 107, 45-76.
2. Raimondeau, S.; Norton, D.; Vlachos, D. G.; Masel, R. I., Modeling of high temperature microburners. *Proc. Comb. Inst.* 2003, 29, 901-907.
3. Vlachos, D. G.; Schmidt, L. D.; Aris, R., Ignition and extinction of flames near surfaces: Combustion of CH<sub>4</sub> in air. *AIChE J.* 1994, 40, (6), 1005-1017.
4. Aghalayam, P.; Vlachos, D. G., The roles of thermal and chemical quenching in NO<sub>x</sub> and fuel emissions: Combustion of surface-stabilized hydrogen/air mixtures. *AIChE J.* 1998, 44, (9), 2025-2034.
5. Masel, R. I.; Shannon, M. Microcombustor having submillimeter critical dimensions, US06193501. 2001.
6. Norton, D. G.; Vlachos, D. G., Combustions characteristics and flame stability at the microscale: A CFD study of premixed methane/air mixtures. *Chem. Eng. Sci.* 2003, 58, 4871-4882.
7. Norton, D. G.; Vlachos, D. G., A CFD study of propane/air microflame stability. *Combust. Flame* 2004, 138, 97-107.
8. Norton, D. G.; Wetzel, E. D.; Vlachos, D. G., Fabrication of single channel catalytic microburners: Effect of confinement on the oxidation of hydrogen/air mixtures. *Ind. Eng. Chem. Res.* 2004, 43, 4833-4840.
9. Veser, G.; Schmidt, L. D., Ignition and extinction in the catalytic oxidation of hydrocarbons over platinum. *AIChE J.* 1996, 42, (4), 1077-1087.
10. Veser, G.; Ziauddin, M.; Schmidt, L. D., Ignition in alkane oxidation on noble-metal catalysts. *Catal. Today* 1999, 47, 219-228.
11. Williams, W. R.; Stenzel, M. T.; Song, X.; Schmidt, L. D., Bifurcation behavior in homogeneous-heterogeneous combustion: I. Experimental results over platinum. *Combust. Flame* 1991, 84, 277-291.
12. Ahn, J.; Eastwood, C.; Sitzki, L.; Borer, K.; Ronney, P. D. In *Catalytic and noncatalytic combustion in heat-recirculating burners*, Proceedings of the

Third Joint Meeting of the U.S. Sections of the Combustion Institute, Pittsburgh, PA, 2003; Pittsburgh, PA, 2003; p E03.

- 13. Deshmukh, S. R.; Mhadeshwar, A. B.; Vlachos, D. G., Microreactor modeling for hydrogen production from ammonia decomposition on ruthenium. *Ind. Eng. Chem. Res.* 2004, 43, (12), 2986-2999.
- 14. Aghalayam, P.; Park, Y. K.; Vlachos, D. G., Construction and optimization of detailed surface reaction mechanisms. *AICHE J.* 2000, 46, (10), 2017-2029.
- 15. Shustorovich, E., Bond-order conservation approach to chemisorption and heterogeneous catalysis: Applications and implications. *Adv. Catal.* 1990, 37, 101-164.
- 16. Shustorovich, E.; Sellers, H., The UBI-QEP method: A practical theoretical approach to understanding chemistry on transition metal surfaces. *Surf. Sci. Rep.* 1998, 31, 1-119.
- 17. Mhadeshwar, A. B.; Kitchin, J. R.; Barteau, M. A.; Vlachos, D. G., The role of adsorbate-adsorbate interactions in the rate controlling step and the most abundant reaction intermediate of  $\text{NH}_3$  decomposition on Ru. *Cat. Lett.* 2004, 96, (1-2), 13-22.
- 18. Ganley, J. C.; Seebauer, E. G.; Masel, R. I., Porous anodic alumina posts as a catalyst support in microreactors for production of hydrogen from ammonia. *AICHE J.* 2004, 50, (4), 829-834.
- 19. Losey, M. W.; Jackman, R. J.; Firebaugh, S. L.; Schmidt, M. A.; Jensen, K. F., Design and fabrication of microfluidic devices for multiphase mixing and reaction. *J. MEMS* 2002, 11, (6), 709-717.
- 20. Deshmukh, S. R.; Mhadeshwar, A. B.; Lebedeva, M. I.; Vlachos, D. G., From density functional theory to microchemical device homogenization: model prediction of hydrogen production for portable fuel cells. *Int. J. Multiscale Comput. Eng.* 2004, 2, (2), 221-238.
- 21. *Kirk-Othmer Encyclopedia of Chemical Technology*. Wiley: 1999.
- 22. Dugger, G. L., Effect of initial mixture temperature on flame speed of methane-air, propane-air and ethylene-air mixtures. *NACA Report 1061* 1952, 105-116.

## Chapter 12

# Fuel Processing in Catalytically Coated Microreactors for Low-Power Fuel Cell Applications

**V. Cominos, V. Hessel, C. Hofmann, G. Kolb, H. Pennemann,  
and R. Zapf**

**Institut für Mikrotechnik Mainz GmbH, Carl-Zeiss-Str. 18–20,  
D–55129 Mainz-Hechtsheim, Germany**

A number of state-of-the-art low power fuel cell systems for portable applications and for stand-alone auxiliary power units exist. The commercialisation of the portable power systems based on direct methanol fuel cells is foreseen by the various companies to be on average within 2005 even though what is predominantly available to-date are prototypes. Based on some recent press releases not all technical problems seem to have been resolved thus leading in some cases to a further delay in market releases. As the demand for even higher power output grows, the typical power density of direct methanol fuel cells may well prove to be insufficient. Thus, processing of various fuels such as methanol and propane to clean hydrogen continues to play a role in low power fuel cell applications (< 200 W). The work carried out at IMM within this field is summarised here.

## Introduction

The on-going drive to achieve more compact and efficient fuel cell systems for low power applications has drawn the attention of scientists in the field of microtechnology as is evident from the activities of a number of research institutes and universities such as Pacific Northwest National Laboratory (1), Eindhoven University of Technology (2), Massachusetts Institute of Technology (3) and Stevens Institute of Technology (4), to name but a few. Microtechnology offers new possibilities for such processes as they can be run at short residence times with higher heat and mass transfer phenomena.

Low power applications and more specifically portable power (< 100 W) promises to be the first commercial market for fuel cells, according to a market survey carried out by Fuel Cell Today (5), since the consumer electronics is currently in a race to find an alternative to nickel cadmium and lithium ion batteries as they stand to hit a barrier due to the demand for increasingly faster processors and higher-resolution displays which inevitably increase the overall power required. In the same survey, it is stated that currently there are now more organisations active in portable fuel cell applications than in any other sector of the fuel cell industry. The number of portable systems built has increased dramatically during the last three years, from less than 1000 portable systems built in 2001 to more than 3500 in 2003 (5). This growth is accounted partly by the fact that there has been an increase in the number of companies which have turned their attention to the development of portable fuel cell systems.

Information regarding the specifications of the various prototypes pursued is not extensively available. It is known that in 2003 Toshiba displayed a laptop incorporating a 12 W (20 W maximum output) direct methanol fuel cell (DMFC) system with fuel storage volume of 50 cc and 100 cc allowing operation of the device up to 5 hours and 10 hours respectively. The laptop with the 100 cc fuel storage weighed 900 g (6). A new version was exhibited in Cebit 2004, Germany, where Toshiba stated that the new laptop had an energy density five times that of a typical lithium-ion battery (7). NEC displayed a laptop in 2003 incorporating a DMFC system with 14 W average output (24 W maximum output) which weighed 900 g with a fuel storage volume of 300 cc (8). Even less specifications are known about some Casio and Motorola prototypes (9, 10, 11) which have systems based on proton exchange membrane fuel cells (PEMFC).

It is interesting to note, though, that to-date most companies have only produced one or two prototypes each (see Figure 1) and despite continuous press releases announcing the commercialisation of laptops running on fuel cells within 2004 (e.g. Toshiba (6), NEC (8), Casio (9)), there have been some announcements indicating a postponement by another year (12). There is of course a strong intent to commercialise such systems in the very near future, an

indication being that in March 2003 nearly all Japanese companies involved in this sector joined their efforts in order to create a single set of standards for fuel cells employed in laptops, mobile phones and other portable devices such as Portable Digital Assistants (PDAs).

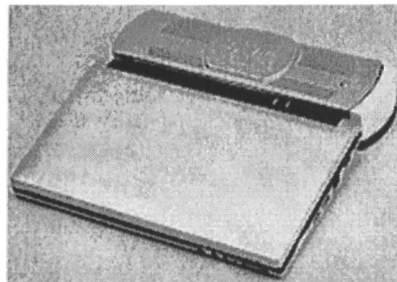


*Figure 1: Toshiba prototype laptop with a 12 W direct methanol fuel cell system*  
 (Source: Reproduced with the kind permission of Toshiba Corporation from reference 6)

According to a news article, dated 1/10/03, Casio Computer Co, Ltd is reported to see a great potential for fuel cells in computer and portable electronic product applications (13). Casio predicts that for laptops, the current rechargeable batteries will be replaced with fuel cells to become the mainstream. As for digital cameras and PDAs, it is presumed that fuel cells, lithium manganese primary batteries and the next generation lithium-ion batteries will co-exist. For the even lower power output field (such as Walkmans and radios) it predicts that in addition to fuel cells, primary batteries including alkaline manganese batteries and rechargeable batteries including electric double layer capacitor, solar batteries and energy sources using natural energies such as human body temperature and movement, will be introduced. In the field where high density energy of 1 000 Whr/L or higher is required, such as in laptops, Casio predicts that among fuel cells, DMFCs will be insufficient in generating enough power density and thus PEMFCs will be in use. At present, the power density of DMFC is 50 mW/cm<sup>2</sup> and the company claims that this needs to reach 100 mW/cm<sup>2</sup> before they can be used. Casio is thus pursuing the development of a PEMFC system which requires methanol to be reformed to hydrogen in order to power laptops.

Other low power applications include stand-alone auxiliary power units (APU) for use in remote locations or for recreational vehicles (such as caravans and yachts) where they can also be used in combination with conventional technologies. In such applications, devices are required to operate intermittently. They offer a huge weight reduction from lead acid batteries and are independent of time of day and weather (that is, they do not need sun light as

competing solar panels do), they are silent and have lower emissions than conventional generators. They do not require to be significantly small in size as space is less of an issue here. This is a niche market but it could also be seen as a first step towards bringing fuel cells closer to consumers and to mass markets.

To our knowledge, Smart Fuel Cell AG is the only company to-date which sells fuel cell systems for recreational vehicle applications. The unit shown in Figure 2 is based on a DMFC which provides 25 W continuous power (14).

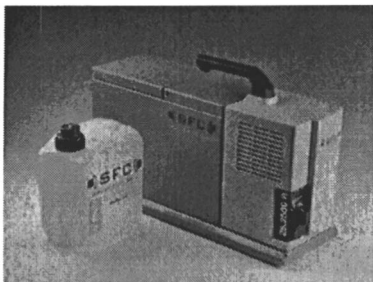


*Figure 2: Smart Fuel Cell SFC A25 small stationary fuel cell unit (25 W)*  
 (Source: Reproduced with the kind permission of Smart Fuel Cell SFC AG from reference 14)

The size of this unit is 465 mm x 290 mm x 162 mm and weighs 9.7 kg including the fuel tank. The fuel tank itself weighs 2 kg. A comparable energy content of lead-acid batteries weighs about 100 kg. The company also markets this unit as a remote industrial power source for traffic and telecommunications systems, danger warning and weather stations. It can also be used to charge batteries.

Most manufacturers addressing low power fuel cell applications have been found to be pursuing the DMFC technology (e.g. SFC, Toshiba, NEC, Motorola) as opposed to PEMFC (only Casio and Motorola to our knowledge). DMFCs are receiving increasing attention and their share of the market has grown considerably in the last years as the liquid fuel requires no reforming and the systems operate at near room temperature. As customers, though, continue to place greater demands on the previous-mentioned devices which in turn require manufacturers to incorporate applications which consume even greater amounts of power, eventually DMFCs with power densities of 50 mW/cm<sup>2</sup> may well not be able to satisfy these demands. Thus, PEMFCs can be seen to have some advantage over DMFCs in this field. This is why companies such as Casio and Motorola are also investigating the application of PEMFCs for their devices. In addition, DMFC further need to overcome some obstacles for power outputs > 100 W which are typically needed for applications such as recreational vehicles. Thus, PEMFCs have great potential in this field of application.

Regarding the choice of fuel, methanol is probably the cheapest and simplest way of supplying fuel to PEMFC for portable applications. Alternatives such as metal hydride canisters and compressed hydrogen cylinders have lower energy densities and this is of importance where size is a crucial factor. Methanol can be easily supplied in disposable or refillable cartridges in the same way that butane is supplied for cigarette lighters. It is thought to be unlikely that consumer markets, where fuel cells will principally compete with Li-ion batteries, will support the cost of hydrogen storage and distribution whether in metal hydride or high pressure canisters (5). For applications such as APUs for stand-alone systems or for recreational vehicles, propane is also a strong candidate due to its easy storage and existing infrastructure.

Thus, fuel processing for providing PEMFC with clean hydrogen has prospects. Current examples, though, of complete fuel processing systems which convert fuel to clean hydrogen for PEMFC are not commonly displayed. The *Zentrum für Brennstoffzellen Technik – ZBT* (Centre for Fuel Cell Technology), based in Germany, displayed at the 2004 Hanover Fair a 300 W PEM auxiliary power unit running on butane, or other similar fuels, for small sailing boats.

The present chapter is not meant to give a review of worldwide developments in the field of fuel cells systems using microtechnology but instead it is aimed to provide a short overview of some current activities carried out by scientist working at the Institut für Mikrotechnik Mainz GmbH (IMM) in the field of fuel processing of methanol and propane using catalytically coated microreactors for obtaining clean hydrogen for low power fuel cell applications ranging up to 200 W.

### Catalytic Fuel Processing Devices

A typical fuel processing flowsheet is shown in Figure 3. For liquid fuels an evaporator is required in addition to the catalytic devices, namely the reformer, water gas shift, selective oxidation and burner reactors. Even though IMM has carried out work on fuel evaporators it will not be discussed here as it is not a catalytic process.

To-date, microstructured reactors have been realized and tested at IMM for methanol and propane steam reforming and further CO-cleanup. Four devices incorporating microstructured features with catalytic coatings were designed and constructed within the framework of the European project entitled 'Micro reactor technology for hydrogen and electricity' (MiRTH-e) where the aim was to realize devices for a 100 W fuel processing unit. Devices shown in Figures 4, 5, 10 and 11 were designed and constructed through the collaboration between IMM, Eindhoven University of Technology (TU/e) and Netherlands Energy

Research Foundation (ECN). The first device (Figure 4) was an electrically heated catalyst test unit used for testing steam reforming and selective oxidation catalysts. It could incorporate 15 plates each with 40 channels and channel dimensions of  $0.5 \times 0.35 \times 50 \text{ mm}^3$ . The second device was a coupled reformer-burner unit (Figure 5) which was tested by our project partners at TU/e using an ECN catalyst. 64 plates made up the device each with 27 channels and typical channel dimensions of  $1 \times 0.1 \times 30 \text{ mm}^3$ .

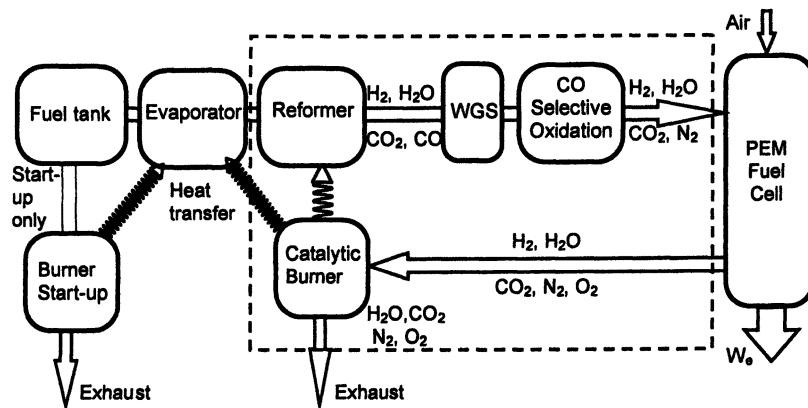


Figure 3: Devices typically present in a fuel processor for PEM fuel cells

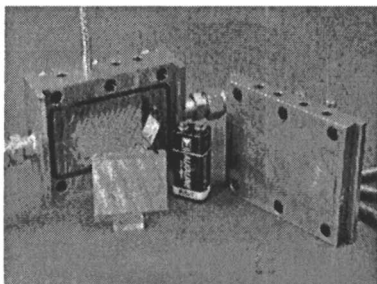


Figure 4: MiRTH-e catalyst test device

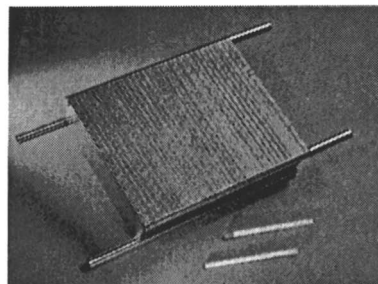


Figure 5: MiRTH-e integrated reformer-burner reactor

Typical results obtained using the test device, with a  $\text{Cu}/\text{ZnO}/\text{Al}_2\text{O}_3$  catalyst under methanol steam reforming conditions, are shown in Figure 6. In this example, the plates had been coated with catalyst at IMM by applying manually a  $\gamma$ -alumina washcoat onto the entire length of the etched stainless steel channels. A 20 % alumina suspension was prepared from  $\gamma$ -alumina (purchased from Alfa Aesar) and deionised water. The suspension also consisted of 5 % polyvinyl

alcohol binder (purchased from Fluka) and 1% acetic acid. The channels were then filled with the suspension and any excess on the top of the channel walls was wiped off. The washcoated plates were then calcined for 1 hour at a temperature of 600°C and subsequently placed in vacuum to remove air from the pores. Carbon dioxide was then passed to fill the pores as it subsequently readily dissolved in the nitrate solutions (purchased from Fluka) which were used for impregnating the alumina with copper and zinc.

A flowrate of 500 ml<sub>N</sub>/min was used (0.6 s at S.T.P.) at various temperatures and a steam to carbon ratio of 2.0. From Figure 6 it is evident that the maximum methanol conversion obtained was approximately 80 % at a temperature of 290°C. Hydrogen yield inevitably increased with increasing temperature while the selectivity decreased slightly. Carbon monoxide selectivity increased with temperature but never exceeded 1.3 %. A more detailed analysis of the results obtained can be found elsewhere (15).

At a temperature of 290°C, 50 % of the off-gas was hydrogen while the unconverted methanol made-up 2 % of the off-gas. The remaining species were water (28 %), carbon dioxide (19 %) and carbon monoxide (0.25 %). The amount of hydrogen produced was enough to power a 33 W fuel cell assuming a fuel cell efficiency of 55 % and hydrogen utilisation of 90 %. Results obtained using the ECN catalyst in the more sophisticated final 100 W reformer-burner device (Figure 5) will be reported by our project partners from TU/e in the near future.

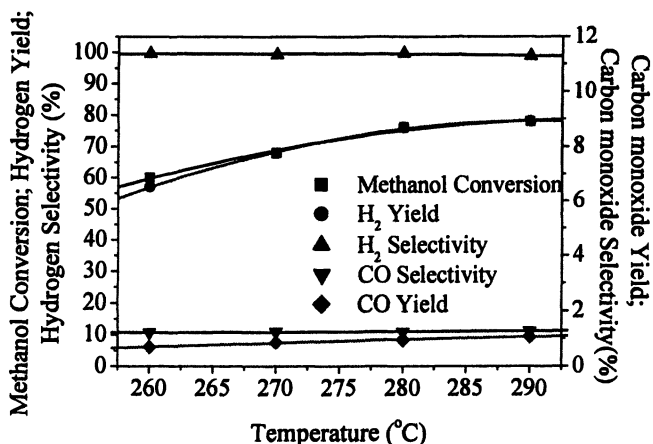


Figure 6: Hydrogen conversion, hydrogen and carbon monoxide yield and selectivity at various temperatures

Propane steam reforming has also been investigated at IMM within the framework of a German funded project (entitled, 'Realisation of a miniaturised

reformer for on-board hydrogen production') using the plate reactor shown in Figure 7. The two parts with the catalytically coated channels were welded together to form a compact device. Each plate consisted of 14 channels with typical dimensions of  $0.5 \times 0.25 \times 25 \text{ mm}^3$ . The procedure for applying both commercial and home-made catalysts was carried out similarly to that for the methanol steam reforming catalyst with the exception, of course, being that there was no impregnation step after applying a washcoat of the commercial catalyst.

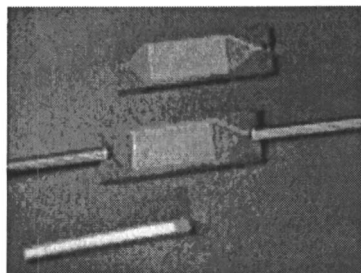


Figure 7: Catalytically coated plate reactor

A number of catalysts were tested under propane steam reforming conditions ( $100 \text{ ml}_N/\text{min}$ ; 80% nitrogen, rest propane and water), the most active, selective and stable of which was a 3.5 wt% Rh/ 3.5 wt% Pt/CeO<sub>2</sub> catalyst. Figure 8 shows the effect of steam to carbon ratio at various temperatures on propane conversion over fresh Rh/Pt/CeO<sub>2</sub> catalyst samples. The molar fraction of the water was kept constant while the propane fraction at the feed was varied in order to achieve the different ratios. The flowrate was kept at all times constant. The residence time at S.T.P. was 0.007s.

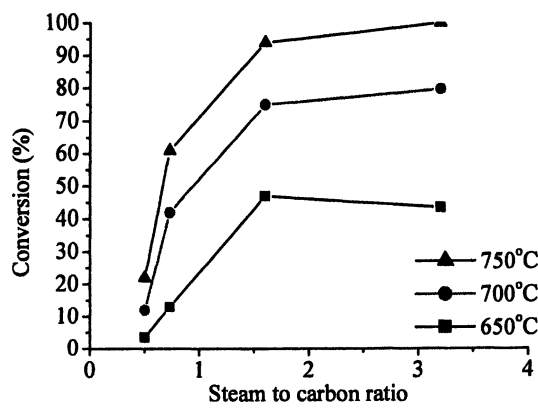


Figure 8: Propane conversion at various temperatures and s/c ratios

An overall increase in propane conversion with increasing steam to carbon ratio took place at all temperatures. At steam to carbon ratios higher than 1.6 the additional steam had however a limited effect on the conversion. The relative increase in conversion with increasing temperature was low regardless of the steam to carbon ratio thus suggesting mass transfer limitations. The amount of hydrogen produced in such a device at a residence time of 0.007s (S.T.P.) could theoretically power a 12 W fuel cell assuming 55 % fuel cell efficiency and 90 % hydrogen utilisation (16). This device can be easily scaled-up for power applications up to 200 W.

Water gas shift reactors are also typically incorporated in fuel processors (with the exception of fuel processors of methanol) as the carbon monoxide levels can only be reduced stepwise. Low and high temperature water gas shift reaction experiments were carried out at IMM using a range of catalysts incorporating metals such as Pt, Pd, Rh, Ru, Fe and Au in addition to washcoats such as  $\text{Al}_2\text{O}_3$ ,  $\text{CeO}_2$ ,  $\text{TiO}_2$  and  $\text{ZrO}_2$ . The tests were carried out using similar reactors such as the one shown in Figure 7 while the reactant gas composition was 55 %  $\text{H}_2$ , 14%  $\text{CO}_2$ , 6% CO and 25%  $\text{H}_2\text{O}$ . Typical results obtained from the low temperature water gas shift experiments at 300°C and flowrate of 30  $\text{mL}_\text{N}/\text{min}$  are shown in Figure 9. It is evident that 4 wt% Pt/ 4 wt% Ru/ 13 wt%  $\text{CeO}_2/\text{Al}_2\text{O}_3$  was the most active catalyst (yet the most selective with respect to methane) while three catalysts (11 wt% Ru/ $\text{ZrO}_2$ , 3 wt% Au/ $\text{TiO}_2$  and the commercial 88 wt%  $\text{Fe}_2\text{O}_3$ / 9 wt%  $\text{Cr}_2\text{O}_3$ / CuO) proved to be entirely inactive. Pt/Rh/ $\text{CeO}_2/\text{Al}_2\text{O}_3$  showed also signs of methane production (selectivity of 35 % w.r.t. methane) while all other active catalysts showed no methane production.

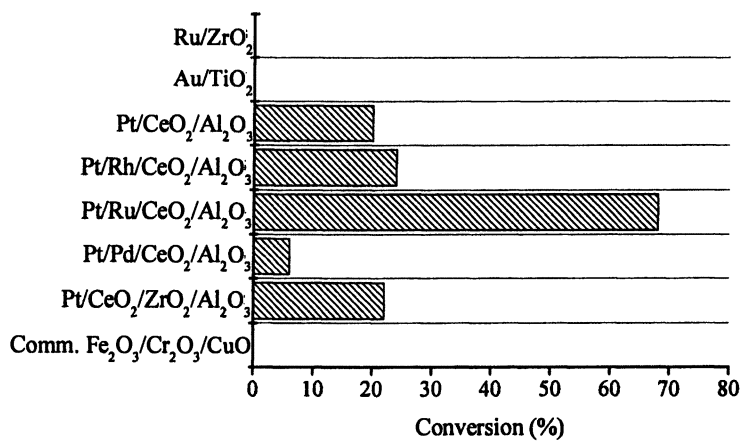


Figure 9: Carbon monoxide conversion over different catalysts at 300°C

The final step in the CO clean-up typically present in a fuel processing system is carried out in a selective oxidation reactor. Carbon monoxide levels at the exit of a water gas shift reactor continue to be too high for PEM fuel cell operation. A selective oxidation reactor brings levels down to 10 ppm.

Figure 10 shows the first generation integrated selective oxidation-heat exchanger reactor designed and fabricated within the framework of the MiRTH-e project. The reactor incorporated heat exchanging plates in addition to catalytically coated plates and had an overall size of  $66 \times 53 \times 52 \text{ mm}^3$ . The aim was to have a flexible device where the catalytically coated plates (with channel dimensions of  $0.25 \times 0.187 \times 30 \text{ mm}^3$ ) could be exchanged while at the same time the temperature of the reformatre stream could be brought down to the temperature of approximately  $150^\circ\text{C}$  (from approximately  $270^\circ\text{C}$ ) for catalytic selective oxidation of the carbon monoxide to take place. The exiting stream needed then to be further cooled by a second heat exchanging part to a temperature of approximately  $65^\circ\text{C}$  which would be low enough for it to enter a low temperature PEM fuel cell. The cooling stream was meant to be the one coming from the fuel cell cathode. During the experiments, a nitrogen stream was used instead.

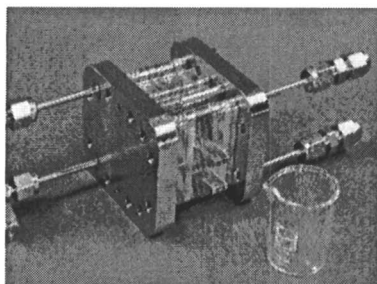


Figure 10: MiRTH-e integrated Selox-heat exchanger reactor (1<sup>st</sup> generation)

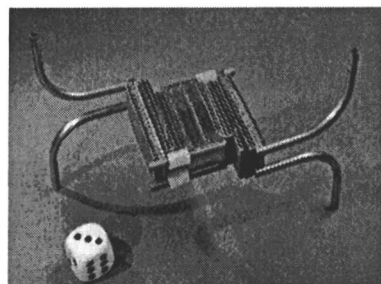


Figure 11: MiRTH-e integrated Selox-heat exchanger reactor (2<sup>nd</sup> generation)

A second generation of this selective oxidation reactor was made where the plates were welded together thus making the device more compact (approximately five times smaller than the previous device) and faster to heat up. Two such devices were made; one from steel (Figure 11) and one from aluminium (not shown here) in order to minimise even further the weight of devices but also the volume. The plate geometry in both was longer and narrower as compared to the first generation so as to enhance temperature differences (typical channel dimensions were  $1 \times 0.1 \times 30 \text{ mm}^3$ ). Unfortunately, the welding of aluminium proved to be difficult and even though the structures could be formed they were not leak tight and thus not suitable for operation.

Figures 4, 10 and 11 also illustrate the progress made in the integration of devices. The first device (the catalytic test device) was a separate electrically heated catalytic unit. In the second stage, instead of making a separate selective oxidation reactor and a separate heat exchanger the two were coupled into one structure thereby moving towards balancing the overall heat input and output of the system. The equivalent was done with the reformer which was coupled to a burner unit. This meant the lack of need of electrical heating for steady state operation and the elimination of tubing thus making the devices more compact. Progress was further made by moving from structures requiring gaskets for sealing purposes, to welded ones. Thus, volume was further decreased and efficiency further increased. Attempts to decrease the weight of devices by using aluminium were unfortunately not successful as already mentioned. It should be noted at this point that all devices shown have tubes at their inlets and outlets as they were required to be suitable for laboratory testing.

The integrated reactor-heat exchanger device shown in Figure 10 was initially used to test various catalysts (such as Rh, Pt and Ru) and washcoats (for example  $\text{Al}_2\text{O}_3$  and  $\text{CeO}_2$ ) combinations prepared by IMM. Typical results for six different catalyst systems are shown in Figure 12.

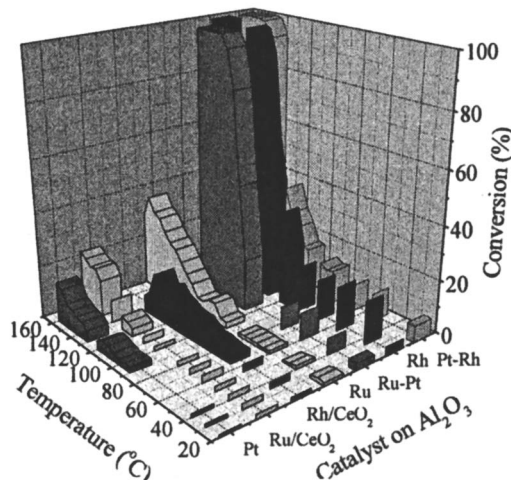


Figure 12: Carbon monoxide conversion with respect to temperature over various catalysts

2.5 wt% Ru/ 2.5 wt% Pt/  $\text{Al}_2\text{O}_3$ , 5 wt% Rh/  $\text{Al}_2\text{O}_3$  and 2.5 wt% Pt/ 2.5 wt% Rh/  $\text{Al}_2\text{O}_3$  catalysts were found to be most active, achieving a carbon monoxide reduction from 12 000 ppm to below 4 ppm (detection limit of GC used) at temperatures of 126°C, 140°C and 144°C respectively and flowrate of 500  $\text{mL}_\text{N}/\text{min}$ . Pt-Rh/ $\text{Al}_2\text{O}_3$  was found to be the most stable with time (tested up

to 20 hours) while its hydrogen selectivity decreased to 88 % at 140°C. The second generation selective oxidation reactor was tested by our project partners in TU/e who applied an ECN catalyst (2).

Catalytic burners have also been realized at IMM such as the one shown in Figure 13. Burners are required in a fuel processing system in order to burn the unutilized hydrogen coming out of a PEM fuel cell. The heat produced can be supplied to units such as the reformer (as is the case with the reactor shown in Figure 5) or to the evaporator. Catalytic burners though may also be used for burning part of the fuel during start-up. Figure 14 shows some results obtained from the catalytic burning of propane over a home-made 5 wt% Pt/Al<sub>2</sub>O<sub>3</sub> catalyst at a molar oxygen to propane ratio of 5 and 7.

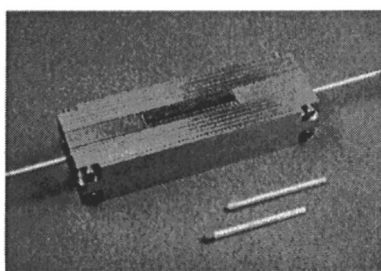


Figure 13: Catalytic burner

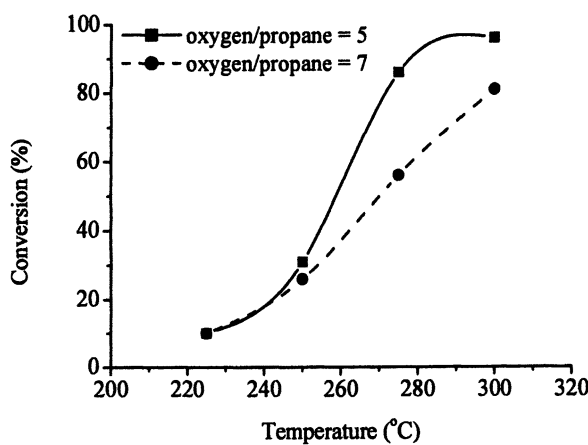


Figure 14: Propane conversion at various temperatures and propane/oxygen ratios

50 % propane conversion was achieved at a temperature of approximately 260°C with an oxygen to propane ratio of 5 while the same conversion was achieved at a temperature of approximately 270°C with an oxygen to propane

ratio of 7. It is also worth noting that the catalyst performed better in the presence of some sulphur which is typically found in low grade propane. The promotion effect of sulphate species forming on the surface have also been reported in literature (17). Better results were not obtained when applying a commercial Pt/Al<sub>2</sub>O<sub>3</sub> catalyst.

### **Applications of the Present Microreactors**

The power output of some microreactors presented here are within the range or higher than what electronics manufacturers currently typically aim for portable devices. Other reactors such as the propane reformer and water gas shift test reactors have a lower power output as to what is typically needed for a stand alone APU system. All reactors though can be scaled to the power output required by the various applications. The conceptual design, for example, of a complete MiRTH-e system, incorporating conventional valves and methanol and oxygen tanks, has been estimated to have an overall size of 280 mm x 100 mm x 400 mm. This includes a 100 W fuel cell of 1 l in size. Without a doubt the MiRTH-e system is not sufficiently small so as to be integrated into portable devices such as laptops. All reactors, though, have potential to be applied in stand-alone systems for use in remote locations or in combination with conventional technologies for use in recreational vehicles, such as caravans and yachts, in order to supply power for satellite dishes, lights, or refrigerators or even laptops to be used inside the vehicles. They offer a huge weight reduction from lead acid batteries, they are independent of time of day and weather (in contrast to technologies such as solar panels), they are silent and have lower emissions than conventional generators. They do not require significant reduction in size as space is less of an issue here.

### **Conclusions and outlook**

Significant steps have been made at IMM within the framework of projects regarding the design, construction and operation of novel catalytically coated microreactor devices for the fuel processing part of a PEM fuel cell system. Issues of start-up and overall system optimisation remain as these have until now been beyond the scope of the projects. It is necessary for these issues though to be resolved in the near future. For this, the input of a fuel cell manufacturer and of an end-user is required. The probability of these systems being applied in a niche market such as recreational vehicles is higher than in a mass market such

as laptops which nevertheless is a step towards bringing the fuel cell closer to the consumer.

### Acknowledgements

We would like to thank the European Commission for the funding of the MiRTH-e project (contract no. EN6K-CT-2000-00110) and our project partners namely, Eindhoven University of Technology, University of Twente, Netherlands Energy Research Foundation, Centre Nationale de Recherche Scientifique-LSGC and Shell Research and Technology Centre. In addition, we acknowledge the financial support from the *Stiftung Rheinland-Pfalz für Innovation* for funding the work carried out on propane reforming.

### References

1. Hu, J.; Wang, Y.; VanderWiel, D. P.; Chin, Y.; Palo, D.R.; Rozmiarek, R. T.; Dagle, R. A.; Cao, J.; Holladay, J. D.; Baker, E. G. *Chem. Eng. Journal* **2003**, *93* (1), 55.
2. Delsman, E. R.; de Croon, M. H. J. M.; Pierik, A.; Kramer, G. J.; Cobden, P.D.; Hofmann, C.; Cominos, V.; Schouten, J. C. *Chem. Eng. Sci.* **2004**, submitted.
3. Arana, L. R.; Schaevitz, S. B.; Franz, A. J.; Jensen, K. F.; Schmidt, M. A. *Proc. IEEE Int. Conf. MEMS*, Las Vegas, **2002**, 232.
4. Bednarova, L.; Ouyang, X.; Chen, H.; Lee, W. Y.; Besser, R. S. *Am. Chem. Soc. Div. Fuel Chem. Prepr.* **2003**, *48* (2).
5. Cropper, M., <http://www.fuelcelltoday.com/FuelCellToday/IndustryInformation/IndustryInformationExternal/IndustryInformationDisplayArticle/01588.631.00.html>, **2003**, viewed 23rd November, 2003.
6. Toshiba press release, [http://www.toshiba.co.jp/about/press/2003\\_03/pr0501.htm](http://www.toshiba.co.jp/about/press/2003_03/pr0501.htm), **2003**, viewed 27th October, 2003.
7. Toshiba press release, [http://www.toshiba.co.jp/about/press/2004\\_03/pr1701.htm](http://www.toshiba.co.jp/about/press/2004_03/pr1701.htm), **2004**, viewed 27th April, 2004.
8. NEC press release <http://www.nec.co.jp/press/en/0306/3002.html>, **2003**, viewed 28th October, 2003.
9. Casio press release, **2002**, <http://world.casio.com/info/2002/fuelcell.html>, viewed 27th October, 2003.
10. Motorola press release, [http://www.motorola.com/mediacenter/news/detail/0.1958.468\\_244\\_23.00.html](http://www.motorola.com/mediacenter/news/detail/0.1958.468_244_23.00.html), **2001**, viewed 29th October, 2003.

11. Motorola press release [http://www.motorola.com/mediacenter/news/detail/0,1958,3099\\_2539\\_23,00.html](http://www.motorola.com/mediacenter/news/detail/0,1958,3099_2539_23,00.html), 2003, viewed 29th October, 2003.
12. Kotadia, M., [http://zdnet.com.com/2100-1103\\_2-5086066.html](http://zdnet.com.com/2100-1103_2-5086066.html), 2003, viewed 27th October, 2003.
13. Geiger, S., <http://www.fuelcelltoday.com/FuelCellToday/IndustryInformation/IndustryInformationExternal/NewsDisplayArticle/0,1602,3462,00.html>, 2003, viewed 29th October, 2003.
14. Product description of SFC Smart Fuel Cell AG, [http://www.smartfuelcell.de/en/produkte/binaries/a25\\_datasheet.pdf](http://www.smartfuelcell.de/en/produkte/binaries/a25_datasheet.pdf), viewed November, 2003.
15. Cominos, V.; Hardt, S.; Hessel, V.; Kolb, G. ; Löwe, H.; Wichert, M.; Zapf, R. *Chem Eng Comm*, 2005, 192 (5), 1.
16. Kolb, G.; Zapf, R.; Hessel, V.; Löwe, H. unpublished results of IMM.
17. Corro, G.; Montiel, R.; Vazquez, L. C.; *Catal Comm* 2002, 3 (11), 533.

## **Chapter 13**

### **Integrated Methanol Fuel Processors for Portable Fuel Cell Systems**

**Daniel R. Palo, Jamie D. Holladay, Robert A. Dagle,  
and Ya-Huei Chin**

**Battelle, Pacific Northwest Division, P. O. Box 999, MS K6-24,  
Richland, WA 99352**

To meet the growing needs of the U.S. military for portable power, Battelle, Pacific Northwest Division (Battelle) is developing a portable power system designed to provide 100-150 watts of electric power for tomorrow's soldier. Battelle's patented micro-channel process technology and highly active and selective steam reforming catalysts enable devices that are small and light, and provide a reliable stream of hydrogen-rich gas to power small proton exchange membrane (PEM) fuel cells. Fuel processors developed under this project, and operating on methanol, have achieved thermal efficiencies of up to 85%, yielding outputs up to 300 W<sub>e</sub>, and providing projected energy densities of up to 2300 Whr/kg fuel. This work was sponsored by the U.S. Army Communications-Electronics Command and the Office of Naval Research.

As the dismounted soldier becomes the beneficiary of advanced electronics and communications technology, the power needs of current and future forces become quite demanding. Since batteries have relatively low energy densities, with limited room for improvement, the volume and mass of battery power become overly burdensome when that power is required for extended missions (three days or greater). A suitable replacement is needed which drastically increases the energy density available to the soldier while retaining as much simplicity as possible. Two main options can be pursued in this regard. Primary battery power can be replaced with an alternative, such as 1) a hybrid fuel cell/battery system (15-50 W) operating on a liquid fuel, or 2) primary batteries coupled with a portable battery charger (100-300 W) operating on liquid fuel. Regardless of the option chosen, each promises to reduce soldier fatigue and/or increase mission duration by drastically increasing the available energy density of the power system.

The energy densities of various batteries and fuels are shown in Table 1 for comparison. While currently accepted battery technology can provide energy densities no higher than 400 Whr/kg, alternatives like compressed hydrogen, sodium borohydride, and liquid hydrocarbons offer much higher energy densities, reaching into the 1000's of Whr/kg. Each alternative power source, however, has its advantages and disadvantages.

**Table 1. Energy density of various batteries and fuels, listed in order of increasing energy density.**

<i>Fuel</i>	<i>Energy Density (Whr/kg)</i>	<i>Comments</i>
BB-2590	81	Secondary
BA-5590	150	Primary
BA-5390	235	Primary
BA-8180	345	Primary Zn-Air battery, large unit
Compressed Hydrogen	500-1000	5000 psig, value includes container weight
Sodium Borohydride	3600	$[\text{NaBH}_4 + 2 \text{H}_2\text{O}]$ weight only
Methanol	5500	Based on lower heating value of fuel
Most Liquid Hydrocarbons	~12,400	Based on lower heating value of fuel
Hydrogen Gas	33,200	Unpackaged
Nuclear Material	2,800,000	Raw power

For instance, hydrogen gas has a very high energy density, but once it is packaged, it looks much less favorable. Similarly, hydride storage systems such as sodium borohydride offer attractive energy density values, but materials

handling and cost issues continue to plague these types of systems. Liquid hydrocarbon fuels such as methanol or synthetic diesel can provide even better energy densities than the other technologies listed, and they offer a familiarity and availability that the others cannot provide, but they must undergo significant processing to extract PEM-quality hydrogen.

For this reason, when considering methanol as a fuel, direct methanol fuel cells (DMFCs) are often discussed. Even if a system were limited to methanol as fuel, the PEM system has several advantages over a DMFC system, as shown in Table 2. Specifically, the PEM system offers much higher MEA power density, much lower platinum loading, and much higher stack power density than a DMFC. These advantages lead to decreased mass, volume, and cost over a DMFC system.

**Table 2. Comparison of direct-methanol and reformate/hydrogen fuel cell technology (1,2,3,4,5).**

Parameter	Units	Direct Methanol	Reformate/Hydrogen
MEA Power Density	$\text{mW/cm}^2$	60	350
Total Platinum Loading	$\text{mg/cm}^2$	4.8	0.25-0.8
Stack Power Density	W/L	24	250
Stack Electric Efficiency	% present % projected	30 40	45 50

## Approach

Battelle, Pacific Northwest Division (Battelle) has been developing solutions for converting liquid hydrocarbon fuels into hydrogen-rich gas for more than five years. Such fuel processing for portable power applications must not only be efficient, but also small and lightweight, lest the high energy density of liquid fuels be offset by the large size of the processing system.

The approach we have taken is based on the combination of microchannel reactors and advanced fuel processing catalysts. While the microchannel architecture provides rapid and efficient heat transfer, our advanced catalysts are tailored to take full advantage of the thermal properties of the reactors. The result is that fuel conversion processes that would normally have reactor residence times on the order of seconds, now have residence times on the order of 0.01 to 0.10 second. This provides the basis for a compact device with high throughput – ideal for portable fuel processing.

Advances in microchannel fuel processing have enabled the development of portable power devices based on hydrocarbon steam reforming and PEM fuel cells. Compared to other competing technologies, a PEM fuel cell system operating on liquid fuels has several advantages, including

- The high energy density of liquid fuels,
- The easy transport of such fuels in bulk or in pre-packaged modules,
- The absence of solid waste when the liquid fuel is spent (such as would be the case in other hydrogen storage scenarios),
- The availability of such fuels at low cost, and
- The familiarity of the average soldier with liquid fuels.

### System Assumptions

Fuel processing for fuel cell applications is widely reported in the literature (6,7,8), and system metrics do not necessarily have uniform definitions. For this reason, our system assumptions are explained here.

In order to estimate fuel processor performance in the absence of a fuel cell, investigators make certain assumptions about the complete system. Some general conventions are often used for thermal and electrical efficiency, as explained below, along with the specific fuel cell and system assumptions pertinent to the present work.

The thermal efficiency ( $\varepsilon_t$ ) of the fuel processor is given by  $\varepsilon_t = \frac{LHV_{H2}}{LHV_{fuel}}$ , where  $LHV_{H2}$  and  $LHV_{fuel}$  are the lower heating values for the

hydrogen produced and the fuel consumed, respectively. However, since the fuel cell does not convert 100% of the heating value of the hydrogen to electric power, the electric efficiency ( $\varepsilon_e$ ) of the fuel processor and fuel cell system is

given by  $\varepsilon_e = \frac{P_{FC}}{LHV_{fuel}}$ , where  $P_{FC}$  is the gross electric power out of the fuel

cell. The value of  $P_{FC}$  is affected by two parameters, the fuel cell hydrogen utilization ( $\mu_{FC}$ ) and the fuel cell conversion efficiency ( $\varepsilon_{FC}$ ), according to  $P_{FC} = LHV_{H2} \cdot \mu_{FC} \cdot \varepsilon_{FC}$ .

Fuel cells that operate on reformate gas are designed with flow-through anodes, which allow the inert components ( $CO_2$ ,  $CH_4$ , etc.) to pass through the cell without accumulating. Because of this flow-through design, not all of the  $H_2$  in the reformate is utilized, and some of it exits with the other gases. Hydrogen utilization for reformate fuel cells typically ranges from 70-90%, depending on electric load and other factors. Furthermore, all fuel cells have a limited conversion efficiency, where some of the energy is converted to heat. The

present study assumes 80% hydrogen utilization and 60% fuel cell conversion efficiency.

Given these assumptions, the net power out of the fuel cell is equal to 48% of the LHV of the H<sub>2</sub> produced in the fuel processor, which means the expected electric efficiency of the bare system is given by

$$\varepsilon_e = \frac{0.48 \cdot LHV_{H2}}{LHV_{fuel}} = 0.48 \cdot \varepsilon_t. \text{ This equation, however, does not account for}$$

parasitic power losses in the system (pumps, controllers, etc.), nor does it account for power conversion inefficiencies through the power electronics. Further assumptions must be made regarding these losses in order to report a realistic projected system efficiency. The resulting overall system efficiency

$$\text{calculation, then, is given by } \varepsilon_e(\text{net}) = \frac{P_{FC} - P_{par} - P_{pc}}{LHV_{fuel}}, \text{ where } P_{FC} \text{ is the}$$

gross fuel cell power output,  $P_{par}$  is the parasitic power requirement, and  $P_{pc}$  is the power conversion loss through the power electronics. This means that, while high thermal efficiency in the fuel processor is an important parameter, it is only the beginning when considering the efficiency of a complete power system. In this report, we focus on the thermal efficiency of the integrated steam reformer, which provides the basis for a highly efficient power system.

## Fuel Processing for Fuel Cells

The conversion of liquid hydrocarbon fuels to useful electricity in a PEM fuel cell system requires the following steps. Those in parentheses may be omitted depending on system requirements or fuel choice.

- Vaporization and preheating of fuel and water – assuming steam reforming
- Initial conversion of fuel to reformat
- (Secondary conversion of initial products to increase hydrogen content)
- Reduction of CO concentration to appropriate level for PEM fuel cell
- (Cooling of product gas before feeding to PEM fuel cell)
- Feeding product gas and air to fuel cell stack
- Application of appropriate load to fuel cell stack to draw electricity

The way this is normally embodied in a steam reforming-based system is shown in Figure 1. If the fuel is methanol, it can generally be pre-mixed with the water and the combined stream can be vaporized in a single unit. The steam reforming reactor converts the fuel and water to a hydrogen-rich gas which also contains significant amounts of carbon dioxide, carbon monoxide, and possibly

methane. If the steam reforming occurs at high temperatures, or if the reforming catalyst exhibits poor selectivity, carbon monoxide concentration will be too high for typical CO cleanup technology, and the stream must be processed through a water-gas shift reactor, which decreases the CO concentration to roughly one percent, and in turn produces additional hydrogen.

The final CO cleanup step is chosen based on a number of considerations, such as the type of PEM fuel cell being used, the size of the system, and the amount of CO that must be mitigated. The most common approaches include preferential CO oxidation, selective CO methanation, and separation through a hydrogen-permeable membrane (usually made from Pd or a Pd alloy).

The stream exiting the fuel processing system is fed to the fuel cell, along with an oxidant, usually air (not shown) and the electrochemical reaction of hydrogen with oxygen produces electric power and heat. Unused hydrogen and other combustible gases exiting the fuel cell anode can be utilized in the system combustor for their heating value, increasing the system thermal efficiency.

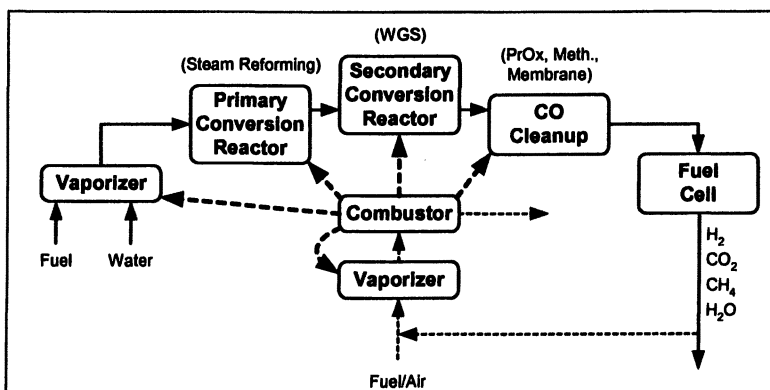


Figure 1. Typical embodiment of steam reforming-based fuel cell system (simplified). Solid flow lines indicate process streams; heavy dashed lines indicate heat flow from combustor to process units; light dashed lines indicate combustor flow streams.

## Microchannel Architecture and Advanced Catalysts

Fuel processing efforts at Battelle have benefited from the synergistic combination of microchannel reactor architecture and advanced fuel processing catalysts. Increasingly, the chemical process industry is becoming familiar with the vastly improved heat and mass transfer capabilities of microchannel architecture. This alone is enough advantage to enable heat and mass exchangers

with vastly improved performance, as seen in the Battelle-designed microchannel vaporizers developed for automotive fuel processing (9).

However, in achieving the same sort of advances in catalytic processes, it is not enough to merely improve heat and mass transport in the system. If the processing catalyst was designed for a system with low heat transfer, for instance, it is not likely to show marked improvement in performance when deployed in a microchannel environment. For this reason, significant investments have been made by Battelle in the development of highly active (as well as selective) fuel processing catalysts which are specifically suited for deployment in microchannel devices. This includes not only the catalyst formulation, but also the form, as the catalyst must be deployed in a microchannel in such a way that pressure drop is minimized while heat and mass transfer are maximized along with surface area. Successfully performing this balancing act is truly what makes microchannel reactors unique.

Additional microtechnology advantages can be realized in the area of system integration. The intelligent integration of unit operations in a single device places the exothermic operations in close proximity to the endothermic ones. A simple example of this is the close coupling of a combustion process with an endothermic reaction such as steam reforming. The result is that heat can be released and transferred within the same device, reducing environmental losses and improving heat transfer. In other parts of the device, process heat can be recovered through efficient heat transfer in small, effective recuperative vaporizers and/or preheaters. The above example describes the essential workings of the integrated fuel processors being discussed in this paper.

## Methanol Reforming Catalysts

We have previously reported on the specific methanol steam reforming catalyst being utilized in our devices, and the details will not be recounted here (10,11,12). However, general performance of the catalyst will be discussed, as it plays directly into the development of a reforming scheme for methanol. Most of the focus in methanol steam reforming has been on the copper-based catalyst and variations thereof. The copper catalyst is desirable for several reasons, not the least of which is its ability to selectively catalyze the conversion of methanol to low-CO reformate. However, this catalyst has several significant drawbacks, including its pyrophoric nature and its tendency to deactivate at high temperature.

Our approach has been to use a palladium-zinc catalyst which:

- Is non-pyrophoric, and stable in air at up to 250 °C,
- Has high activity and selectivity at temperatures up to 400 °C,
- Produces no methane at temperatures below 400 °C,

- Demonstrates excellent stability under reaction conditions, and
- Is easily regenerated, and can be reduced *in situ*.

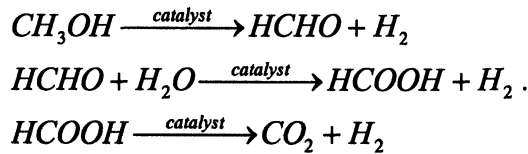
In portable applications, for kinetic reasons, it is desirable to operate steam reformers at higher temperatures. The faster kinetics achieved at higher temperatures result in smaller devices and/or higher throughput. However, higher temperatures also generally result in higher CO selectivity. This is due to the thermodynamics of the water-gas shift reaction,

$H_2 + CO_2 \rightleftharpoons H_2O + CO$ . At higher reforming temperatures, this equation is shifted to the right, reducing the amount of hydrogen available and increasing the amount of carbon monoxide that must be mitigated before feeding the reformate to a PEM fuel cell.

The Pd/ZnO catalyst we employ combines the following desirable characteristics:

- Favorable higher temperature operation (300-400 °C),
- Non-decomposition reaction pathway, and
- Lack of water-gas shift activity.

The first item allows for the favorable reformer kinetics and greater throughput mentioned earlier. The second and third items result in low CO selectivity, actually providing a product stream containing less than equilibrium amounts of CO. It has been proposed (13) that this is accomplished through a mechanism such as



This reaction sequence does not include the decomposition of methanol to CO, and does not contain CO as an intermediate in the formation of CO<sub>2</sub>. As a result, less-than equilibrium amounts of CO can be produced during the steam reforming of methanol at high throughput. The steam reformers described here typically operate at gas hourly space velocities of 30,000 hr<sup>-1</sup> to 60,000 hr<sup>-1</sup>, which does not allow time for the shift mechanism to have much of an impact. This is illustrated in Figure 2, where the CO concentration in the dry reformate and predicted equilibrium concentration are plotted as functions of temperature. The quantitative benefit can be seen by comparing the actual and predicted operating temperatures to achieve a CO concentration of 0.8%. The integrated reformer can be operated at up to 300 °C while maintaining CO ≤ 0.8%. However, equilibrium calculations would predict a necessary operating temperature of no more than 180 °C. The result is a 120 °C increase in operating temperature for the same CO concentration, resulting in a 200-fold increase in reaction rate (12).

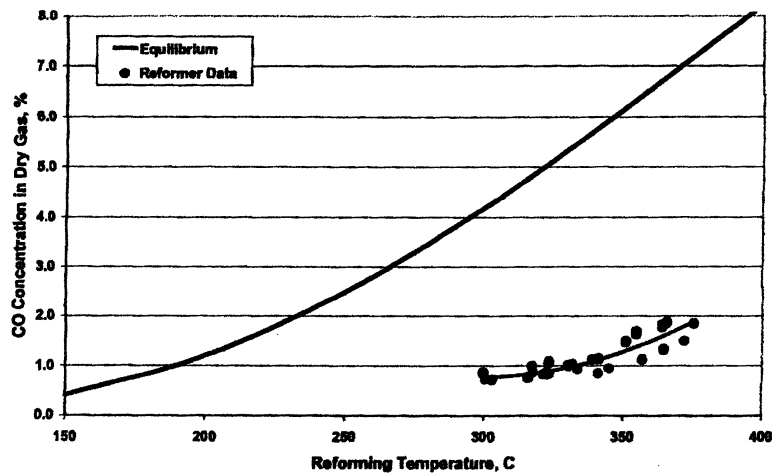


Figure 2. CO concentration in dry reformate as a function of reactor temperature. Equilibrium (solid dark line) and reactor results (data points) obtained for steam:carbon ratio of 1.2 at methanol conversions >95%.

### Breadboard Fuel Processor

We previously reported on the breadboard demonstration of a methanol steam reforming process train (14). The breadboard system consisted of a catalytic steam reformer, catalytic combustor, and two recuperating vaporizers, as shown in Figure 3.

After startup, the system operated in a thermally independent manner with a calculated electric equivalent output of 13-14 W. The demonstrated thermal efficiency at this condition was 45%. The reformate exiting the system contains roughly one percent CO on a dry gas basis, and therefore no water-gas shift reactor is required for this system. However, the reformate does require final CO cleanup, a subject which will not be addressed in this paper.

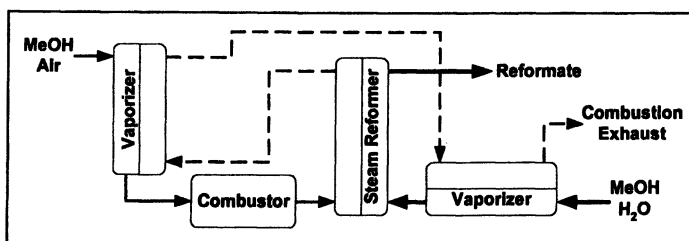


Figure 3. Breadboard demonstration system for methanol steam reforming.

Since reporting the breadboard results, our efforts have focused on the integration of these unit operations into a single reactor "block" over a wide power range. These integration efforts have included the combustor, steam reformer, vaporizers, and recuperators, but not the final CO cleanup step. Integration of these several unit operations into a single device illustrates the versatility and utility of microchannel-based devices, and demonstrates the efficiency gains that can be made when complementary unit operations are close-coupled in the same device.

### Integrated Methanol Fuel Processors

Over the past three years, and based on the technology previously discussed, we have developed integrated methanol steam reformers at various sizes suitable for portable power applications. Earlier work was focused on smaller units in the 20-W range, while more recent work has demonstrated devices sized for more than 100 W of electric equivalent output. Regardless of size, these devices have common properties, as listed in Table 3.

For laboratory testing, the liquid streams are fed to the reactor by HPLC pumps or syringe pumps. Since the fuel being reformed is methanol, a pre-mixed methanol/water solution is fed to the integrated reformer. A separate pure methanol reservoir is used to feed the system combustor. Air is supplied through a mass flow controller. Initial heat-up of the reactor (to ~65 °C) is accomplished by hydrogen combustion, after which methanol combustion provides the necessary process heat.

More recently, small liquid and air pumps have been implemented, as well as a hydrogen ballast (metal hydride canister), as a precursor to the systemization of this reforming process. Extensive investigations have also been conducted regarding the mitigation of the CO present in the reformat, testing other balance of plant components, and identifying appropriate fuel cell technologies.

Figure 4 shows an example of the integrated steam reformers being discussed. The device pictured has a design output of 20 W, and is constructed of 316 stainless steel. Figure 5 indicates the flow paths taken by the two process streams in the integrated reformers. Depending on the system configuration and the desired reformat outlet temperature, the reformat stream can be obtained from either of two different outlet ports on the reactor. Using the standard reformat outlet port allows for substantial heat recuperation from the reformat stream, and yields a reformat temperature on the order of 150-180 °C when the reformer is operating at 300-350 °C. If the alternate outlet port is employed, the reformat exit temperature is generally in the 250-300 °C range, resulting in a slight decrease in thermal efficiency.

**Table 3. Common properties of the 20-, 50-, 100-, and 150-W integrated methanol steam reformers developed for portable power applications.**

Material	316 stainless steel
Fabrication Method	Diffusion bonding and welding
Unit operations	Catalytic steam reforming, catalytic combustion, vaporization (2), heat recuperation (2)
Combustor feed stream	Methanol and air
Reformer feed stream	Methanol/water premix (60 wt% methanol, 1.2:1 steam to carbon ratio)
Operating temperature	300-350 °C
Reformate composition	~71% H <sub>2</sub> , ~24% CO <sub>2</sub> , ~4.8% H <sub>2</sub> O, ~0.8% CO
Methanol conversion	95-100%

With this reactor configuration, the choice of exit port, and thus exit temperature, will depend on the nature of any downstream processes being employed for removal of the CO present in the reformate. If the reformate is being fed to a membrane separator, a higher outlet temperature will be required. However, if catalytic CO cleanup is employed, a lower outlet temperature is more desirable. To a certain extent, the reactor operating temperature can be adjusted to provide a more desirable reformate exit temperature. Since this reactor is not intended to be a stand-alone unit, but coupled to a larger system, these temperature and heat recuperation issues need to be appropriately weighed for each application.



*Figure 4. Example of 20-W integrated methanol steam reformer, containing catalytic combustor, vaporizers, recuperators, and catalytic steam reformer.*

Table 4 lists important performance parameters for each integrated reformer design developed, from 20 W up to 150 W nominal power output. Over the

course of the work, the integrated steam reformer was successively scaled up from the original 20-W target to meet the changing needs of the portable power application it was designed to support. The final reactor design point was 150 W, which was intended to support a 150-W fuel cell and a net 100-W to 120-W power system. The values reported in Table 4 were obtained while maintaining a methanol conversion of at least 95%, as performance reported at lower conversion can be misleading.

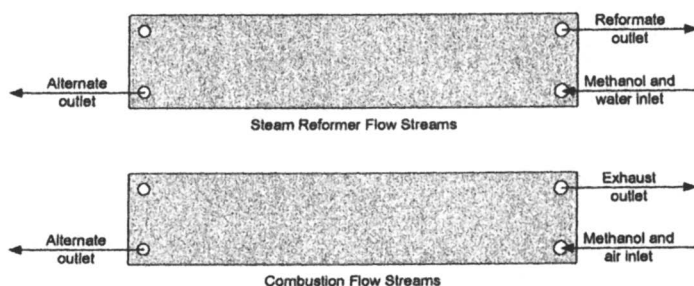


*Figure 5. Front and back face views of integrated methanol steam reformer, indicating locations of process flow streams.*

The three devices with nominal powers of 20, 50, and 100 W all belong to the same family of designs, based on the same footprint. Each design performed well above its rated power, and further investigation would likely yield even wider windows of operation for these reactors. However, as output is pushed upward, this requires higher temperatures of operation, which inevitably lead to higher CO levels. While the increased CO concentration remains well below that predicted by thermodynamic equilibrium, it nonetheless makes the downstream CO cleanup more difficult and significantly reduces the hydrogen yield.

Specific lifetime testing was not conducted on these devices, but the cumulative time on stream for one of the 50-W units is illustrative of the durability of the catalysts and devices. This particular unit was operated for over 300 hours of non-continuous use in daily laboratory testing, during which it endured more than 60 thermal (on/off) cycles. By the time this device was taken off-line, it had displayed no noticeable degradation in performance.

Scale-up of the original 20-W design was limited to about 100 W (nominal), so a second design with larger footprint was developed in the production of a 150-W reactor. Because of the change in design templates and the lack of optimization at this point, the 150-W design does not yield the same level of performance as the 50-W or 100-W designs in terms of efficiency and power density. However, it does perform quite well, yielding just under 80% efficiency and maintaining low CO levels at high conversion.

Optimization of these reactor designs for specific applications is expected to further increase thermal efficiency and responsiveness. Materials of construction other than stainless steel have not been investigated, however, significant advantages may be realized by using a lighter material.

**Table 4. Physical and performance parameters for integrated methanol steam reformers developed for portable power applications.**

Design Power, W <sub>e</sub> <sup>a</sup>	20	50	100	150
Demonstrated Power, W <sub>e</sub> <sup>b</sup>	6-34	26-54	45-150	60-300
Demonstrated Thermal Efficiency, % <sup>c</sup>	38-63	62-84	78-85	71-78
Estimated System Electrical Efficiency, % <sup>a</sup>	18-30	30-40	37-41	34-37
Estimated Fuel Specific Energy, Whr/kg <sup>d</sup>	1000-1680	1680-2240	2070-2300	1900-2070
Mass, g	65	105	155	245
Volume, cm <sup>3</sup>	11	19	28	67
Power Density at Design Power, W/L <sup>e</sup>	1750	2680	3650	2240
Specific Power at Design Power, W/kg <sup>f</sup>	300	470	650	470

<sup>a</sup> Based on fuel cell having 60% conversion efficiency and 80% hydrogen utilization  
<sup>b</sup> Performance values are reported for methanol conversion >95%  
<sup>c</sup> Based on lower heating values of methanol and hydrogen  
<sup>d</sup> Specific energy based on fuel weight; system specific energy will depend on complete system size and weight  
<sup>e</sup> Power density and specific power numbers are for reactor hardware only

## Conclusions

Compact, efficient, integrated methanol fuel processors have been developed for portable power applications ranging from 20-W to 150-W nominal output. These devices contain all necessary unit operations to convert a methanol/water mixture to a high-H<sub>2</sub>, low-CO reformate stream, significantly simplifying the downstream CO cleanup process. Included in each device, regardless of design power, are two vaporizer/preheaters, two recuperators, a catalytic combustor, and a catalytic methanol steam reformer. The excellent performance of these reactors is enabled by the combination of a novel,

advanced, selective, methanol-specific reforming catalyst and efficient microchannel device architecture. The resulting thermal efficiency of up to 85% and fuel-based specific energy of up to 2300 Whr/kg illustrate the excellent performance of these devices.

Dozens of thermal cycles and hundreds of hours of non-continuous operation have been demonstrated on a single device without degradation in performance. Reformate CO concentrations were maintained well below the levels predicted by thermodynamic equilibrium calculations. Furthermore, the methanol reforming catalyst has excellent stability, being non-pyrophoric and, in fact, withstanding exposure to air at temperatures up to 250 °C.

### Acknowledgements

Funding for this work was provided by the U.S. Army Communications-Electronics Command and by the Office of Naval Research, and their support is gratefully acknowledged.

### Literature Cited

1. Hoogers, G. *Fuel Cell Technology Handbook* (G. Hoogers, ed.) (CRC Press, New York, 2003) pg. 1-4.
2. Srinivasan, S.; Davé, B.; Murugesamoorthi, K.; Parasarathy, A.; Appleby, A. *Fuel Cell Systems* (L.J.M.J. Blomen and M.N. Mugerwa ed.) (Plenum Press, New York, 1993) p 70.
3. Thompsett, D. *Fuel Cell Technology Handbook* (G. Hoogers, ed.) (CRC Press, New York, 2003) pg. 6-1 to 6-23.
4. Gottesfeld, S. *Small Fuel Cells for Portable Power Applications 2002*, Washington D.C. April 21-23, 2002.
5. Ren, X.; Davey, J.; Pivovar, B.; Dinh, H.; Rice, C.; Gottesfeld, S.; Zelenay, P. *Fuel Cell Technology: Opportunities and Challenges - AIChE Topical Conference Proceedings*, New Orleans, March 10-14, 2002, p. 505.
6. Holladay, J.; Jones, E.; Wang, Y. *Chem. Rev.* 2004 (in press).
7. Krumpelt, M.; Krause, T.; Carter, J.; Kopasz, J.; Ahmed, S. *Catal. Today* 77(1/2) 3-16 (1 December 2002).
8. Song, C. *Catal. Today* 2002, 77(1/2), 17.
9. Whyatt, G.; Brooks, K.; Davis, J.; Fischer, C.; King, D.; Pederson, L.; Stenkamp, S.; Tegrotenhuis, W.; Wegeng, R. *DOE Hydrogen and Fuel Cells Merit Review*, May 2003.

10. Hu, J.; Wang, Y.; VanderWiel, D.; Chin, C.; Palo, D.; Rozmiarek, R.; Dagle, R.; Cao, J.; Holladay, J.; Baker, E. *Chem. Eng. J.* **2003**, *93*, 55.
11. Chin, Y.-H.; Dagle, R. A.; Hu, J.; Dohnalkova, A. C.; Wang, Y. *Cat. Today* **2002**, *77*, 79.
12. Cao, C.; Xia, G.; Holladay, J.; Jones, E.; Wang, Y. *Appl. Catal. A: Gen.* **2004**, *262*, 19.
13. Iwasa, N.; Masuda, S.; Ogawa, N.; Takezawa, N. *Appl. Catal. A: Gen.* **1995**, *125*, 145.
14. Palo, D. R.; Holladay, J. D.; Rozmiarek, R. T.; Guzman-Leong, C. E.; Wang, Y.; Hu, J.; Chin, Y.-H.; Dagle, R. A.; Baker, E. G. *J. Pwr. Sources* **2002**, *108*, 28.

## **Chapter 14**

### **Engineering Aspects of Designing the Components in a Microchannel Fuel Processor**

**Q. Ming, A. Lee, J. Harrison, and P. Irving**

**InnovaTek, Inc., 350 Hills Street, Suite 104, Richland, WA 99352**

Comparison of a tubular reforming reactor with a microchannel reactor indicates that a microchannel design offers enhanced thermal transfer and therefore facilitates the steam reforming reaction. A simulation study showed that with proper temperature management, CO conversion in a water gas shift reactor increases as reactor size decreases. Uniquely engineered steam reforming and water gas shift catalysts were developed to allow the application of microchannel technology in a fuel processor. A comparison of test results indicates that the engineered catalyst in a microchannel environment provides methane and diesel steam reforming performance that exceeds that of a granulate catalyst in a conventional tubular reactor.

### **Introduction**

A fuel processor that converts available fossil fuels to hydrogen rich gas offers an alternative that allows the use of fuel cell technologies with the existing fuel infrastructure. This will allow a quicker transition to the time when a hydrogen transportation and distribution infrastructure is established.

Characteristics such as size, start-up time, and dynamic response to the power demand will determine successful market penetration for integrated fuel processor/fuel cell systems for portable and transportation applications.

InnovaTek has been developing a diesel fuel reformer based on the steam reforming process for applications in the power range of 1-5 kW. After successful demonstration of our first prototype system in 2001 [1], the system has been further optimized by redesign of the major components, emphasizing compactness, improved thermal and mass transfer, and system efficiency.

A typical industrial steam-reforming reactor is made of a few hundred high temperature alloy tubes with a diameter in the range 7-13 cm, and length of 7.5-12 m[2, 3]. The heat flux to the catalyst bed in a typical top fired furnace can reach 120 kW/m<sup>2</sup> [4] at the entrance zone where a high temperature gradient across the tubes exists. An average heat flux of 80 kW/m<sup>2</sup> has been reported [3]. When this design is scaled down to 1-5 kW, the heat flux to the catalyst bed becomes particularly problematic due to the high transfer resistance [3]; therefore, reactors using this design are large and often restricted for use in applications where the reactor size is not major factor.

We have engineered a reactor design that provides a very high surface to volume ratio for improving heat transfer while maintaining the compactness of the reactor. The reactor is built on a microchannel structure [5, 6] that allows rapid heat and mass transport, thus providing the potential to meet the requirements of compactness, quick start up time and response to changes in hydrogen demand.

Another major engineering achievement was to support InnovaTek's proprietary catalysts [7] on a monolithic form to suit the new reactor design. The depth of the catalyst bed in a microchannel reactor is typically less than a few hundred microns. Therefore conventional packing of granulate catalyst is not applicable. A uniquely engineered steam reforming catalyst was developed to allow the application of microchannel technology in the fuel processor. The catalyst is supported on a high temperature resistant alloy (HTRA) providing sufficient thermal stability, mechanical strength, and other unique properties.

## Defining the System

Figure 1 is a schematic of a simplified process diagram. The liquid diesel fuel and steam are injected via a miniature fuel injector. The diesel is atomized and then vaporized by high temperature steam prior to the catalyst bed. The raw

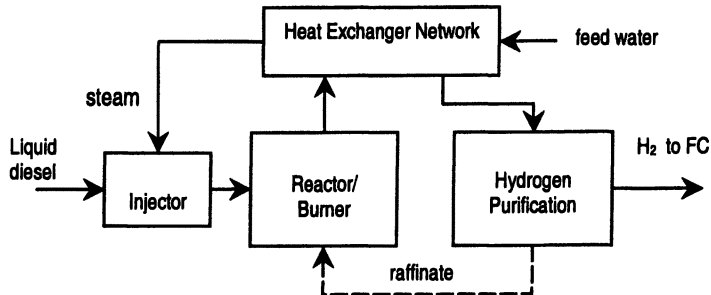


Figure 1. Process diagram schematic

reformate heats the feeding water in a heat exchanger network, thus cooling down to a suitable temperature for the hydrogen purification subsystem. Two alternative subsystems for hydrogen purification have been developed for different applications: 1) water gas shift reaction combined with preferential oxidation, and 2) palladium alloy membrane separation.

In this system, there are two hot streams (reformate gas, combustion gas) and two cold streams (feed water and combustion air). Accordingly there are several different process configurations that determine the cost, efficiency, complexity, and operating flexibility of the system. A comprehensive model was developed to calculate the mass and energy balances of the entire system. The model has been used to optimize system design by evaluating different process configurations, and to develop the specifications for the design of the components.

## Design of the Components

### Steam Reforming Reactor

The objective of reactor design is to facilitate a high heat transfer rate (Watt or Joule/s) to the endothermic reforming segment of the reactor. Heat transfer toward the catalyst bed is supplied by flowing high temperature combustion exhaust gas along the catalyst bed, and is dominated by convection heat transfer as Newton's law of cooling. An increase in heat transfer rate can be achieved by increasing the transfer surface area and/or overall heat transfer coefficient  $U$  ( $\text{W}/(\text{m}^2 \cdot \text{K})$ ) that has a series of components, including hot side convection, wall conduction, and cold side convection.

The difficulty in scaling down a tubular reactor to 1-5 kW range is that the transport restriction becomes significant. An industrial reforming reactor is typically operated at a high Reynolds number [3]; therefore, heat flux can reach as high as  $120 \text{ kW/m}^2$  [4] at the entrance of the reactor tube, with an average of  $85 \text{ kW/m}^2$  [3]. However, heat flux for a bench scale sized reactor ( $\varnothing=20 \text{ mm}$ ) has been reported to be only  $17.4 \text{ kW/m}^2$  [3]. Achieving a sufficiently large heat transfer surface in these small reactors requires reducing the diameter of the internal tube bundle. This creates a challenge in both manufacturing (a large number of very small welds) and operation (high pressure drop).

A tubular reactor that was fabricated from high temperature resistant alloy is shown in Figure 2. Three 1/2-inch-diameter Inconel tubes were used to increase the surface area for improved heat transfer between combustion exhaust gas and the catalyst bed inside the three tubes. The tubular reactor was tested for steam reforming of ultra low sulfur diesel (obtained from Chevron Phillips Chemical, TX). The heat flux for the tubular design was calculated to be in the range of  $30\text{-}40 \text{ kW/m}^2$  with the temperature difference between hot exhaust gas and catalyst bed being around  $150^\circ\text{C}$ . The heat flux was higher than the  $17.4 \text{ kW/m}^2$  reported in [3] due, in part, to the radiation heat transfer.

A microchannel reactor was developed (Figure 3) based on a design that was constructed to provide thin, flat channels for both hot (burner exhaust gas)

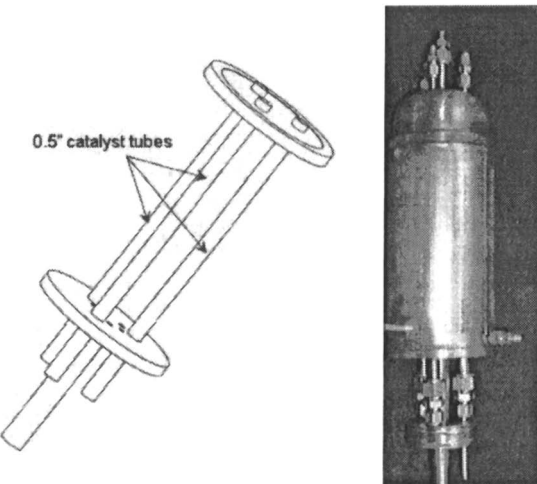


*Figure 2. The design (left) and hardware (right) of conventional tubular reactor with three catalytic tubes for increased heat transfer surface area*

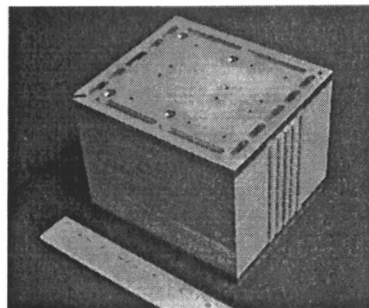


*Figure 3. InnovaTek's proprietary microchannel steam reforming reactor*

and cold (reactants) fluids separated by very thin metallic separators and that incorporates design features that provide rapid heat and mass transport. The microchannel configuration provides a high ratio of heat transfer surface area to volume of catalyst to facilitate the heat transfer required for the endothermic steam reforming reaction. For approximately the same reactor size, the 0.147 liter catalyst bed volume for the microchannel design is over three times greater than that for the tubular design (Table I). The heat transfer area ( $0.289\text{ m}^2$ ) of the microchannel design is over ten times larger than that ( $0.024\text{ m}^2$ ) of the tubular design. This will allow a much higher rate of hydrogen production per unit volume for the microchannel design.

**Table I. Comparison of Tubular and Microchannel Reactor Design**

<i>Reactor</i>	<i>Total Reactor Volume (liter)</i>	<i>Catalyst Volume (liter)</i>	<i>Heat Transfer Area (<math>\text{m}^2</math>)</i>	<i>Allowable Heat Duty (kW)</i>
Tubular	1.26	0.04	0.024	1.01
Microchannel	1.24	0.147	0.289	4.74

The microchannel reactor also provides a higher heat transfer coefficient. The convection heat transfer coefficient,  $h$  ( $\text{W}/\text{m}^2\cdot\text{K}$ ), is correlated with thermal conductivity,  $k$  ( $\text{W}/\text{m}\cdot\text{K}$ ), hydraulic diameter,  $D_h$  (m), through the Nusselt number,  $Nu$  as  $h=Nu\times k/D_h$ . In a laminar flow regime, the convection heat transfer coefficient of 1824  $\text{W}/\text{m}^2\cdot\text{K}$  is estimated [8] using a thermal conductivity of 0.239  $\text{W}/\text{m}\cdot\text{K}$  for the reforming stream at reaction temperature, while for the combustion exhaust gas side, a heat transfer coefficient of 400

$\text{W/m}^2\text{K}$  is calculated with a thermal conductivity of  $0.078 \text{ W/m}\cdot\text{K}$ . By omitting the fouling factors and thermal transfer resistance of the metallic thin wall, an overall heat transfer coefficient of  $328 \text{ W/m}^2\text{K}$  is estimated. From the heat transfer perspective alone, a temperature difference of  $50^\circ\text{C}$  between hot and cold streams will allow  $4.74 \text{ kW}$  to be transferred for the microchannel design, while only about  $1 \text{ kW}$  is transferred in the 3-tubular design even with a temperature difference of  $150^\circ\text{C}$ .

### Water Gas Shift Reactor

The water gas shift (WGS) reaction ( $\text{CO}+\text{H}_2\text{O} \rightarrow \text{H}_2+\text{CO}_2$ ) catalytically converts CO, a poison to PEM fuel cells, to  $\text{CO}_2$  with the co-production of additional  $\text{H}_2$ . It has been used as a subsystem to reduce CO concentration to a level typically less than 1% by volume. WGS reaction is a moderately exothermic process and, in most plants, is conventionally implemented in a fixed bed adiabatic reactor [2, 4]. Under adiabatic conditions, CO conversion in a single bed of catalyst is thermodynamically limited. Using high temperature (HT) and low temperature (LT) two beds with internal cooling (Figure 4 top) can reduce thermodynamic limitations to the reaction, thus increasing CO conversion. By appropriate design, the integration of heat exchanging and WGS reaction into one device can perform dual functions (Figure 4 bottom), and such integration provides a preferred temperature profile for the water gas shift reaction. An optimal temperature distribution [9] can drastically reduce the overall size of the reactor when compared with the reactors operated at other conditions. Assuming a packed bed plug flow, we conducted a similar simulation as reported in [9, 10] with one of our reactor designs using the reaction rate equation for a precious metal catalyst reported by TeGrotenhuis *et al* [9]. Figure 5 shows the temperatures and CO conversions along the catalyst bed for adiabatic and optimal temperatures. The operation of the reactor in an adiabatic

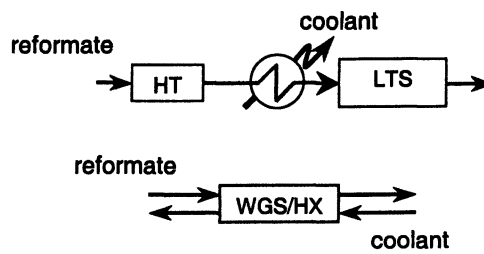


*Figure 4. The schematic of a flow diagram for a water gas shift system with two-bed design (above), and heat exchanger type one bed design (bottom)*

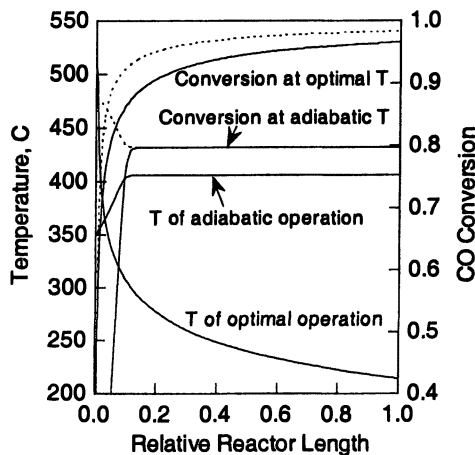


*Figure 5. The comparison of CO conversion for a water gas shift reaction at two different operating conditions: adiabatic and optimal; the equilibrium conversions are shown in dot line for both conditions*

mode results in a temperature increase of about 50°C across the catalyst bed, while if the reactor is operated under optimal conditions, there is a temperature difference, inlet to outlet, of over 250°C.

The adiabatic reactor results in a CO conversion of about 80% (Figure 5) compared with better than 95% for the reactor operated at optimal temperature conditions. The lower CO conversion for the adiabatic reactor is due to a higher exit temperature (over 400°C) toward the end of reactor. The CO conversion can be increased in an adiabatic system by lowering the inlet temperature (e.g. to 350°C) of the feed, but a lower inlet temperature will result in a slower reaction rate, thus requiring a longer catalyst bed. The reactor operated at an optimal temperature condition has much improved conversion. This conversion is still less than the equilibrium conversion (shown as dashed lines in Figure 5) due to the slower reaction rate at the lower temperature range. The reactor operated at optimal conditions outperforms the reactor operated at adiabatic conditions for any reactor length as shown in Figure 5.

Figure 6 shows the design (left) and fabricated hardware (right) of a microchannel heat exchanger type water gas shift reactor. In this design, reformate (reforming product) is fed through reforming product inlet and flows through the catalyst bed, and exits from the outlet. Fluid (e.g. H<sub>2</sub>O) acting as a

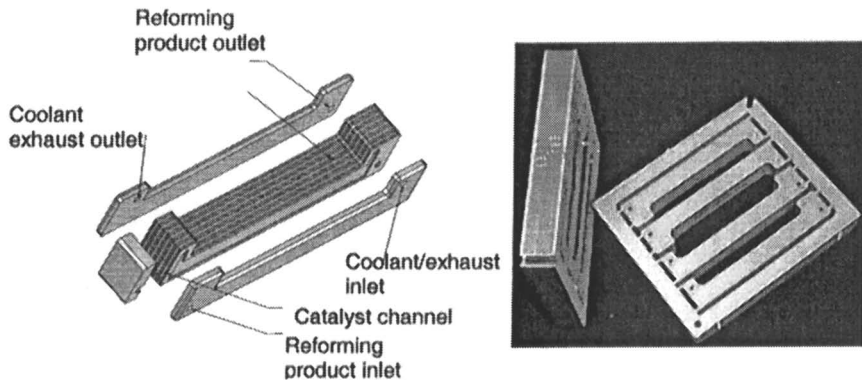


*Figure 6. The design (left) and hardware (right) of microchannel heat exchanger type water gas shift reactor*

heat sink flows through alternative channels of the assembly, creating a temperature profile along the catalyst bed of the reactor. Careful design of process parameters (e.g. flow rates) and channel dimensions provides the potential to create a temperature profile close to the optimal temperature distribution shown in Figure 5. This design provides two additional significant advantages: small reactor volume and fast start up time. The small reactor volume is attributed to proper management of the temperature profile, while a fast start up can be accomplished by flowing hot exhaust gas during start up, instead of the coolant used at steady operation, through "heat sink" channels.

### Catalysts

Conventional granulate catalyst may not be suitable for microchannel reactors. The small granulate particle size required to achieve uniform packing can create a large pressure drop across the channels, while large particles produce non-uniform flow that results in possible hot spots. We have developed monolithic catalysts whose structures were specifically tailored to suit the microchannel reactor designs. Both the porous and dense monolithic supporting materials consisted of a high temperature resistance alloy (HTRA) that was selected to offer high thermal stability, sufficient mechanical strength, and high thermal conductivity. With appropriate oxidation conditions, HTRA forms a desirable surface with a textured whisker ( $\text{Al}_2\text{O}_3$ ) structure as shown in Figure 7. The average size of whiskers is less than  $1\mu\text{m}$ . The whiskers completely cover the metal surface, thus substantially improving the adhesion of catalyst coatings to the substrate.

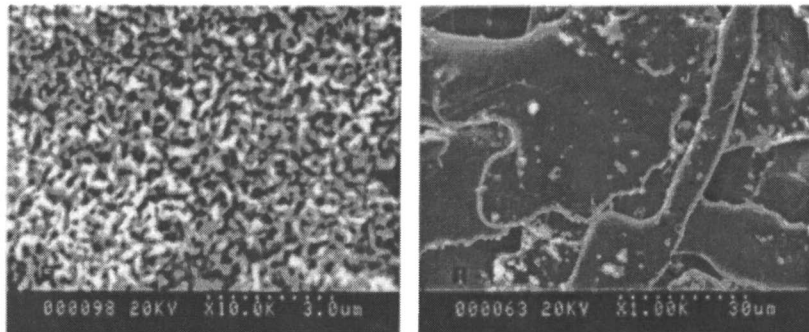


*Figure 7. The microstructures of (left) dense and (right) porous high temperature resistance alloy after pretreatment*

The steaming reforming catalysts were prepared by washcoating (dip coating process) the HTRA with a suspension that was made of the impregnated catalyst, deionized water, and ceramic binder. The viscosity of the suspension was adjusted by changing the acidity of the solution to create suitable slurry for the coating. The final step was the calcination of the catalyst. The process can be repeated if a high metal loading is required.

HTRA alone has a very low BET surface area ( $0.07 \text{ m}^2$  per gram). With catalyst coating, the BET surface area was increased to  $7.33 \text{ m}^2$  per gram or  $37 \text{ m}^2$  per ml volume. This corresponds to a surface area of  $101 \text{ m}^2/\text{g}$  based on the ceramic coating alone. This number matches the surface area of the initial oxide material. The measured average pore diameter of 8 nm (Figure 8) also matches that of the starting oxide. The cumulative pore volume was measured to be  $0.015 \text{ cc/g}$  as shown in Figure 8 and corresponds to  $0.22 \text{ cc/g}$  for the coated ceramic. This value is less than the  $0.77 \text{ cc/g}$ , the pore volume of the initial oxide. The loss of pore volume is due to the grinding step during the preparation process.

The engineered catalysts were tested for steam reforming of both methane and diesel fuel. The test was conducted in a single channel reactor with the catalyst channel dimension of  $0.35'' \times 0.04'' \times 4''$  heated by an electrical furnace. The temperature at the exit of the catalyst bed was controlled at  $850^\circ\text{C}$ , while another thermocouple monitored the temperature at the entrance of the catalyst bed. The temperature difference between exit and entrance of the catalyst bed was within  $50^\circ\text{C}$ . The steam/C ratio was controlled at 2.5 for steam reforming of methane. Nearly complete methane was converted at a gas hourly space velocity (defined as the volume of feed at STP/volume of catalyst) of  $100,000 \text{ hr}^{-1}$ . Increasing the GHSV to about  $341,000 \text{ hr}^{-1}$ , the methane conversion dropped to

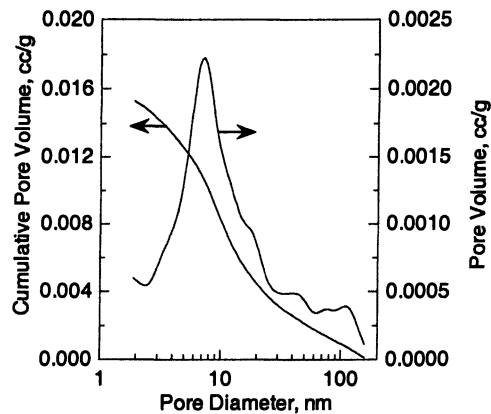


Figure 8. The average pore diameter and pore volume distribution of catalyst

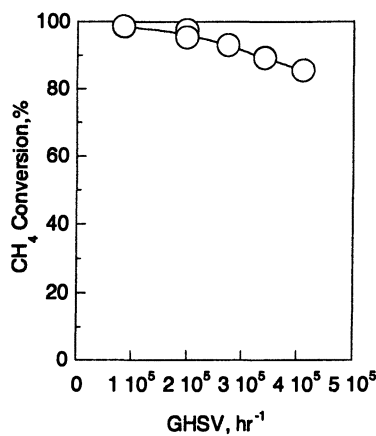
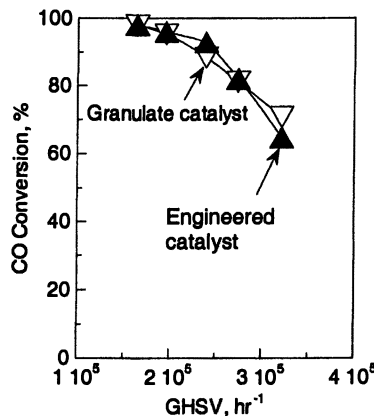


Figure 9. Methane conversion versus gas hourly space velocity during steam reforming of methane; reaction temperature: 850 °C, H<sub>2</sub>O/C ratio: 2.5

about 90% as shown in Figure 9. For steam reforming of diesel fuel, a vaporizer was connected to the reforming reactor which was heated by a 400 watt cartridge heater to ensure the complete vaporization of diesel (high boiling point, HBP=366°C) and water mixture prior to entering the catalyst channel. The test was conducted with a diesel flow rate of 0.1 ml/min and H<sub>2</sub>O flow rate of 0.55 ml/min. The hydrogen concentration in the reformate product was about 70% on a dry basis, with about 13.5% CO and 16.5% CO<sub>2</sub> generated. No

methane was detected during the test. A stable product flow rate of 420 sccm was measured by a DryCal flow meter (Bios International, NJ) for a test of 14 hours. The engineered catalyst showed similar diesel conversion and selectivity for steam reforming of ultra low sulfur diesel to the granulate catalyst reported in [1], but with a GHSV for the engineered catalyst over 3 times higher than that for granulate catalyst (300-500  $\mu\text{m}$ ), thus allowing a higher hydrogen production rate per unit volume of catalyst.

An engineered water gas shift catalyst was also prepared according to the procedure described for the preparation of steam reforming catalyst. The catalysts were tested and compared with the granulate catalyst. A gas mixture consisting of 71.5%  $\text{H}_2$ , 13.5%  $\text{CO}_2$ , and 15% CO was fed with steam into the catalyst bed at 350°C. Granulate catalyst (0.2 grams at 300-500  $\mu\text{m}$ ) was diluted with inert  $\text{Al}_2\text{O}_3$  granulates with the same size range and then packed in a catalyst bed of 4"  $\times$  0.35"  $\times$  0.04" formed by two plates. The weight of engineered catalyst was about 0.82 gram with active metal loading the same as granulate catalyst. At relatively low space velocity (e.g. 150,000  $\text{hr}^{-1}$ ), nearly complete CO conversion was obtained for both catalysts as shown in Figure 10, while at a higher space velocity (e.g. 330,000  $\text{hr}^{-1}$ ), the engineered catalyst shows comparable performance (CO conversion and selectivity) for converting CO to  $\text{CO}_2$  with the granulate catalyst. The high catalytic activity of the engineered catalyst allows the implementation of a heat exchanger type microchannel water gas shift reactor that offers the advantages mentioned above.



*Figure 10. Comparison of granulate and engineered catalysts for the water gas shift reaction; both catalysts had the same amount of metal loadings; the feed rate of water was 0.3 g/min and the feed rate of simulated reformate varied from 76 to 540 ml/min*

### Fuel Injector and Heat Exchangers

A miniature fuel injector (Figure 11) was developed for feeding liquid diesel fuel into the reforming reactor to minimize the carbon formation. The liquid diesel was atomized by high temperature steam by the fuel injector and diesel was completely vaporized prior to entering catalyst channels. The formation of a continuous liquid diesel jet through the atomizing nozzle and prevention of vapor locking are two most important engineering aspects during the design of injector.

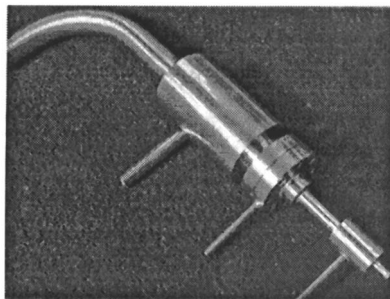


*Figure 11. The miniature injector developed for liquid diesel injection*

A mixture of diesel/steam from the injector was characterized experimentally by Laser Rayleigh Scattering (LRS) [11]. Figure 12 shows the trace signals from the LRS diagnosis of two different injectors operated at similar conditions using pump diesel from a local gas station. In this setup a zero trace signal indicates no scattering, while a large deviation from the mean value indicates a poor diesel/steam mixture with incomplete vaporization. The improvement of performance by our advanced design is clearly shown in the Figure 12 where the signal deviation (standard deviation/mean deviation) for the second generation injector (18%) is significantly reduced from that for the first prototype (43%). The ratios of standard deviation/mean deviation obtained from the same LRS test for helium and nitrogen gas were reported to be about 5% [12].

Additional essential components for an efficient system are the heat exchangers that recover heat from either the reformate gas or the combustion exhaust stream to preheat combustion air and to vaporize the water. A water vaporizer of 4.3 cubic inches was developed with a heat transfer density of 10.1 watt/cm<sup>3</sup>, very close to the 11 watt/cm<sup>3</sup> reported for a large system [13]. We also

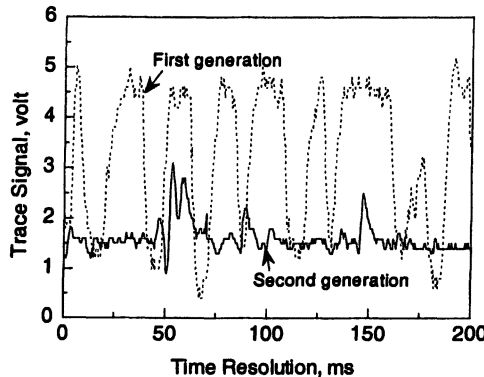


*Figure 12. The trace signals from Laser Rayleigh Scattering diagnosis of two generations of injectors developed by InnovaTek.*

designed a single module of about 12 cubic inches that combined three compact heat exchangers (including a recuperator) with a total heat transfer duty of 1.12 kW. In this module, the three compact heat exchangers are sequentially heated by one common source, combustion exhaust gas, to achieve the compact design.

### Concluding Remarks

Microchannel reactors offer the potential to produce a step function change in cost and size of steam reformers for hydrogen production in fuel cell power systems. Reformers that can use infrastructure fuels such as gasoline and diesel for the production of hydrogen are a critical bridging technology to transition to a hydrogen economy. Engineers at InnovaTek have designed, tested and are integrating unique micro-structured components that will achieve a novel, compact, and efficient processor for complex hydrocarbon fuels. An additional focus is to improve the design for manufacturability of these components and the catalyst systems with the objective of achieving further cost reductions that will lead to the production of low cost hydrogen.

### Acknowledgement

The funding for this work was supplied in part by the US Army under contract DAAD05-990D-7014 and US Department of Energy under contract DE-FC36-99GO10452. The Navel Office of Research under Contract N00014-

03-0043 and Washington Technology Center under contract WTC F01-A1 also supported this work.

The authors wish to acknowledge the support of their colleagues David Willford and Trevor Moeller. We also acknowledge the support from Prof. Philip Malte at the University of Washington, and Prof. Patrick Pedrow at Washington State University during their collaborations with InnovaTek.

## References

1. Ming, Q.; Dickman, T.; Lee, A.; Stephens, R. In *2003 Fuel Cell Seminar Abstract*, November 3-7, 2003, pp 586
2. Ridler, D. E.; Twigg, M. V., In *Catalyst Handbook, 2<sup>nd</sup> Ed.*; Twigg, M. V. Ed.; Manson Publishing: London, 1996; pp 225
3. Rostrup-Nielsen, J.R.; Christiansen, L.J.; Hansen, J.H. *Appl. Catal.* **1988**, 43, 287-303
4. Rase, H. F. *Handbook of Commercial Catalysts: heterogeneous catalysts*, CRC Press: New York, 2000; pp 403
5. Wegeng, R. S.; Pederson, L. R.; TeGrotenhuis, W. E.; Whyatt, G. A. *Fuel Cells Bulletin*, **2002**, 28, 8-13
6. Matson, D. W.; Martin, P. M.; Stewart, D. C.; Tonkovick, A. L. Y.; White, M.; Zilka, J. L.; Roberts, G. In *Microreaction Technology, IMRET 3: Proceedings of the Third Inter. Conf. on Microreaction Technol.*; Ehrfeld, W. Ed.; Springer: New York, 1999; pp 62
7. Ming, Q.; Healey, T.; Allen, L.; Irving, P. *Catal. Today* **2002**, 77, 51-64
8. Incopera, F. P.; DeWitt, D. P. *Fundamentals of Heat and Mass Transfe*, 5<sup>th</sup> Ed.; John Wiley & Sons: New York, 2002; pp 496
9. TeGrotenhuis, W. E.; King, D. L.; Brooks, K. P.; Golladay, B. J.; Wegeng, R. S. In *6<sup>th</sup> Inter. Conf. on Microreaction Technol. and AIChE Spring National Meeting*, New Orleans, March 10-14, 2002
10. Zalc, J. M.; Loffler, D. G. *J. Power Sources* **2002**, 111, 58-64
11. Espey, C.; Dec, J. *Combust. Flame* **1997**, 109, 65-86
12. Philip Malte, University of Washington, personnel communication, 2003
13. Whyatt, G. A.; TeGrotenhuis, W. E.; Greeting, J. G.; Davis, J. M.; Wegeng, R. S.; Pederson, L. R. In *Microreaction Technology, IMRET 5: Proceedings of the Fifth Inter. Conf. on Microreaction Technol.*; Matlosz, M.; Enrfeld, W.; Baselt, J.P. Ed.; Springer: New York, 2001; pp 303.

## Chapter 15

### Fuel Reformation: Microchannel Reactor Design

**K. P. Brooks, J. M. Davis, C. M. Fischer, D. L. King, L. R. Pederson,  
G. C. Rawlings, V. S. Stenkamp, W. TeGrotenhuis, R. S. Wegeng,  
and G. A. Whyatt**

**Pacific Northwest National Laboratory, P.O. Box 999, Richland, WA 99352**

Fuel processing extracts hydrogen from conventional vehicle fuel and allows fuel cell powered vehicles to use the existing petroleum fuel infrastructure. Kilowatt scale microchannel steam reforming, water-gas shift, and preferential oxidation reactors are being developed to meet DOE-required system performance metrics. Microchannel design effectively supplies heat to the highly endothermic steam reforming reactor to maintain high conversions, controls the temperature profile for the exothermic water gas shift reactor, which optimizes the overall reaction conversion, and removes heat to prevent unwanted hydrogen oxidation in the preferential oxidation reactor. The reactors combined with microchannel heat exchangers, when scaled to a full sized 50 kWe automotive system, will be less than 21 L in volume and 52 kg in weight.

A fuel cell powered car provides the potential for greater fuel efficiency and less pollution than conventional gasoline engines. Although on-board hydrogen storage technology is being pursued, an alternative approach is to process a liquid hydrocarbon fuel to produce a hydrogen-rich gas stream suitable for consumption by a fuel cell. This approach has the advantage of using the current gasoline infrastructure while providing a transition technology between conventional gasoline engines and zero-emission, fuel cell-based electric vehicles. Conventional technology for hydrocarbon fuel processing and CO clean-up experiences heat and mass transfer limitations. These limitations often result in longer residence times, larger equipment, and low efficiency. DOE-EE/RE's FreedomCAR Program has tasked Pacific Northwest National Laboratory with applying microchannel architectures where appropriate in a fuel processing system to develop the technology for a 50 kWe fuel processor that is smaller than one cubic foot (1). A prototype micro-channel-steam reforming based fuel processor at 2 kWe scale is being developed that attempts meet DOE performance targets when scaled up to 50 kWe. The other FreedomCAR targets for this system are shown in Table I. Of particular interest in the work described here are the size and weight (as specified in the power density and specific power requirements), the rapid start up time, and the CO content in the product. While developing catalysts that help meet these requirements is a significant part of this effort, the focus of this report is to discuss the features of the hardware to meet these requirements.

**Table I: DOE-EE/RE's Freedom CAR Program 2005 Targets (2)**

<i>Feature</i>	<i>Target</i>
Power density	700 W/L (< 71 L)
Specific power	700 W/kg (< 71 kg)
Energy efficiency	78%
Start-Up Energy	2 MJ
Cold startup	< 1 minute
Transient response	5 seconds
CO content in product	10 ppm (steady state)
Durability	4000 hours

The reactors that are under development for this fuel processor use the steam reforming, water-gas shift (WGS), and preferential oxidation reactions (Figure 1). The steam reforming reacts a hydrocarbon fuel with steam to produce a mixture of hydrogen, carbon monoxide, and carbon dioxide. Because steam reforming is endothermic, providing a mechanism to conduct the heat to the reaction is important in maintaining high throughput rates. To minimize the need for added heat in the reaction, partial oxidation or autothermal reforming is often used. While these are not as efficient as steam reforming in producing hydrogen for a fuel cell, they are

exothermic and heat neutral, respectively. Microchannel reactors, with their high surface area per unit volume and short heat transfer distances, provide a means to efficiently add heat to this reaction, reduce diffusion resistance, and maintain rapid kinetics. With a sufficiently efficient system, enough fuel value can be obtained from burning the anode exhaust gas to provide the required heat to drive the endothermic steam reformer.

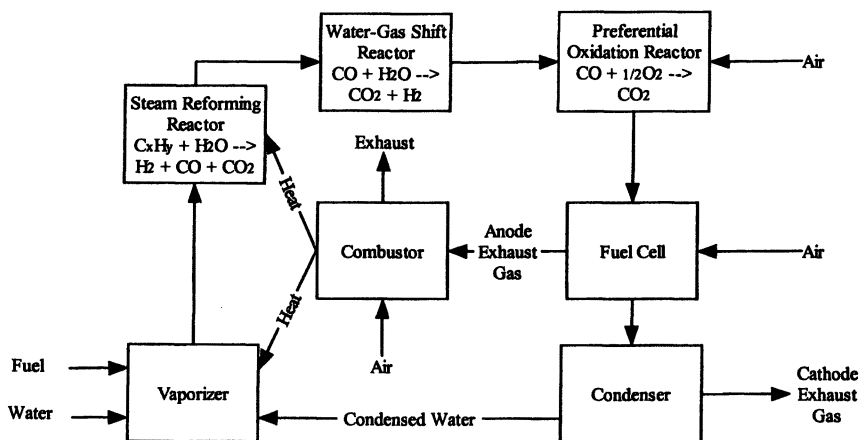


*Figure 1. Generic Process Flow Diagram of a Fuel Processor  
(Not all heat exchangers, recuperators, and air flows are shown)*

While the steam reforming reaction is generally operated at  $> 650^{\circ}\text{C}$  and is endothermic, the WGS reaction operates less than  $400^{\circ}\text{C}$  and is mildly exothermic. The purpose of this reaction is to increase the hydrogen content of the product stream from steam reforming and to decrease the CO concentration to less than 1%. The WGS reaction is equilibrium limited, and the temperature must be reduced to below  $270^{\circ}\text{C}$  in order to meet the FreedomCAR 1% CO target. However, at these lower temperatures, the reaction kinetics are slow. Generally this reaction is performed in two adiabatic steps separated by a heat exchanger. The high temperature shift reactor is small due to the fast kinetics, but in order to meet the 1% CO target, the second low temperature shift reactor is quite large. For this reaction, microchannels provide a means of removing heat to balance equilibrium conversion and kinetics to reduce the size of the low temperature WGS reaction and eliminate the need for a separate heat exchanger.

DOE FreedomCAR requires that the feed to the proton exchange membrane (PEM) fuel cell be less than 10 ppm CO during steady state operation. One approach to reduce the CO concentration in the WGS product stream is to use the preferential oxidation (PROX) reaction. In this reaction the hydrogen and CO compete for the oxidation reaction. By using the appropriate catalyst and process

conditions, all of the CO is oxidized while only a small fraction of the larger concentration of H<sub>2</sub> reacts. Higher temperatures result in a less selective CO oxidation reaction and larger amounts of hydrogen react. At lower temperatures the reaction kinetics are slower and incomplete CO conversion results. For the catalysts studied at PNNL, a reaction temperature near 200°C optimizes this balance. Micro-channel reactors allow heat removal within the reactor to maintain this strongly exothermic reaction at near constant temperature.

### Steam Reformer Reactors and Testing

For the steam reforming work performed here, the hydrocarbons studied have included methanol, ethanol, methane, propane, butane, isooctane, a synthetic diesel fuel, and a fuel mixture called benchmark fuel, which is a blend of hydrocarbons that was developed to simulate a sulfur-free gasoline (3). Reactors were first fabricated from 316 stainless steel and tested. If the design was successful, they were then fabricated from Inconel 625 to allow testing at higher temperatures.

For the steam reforming reaction with these hydrocarbons, higher steam to carbon (S:C) ratio is favorable thermodynamically, but typically reduces conversion due to the reduction in residence time and the reaction's kinetic limitations. In contrast, having insufficient steam can cause carbon deposition which would then lead to lower conversion over time. A higher S:C ratio also results in an energy penalty caused by the need to heat and vaporize more water. Higher temperatures also result in higher throughputs, limited primarily by the reactor materials. Figure 2 illustrates the effect of reformate temperature on the reformer productivity for several hydrocarbons tested in an inconel 625 microchannel steam reforming reactor. This 51 cc core reactor was developed to produce an equivalent of 2 kWe and reach temperatures up to 900°C. It was based on the design in Ref 3, but was fabricated from inconel to permit high operating temperatures.

These tests were performed with a Battelle-developed precious metal catalyst(4) at a S:C ratio of 3:1 and are based on a hydrocarbon conversion of greater than 99%. As can be seen from the figure, higher temperatures yield higher catalyst productivity. For example, the productivity for benchmark fuel tripled as the temperature was increased from 650°C to 850°C. The higher productivity results in a smaller reactor. This not only provides a smaller envelope for the reformer but also reduces the thermal mass of the system to improve start-up time. Higher temperatures also improve the catalyst's sulfur tolerance. However, by increasing the temperature, the CO:CO<sub>2</sub> ratio in the product stream increases, increasing the load on the WGS reactor.

A recently developed steam reforming reactor is shown in Figure 3. In this design, the hot air from combustion of the unused anode gas heats the reformer. These gases pass through short microchannels in reactor thickness dimension. The reformate gas travels crossflow to the combustion air across the width of the reactor. These microchannels contain the previously mentioned precious metal

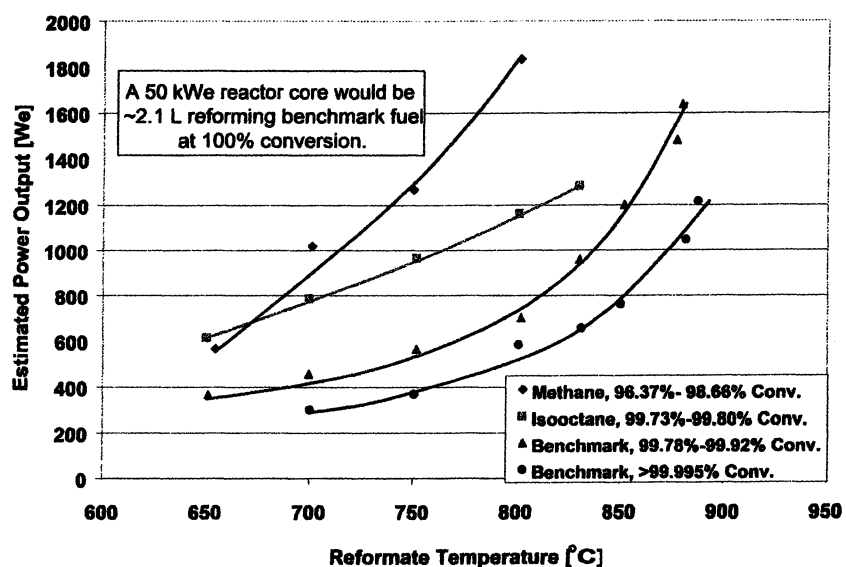
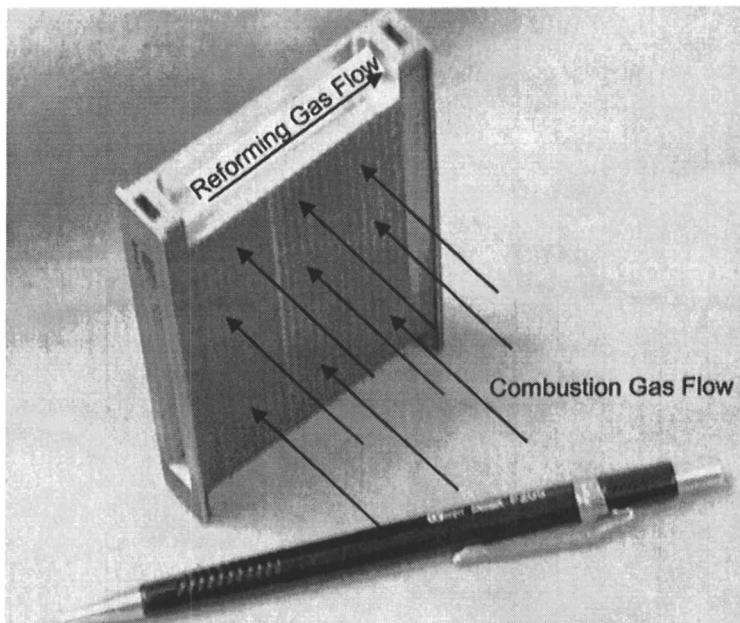


Figure 2. Increase in processing rate with increasing temperature in a microchannel steam reformer with various fuels. Electrical power estimate assumes 90% conversion in a WGS and 44% efficiency in a PEM fuel cell.

catalyst. The panel is 65 cm<sup>3</sup> in volume for both the reforming and combustion sides (including headers) and has been designed for 500 We operation at 650°C with a pressure drop of approximately 1 inch H<sub>2</sub>O across the combustion gas side of the reformer panel.



*Figure 3. 500 We low pressure drop, stainless steel, microchannel steam reformer.*

This design was used to obtain high heat transfer, low pressure drop, and to prevent overheating of the reaction panel with the hot combustion gases. The short diffusion lengths and laminar flows within the microchannel provide the high heat transfer. The short distance across the panel and the low velocity due to the large number of parallel channels result in a low pressure drop. By using an interleaved approach, where each combustion channel is directly next to two reaction channels, heat must be transferred only between the metal shim separating these two streams (Figure 4). A reasonable reaction panel metal temperature is maintained by making the height of the microchannels for the reforming reaction zone much smaller than those on the air side and by using a thin panel. Because the convection coefficient for the reformate is higher than the air side, the temperature of the metal in the reactor is closer to the reforming temperature (~ 750°C) than the combustion air temperature (~ 900°C). Thin panels increase conduction of the panel front to back

to reduce the metal temperature gradient, allowing higher gas temperatures without excessively high metal temperatures. These higher temperatures increase the system processing rate.

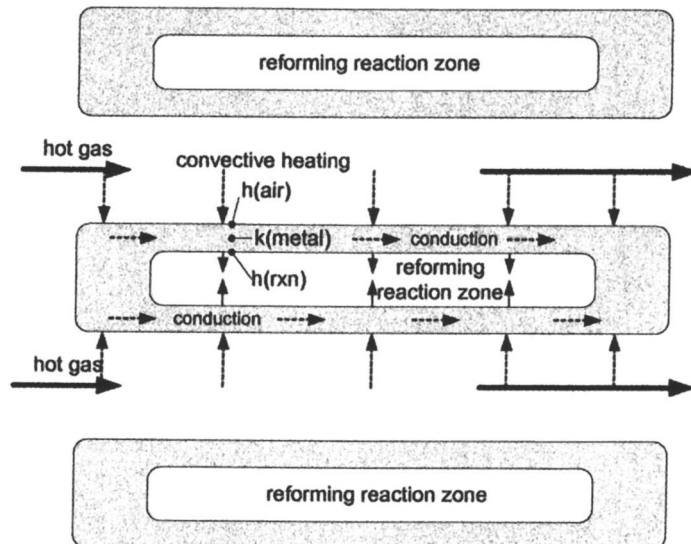


*Figure 4. Schematic of low pressure drop microchannel steam reformer panel configuration.*

Since the steam reforming reactor is the highest temperature component of the fuel processor, it must be small enough to allow fast heat up during reactor start-up. A single reforming panel was tested to determine the rate of cold start-up using isooctane as the fuel. The results are shown in Figure 5. The reformer was heated using a spark-ignited hydrogen combustor and high air flows. Temperatures were monitored in the combustion gas both before and after the reformer as well as in the entrance and exit to the reforming stream. The initial combustion gas flows were approximately 1100 slpm (10% H<sub>2</sub> in air). Hydrogen combustion was used for experimental convenience. Testing on an atomized gasoline combustor to support startup has been performed successfully in separate experiments. The water and fuel pumps for steam reforming were started within 3 seconds of the introduction of combustion gases. Initially the fuel flow was 9.04 cc/min. The combustion air was heated from ambient to 700°C in less than 5 seconds for a final average air temperature of 850°C. Full reformate flow was reached in 12 seconds. Once full

reformate flow was reached the fuel flow was reduced to 2.2 cc/min. At full reformate flow, the reformate thermocouple measured only 350°C. However, based on the composition of the feed and reformate, the equilibrium reformate temperature was in excess of 650°C. Thermal lag in the unheated reactor outlet header and connecting tubing prior to the thermocouple measurement is probably responsible for the lower temperature. A more accurate measure of the reformate temperature would probably be the combustion gases after passing through the reformer heat exchanger. These showed an average temperature of 550°C. The cycling of the reformate flow during steady state is the result of cycling in the fuel piston pump. A pulse dampener would reduce this cycling but would slow the response time.

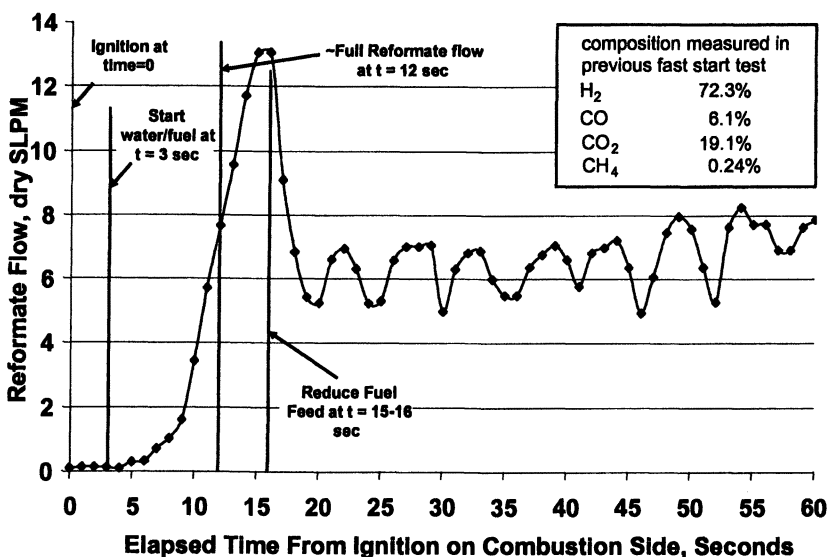


Figure 5. Steam reforming rapid start-up experiment with the 500 We panel with isoctane fuel: reformate flow on a dry basis.

During start-up, the S:C ratio was increased to about 24:1. This high S:C ratio provides many advantages. The high steam flows provide high S:C ratio at the reformer, reducing CO content in the reformate. Low CO reduces demand for WGS activity during startup when the WGS reactor has not reached its operating temperature. High steam flows would also provide a greater heat content to warm the reformate recuperator and WGS-PROX reactors. Once the WGS and PROX

reactors have reached their operating temperatures, the S:C ratio can be reduced to improve system efficiency.

### Water–Gas Shift Reactor and Testing

The goal when operating the WGS reactor is to develop an optimum thermal profile down the length of the reactor that will result in the highest reaction rate while maintaining the CO concentration far enough away from equilibrium to allow continued conversion to occur. The optimal temperature profile developed mathematically in previous work is shown in Figure 6 (5). In this figure, most of the conversion, 82%, occurs in the first third of the reactor, and the remaining two-thirds of the reactor is required for the remaining 8% of conversion, a direct result of much lower activity as the temperature decreases. Furthermore, the optimal temperature profile calls for a rapid decrease in temperature—from 665°C at the inlet to 400°C at eight percent of the reactor. This is also where two-thirds of the heat of reaction is being generated, adding to the unbalanced heat load at the inlet end of the reactor.

The ideal profile is difficult to implement in an actual reactor due to the sharp temperature gradients required. A reactor was developed that provides many of the features of this ideal temperature profile. The expected temperature profile of this combined adiabatic/differential reactor is shown in Figure 7. In this reactor, the exothermic reaction in the adiabatic section heats the feed gas from 340 to 410°C. It then enters the differential temperature section where the gas is cooled from 410°C to 275°C as the reaction progresses. Similar to the approach taken here, conventional WGS systems use two reactors. However, the conventional system uses two adiabatic reactors with a heat exchanger between them. Based on modeling, the differential reactor will result in 43% reduction in size of the conventional second stage adiabatic reactor. This does not include the additional size reduction from the loss of the additional heat exchanger, which is not required for the differential approach.

The benefit of a differential section of this reactor can best be described with the results of previous experiments done with only a differential reactor (Figure 8). This approach was validated with a low temperature shift reactor operating at 76,000 GHSV with a steam to dry gas ratio of 0.52:1 and an initial inlet CO concentration of 4.6% and the balance was H<sub>2</sub> and CO<sub>2</sub>. When operated as an isothermal reactor, at higher temperatures, the minimum CO concentration was limited by the equilibrium of the WGS reaction. As the temperature decreased, the equilibrium CO concentration continued to decrease, but the reaction kinetics also decreased. At sufficiently low temperatures, equilibrium conversions were not possible because of the slow reaction kinetics. This resulted in an increase in CO concentration

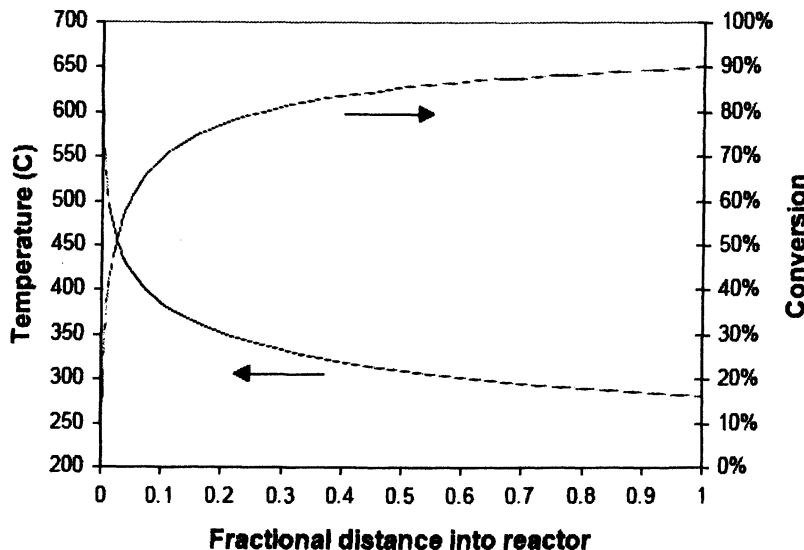


Figure 6. Representative optimum temperature profile and corresponding conversion profile for a water gas-shift reactor with a steam reformate feed at an initial composition of 9% CO, 9% CO<sub>2</sub>, 36% H<sub>2</sub>O, and 45% H<sub>2</sub>.

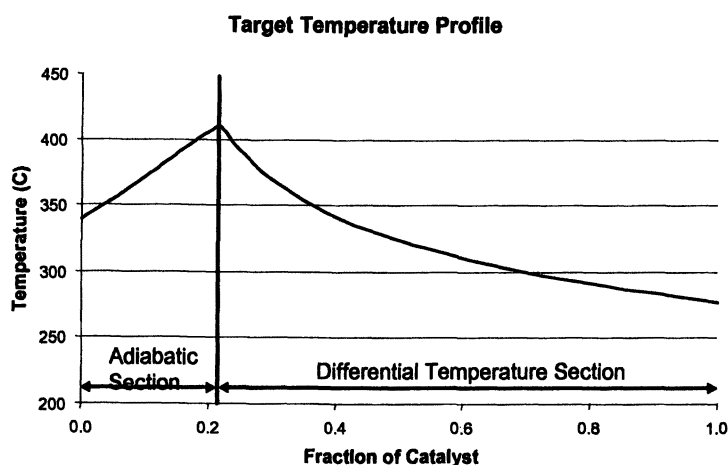


Figure 7. Temperature profile model of the hybrid WGS reactor with an adiabatic section followed by a differential reactor with integral, co-current heat exchanger.

out of the reactor. With a differential reactor, the CO concentration was able to reach levels lower than the isothermal case because the reactor inlet is at higher temperatures with favorable reaction kinetics, and the exit is at a lower temperature where only small CO conversion is required to maintain the concentration near equilibrium in spite of the slow kinetics.

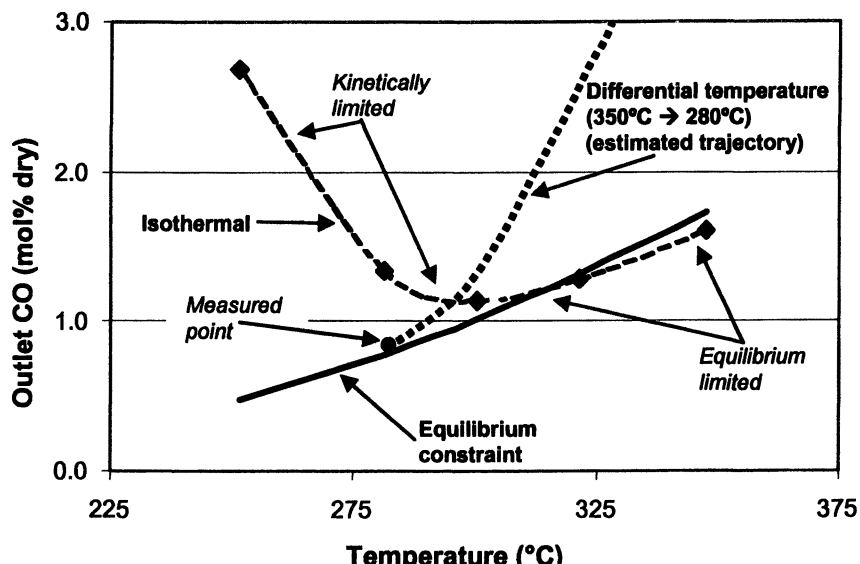


Figure 8. Experimental results of microchannel low temperature shift WGS reactor outlet CO concentrations under both isothermal and differential conditions compared to equilibrium. Note: 76,000 GHSV, 0.52 steam/dry gas, 4.6% CO feed. The differential temperature trajectory was estimated based on mathematical modeling.

This previous work on WGS at PNNL used an interleaved approach for reaction cooling in the second differential stage similar to that used for the steam reforming system. Air flow between the reaction gases and the coolant air was counter flow. Results from this testing was less than ideal. Heat transfer between the cooling air and the reactor was too high and the ideal temperature profile could not be achieved. For example, in order to cool the reactor exit down to 270°C, the reaction gases at the hot end of the reactor were quenched. Or, to maintain high temperature at the entrance, the reduced exit temperature could not be achieved.

To address these issues, a second reactor was designed with the adiabatic and differential sections combined in a single reactor (Figure 9, left). The heat transfer resistance was increased by placing the microchannels side by side and allowing cooling to occur from the catalyst through a fin and into the cooling

channel (Figure 9, right). The cooling channels were perpendicular to the reaction channels. Cooling gases passed cocurrent with the reaction gases. The cocurrent flow and reduced heat transfer resulted in a temperature asymptotic profile rather than a linear one, which is closer to the ideal in Figures 6 and 7.

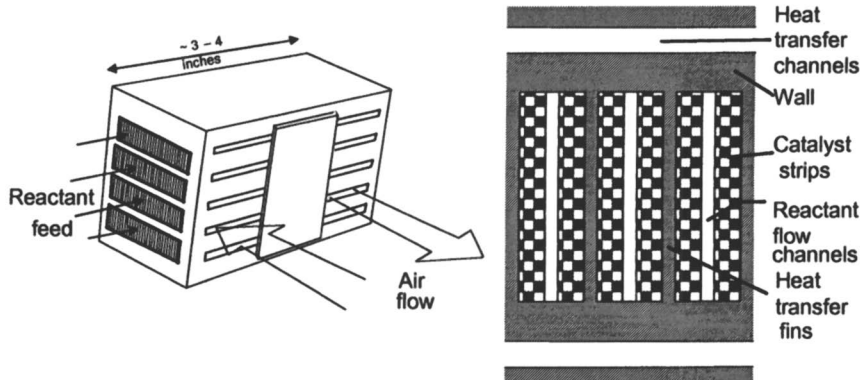


Figure 9. The WGS reactor (left) and schematic of the flow and heat transfer channels within the reactor (right).

This reactor also had the added advantage of increasing the total amount of catalyst that can be loaded into a given volume of reactor. For the interleaved approach, significantly less than half of the reactor is catalyst because of the high fraction of cooling channel interleaved metal. At high differential pressure between the two streams, this becomes even more significant as the metal thickness must increase and the span of the microchannel must decrease. For this reactor, the catalyst made up more than half of the overall volume of the reactor (52%).

This reactor was run over a range of air flow rates to evaluate the benefits of the reactor design. For the work done here, the composition of the feed stream is shown in Table II. The reactor was designed for 2 kWe throughput (corresponding to 29 slpm dry gas feed and a 44% efficient fuel cell). At more or less adiabatic conditions, the CO concentration is greater than 2% (zero air flow) (Figure 10). By increasing the cooling air flow, the temperature at the exit can be reduced and CO concentrations below 1% are possible. During testing, the differential section ranged from 350–400°C at the inlet to 250–300°C at the outlet. For flow rates up to 2 kWe, the exit CO concentration remained within a few percent of the equilibrium concentration. Exit CO concentrations of < 1% were possible with the reactor flows up to 2.5 kWe. As seen in the figure, there is an air flow rate where the minimum CO concentration can be achieved exiting the differential section. Higher flowrates tend to quench the reaction prematurely and lower flow rates do not decrease the temperature at the exit sufficiently to obtain a low equilibrium concentration driving

force. The GHSV for this reactor at 2 kWe was 64,000 overall. The reactor was loaded with a commercially available SudChemie precious metal catalyst.

**Table II. Composition of WGS Feed**

Component	Dry Basis Composition	Wet Basis Composition
H <sub>2</sub>	74%	49.3%
CO	12%	8%
CO <sub>2</sub>	14%	9.3%
H <sub>2</sub> O		33%

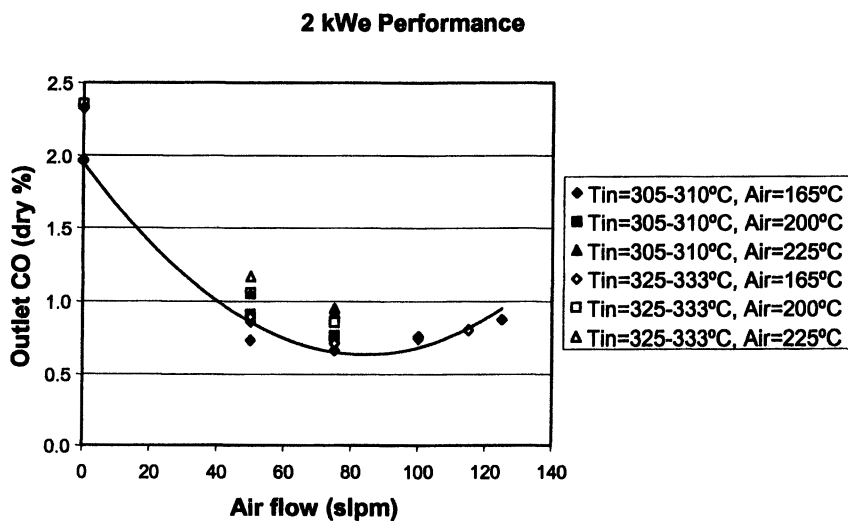


*Figure 10. Outlet CO composition for the hybrid adiabatic/differential temperature WGS reactor over a range of coolant flow rates for 2 kWe syngas flow. Syngas (Tin) and air inlet temperatures (Air) are provided.*

Unlike the differential section that followed the expected profile closely, the adiabatic section had a temperature rise of approximately 30–40°C. This is less than the expected 60°C. This reduced temperature is probably caused by heat losses to the differential temperature side of the reactor. These heat losses actually improved the reactor performance by allowing the temperature to approach

equilibrium at a lower temperature resulting in CO concentrations of ~ 2–3% at the exit of the adiabatic section rather than the expected ~ 4% equilibrium value at 410°C.

### Preferential Oxidation Reactor

The goal of the PROX reactor was to receive the 1% CO product from the WGS reaction and produce an outlet CO concentration of less than 10 ppm using an O<sub>2</sub>:CO ratio of 1:1 or less. This stream can then be used as feed to a PEM fuel cell without poisoning the membrane. For this transportation application, the size and weight of the reactor was also to be minimized.

To meet these criteria, a reactor was developed that attempted to maintain the temperature within the reactor as near constant as possible. The reactor was designed with multiple chambers of catalyst (Figure 11). Sandwiched between each of these catalyst stages are thin heat exchanger panels that allow reaction gases to flow through them. The catalyst is coated on high thermal conductivity porous material. Due to the close contact between the catalyst and the heat exchanger panel, heat generated by the strongly exothermic reaction is transferred both by convection through the gases and conduction through the foam to the heat exchanger panel. To further control the reaction and maintain an isothermal temperature profile, the air is added in small quantities at each of the four stages of the reactor rather than once at the beginning.

The advantages of this particular reactor are as follows. This reactor design can have significantly higher than 50% of its volume in catalyst and yet still control the reaction temperature. For the reactor developed, the catalyst accounted for nearly 70% of the volume (excluding outside walls and headers). This approach also allows a change in catalyst quantity and size down its length. In the front end of the reactor where most of the reaction is occurring and thus most of the heat is generated, less catalyst can be used and the heat exchangers can be closer together. Further down the reactor more catalyst can be used with fewer heat exchangers. The microchannel heat exchanger panel provides for low pressure drop, and small volume temperature control, which are integral to the reactor.

Before the reactor was developed, testing was performed on several commercially available catalysts both at first stage CO concentrations (1%) and second stage low CO concentrations (330 ppm). Catalysts were found with high selectivity and activity. The first stage catalyst selected was a SudChemie non-precious metal catalyst. Sample results of testing this catalyst are shown in Figure 12. Conversions of ~ 97% were achieved at ~ 200°C to yield approximately 300 ppm CO exiting the first stage. Increasing the temperature above 200°C resulted in complete O<sub>2</sub> conversion and a reduction in selectivity toward the CO oxidation reaction.

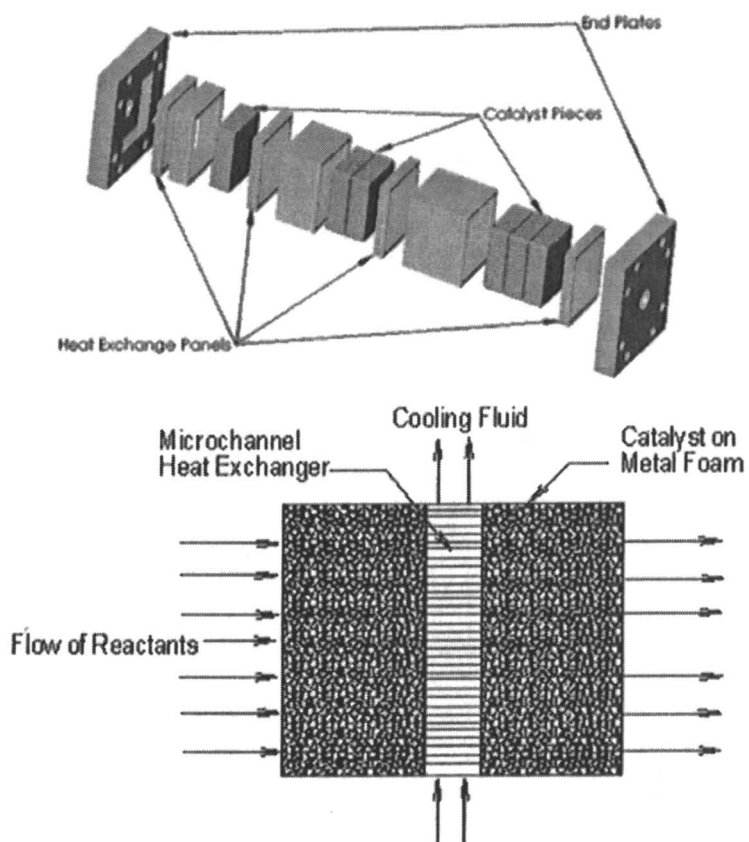


*Figure 11. Design of the PROX reactor (top). Catalyst foams are sandwiched between heat exchanger panels to maintain the reaction temperature nearly constant (bottom).*

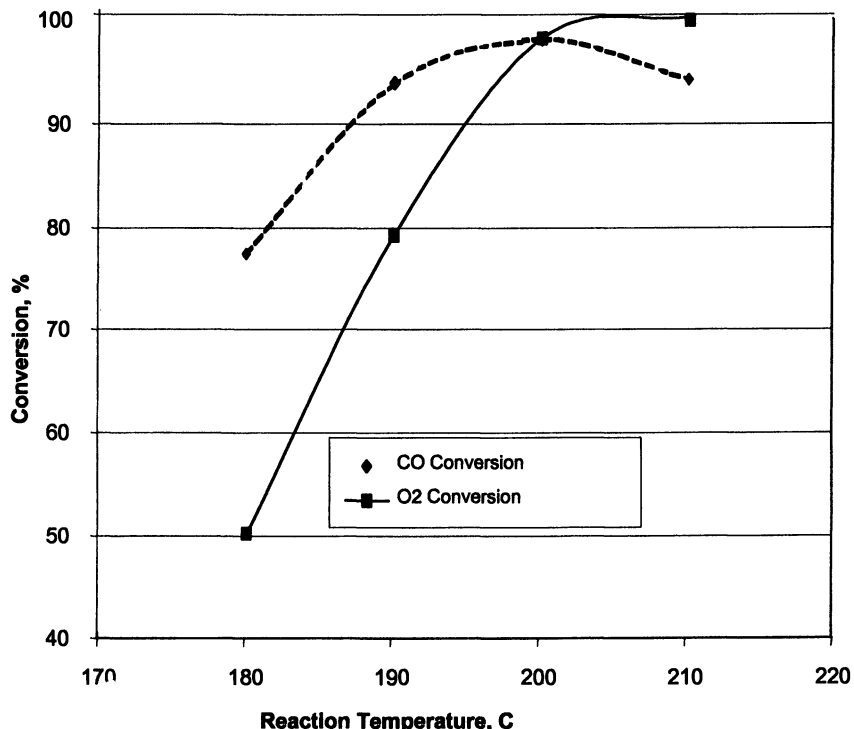


Figure 12. Results of SudChemie non-precious metal first stage PROX catalyst at  $O_2:CO = 1.0$ , steam to gas = 0.3, a feed CO concentration of 1% CO, and GHSV = 100K.

The second stage catalyst was selected from two Engelhard precious metal catalysts. Sample results of this test are shown in Figure 13. Once again conversions of > 97% were possible, but only over a very limited temperature range. The higher temperature catalyst was selected because it had a wider range of operating temperatures and operated at a temperature very similar to that of the first stage catalyst (200°C).

To meet the 10 ppm CO limits, a microchannel reactor with four chambers was developed and loaded with three of the four chambers using SudChemie first stage catalyst and the final chamber with the Engelhard second stage catalyst. Using this configuration, the first three chambers containing first stage catalyst oxidized the CO from ~1% to ~300 ppm and the final chamber containing second stage catalyst oxidized the remaining CO from 300 ppm to < 10 ppm. The higher temperature Engelhard catalyst was employed to allow the entire reactor to operate at 200°C.

For the 2 kWe testing performed with the reactor shown in Figure 11, an oil bath was used to cool the heat exchanger panels and maintain the temperature near 200°C. In an actual test, pressurized water at its boiling point would probably

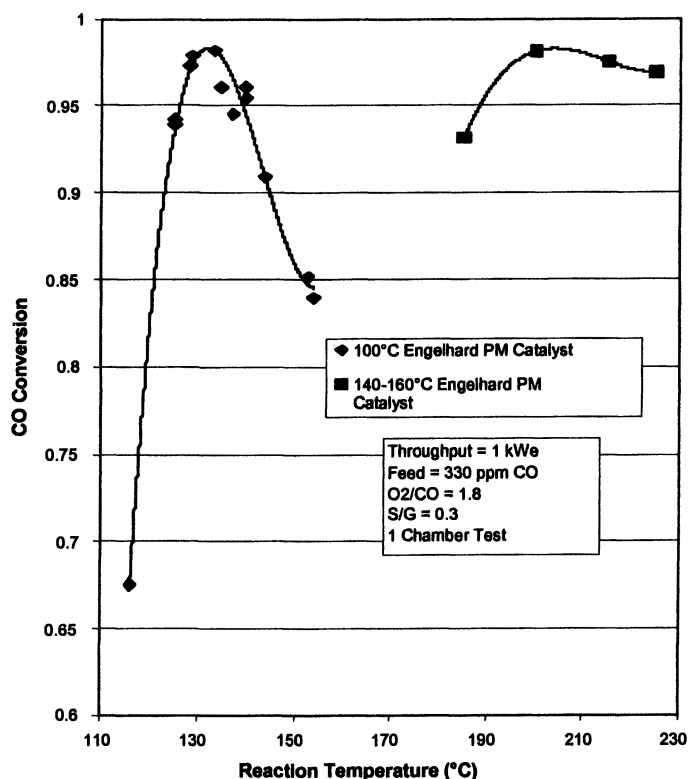


Figure 13. Results of Two Engelhard PM second stage PROX catalysts as a function of temperature at a GHSV of 200K.

**Table III. Composition of the PROX Reactor Feed**

<i>Component</i>	<i>Dry Composition</i>	<i>Wet Composition</i>
H <sub>2</sub>	79%	60.8%
CO	1%	0.8%
CO <sub>2</sub>	20%	15.4%
H <sub>2</sub> O	--	23.1%

be used to control the reaction temperature. The composition of the feed stream for this testing is shown in Table III.

As shown in Figure 14, this reactor was able to reach less than 10 ppm CO for a starting concentration of 1% with an overall O<sub>2</sub>:CO addition of 1.2:1. This was accomplished by adding only O<sub>2</sub>:CO in the ratio of 0.5:1 (stoichiometric) and then progressively adding a higher O<sub>2</sub>:CO ratio to each chamber. The last chamber had an O<sub>2</sub>:CO ratio of approximately 6:1. However, due to the low CO concentration in this chamber, the amount of air actually added was very small and the overall hydrogen loss due to the unfavorable reaction was only approximately 1%. Additionally, there was a higher catalyst loading on the metal foams of each progressive chamber of the reactor. The overall GHSV was 93,000 for a 2 kWe equivalent flow of hydrogen.

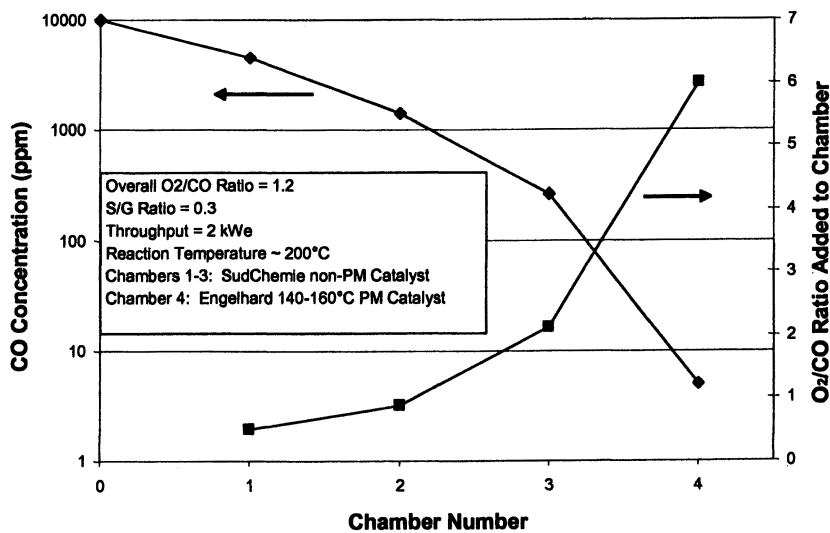


*Figure 14. CO concentration and O<sub>2</sub>:CO ratio addition in each chamber for the 2 kWe PROX Reactor*

A characteristic temperature profile for this reactor is shown in Figure 15. In this case only the non-precious metal first stage PROX catalyst was tested.

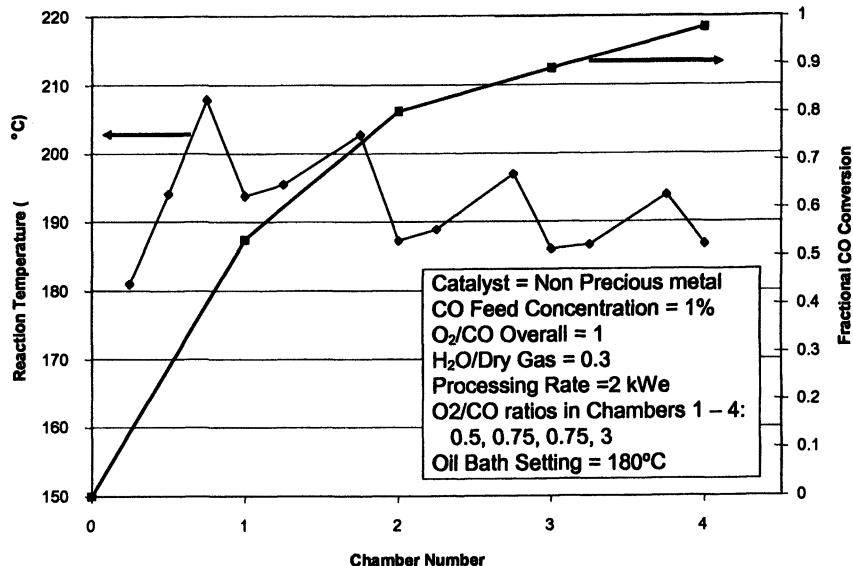


Figure 15. Temperature profile within the 2 kWe PROX reactor as a function of chamber number and CO conversion.

Measurements were taken both within the catalyst in each chamber and before and after the catalyst in each chamber. The temperature remained within  $\pm 20^\circ\text{C}$  throughout the reactor, rising within the catalyst and then decreasing as it passed through the series of microchannel heat exchangers. Since the overall expected temperature rise of the reaction under adiabatic conditions is greater than  $100^\circ\text{C}$ , these results indicate significant temperature control using the staged heat exchanger and air addition approach.

## Conclusion

Microchannel reactors have made it possible to effectively supply heat to highly endothermic reactions and to control temperature for highly exothermic reactions. In the work performed here, microchannel reactors have been used to effectively supply heat to the steam reforming reactor to maintain a high throughput rate, control heat removal in the WGS reactor to optimize the overall reaction conversion, and remove heat to prevent the unwanted hydrogen oxidation reaction

in the PROX reactor. These reactors were done with kilowatt-scale flows to allow scaling of this prototype to a full-scale 50 kWe reactor system. By scaling up these reactors, the size goals of the DOE-EE/RE's FreedomCAR Program can be estimated (See Table IV). The volume and weight goals of 71 kg and 71 liters appears feasible with the current microchannel architecture approach.

**Table IV. Estimated size and mass of the 50 kWe fuel reforming system based on current experimental results.**

<i>Device</i>	<i>Mass (kg)</i>	<i>Volume (L)</i>
Steam Reformer	4.36	1.1
Water Vaporizer	7.44	0.8
Air-Air Preheater	24.68	8.1
Recuperator	1.8	0.3
WGS Reactor	7.20	3.4
PROX Reactor <sup>a</sup>	6.60	7.0
<b>Total</b>	<b>52.08</b>	<b>20.7</b>

<sup>a</sup> PROX values are based on direct scaling of an experimental prototype not optimized for size. Significant size reductions are expected.

### References

1. Wegeng, R. S.; Pederson, L. R.; Tegrotenhuis, W. E.; Whyatt, G. A.; Saffell, B. J. *Fuel Cells Bulletin*, 2001, 3(28), 1-6.
2. Hydrogen, Fuel Cells & Infrastructure Technologies Program Multi-Year Research, Development and Demonstration Plan 2003-2010, U.S. Department of Energy, Energy Efficiency and Renewable Energy, Draft 6/03/03.
3. Whyatt, G. A.; Fischer, C. M.; Davis, J. M. "Progress on the Development of a Microchannel Steam Reformer for Automotive Applications," AIChE 2002 Spring National Meeting, March 10-14, 2002.
4. Wang, Y.; Vanderwiel; D. P.; Tonkovich, A. Y., US Patent 6,734,137. 2004.
5. TeGrotenhuis, W.E; King, D.L.; Brooks, K.P. ; Golladay, B.J.; Wegeng, R.S. March 2002. "Optimizing Microchannel Reactors by Trading-Off Equilibrium and Reaction Kinetics through Temperature Management." AIChE Spring National Meeting. New Orleans, LA.

## Chapter 16

### **Microchannel Reactors for Intensifying Gas-to-Liquid Technology**

**Kai T. Jarosch<sup>1</sup>, Anna Lee Y. Tonkovich<sup>1</sup>, Steven T. Perry<sup>1</sup>,  
David Kuhlmann<sup>1</sup>, and Yong Wang<sup>2</sup>**

**<sup>1</sup>Velocys Inc., 7950 Corporate Boulevard, Plain City, OH 43064**

**<sup>2</sup>Pacific Northwest National Laboratory, Richland, WA 99301**

Microchannel devices increase process intensity for major unit operation building blocks, including chemical reactors, by reducing heat and mass transfer distances. Observed volume reductions range from 10 to 1,000 times that of conventional technology. Microchannel technology is being commercialized for both steam methane reforming and Fischer-Tropsch (FT) synthesis. Synthesis gas formation in methane reformers with integrated combustion has been demonstrated where conversions approach equilibrium at contact times less than 10 milliseconds (ms), temperatures near 925°C, at a pressure of 25 atmospheres (atm). FT synthesis has been demonstrated in a microchannel reactor over a Co/Re-Al<sub>2</sub>O<sub>3</sub> catalyst at a pressure of 41 atm and temperature of 250°C. Carbon monoxide conversion was greater than 69%, while selectivity to methane was below 11% at a contact time of 308 ms. In addition, the required manufacturing methods and technology to produce large-capacity microchannel reactors have been developed and demonstrated.

## Introduction

One attractive area for microchannel technology is the FT gas-to-liquids (GTL) process. The conventional process involves three reactions, one endothermic and two exothermic. The endothermic reaction is steam reforming of a hydrocarbon to make synthesis gas. One of the exothermic reactions is a combustion reaction required to provide the heat for reforming. The second exothermic reaction is the FT synthesis reaction. A methane steam reforming reactor that intimately couples catalytic combustion with the endothermic steam reforming of methane has been demonstrated. In addition, an FT reactor that couples the exothermic formation reaction with partial boiling heat removal has been developed.

Successful commercialization of microchannel processes requires not only robust design and catalyst performance, but also the development of manufacturing methods and technology (*1*) that are technically feasible and cost-effective. To that end, a manufacturing supply chain and manufacturing technology capable of meeting these goals has been developed.

## Manufacturing Microchannel Devices

The most common method of manufacturing microchannel devices is to laminate or diffusion bond thin sheets of metal, plastic or ceramic so that each layer has a defined geometry of channels and openings through which to convey fluids (Figure 1). After the individual layers are created, they are stacked in a prescribed order to build up the lamination. This completed stack is then diffusion bonded to prevent fluids from leaking into or out of the device or between streams. After bonding, the device is trimmed to its final size and prepared for attachment of pipes and manifolds. An additional step for devices in which catalytic reactions occur is to integrate the catalyst into the device prior to final assembly.

Feature creation methods include photochemical etching, milling, drilling, electrical discharge machining, laser cutting, and stamping. The most economical method for mass manufacturing is stamping (*2*). In stamping, care must be taken to minimize distortion of the material and maintain tight tolerances of channel geometries.

Stacking the layers is another technical issue that needs to be addressed for technical and commercial success. Several requirements are key to the stacking process:

- Prevent distortion
- Maintain shim alignment
- Ensure that layers are stacked in the proper order.

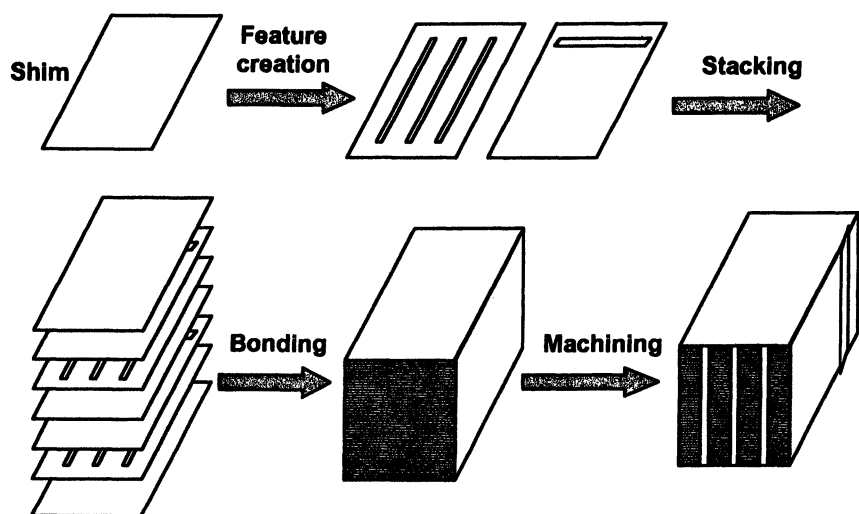


*Figure 1. The basics of microchannel device fabrication.*

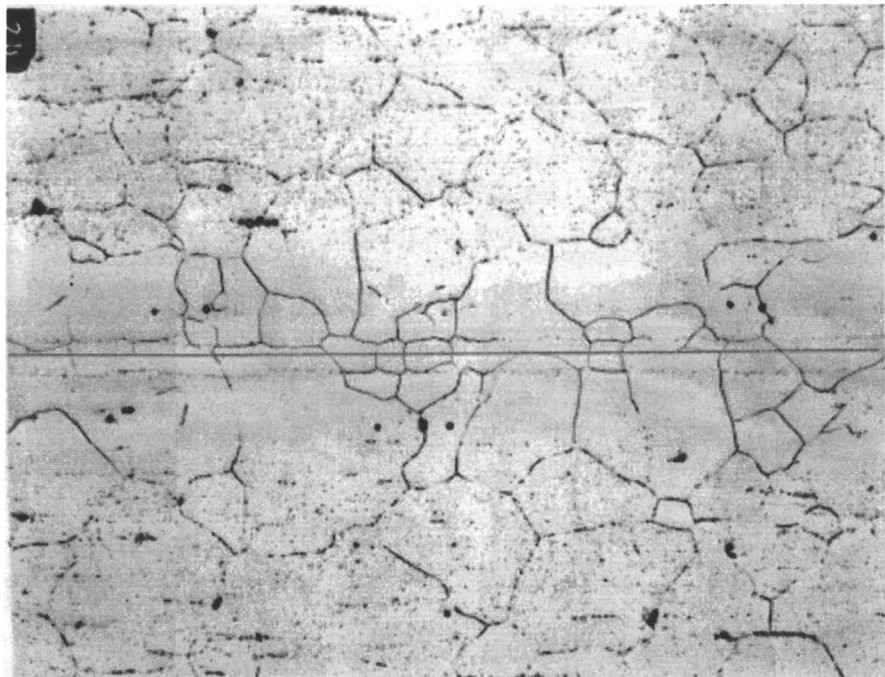


*Figure 2. 200X Photomicrograph of diffusion bonded microchannel layers.  
(See page 3 of color insert.)*

The stack is bonded through a diffusion process. In this process, the stack is subjected to elevated temperatures and pressures for a precise time period to achieve the desired bond quality. Selection of these parameters has required extensive modeling and experimental validation to find the correct bonding conditions that enable sufficient grain growth between the metal layers. After bonding, the metallurgical properties of the device approach parent material.

Figure 2 shows a typical micrograph of bonded microchannel layers. The solid line bisecting Figure 2 denotes the location of the interface between layers. Note the substantial metallurgical grain growth across this former shim boundary. This type of grain growth is indicative of high-quality bonds.

After bonding, the next major manufacturing step is machining the device. A number of processes have been used, including conventional milling with high-speed cutters, as well as highly modified electrical discharge machining techniques. A full-sized bonded reactor sub-unit (made up of many hundreds of shims) that has undergone post-bonding machining operations can be seen in Figure 3.

The final step in manufacturing is catalyst integration, including precise insertion and in situ application.



*Figure 3. Full-scale reactor after bonding and access machining ready for manifolding.*

### FT GTL Reaction

The GTL process, as it is known today, is the result of concerted technical effort at the turn of the last century to produce motor fuels from Germany's plentiful coal supplies (a solid-to-liquid process). Following in the footsteps of Friedrich Bergius, two German scientists (Franz Fischer and Hans Tropsch), working in the 1920s, discovered that mixtures of CO and hydrogen could be converted to higher hydrocarbons over iron and cobalt catalysts (3,4). The technology was successfully commercialized, as a result of government subsidy, and developed further during World War II. Interest in the FT process waned in the post-war years, but was adopted by Sasol during international sanctions on the Republic of South Africa.

### **Conventional Processes for GTL Conversion**

At present, only two companies, Sasol and Shell Gas and Power, are operating commercial FT processes. Using low-grade coal as a starting point, Sasol's South African operations employ a number of reactor technologies (tubular fixed bed, slurry bed, fluid bed and circulating fluid bed) to produce approximately 150,000 barrels per day (BPD) of motor fuels (5). Shell's Bintulu plant uses natural gas as a starting point and uses a tubular fixed bed reactor and cobalt catalyst system to produce 12,500 BPD (5).

Apart from the commercial operations mentioned above, several small demonstrations of FT processes are under way. ConocoPhillips operates a 400-BPD demonstration plant that combines partial oxidation for syngas production and a fluidized bed for the FT reaction (5). BP operates a 100-BPD demonstration plant based on its compact, fixed bed reformer technology and Davy Process Technology's FT technology (5). In addition to these demonstrations, Syntroleum and Marathon Oil are operating a 70-BPD plant as part a U.S. Department of Energy program (6). At a larger scale, Sasol and Chevron are planning to complete a 34,000-BPD GTL joint venture plant in Qatar by 2005 (5). Consideration is being given to expanding the capacity of this plant to 100,000 BPD by 2009. Also in Qatar, Shell and Qatar Petroleum are planning a 140,000-BPD GTL plant in Ras Laffan City to be completed in 2009 (5).

### **Microchannel Processes for GTL Conversion**

In spite of varying levels of commercial interest, a steady stream of work has been reported both in the technical and patent literature for catalysts and conventional-scale reactors and processes related to GTL via the FT reaction; but up to the present, very little work has been reported on the application of microchannel technology to the FT process. To date only Pacific Northwest National Laboratory (7,8), Statoil of Norway (9), GTL Microsystems (10), Velocys (11), and Institute for Micromanufacturing at Louisiana Tech University (12) have reported conducting the FT reaction under microchannel conditions.

The work at PNNL (7,8) focused on developing catalysts with high activities to make use of the advantages inherent to microchannel technology (high heat and mass transfer rates) and on the integration of these catalysts with suitable engineered supports. The engineered catalyst forms were tested in a microchannel reactor with a critical dimension of 1.5 millimeters, and the catalyst was kept in a close-to-isothermal state by two adjacent coolant containing microchannels. CO conversion of up to 84%, combined with

methane selectivity of 9%, was obtained with contact times as short as 2 seconds (1800 hr<sup>-1</sup> GHSV).

Schanke, Bergene, and Holmen (9) reported the use of a monolith type structure for the FT reaction, where cooling is provided by recirculating cold FT product. A CO conversion of 27% was observed over the high surface area monolith at 195°C and a gas hourly space velocity of 4.06 hr<sup>-1</sup>. FMC Technologies and Accentus have formed a joint venture company to commercialize a microchannel GTL FT process based on a proprietary catalyst (10). Kuila *et al* at Louisiana Tech (12) reported the use of cobalt, iron, and ruthenium sol-gel catalysts for FT in 5-micrometer ( $\mu\text{m}$ ) and 25- $\mu\text{m}$  microchannels and obtained conversions of CO as high as 73%, but experienced significant loss of catalyst activity (85%) over 17 hours.

The conventional reactor concepts for producing GTL products through FT synthesis are limited by heat transfer and mass transfer. Microchannel technology is able to mitigate the restrictions of both heat and mass transfer to exploit the underlying catalyst potential. The short distances characteristic of a microchannel alleviate external mass transfer limitations. In this work, the heat transfer limitations are overcome by coupling the exothermic FT synthesis with heat transfer via steam generation.

The authors further discuss higher productivity rates with low selectivity to methane in a microchannel reactor. The work is differentiated from previous work by the use of a substantially smaller reaction channel than that reported previously by Wang *et al* (7,8) or greater stability than those reported by Kuila *et al* (12) or much greater space velocity than that reported by Schanke *et al* (9).

### Integrated Steam Reforming and Combustion Reactors

One advantage of microchannel technology over conventional technology is that it enables the close coupling of heat generation and heat adsorption. This allows highly endothermic reactions, such as steam reforming (49.3 kilocalorie per gram mol [kcal/mol]), that are normally heat transfer limited (13) in conventional technology to be closely coupled to highly exothermic reactions such as the combustion of hydrogen (57.8 kcal/mol) or methane (147.5 kcal/mol). In this case, the microchannel advantage allows for the intensification of heat transfer. The reported integrated combustor reformers has been operated to obtain heat flux as high as 100 W/cm<sup>2</sup> (14); thus, the microchannel reactors operate with heat fluxes more than one order of magnitude greater than those that can be obtained in conventional systems (1 W/cm<sup>2</sup>) (15,16). This, combined with the very short distances involved for mass transfer, allows the full kinetic potential of the catalyst to be exploited.

Integrated reformer-combustor reactor results have been evaluated over a wide range of feed compositions, operating at high temperatures ( $>900^{\circ}\text{C}$ ) and high pressures (up to 25 atm) and short contact times ( $< 10$  ms). The physical description and operational details of such devices are extensively reported elsewhere by Tonkovich *et al* (15). Details of how such a device can be fabricated are given by Tonkovich *et al* (1). Typical results obtained in a six repeating unit device are presented in Figure 4 (15). In this case, the reactor was operated with a near equilibrium conversion of the steam reforming reaction at  $865^{\circ}\text{C}$  and pressure of 12 atm with a contact time of less than 9 ms. Over the entire 300-hour demonstration, the steam reformer achieved equilibrium conversion of methane (approximately 90%) with no signs of deactivation. Additional description of the reforming catalyst is presented by Wang *et al* (17) and of the reactor technology by Tonkovich *et al* (18).

A second advantage of microchannel technology over conventional is that

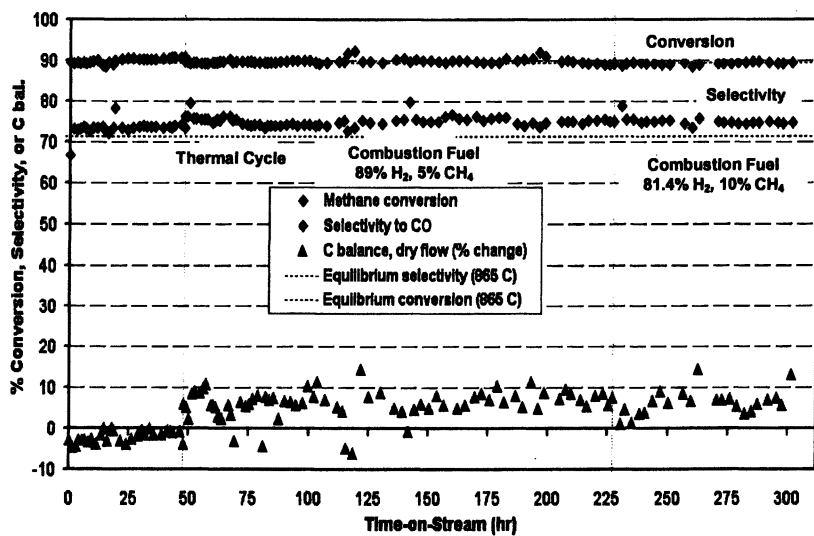


Figure 4. Performance with time on stream for a multi-channel integrated steam reformer-combustor reactor.

catalytic combustion can be employed. This permits very low levels of nitrogen oxide ( $\text{NO}_x$ ), CO, and hydrocarbon emissions. The integral combustion supporting the steam reforming shown in Figure 4 was conducted at a contact time of less than 9 ms using 30 to 35% excess air. The maximum metal temperature was less than  $925^{\circ}\text{C}$ . Under these conditions, the emissions from

the combustion contained less than 10 ppm of NO<sub>x</sub>. The flexibility of the microchannel combustor was demonstrated by changing the fuel composition from 89 mol% hydrogen with 5 mol% methane to 81.4 mol% hydrogen and 10 mol% methane, with no change in reformer performance.

### FT Synthesis in a Microchannel Reactor

The FT reaction has been demonstrated in a microchannel reactor over a powdered Co/Re-Al<sub>2</sub>O<sub>3</sub> catalyst with a Co to Re molar ratio of 21:1. The reactor employed in this study was fabricated from SS316 and consists a process microchannel with a gap of 0.51 mm, width of 1.27 cm and length of 8 cm. Temperature in the catalyst bed is estimated via a series of thermocouples placed in wells that are located 0.75 cm, 2.0 cm, 3.3 cm and 4.6 cm up from the outlet of the process microchannel. Of the 8 cm process flow length only 2.5 to 3 cm is taken up by catalyst the balance being either open or filled with wadding material, such as quartz wool, to retain the catalyst. The wadding material takes up ~1 cm on either side of the catalyst bed. The catalyst bed itself is located in the process channel in such a manner as to allow two or more thermocouples to be aligned with the catalyst bed. By loading the channel in this manner the balance of the process microchannel (2 – 3 cm) can be used to preheat the feed gasses. The process microchannel is externally jacketed such that coolant fluid such as water or a heat transfer oil can be circulated co- or counter currently to the flow of fluid in the process channel.

### *Catalyst Preparation and Pretreatment*

The catalyst was prepared by first calcining a sample of Al<sub>2</sub>O<sub>3</sub> support at 650°C and then performing 3 impregnations using an aqueous solution containing 30% Co (from cobalt nitrate) by weight and 4.5% Re (from Perrhenic acid) by weight. After the first and second impregnations the catalyst was dried in an oven for 12 hours at 90°C. After the final impregnation step the catalyst is calcined by heating the catalyst to 350°C at a rate of 1°C per minute and holding at 350°C for 3 hours. Catalyst prepared by this method had a particle size in the range of 177 to 250 microns. The metal dispersion was found to be 5.4%.

After preparation, a 0.19 gram sample was loaded into the reactor channel forming a 3 cm deep bed of catalyst. The catalyst was then activated by alternating reduction (3 cycles) and oxidation (2 cycles). In the first reduction cycle 41 sccm of 5 vol% hydrogen (balance He) was allowed to flow over the catalyst at close to ambient pressure. The reactor was then heated from 20°C to 250°C over a period of 3.8 hours and held at that temperature for additional 8

hours. The temperature was then increased to 400°C over a period of 2.5 hours and held at that temperature for additional 12 hours. The 5 vol% hydrogen gas flow was then replaced with He only at the same flow rate and the reactor was allowed to cool to ambient temperature over a period of 13.2 hours. This reduction cycle was followed by an oxidation cycle in which 30 sccm of He gas containing 2 vol% oxygen was allowed to flow over the catalyst at close to ambient pressure. The temperature was then increased from 22°C to 350°C at a rate of 1.5°C per minute. The reactor was then held at 350°C for 2 hours. The 2 vol% oxygen stream was then replaced with He only at the same flow rate and the reactor was allowed to cool to ambient temperature. The total time for this cooling and purging step was 18.1 hour.

The first oxidation step was then followed by the second reduction cycle that was alike in all respects to the first with the exception that the final cooling and purging step lasted 24 hours. The second reduction cycle was followed by the second oxidation cycle. This cycle was alike in all respects to the first with the exception that the cooling and purging step lasted 22 hours. The last step in catalyst activation involved flowing 41 sccm of the 5 vol% hydrogen gas through the reactor heating the reactor from 24°C to 250°C at a rate of 1°C per minute. Once at 250°C the reactor was held at this temperature for one half hour. After this soak period the reactor was heated to 375°C at a rate of 1°C per minute and held at this temperature for 12 hours. The reactor was then allowed to cool to 160°C and pressurized to 400 psig under the same 5 vol% hydrogen atmosphere. In this manner the catalyst was activated and the reactor ready for operation.

#### *Experimental Set-Up*

The reactor described above was installed in a test enclosure and the gas mixtures required for catalyst activation and reactor operation were provided via a bank of mass flow controllers. The two phase product stream from the reactor was directed to a cold trap in which the condensable fraction was collected. Once the condensable had been removed from product stream the remaining product gas passed through the back pressure regulator to an on-line gas chromatograph. The test set-up included the capacity to allow the feed to bypass the reactor and in this manner the feed gas composition could be periodically checked. The conversion of carbon monoxide was determined using the inlet flow of carbon monoxide, the fraction reported in the outlet dry gas, and the outlet dry gas flow rate. Selectivity to methane was calculated by dividing the outlet flow of methane by the amount of carbon monoxide converted. The feed composition was a fixed mixture of hydrogen (61 vol%), carbon monoxide (35 vol%) and helium (4 vol%).

### Microchannel FT Results and Discussion

The reactor was brought on line at a pressure of 21 atm and a temperature of 180°C. The reactor temperature and contact time were adjusted until a steady state condition of 225°C was reached at a contact time of 288 ms (12,500 hr<sup>-1</sup> GHSV). At this point the catalyst had 320 hours time-on-stream and the conversion of carbon monoxide was 47% and the selectivity to methane 10%. For the next 481 hrs time-on-stream the pressure and feed flow rate were fixed, and at 801 hours time-on-stream the pressure was increased from 21 to 41 atm. The increase in pressure increased the conversion of carbon monoxide to 56% and reduced the methane selectivity to ~7%. At 933 hours time-on-stream a temperature ramp was started to take the reactor from 225°C to 250°C and the contact time was increased from 288 ms to 308 ms (11,688 hr<sup>-1</sup> GHSV). The reactor reached thermal steady state at 1104 hours time-on-stream (see Figure 5). The reactor was operated under constant conditions for the next 765 hours over which time the average values of CO conversion and methane selectivity were 69.7% and 10.5% respectively.

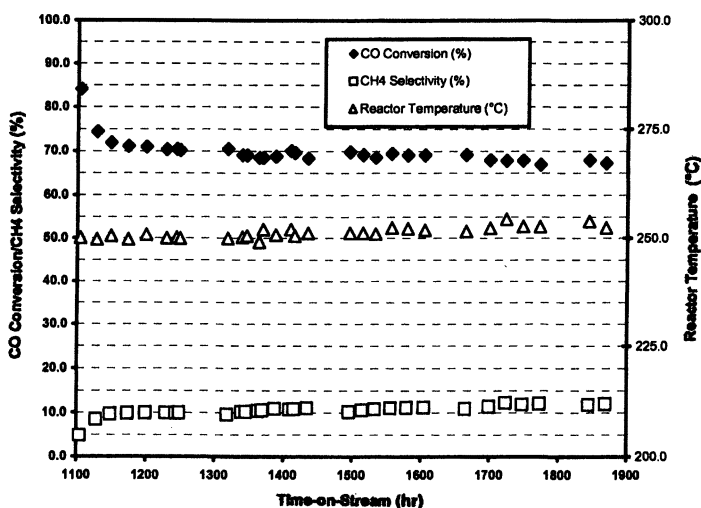


*Figure 5. Performance with time on stream for a microchannel FT reactor.*

Based on the performance of the microchannel FT technology demonstrated, reactor productivity is estimated to be on the order of 85 bbl/tonne. Thus, the productivity is seven times that of conventional tubular fixed bed technology and

8.5 times that of conventional slurry technology (~12 barrels per metric ton) (19). In terms of catalyst productivity, the microchannel FT technology demonstrated in this work is estimated to be 1,700 kilograms (kg)/m<sup>3</sup>/hr compared with 700 to 800 kg/m<sup>3</sup>/hr for tubular fixed bed or 350 kg/m<sup>3</sup>/hr for slurry bed technology (19).

### Economic Impact

Process intensification achieved by applying microchannel technology almost always involves a dramatic reduction in size and thus a reduced process footprint. For some specialized applications (such as off-shore installations, mobile installation, fine chemical production, distributed source production, or military use), this reduction of footprint may be sufficient to make the technology attractive. An economic advantage may be derived from both capital and operating costs.

A detailed capital cost estimate for a 30,000-BPD GTL plant, as well as a capital cost model for GTL plants based on its microchannel technology has been developed. Each of the major unit operations required for a green field demonstration site have been sized. Quotes for major equipment were compiled along with a detailed cost estimated P&ID for installation. Both ISBL and OSBL estimates were complete.

The capital cost comparison is presented in Figure 6, along with a proprietary model for the cost of conventional GTL and data for various plants operating with current conventional technology. From the modeling conducted, it is evident that the reported microchannel technology has a large capital cost advantage over conventional technologies for plant capacities below 50,000 BPD. The 30,000-BPD plant was estimated to have an installed cost of \$20,000/BPD compared with approximately \$30,000/BPD for Sasol-Chevron's Nigerian operation. At capacities above 50,000 BPD, microchannel technology remains competitive with conventional operations on a capital cost basis; however, the margin decreases sharply as plant capacity increases to near 100,000 BPD.

A detailed analysis and comparison of operating expenses between microchannel technology and conventional technologies has not been completed, but the operating costs of a microchannel process are not expected to exceed those of conventional technologies with similar capacity.

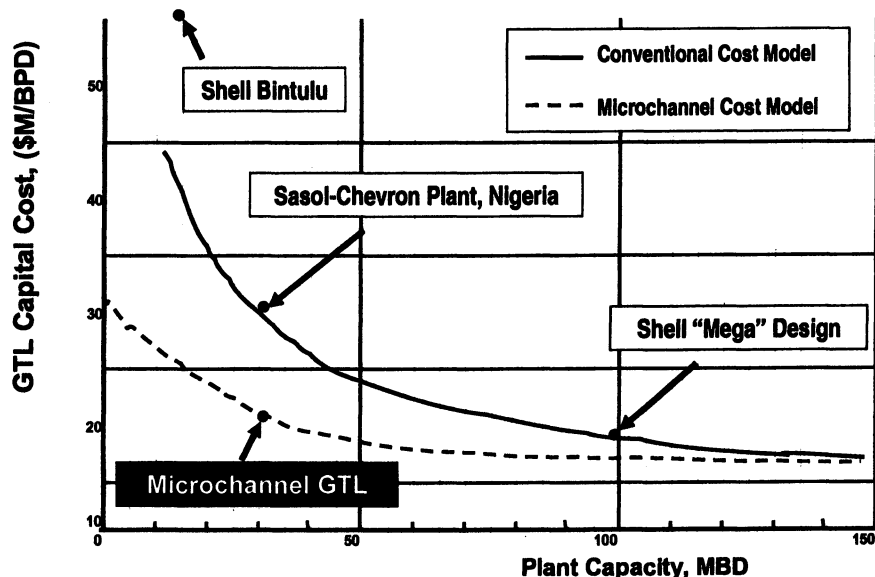


Figure 6. Comparison of microchannel GTL process versus conventional technologies.

### Summary and Conclusions

Based on the experimental demonstration results and cost model results reported here microchannel technology has significant capital cost advantages over conventional technology in the for land based applications smaller than 50,000 BPD. In addition to these cost advantages the FT reaction has been demonstrated in microchannel reactor achieving significant increases in productivity and catalyst stability over previously reported systems. Specifically high conversions of methane (70%) combined with low selectivity to methane (11%) at a short contact time (308 ms) were achieved. In addition, the catalyst appeared to have approached steady state operation with 1869 hours total time on stream, 765 hour of which were at the stated conditions.

## References

- 1 Tonkovich, A.; Roberts, G.; Fitzgerald, S. P.; Werner, T. M.; Schmidt, M. B.; Luzenski, R. J.; Chadwell, G. B.; Mathias, J. A.; Gupta, A.; Kuhlmann, D. J.; Yuschak, T. D.; US Patent US 2004/0099712 A1, 2004, patent application.
- 2 Werner, T.M., Schmitt, S.C., Daymo, E. A., Wegeng, R.S., "Microchannel Gasoline Vaporizer Unit Manufacturing Cost Study", PNNL-12226, June 1999.
- 3 Strange, A. M.; AIChE 2003 Spring National Meeting, New Orleans, LA, 2003.
- 4 Anderson, R.B., *The Fischer-Tropsch Synthesis*, Academic Press, Inc., 1984.
- 5 Hairston, D., *Chemical Engineering*, May, 2004, p 23.
- 6 Bureau of International Information Programs, U.S. Department of State, Press Release October 3<sup>rd</sup> 2003, <http://www.useu.be/Categories/Energy/Oct0303CleanFuelPlant.html>
- 7 Wang, Y; Vanderwiel, D. P.; Tonkovich, A.Y.; Gao Y.; Baker, E. G.; US Patent 6,451,864, 2002.
- 8 Wang, Y; Vanderwiel, D. P.; Tonkovich, A.Y.; Gao, Y.; Baker, E. G.; US Patent 6,558,634, 2003.
- 9 Schanke, D.; Bergene, E.; Holmen, A.; US Patent 6211255, 2001.
- 10 Snyder, R. E.; World Oil June, 2003 URL [http://www.worldoil.com/magazine/MAGAZINE\\_DETAIL.asp?ART\\_ID=2062&MONTH\\_YEAR=Jun-2003](http://www.worldoil.com/magazine/MAGAZINE_DETAIL.asp?ART_ID=2062&MONTH_YEAR=Jun-2003).
- 11 Mazanec, T., *PTQ*, October, 2003, p 149.
- 12 Kuila, D; Nagineni, V. S.; Zhao, S; Indukuri, H.; Liang, Y.; Potluri, A.; Siriwardane, U; Seetala, N; Fang, J.; MRS Spring Meeting, San Francisco, CA, 2004.
- 13 Rostrup-Nielsen, J. *In Catalysis Science and Technology*; Anderson, J., Boudart, M., Ed; Springer-Verlag: New York, NY, 1984; Vol. 5.
- 14 Tonkovich A., Qiu, D., Long L.Q., Yang B.L., Yuschak T., Perry S.T., US2004/0228781A1, 2004, patent application.
- 15 Tonkovich, A.Y.; Roberts, G.; Fitzgerald, S.P.; Neagle, P.W.; Qium D.; Schmidt, M.B.; Perry, S.T.; Hesse, D. J.; Luzenski, R.J. ; Chadwell, G.B.; Peng, Y.; Mathias, J.A.; Gano, N.P.; Long, R.Q.; Roger, W.A.; Arora, A.; Simmons, W.W.; Yang, B.L.; Kuhlmann, D.J.; Wang, Y.; Yuschak, T.D.; Forte, T.; Monahan J.A.; Jetter, R.; US Patent US 2004/0033455 A1, 2004, patent application.
- 16 Tonkovich, A. Y.; Call, J. C.; Jimenez, D. M.; Wegeng R. S.; Drost, M.K.; *AIChE Symposium Series* 1996,310, p 119-128.

- 17 Wang, Y., Chin, Y., Rozmiarek, R., Johnson, B., Gao, Y., Watson, J., Tonkovich, A., VanderWiel, D., *Catalysis Today*, **2004**, 98, 575-581.
- 18 Tonkovich, A. L.Y.; Perry, S.; Wang, Y.; Rogers, W.A.; Qiu, D.; Peng, Y. *Chem. Eng. Sci.* **2004**, 59(22&23), 4819-4824.
- 19 Hoek, A., *The Shell Middle Distillate Synthesis Process – Facts, Technology and Perspective*. Presented at CatCon, Houston TX, May 2003.

## Chapter 17

### Microchannel Catalytic Processes for Converting Biomass-Derived Syngas to Transportation Fuels

Chunshe Cao, Yong Wang\*, Susanne B. Jones, Jianli Hu,  
X. Shari Li, Douglas C. Elliott, and Don J. Stevens

Pacific Northwest National Laboratory, 902 Battelle Boulevard,  
MSIN K8-93, Richland, WA 99352

In this paper, a catalytic microchannel reactor integrated with highly efficient heat exchangers was used to demonstrate the significantly improved Fischer-Tropsch (FT) productivity by minimizing heat and mass transfer limitations in this three phase reaction system. A factor of up to 15 process intensification can be achieved for FT synthesis using microchannel reactors. In order to achieve high yields of naphtha and diesel range of hydrocarbons (C<sub>5</sub>-C<sub>19</sub>), we have developed a unique structured catalyst system suitable for the deployment in microchannel reactor applications. This engineered catalyst structure is based on metallic monolith supports, uniformly coated with an improved catalyst formula. Such an ordered catalyst structure has the advantages of higher thermal conductivity and more reduced mass transfer resistance compared to the conventional catalysts. By tailoring the mass transfer limitations, we have demonstrated that this engineered catalyst produces hydrocarbons with narrower carbon distributions (mainly < C<sub>25</sub>) than a conventional particulate catalyst at similar conversion and methane selectivity. In particular, majority of the synthesis products fall into the gasoline and diesel range. This unique product distribution, in turn, has a positive impact on process economics since a milder or no hydrocracker will be required in downstream product processing.

## Introduction

Production of clean transportation fuels from renewable and sustainable biomass is receiving growing attention in recent years due to the concerns with climate change and the need for energy diversity (1). Biomass feedstock provides unique renewable features since carbon dioxide emissions from its use are absorbed by newly grown biomass (2,3).

Conversion of biomass to fuels generally goes through one of the two routes of thermal upgrading processes: pyrolysis for direct production of liquid oil or gasification for syngas production. As shown in Figure 1, the biomass feedstock needs first be pretreated for conversion for both processes. The pretreatment includes the unit operations such as grinding and drying. Pyrolysis route

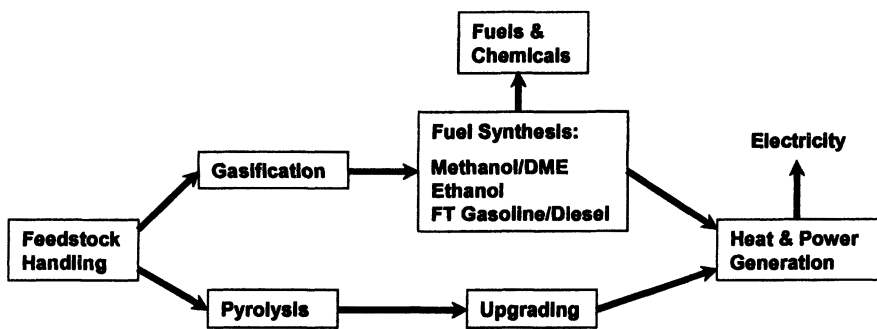


Figure 1. Biomass conversion to fuels and energy

typically requires that the pyrolysis oil is upgraded by hydrotreating to provide deoxygenated high heating value oil for heat and power generation. The syngas generated from the gasification route can be converted to liquid hydrocarbon fuels using technologies such as FT synthesis. Since various process options in the gasification can be chosen such as atmospheric and pressurized, air-blown and oxygen-blown, a wide range of syngas compositions with H<sub>2</sub>/CO ratios varying from 0.45 to 2 can be produced. Consequently, to suit the FT synthesis, the H<sub>2</sub>/CO ratio needs to be adjusted using gas conditioning processes such as water gas shift (WGS) and/or methane steam reforming (SMR). Prior to the gas conditioning, any contaminants such as H<sub>2</sub>S, NH<sub>3</sub>, dust and alkalis also need to

be removed or significantly reduced to avoid catalyst poisoning. Another major gas cleaning step is the costly carbon dioxide removal from syngas mixtures prior to FT synthesis.

A further economic constraint in conversion of biomass to fuels is associated with the distributed nature of biomass feedstocks. In another word, biomass feedstocks may not be near existing chemical or petrochemical plants and are not economic to centralize. Even the largest gasifiers can not process more than 1000 ton biomass/day which is equivalent to about 1100 bpd liquid FT fuels and about a factor of 20 smaller than the scale at which conventional gas-to-liquid (GTL) plants are economic (Figure 2) (4). Centralizing syngas from gasifiers is not an economic option since there is no existing pipeline in the US through which the syngas can be transferred to large central facilities. Therefore, an enabling technology is needed for biomass conversion to fuels.

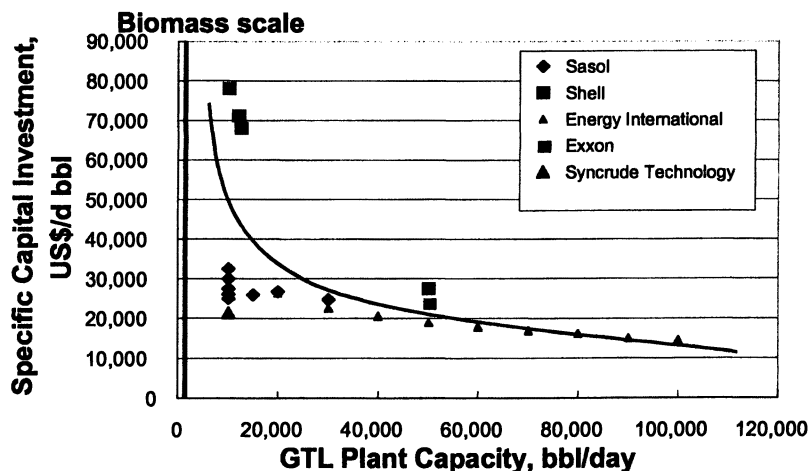


Figure 2. Conventional GTL plant capital investment

Microchannel reactors, which have been developed by PNNL for the past decade (5,6,7,8,9), are modular and less dependent on the economy of scale. Microchannel reaction technology provides a potential breakthrough solution to the challenge of deploying biomass conversion to fuel processes. These reactors have a sandwich-like multi-layer structure consisting of a large number of closely spaced channels with a gap of less than 2mm, which reduces heat and mass transport distance and greatly enhances heat and mass transfer efficiency. Heat transfer is further enhanced due to the high surface-to-volume ratio achievable in microchannel reactors. Such high heat transfer efficiency permits the isothermal operation of highly exothermic FT synthesis at higher reaction temperatures without sacrificing the selectivity. The improved mass transfer

mitigates the mass transport problems typically associated with conventional fixed-bed and slurry reactors for FT synthesis. In addition to heat and mass transfer improvement, the unique layered sheet architecture of microchannel reactors allows the integration of gas conditioning and reactant/product heat exchange within a single unit to improve the thermal efficiency and reduce the capital cost. Consequently, microchannel reactors potentially allow process intensification for FT synthesis.

In this paper, a new type of highly active and selective cobalt based catalyst and its engineered structures based on metal substrates suitable for microchannel reactors have been developed. This study centers on the catalyst development and their unique performance in microchannel reactors to meet the biomass conversion requirements. The potential elimination of costly CO<sub>2</sub> separation and hydrocracking steps using microchannel reactors and the subsequent impact on the capital investment are evaluated.

## Experimental

### Catalyst Preparation.

Acidic  $\gamma$ -Al<sub>2</sub>O<sub>3</sub> (Sasol) with an average particle size of 45 $\mu$ m was precalcined at 500°C in air for 2 hours prior to impregnation. This support has a spherical shape and uniform particle distribution. An aqueous solution of cobalt nitrate hexahydrate (Co(NO<sub>3</sub>)<sub>2</sub>.6H<sub>2</sub>O) (98% purity, Aldrich) and Perrhenic acid (HReO<sub>4</sub>) (Engelhard, 53.29wt% P.M.) was impregnated onto the  $\gamma$ -Al<sub>2</sub>O<sub>3</sub> support using a multi-step incipient-wetness impregnation method. After each impregnation, the catalysts were dried in air at 90°C for 8 hrs followed by calcination at 350°C for 3 hours. Five sequential impregnations were used to give final formulated catalyst with 30wt%Co and 4.5wt%Re on alumina. The synthesized powder catalyst has a surface area of 60m<sup>2</sup>/g and pore volume of 0.14 cm<sup>3</sup>/g.

An engineered catalyst is based on an aluminum monolithic substrate due to its high thermal conductivity. The substrate was microstructured with double-side alternative valleys and peaks as shown in Figure 3. The width of each valley is 254 $\mu$ m, the valley depth is 635 $\mu$ m, and the peak width is 254 $\mu$ m. The overall dimensions of each monolith are 12.7mm x 1.5mm x 31.8mm. The surface of aluminum substrate was first oxidized in air at 550°C to enhance the adhesion to catalyst layers, and dip coated with a solution of PQ Al<sub>2</sub>O<sub>3</sub> (Nyacol), pluronic F-127(HO(CH<sub>2</sub>CH<sub>2</sub>O)<sub>106</sub>(CH<sub>2</sub>CH(CH<sub>3</sub>)O)<sub>70</sub>(CH<sub>2</sub>CH<sub>2</sub>O)<sub>106</sub>H), and ethyl alcohol (Aldrich) mixture at 1:0.9:3.5 weight ratios. The aluminum substrate was

then dried at 100°C for 20 minutes. The dipping and drying cycle was repeated to achieve the target alumina loading and coating thickness. Finally, the monolith was calcined at 450°C for 4 hours to remove F127. An aqueous solution of cobalt nitrate hexahydrate ( $\text{Co}(\text{NO}_3)_2 \cdot 6\text{H}_2\text{O}$ ) (98% purity, Aldrich) and Perrhenic acid ( $\text{HReO}_4$ ) (Engelhard, 53.29wt% P.M.) was co-impregnated onto the alumina layer to achieve desired Co and Re loadings, followed by drying in air at 90°C for 8 hrs and calcination at 350°C for 3 hours. As a typical example, the monolith has a catalyst coating thickness of  $15\mu\text{m}$ , a surface area of  $140\text{m}^2/\text{g}$  of active coating layer, an average pore size of  $95\text{ \AA}$ , and about 30 wt% Co (relative to active coating layer) with an atomic Co/Re ratio of 21.

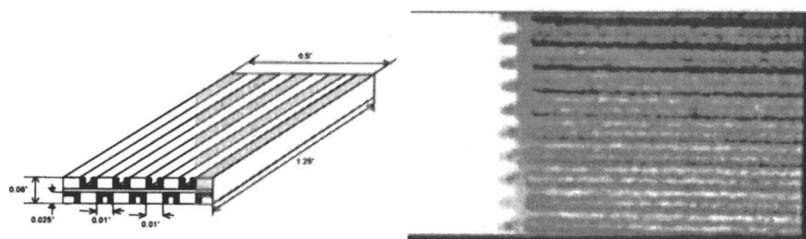


*Figure 3. Engineered catalyst tailored for a microchannel reactor*

### Activity Testing

Experiments were carried out in a microchannel reactor system to maintain isothermal conditions for the highly exothermic FT synthesis reactions. The details of this reactor are described elsewhere (10). The channel gap of the reactor is 1.5mm wide and the channel width is 12.7mm. Powdered catalysts were packed into the channel. For engineered catalyst testing, two pieces of the mini-structured catalysts described above were snugly inserted in the microreactor providing the total length of the catalyst bed of 63.6mm. There was essential no gap between the monolithic catalyst pieces and the reactor walls. Four thermocouples along the catalyst bed indicated that the temperature gradient within the catalyst bed is less than 1 °C under the targeted reaction conditions. After catalyst was activated in hydrogen at about 400°C for 8 hours, a syngas feed with  $\text{H}_2/\text{CO}$  ratio of 2 was introduced and FT synthesis was conducted at pressures from 10 to 40atm. Hydrocarbons and water in the effluent were condensed in a chilled vessel. Non-condensed gases were analyzed using an on-line gas chromatography (Agilent QUADH G2891A with Molsieve 5A, PoraPlotQ columns) to determine CO conversion and light product selectivity.

Condensed liquid wax products were analyzed with a HP5890 GC with a DB-5 column (15m long, 0.32mm i.d., 0.25um film thickness) connected to an FID detector.

## Results and Discussion

### Intensification of FT Process with an Improved Catalyst

To demonstrate the potential of FT process intensification achievable in microchannel reactors, as-synthesized powder catalyst was packed in the microchannel reactor described in the Experimental section. The reaction temperature and gas flowrate were increased while maintaining a single-path CO conversion of 63% and methane selectivity of less than 10%. At 20atm and 235°C with H<sub>2</sub>/CO=2, the highest GHSV achieved was 60,000 hr<sup>-1</sup> which corresponds to a contact time of 0.06 second (contact time is defined as catalyst bed volume divided by the feed gas flowrate at standard temperature and pressure). Under these reaction conditions, steady catalyst performance was observed over a time-on-stream of more than 100 hours. Table 1 summarizes comparison with the best performances in conventional fixed bed and slurry bed reactors reported in the open literature (11). Apparently, GHSV is about 15 times faster and the C5+ productivity is about 10 times higher than the conventional tubular fixed bed reactor.

*Table 1. Comparison of productivity enhancement*

	Slurry (10)	Tubular Fixed Bed (10)	Microchannel*
GHSV, v/v/hr	750-1,000	3,000-4,000	60,000
Cat Productivity kg/m <sup>3</sup> /hr	350	700-800	7400

\* P=20atm, T=235°C, H<sub>2</sub>/CO=2, CO conversion: 63%, CH4 selectivity: 10%

The superior catalyst performance results from the effective heat and mass transfer characteristics of the microchannel reactor. The microchannel reactor with active heat removal provides near-isothermal environment, allowing the catalyst being operated at higher average temperature, which leads to high single-pass conversion at high GHSV. The efficient heat removal also minimizes the presence of hot spots in the catalyst bed, leading to low methane selectivity. A reactor modeling described elsewhere (10,12) showed that a conventional

fixed bed reactor exhibits significant temperature gradients. Under similar reaction conditions, the temperature gradient in a fixed-bed micro-tubular reactor (4mm ID) is as high as 30°C, which could significantly promote the methanation reaction. In contrast, the microchannel reactor has a near isothermal temperature distribution with temperature gradient less than 1.5°C. Such an excellent temperature control also allows deployment of more active catalyst to improve space-time yield.

### The Effect of CO<sub>2</sub>

Since the syngas generated via biomass gasification process contains significant amount of CO<sub>2</sub>, it is important to evaluate the effect of CO<sub>2</sub> on the FT synthesis performance. In particular, catalyst tolerance to CO<sub>2</sub> during the FT synthesis needs to be evaluated to justify the necessity of costly CO<sub>2</sub> removal. In a series of controlled experiments, syngas partial pressure was kept at 21 atm with a H<sub>2</sub>/CO ratio of 2 while CO<sub>2</sub> partial pressure was systematically increased from 0, 2 and to 5.6 atm, which corresponds to CO<sub>2</sub> composition of 0%, 8.3%, and 20% in the feed gas (note that N<sub>2</sub> with partial pressure of 0.85atm was used as the GC internal standard in the feed mixture). As can be seen in

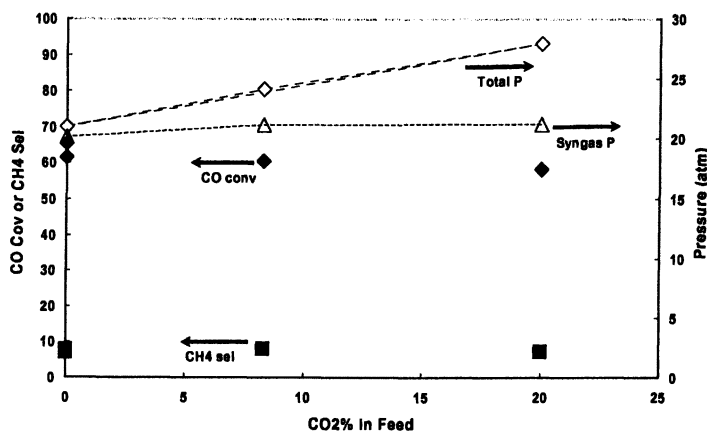


Figure 4. The effect of CO<sub>2</sub> on the Fischer-Tropsch synthesis (GHSV based on syngas: 22,500hr<sup>-1</sup>, 224°C, H<sub>2</sub>/CO=2

Figure 4, at a syngas GHSV of 22,500hr<sup>-1</sup>, 224°C, H<sub>2</sub>/CO=2, and 21atm of syngas partial pressure, CO conversion and CH<sub>4</sub> selectivity are independent of CO<sub>2</sub> partial pressure within the range studied. There was no significant effect on catalyst life over 120 hours of time-on-stream. In another word, CO<sub>2</sub> had

essentially no effect on the FT synthesis at up to 20% CO<sub>2</sub> in the feed gas using the current Co/Re catalyst. Therefore, it is recommended that further studies need to be done to determine whether the costly CO<sub>2</sub> separation step can be eliminated.

### Tailoring of Product Distribution

To further evaluate the effects of mass transfer limitation on the FT performances without the concern of significant pressure drop typically associated with the smaller catalyst particles, an engineered monolith substrate coated with Co/Re catalyst as described in the Experimental was evaluated in the microchannel reactor. In particular, the diffusion resistance was tailored by changing the coating thickness of catalytic materials on the engineered substrate. In a typical example, an engineered monolith with a catalyst coating thickness of 15 $\mu$ m was compared with powder catalysts of 45 $\mu$ m diameter. Both catalysts have similar Co loading (30wt%) and Co/Re ratio (21). Their performances were evaluated in the microchannel reactor under identical WHSV (weight hourly space velocity) with H<sub>2</sub>/CO=2 at 250°C. The product distribution and methane selectivities for both forms of catalysts are compared in Figure 5.

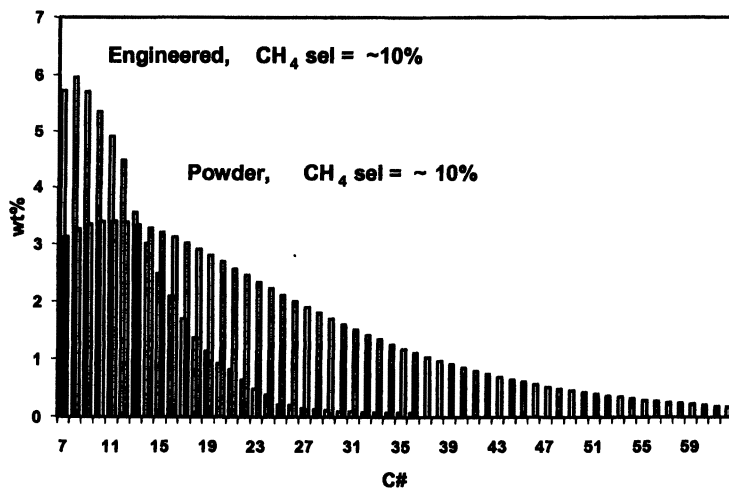


Figure 5. Tailoring the FT product distributions (H<sub>2</sub>/CO=2, 250°, WHSV=3.73 gCO/gcat/hr)

Under similar CO conversion (about 70%) and methane selectivity (about 10%) , the engineered monolith catalyst exhibits a unique narrower product distribution. This is likely due to improved mass transfer with the engineered catalyst, which has a thinner catalyst layer (15 $\mu$ m) than the particle size of powder catalysts used in fixed bed reactors (about 45 $\mu$ m). Shorter intra-particle mass diffusion pathway in the engineered catalysts potentially disfavor the secondary reactions via olefin readsorption (13), which reduces chain growth probability of the products and leads to a narrow product distribution. A narrow product distribution is known to be achieved at short residence time or high reaction temperature or low pressure using conventional reactors and catalysts but at the expense of higher methane selectivity (14). The fact that a narrow product distribution can be achieved without increased methane selectivity using engineered catalyst may be due to the lower local H<sub>2</sub>/CO ratio on the catalyst. Under the Fischer-Tropsch synthesis conditions, internal pores within the catalyst are normally filled with liquid hydrocarbons, through which hydrogen has much higher diffusivities than CO (15). This could result in much higher H<sub>2</sub>/CO ratio inside a pellet or powder catalyst than that in the bulk feed, which favors methanation. A thinner catalyst layer with the engineered catalyst, on the other hand, could result in a relatively lower local H<sub>2</sub> concentration within the catalyst, which minimizes the selectivity to methanation. A particular advantage with a narrow range of hydrocarbon liquid product distribution and low methane selectivity is that no hydrocracker or only milder hydrocracker is needed for gasoline or diesel productions from FT product which reduces capital and operation costs.

### Process Economic Analysis

To evaluate the potential economic advantages of microchannel reactors for FT synthesis from biomass syngas, the capital investment was estimated for a plant at a scale of 1,100 barrels per day, equivalent to a gasification plant capable of processing 1,000 dry tons of biomass. Equipment included in the capital calculations are water removal, FT reactor(s), and product separation units. Both conventional and microchannel FT reactors are single pass. The estimation does not include equipment for production of syngas or power recovery. The cost of conventional FT process was scaled down using the data from references (16) and (17). An overall installation factor of 4.1 was used to obtain total capital investment costs from purchased equipment price. Equipment sizes were based on a Chemcad<sup>®</sup> model of the FT synthesis step using syngas composition based on IGT gasifier followed by cleanup and reforming (2, 18). The potential capital cost advantages of the microchannel FT process over the conventional FT process are summarized in Figure 6. If the advantage with microchannel

reactors is only from high GHSV ( $60,000\text{hr}^{-1}$ ) operation as aforementioned, the capital investment reduces from about \$36M to about \$33M. If the narrow product distribution can be achieved using

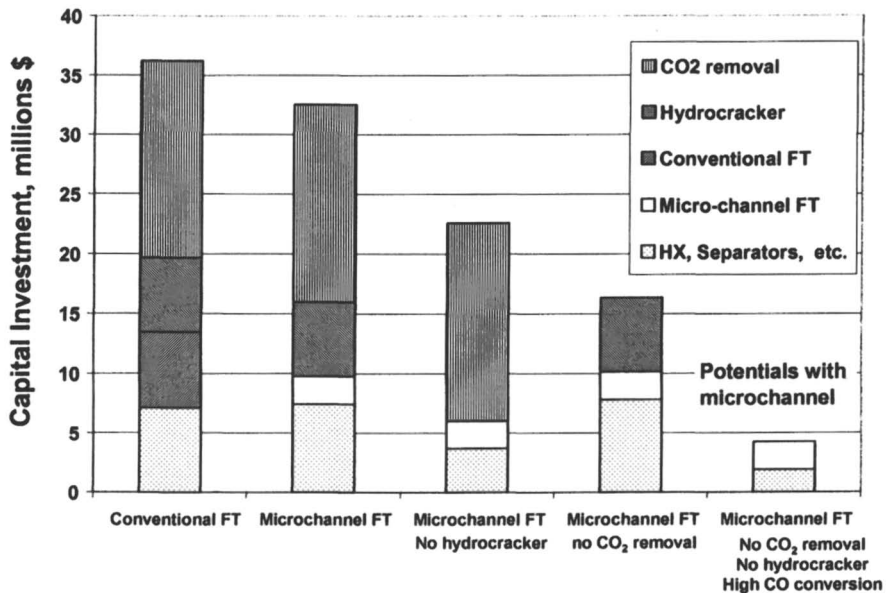


Figure 6. Preliminary capital investment costs for converting syngas to Fischer-Tropsch fuels at 1,100 bpd (GHSV:  $60,000\text{hr}^{-1}$ )

engineered catalyst and no hydrocracker is needed, a significant capital investment reduction from conventional FT process can be realized (from \$36M to \$23M). Capital investment can be further reduced to about \$16M if CO<sub>2</sub> removal can be avoided since the preliminary results indicated that CO<sub>2</sub> has no negative impact on the FT performances on the catalyst studied. The above capital investment estimation was based on a single pass CO conversion of 70%. It can be envisioned that a higher CO conversion, such as 90%, may be achieved if the unique layered sheet architecture of microchannel reactors allow the readily integration of *in-situ* water separation during FT synthesis to avoid catalyst deactivation. This could further reduce the capital investment to about \$5M.

## Conclusion

Microchannel reactor technology potentially provides an enabling technology to economically convert biomass derived syngas to liquid transportation fuels such as gasoline and diesel. A factor of up to 15 process intensification can be achieved for FT synthesis using microchannel reactors. A unique engineered monolith-type catalyst has been demonstrated to provide narrow product distribution when integrated with microchannel reactors. The superior performances demonstrated using microchannel reactors have great potential in the reduction of capital investment for the FT synthesis.

## Acknowledgements

This study was made with Government support under Contract DE-AC0676RLO1830 awarded by the U.S. Department of Energy. The authors gratefully acknowledge the support through US DOE EE Renewable Energy, Office of the Biomass Program. This work was performed in the Environmental Molecular Sciences Laboratory, a national scientific user facility sponsored by the US Department of Energy's Office of Biological and Environmental Research and located at Pacific Northwest National Laboratory in Richland, WA.

## Reference

1. Chum, H.L.; Overend, R.P. *Fuel Processing Technology*, **2001**, *71*, 187-195.
2. Tijmensen, M.; Faaij, A.; Hamelinck, C.; van Hardeveld, M. *Biomass and Bioenergy* **2002**, *23*, 129-152.
3. Faaij, A.; Hamelinck, C.; Tijmensen, M. In *Proceedings of the First World Conference on Biomass for Energy and Industry*; Kyritsis, S. et al., Ed.; James & James Ltd: London, UK, 2001; 1/2, p687-690.
4. van Berge, P.J.; Barradas, S; Caricato, E.A.; Sigwebela, B.H.; and van de Loosdrecht, J. Worldwide Catalyst Industry Conference, CatCon2000, June 12-13, 2000, Houston, Texas.
5. Wegeng, R.S.; Drost, M.K.; McDonald, C.E. US 5,611,214, 1997.
6. Bennett, W.D.; Martin, P.M.; Matson, D.M.; Roberts, G.L.; Stewart, D.C.; Tonkovich, A.L.Y.; Wang, Y.; Zilka, J.L.; Schmitt, S.C.; Werner, T.M. US 6,192,596, 2000.
7. Tonkovich, A.L.Y.; Roberts, G.L.; Call, C.J.; Wegeng, R.S.; Wang, Y. US 6,200,536B1, 2001.

8. Tonkovich, A.L.Y.; Wang, Y.; Fitzgerald, S.P.; Marco, J.L.; Roberts, G.L.; Vanderwiel, D.P.; Wegeng, R.S. US 6,488,838, 2002..
9. Wang, Y.; VanderWiel, D.P.; Tonkovich, A.L.Y.; Gao, Y.; Baker, E.G. US 6,491,880, 2002.
10. Cao, C.; Xia, G.; Holladay, J.D.; Jones, E.O.; Wang, Y. *Appl. Catal. A: General*. **2004**, 262 19-29.
11. Hoek, A. In *The Catalyst Group Resources, Inc.*, 7th Annual Worldwide Catalyst Industry Conference & Exhibition, CatCon2003, Houston, TX, 2003.
12. Cao, C.; Wang, Y. "Modeling a microchannel reactor for Fischer-Tropsch synthesis", manuscript in preparation.
13. Iglesia, E.; Reyes, S.C.; and Madon, R.J. *J.Catal.*, **1991**, 129, 238-256.
14. Dry, M. E. *Catal. Today*, **2002**, 71,227-241.
15. Van Der Lann, G. P.; and Beenackers, A. A. C. M. *Catal. Rev.-Sci. Eng.*, **1999**, 41(3&4), 255-318.
16. Hamelinck, C.; Faaij, A.; den Uil, H.; Boerrigter, H. Utrecht University, *Production of FT Transportation Fuels from Biomass: Technical Options, Process Analysis and Optimisation and Development Potential*, Report NWS-E-2003-08, March 2003.
17. SRI PEP Report No. 135C, *Opportunities for Gas-To Liquid Technologies*, February 2000.
18. Stevens, D.J., *Review and Analysis of the 1980-1989 Biomass Thermochemical Conversion Program*, National Renewable Energy Laboratory/TP-421-7501, September 1994.

## **Chapter 18**

### **Flow-Induced Phase Inversion Phenomenon in Process Intensification and Microreactor Technology**

#### **Preparation and Applications of Nanostructured Microporous Polymers and Metals**

**G. Akay<sup>1,2</sup>, M. Dogru<sup>1</sup>, B. Calkan<sup>1</sup>, and O. F. Calkan<sup>1</sup>**

<sup>1</sup>**Process Intensification and Miniaturization (PIM) Centre, School of  
Chemical Engineering and Advanced Materials, Newcastle University,  
Newcastle upon Tyne NE1 7RU, United Kingdom**

<sup>2</sup>**Institute of Nanoscale Science and Technology, Newcastle University,  
Newcastle upon Tyne NE1 7RU, United Kingdom  
(<http://www.Newcastle.ac.uk/PIM>)**

Process Intensification (PI) based on Flow Induced Phase Inversion (FIPI) phenomenon is reviewed briefly. The relationship between PI and process miniaturization through micro-reactor technology is considered in terms of micro-reactors and phenomenon based process intensification. The significance of FIPI in micro-reactor technology is considered in more detail. In order to achieve phenomenon based process intensification, it is necessary to conduct processes in micro-scale which provides extended surface area and enhanced selectivity through the interactions between the reactants / products and the micro-reactor environment. Strong interactions can be achieved by providing specific chemical functionality, surface area and accessibility within the micro-environment. These conditions are achieved by using nano-

structured micro-porous polymers or metals with controlled chemical structure in which arterial pores provide accessibility and nano-pores provide surface area and functionality. We examined the preparation of sulphonated micro-cellular PolyHIPE Polymers prepared through a High Internal Phase Emulsion (HIPE) polymerization route and subsequently sulphonated using sulfuric acid which is already present within the pores of the micro-porous polymer. In the preparation of such polymers, FIPI is used to control the pore size and prevent the emulsion separation during polymerization as a result of sulfuric acid presence. PolyHIPE Polymers were also used as template in the preparation of nano-micro-porous metals/alloys which can be used as intensified catalyst or catalyst support. These catalysts also provide accessibility for the reactants and products through the arterial micro-pores connecting the nano-pores which provide catalytic activity and surface area.

## Introduction

Process Intensification (PI) represents a novel design strategy which aims at the reduction in the processing volume by at least an order of magnitude, compared with the existing technology, without any reduction in process output. However, this is a restricted view of PI and it is also relativistic. Operations at very high processing rates in small processing volumes can result synergy underpinning the intensification of the process as in 'Phenomenon Based Process Intensification. The relativistic nature of the definition requires a standard against which one can compare the intensified processes. Initially, PI represented a design objective driven primarily by cost savings, since a significant part of the plant cost is associated with piping, support structures and civil engineering items (1-3). On the other hand, Process Miniaturization (PM) in the chemical industry and biology is well known in the form of analytical equipment and sensors where miniaturization is an essential design objective. Therefore, for a given production objective (or processing rate) PI and PM represent respectively, top-down and bottom-up approaches in the design of an intensified and miniaturized process. These two design approaches can be integrated with the objective of plant size reduction and significantly enhanced efficiency, to provide major savings on capital and operating costs.

However, the integration of Process Intensification and Miniaturization (PIM) also creates synergy in achieving intensified processes, novel product forms and size dependent phenomena which in turn provides novel intensified processes (4-6). PIM is seen as an important element of sustainable development since PIM can deliver: (i) At least a ten fold decrease in process equipment volume; (ii) Elimination of parasitic steps (such as side reactions) and unwanted by-products, thus eliminating some downstream processing operations; (iii) Inherent safety due to reduced reactor volume; (iv) Novel product forms (v) Energy, capital and operating cost reduction and an environmentally friendly process; (vi) Plant mobility, responsiveness and security; and (vii) A platform for other technologies.

Furthermore, the miniaturization of a process can result in a 'size dependent phenomenon' (4-6) which in turn can be used to underpin an intensified process. Therefore, such processes are called Phenomenon Based Process Intensification, or because of its nature, they can also be called 'Inherently Intensive Processes' (3). Processes which are intensified by virtue of the intensification of the driving force(s), such as extended surface area, high temperature / pressure / deformation rate, are called Physical Process Intensification. This classification widens the scope of PI and highlights the importance of process miniaturization in intensification. Size dependent phenomenon which forms the basis of the inherently intensive processes, also contributes to the understanding of chemical and biological processes in confined environment.

A prerequisite in the investigation of a size dependent phenomenon is the ability to fabricate suitable environment to carry out the chemical / biochemical processes and to incorporate the reactants or catalysts within such an environment in sufficient concentration. Furthermore, the control of the size of environment and its physical/chemical structure is also necessary in the optimization of the conditions leading to the selectivity and intensification of the target processes.

Flow Induced Phase Inversion (FIPI) phenomenon has been used as the basis of process intensification as well as in the preparation of micro-porous polymers (with or without superimposed nano-structure) which are now used in process intensification and miniaturization and in the investigation of size dependent phenomena in biological and chemical systems (4-6).

#### **Flow Induced Phase Inversion (FIPI) and Process Intensification**

FIPI is most readily observed in multi-phase systems and most unambiguously in emulsions. It was applied to the intensive structuring of materials such as agglomeration, microencapsulation, detergent processing,

emulsification, latex production from polymer melt emulsification etc. (7-18). Diagrammatic illustration of FIPI is shown in Figure 1. When a material-A is mixed with material-B, in the absence of any significant deformation, the type of dispersion obtained ([A-in-B] or [B-in-A]) is dictated by the thermodynamic state variables, TSVs (concentration, viscosity of components, surface activity, temperature, pressure). If the prevailing TSVs favour the formation of [A-in-B] -dispersion, phase inversion to [B-in-A] -dispersion can be achieved by changing the TSVs (thermodynamically driven process).

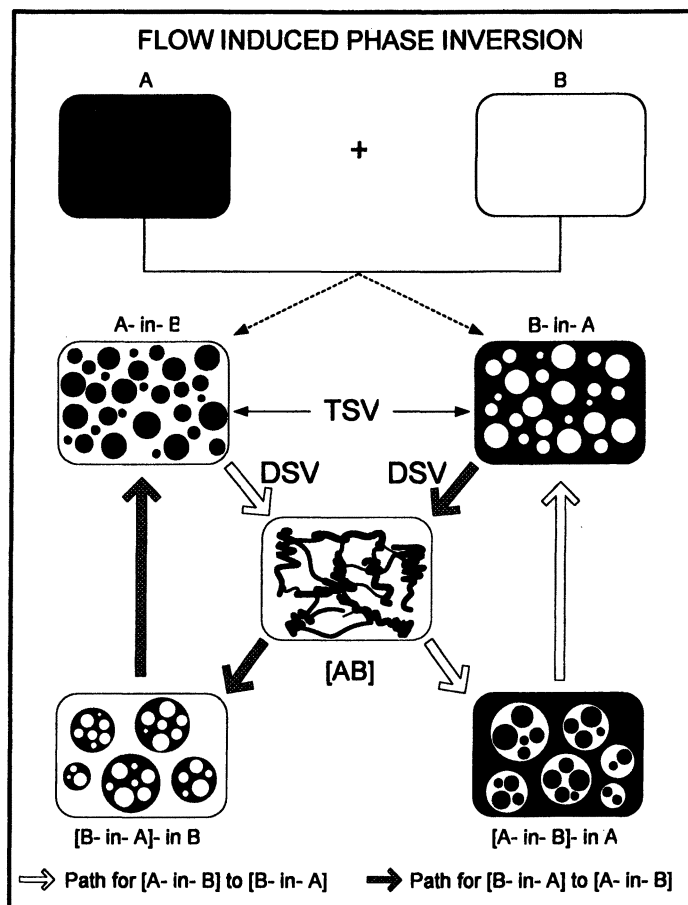


*Figure 1. Isothermal Flow Induced Phase Inversion (FIPI) paths for the inversion of [A-in-B] or [B-in-A] emulsions through a co-continuous unstable emulsion phase [AB]. TSV= Thermodynamic state variable; DSV= Deformation state variable.*

Alternatively, the dispersion can be subjected to a well-prescribed deformation, characterised by its rate and type (deformation state variables, DSVs) in order to invert the dispersion under constant thermodynamic conditions; this phenomenon is known as Flow Induced Phase Inversion. It is found that FIPI is not catastrophic and the dispersion goes through an unstable co-continuous state denoted by [AB], followed by a relatively stable multi-dispersion state denoted as {[A-in-B]-in-A}, before complete phase inversion to [B-in-A]. Therefore, the interchange ability of TSVs with DSVs forms the basis of FIPI-processes.

The characteristics of the micro-structure formed (such as emulsion droplet size) are dependent on the type of micro-structure, type of deformation (shear, extension or combined), and deformation rate as well as the TSVs. In order to maximise the fluid micro-structure/flow field interactions, the flow field must be uniform which requires the application of the flow field over a small processing volume. There are several equipment such as Multiple Expansion Contraction Static Mixer (MECSM) or its dynamic version called Controlled Deformation Dynamic Mixer (CDDM) which are most suitable for process intensification in the preparation of emulsions or micro-structured materials (7-10). FIPI-based process intensification techniques can be further facilitated by using non-isothermal FIPI (11-14). Therefore, isothermal and non-isothermal FIPI phenomena represent the first examples of Phenomenon Based Process Intensification, when very high deformation rates and small processing volumes are required in order to achieve novel products in very fast processes.

The importance of FIPI in process intensification is two fold. It can be used to promote phase inversion without changing the thermodynamics of the system to obtain a higher entropy state or, it is possible to delay phase inversion while reducing the system entropy (8). These attributes of FIPI were utilised in devising intensive processes in materials structuring such as agglomeration, microencapsulation, detergent processing, emulsification, latex production from polymer melt emulsification etc. (7-18). FIPI was also used in the preparation of High Internal Phase Emulsions (HIPEs) which were subsequently polymerised to produce micro-porous polymers with controlled pore size (6,19) and used in process intensification and micro-reactor technology.

### **Microporous Polymers and Their Application in Process Intensification and Micro-reactor Technology**

Micro-porous polymers have been used in the intensification of several processes encountered in nuclear, petroleum, bio-conversion, tissue engineering, chemical and environmental technologies (4-6, 19-25). The advantages of PolyHIPE Polymer and its metallic form are associated with the accessibility of

their pores, controllability of the pore and interconnect structures, versatility of fabrication and chemical modification of their walls. The structure of these materials is shown in Figure 2 (a-d). These materials can be manufactured over a wide range of pore size,  $D$ , ( $0.5 \mu\text{m} < D < 5000 \mu\text{m}$ ) and interconnect size,  $d$  ( $0 < d/D < 0.5$ ). Pores with size above  $\sim 200 \mu\text{m}$  are obtained through a coalescence polymerisation route (6).

These attributes are utilised in devising intensified processes as well as in the discovery of several size dependent phenomena especially in biology which are subsequently utilised in bioprocess intensification. Currently, PolyHIPE Polymers (both hydrophobic and hydrophilic versions) are used in the intensification of stable water-in-oil emulsion separation (demulsification) (20),

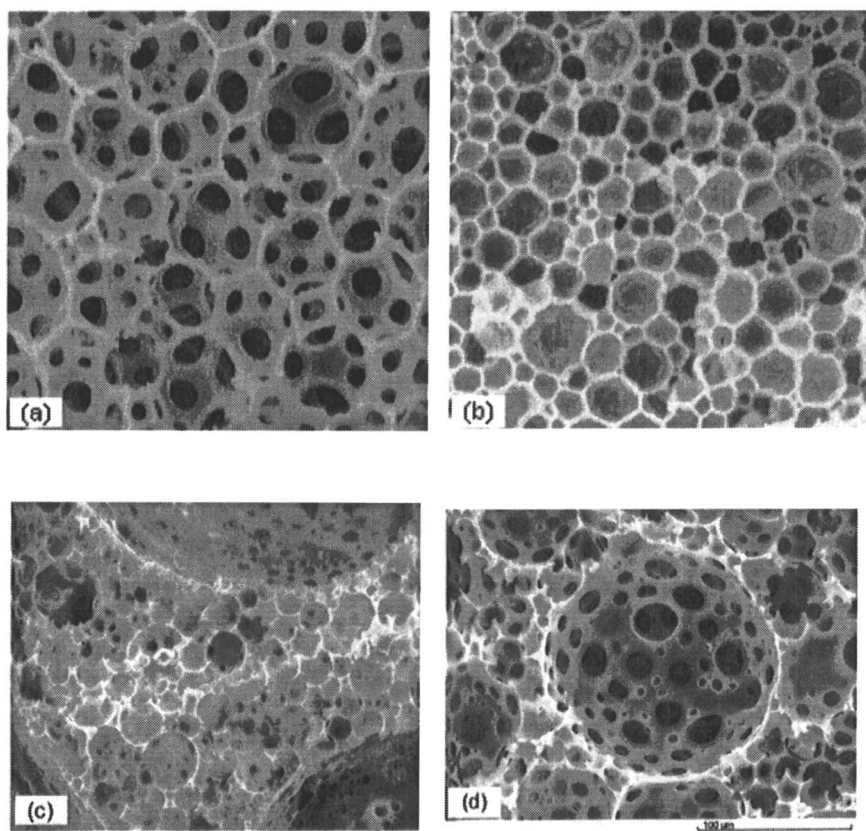


*Figure 2. Basic PolyHIPE Polymer structures: (a) Primary pores with large interconnecting holes, (b) Primary pores with nano-sized interconnecting holes, (c) Large coalescence pores (3 such pores are partially shown) dispersed into the primary pores in the process of coalescence; (d) Detail of the coalescence pores. Note that these pore structures can be prepared over a wide size range.*

gas-liquid separation as applied to tar and water removal from biogas produced through the gasification of biomass (21,22), bioprocess intensification (4,23,24) tissue engineering (5,6,24) and metal ion/toxin removal from contaminated water (25). The processing and chemical structure of these materials are also available (23-25). The accessibility of the pores increases both the rate and capacity of metal ion removal. In currently available ion-exchange resins, only the outer most part of the resin beads are utilised since, as soon as the resin surface is saturated or fouled, metal ion removal rate and capacity are drastically reduced.

Utilisation of PolyHIPE Polymers in the above cited areas require: i) Ability to produce PHP with a desired internal architecture (i.e., pore/interconnect size, presence of arterial channels), ii) Ability to form monolithic structures; iii) Ability to chemically/biologically functionalise the PHP for specific application. In order to commercialise such devices / applications, it is also important to ensure that the preparation and functionalisation of PHP is sustainable (economic, environmental and social acceptance). The use of highly expensive and toxic monomers and the generation of excessive waste during processing and/or functionalisation of these materials are not sustainable. Crosslinked styrene - divinyl benzene copolymer based PHP is a very useful starting material and sulfonated form of this PHP has been widely used where hydrophylicity is required (20, 25). However, currently available techniques of sulphonation (20, 25-30) are not sustainable due to the production of excessive waste acid after the sulphonation process and the inability of acid to penetrate into the material. In this study, we also introduce a novel sustainable sulphonation technique.

### **Nano-Structured Micro-Porous Materials and Intensified Catalysis**

Nano-structured micro-porous catalysts or catalyst supports offer intensified catalysis since they provide enhanced surface area which is accessible to the reactants and products through a network of channels feeding into the regions of catalytic activity. In non-structured catalysts, although the surface area might be large, they are often not accessible as a result of surface fouling and the diffusion resistance can slow down the rate of reaction. Catalysts are either deposited as a thin film on a support or they are used as pellets. These two techniques have certain drawbacks: in coated systems, catalyst adhesion can be non-uniform and weak while the accessibility of the active sites within the interior of the catalyst is hindered due to low porosity.

In this study, micro-porous materials were used as templates for the solution deposition of metals which were subsequently heat treated to obtain porous metallic structures where the size of the pores ranged from tens of microns to tens of nano-meters thus eliminating the problems of accessibility and poor adhesion. The technique differs fundamentally from the compression based systems where the porosity is reduced as a result of compaction. Furthermore, the mechanisms of metal deposition within micro-pores and nano-structure formation are novel. The importance and current fabrication techniques of porous metallic systems can be found in (31).

## Experimental

### Materials and Techniques

#### Materials

Styrene, DVB (Divinyl benzene), Sorbitan Monooleate (Span 80), Nickel Chloride, Sodium Hypophosphate Hydrate, Ammonia, Lauroyl Peroxide and Isopropanol were purchased from Merck. All the chemicals (reagent grade) were used without further purification.

#### Preparation of Micro-cellular Polymers

PolyHIPE Polymers (PHP) were prepared through a high internal phase emulsion polymerization route using the technique given in (4-7, 19-20,24,27). The acronym, PHP and the name of these polymers reflect their processing history (4-7). The techniques used in this study ensure the preparation of micro-porous polymers with well controlled internal architecture, pore and interconnect sizes and their distributions (24).

The high internal phase emulsion (HIPE) was prepared initially. The continuous phase of HIPE, which eventually undergoes polymerization and crosslinking, contained 14 wt % surfactant (Span 80), 78wt% monomer (styrene) and 8 wt% crosslinking agent (divinyl benzene). In some cases, oil soluble initiator, lauroyl peroxide was also used at 1% level in which case the weight percent of styrene was reduced to 77%. This reactive mixture was placed at the bottom of a mixing vessel (internal diameter was 12 cm) and 220 cm<sup>3</sup> dispersed phase (water containing 1% potassium persulphate as polymerization initiator) was dosed into the continuous phase while mixing. We used either oil phase or aqueous phase initiator. When the polymers were prepared for sulphonation experiments, the aqueous phase contained 10 % sulfuric acid.

Mixing was conducted using 3 flat paddles (diameter was 9 cm) which were stacked at right-angles to each other and the bottom impeller was as close to the bottom of the vessel as possible. Rotational speed of the impellers was 300 rpm. The phase volume of the aqueous phase was 85%. The control of pore and interconnect sizes in the micro-porous polymer is achieved mainly through the control of temperature of emulsification, mixing speed and time. Details of the process to obtain a given pore size and structure are available in (6,24).

After the preparation of the emulsion, it was transferred to plastic containers with internal diameter 2.6 cm and polymerized at 60 °C for at least 8 hours.

After polymerization, polymer was cut into 0.4 cm thick disks and used in sulphonation experiments. These polymer disks were then dried under vacuum and stored for use in subsequent modifications or applications.

### **Sulphonation Technique**

Samples in the form of disks were placed in a pre-heated oven and kept there for a preset length of time for sulphonation. Some of the samples were dried under vacuum at 60 °C in order to increase the acid concentration from 10% to 70% before sulphonation so as to accelerate the rate of sulphonation. After sulphonation, they were washed in a mixture of water / iso-propanol to remove all the residual monomer/crosslinker, initiator and excess sulfuric acid. Polymer disks were then dried under vacuum and stored for examination and for the determination of degree of sulfonation using the method described in (20,27).

### **Metallization of PolyHIPE Polymer**

#### *Electroless Deposition Solution*

In each electroless nickel deposition experiment we used a solution of 5 grams Nickel Chloride, and 40 grams of Sodium Hydrophosphate Hydrate both dissolved in 300 mL double distilled water. Solution pH was adjusted to 11.5 by adding 40 mL ammonium hydroxide solution (35% concentration). This solution was passed through the template polymer with periodic washing with water. The procedure was repeated by reversing the deposition direction in order to provide uniform metal distribution across the thickness of the template.

#### *Preparation of Template PolyHIPE Polymer (PHP) for Metal Deposition*

PHP template was prepared using 78% styrene, 14% Span 80 and 8% divinyl benzene in the oil phase. The aqueous phase contained 1% potassium persulphate in double distilled water. Phase volume of the template PHP was 95% in order to obtain highly open pore polymer. The emulsion preparation was conducted in the mixer as described above using agitator speed of 300 rpm. Dosing was completed in 1 minute and another 2 minute mixing was allowed. The temperature of the aqueous phase was 60 °C. The resulting polymer was washed in water and iso-propanol and pore size was evaluated using SEM. In order to accelerate the metal deposition, it is possible to include nickel ions (such as nickel chloride) in the aqueous phase. Although this also insures uniform deposition of some metal without the use of the metal bath, the emulsion can become unstable and form coalescence pores as described previously (6).

### *Deposition Equipment*

The flow diagram of the metal deposition is shown in Figure 3 (a). A metal deposition cell was constructed as illustrated in Figure 3 (b). The deposition cell houses the template PHP in the form of a disk (4 mm thick and 26 mm in diameter). Referring to the Figure 3 (b), PHP template sample (S) is sandwiched between two Teflon flow distributors (D) at the end of the Teflon flow channel (C) bored into the holders (A) which also act as support for PHP. The whole assembly was then placed between two circular brass blocks (B) which are electrically heated using a band heater (E). Note that the PHP template is in direct contact with the brass holder to provide direct heating. Temperature of the PHP template was monitored using a thermocouple (T) in contact with the polymer. All parts of the flow cell which are in direct contact with the metal bath solution are made of Teflon in order to prevent metal deposition in the flow channels. The metal bath solution was kept at room temperature and was pumped into the deposition cell using a syringe pump at a rate of 2 mL/min. In order to cause metal deposition within the pores of the template polymer, the temperature of the solution was raised to 90 +/- 3 °C. In order to achieve this, the deposition cell was charged with demineralized water at 97 °C for 5 minutes at a rate of 40 ml/min while keeping the band heater at 90 °C. This was followed by the syringe pumping of the metal bath solution. After pumping 50 ml solution, the deposition was stopped and hot water washing was renewed and the cycle was repeated. After using 300 ml metal bath solution, the direction of flow was reversed until sufficient amount of metal was deposited. It is possible to reverse the flow direction after each 50 ml deposition and washing in order to obtain more uniform deposition.

### **Scanning Electron Microscopy (SEM)**

Fracture surface of samples were examined using a scanning electron microscope (Cambridge S 240). Non-conducting specimens (i.e., initial hydrophobic PHP) were coated with carbon, while sulphonated or metallized samples were examined after washing and drying as they are already conductive.

## **Results and Discussion**

### **Sulphonation**

The variation of sulphonation degree with time as a function of processing conditions is shown in Figures 3-5. As seen, the degree of sulphonation increases with time and it reaches a plateau value at ca. 60% (Figure 4). As expected, the rate of sulphonation increases with increasing temperature as well

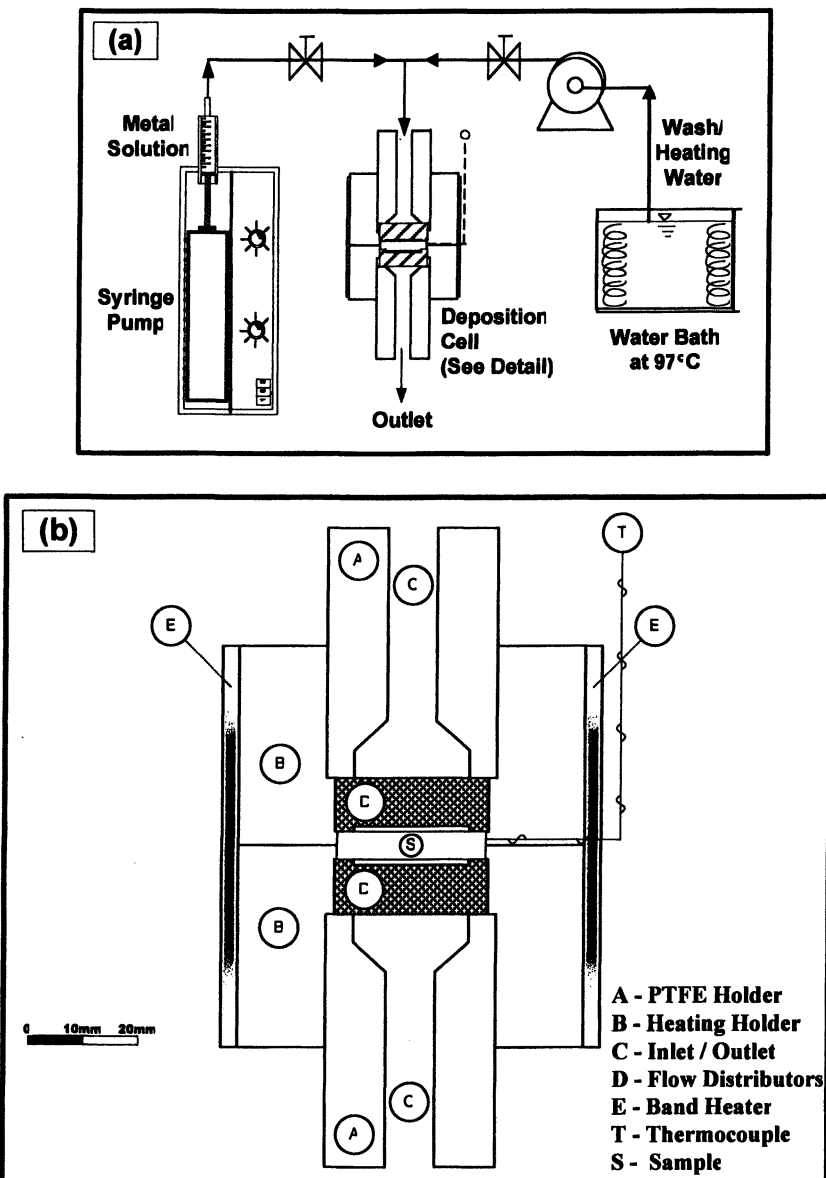


Figure 3. Metal deposition equipment: (a) Flow diagram, (b) Detail of the metal deposition cell

as with the concentration of the acid within the pores of the polymer (Figure 5). The asymptotic value of sulphonation is higher when concentrated acid is present or when potassium persulphate is used as initiator although the rate of sulphonation is reduced initially compared with oil soluble initiator, lauroyl peroxide (Figure 6).

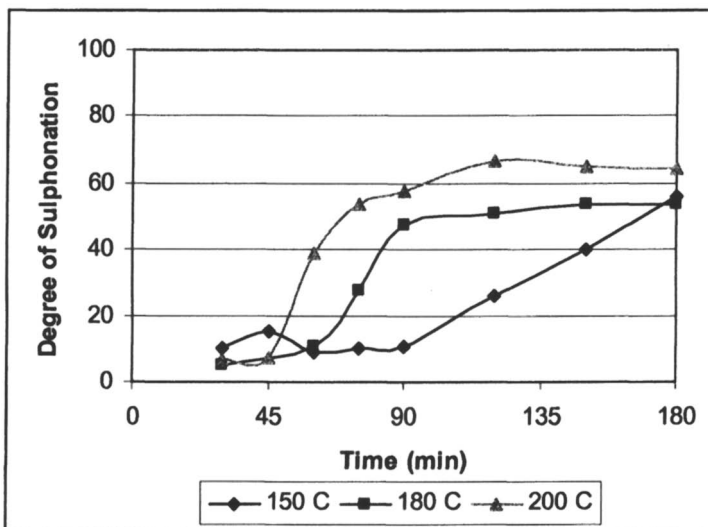


Figure 4. Variation of sulphonation degree with time at various temperatures when PHP contained 10% sulfuric acid with lauryl peroxide as initiator

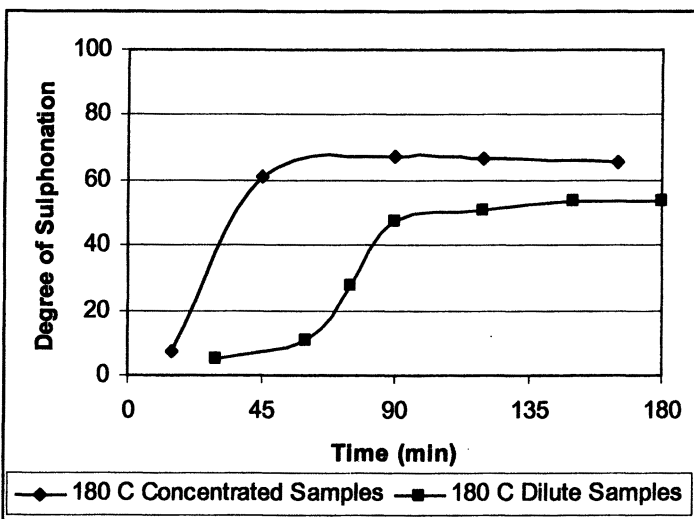


Figure 5. Variation of sulphonation degree with time at 180 °C as a function of acid concentration in PHP. Dilute samples contained 10% acid while the concentrated samples contained 70% acid with Lauroyl Peroxide as initiator.

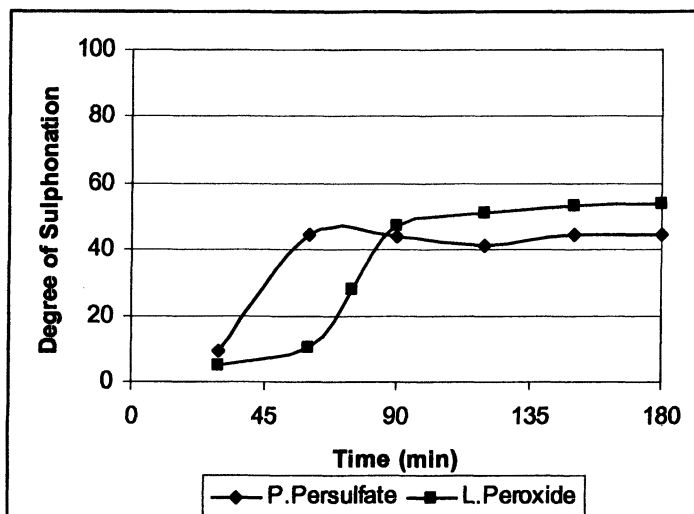
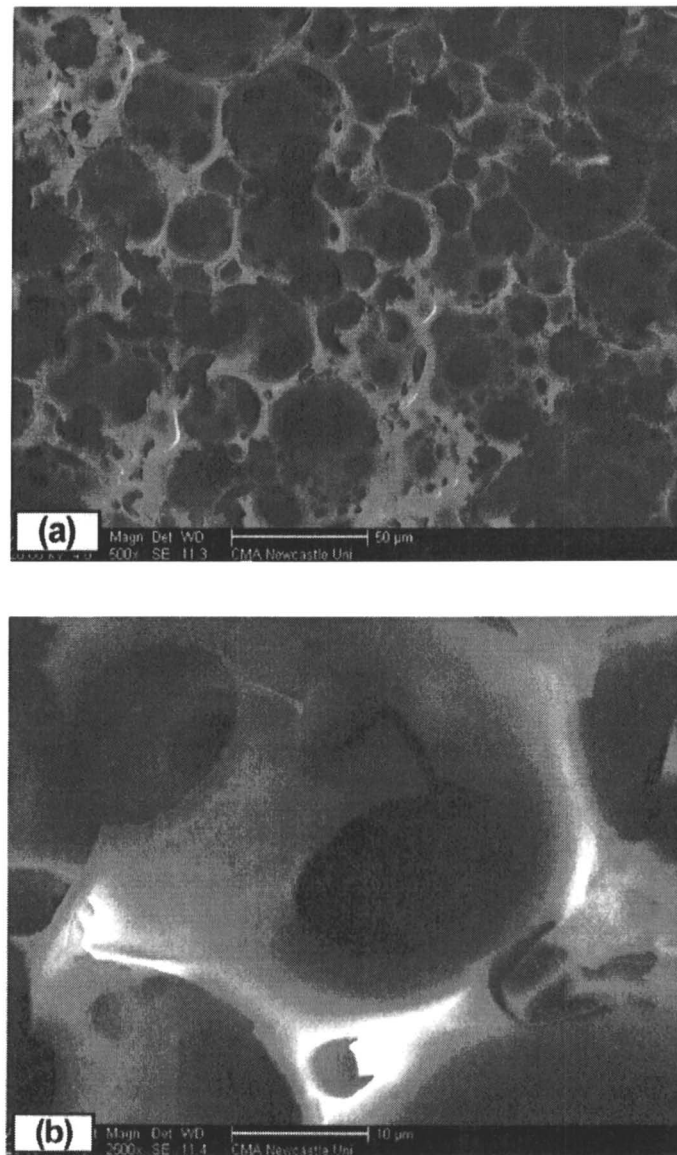


Figure 6. Variation of sulphonation degree with time at 180 °C as a function of initiator type (Potassium Persulphate or LauroylPeroxide) when PHP contained 10% sulfuric acid.

### Structure of Sulphonated Micro-porous Polymers

Typical structure of sulphonated PHP is illustrated in Figure 7 (a,b). These Scanning Electron Micrographs indicate that the 'coalescence' pores are dominant because of the presence of sulphuric acid which destabilizes the emulsion during polymerization. Therefore, water droplet coalescence and polymerization / cross-linking reactions proceed at the same time, leading to the formation of coalescence pores dispersed into the primary pores. The size and volume fraction of coalescence pores is dependent on the size of the primary pores as well as the rate of polymerization and temperature. The walls of the coalescence pores are thicker and they can contain primary walls as illustrated in Figure 7(b).

These sulphonated polymers are also electrically conductive and therefore they can be examined under SEM without the application of a conductive coating (carbon or gold) and microanalysis can be performed including carbon analysis on the sample.



*Figure 7. SEM micrograph of coalescence pores produced through HIPE polymerization using 10% sulphuric acid solution followed by sulphonisation at 180 °C for 180 minute. Note the presence of primary pores within the walls.(a) General view; (b) Detail*

**Metallization***Metal Deposition Characteristics*

The deposition of metal (nickel) within the pores is in the form of metal grains. Figure 8 (a,b,c) illustrate the metal deposition behavior in which the metallic grains as well as the polymer structure can be identified clearly since the deposition is at the early stages of the experiments (300 ml solution used). It can be seen that a relatively thick (ca. 25  $\mu\text{m}$ ) and low porosity, dense skin layer is formed even at an early stage (Fig. 8b). The morphology of this layer differs from the grainy morphology of the inner structure which is detailed in Fig 8 (c): large interconnected arterial pores formed by the metal grains follow the contours of the template polymer.

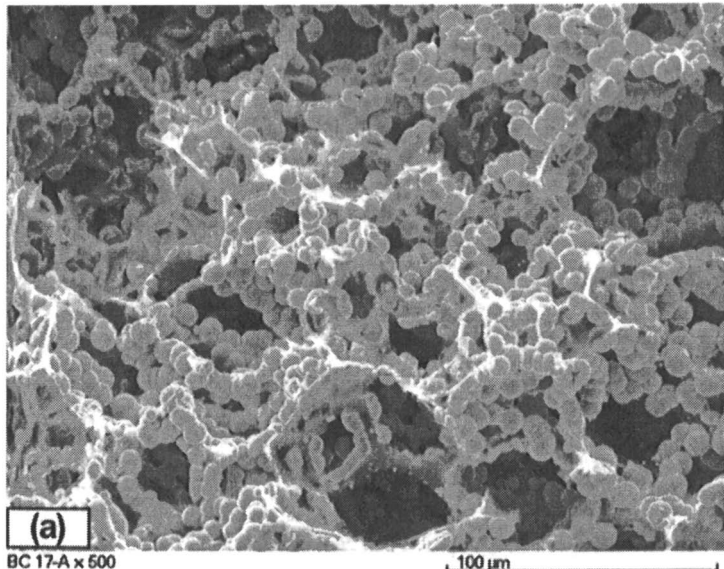


*Figure 8. Appearance of the polyHIPE template and metal deposit at the early stages of deposition, after passing 300 ml solution through the template*  
(a)Inner structure; (b) Skin formation; (c) Detail of the inner structure.

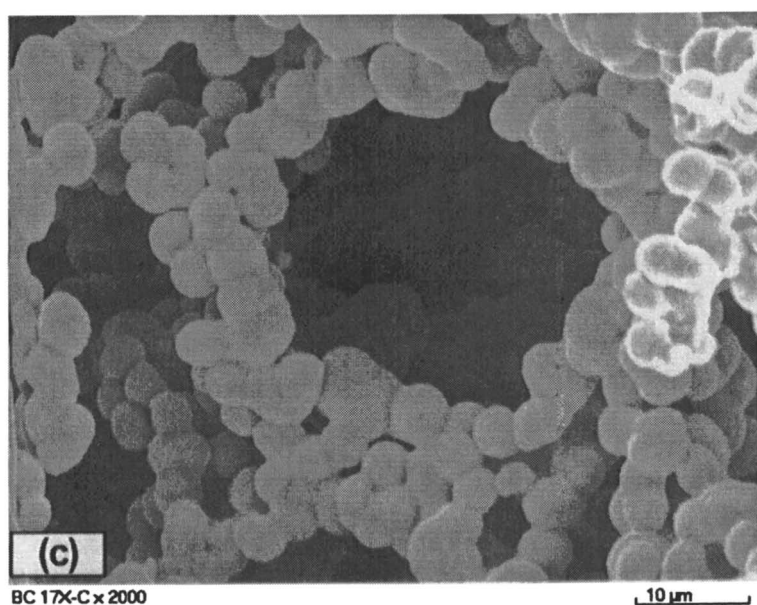
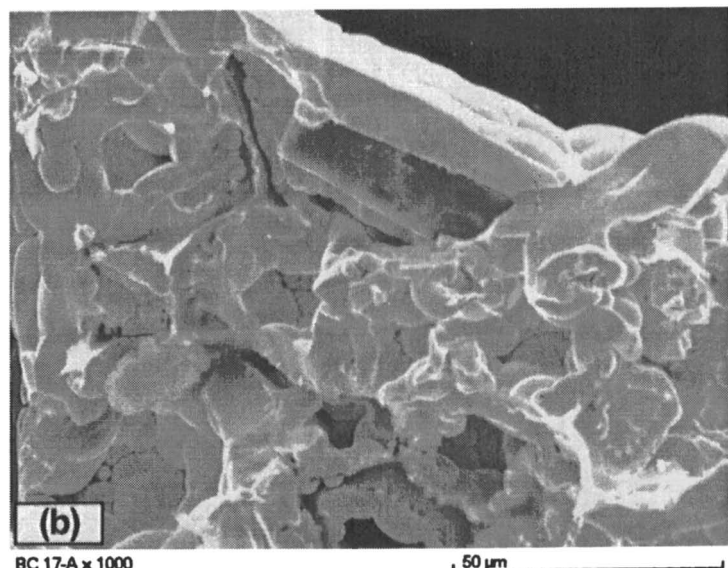
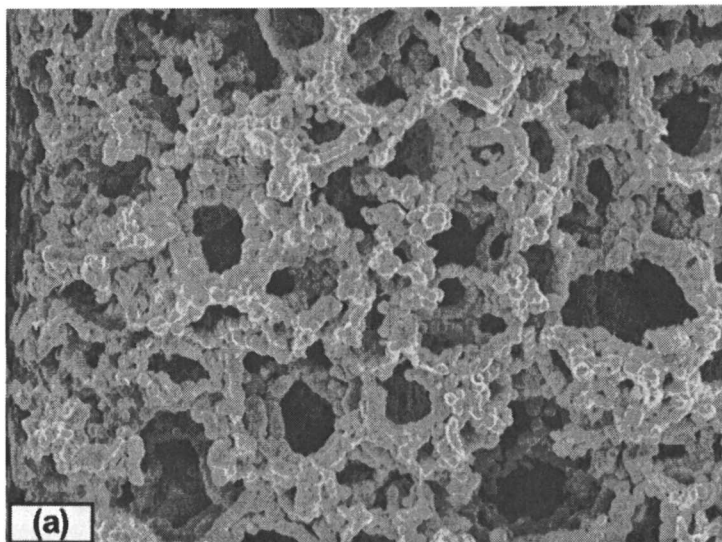


Figure 8. *Continued.*

*Effect of annealing temperature on the nano-structure of metal grains*

After the metal deposition is completed (approximately  $3.2 \pm 0.3$  gram metal deposition is achieved, using a polymer template of 0.085 gram) the polymer/metal deposit is gradually heated in a furnace to  $600^\circ\text{C}$  or  $800^\circ\text{C}$  or  $1000^\circ\text{C}$  at the maximum rate of  $20^\circ\text{C}/\text{min}$  so that the heating time is 60 min in all cases. Upon reaching to the target temperature, the material was kept for one hour and subsequently taken out to cool outside the oven. These materials were then examined under SEM. Figure 9 (a) illustrates the general appearance of the porous metal. It can be seen that a 3D micro-porous metal structure is formed by the partial fusing of the metal grains as shown in Figure 9 (b). The average grain size before heat treatment (one hour heating from  $25^\circ\text{C}$  and one hour annealing at the target temperature) is ca.  $6 \pm 2 \mu\text{m}$ . Average grain size increases slightly after an one hour annealing at  $600^\circ\text{C}$  to  $7 \pm 2 \mu\text{m}$  but it increases with increasing temperature: to  $14 \pm 2 \mu\text{m}$  at  $800^\circ\text{C}$  and remains at this level when the temperature is at  $1000^\circ\text{C}$ .



*Figure 9. Typical inner structure of the porous metal after heat treatment at  $600^\circ\text{C}$  for 1 hr following the passing of 680 ml metal bath solution (a) General appearance, (b) Fused structure of the metal grains.*

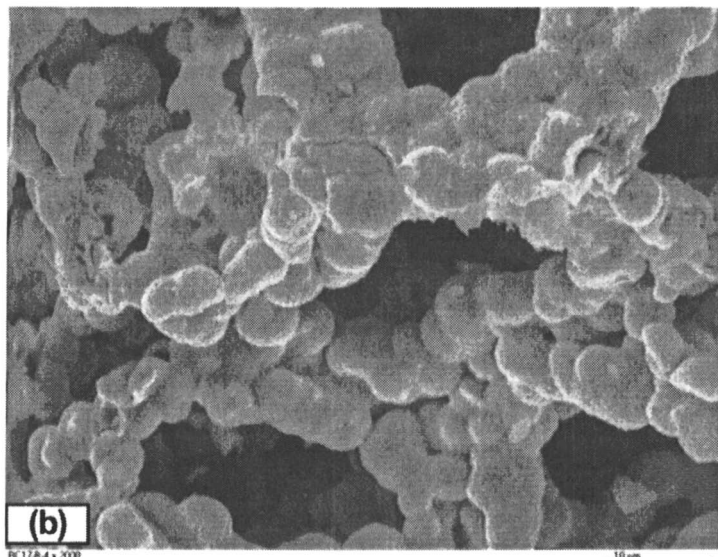


Figure 9. *Continued.*

#### *Nano-structure of the Metal Grains*

A close examination of the grain structure indicates that the grains contain nano-pores and both the pore density and pore size are dependent on the heat treatment temperature as illustrated in Figure 10 (a,b,c). Number density of the pores decreases with increasing heat treatment temperature as temperature is increased from 600 °C (Figure 10.a) to 800 °C (Fig. 10 b) and to 1000 °C (Figure. 10 c). Surface pore size initially increases with increasing temperature but at 1000 °C, surface pore size starts decreasing as shown in Figures 10 (a,b,c).

A closer examination of the metal grain structure (i.e., fractured metal grains) shows that, inside the metal grains the material is also porous with a mixture of micron- and nano-sized pores as shown in Figure 11.

#### **Conclusions**

Flow induced phase inversion (FIPI) phenomenon was utilized in controlling the pore size and stability of microcellular PolyHIPE Polymer which was subsequently modified to obtain monolithic functional polymers or nano-structured micro-porous metals which can be used in micro-reactor technology or intensified catalysis. Understanding of the FIPI phenomenon delivers not only several Phenomenon Based Process Intensification techniques, but also enables the preparation of micro-cellular structures which can be used in micro-reactor technology and process intensification.

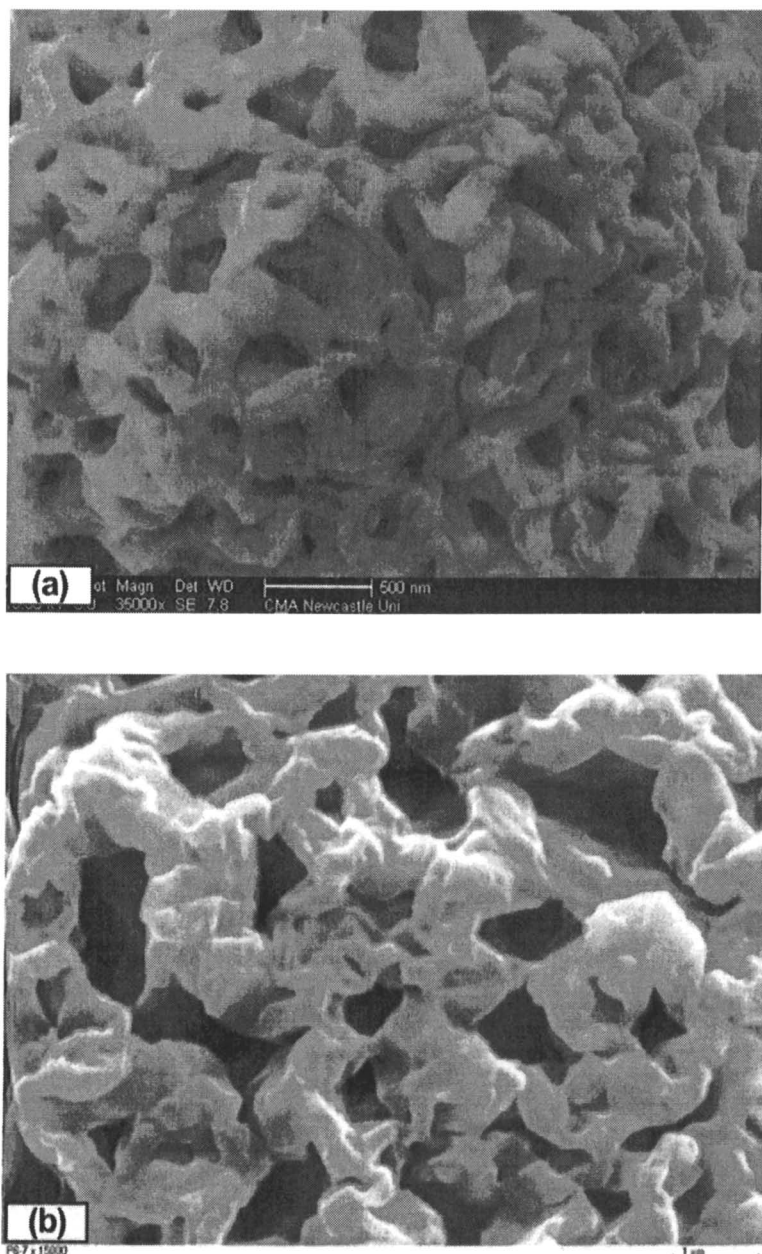


Figure 10. The effect of annealing temperature on the metal grain surface pore size and pore number density: (a)  $T = 600^\circ\text{C}$  (b)  $T = 800^\circ\text{C}$  (c)  $T = 1000^\circ\text{C}$ .

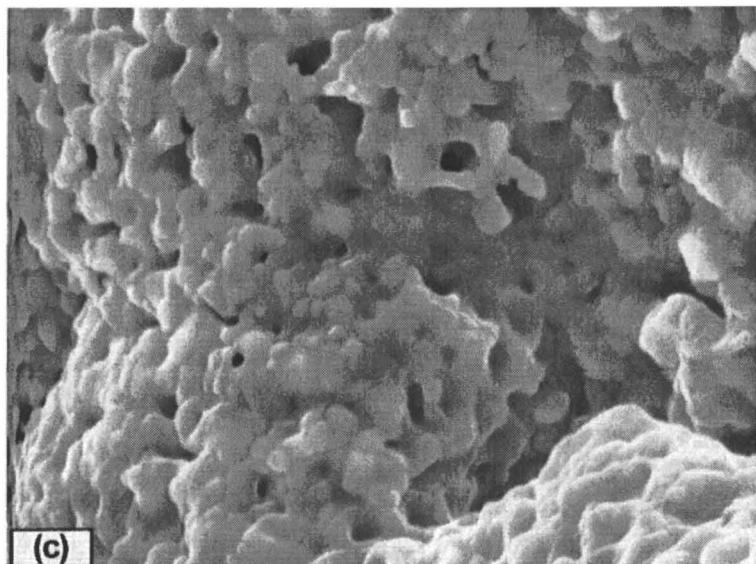


Figure 10. *Continued.*

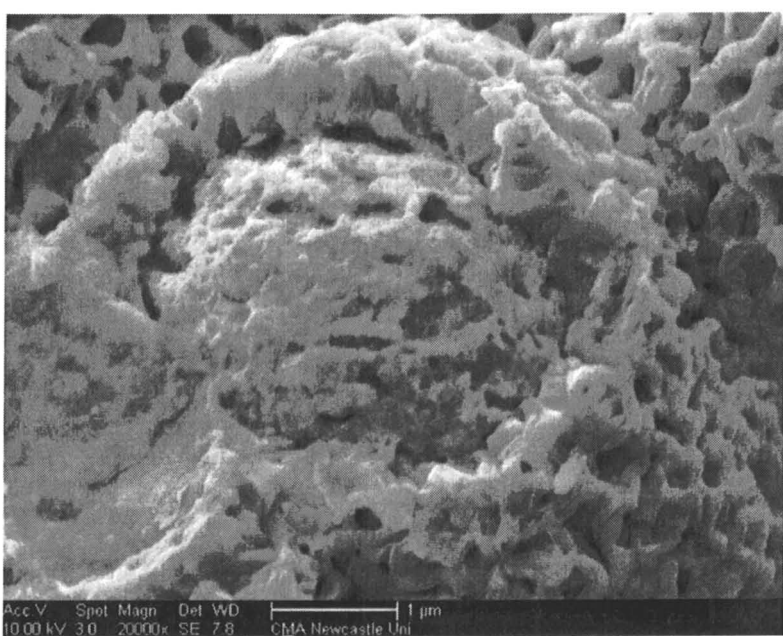


Figure 11. Fracture surface of the metal grains revealing their inner structure. There appears to be phase separation between the skin and the core which is also porous with large as well as very small pores. Heat treatment was conducted at 600 °C for two hours (1 hr slow heating plus 1 hour constant temperature annealing).

However, these monolithic micro-porous structures often require chemical or biological functionalization. The chemical functionalization through sulphonation of the original crosslinked styrene-divinylbenzene co-polymer is important in several applications of PolyHIPE Polymers. The currently available sulphonation technique is highly wasteful as it produces large quantities of dilute sulfuric acid and can not be used in the sulphonation of thick monolithic structures. In the present technique, PolyHIPE Polymer is produced using sulphuric acid as the internal phase at the emulsification stage. Since sulfuric acid is already present within the pores of the polymer, the use of excess acid and the need for its penetration into the pores are avoided.

Unlike the previous attempts (32, 33) to produce strong micro-porous metals, we used basic solution which results in grain formation and faster deposition. Furthermore, there is no need for the sensitization of the polymer using metals such as palladium and chemical agents used in smooth metal deposition. During heat treatment, metallic grains fuse and a skin/core structure is formed. Grain fusing and subsequent size enlargement is enhanced with temperature. Metal grains (size ca. 6-14  $\mu\text{m}$ ) have surface skin pores in the range of 200 nm going across the skin of ca. 1  $\mu\text{m}$ . Similar to the bulk structure, the core itself is also porous with micron and nano sized pores confined to domains of ca. 6-14  $\mu\text{m}$  diameter. The micro-pores in these materials make nano-pores accessible to the reactants hence we can expect the acceleration of the reaction rates while the nano-sized pores providing surface area for reaction. Similar to chemically (or indeed biologically) functionalized PolyHIPE Polymers, these metallic structures can be fabricated in monolithic forms, making them ideal for high temperature micro-reactor applications.

## Acknowledgements

We are grateful to the UK Engineering and Physical Sciences Research Council (EPSRC), UK Department of Trade and Industry, Avecia / Cytec, BLC Research, BP Amoco, Ecoprotech Ltd., Exxon Mobil, Intensified Technologies Incorporated (ITI), Morecroft Engineers Ltd., Safety-Kleen Europe, Triton Chemical Systems, Willacy Oil Services Ltd., for their support.

## References

1. Akay, G., Mackley, M.R., and Ramshaw, C. Process Intensification: Opportunities for Process and Product Innovation, In *IChemE Research Event*; Chameleon Press, London, 1997; Vol. 1, pp. 695-703.

2. Stankiewicz, A., Moulijn, J.A., *Ind. Eng. Chem. Res.* **2002**, 41, 1920-1924.
3. Akay, G. Bioprocess and chemical process intensification. In *Encyclopedia of Chemical Processing*, Ed: Lee, S., Marcel Dekker, NY, 2005.
4. Akay, G., Erhan, E., and Keskinler, B. Bioprocess intensification in flow through monolithic micro-bioreactors with immobilized bacteria. *Biotech. Bioeng.*, in press.
5. Akay, G., Birch, M.A., and Bokhari, M.A., *Biomaterials*, **2004**, 25, 3991-4000.
6. Akay, G., Dawnay, S., and Price, V.J., European Patent 1,183,328 June 3, 2002.
7. Akay, G. Flow induced phase inversion in powder structuring by polymers. In *Polymer Powder Technology*; Narkis, M.; Rosenzweig; Eds.; Wiley: New York, 1995; pp. 542-587.
8. Akay, G., *Chem. Eng. Sci.* **1998**, 53, 203-223.
9. Akay, G., Irving, G.N., Kowalski, A.J., and Machin, D. Process for the production of liquid compositions. European Patent 799,303. October 31, 2001.
10. Akay, G., Irving, G.N.; Kowalski, A.J.; Machin, D. Dynamic mixing apparatus for the production of liquid compositions. US Patent 6,345, 907, February 12, 2002.
11. Tong, L. and Akay, G., *J. Materials Sci.*, **2002**, 37, 4985-4992.
12. Akay, G., L.Tong, L., and Addleman, R., *Ind. Eng. Chem. Research*, **2002**, 41, 5436-5446.
13. Akay, G. and Tong, L., *J. Materials Sci.* **2003**, 38, 3169- 3181.
14. Akay, G. and Tong, L., *Int. J. Transport Phenomena*, **2003**, 5, 227-245.
15. Akay, G. and Tong, L., *J. Colloid Interface Sci.* **2001**, 239, 342-357.
16. Akay, G., Tong, L., Hounslow, M.J. and Burbidge, A.S., *Colloid and Polymer Sci.*, **2001**, 279, 1118-1125.
17. Akay, G., Tong, L., Bakr, H., Choudhery, R.A., Murray, K., and Watkins, J., *J. Materials Sci.*, **2002**, 37, 4811-4818.
18. Akay, G., *The Chemical Engineer*, **2004**, 752, 37-39.
19. Akay, G. Method and apparatus for processing flowable materials. International Patent Application. PCT Publication WO 2004/004880, January 15, 2004.
20. Akay, G. and Vickers, J. Method for separating oil in water emulsions, European Patent 1,307,402 May 7, 2003.
21. Dogru, M. and Akay, G. Gasification, International Patent Application, PCT/GB2004/004651, November 9, 2004.
22. Akay, G., Dogru, M., Calkan, O.F. and Calkan, B. Biomass processing in biofuel applications. In: *Biofuels for Fuel Cells: Biomass fermentation towards usage in fuel cells*, Lens, P., Westermann, P., Haberbauer M., and Moreno, A.; Eds., IWA Publishing, London, 2005, Ch. 4.

23. Erhan, E., Yer, E., Akay, G., Keskinler, B., and Keskinler, D., *J. Chem. Technol. Biotech.* **2004**, *79*, 195-206.
24. Akay, G., Bokhari, M.A., Byron, V.J., and Dogru, M. Development of nano-structured micro-porous materials and their application in bioprocess – chemical process intensification and tissue engineering. In: *Recent trends and developments in chemical engineering*, Galan, M. A. and Del Valle, E.M.; Eds., Wiley, London, 2005.
25. Wakeman, R.J., Bhumgara, Z.G., and Akay, G., *Chem. Eng. Journal*, **1998**, *70*, 133-141.
26. Williams, J.; Wroblewski, D.A. , *Langmuir*, **1988**, *4*, 656-662.
27. Akay, G., Bhumgara, Z., and Wakeman, R.J., *Chem. Eng. Res. Design*, **1995**, *73*, 782-797.
28. Cameron, N.R., Sherrington, D.C., Ando, I., and Kurosu, H., *J. Mater. Chem.*, **1996**, *6*, 719-726.
29. Haq, Z., Porous crosslinked absorbent polymeric materials, US Patent, 4536521 (1985).
30. Kucera, F., and Jancar, J., *Polym. Eng. Sci.*, **1998**, *38*, 783-792.
31. Banhart, J., *Progress in Materials Sci.*, **2001**, 559-632.
32. Sotiropoulos, S., Brown, I.J., Akay, G., and Lester, E., *Materials Letter*, **1998**, *35* , 383-391.
33. Brown, I.J., and Sotiropoulos, S. *J. Appl. Electrochem.*, **2001**, *31*, 1203-1212.

## Chapter 19

# New Catalytic Polymeric Membranes Incorporating Ti(IV) Trialkanolamines Complexes: Synthesis, Characterization, and Application in Catalysis

M. G. Buonomenna<sup>1,\*</sup>, E. Drioli<sup>1,2</sup>, G. Licini<sup>3,\*</sup>, and P. Scrimin<sup>3,4</sup>

<sup>1</sup>Department of Chemical Engineering and Materials, University  
of Calabria, I-87030 Arcavacata di Rende (CS), Italy

<sup>2</sup>Research Institute on Membrane Technology ITM-CNR c/o University  
of Calabria, I-87030 Arcavacata di Rende (CS), Italy

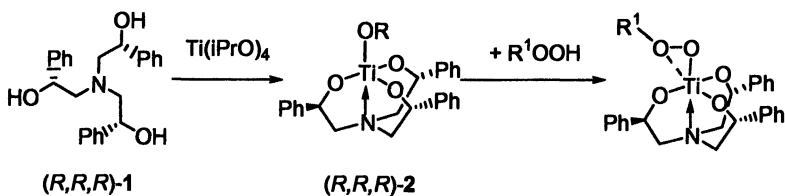
<sup>3</sup>Department of Chemical Science, University of Padua, I-35131,  
Padua, Italy

<sup>4</sup>Research Institute of Membrane Technology, ITM-CNR Padua Section,  
Padua, Italy

The incorporation of chiral homogenous catalyst, Ti(IV)/(R,R,R)-tris-(2-phenylethanol)amine, in polymeric membranes provided the first asymmetric catalytic Ti(IV)-based membranes, stable and efficient as heterogeneous catalysts for stereoselective sulfoxidations and chemoselective oxidations of secondary amines to nitrones by alkyl hydroperoxides. Polyvinylidene fluoride (PVDF) -based catalytic membranes gave the best results affording products in short reaction times, high yields and high selectivity using as little as 1% of catalyst, comparable with the performances of the corresponding homogeneous system. The PVDF-Ti stability is reasonably good and catalyst activity increases with no loss of selectivity in the subsequent uses of the same membrane.

Chemical processes catalysed by homogeneous transition metal complexes are of critical importance for fine and basic chemical industry. The majority of such metal catalysts are very often rather expensive, they are scarcely environmental compatible or even toxic. The current trend towards a sustainable chemistry has given life to a continuously increasing number of new strategies for catalyst immobilization, enabling an easy recovery, re-use and disposal at low costs of the catalyst<sup>1</sup>, even if this is usually associated with decreased selectivity and lower chemical yields. A possible solution to the problem could be the development of catalytic polymeric membranes, in which a Process Intensification Strategy<sup>2</sup> can be applied: no catalyst recovery is required, catalysts have longer life and the intact structure of the catalyst should be preserved inside the polymeric membranes, providing no loss of activity and selectivity. As a proof of principle, Ru-BINAP,<sup>3</sup> Rh-DUPHOS and Jacobsen catalyst<sup>4</sup> for epoxidation of simple olefins<sup>3</sup> were entrapped in polydimethylsiloxane matrices affording performances comparable to the analogous homogeneous systems.<sup>5</sup> As far as oxygen transfer catalysis is concerned, the Sharpless-Katsuki epoxidation system<sup>6</sup> launched the rich field of titanium catalyzed asymmetric oxidations.<sup>7</sup> Since that breakthrough, chiral Ti(IV) alkoxides have been used to catalyze a variety of oxidative transformations affording highly stereoselective processes in the allylic alcohol epoxidation,<sup>6</sup>  $\beta$ -hydroxyamine N-oxidation<sup>8</sup> sulfoxidation,<sup>9</sup> as well as in the Baeyer-Villiger oxidation of cyclobutanones.<sup>10</sup>

We have recently reported that tetradentate alkoxide ligands, namely C<sub>3</sub>-symmetric trialkanolamines 1, provide very stable titanium(IV) complexes (Scheme 1).<sup>11</sup>



*Scheme 1. Synthesis of titanatrane complex (R,R,R)-2 and the corresponding peroxocomplex (R,R,R)-3 by reaction of (R,R,R)-tris-(2-phenylethanol)amine 1 with Ti(iPrO)<sub>4</sub>.*

In the presence of alkyl hydroperoxides, such species are able to catalyze the asymmetric sulfoxidation of alkyl aryl sulfides with ee's up to 84% and with

unprecedented catalytic efficiency, reaching 1000 turnover numbers (TON)<sup>12</sup> and the oxidation of secondary amines to nitrones with high chemoselectivities, quantitative yields and TON up to 1400.<sup>13</sup>

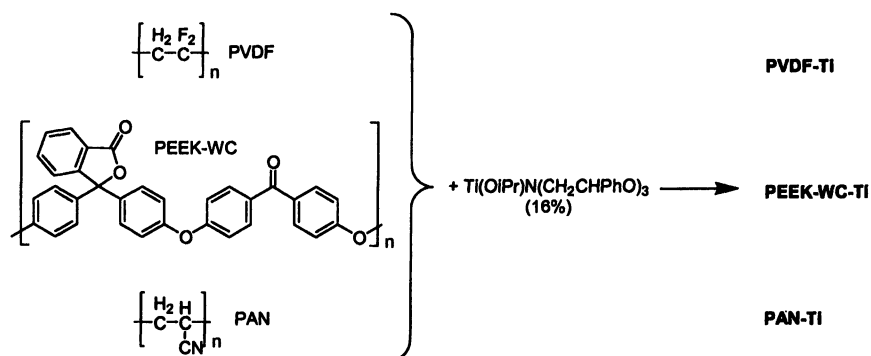
Beside the fact that the oxygen transfer process affords in both cases the corresponding products with high chemical yields and good selectivities, the Ti(IV) catalyst showed to be rather robust under the reaction conditions, which require the presence of large quantities of alkylperoxide<sup>12</sup> and, in the case of secondary amine oxidation, affords stoichiometric amount of water.<sup>13</sup> The structure in solution of the Ti(IV) catalyst **2** and of the corresponding peroxy active species **3** has been elucidated via the combined use of <sup>1</sup>H NMR and mass spectrometry.<sup>14</sup> They consist of stable titanatrane units in which the apical alkoxy ligand can easily exchange with other hydroxyl derivatives present in solution (for example iso-propanol, alkyl hydroperoxides or the trialkanolamine itself). In the presence of an excess of alkyl hydroperoxide they afford quantitatively the monomeric peroxycomplex **3**, which is the active species in the oxygen transfer process.<sup>14</sup>

For all these reasons, titanatrane complexes **2** seemed to us good candidates for preparing Ti(IV) polymeric catalytic membranes to be used in selective oxygen transfer reactions. In fact the catalysts should be robust enough to survive the conditions required for membrane preparation. Once in the polymeric matrix, their stability should improve because of minimized secondary hydrolysis reactions and therefore extending the life of the catalysts. Obviously, the recycling of the catalytic membrane will increase the total TON of the process. Here we report on the preparation and characterization of different catalytic membranes incorporating Ti(IV)/(R,R,R)-tris(2-phenylethanolamine)-**2** and their application for heterogeneous oxidation of a model sulfide, benzyl phenyl sulfide, and a model secondary amine, dibenzyl amine.

### Catalytic Membranes Synthesis and Characterization

The preformed Ti(IV) (R,R,R)-tris(2-ethanol)amine complex<sup>11</sup> (16%/w) has been entrapped in different polymeric membranes using a phase inversion

technique induced by a nonsolvent: DMA and water were respectively employed as solvent and nonsolvent. Three polymers, all characterized by a high thermal, chemical and mechanical stability, were used for the preparation of catalytic membranes: polyvinylidene difluoride (PVDF),<sup>15</sup> a modified polyether-etherketone (PEEKWC)<sup>16</sup> and polyacrylonitrile (PAN)<sup>17</sup> (Scheme 2).

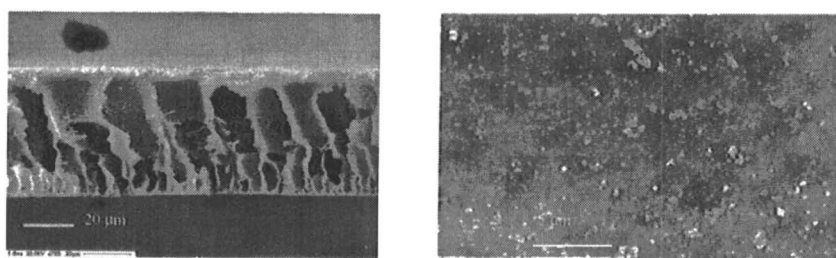


**Scheme 2. Synthesis and structural unit of polymeric membranes incorporating Ti(IV) complex.**

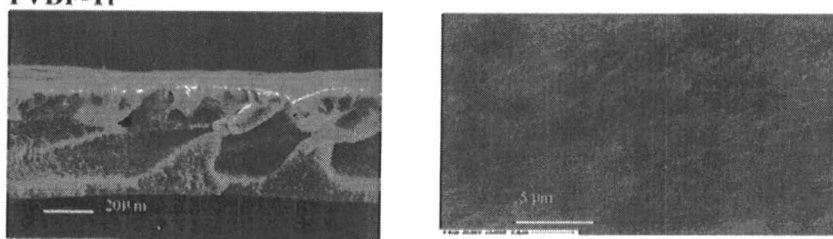
The top surfaces and the cross section morphology of the membranes have been examined by scanning electron microscopy (SEM). According to the synthetic procedure, in all the cases the catalyst embedding results in the formation of asymmetric hybrid membranes (Figure 1).

SEM analysis shows a strong difference in the membrane morphology by changing the polymer in the casting solution. Figure 1 shows that the morphology of membranes varies from porous finger-like with elongated macrovoids for PEEKWC-Ti and highly asymmetric structure with a dense skin layer for PVDF-Ti to an asymmetric dense for PAN-Ti. A smooth surface for PEEKWC-Ti and PVDF-Ti membranes is obtained whereas a large number of small pores is observed on the top surface of PAN-Ti membrane.

PEEKWC-Ti



PVDF-Ti



PAN-Ti

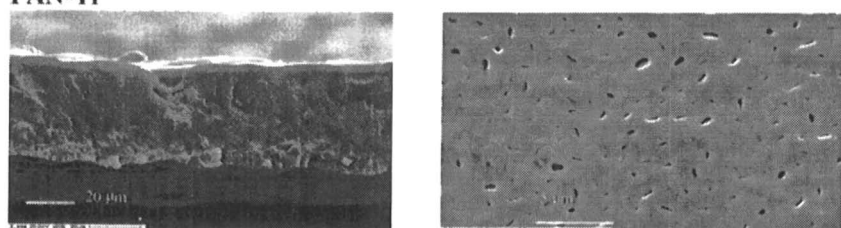
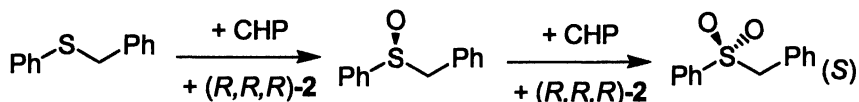


Figure 1. Cross sections (left) and top surface (right) morphology of the catalytic membranes, examined by scanning electron microscopy (SEM)

## Catalytic Membrane Reactivity

The screening of activity of the different catalytic membranes [PVDF-Ti, PEEKWC-Ti, PAN-Ti] has been assessed in the oxidation of benzyl phenyl sulfide and dibenzylamine, chosen as model substrates. The membrane performances were investigated under batch conditions using an equal active surface and comparable amount of total catalyst loading. In order to have a better comparison of the results, the reactions were carried out under the best conditions selected for the homogeneous reactions. Due to the solubility of PEEKWC in chlorinated solvents (chloroform or 1,2-dichloroethane, DCE), which are the most suitable ones for the homogeneous reactions, the reactivity as been also explored in acetonitrile.

Initially the reactivity of the catalytic membranes has been tested in the sulfoxidation reaction in order to have also indirect evidence on the nature of the catalyst and active species embedded in the different membranes (Scheme 3).



*Scheme 3. Stereoselective oxidation of benzyl phenyl sulfide by cumyl hydroperoxide (CHP) catalyzed by Ti(IV) complex (R,R,R)-2.*

Chiral sulfoxides are an important class of compounds that find increasing applications as chiral auxiliaries in asymmetric synthesis<sup>18</sup> and recently as biological active molecules.<sup>19</sup>

Preliminary tests on the catalytic membranes indicated that catalyst leaching was not a severe problem. In fact, after washing the membrane one-two times with the solvent of the reaction, no significant amount of catalyst or free trialkanolamine ligand could be detected anymore in solution via <sup>1</sup>H NMR.

In the sulfoxidation reaction, due to the occurrence of two cooperative stereoselective processes, i.e. the asymmetric oxidation of the sulfide and the subsequent kinetic resolution for the over oxidation of sulfone, the enantiopurity of the sulfoxide increases during the course of the reaction.

In Table 1 the results obtained with PVDF-Ti and PEEKWC-Ti are reported, together with the one obtained under homogeneous conditions.

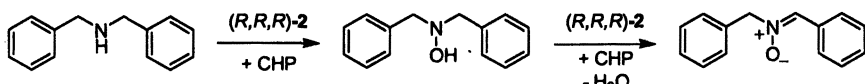
**Table I. Oxidation of benzyl phenyl sulfide with CHP catalyzed by Ti(IV) complexes.<sup>a</sup>**

#	Catalyst	Solvent	Time, h	Conversion, %	SO:SO <sub>2</sub>	e.e. (S) %
1	Ti(IV)-2	DCE	4	94	56:44	69
2	PVDF-Ti	DCE	5	93	59:41	67
3	Ti(IV)-2	CH <sub>3</sub> CN	1	15	90:10	44
4	PEEKWC-Ti	CH <sub>3</sub> CN	100	8	100:0	40

a. Reaction conditions: [Substrate]<sub>0</sub>=0.1M; [CHP]<sub>0</sub>= 0.1 M, [catalyst]= 0.01 M, T= 0°C.

It is noteworthy that in both cases the catalytic membranes were able to activate CHP and (S)-benzyl phenyl sulfoxide was produced with stereoselectivities comparable to the homogeneous systems, even if reactivities are rather diverse. Despite the fact that reactions in DCE are intrinsically faster than in CH<sub>3</sub>CN, PVDF-Ti catalytic membrane (Table I, entry 2) undoubtedly gave the best results affording high conversions into products with e.e.'s comparable to the homogeneous system (Table I, entry 1). On the other hand, PEEKWC-Ti afforded only the sulfoxide in much lower yields (8%) and much longer reaction times (100 hr) (Table I, entry 3). These data seem to indicate that both membranes maintain catalyst integrity and that in the more hydrophobic membrane, PVDF-Ti, the reactivity of the system is not significantly depleted. The reactivity of the catalytic membranes has been also tested in the secondary amine oxidation to nitrones. Nitrones are versatile and valuable synthetic intermediates for the synthesis of heterocycles<sup>20</sup> and natural products<sup>21</sup> and they are also effective spin trap reagents.<sup>22</sup> They can be synthesized by oxidation of secondary amines or the corresponding hydroxylamines.<sup>23</sup> Quite often the oxidation reaction suffers from limited chemoselectivity such that a significant amount of hydroxylamine is recovered. With highly reactive nitrones, over-oxidation and hydrolysis can be significant problems.

The titanium alkoxide catalyst 2 is the first reported Ti-based catalyst effective for this reaction (Scheme 4).<sup>13</sup>



**Scheme 4. Chemoselective oxidation of dibenzyl amine by cumyl hydroperoxide (CHP) catalyzed by Ti(IV) complex (R,R,R)-2**

In the homogeneous reaction, the catalyst is protected from hydrolysis by co-produced water by the combined use of the tightly binding trialkanolamine

ligand and, eventually, the addition of molecular sieves. Therefore nitrones can be obtained in high yield (up to 98%) under homogeneous, anhydrous conditions in short reaction times (2-7 h) and good selectivity with as little as 1% catalyst.<sup>13</sup> The reactivity of the catalytic membranes has been tested in the oxidation of dibenzyl amine. Reactions have been carried out also in this case under the optimized conditions for the homogeneous catalyst and the course of the reactions has been monitored via <sup>1</sup>H NMR. In Figure 2 are reported the kinetic profiles for the nitrone formation in acetonitrile at 60°C obtained using the homogeneous catalyst, PVDF-Ti, PEEKWC-Ti and PAN-Ti catalytic membranes.

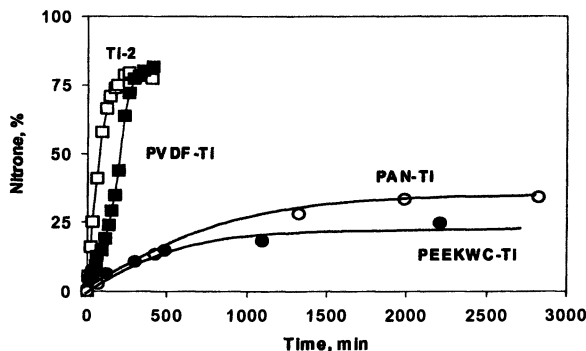


Figure 2. Nitrene formation in the oxidation of dibenzylamine with CHP catalyzed by Ti(IV) complexes:  $[Substrate]_0 = 0.1 M$ ;  $[CHP]_0 = 0.4 M$ ,  $[Catalyst] = 0.01 M$ ;  $CD_3CN$ ;  $T = 60^\circ C$ . , (□) homogeneous system, (■) PVDF-Ti, (○) PAN-Ti; (●) PEEKWC-Ti.

As in the previous case, all the three catalytic membranes were able to activate CHP for the oxygen transfer process but once again with rather different performances. Reactions performed with PAN-Ti and PEEKWC-Ti gave low and slow conversion of the reagent (30-40%) affording the nitrene in comparable amounts with N-benzylidene benzylamine and benzaldehyde (data not shown).

On the contrary, PVDF-Ti catalytic membrane efficiently catalyses the oxidation affording the nitrone in good yields (80%) and short reaction times, comparable to the ones of the homogeneous system.

The oxidation with catalytic membrane PVDF-Ti was also tested in chloroform. The comparison of the performances of the system in the two solvents is reported in Figure 3.

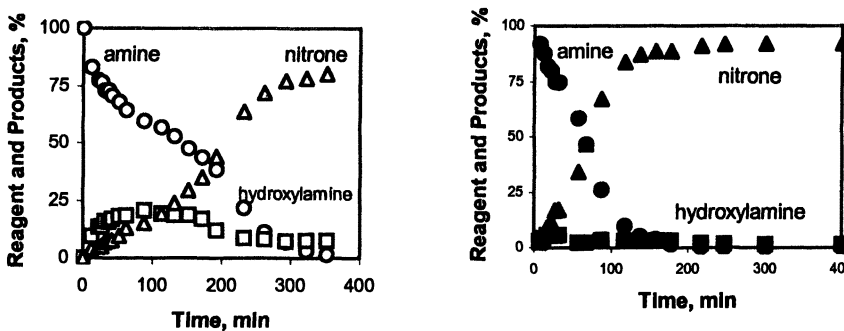


Figure 3. Oxidation of dibenzylamine with CHP catalyzed by PVDF-Ti catalytic membrane: [Substrate]<sub>0</sub> = 0.1 M; [CHP]<sub>0</sub> = 0.4 M, [Catalyst] = 0.01 M; T = 60°C, m.s. = 250 mg/mmol a. in CD<sub>3</sub>CN; (○) dibenzylamine, (□) hydroxylamine, (Δ) nitronate, and b. in CDCl<sub>3</sub> (◆) dibenzylamine, (■) hydroxylamine, (▲) nitronate.

In chloroform the reaction occurs even faster [t<sub>1/2</sub>(CDCl<sub>3</sub>) = 65 min vs t<sub>1/2</sub>(CH<sub>3</sub>CN) = 140 min] and the nitronate was recovered in higher chemical yield (92%) and almost complete chemoselectivity (only traces of imine and hydroxylamine were detected).

The performance of the PVDF-Ti catalytic membrane has been also evaluated on the basis of system recycling. A set of experiments was carried out in order to examine its activity along five oxidation runs. After each experiment the membrane was removed from the reaction vessel, washed in chloroform in order to remove adsorbed reagent or products, and recycled. The results are reported in Table III.

**Table III. Oxidation of dibenzylamine with CHP catalyzed by PVDF-Ti catalytic membrane, catalyst recycling<sup>a</sup>**

<i>RUN</i>	<i>Time</i> <sub>1/2</sub> , <i>min</i>	<i>Nitrone, %</i>
I	39	92
II	10	90
III	14	90
IV	14	90
V	23	90

a. Reaction conditions: [Substrate]<sub>0</sub>= 0.1M; [CHP]<sub>0</sub>=0.4 M, [Catalyst]= 0.01 M; T=60°C, CDCl<sub>3</sub>, m.s.= 250 mg/mmol in run 1, 500 mg/mmol runs 2-5.

**Table IV. Effect of substrate/catalyst ratio on oxidation of dibenzylamine catalyzed by PVDF-Ti membrane or the homogeneous catalyst Ti(IV)-2 in CDCl<sub>3</sub> at 60°C.<sup>a</sup>**

<i>[Sub]</i> <sub>0</sub> , <i>M</i>	<i>Sub/Cat</i>	<i>Catalyst</i>	<i>Time</i> ,	<i>Nitrone %</i>
			<i>h</i>	
0,1	10:1	PVDF-Ti	3	100
		Ti(IV)-2 <sup>b</sup>	2.5	100
1	100:1	PVDF-Ti	3	90
		Ti(IV)-2 <sup>b</sup>	1	100
1	1000:1	PVDF-Ti	71	65 <sup>d</sup>
		Ti(IV)-2 <sup>b</sup>	100	68 <sup>e</sup>

a. Reaction conditions: [catalyst]= 0.01 M, dibenzylamine, CHP (4 equiv) and 4A molecular sieves in CDCl<sub>3</sub> at 60 °C., b. see ref. 13. c. complete reagent conversion; other products: *N*-benzylidene benzylamine (15%), PhCHO (15%). d. complete reagent conversion; other products: *N*-benzylidene benzylamine (10%), PhCHO (22%).

It is noteworthy that the catalytic activity of the PVDF-Ti membrane was maintained for all five runs, affording comparable yields in nitrone (90%). Interestingly, reaction rates in all five runs were higher than the first one: highly functional surfaces result from changes in surface properties that make the system more efficient, more effective in agreement with the Process Intensification strategy. The increased reactivity could originate from modifications of the polymeric membrane that render available a larger quantity of the catalyst or enhance the Lewis acidity of the metal complex. This important aspect will be addressed in future studies.

The catalytic activity of the PVDF-Ti catalytic membrane was also tested. Different dibenzylamine oxidation reactions were carried out increasing substrate/catalyst ratios from 10:1 to 1000:1 (table IV).

The results reported in Table IV show that complete conversion of dibenzylamine and >90% selectivity for the nitrone could be achieved also in the presence of 1% of catalyst. It is noteworthy that, in order to maintain the catalyst concentration at 0.01M, these reactions were performed neat. However, further increasing the ratio to s/c = 1000 (which necessarily dropped the catalyst concentration to 0.001M) resulted in a severe deterioration of chemoselectivity, in analogy with what observed also in the homogeneous system.<sup>13</sup>

## Conclusions

Novel heterogeneous oxidation catalysts have been synthesized by embedding Ti(IV)/trialkanolamine complexes within polymeric membranes. The characterization of the catalytic membranes and the reactivity studies allowed to: (i) identify the PVDF-W1-Ti catalytic membrane as the best system where the catalyst structure is preserved from hydrolysis; (ii) exclude the occurrence of competing homogeneous pathways; (iii) verify the stability of the embedded catalyst during recycling. The heterogeneous oxidation of sulfides and secondary amines proceeds completely in comparable times with the homogeneous system, yielding sulfoxides and nitrones, highly valuable synthetic products, with high selectivity. Further research work will be focused to a better understanding of the membrane-based catalyst orientation in order to improve the synthetic potential of the methodology.

## References

- <sup>1</sup> Kirschning, A.; Monenschein, H.; Wittenberg, R. *Angew. Chem. Int. Ed.* **2001**, *40*, 650.
- <sup>2</sup> Stankiewicz, A.; Moulijn, J.A. *Chem. Eng. Prog.* **2000**, *96*, 22.
- <sup>3</sup> Vankelecom, I.F-J. and Jacobs, P.A. *Cat. Today* **2000**, *56*, 147.
- <sup>4</sup> Neys, P. E. F.; Severeyns, A.; Vankelecom, I. F. J.; Ceulemans, E.; Dehaen, W.; Jacobs, P.A. *J. Mol. Catal. A* **1999**, *144*, 373.
- <sup>5</sup> Vankelecom, I. F. J. *Chem. Rev.* **2002**, *102*, 3779.
- <sup>6</sup> Gao, Y.; Hanson, R. M.; Klunder, J. M.; Ko, S. Y.; Masamune, H.; Sharpless, K. B. *J. Am. Chem. Soc.* **1987**, *109*, 5765; Johnson, R. A.; Sharpless, K. B. *Catalytic Asymmetric Epoxidation of Allylic Alcohols in Catalytic Asymmetric Synthesis, Second Edition*; pp. 231-285, Ojima, I., Wiley-VCH Publisher: New York, **2000** and references therein.
- <sup>7</sup> Ojima, I. *Catalytic Asymmetric Synthesis, Second Edition*; Wiley-VCH Publisher: New York, **2000**.
- <sup>8</sup> Miyano, S.; Lu, L. D.-L.; Viti, S. M.; Sharpless, K. B. *J. Org. Chem.* **1983**, *48*, 3608.
- <sup>9</sup> Kagan, H.B, *Asymmetric Oxidation of Sulfides*, in *Catalytic Asymmetric Synthesis, Second Edition*; pp. 327-356, Ojima, I., Wiley-VCH Publisher: New York, **2000** and references therein.
- <sup>10</sup> Lopp, M.; Payn, A.; Kanger, T.; Pehk, T. *Tetrahedron Lett.* **1996**, *37*, 7583.
- <sup>11</sup> Di Furia, F.; Licini, G.; Modena, G.; Motterle, R.; Nugent, W. A. *J. Org. Chem.* **1996**, *61*, 5175.
- <sup>12</sup> Licini, G.; Bonchio, M.; Modena, G.; Nugent, W.A. *Pure Appl. Chem.* **1999**, *71*, 463.
- <sup>13</sup> Forcato, M.; Nugent, W.A.; Licini, G. *Tetrahedron Lett.* **2003**, *44*, 49.
- <sup>14</sup> Bonchio, M.; Licini, G.; Modena, G.; Bortolini, O.; Moro, S.; Nugent, W.A. *J. Am. Chem. Soc.* **1999**, *121*, 6258.
- <sup>15</sup> Bottino A.; Camera Roda G.; Capannelli G. and Munari, S., *J. Membr. Sci.* **1991**, *57*, 1.
- <sup>16</sup> Buonomenna, M.G.; Figoli, A.; Jansen, J.C. and Drioli E. *J. App. Polym. Sci.* **2004**, *92*, 576.
- <sup>17</sup> Khayet, M.; Feng, C.Y.; Khulbe, K.C.; Matsuura, *Polymer* **2002**, *43*, 3879.
- <sup>18</sup> Carreno, M. C. *Chem. Rev.* **1995**, *95*, 1717.
- <sup>19</sup> Pichen, P. *Asymmetric Synthesis of Sulfoxides: Two Case Studies in Chirality in Industry II*, Collins, A.N.; Sheldrake, G.N.; Crosby, J. Eds. Pp 381-390,

Wiley, New York, 1997. Blaser, H.U.; Spindler, F.; Studer, M. *Applied Catalysis A: General* **2001**, *221*, 119.

<sup>20</sup> Gothelf, K. V.; Jørgensen, K. A. *Chem. Rev.* **1998**, *98*, 863.

<sup>21</sup> Bloch, R. *Chem. Rev.* **1998**, *98*, 1407.

<sup>22</sup> Tanner, D. D. *Advances in Free Radical Chemistry*, JAI Press: Greenwich, CT, 1990.

<sup>23</sup> Murahashi, S.-I. *Angew. Ch. Int. Ed. Engl.* **1995**, *34*, 2443.

## Chapter 20

# Enhancement of Micromixing Tees Using Ultrasound Energy

L. Zeng and J. Palmer\*

Chemical Engineering Program, Louisiana Tech University,  
Ruston, LA 71272

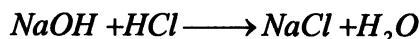
Microfluidic opposed mixing tees were tested with hydraulic diameters of 100  $\mu\text{m}$ , 177  $\mu\text{m}$ , and 254  $\mu\text{m}$ . Mixing performance was characterized by feeding one stream with hydrochloric acid and another stream with sodium hydroxide and dimethoxypropane. Under ideal mixing conditions, the instantaneous neutralization of sodium hydroxide with hydrochloric acid would prevent the catalytic hydrolysis of dimethoxypropane. Therefore, higher conversions of dimethoxypropane in this fast, competitive reaction is an indication of lower mixing performance. For a constant Reynolds Number, the mixing performance was increased by decreasing the channel dimensions. Ultrasound energy was externally applied to all three reactors and was found to increase mixing performance. Challenges in sealing the 100  $\mu\text{m}$  mixer precluded operation at comparable pressures achieved with the 177 and 254  $\mu\text{m}$  mixers. The highest mixing performance was observed with the 177  $\mu\text{m}$  diameter mixer using a combination of pump work and ultrasound energy. A combination of ultrasound energy and pump work was demonstrated to be the most efficient mode of providing mixing for the 254  $\mu\text{m}$  system. Therefore, externally applied ultrasound energy can be an effective and efficient means of improving the mixing performance of microfluidic systems.

## Introduction

Chemical reactors operating with homogeneous, liquid phases must begin with the mixing of two fluids. The product distribution of fast reactions with competitive pathways can be influenced by the intensity of this initial mixing (1). Reactions with half-lives of  $10^3$  to  $10^6$  seconds are considered sufficiently rapid to warrant special consideration. Researchers (2-6) have studied the effects of mixing on fast, competitive reactions in conventional scale reactors. In recent years, researchers have explored the use of microfluidic devices for synthesis. Microfluidic devices present unique challenges to mixing due to the predominance of laminar flow regimes within these structures. Ehrfeld *et al.* (7) authored a text describing a number of mixing strategies that have been tried on the microscale. Hessel, *et al.* (8) recent text provides many new designs along with applications and design equations of many of the previous approaches. One common approach is to minimize the thickness of the two contacting streams. These and other designs rely on the geometry of the microchannel to facilitate a passive mixing process. The research of utilizing externally applied energy to create an active micromixer has been limited to date. Active mixing devices have been demonstrated in microfluidics operating at very low Reynolds Numbers (9, 10). The microfluidics operating at low Reynolds Numbers are applicable to analytical sample preparation, process development, and catalyst/drug discovery; applications that seek to extract the maximum information from the minimum amount of sample. However, for synthesis, much higher flow-rates and therefore Reynolds Number can be achieved. The application of external energy to enhance the performance of a fast, competitive reaction in a device operating at a relatively high Reynolds Number has not been explored.

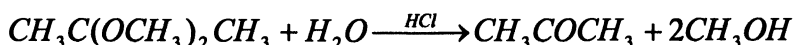
Ultrasound energy is a method that has been utilized to increase the performance of both continuous (11) and semi-batch (12) conventional sized reactors. Monnier *et al.* (13) investigated ultrasound enhanced micromixing in a 50 ml flow cell. Yang *et al.* (14) presented the integration of a piezoelectric material in a microfluidic mixer. The mixing chamber was 6000  $\mu\text{m}$  long, 6000  $\mu\text{m}$  wide, and 60  $\mu\text{m}$  deep. The mixing time as measured by imaging the mixing of water with a fluorescent dye was estimated to be 2 s. In this study, ultrasound energy will be applied to a microfluidic mixing tee operating at relatively high Reynolds Numbers to enhance the mixing performance for fast, competitive reactions.

A number of model reactions have been discussed in the literature for characterization of mixing performance (15-18). The fast, competitive reaction utilizing dimethoxypropane and presented previously by Walker (19) was the reaction employed to characterize mixing performance in this study. In this system, a solution of dimethoxypropane, sodium hydroxide, ethanol, and water is mixed with a solution of hydrochloric acid, ethanol, and water. The two competing reactions are the very fast hydrolysis of dimethoxypropane catalyzed by hydrochloric acid, and the near instantaneous neutralization of hydrochloric acid with the sodium hydroxide. The hydrolysis products of dimethoxypropane is acetone and methanol. Therefore, the conversion of dimethoxypropane to methanol and acetone is inversely proportional to the mixing performance of a given device.



Reaction A – Fast

$k = 1.3 \times 10^{11} \text{ m}^3/\text{kmol s}$  @25°C



Reaction B – Slow

$k = 700 \text{ m}^3/\text{kmol s}$  @25°C

## Experimental

The following chemicals were obtained from Aldrich chemical and used without further purification: 2,2-dimethoxypropane, 98%; ethyl alcohol, absolute, 200 proof reagent grade; sodium hydroxide pellets, 97+% reagent grade; hydrochloric acid, 37% reagent grade; sodium chloride, 99+% reagent grade. Type 1 Reagent Grade Water (RGW) was obtained using a Barnstead Series 1090 E-Pure reverse osmosis purifier and was utilized for all experiments.

A Hewlett Packard 5890 Series II gas chromatograph with a 30 m HP-FFAP column and a flame ionization detector was employed to determine the concentration of the resulting methanol and therefore determine the conversion of the reaction. A lower conversion of dimethoxypropane was an indication of

higher mixing performance. Ethanol was present in both solutions at a constant concentration of 25 weight percent for solvation of the dimethoxypropane and for use as an internal standard to measure the extent of reaction of dimethoxypropane.

The two reactants were fed into an opposed mixing tee at equal mass flow-rates. Table I depicts the composition of the two feed streams. The 5% molar excess of sodium hydroxide was necessary to ensure complete neutralization of the hydrochloric acid after the mixing of the streams. The catalytic hydrolysis of dimethoxypropane requires that no residual quantities of hydrochloric acid are present after the mixing of the two streams, otherwise the performance of the mixing environment would not be measured.

**Table I – Concentrations of reactants in aqueous solutions, balance of solution is Type 1, Reagent Grade Water**

<b>Component</b>	<b>Mass Fraction</b>	<b>Molar Concentration (gmol/m<sup>3</sup>)</b>
Feed 1		
Dimethoxypropane	0.07	648
Ethanol	0.25	
Sodium hydroxide	0.028	680
Sodium chloride	0.0197	324
Feed 2		
Hydrochloric acid	0.0237	648
Ethanol	0.25	

Figure 1 depicts the complete experimental apparatus. A Lab Alliance Series III pump with a PEEK head was used to feed in each reactant into the mixing tee. Three Ohaus Explorer balances with a resolution of 10 mg were used to measure the mass of each reactant feed solutions and the product to ensure that the proper mass flow of each stream had been achieved. Ultrasound energy was provided by a Sonics VC-750 processor operating at 20 kHz. Three sizes of mixing tees were tested in this study. The 127  $\mu\text{m}$  and 254  $\mu\text{m}$  mixers were commercially available tees with circular dimensions and had the same dimensions for both inlets and outlet streams. A third mixing tee was produced at Louisiana Tech in silicon to achieve smaller internal dimensions. The anisotropic etching in silicon resulted in rectangular dimensions.

The energy required by the Sonics VC-750 processor to maintain a 20 KHz ultrasound is displayed by the instrument. Ultrasound energy measurements were performed on reactors with and without liquid flow. The ultrasound energy reported in this article is the difference of the energy observed for the flow and no flow conditions to account for inductive losses by the probe to the device. Figure 2 and figure 3 depict the position of the ultrasound probe in relation to the 254  $\mu\text{m}$  and 100  $\mu\text{m}$  mixers respectively.

The silicon micomixers were fabricated on 4 inch diameter, 550  $\mu\text{m}$  thick double side polished  $<110>$  wafers coated with 2.5  $\mu\text{m}$   $\text{SiO}_2$ . The pattern was transferred from a chrome mask using a EV 420 mask aligner. A Buffered Oxide Etch was used to remove the  $\text{SiO}_2$  layer, and an Alctel A601 E Inductive Coupling Plasma etched the silicon using the Bosch process. The silicon microchannels were sealed by anodically bonding borosilicate glass to the top surface. The silicon mixer was placed into a Teflon holder to allow an interface with the fluidic connections and provide mechanical support to the borosilicate glass cap. The depth of the entire mixing tee was 100  $\mu\text{m}$ . The width of both inlet portions of the mixer was 33  $\mu\text{m}$  wide while the product outlet was 100  $\mu\text{m}$  wide. The channel widths were chosen to maintain a constant Reynolds Number between each inlet channel and the combined outlet channel. This was achieved because as the volumetric flow-rate doubled in the outlet channel, the hydraulic diameter of the outlet channel was also doubled. Neglecting the volume change of mixing of the two fluids and any differences in density and viscosity, maintaining a constant ratio of volumetric flow-rate to hydraulic diameter will result in a constant Reynolds Number. The outlet channel was 3 cm long while each inlet was 0.5 cm long. The length of the outlet was chosen to ensure complete conversion of the slow reaction at the flow rates of interest.

## Discussion of Results

As stated above, a decrease in conversion in dimethoxypropane is an indicator of improved mixing performance. Figure 4 depicts the trend that as the Reynolds Number for each of the 127  $\mu\text{m}$  and 254  $\mu\text{m}$  mixing tee's was increased, the mixing performance increased. The 100  $\mu\text{m}$  silicon mixer encountered challenges in sealing at the higher pressures, precluding the large variation in Reynolds Number tested for the previous two mixers. For a given Reynolds Number, the mixing performance increased as the diameter of channel inside the mixing tee was reduced.

The pressure of the two feed streams was measured using a gauge integral to each pump. Pulsations from the positive displacement pump were minimized



*Figure 1. Experimental setup. (See page 3 of color insert.)*

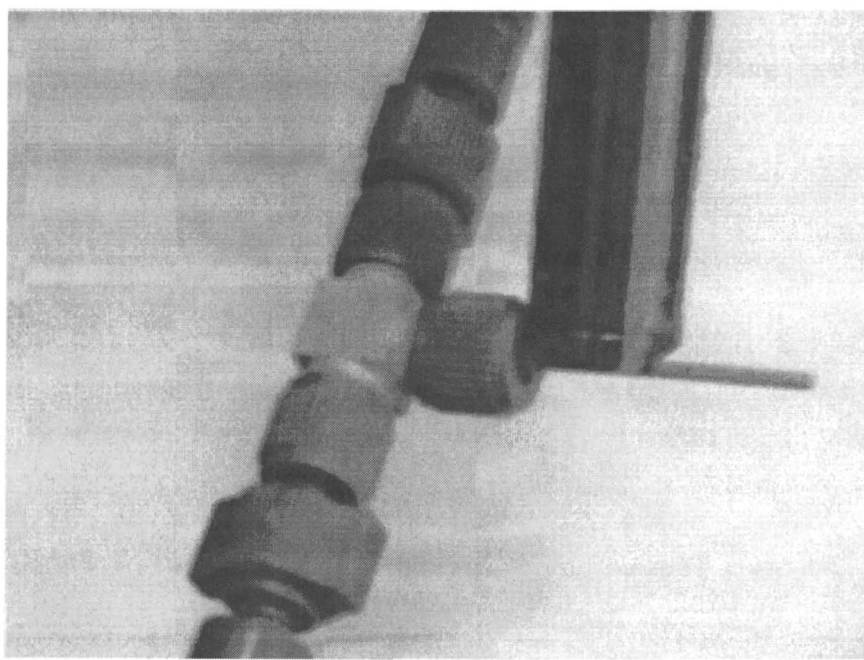


*Figure 2. Ultrasound generator touching 254  $\mu\text{m}$  mixing tee.  
(See page 4 of color insert.)*

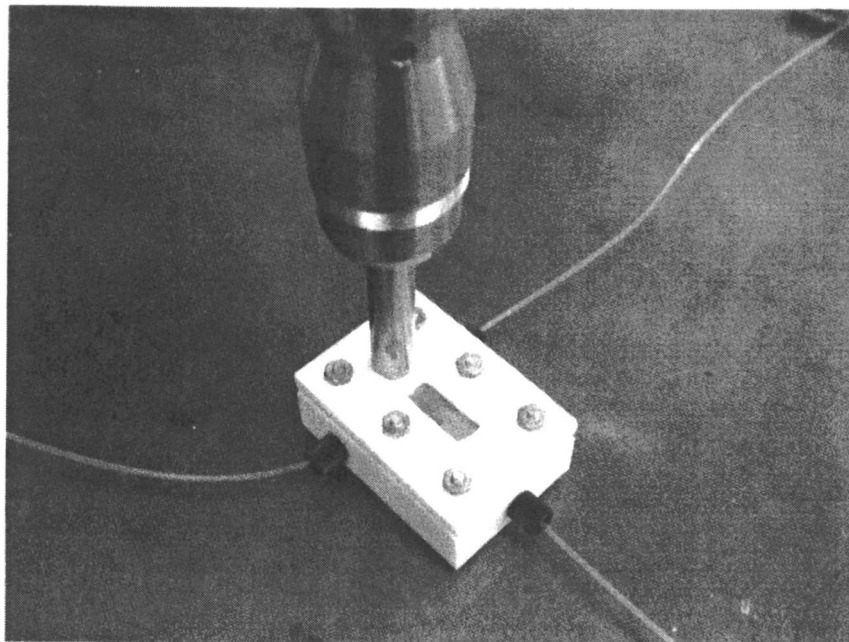


*Figure 3. Ultrasound generator touching 100  $\mu\text{m}$  mixing tee.  
(See page 4 of color insert.)*

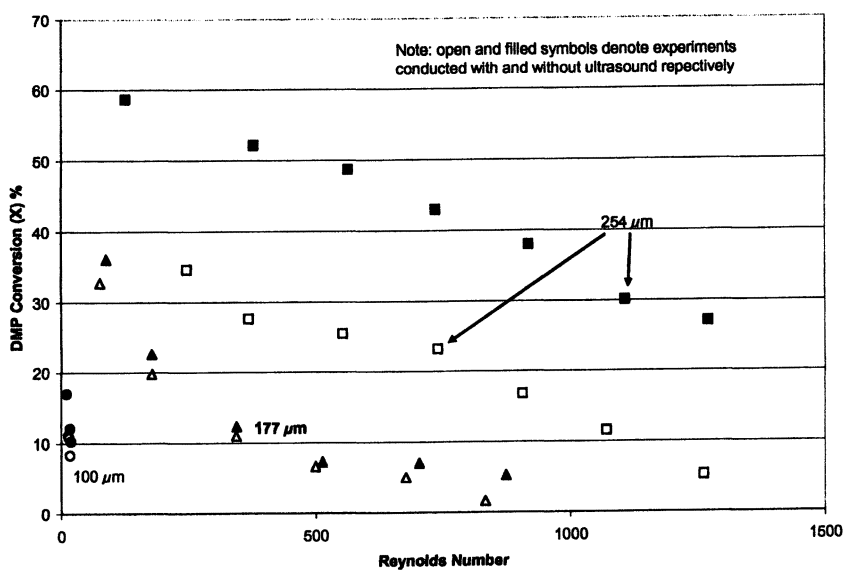


*Figure 4. Mixing Performance of 100, 177, and 254  $\mu\text{m}$  Micromixers as a Function of Reynolds Number.*

due to a diaphragm pulse damper that was part of the system. The pulse damper required pressure above approximately 100 psia before uniform pressures could be obtained. Unfortunately, the 100  $\mu\text{m}$  silicon mixer could not be operated above these pressures due to leaks. Therefore, the pressure data from the 100  $\mu\text{m}$  silicon mixer are suspect and not presented in the following analysis of system energy. Improvements are being implemented to allow operation of much higher pressures in the silicon microchannel.

The total power input into the system was calculated for all experiments considering both ultrasound and pump work. The pump work delivered to the fluid was calculated from the inlet pressure and mass flow-rate of each microchannel feed streams. The experimental section describes how the ultrasound energy delivered to the fluid was measured. Figure 5 depicts the total system power of all three micromixers tested. As in the previous figure, the open and filled symbols denote experiments with and without ultrasound energy respectively.

The 177  $\mu\text{m}$  without ultrasound energy showed a dramatic increase in performance with the initial increases in system power. The increase in power is due to higher flow-rates and therefore higher pressure drops. The lowest conversion for this system was approximately 8%. The addition of ultrasound energy provided a step change in energy fed to the system. 3 Watts of power was fed to the system without substantial gains in performance. However, the additional energy input by the ultrasound was able to improve the performance of the 177  $\mu\text{m}$  reactor at the highest flow-rate tested to produce the highest level of mixing observed in this study. 4% conversion was observed at this highest flow-rate combined with ultrasound energy. Figure 6 depicts the specific work for the 177  $\mu\text{m}$  mixer. With the non-ultrasound experiments, the specific work increased as the pressure and therefore flow-rate was increased. The reverse slope of the ultrasound experiments is indicative of the large amount of energy provided into the mixer from the ultrasound generator. As the flow-rate was increased, the specific work decreased because the homogenizer made up the large majority of the energy into the system and that energy was now being distributed over a larger amount of mass. From the specific work, it is clear that much more energy was being delivered to the mixer than was effectively utilized by the fluid. Increasing the proportion of fluid in the channels by operating several mixers in parallel in a single mixer would likely have increased the efficient utilization of ultrasonic energy.

The 254  $\mu\text{m}$  mixer exhibited the worst performance of the three mixers tested. This low performance is evident from Figure 5 depicting total power input into the system. As stated above, low power in Figure 5 was due to low flow-rates

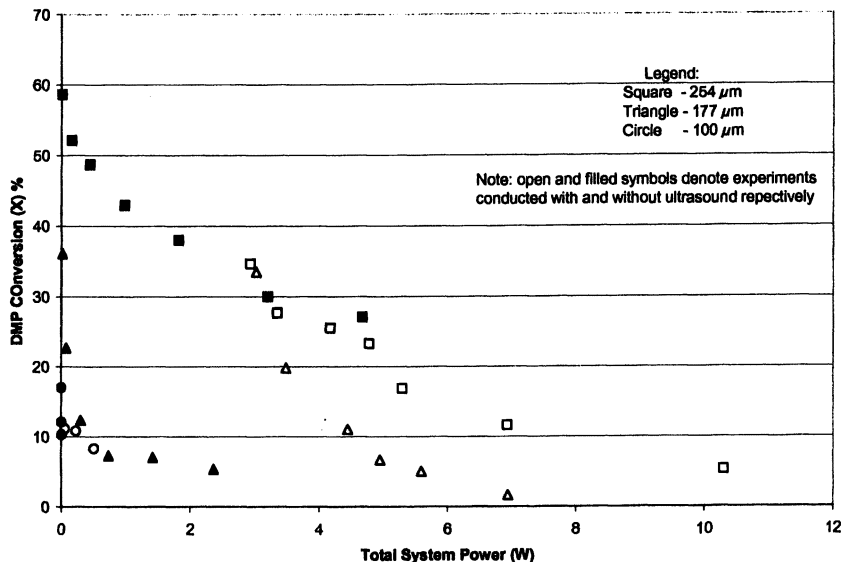


Figure 5. Mixing Performance of 100, 177, and 254  $\mu\text{m}$  Micromixers as a Function of Total System Power (Ultrasound Energy and Pressure Dissipation)

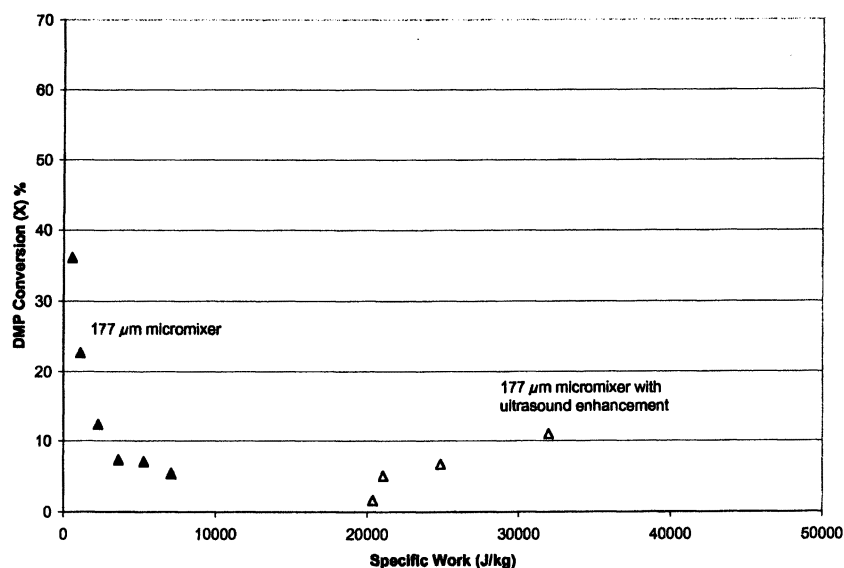


Figure 6. Mixing Performance of 177  $\mu\text{m}$  Micromixers as a Function of Specific Work.

and correspondingly low pressures generated by the system. The mixing performance of the 254  $\mu\text{m}$  system increased nearly linearly with a corresponding increase in system power. The specific work was most interesting for the 254  $\mu\text{m}$  mixer and is depicted in Figure 7. At a combined flow-rate of 8 g/min, the ultrasound enhanced mixer resulted in a conversion of only 35%, but resulted in a specific work of 22,000 J/kg. Experiments conducted without ultrasound at a combined flow-rate of 40 g/min resulted in a lower conversion of 27%. The pressure required for these two feeds was approximately 1050 psig, resulting in a specific work of 6,700 J/kg. Pump work, at least initially, provided a more efficient method of mixing versus the externally applied ultrasound energy. At total flow-rates above 10 g/min, the ultrasound experiments achieve system powers that are comparable to extrapolated performances of the experiments without ultrasound. The ultrasound energy allows mixing performance unachievable due to pressure drop constraints of the pumping system. Therefore, a combination of high-pressure and ultrasound results in the most efficient and effective combination for fast mixing.

Estimates of the mixing times can be calculated based on the literature kinetic rate constant and the concentrations of the dimethoxypropane and hydrochloric acid. Prior literature utilized the resultant concentration of dimethoxypropane and hydrochloric acid that would theoretically exist if the two feed streams combined with no reaction (20). Therefore, mixing times of 480  $\mu\text{s}$  were achieved with the 100  $\mu\text{m}$  system without ultrasound energy. As described above, pressure limitations of this system prevented operation at higher flow-rates that would have reduced this mixing time. The higher pressure allowed by the 177  $\mu\text{m}$  system allowed the mixing time without ultrasound energy to be reduced to 240  $\mu\text{s}$ . The addition of ultrasound energy further reduced the mixing time to 70  $\mu\text{s}$ . The 254  $\mu\text{m}$  system benefited the greatest from the ultrasound energy, with a reduction in mixing time from 1400 to 240  $\mu\text{s}$  as the ultrasound energy was added at the highest flow-rate tested.

## Conclusions

The mixing performance of the opposed mixing tees improved for a constant Reynolds Number as the channel dimension was decreased. An increased amount of pump work was required to maintain a constant Reynolds Number as the channel dimension was decreased. Limitations on the maximum pressure achievable by both the pump and the mixer preclude further increases in mixing performance through pump work. Ultrasound energy, even externally applied as in the manner of this study, is an effective means of adding additional work to the system and therefore promoting faster mixing. The application of ultrasonic

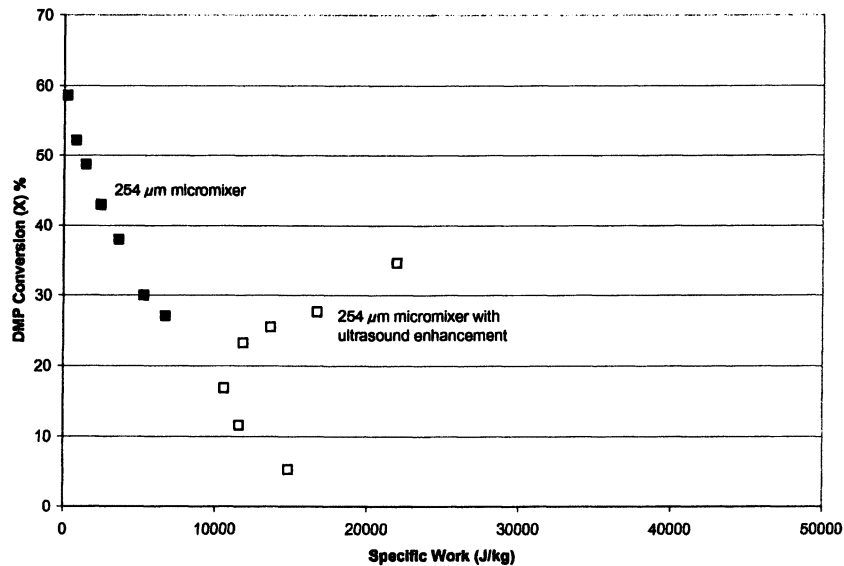


Figure 7. Mixing Efficiency of 254  $\mu\text{m}$  Micromixers as a Function of Specific Work.

energy to very small diameter channels may not be efficient on a per unit mass basis, but does provide the highest level of mixing performance. A combination of pump work and ultrasound energy was demonstrated to give the lowest specific work while maximizing mixing performance. Further studies on smaller diameters channels with suitable sealing to withstand high pressures and the ultrasound energy are ongoing.

### References

1. Levenspiel, O; *Chemical Reaction Engineering*, 2<sup>nd</sup> ed.; NY, New York, 1972.
2. Bourne, J.; Togvstiga, G.; *Chem. Eng. Res. Des.* 1988 vol 66, 26-32.
3. Baldyga, J.; Bourne, J.; *Chem. Eng. Sci.* 1990, vol 45, 907.
4. Bourne, J.; Yu, S.; *Ind. Eng. Chem.* 1994, vol 33, 41-55.

5. Baldyga , J.; Bourne, J.; Zimmerman, B.; *Chem. Eng. Sci.* 1994, *vol 49*, 1937-1946.
6. Knight, C.; Penny, W.; Fasano, J.; Presented at the 1995 AIChE Winter Annual Meeting, Miami Beach, FL, 1995.
7. Hessel, V.; Hardt, S.; Löwe, H. *Chemical Micro Process Engineering*, 1<sup>st</sup> ed.; Weinheim, Germany, 2004.
8. Ehrfeld, W.; Hessel, V.; Löwe, H. *Microreactors – New Technology for Modern Chemistry*, 1<sup>st</sup> ed.; Weinheim, Germany; 2000.
9. Lu, L.; Ryu, K.; Liu, C.; *J. Microelectromechanical Sys.* 2002, *vol 11*, 462-470.
10. Deshmukh, A., Liepmann, D., Pisano, A.; Proceedings of the 11<sup>th</sup> Internaional Conference on Solid State Sensors and Actuators, Munich, Germany, 2001, 950-953.
11. Okada, K; Fuseya, S.; Nishimura, Y.; Matsubara, M. *Chem. Eng. Sci.* 1972, *vol 27*, 529-535.
12. Monnier, H.; Wilhelm, A.M.; Delmas, H. *Chem. Eng. Sci.* 1999, *vol 54*, 2953-2961.
13. Monnier, H.; Wilhelm, A.M.; Delmas, H.; *Chem. Eng. Sci.* 2000, *vol 55*, 4009-4020.
14. Yang, Z.; Matsumoto, S.; Goto, H.; Matsumoto, M.; Maeda, R. *Sen. and Act. A* 2001, *vol 93*, 266-272.
15. Bourne, J.; Kozicki, F.; Rys, P.; *Chem. Eng. Sci.* 1981 *vol 36*, 1643-1648.
16. Bourne, J.; Kut, O.; Lenzner, J.; *Ind. Eng. Chem. Res.* 1992 *vol 31*, 949-958.
17. Fournier, M.; Falk, L.; Villermaux, J.; *Chem. Eng. Sci.* 1996 *vol 51* 5187-5192.
18. Guichardon, P.; Falk, L.; *Chem. Eng. Sci.* 2000 *vol 55*, 4233-4243.
19. Walker, B.; Doctoral Dissertation, Swiss Federal Institute of Technology, Zurich, Switzerland, 1996.
20. Johnson, B.; Prud'homme, R.; *AIChE Journal* 2003 *vol 49*, 2264-2282.

## Chapter 21

# Mixing Principles for Microstructured Mixers: Active and Passive Mixing

Volker Hessel<sup>†</sup> and Holger Löwe

Institut für Mikrotechnik Mainz GmbH, Carl-Zeiss-Str. 18–20,  
D–55129 Mainz, Germany

<sup>†</sup>Corresponding author: [hessel@imm-mainz.de](mailto:hessel@imm-mainz.de)

Microstructured mixers have two major application fields. They are used for mixing operations in the framework of conventional chemical processing as part of ordinary industrial field equipment, i.e. use of multi-scale technology. On the other hand, these tools may be integral part of miniaturised analytical devices like lab-on-a-chip. Mixing is here part of an entire microflow process and orients on a new means of analysis. These two application fields have totally different requirements on their devices: in the first case, capacities range from 1 l/h to several m<sup>3</sup>/h flow for watery systems. In contrast, analytical tests typically demand for consumption of minute sample volumes, which correspond to flows in the  $\mu$ l/h to ml/h range. Especially at such low flow velocities, the often applied pressure-driven or electroosmotic flow mixing, the so-called passive mixing, is not adequate. Here, active mixing principles which rely on external energy are better suited and may be used over periods of several minutes. Examples for both types of mixing principles are given below.

In the following, only the mixing of miscible fluids, mostly liquids, in microstructured mixers is considered. No reference is given to mixing of immiscible fluids generating multi-phase systems, i.e. to emulsification and foaming. In addition, only the mixing principles themselves and sometimes their design issues are explained. No details on the respective devices, their characterization and applications are given for reasons of limited space and consistency within this chapter. Here, selected major references provide further information.

### Active Mixing

#### Electrokinetic Instability Mixing

Fluctuating electric fields can be used for liquid mixing (1). This results in rapid stretching and folding of material lines or sheets, having a similar impact as stirring. Flow instability achieved by oscillating electroosmotic flows are referred to as electrokinetic instability (EKI) (1). A preferred type of oscillation of electric fields is to apply a sinus wave. EKI mixing does not rely on moving parts and is applicable for mixing flows at very low Reynolds number ( $\sim 1$ ).

Full-field images of the entire mixing chamber of an EKI mixer device, yielded by injection of a fluorescence tracer, prove that rapid stretching and folding is indeed given (1). Mixing times of about 2.5 s were deduced from time-resolved images showing the point when a randomly distribution of a fluorescence tracer is achieved (1).

Image power spectra provide further details on the EKI mixing. If no AC field is turned on, an unmixed state is given characterised by a slightly elongated frequency band (1) (see Fig. 1). This is indicative of higher spatial frequencies transverse to the interface and corresponds well to the initial horizontal orientation of the interface. Advective flux arises when EKI mixing is set on and leads to high spatial frequency gradients in the power spectra. New, undiffused fluid interface lengths occur. These high-frequency bands are damped in the final, mixed state, yielding thus isotropic power spectra indicative for good stirring.

The mixing times of the 1<sup>st</sup> generation EKI device were determined by analyzing the flow patterns via fluorescence imaging. After a period of 2 s, the flow becomes unstable and transverse velocities stretch and fold material lines in the flow (1). The initial seeded / unseeded interface becomes rapidly deformed. Finally after about 13 s, a random distribution of the tracer transverse to the applied AC field is achieved. EKI action is visible throughout the whole channel length of 7 mm. The mixing time of a 2<sup>nd</sup> generation EKI, being 2.5 s, is even superior to the performance of the prototype device.

#### Chaotic Electroosmotic Stirring Mixing

A temporal modulation by non-uniform  $\zeta$  potentials along a micro channel's walls can be achieved by superposition of electroosmotic flows. In this way, chaotic advection can be induced leading to a material transport similar to mixing by stirring (see Fig. 2) (2). Non-uniform  $\zeta$  potentials can be obtained by coating the channel's walls with different materials or by using differ-

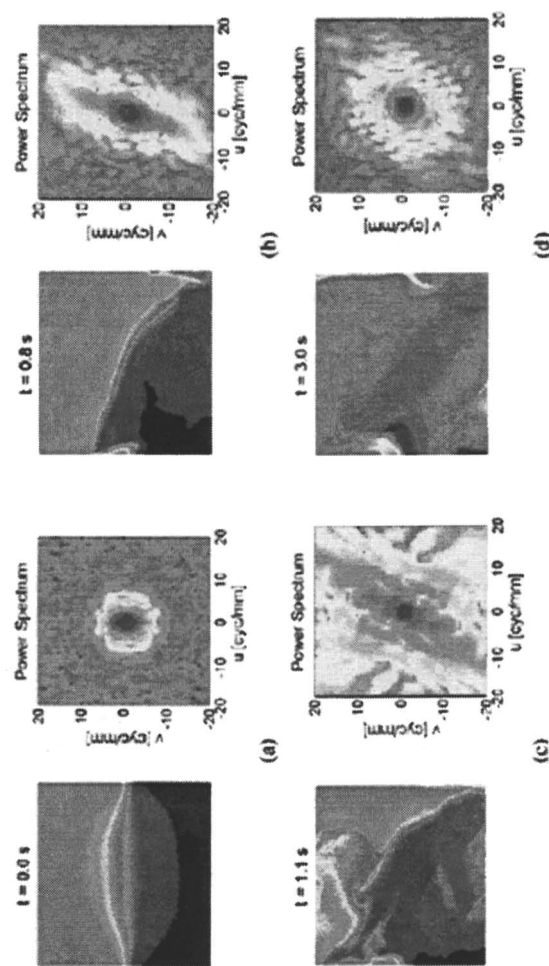


Fig. 1 Power spectra obtained for an electrokinetic mixer (reproduced from (1); Copyright: ACS).

ent buffer solutions. For one concept investigated in detail, such electric fields were achieved by a series of electrodes located under the channel's floor. Both spatial and temporal control of the  $\zeta$  potential was so achieved by imposing an electric field perpendicular to the solid-liquid interface. As an alternative means, the light charging of photosensitive surfaces has been proposed (2).

So far, the chaotic electroosmotic stirring concept has not been transferred into a physical device. Hence, there are no experimental proofs to report. Nonetheless, simulations give first evidence on the mixing efficiency of such devices. In one such simulation study, a square material blob was placed in the center of the channel (2) (see Fig. 2). This is equivalent to inserting a drop of a dye in the channel. Rapid stretching and folding processes, characteristic of chaotic advection, arise when periodically switching between flow fields. Eventually, the blob is spread over the entire cell's area. Hence efficient stirring is given.

### **Magneto Hydro Dynamic Mixing**

The use electric fields for liquid mixing can be extended by combination to a magnetic field (3). For this purpose, a micro channel was equipped with an array of electrodes. A complex electric field with currents in various directions was generated by alternate potential differences. This electric field was then coupled to a magnetic field. By induction of Lorentz body forces for fluid mixing, a cellular motion was achieved which stretches and deforms material lines.

Simulations were performed for the magneto hydro dynamic mixing to predict to which extent and by which pattern the interfaces are stretched which is a qualitative measure of mixing efficiency (3). The evolution of the interface was given as a function of the dimensionless time. An initial bi-layered system forms a vortex-type structure with increasing spiral winding upon time. A quantitative analysis shows that the interface increases slightly faster than a linear function of time (3). This is better than when having diffusion only, but is inferior to the performance of chaotic advection.

These predictions have been corroborated by dye-visualization experiments. Owing to the dc potential difference, a visible flow was clearly induced in a water-filled chamber with a central dyed line by magneto hydro dynamic action (3). Upwards and downwards fluid motion in a rotating fashion was observed.

### **Air-Bubble Induced Acoustic Mixing**

Air-bubble acoustic mixing is a method to mix liquids in micro chambers of comparatively large internal volume (4). An air bubble in a liquid medium can act as actuator and thus achieve liquid mixing. When stimulated by an acoustic field, the bubble surface vibrates. The bubble vibration induces friction forces at the air/liquid interface. In this way, a bulk fluid flow around the air bubble is achieved, termed *cavitation microstreaming* or *acoustic microstreaming*. Circulatory flows lead to global convection flows of "tornado"-type pattern.

The bubble resonance characteristics govern the bubble actuation (4). An insonation frequency equalling the resonance frequency for pulsation has to be set. The frequency of acoustic microstreaming is, as to be expected, strongly dependent on the bubble radius and vice versa.

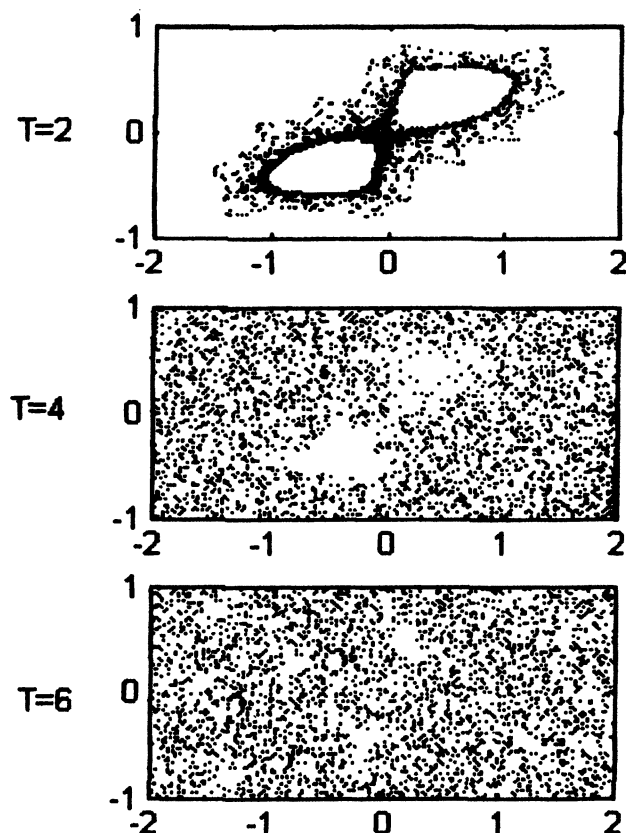


*Fig. 2 Streamline patterns for various electroosmotic flows, showing the transition to chaotic flow (reproduced from (2); Copyright: ACS). T: periodicity of flow switching; the x- and y-axes denote dimensionless numbers for the respective axes of the mixing volume.*

The bubbles are favorably fixed at a solid boundary in specially designed pockets (4). By use of a commercially available piezoelectric (PZT) disk, liquid mixing times of a few seconds were realized. Mixing of comparable volumes solely by diffusion would require several hours.

Initial dye imaging mixing experiments by multiple-bubble microstreaming yielded complete mixing of the micro chamber within 105 seconds (5 kHz; 5 V) (4). Mixing based on pure diffusion in the same volume would have taken about 6 hours. By increasing the peak-to-peak amplitude further optimization of mixing was performed. Now, a mixing time of only 6 seconds results (5 kHz; 40 V) (4). Mixing based on pure diffusion in the same volume would have taken about 8 hours.

The method of multiple-bubble microstreaming has been proven to be particularly suitable for mixing of relatively large mixing chambers. Bubbles with radii of 0.5 mm can stir fluid volumes in a distance with a radius smaller than 2 mm (4). Thus, any micro chamber is suitable for acoustic microstreaming with a depth  $<2$  mm and with an air pocket pitch  $<4$  mm.

#### **Ultrasonic Mixing**

Ultrasound in the kHz region generated by lead-zirconate-titanate (PZT), a piezoelectric ceramic, was applied to liquid mixing in closed volumes such as micro chambers (5). For such configurations, the creation of standing waves has been reported which move liquid streams and induce even turbulent-like eddies.

Compared to other means of creating turbulence in closed chambers, such as mixing by valves, ultrasonic mixing is said to have advantages of a favorably lower sensitivity towards bubbles and of a free choice of the flow ratio between the two liquids to be mixed (5).

In the absence of ultrasonic mixing, two stable separate fluid regions were found in a mixing chamber, as experiments with water and uranine solutions demonstrate (5). A straight interface was given; hence only a low degree of mixing was observed being limited to the interface by slow molecular diffusion. Upon ultrasonic action, turbulence occurred, moving material throughout the whole mixing chamber. From video observation, a mixing time of about 2 s was judged. Further, optimization studies were undertaken such as varying the diaphragm oscillation, but so far did not further contribute to improving mixing.

#### **Moved- and Shaken-Droplet Mixing**

The movement of discrete droplets provides an alternative microfluidic approach to batch processing of miniature volumes and continuously flowing streams (see e.g. (6)). Thereby, large flexibility regarding to the chemical protocols is given, e.g. when needing both short and long processing time scales, overcoming some of the limits of continuous processing. As a further valuable aspect, the footprint area as well as the sample volume for fluidic handling is notably decreased, which is essential for virtually all  $\mu$ TAS applications.

An electrostatic method is used to move the droplets. This so-called electro-wetting effect changes the interfacial tension of the droplets by applying voltage, (6). This implies that polarizable and/or conductive liquids are employed. In a passive variant, the droplets are moved towards each other and simply merged to induce mixing by diffusion (6). A more efficient active mixing means is provided by fast movement of the merged droplet between many electrodes, inducing circulatory flow by shaking and speeding up mixing (see Fig. 3).

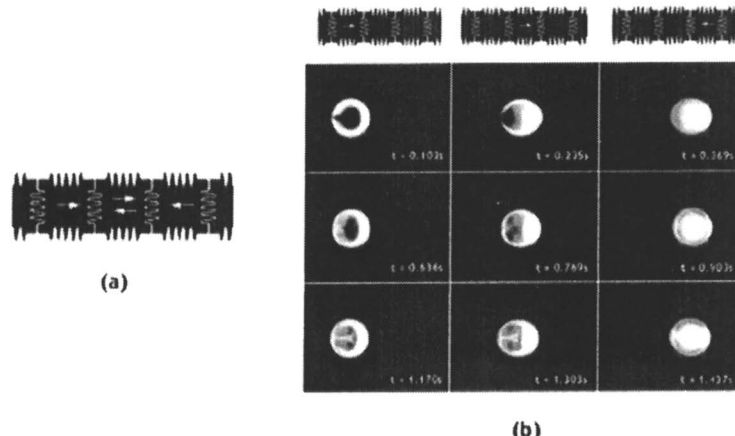


Fig. 3 Fluorescence images of active droplet mixing by a 3-electrode configuration (reproduced from (6); Copyright: RSC). Left: electrode structure; right: dynamic evolution of flow patterns, monitored by fluorescence.

Fluorescence imaging of the dynamic evolution of flow patterns demonstrates that 4-electrode active mixing gives more droplet configurations and achieves better mixing as compared to 2- and 3-electrode mixing (6). The latter configurations suffer from flow reversibility which restores the initial situation with small interfacial areas.

By optimization of design parameters such as the aspect ratio (height-to-width of the electrode chamber mixing is considerably further improved. Mixing times decrease from 15 s to 6 s, when raising the aspect ratio from 0.1 to 0.5 (6). Thereafter, a slight increase of mixing time is observed again. This is owing to the formation of complex flow patterns at aspect ratios of 0.4 to 0.5, whereas only bi-layered structures are found for the small aspect ratios. The latter results in smaller interfacial areas, hence leads to longer mixing times. For aspect ratios  $> 0.5$  mixing times increase owing to the larger volume, i.e. the slightly less efficient generation of interfaces under such conditions.

#### Membrane-actuated Micropumping Mixing

PZT driven valveless micropumps operate at high frequency in the kHz range. By displacement of a membrane fluid volumes are transported. Thereby, a powerful pumping principle is achieved which is claimed to induce locally turbulence (7). This pumping action can be converted into mixing performance,

if a suitable design is provided with two feed inlets entering a pumping chamber and one outlet. Mixing performance was qualitatively proven by flow visualization, albeit no quantitative data are available.

A similar active micropumping mixing relying on fast periodical changes of a mixing-chamber volume by a piezo disk was reported in (8). The design chosen, however, is different and comprises a bottom part containing the inlet and outlet ports and a top part forming the mixing chamber. The thin membrane covers the mixing chamber, the piezo disk is located above. Similar to the pumping action of membrane pumps, fluid motion is achieved in this way.

The mixing efficiency was followed by colorimetric measurement at various frequencies and amplitudes of actuation (100 Hz; 95 – 492  $\mu\text{l min}^{-1}$ ) (8). An optimum signal amplitude between 30 and 40 V was found correspondding to a total membrane stroke of 6-7  $\mu\text{m}$ .

### Electrohydrodynamic Mixing

Surface charges can be generated and accumulated on the boundary of a dielectric material by electromagnetic means (9). This procedure can be transferred to bulk liquid samples. For a non-uniform external electric field, interfacial shear stress in liquids is so induced. This leads to flow motion which tends to eliminate this stress. In this way, new interfaces are formed and mixing can be achieved.

A numerical simulation of the velocity field after applying the electrical field was made at three times, 1, 10, and 10 ms after start of the turning-on of the field (9). The velocity field is considerably changed in this short time scale which usually is indicative of good mixing. Fast mixing was qualitatively confirmed by flow-visualization experiments.

### Micro Impeller Mixing

The majority of conventional mixing problems are solved by batch processing using impellers of numerous types. Many  $\mu\text{TAS}$  applications demand for mixing of liquids in vessels, i.e. mixing chambers, of comparatively extended volumes at comparatively long residence times which somehow resembles batch mixing. Owing to this analogy in technical boundary conditions, it probably is not too far-fetched to develop miniaturised stirrers (10). Claimed advantages of micro impellers are the possibility to adapt the impeller diameter to the mixing volume, to mix large volumes, to perform mixing on-demand (via switching on/off), and flexibility of the mixing approach concerning the choice of liquids.

Mixing of an extended circular mixing chamber (diameter: 2.5 mm; depth: 40  $\mu\text{m}$ ) is complete at after 55 s when using a 3 x 3 array of micro impellers at 600 rpm, as demonstrated by dye flow visualisation and color histograms

### Passive Mixing

#### Vertical Y- and T-Type Configuration Diffusive Mixing

Y- and T-type micro mixers resemble mixing tees which are used for simple, undemanding mixing tasks conventionally. Whereas the latter are typically operated under turbulent-flow conditions, their microstructured analogues use diffusion in laminar regimes for mixing, by virtue of decreasing the distances within a bi-layer. This bi-layer can be arranged vertically or horizontally with respect to the the ground level of the mixing channel.

In a simulation study generic investigations on the impact of design details of Y- and T-type micro mixers on the mixing efficiency of gaseous reactant were made (11). The effect of the inclination angle of the feed channels, i.e. of various Y-designs, is given. The variation of the mixing length, being 1.93 to 2.25 mm, was determined to be fairly small compared to the changes in the feed angle (further details see in (11), being from +45° to -65°. It was further shown that the mixing performance of such Y-feeds is comparable to those with inverse Y-configuration. The latter design is less foot-print consuming, however, suffers from the presence of dead zones. The benefits of using a throttle, revealing a Venturi-type design, for pressure recovery and speeding up mixing were also shown in this work. Varying the throttle diameter from 500 to 10  $\mu\text{m}$  has a considerable effect on the mixing length (11). In this way, the mixing length can be reduced from about 2 mm to less than 0.1 mm. As compared to the design without throttle (see above) a notable improvement in mixing results.

Y-type mixing of liquids (unfocused bi-lamination) is slow for the typical dimensions of today's micro channels. These slow mixing characteristics however can be exploited by purpose, yielding a kind of stop-flow technique. This enables sensing of a reaction at a rather unmixed state and, after stopping the flow, for all stages of the reaction until completion (12). By pulsation of the flow rate this sequence can be repeated many times, leading to a rapid switching between reactant and product flows, e.g. to investigate the kinetics of a reaction. The effective time span between subsequent spectra was only 65 ms, hence providing a high dynamic resolution. In this way, the saponification of methyl monochloroacetate with sodium hydroxide was investigated as a slow reaction which can be monitored by FTIR. Owing to the slow reaction, despite pre-mixing no detectable reaction could be monitored. When stopping the flow, the reaction products chloroacetate and methanol appear. After a few 100 ms reaction time, the reaction is completed.

#### Capillary-force, Self-Filling Bi-laminating Mixing

Mixing applications are also needed for portable tools in medical and environmental analysis, which is preferably done in field experiments on site (13). Here, a mixing principle avoiding any costly and heavy machinery such as

pumps or actuators (e.g. mechanic or electric) is strongly favored. In addition, ruggedness of the mixing principle is a request, because many field samples have particles or are contaminated, different from 'clean' laboratory probes. These demands are fulfilled by self-filling approaches that enable reasonably fast mixing. In one solution realized the liquid is soaked up by capillary forces into a miniature reservoir and sealed by displacing a tiny cantilever, again owing to capillary forces. Now, the second liquid can be filled in a neighboring chamber. Mixing thereafter can be initiated by bi-lamination. Though this is typically a slow process, this is adequate for most field chemical analysis procedures.

Based on general assumptions of diffusion in aqueous solutions, the mixing in the self-filling device is assumed to be in the order of seconds and minutes (13). This is slow compared to other micro mixers, but having a fast mixing time is not a requirement for the target applications of the device, namely field analysis and medical applications.

#### **Focusing Bi-laminating Mixing**

By hydrodynamic focusing (see (14)) via geometric constraints the mixing of bi-laminated streams can be speed up. This concept was originally developed according to the demands of one flow injection analysis (FIA) system (15). As for many other  $\mu$ TAS systems, an easy integration is the governing principle, demanding for minimizing the size of the parts of the integrated system. This is achieved when bi-laminating two liquid streams directly after injection and confining the cross-sectional area to reduce the diffusion distances for mixing. In this way, a passive mixing element of small internal volume can be achieved which easily can be set beforehand a reaction chamber and a detector.

The liquid mixing time was calculated for phenol in an aqueous solution using the bi-laminating focusing mixer (15). For example, a reduction of the channel width from 300  $\mu$ m to 100  $\mu$ m can be reduced from 35 s to 4 s. Experiments with phenol solution confirmed completeness of mixing for flow rates of about 1  $\mu$ l min<sup>-1</sup>.

#### **Bifurcation and Interdigital Multi-Lamination Mixing**

Multi-lamination is a logical extension of the bi-laminating concept, extending the capacity of the mixer and achieving even higher focusing ratios, i.e. faster mixing times. Multi-lamination is based on an alternating arrangement of small fluid compartments, typically multi-lamellae which are then mixed by diffusion. This is realised by alternating feed arrangements (type A-B-A-B- ...), fed into a flow-through mixing chamber.

Fluidic distribution chains of various type connect the alternating feeds to one inlet reservoir each. A widely used branching design is the so-called *interdigital* array given by the displaced superposition of two fork-like chains, termed in analogy to the respectively arranged electrode structures (16-19). The cross-sections of the feed channels and of the reservoirs are chosen in a way that

a sufficiently large pressure drop is developed in order to have flow equidistribution. The direction of the distribution chains can be counter-flow (16) or co-flow (17, 18), the selection of which is mainly governed by microfabrication needs. In the case of counter-flows, the streams have to be redirected before entering the mixing channels, to have a feed co-flow essential for multi-lamination. For distribution-chain co-flows, more delicate fluidic architectures are needed. The chains are usually situated on different levels within the mixer device to prevent intermixing at an too early stage and the ends of the chains are brought to one common level before entering the mixing chamber so that the A-B-type nozzle pattern is established.

Besides single-chain interdigital contacting, interdigital mixers with multiple, parallel platelets were realized (19). In the concrete versions developed, the outlet flows of all levels were guided into the same (large) mixing flow-through chamber. Alternatively, one could think of many separate, numbered-up mixing elements with chambers attached. But this has not been realised so far.

*Bifurcation branching* yields flow equidistribution by structural symmetry, using replicated splitting of one main stream (20). The outlet arrangement thus achieved is basically identical to the interdigital feed concept. The pressure drop of the bifurcation concept is solely governed by the contribution for the flow distribution passage itself and does not need an additional share as the interdigital concept. Contrariwise, it poses much higher demands on the structural precision, since deviations in symmetry will affect the quality of distribution. Moreover, fouling or deposits within the channels are very detrimental, as both will also break the ideal splitting geometry of bifurcation. By fluorescence imaging, a liquid mixing time for 95% mixing of about 15 ms was determined.

Besides these planar arrangements, *3-D alternating cross-injection feeds* were described, one example being the *StarLam* mixer series with stacked thin plates (21). Here, a cross-wise injection along the long axis of the mixing channel is performed. This concept allows one to achieve large capacity, because a simple stacking construction (internal numbering-up of mixing elements) is used to guide flows through many plates. *StarLam* mixers, thus, achieve throughputs as high as several m<sup>3</sup>/h liquid flow. Owing to the large internal diameter of the mixing chamber, turbulent mixing is given for the usual flows applied instead of having multi-lamination flow. If laminar flow could be established for the alternating cross-injection feeds, one would expect that an onion-skin-type pattern is established.

Two types of *StarLam* mixers were compared for their mixing efficiency (21). The efficiency was determined by a competitive reaction approach and is inversely proportional to a measured UV absorption signal, i.e. the extinction, relating to one reaction product, iodine. The small *StarLam300* (300 l/h-range) reaches extinctions as low as 0.1 at maximum flow rate, which is considered to correlate to a good mixing efficiency. Best values known for laboratory micro mixers (still smaller and lower throughput) are 0.01. The large-scale interdigital

concentric microstructured mixer (StarLam3000; 3500 l/h-range) gives a mixing efficiency which is average, equivalent to an extinction of 0.55. From extrapolation of the data it seems possible that this device achieves the same mixing performance as the StarLam 300 at its highest possible flow rates, which so far were not accessible for the mixing characterization experiments due to pump limitations.

As mentioned above for bi-laminating flows (15), *hydrodynamic focusing by geometric constraints* is the right concept to speed up mixing (see Fig. 4) (17, 18). Initially, complex-shaped geometries like sections of an arc were employed, mainly for fabrication reasons. Drawbacks of the early solutions (16) were a too extreme focusing ratio resulting in lamellae of varying thickness and even lamellae tilting and winding at higher Re numbers (17).

Thereafter, triangular focusing chambers were introduced and are now commonly applied, with focusing ratios in the order of several tens. Based on these first achievements and a semi-analytical optimisation study, a novel focusing design, termed *SuperFocus*, was developed which indeed displayed regular focusing with equally spaced lamellae at a liquid mixing time of a few milliseconds only (17, 18). In this way, mixing can be completed within the micro device, and not in the tubing attached. For achievement of throughputs of several hundreds of litres per hour of a watery system, a 2<sup>nd</sup> generation version of the *SuperFocus* mixer was developed later (22). For this device, it could be shown that 128 parallel lamellae can be reduced in their thickness from 610 µm to about 3.7 µm at a focusing factor of 166 (see Fig. 4).

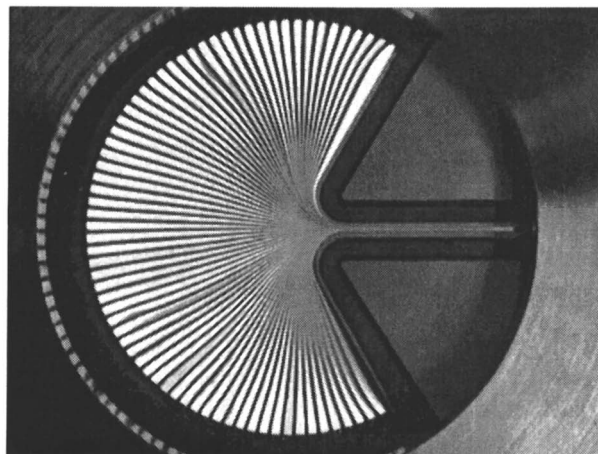


Fig. 4 Dye-imaging of focusing of a multi-laminated flow in a *SuperFocus* mixer (reproduced from (22); Copyright: Wiley-VCH).

### Cyclone Laminating Mixing

Cyclone mixers produce a rotational flow field (23). Thereby, vortex patterns of laminating and focusing streams are formed. The benefits envisaged are that the lamellae are thinned by vortex-folding, at an increase of residence time in the mixer. It is calculated that a full rotation should halve the lamellae width. Therefore, the optimisation parameter may be to have as many rotations as possible. However, these predictions still wait to be proven. In the experimental investigations on mixing with the cyclone mixers given so far only the formation of the vortex flow pattern was confirmed; no details on the mixing time and efficiency were given.

### Split-and-Recombine Mixing

Split-and-recombine (SAR) micro mixers use a distributive mixing approach, based on multiple flow splitting and recombination steps (24-26). Thereby, an originally bi-laminated flow is first divided into two sets of two lamellae. Channel branching is most often used for this purpose (24-26); however, in-channel splitting has been reported as well (25, 26). Concerning the latter case, elevating and descending structures were designed for spatially separated flow guidance of split lamellae within the channel (25, 26).

During the flow passage after splitting, the channel cross-section may be changed to restore that of the incoming stream after recombination of the flows (24, 26). By  $n$ -time repetition of this procedure,  $2^n$  lamellae are achieved. Typical values of  $n$  are 5 to 10, yielding sufficiently small lamellae. The SAR devices differ in the exact design of their split/recombine repeat units, e.g., may have fork-like (25) or vertically curved (26) design.

Friction forces deform the lamellae, if split layers are in direct contact; this drawback is most prominent for in-channel SAR devices (26). Following the same argument, a splitting plane at the beginning of each repeat unit, basically acting like a knife, can be useful for accurate lamellae division (24, 26). SAR mixers were described with and without splitting plane.

SAR mixing can yield nearly perfect multi-lamination patterns, as first evidenced by a dilution-type experiment using a caterpillar micro mixer made from transparent polymer material and equipped with a splitting plane. (see Fig. 5) (26). The feed of bilaminated colorless and colored solutions results in multi-lamination patterns of alternate color, with a doubled number of lamellae per each of the eight mixing stages. However, this is restricted to flows at low Reynolds numbers, typically  $<100$ . Secondary flow superpose the multi-lamination patterns at other flow regimes. This is not entirely negative, since mixing is speed up by these means (however, the underlying patterns are not as regular and directed).

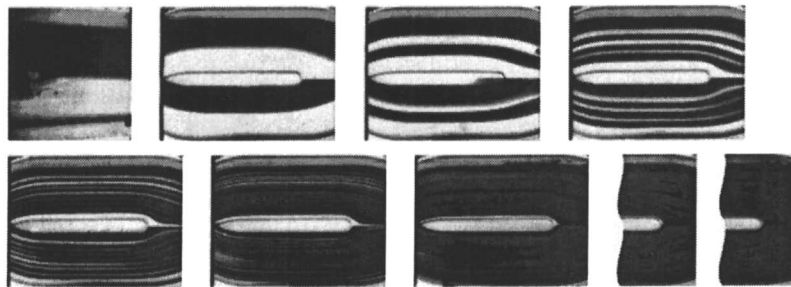


*Fig. 5 Dye-imaging of the increase of lamellae by split-and-recombination in a caterpillar mixer (reproduced from (26); Copyright: RSC).*

Thus, the experiments have shown that with only about eight mixing stages, the same patterns like for multi-lamination mixing are accessible for laminar flows. Accordingly, the mixing times should be in the order of some milliseconds, excluding the time for the 8-stages passage (which is flow-dependent). When operating at higher  $Re$ , secondary-flow patterns arise and it is expected that mixing performance is then equal or better; however, such confirmations need to be done in further investigations.

#### Rotation-and-Break-up Mixing

Whereas being a more unforeseen effect for SAR flows, the intentional use of secondary or rotational flows for mixing has been described as well. This is achieved by in-channel flow structures to stretch and fold fluids. An initially induced rotation of the flow is superposed by a break-up step, which basically serves for flow splitting (27). Rotation-and-break-up mixing is proposed in close analogy to elementary steps proposed for conventional mixing.

The addition of a break-up step in addition to the flow rotation gives positive moments for mixing (27). This leads to an increase of the interfacial area by stretching and folding and producing striations. At low  $Re$  number, fluids were broken up and small fragments of blobs were generated. In this way, more than 70% mixing was achieved for a mixing length of only 4 mm for  $Re$  numbers of 1, 10 and 50. On the contrary, for pure diffusion complete mixing is given after 1, 10 and 50 m for the same  $Re$  numbers. Accordingly, the rotation and break-up concept has a considerable impact on speeding up mixing.

#### Distributive Mixing with Traditional Static Mixer Designs

Whereas SAR in-channel mixers use microstructures at the channel's floor or ceiling for distributive mixing, it is straightforward to apply for the same purpose in-line 3-D flow obstacles, resembling designs of conventional static mixers (28). For instance, intersecting and helical packings are known to per-

form distributive mixing by splitting, rearranging and recombining or stretching and folding of the flow, respectively. Miniaturised versions of such packings were made by 3-D microstructuring techniques with the expectation to induce a comparable action. As simulations show much more complex flow patterns compared to the split-and-recombine (SAR) mixers are generated, not comparable to the lamellae patterns obtained at low  $Re$  number of the SAR devices. When simulating mixing efficiency by particle trajectories (water as fluid;  $Re = 12$ ), it is evident that the intersecting device performs manifold splitting and recombining of the flow, yielding a fine-dispersed system at the end, i.e. achieving a good mixing efficiency (28) (see Fig. 6). In contrast, flow stretching and folding are found for the helical device, resulting in a coarsely textured fluid, which means less efficient mixing. Thus, the simulations predict the intersecting device to be more efficient in creating interfaces for mixing, however at the expense of higher pressure drop, the same behavior is given for the macroscopic static mixer analogues.

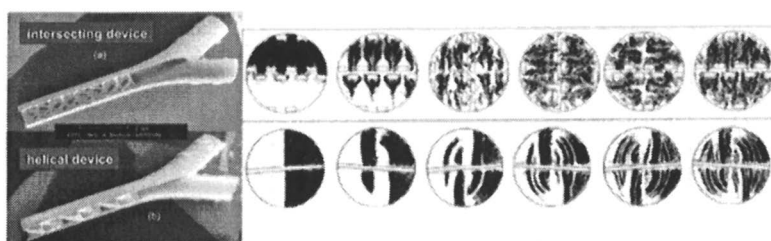


Fig. 6 CFD simulation displaying the interfacial increase by distributive mixing in a device with 3-D internals (reproduced from (28); Copyright: RSC).

#### Secondary Flow Mixing in ZigZag Micro Channels

In zigzag channels the fluid is divided into a main passage, around the 'open' straight conduit and more quiescent zones in the corners (29). The flow in the latter zones can assist mixing by secondary flows at sufficiently high  $Re$  numbers. At these conditions, the flow direction of the main passage is repeatedly bended along the channel's longitudinal axis and so flow rotation in the corners is induced. By means of such recirculation patterns, material is transported transverse to the flow direction and improves the mixing.

The mixing efficiency in zigzag channels is dependent on the  $Re$  number, as to be expected. For  $Re = 80$ , mixing efficiency stays almost constant at 81%. Here, only diffusion causes mixing. For  $Re$  numbers  $> 80$ , a pronounced increase in mixing efficiency takes places, which is owing to the induction of flow circulation patterns. Maximum mixing efficiencies of 99% were achieved at  $Re = 267$  with an optimal meandering pattern; for reference cases, straight channels of similar internal dimensions, lower mixing efficiencies in the range

of 29-86% were found. The better performance here was achieved at the expense of increasing the mixing length.

#### Micro Plume Injection Mixing

When a multitude of small fluid bulbs, 'micro plumes', are injected into a main stream, the fluid interface for diffusive mixing is notably enlarged (30). One design proposed for this purpose was a square mixing chamber with a sieve bottom through which one of the fluids has to be fed. The other fluid, i.e. the main stream, is guided through the mixing chamber, oriented at 90° relative to the feed channel of the injected fluid.

Flow visualization experiments by means of VIS absorption and fluorescence proved complete mixing at a flow rate of about  $1 \mu\text{l s}^{-1}$  (30).

#### Passive Chaotic Mixing by Posing Grooves to Viscous Flows

Grooves oriented at an oblique angle on the ground level of a micro channel are known to induce transverse flows by using a steady axial pressure gradient (31). These grooves pose an anisotropic resistance to viscous flows, mainly in the orthogonal direction. In this way, an axial pressure gradient is built up and generates a mean transverse component of the flow. The flow originates at the floor structures and circulates back across the top of the channel, giving helical streamlines for the full flow (see Fig. 7, top).

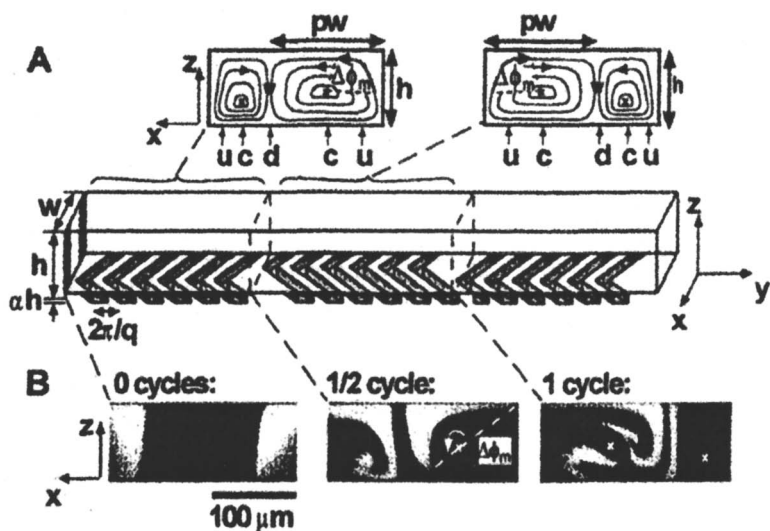


Fig. 7 Schematic of the herringbone microstructure and its flow circulation; fluorescence images of flow patterns (reproduced from (31); Copyright: AAAS).

The functioning of grooves was proven under pressure-driven (31) and electroosmotic flow (32) conditions.

Confocal fluorescence imaging of the cross-sections of the flow in the micro channel demonstrate the superior mixing quality of the staggered herringbone mixer, even at high  $Pe$  numbers, by showing the folding of the fluid layers and the respective increase in interfacial area ( $9 \times 10^5$ ) (31) (see Fig. 7, bottom). For a simple channel without any grooves nearly no mixing is detected and for the mixer with an array of multiple obliquely oriented, straight grooves incomplete mixing is found, even after 30 mm flow passage. A quantitative analysis of these data shows that the SHM mixer performs well over a large range of  $Pe$  numbers. The mixing length required for 90% mixing increases by less than a factor of 3 from the lowest to the highest  $Pe$  number. The straight-grooved mixer and the non-grooved channel have much reduced performance. For example, at  $Pe = 10^4$  the a simple, non-grooved channel requires 100 cm for mixing completion, whereas 1 cm is sufficient for the staggered herringbone mixer (SHM).

#### Passive Chaotic Mixing by Twisted Surfaces

Chaotic flow motion is given for time dependent two-dimensional velocity fields and for three-dimensional velocity fields (33). One option for generation of such complex fields is to guide the flow close to structured surfaces, e.g., placed on a channel's bottom, starting from a T-type flow inlet configurations.

Mass contour fraction plots were simulated for gas mixing in three T-type mixer designs with internals – comprising inclined, oblique and wave-like structures (these elements being repeated four times) - at an inlet velocity of  $2.0 \text{ m s}^{-1}$  (33). It turned out that the inclined design gave best results, although the other designs were only slightly inferior.

#### Time Pulsing Mixing

Time pulsing of flows means varying the flow rates of the feed streams, which can be simply realized by programming the respective pumps (for pressure-driven feed) (34). Besides from this simple T-type injection of two flows, advanced time pulsing is given when superposing multiple flows in more intricate microstructures with unsteady cross-flow injection and a steady-flow in a main channel (35).

In the first and simpler case, it was shown by simulations that mixing indeed can be enhanced by simple periodical variation of the flow rates in the inlet channels, without any need for further moving parts or complex fluid architectures (34). A low frequency sinusoidal flow rate is superimposed upon a steady flow rate. For steady state inlet velocities of 1.0 mm/s time-dependent inlet velocities of the form  $1.0 + 7.5 \sin(5 \times 2\pi t)$  mm/s were used, with  $t$  being the time. In further experiments, two periodical flows were superimposed, yielding best results at  $180^\circ$  phase difference (see Fig. 8).

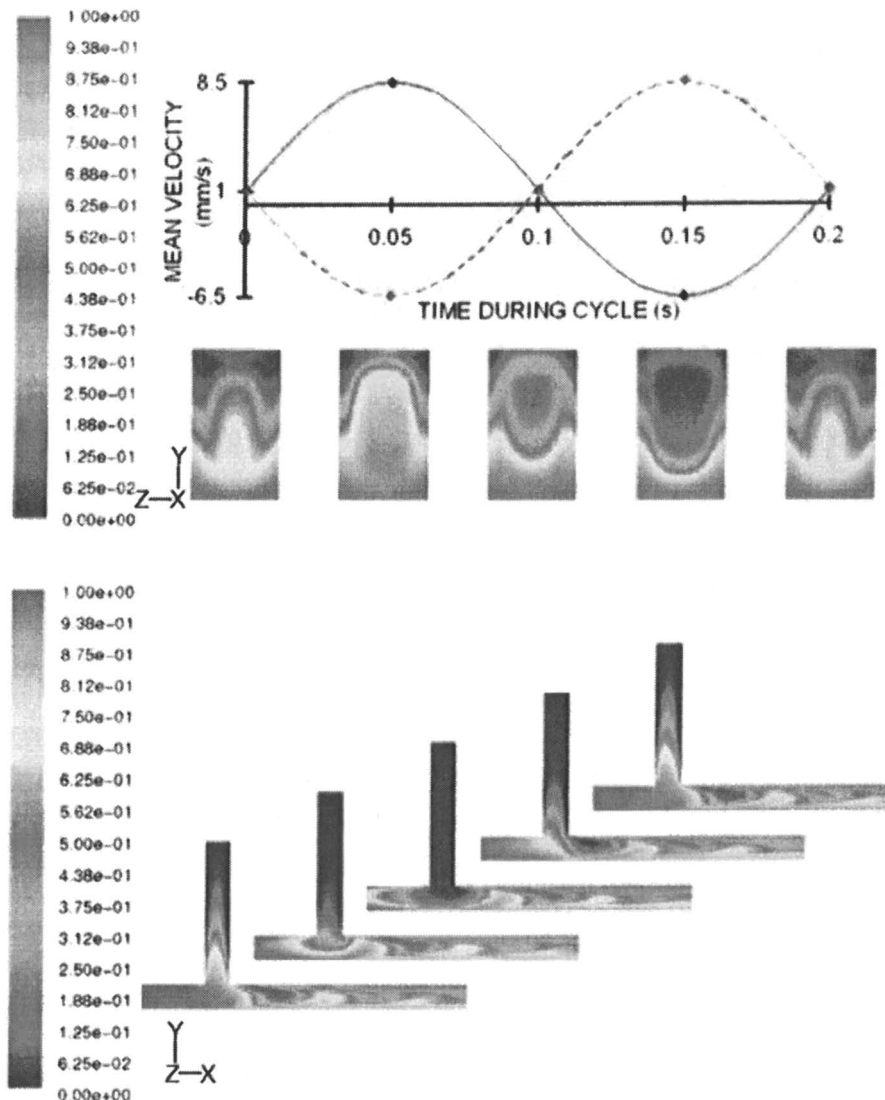


Fig. 8 CFD simulations of the concentration profiles for 180°-time pulsing operation for pressure-driven flows (reproduced from (34); Copyright: RSC).

Top: mass-contour plots for the channel's cross-section showing the deformation of the fluid interface; bottom: mass-contour plots along the channel's flow axis, giving similar information.

When pulsing both inlet flow rates with phase differences of 90° and 180° the degree of mixing is notably increased, actually being more than doubled, as compared to one-inlet-flow pulsing, respectively, at the same amplitude and frequency (34).

This concept can be extended to the multiple, pulsing injection of flows into one micro channel, thus creating chaotic advection; such devices are so far hypothetical and certainly would require a complex control system (35). A detailed simulation study describes the effect of the variation of the amplitude and angle frequency of the perturbation for a multi-injection design. For a given parameter set, the coexistence of chaotic and quasi-periodic areas is found (see Fig. 9).

An increase of the amplitude from there at fixed frequency results in the formation of chaotic areas. These zones are not homogeneously distributed within the bulk fluid. At still higher amplitude, the so-called KAM (Kolmogorov Arnold Moser) curves, positioned at the interfaces between chaotic and quasi-periodic areas, break up to islands. As a special feature, outer and inner chaotic areas are found.

#### **Bimodal Intersecting Channel Mixing**

This mixing concept is the micro-scale equivalent of ‘macroscopic’ mixing in regular packed-bed packings used for capillary electrochromatography column (CEC) operation (36). This specific application in the sub-15 nl volume range demands for mixers that have an order of degree smaller internal volumes, i.e. a few 100 pl or less; today’s micro mixers have however larger volumes. Packed-bed mixing profits from transverse mixing along the flow path of fluids flowing around the obstacles. The direct attempt – using highly regular micromachined packed beds – so far failed to achieve sufficient transverse mass transfer owing to heterogeneities in their flow path. Therefore, a bimodal structure was realized with a main flow having fluid convection and intersecting side streams achieving fast diffusion, termed trans-channel coupling. This resembles voids in the packed beds which owe to convective transport besides the diffusive transport happening in the interstices. These voids meander along the residual packed bed volume so that the respective modal microstructure has a zig-zag main path. In this way, a main stream is split repeatedly in smaller side streams which after a passage merge again with the main stream.

Microscopy images and fluorescence intensity profiles were recorded for bi-laminated streams before and after passage through the micro mixer (36). The unmixed state displays, as to be expected, two separated areas, divided by a thin interface. Accordingly, the corresponding fluorescence intensity profile has two distinct zones with maximum and zero concentration of the dye separated by an about 25  $\mu$ m thin mixed interface. When this stream was mixed by the micro mixer, a rather uniformly colored microscopy image and even fluorescence intensity profile were found which indicate that complete mixing has been occurred.

#### **Coanda Effect Mixing**

The exploitation of the Coanda effect is one of many means to achieve a second passive momentum to speed up mixing in addition to diffusion (37). The flow patterns of the Coanda effect are well known from studies of in-plane micro valves and micro pumps. Recently, it was thus aimed at transferring this know-how for design of a micro mixer (37). Central element of this device is a

Tesla structure which redirects the flow and thereby induces collision of streams.

The basic functioning of the above mentioned micro mixer was sketched by comparison to the mixing performance of three similar designs which, however, were missing one essential part of the design of the Coanda mixer. These structures were a Coanda design without wing, a T-type mixer and a ring-type mixer (37). The analysis of the corresponding flow patterns at  $50 \mu\text{l min}^{-1}$  by a dilution-type experiment clearly reveals the onset of mixing for the "real" Coanda structure, whereas all three other designs do not give any visual hint for mixing.

### Cantilever-valve Injection Mixing

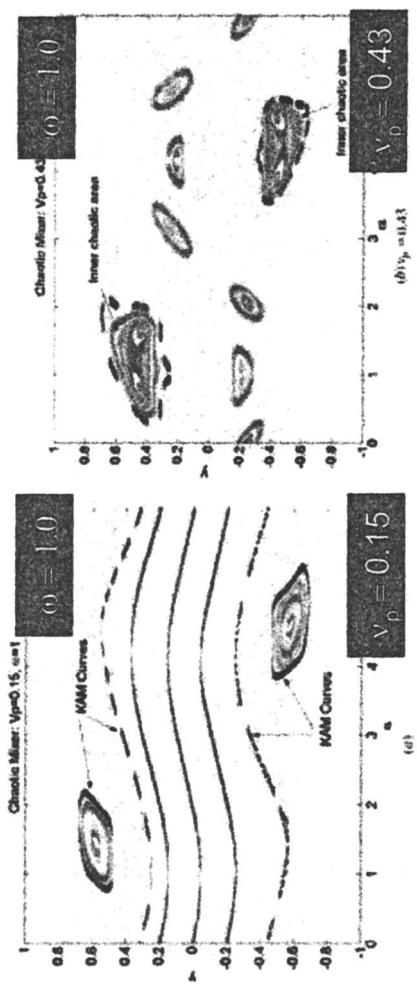
A cantilever-plate flapper valve was utilized for injection of volumes into a main stream and performing mixing in a flow-through chamber (38).

The self-filling principle was confirmed by introducing two colored solutions serially into the channels (38). Based on general assumptions of diffusion in aqueous solutions, the mixing in the self-filling device is assumed to be in the order of seconds and minutes. This is slow compared to other micro mixers, but having a fast mixing time is not a requirement for the target applications of the device, namely field analysis and medical applications.

### Serial Diffusion Mixer for Concentration Gradients

Not in all cases, fast completion of mixing is the task of the mixing device. Devices for partial mixing were built for the generation of defined concentration gradients in a flowing stream (39). This has many practical analytical uses, e.g. for drug screening. Concentration gradients can be continuous and discontinuous. The first have a concentration continuously decreasing along the channel, whereas the latter exhibit a spontaneous change in concentration at a certain locations and have near-constant concentration in between, similar to a step-like profile. Specialty microfluidic networks were developed for realization of both types of concentration gradients within one device. One solution uses multiple serial contacting of a main stream with side flows at certain, spatially confined locations. Mixing occurs here via diffusion for a short, defined time. The main stream concentration in the passages between the contact zones is not changed from external sources, albeit 'internal' concentration equilibration within the flow is achieved.

The basic functioning of the mixer was proven using fluorescent dye and buffer solutions. For example, a discontinuous concentration gradient was built up as evident from the presence of three distinct concentration plateaus measured by the fluorescence intensity (39).



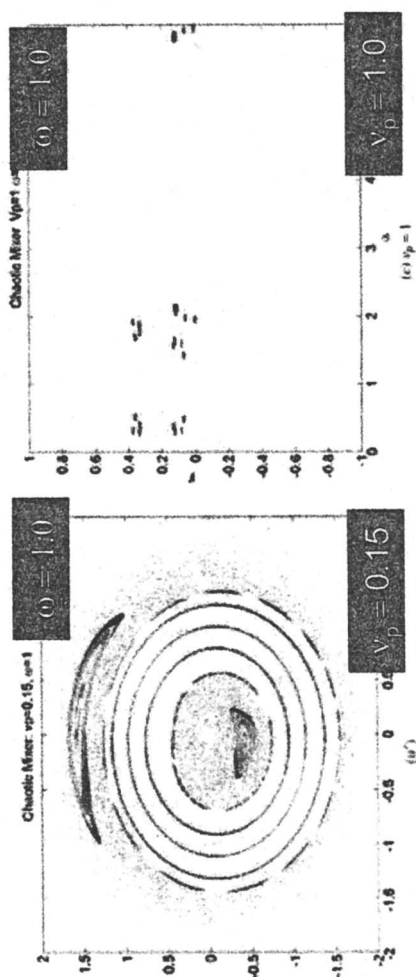


Fig. 9 Poincaré sections displaying non-chaotic and chaotic zones at various amplitudes and angle frequencies (reproduced from (35); Copyright: IOP).  $\alpha$ : angle frequency;  $v_p$ : amplitude;  $\alpha$ : angle;  $y$ : position vector of a particle. The Poincaré section (a') is a variation of the mapping formula:  $(y_m + 1)$  as radius,  $\alpha$  as angle, draw in polar coordinate. This mapping has the advantage of showing a continuation of angle  $\alpha$  (also means time).

### Jet Collision Mixing

The collision of jets is a channel-free (non-guided) microfluidic means for mixing, especially applicable to particle-containing or precipitating solutions. At high fluid velocity and thus energy, turbulent mixing can be accomplished (40). Even under laminar conditions, collision mixing may be adequate, when no other type of micro mixer may be suited, e.g. for the reasons given above, and nonetheless drivers for microfluidic processing are given (41).

Jets can be collided frontal, i.e. at 180° angle, bringing the energy input at maximum (40). In a specialty high-energy mixer device, the fluid virtually is “atomised” in this way and needs to be surrounded by a mixing chamber to be re-collected. A more “soft” contact is given for an Y-type flow configuration at much lower collision energies (41). The two jets simply merge forming a third one, rather than being disrupted into pieces. Under certain conditions, however, a separated, bi-laminated fluid system is achieved here.

Different types of flow were found for the latter type of impinging jet mixer, dependent on the flow rate (41). At low flow rates, the two fluids merge immediately after leaving the outlets, wet the mixer surface and finally form droplets. At increasing flow rate, the frequency of the droplets increases and results in merging to a jet. These flow regimes were referred to as “wobbly”, “Y-type”, “T-type”, “fan-shaped”, and “fanned-out” jets, the latter presenting the desirable flow patterns.

A chemical method based on competitive reactions was used for the analysis of mixing quality (41). An analysis of the mixing quality of nine different impinging jet mixers in the flow range from 300 to 1500 ml h<sup>-1</sup> revealed an increase in mixing quality, with increasing flow rate until a constant, low level is approached. Clear advantages of the smaller-sized devices became evident, indicating here a higher degree of mixing. The best designed device was tested for three reactions of known high fouling sensitivity owing to fast and heavy particle formation during reaction. This included the amide formation from acetyl chloride and n-butyl amine in THF which could be performed for several hours in the impinging-jet micro mixer at high yield.

### Conclusions

A multitude of mixing principles for mixing of fluids in miniature spaces is available; maybe this “bunch” is already even too large for the newcomer in the field interested in using the devices for his purposes. Under high-velocity flow conditions, typical for chemical engineering applications, pumping energy is usually sufficient to perform mixing by passive means. Several ways to utilize this concept have been proposed and validated, including flow division and recombination, flow compression, flow structuring by internals within the channels, etc. In the field of analytics, the fluids are processed typically much

longer and thus active mixing principles relying on external energy sources are more widely employed.

Initially, most of the mixing principles have been verified by building devices and testing them with simple flow visualization techniques; the experiments being ruled by the predictions of CFD simulations made in advance. More and more elaborate analytics are being used these days, giving quantitative performance characterization. In future, a detailed benchmarking is needed for proper mixing comparison between the different micro mixers themselves, at best using dimensionless parameters. Also, the micro devices need to be benchmarked to conventional equipment.

Since the micro devices are not used for the same purpose and correspondingly target functions, a mixing-efficiency comparison provides first insight, but may not be the only and most important figure of merit. While for the one type of mixer slow mixing may be acceptable, it may not for another micro mixer. Thus, apart from a pure technical comparison, other parameters may be of importance for the selection of one micro device, which are, for example, reliability and robustness, weight/volume savings, and naturally costs and commercial availability of the device. Concerning the latter, the functioning of the micro device has to obey the laws ruled by economic calculations, as e.g. made in the framework of establishing chemical production processes with their OPEX and CAPEX costs. This will finally lead to a much more differentiated view of the performance of some microstructured mixers. Thus, in future we will see a commercial documentation aside the scientific one which has already started, given by a few hundred papers in the field.

## References

- (1) Oddy, M. H.; Santiago, J. G.; Mikkelsen, J. C. *Anal. Chem.* **2001**, 73 (24) 5822-5832.
- (2) Qian, S.; Bau, H. H. *Anal. Chem.* **2002**, 74 (15) 3616-3625.
- (3) Bau, H. H.; Zhong, J.; Yi, M. *Sensors and Actuators B* **2001**, 79 207-215.
- (4) Liu, R. H.; Lenigk, R.; Druyor-Sanchez, R. L.; Yang, J.; Grodzinski, P. *Anal. Chem.* **2003**, 75 (8) 1911-1917.
- (5) Yang, Z.; Matsumoto, S.; Goto, H.; Matsumoto, M.; Maeda, R. *Sensors and Actuators A* **2001**, 93 266-272.
- (6) Paik, P.; Pamula, V. K.; Fair, R. B. *Lab Chip* **2003**, 3 253-259.
- (7) Yang, Z.; Goto, H.; Matsumoto, M.; Yada, T. In *Micro Total Analysis Systems*; Harrison, J.; van den Berg, A., Eds. Kluwer Academic Publishers: Dordrecht 1998; pp 177-180.
- (8) Woias, P.; Hauser, K.; Yacoub-George, E. In *Micro Total Analysis Systems*; van den Berg, A.; Olthuis, W.; Bergveld, P., Eds. Kluwer Academic Publishers: Dordrecht 2000; pp 277-282.

(9) Choi, J.-W.; Hong, C.-C.; Ahn, C. H. In *Micro Total Analysis Systems*; FRamsey, J. M.; van den Berg, A., Eds. Kluwer Academic Publishers: Dordrecht 2001; pp 621-622.

(10) Lu, L.-H.; Ryu, K. S.; Liu, C. In *Micro Total Analysis Systems*; Ramsey, J. M.; van den Berg, A., Eds. Kluwer Academic Publishers: Dordrecht 2001; pp 28-30.

(11) Gobby, D.; Angelis, P.; Gavrilidis, A. *J. Micromech. Microeng.* **2001**, 11 126-132.

(12) Hinsmann, P.; Frank, J.; Svasek, P.; Harasek, M.; Lendl, B. *Lab Chip* **2001**, 1 16-21.

(13) Seidel, R. U.; Sim, D. Y.; Menz, W.; Esashi, M. In *Microreaction Technology: 3rd International Conference on Microreaction Technology, Proc. of IMRET 3*; Ehrfeld, W., Ed. Springer-Verlag: Berlin 2000; pp 506-513.

(14) Knight, J. B.; Vishwanath, A.; Brody, J. P.; Austin, R. H. *Phys. Rev. Lett.* **1998**, 80 (17) 3863.

(15) Veenstra, T. T.; Lammerink, T. S. J.; Elwenspoek, M. C.; van den Berg, A. *J. Micromech. Microeng.* **1998**, 9 199-202.

(16) Ehrfeld, W.; Golbig, K.; Hessel, V.; Löwe, H.; Richter, T. *Ind. Eng. Chem. Res.* **1999**, 38 (3) 1075-1082.

(17) Hessel, V.; Hardt, S.; Löwe, H.; Schönfeld, F. *AIChE J.* **2003**, 49 (3) 566-577.

(18) Hardt, S.; Schönfeld, F. *AIChE J.* **2003**, 49 (3) 578-584.

(19) Ehlers, S.; Elgeti, K.; Menzel, T.; Wießmeier, G. *Chem. Engin. Proc.* **2000**, 39 291-298.

(20) Bessoth, F. G.; deMellow, A. J.; Manz, A. *Anal. Commun.* **1999**, 36 213-215.

(21) Werner, B.; Hessel, V.; Löb, P. *Chemie Ingenieur Technik, Sonderheft Mikroverfahrenstechnik (Ed. Hessel, V.)* **2004**, 76 (5) in print.

(22) Löb, P.; Dreser, K. S.; Hessel, V.; Hardt, S.; Hofmann, C.; Löwe, H.; Schenk, R.; Schönfeld, F.; Werner, B. *Chem. Eng. Technol.* **2003**, 27 (3) 340-345.

(23) Böhm, S.; Greiner, K.; Schlautmann, S.; de Vries, S.; van den Berg, A. In *Micro Total Analysis Systems*; Ramsey, J. M.; van den Berg, A., Eds. Kluwer Academic Publishers: Dordrecht 2001; pp 25-27.

(24) Branebjerg, J.; Gravesen, P.; Krog, J. P.; Nielsen, C. R. *IEEE-MEMS'96*, San Diego, USA, 12 - 15 Febr., 1996; pp 441-446.

(25) Schwesinger, N.; Frank, T.; Wurmus, H. *J. Micromech. Microeng.* **1996**, 6 99-102.

(26) Schönfeld, F.; Hessel, V.; Hofmann, C. *Lab Chip* **2004**, 4 65-69.

(27) Park, S.-J.; Kim, J. K.; Park, J.; Chung, S.; Chung, C.; Chang, J. K. *J. Micromech. Microeng.* **2004**, (14) 6-14.

(28) Bertsch, A.; Heimgartner, S.; Cousseau, P.; Renaud, P. *Lab Chip* **2001**, 1 56-60.

(29) Mengeaud, V.; Josserand, J.; Girault, H. H. *Anal. Chem.* **2002**, 74 4279-4286.

(30) Miyake, R.; Lammerink, T. S. J.; Elwenspoek, M.; Fluitman, J. H. J. *IEEE-MEMS'93*, Fort Lauderdale, USA, Febr., 1993; pp 248-253.

(31) Stroock, A. D.; Dertinger, S. K. W.; Ajdari, A.; Mezic, I.; Stone, H. A.; Whitesides, G. M. *Science* **2002**, 295 (1) 647-651.

(32) Johnson, T. J.; Locasio, L. E. *Lab Chip* **2002**, (2) 135-140.

(33) Jen, C.-P.; Wu, C.-Y.; Lin, Y.-C.; Wu, C. Y. *Lab Chip* **2003**, 3 73-76.

(34) Glasgow, I.; Aubry, N. *Lab Chip* **2003**, 3 114-120.

(35) Niu, X.; Lee, Y.-K. *J. Micromech. Microeng.* **2003**, 13 454-462.

(36) He, B.; Burke, J.; Zhang, X.; Zhang, R.; Regnier, F. E. *Anal. Chem.* **2001**, 73 (9) 1942-1947.

(37) Hong, C.-C.; Choi, J.-W.; Ahn, C. H. In *Micro Total Analysis Systems*; Ramsey, J. M.; van den Berg, A., Eds. Kluwer Academic Publishers: Dordrecht 2001; pp 31-33.

(38) Voldman, J.; Gray, M. L.; Schmidt, M. A. In *Micro Total Analysis Systems*; Harrison, J.; van den Berg, A., Eds. Kluwer Academic Publishers: Dordrecht 1998; pp 181-184.

(39) Yang, M.; Yang, J.; Li, C.-W.; Zhao, J. *Lab Chip* **2002**, 2 158-163.

(40) Penth, B. WO 00/61275, 1999.

(41) Schenk, R.; Hessel, V.; Werner, B.; Ziogas, A.; Hofmann, C.; Donnet, M.; Jongen, N. *Chem. Eng. Trans.* **2002**, (1) 909-914.

## Chapter 22

### Gas–Liquid Processing in Microchannels

**Ward TeGrotenhuis<sup>1</sup>, Susie Stenkamp<sup>1</sup>, and Alvin Twitchell<sup>2</sup>**

<sup>1</sup>**Battelle Memorial Institute, Pacific Northwest Division,  
Richland, WA 99352**

<sup>2</sup>**Washington State University Tri-Cities, 2710 University Drive,  
Richland, WA, 99354**

Processing gases and liquids together in microchannels having at least one dimension <1 mm has unique advantages for rapid heat and mass transfer. One approach for managing the two phases is to use porous structures as wicks within microchannels to segregate the liquid phase from the gas phase. Gas-liquid processing is accomplished by providing a gas flow path and inducing flow of the liquid phase through or along the wick under an induced pressure gradient. A variety of unit operations are enabled, including phase separation, partial condensation, absorption, desorption, and distillation. Results are reported of an investigation of microchannel phase separation in a transparent, single-channel device. Next, heat exchange is integrated with the microchannel wick approach to create a partial condenser that also separates the condensate. Finally, the scale-up to a multi-channel phase separator is described.

## Introduction

Devices based on microchannel architecture, developed by Battelle and Pacific Northwest National Laboratory, have enabled process intensification—high throughput per unit hardware volume—of many unit operations, including heat exchange, reactions, and separations (1,2). With these devices, thermal and chemical processing takes place through an array of channels having at least one dimension that can range from a few millimeters to just a fraction of a millimeter. Consequently, extremely rapid heat and mass transfer rates occur that allow for orders of magnitude reduction in hardware volume and mass. Performing unit operations involving both gases and liquids in microchannels, however, presents unique challenges for managing and controlling the two phases.

Past approaches for processing gases and liquids together in small channels have included using interfacial tension to prevent intermixing of the phases. In some cases, the approach has been accomplished with planar porous contactor plates that are non-wetting for one of the phases, which then allows the two phases to flow along opposite sides to facilitate mass transfer without being mixed (3,4). In a similar approach, two straight microchannels, each carrying one phase, are constructed to overlap slightly such that the interface between the phases is pinned at the gap. This configuration allows the two phases to flow through their respective channels, remaining segregated while achieving mass transfer (5).

In this effort, a new wicking approach is taken for processing multiple phases in microchannels, which is to employ a thin, permeable structure as the flow medium for one phase while allowing the other phase to flow through an open channel in the same way that vapor and liquid recirculate within a heat pipe (6). One phase, typically the liquid, is preferentially wetting for the porous wick and resides in the wick because of capillary forces.

This ability to segregate the phases within a microchannel facilitates a number of possible unit operations, including phase separation, partial condensation, evaporation, absorption, desorption, and distillation (7). The focus of this paper is phase separation and partial condensation. However, the advances in controlling gas and liquids in microchannels, while also heating and cooling, enable other unit operations as well.

## Theory of Operation

The common elements among the family of Microwick technologies—those utilizing wicks to segregate gases and liquids in microchannels—are thin, planar

porous structures. Figure 1 illustrates the basic architecture for the specific case of phase separation. The rectangular channel is deeper than the thickness of the wick to provide an adjacent open plenum for gas flow. Because the porous wick is wetting for the liquid, the liquid preferentially sorbs into it and is held there by capillary forces as long as the wick is kept at a lower pressure. In addition, the gas will not displace the liquid from the wick as long as the pressure difference does not exceed a maximum value, referred to as the breakthrough pressure, which is determined from the Young-Laplace equation (8),

$$\Delta P_{BT} = \frac{2 \sigma \cos(\theta)}{r_p} \quad (1)$$

where  $\sigma$  is the surface tension of the liquid,  $\theta$  is the contact angle between the liquid and the wick material, and  $r_p$  is the pore radius.

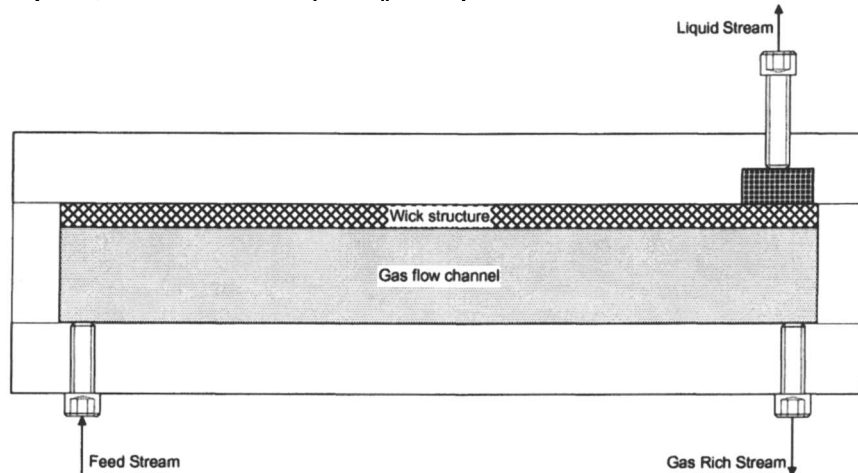


*Figure 1. Schematic of microchannel phase separator with liquid flow along wick from left to right to liquid stream outlet.*

Gas-liquid processing generally requires flow of the liquid through the porous structure, which is characterized by Darcy's equation (8),

$$K = \frac{\mu_L L Q}{A \Delta P} \quad (2)$$

where  $K$  is the permeability coefficient,  $\mu_L$  is the viscosity of the liquid,  $L$  is the length of the flow path,  $Q$  is the volumetric flow rate of liquid,  $A$  is the flow area, and  $\Delta P$  is the liquid pressure drop. In some cases, the liquid flows in the plane

of the wick, such as from left to right in Figure 1. In other cases, the liquid flows primarily through the wick perpendicular to the plane of the wick, in which case  $A$  is the area of the wick and the flow length,  $L$ , is the wick thickness. When the primary purpose is phase segregation flow is generally through the wick to maximize flow area and minimize flow resistance for maximum processing capacity. In the partial condenser device described herein, liquid flow is a combination of flow in the plane and flow perpendicular through the wick.

Furthermore, layered wick structures can be employed with the top layer adjacent to the gas flow channel having high porosity and high permeability to provide good sorption capacity, and the lower level, typically referred to as the pore throat, having a tighter pore structure to give increased breakthrough pressure and thus preclude gas intrusion into the liquid outlet. The devices used in this work employ two layers, a wicking layer and a pore throat layer.

Another important aspect of phase segregation is capturing the liquid entrained in the flowing gas stream. Possible mechanisms for recovering the liquid phase include hydrodynamics, inertial capture, imposed forces on liquid droplets, and Brownian motion. In the devices reported here, liquid capture occurs primarily by hydrodynamic and inertial forces. Hydrodynamic forces are attributed with two-phase flow behavior, which can range from annular and stratified flow to slug flow to bubbly flow (9). Two-phase flow behavior has been mapped for a variety of geometries and environments (10-14). Presumably, if the device can be operated in a flow regime where the phases are naturally segregated, such as in annular or stratified flow, then the liquid phase can be brought into contact with and sorbed into the porous wicks. Inertial forces arise from centripetal acceleration when a fluid stream changes direction, and can also be used effectively in microchannels for capturing larger particles. Direct forces can be applied to the liquid droplets by gravity or other imposed fields which can be deployed in microchannels. Random motion, referred to as Brownian motion, will cause droplets smaller than 10 microns to diffuse from the flow field given sufficient residence time (8). Direct forces and Brownian motion are not primary separation mechanism in the devices described here.

## Phase Separation

Initial efforts in performing phase separation using wicking concepts were performed with the transparent, single channel, device shown in Figure 2, oriented horizontally with the gas channel located above the liquid channel. As discussed below, these initial investigations provided important insights into the principles and relative importance of mechanisms in achieving separation of gases and liquids using porous materials in microchannels.

The open gas flow channel of the test device was 7.3 cm x 1.4 cm x 0.27 cm, while the adjacent liquid channel was 8 cm x 2 cm x 0.064 cm, consisting of Pall Supramesh Z sintered metal porous material overlying a 70-mesh woven stainless steel screen. The permeability of the Pall Supramesh Z was measured to be  $1.8 \times 10^{-10}$  cm<sup>2</sup>. The device was tested with water, decane, and 4 cp and 14 cp water-glycerin mixtures to investigate the relative importance of liquid density and surface tension. Air and liquid were mixed at a 1/8-inch Tee fitting before being introduced into the device. Additional details of the single channel device, apparatus, and experimental procedures can be found in TeGrotenhuis and Stenkamp (15).

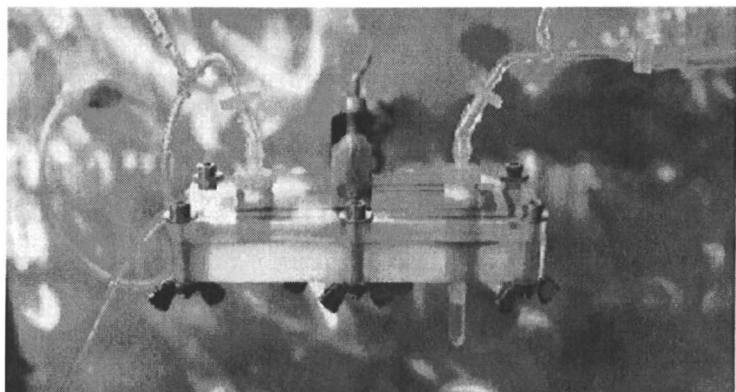


*Figure 2. Single-channel, microchannel phase separator test device.*

Experiments were performed at increasing liquid flow rate at constant gas flow and pressure difference between the gas and liquid outlets. At low liquid flows, recovery of liquid from the flowing gas stream was complete, and very little hold-up of liquid water was observed in the liquid channel, as indicated by Figure 3. In this operating regime, the primary mechanism for capturing water from the gas channel is by impaction of the droplets against the pore throat as the flow enters perpendicular to plane of the channel.

The incipient liquid breakthrough point is a function of a number of parameters, including the gas flow rate, the pressure difference across the pore throat, and the properties of the liquid. The pressure difference across the pore throat determines the maximum liquid flow capacity by Equation 2, and the pore throat utilization is determined as the ratio of maximum liquid removal capacity divided by the pore throat flow capacity at a give pressure difference. In the experiments, the pore throat utilization varied between 10% and 90% and generally decreased with increasing gas and liquid flows, as expected.

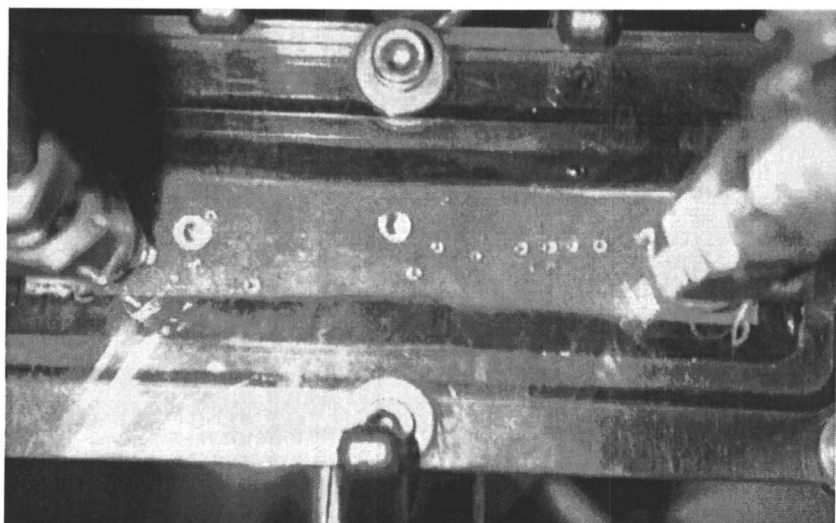


*Figure 3. View of device top with flow rates of 2 mL/min of water and 1 SLPM of air. The pressure drop across the pore throat is 12 inches of water. No breakthrough is observed.*

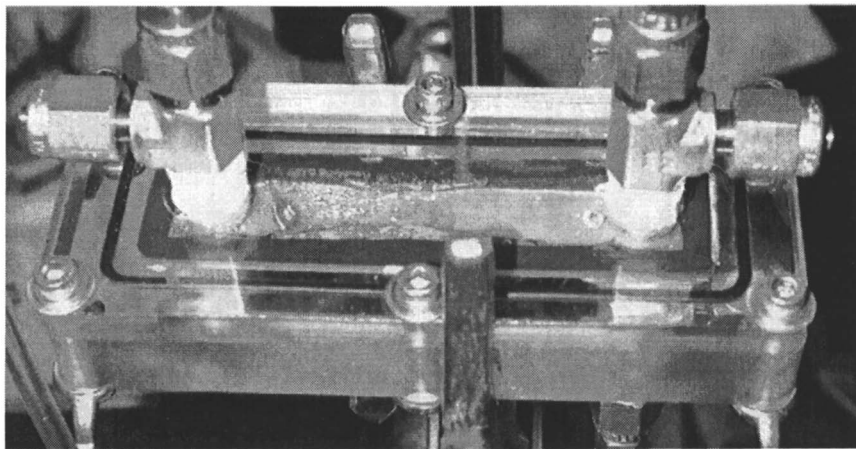


*Figure 4. Device running with flow from left to right at flow rates of 40 mL/min of water and 1 SLPM of air. The pressure difference across the pore throat is 12 inches of water. No breakthrough is observed.*

In addition to the limitation of pore throat flow capacity, hydrodynamic limits within the gas channel were also uncovered through dimensional analysis. The superficial gas and liquid Reynolds numbers are defined as  $Re_{GS} = \rho_G U_{GS} D_h / \mu_G$  and  $Re_{LS} = \rho_L U_{LS} D_h / \mu_L$  (12), where  $\rho$  is density,  $D_h$  is the hydraulic diameter of the gas channel,  $\mu$  is viscosity, and subscripts  $G$  and  $L$  refer to gas and liquid phase, respectively. The superficial velocity,  $U_s$ , is the volumetric flow of a given phase divided by the gas channel cross-sectional area. The Suratman criterion, which is based on the Suratman number defined as  $Su = \sigma D_h \rho_L / \mu_L^2$  (12), for the slug to annular flow transition for two-phase flow in microgravity (12) is also predictive of the incipient breakthrough of liquid from the separator, as shown in Figure 5. This indicates that hydrodynamic forces dictating two-phase flow behavior in the gas channel are important for segregating the liquid from the gas and allowing liquid to be siphoned from the gas channel through the pore throat. Consequently, flow maps, such as the Suratman criterion, are useful tools for predicting the onset of slug flow behavior of the two-phase mixture in the gas channel leading to inadequate phase separation.

The other important consideration of phase separator performance is the exclusion of gas from the liquid flow channel. In this case, capillary forces preclude gas intrusion into the pore throat, as described by Equation 1 above. The Supramesh pore throat material is believed to have a maximum pore radius of 15 microns, and measured contact angles and surface tensions were used to calculate breakthrough pressures for each of the liquids. Breakthrough of gas through the pore throat occurred at pressure differentials as low as 30% of the

calculated breakthrough pressure. This can be attributed to pressure fluctuations, potential for contamination lowering the contact angle and surface tension during the experiments, and the potential presence of larger pores.

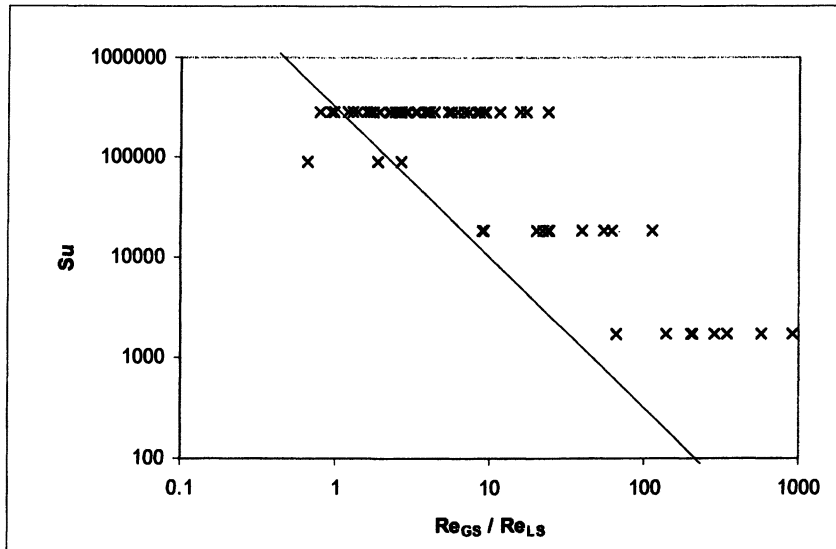


Figure 5. Map of the transition to breakthrough of liquid out of the device as determined by the Suratman number and the ratio of the gas to liquid Reynolds numbers. The line corresponds to the slug-annular transition found for two-phase pipe flow in microgravity (12).

### Partial Condensation and Phase Separation

Microchannel architectures are scaled up by stacking the planar channels to form an array of parallel channels that will accommodate the required processing rates. A second set of channels can then be interleaved that are in intimate thermal contact with the first set to provide active heat exchange between two fluids flowing through the two sets of channels. By interleaving heat exchange channels with microchannel phase separation channels, a partial condenser with phase separation is constructed. In the device described here, the heat exchange channels are constructed for air-cooling with low pressure drop in cross-flow.

An exploded-view schematic of the stacked components that form the partial condenser is shown in Figure 6. Three components are stacked with gaskets in between. On the bottom and top are arrays of 142 heat exchange channels that are 0.61 mm x 2.5 mm in flow profile and 3.05 cm long. The slots are separated

by 0.25-mm webs that serve as heat exchange fins to enhance air side heat exchange. The heat exchange elements are aluminum and weigh 23.5 g each. Condensing flow channels are located adjacent to the heat exchange channels separated by a 0.25-mm thick wall. Condensing flow channels are formed by ridges, as shown in Figure 7, and are 0.25 mm deep, 4.3 mm wide, and 14.5 cm long. There are five channels formed by each condensing element for a total of 10 microchannels for condensing heat exchange.

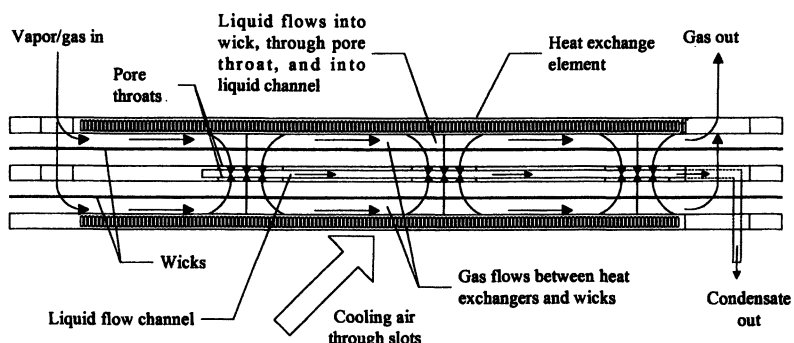


*Figure 6. Schematic of an exploded view of the microchannel partial condenser and phase separator.*

Adjacent to the condensing channels are thin wicking structures intended to absorb condensate from the condensing flow channels. At the center of the stack is the separator element shown in Figure 8. An interior liquid flow channel is hydraulically connected to the absorbent wicks on each side by three pore throat windows that are 2.5 cm x 1.3 cm and consist of the Pall Supramesh Z material. The average measured permeability of the pore throat material in the separator is  $6 \times 10^{-10} \text{ cm}^2$ , and the breakthrough pressure is approximately 4.4 kPa. A tube connected to one end of the liquid channel allows condensate to be siphoned from the device by maintaining the liquid outlet at a slightly lower pressure than the condensing channels.

A mixture of vapor and non-condensable gas is fed into a header region at one end and distributed into the array of condensing flow channels. Air blowing cross-current through vertical slots in the heat exchange elements cools the gas mixture and condenses the vapor flowing through the microchannels. The objective is to operate the device in the appropriate flow regime, whereby the liquid can be effectively transported from the condensing surface to the wick without entraining liquid in the flowing gas and transporting it to the gas outlet.

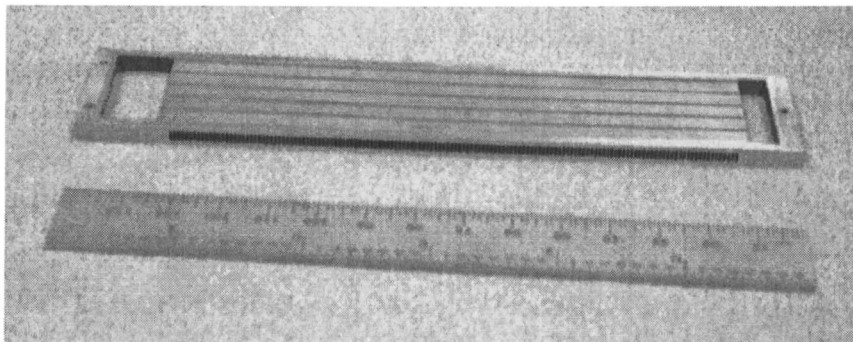


*Figure 7. Heat exchange element of the partial condenser is shown along with a 6-inch ruler for scale.*

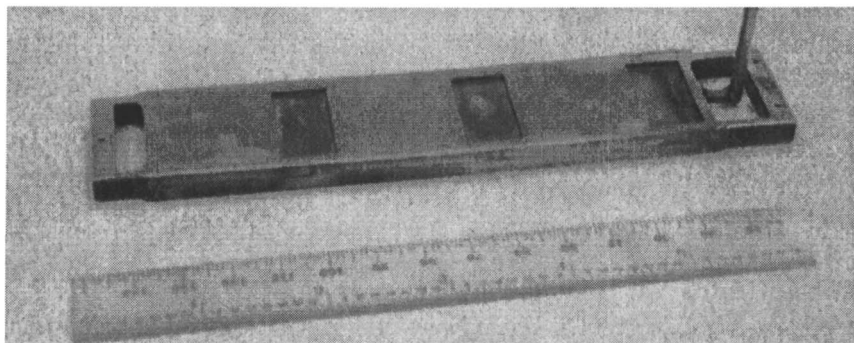


*Figure 8. Phase separator of the partial condenser is shown along with a 6-inch ruler for scale.*

The performance of the partial condenser and phase separator was tested on NASA's KC-135 reduced gravity aircraft. The aircraft performs parabolic maneuvers every 1 to 1.5 minutes, thereby achieving short periods of reduced gravity lasting about 20 seconds alternating with periods of hyper-gravity as the plane pulls out and regains altitude. Zero gravity is typically represented by less than 0.04 g, while 1.8 g is the maximum. Parabolas are performed in sets of 10 to 12 separated by 1- to 3-minute breaks as the aircraft turns around. Typically, 40 parabolas are performed during a given flight.

For performance testing of the device, mixtures of air and steam were fed at temperatures of 70-95°C and cooled to less than 40°C. Condensate was successfully separated from the gas stream in the absence of gravitational forces over a range of operating conditions. Additional details of the test apparatus and the experimental procedure are given in TeGrotenhuis and Stenkamp (16).

Breakthrough of the condensate to the gas outlet tended to occur at higher condensing stream flow rates and at increasing outlet temperature gas stream, as indicated by the data in Figure 9. The importance of outlet condensing stream temperature is attributed to increased condensation near the outlet of the condensing flow channels at the higher outlet temperatures, which increased the opportunity for liquid entrainment. Flow capacity of the pore throats of the separator was not a significant factor. Breakthrough of gas into the condensate stream rarely occurred during the reduced gravity experiments as long as the difference in pressure between the inlet and the liquid outlet was maintained below the breakthrough pressure of 4.4 kPa.

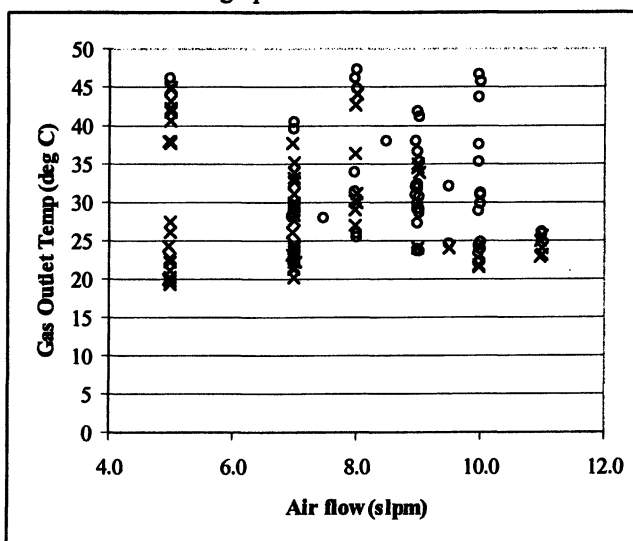


*Figure 9. Compilation of phase separation effectiveness at varying condensing stream air flow rates and gas outlet temperatures where liquid breakthrough occurred (o) and did not occur (x).*

The limited duration of the low gravity flights and the relatively large thermal inertia of the condenser-separator housing and piping presented a challenge for achieving steady-state temperatures and heat balances (16).

Average heat fluxes across the primary heat transfer area, based on the calculated enthalpy change of the hot stream, ranged from 1 up to almost 7 W/cm<sup>2</sup>, depending on the flow rate and fraction of water in the feed. The mean overall heat transfer coefficient,  $U_m$ , was calculated by dividing the average heat flux by the log-mean temperature difference (LMTD) for cross-flow heat exchange using inlet and outlet gas temperatures. The mean overall heat transfer coefficient is a function of the water content of the feed, as seen in Figure 10.

Heat transfer power density and specific power are critical parameters when size and weight are important. Using only the size and weight of the heat exchange elements, calculated heat transfer energy densities exceeded  $10 \text{ W/cm}^3$ , and specific powers exceeded 5000 W/kg.

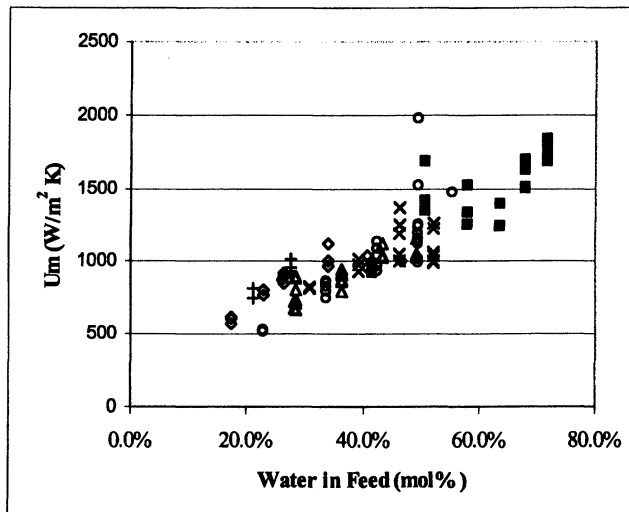


Figure 10. Mean overall heat transfer coefficient versus percent water in the feed at condensing stream air flows of 11 SLPM (+), 10 SLPM (◊), 9 SLPM (Δ), 8 SLPM (x), 7 SLPM (○) and 5 SLPM (■).

### Phase Separation Scale-up

With microchannel technologies, the process of scale-up involves increasing the number of channels to meet a productivity objective. Among the challenges with numbering up includes good flow distribution among the channels. In this work, scale-up of microchannel gas-liquid processing has been pursued for the application of recovering water from the cathode effluent of a polymer electrolyte membrane (PEM) fuel cell power system for the NASA. In this application, water produced at the cathode of the fuel cell must be recovered from a pure oxygen stream being recycled back to the cathode. The specifications for the water separator required for a 5-kWe fuel cell system are

- Remove 40 ml/min water from cathode effluent.
- Process 2.7 to 54.3 SLPM of humidified oxygen.
- Operate at pressures from 45 to 75 psia and a temperature of 80°C.
- Do not exceed a pressure drop of 5 psid.

- Operate effectively in zero gravity up to 3 g.

In addition, materials of construction must be compatible with a high oxygen concentration. Furthermore, the device must respond to transients in fuel cell load (load following), and have an operating life of 10,000 hours. Size and weight are also of paramount importance for space applications.

The multi-channel phase separator shown in Figure 11 was designed and built to meet the above requirements. Good flow distribution between the channels was achieved by designing the pressure drop in the entrance header to be small compared to the pressure drop in each channel, thus allowing the flow to distribute evenly in the header before entering the channels. The design calls for three gas flow channels 3 cm wide x 5 cm long. The separator is constructed by stacking components, allowing the height of the gas channels to be determined by the thickness of spacer bars, which can be varied. Testing was performed with a gas flow channel height of 2 mm. Thin absorbent materials supported by metal screens to provide stiffness, and located above and below the gas channels, are used for absorbing the water from the gas flow channels. Thin cotton cloth was used in this case, although more inert materials, such as ceramic cloth or woven Kevlar, will be required for pure oxygen atmospheres. The absorbent material was pressed up against Pall Supramesh Z sintered metal pore throats with an active area of 3.0 cm x 6.9 cm. The pore throats are fit into frames that define liquid flow channels having dimensions of 3.0 cm x 5.6 cm and 0.2 cm deep with a 1/16"-ID tube welded onto one end to form an outlet for the captured water. Consequently, there are three gas flow channels bounded by four liquid channels. The bottom liquid channel, pore throat, and absorbent material extend over the full bottom of the separator, as shown in Figure 12.

The operation of the device is depicted in Figure 12. The mixture of gas and liquid flow into the inlet header of the device, turns 90 degrees, and distribute among the three gas flow channels where the liquid is removed by absorbing into the wicking materials. The gas then flows to an outlet header and exits the device. The liquid outlets from the four liquid flow channels are maintained at slight negative pressure relative to the flowing gas stream to siphon the liquid from the device.

For the device to operate correctly, a pressure difference between the gas and liquid channels is required, which cannot exceed the breakthrough pressure of the pore throat material or about 20 inches of water column (0.72 psi). An Alicat Scientific, Model PCLR-1PSID-D differential pressure controller was used for active control of the pressure difference. The active control element is a gate valve located in the piping of the outlet gas stream.

The device has been tested in the laboratory at the Pacific Northwest National Laboratory, in a test stand at the NASA Johnson Space Center, and in reduced gravity on NASA's KC-135. In normal gravity, the device was operated in three orientations: 1) gas inlet and outlet pointing upward as shown in Figure 11, 2) upside down, and 3) with the liquid outlets pointing downward. Device performance in normal gravity was largely independent of the orientation of the separator.

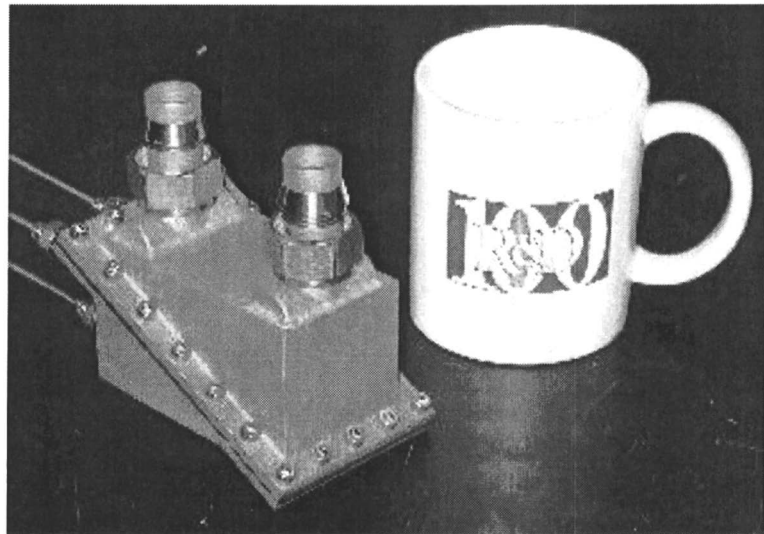


Figure 11. Multi-channel microchannel phase separator designed to remove water from the cathode effluent of a 5-kWe PEM fuel cell system.

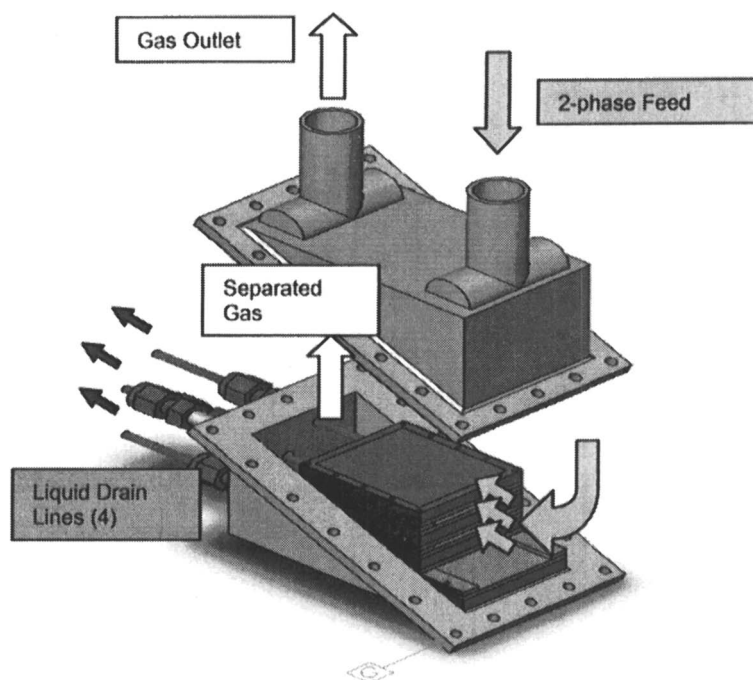


Figure 12. Schematic showing operation of the multi-channel phase separator.

Separator performance can be characterized by the maximum liquid recovery rate without breakthrough of liquid to the gas outlet or liquid to the gas outlet at a given gas flow and constant operating parameters. Separator performance in upward orientation is summarized in Table 1 for operation in normal gravity at three operating pressures, two gas flows and varying differential pressures across the pore throat. The last column gives the maximum flow rate at which 100% liquid removal occurs. It can be seen that with sufficient pressure differential, the maximum liquid recovery rate exceeds the liquid flow limit of the system. However, as the pressure differential decreases, the liquid capacity decreases until eventually complete separation of the phases becomes difficult and unpredictable. Furthermore, this minimum pressure differential is dependent on the operating pressure. At 45 psia, separation becomes unstable below 4.4 inches of water differential pressure, while the unstable point appears to be about 5.3 inches of water when the pressure is increased to 70 psia. This implies that a larger driving force is required across the pore throat for good separation as pressure increases.

The multi-channel separator has two primary mechanisms by which water is captured from the flowing gas stream. The first results from inertial forces on the higher density liquid phase that will cause the liquid to impact the absorbent material on the bottom of the inlet header as the gas flow turns 90°. Liquid inertia will tend to increase the fraction of liquid going to the bottom liquid channel. The second mechanism is hydrodynamic capture as the stream flows through the microchannels, because the liquid will preferentially migrate to the corners and walls in the appropriate flow regime.

As pressure increases, density of the gas increases, causing the average velocity of the entire stream to decrease, and reducing the inertia of the entrained liquid. Consequently, the effectiveness of the inertia mechanism for capturing the liquid is diminished with increasing pressure. Furthermore, the distribution of liquid between the channels is expected to improve.

The flow map for the separator is not well-characterized, and even the flow and composition of the stream passing through a given channel is not known. Therefore, the ability to correlate performance to established flow maps is difficult. However, the impact of pressure on critical two-phase flow parameters can be examined for qualitative trends. As pressure increases, the gas density increases; the gas superficial velocity,  $U_{GS}$ , decreases; and the liquid density and superficial velocity remain unchanged. As a result, the gas and liquid superficial velocities remain unchanged, as does the Suratman number. Consequently, the Suratman flow used for correlating single channel performance is unaffected by change in pressure. However, the Bousman (13) flow map suggests that the decrease in gas superficial velocity will move the flow behavior toward slug flow, increasing the likelihood of slugs being formed and carried from the device. Therefore, increasing pressure may affect both the inertia and hydrodynamic mechanism for liquid capture. Further study is required to discern their relative importance.

*Table 1. Maximum liquid removal capacity of the multi-channel separator oriented upward in normal gravity.*

Operating pressure (psia)	Gas flow (SLPM)	Pressure differential (in.H <sub>2</sub> O)	Max. liquid removal (ml/min)
16	20	7.8	> 140
16	20	6.0	> 180
45	20	6.0	> 160
45	20	5.5	> 180
45	55	14.1	> 110
45	55	12.2	> 110
45	52	5.5	> 180
45	55	4.4	40
70	20	6.4	> 180
70	20	5.5	120
70	20	5.0	80
70	55	20.2	> 110
70	55	7.8	50
70	55	5.5	60
70	55	5.3	40

During testing on board NASA's KC-135 reduced gravity aircraft, the separator was able to achieve complete separation of a mixture of gas and liquid during low and high gravity. The most problematic period was during transitions between reduced gravity and hyper gravity, when a small amount of liquid frequently escaped from the liquid outlet and/or gas intruded to the liquid outlets. The challenge of achieving relatively steady performance during the short periods of reduced gravity was confounded by difficulties in establishing a constant differential pressure across the pore throats with the differential pressure controller. This active control element was unable to maintain a constant control point during transitions in the gravity level and typically would not stabilize during the 20 seconds in reduced gravity. Consequently, the operating conditions were not stable or reproducible between experiments, making it difficult to quantify separator performance as a function of operating parameters.

Despite the difficulty with transients, complete separation of the phases was successfully achieved over a wide range of operating conditions. At the low end of gas flow, complete separation was achieved with 120 mL/min of water and 20 SLPM of air flow at an average pressure differential of 8.6 inches of water. On the other hand during a different parabola, some liquid breakthrough to the gas outlet was observed at 64 mL/min of water and 20 SLPM of air flow and at an average pressure differential of 7.1 inches of water. When the air flow rate was

increased to 95 SCFM, up to 43 mL/min of water was successfully recovered with a pressure differential of 9.2 inches of water.

## Conclusions

A novel approach for gas-liquid processing in microchannels has been described. In this approach, a transparent, single-channel device was used to understand the relative importance of mechanisms for separating entrained liquid from a flowing gas stream. The flow capacity of the wick as dictated by Darcy's Law is important, as are the hydrodynamic forces that dictate two-phase flow behavior. As the two-phase flow approaches conditions of slug flow, the likelihood of water breakthrough to the gas outlet increases, and phase separation effectiveness is compromised. The occurrence of water breakthrough in the device corresponded with the transition to slug flow as described by Jayawardena (12).

The planar microchannel architecture provides the opportunity to easily integrate heat exchange into devices. An aluminum gas-liquid phase separator, constructed with cross-flow air heat exchange channels, was tested as a partial condenser. The device operated effectively in normal gravity and reduced gravity, with high power density and specific power, while effectively recovering condensate.

A multi-channel phase separator, built to recover water from the cathode effluent of a 5-kWe PEM fuel cell was operated in multiple orientations in normal gravity, in reduced gravity, and in hyper gravity. Its performance was found to depend on operating pressure, which effects the liquid capture mechanisms, including inertial capture and hydrodynamics.

While the work described here focused on phase separation and partial condensation, the successful operation of this device creates new opportunities for process intensification with other unit operations.

## References

1. Wegeng, R. S.; Pederson, L. R.; TeGrotenhuis, W. E.; and Whyatt, G.A.; *Fuel Cells Bulletin* January 2001, 28, 8-13.
2. Ehrfeld, W.; Hessel, V.; Kiesewalter, S.; Lowe, H.; Richter, Th., Schiewe J. Microreaction Technology: Industrial Prospects, Proceedings of the Third International Conference on Microreaction Technology, Springer, Berlin, 2000, pp. 14-35.

3. TeGrotenhuis, W.E.; Cameron, R.; Butcher, M.G.; Martin, P.M.; Wegeng, R.S. *Sep. Sci. Technol.*, 1999, 34(6&7), 951-974.
4. Drost, M.K.; Wegeng, R.S.; Friedrich, M.; Hanna, W.T.; Call, C.J.; Kurath, D.E. U.S. Patent 6,126,723, 2000.
5. Shaw, J.E.A.; Simpson, R.I.; Bull, A.J.; Simper, A.M.; Holmes, R.G.G. U.S. Patent 5,961,832, 1999.
6. Faghri, A. *Heat Pipe Science and Technology*; Taylor & Francis: Washington, DC, 1995.
7. TeGrotenhuis, W.E.; Wegeng, R.S.; Whyatt, G.A.; Stenkamp, V.S.; Gauglitz, P.A. U.S. Patent 6,666,909, 2003.
8. Adamson, A.W. *Physical Chemistry of Surfaces*; Fourth Edition; John Wiley & Sons: New York, 1982.
9. Carey, V.P., *Liquid-Vapor Phase-Change Phenomena*, Hemisphere Pub. Corp., Washington, 1992.
10. Mandhane, J.M.; Gregory, G.A.; and Aziz, K. *Int. J. Multiphase Flow* 1974, 1, 537-553.
11. Taitel, Y.; Dukler, A.E. *AICHE J.* 1976, 22, 47-55.
12. Jayawardena, S.; Balakotaiah, V.; Witte, L.C. *AICHE J.* 1997, 43(6), 1637-1640.
13. Bousman, W.S. Ph.D. Thesis, University of Houston, Houston, TX, 1994.
14. Dukler, A.E.; Fabre, J.A.; McQuillen, J.B.; Vernon, R. *Int. J. Multiphase Flow* 1988, 14(4), 389.
15. TeGrotenhuis, W.E.; Stenkamp, V.S. *NASA Report: NASA/CR—2001-210955*, 2001.
16. TeGrotenhuis, W.E.; Stenkamp, V.S. *First International Conference on Microchannels and Minichannels*, S.G. Kandlikar, Ed., ASME: New York, NY, 2003; 699-706.

## Chapter 23

# Process Intensification in Water-in-Crude Oil Emulsion Separation by Simultaneous Application of Electric Field and Novel Demulsifier Adsorbers Based on Polyhipe Polymers

G. Akay<sup>1,2</sup>, Z. Z. Noor<sup>1</sup>, M. Dogru<sup>1</sup>

<sup>1</sup>Process Intensification and Miniaturization (PIM) Centre, School of Chemical Engineering and Advanced Materials, Newcastle University, Newcastle upon Tyne NE1 7RU, United Kingdom

<sup>2</sup>Institute of Nanoscale Science and Technology, Newcastle University, Newcastle upon Tyne NE1 7RU, United Kingdom  
(<http://www.Newcastle.ac.uk/PIM>)

A novel process intensification technique has been demonstrated in the demulsification (separation) of highly stable water-in-crude oil emulsions through the superimposition of an electro-static separation field with micro-porous demulsifier adsorbers which are prepared through a high internal phase emulsion polymerization route and subsequently sulphonated. These materials are also known as PolyHIPE Polymers (PHP). The hydrophilic version of PHPs is also an excellent ion exchanger and therefore during the demulsification process, they not only remove the surface active species from the crude oil, but they also remove ionic moieties thus acting as a combined demulsifier and adsorber. Although these materials can be used to demulsify stable emulsions very effectively, they are ineffective in highly stable emulsions. The same is also true for electro-static

emulsion separators. The combination of these two techniques appears to create synergy which results in the intensification of the separation process. Experiments were carried out using a model emulsion with highly viscous crude oil and model sea-water aqueous phase. An electro-static separator was used and the effects of emulsion flow rate and electric field strength were evaluated using 0.5 gram PHP demulsifier adsorber in 1 kg 50:50 water-in-oil emulsion. Complete demulsification was achieved at high flow rates or low electric field strengths when electro-static separation was not effective without the PHP demulsifier adsorber.

## Introduction

There are circumstances when the separation of emulsions is required. This process is known as demulsification. Demulsification is readily achieved in coarse emulsions but in highly stable, fine emulsions, demulsification process can be complex. Demulsification is most important in crude oil / water emulsions which can contain up to 90% water but yet it is still economically viable to remove water in the recovery of oil. Another important application of demulsification is in the nuclear re-processing when a highly stable and viscous water-in-oil emulsion (called interfacial crud) is formed which reduces the heat transfer rates as a result of equipment fouling. Stable emulsions are also produced in process industries which can cause environmental problems. Demulsification can also allow the recycling of the emulsion phases. In this study we only consider the demulsification of water-in-crude oil emulsions.

There are a number of well established mechanical, chemical and electrical demulsification techniques available, including the use of hydrocyclones, centrifuges, pH adjustment, steam/air stripping, membrane filtration, electric field and the addition of chemicals known as demulsifiers (1-11). The common purpose in these techniques is to cause the coalescence of the dispersed phase droplets which are stabilised by the surface-active materials present in the emulsion. In water-in-crude oil emulsions, the type and concentration of indigenous surface active materials are dependent on the oil-field. These indigenous surface active materials are responsible for the formation of relatively stable emulsions as a result of mixing of crude oil with water as this mixture is pumped from the oil well. Most of the crude oil demulsification techniques cited above have been developed for on-shore separation where the availability of space and storage facilities are not restricted and the oil viscosity is not high. However, this is not the case in offshore crude oil production, although oil-water separation at source of production has several advantages. Most importantly,

separation at source can utilise the potential energy of the crude oil (namely, high temperature and pressure) in destabilising the water-in- crude oil emulsion which in turn reduces the cost of pumping of the produced water and subsequent re-heating of the crude oil for separation. Thermal de-stabilisation of emulsions is well known. Recently, it was shown that the emulsion stability decreases with increasing pressure (10) and hence separation at source (either on the off-shore oil platform or on the sea-bed or down hole) can be economically desirable, socially acceptable and technologically safe.

Conventional methods of demulsification may take days, due to large hydraulic residence time. Due to the large volumes of crude oil and slow rate of separation, the mechanical systems such as gravity settling, hydrocyclones, centrifugal separators and stripping columns are large and costly as the concentration of water in the emulsion increases due to the advancing age of the oil wells. Therefore, the current technology can not be used in off-shore applications especially when the emulsions are highly stable. What is needed is an intensified process which requires extremely fast demulsification rate with small processing volume in a continuous process.

Recently, such a process has been disclosed (9). This process consists of two elements. Firstly, it was discovered that hydrophilic micro-porous polymers are highly effective as demulsifiers for the removal of surface active species from emulsions (interfacial crud) produced during the nuclear re-processing of spent radio-active fuel. This was also true for water-in-crude oil emulsions. These micro-porous polymers are prepared through a high internal emulsion (HIPE) polymerisation route and are known as PolyHIPE Polymer (PHP) (11-15). Secondly, these polymers are also very effective for the removal of metal ions through an ion exchange mechanism (11, 14). Furthermore, they also adsorb organic toxins due to the presence of hydrophilic and hydrophobic domains on the walls of the porous structure. Consequently, these polymers are named as demulsifier adsorbers.

A very useful hydrophobic PHP is based on cross-linked styrene-divinyl benzene. These materials can be manufactured over a wide range of pore size, D ( $0.5 \mu\text{m} < D < 5000 \mu\text{m}$ ) and interconnect size, d ( $0 < d/D < 0.5$ ). Pores with size above  $\sim 200 \mu\text{m}$  are obtained through a coalescence polymerisation route as described previously (13-15). Post polymerisation chemical functionalization (such as sulphonation) can be achieved by incorporating the necessary chemical species in the oil or aqueous phase during the emulsification stage in order obtain uniform chemical structure (14). This technique is especially useful and economically necessary in the sulphonation of monolithic materials.

PolyHIPE Polymers have been used in several chemical process intensification as well as support for animal cells and bacteria in tissue engineering and bioprocess intensification (16-19). They are also useful in the separation of tar and water from gases produced through the gasification of

biomass (20). PolyHIPE polymers are used as templates for the manufacture of nano-structured micro-porous metals used in intensified catalysis (11). The imposition of nano-structure in the PolyHIPE Polymer is also possible (13) where the micron-thick pore walls have nano pores present. These nano-structured micro-porous polymers therefore provide enhanced surface area which is accessible to reactants as a result of the pore size gradient.

The use of electrostatic separation of water-in-crude emulsions has several advantages such as low power consumption due to low electrical current across the dispersion (3). This technique is independent of moving parts so it is free from mechanical breakdown. Combining electrical separation technology with various other techniques such as centrifugal separation (5-7), heating (8) and addition of chemicals was found to create synergy.

Demulsifiers have become an increasingly popular method in destabilising emulsions especially in oil and petroleum industries. Demulsifiers can also be used as pre-treatment to inhibit emulsification process by adding them to the crude oils (21). Demulsifiers are blend of several chemical compounds with different chemical structures (22,23) and broad distribution of molecular weight. Normally, demulsifiers used for crude oil destabilisation are polymeric. Since sulphonated PolyHIPE Polymers appear to selectively remove surfactants (24-26) thus causing demulsification (9), in this study we investigate the use of sulphonated PolyHIPE Polymer as demulsifier adsorber in the presence of high voltage electric field in order to intensify the demulsification of water-in-crude oil emulsions.

## Material and Experimental Method

### Materials

The crude oil (from Harding Field in the North Sea) was supplied by BP Amoco. It has a specific gravity of 0.80 mg/L. The crude oil is Newtonian over the experimental shear rate range (up to 1000 s<sup>-1</sup>) with viscosity (measured by HAAKE VT550 viscometer at 25°C) 153 mPa.s. A model sea water was used as the internal phase which contained CaCl<sub>2</sub>, MgCl<sub>2</sub> and NaCl. These chemicals were obtained from Merck and they were used as received. De-ionised water was used in the preparation of the model sea-water. The PolyHIPE Polymer demulsifier adsorber used in this study was previously developed (9). The preparation of this material is described in (13). It is a sulphonated PHP in the form of granules with the size range of 700 to 1000 µm.

### *Emulsion Preparation*

Water-in-crude oil emulsions had equal phase volumes of oil and water phases. The aqueous phase contained: 28.1 g/L NaCl; 0.6 g/L CaCl<sub>2</sub>; 5.0 g/L MgCl<sub>2</sub>; and had a density of 1.021 g/mL. No synthetic surfactant was used in the preparation of the emulsions since the crude oil has indigenous surfactants present. The model emulsion used in this experiment was prepared in a stainless steel, laboratory scale mixer at room temperature. The mixer had a diameter of 12 cm and an approximate nominal capacity of 550 ml. The temperature of the vessel was controlled by water circulation. The stirrer was powered by an electric motor allowing rotation speeds over a range of 200 to 2000 rpm. The mixing was conducted using two 100 mm diameter flat paddles at 90 degrees to each other. Details of the equipment are given in (9,10).

The emulsions were prepared at a volume of 500 ml (i.e. 250 ml crude oil and 250 ml aqueous phase). First, the oil phase was placed into the vessel and aqueous phase was pumped in five minutes while mixing at 2000 rpm. Mixing was continued for another 15 minutes and the resulting emulsion was transferred to a holding container where it was mixed with the PHP demulsifier adsorber. In order to avoid any aging effects, this emulsion was used immediately in the separation experiments. The viscosity of the emulsion was slightly shear thinning at the highest shear rates available in the Haake Viscometer. At the shear rate of 1000 s<sup>-1</sup> 50:50 water-in-crude oil emulsion had viscosity of 1030 mPa.s. Its conductivity was 0.8  $\mu$ S/cm at 25°C and the emulsions showed no sign of separation within 4 weeks of preparation.

### *Oil/Water Separation*

The oil-water separation experiments were carried out using a Perspex electric field separation cell. The cell consists of two blocks held together with six plastic screws and bolts (Figure 1). The emulsion is fed into the circular central flow channel (2 cm diameter) from the central inlet port and the samples are collected from the top and bottom outlets after passing through the stainless steel electrodes as shown in Figure 1. A rubber seal between the blocks stops the leakage of the emulsion.

Before the separation under high voltage electric field, 0.5 g demulsifier adsorber was added to 1 kg emulsion. This mixture was constantly stirred using a magnetic stirrer through out the experiment. The bottom electrode was earthed and the top electrode was connected to high positive potential. The latter electrode was fully insulated using several layers of lacquer providing a vertical electric field. High voltage (up to 30kV) DC electric field was available to apply to the top electrode by gradually increasing from zero. An ammeter was present

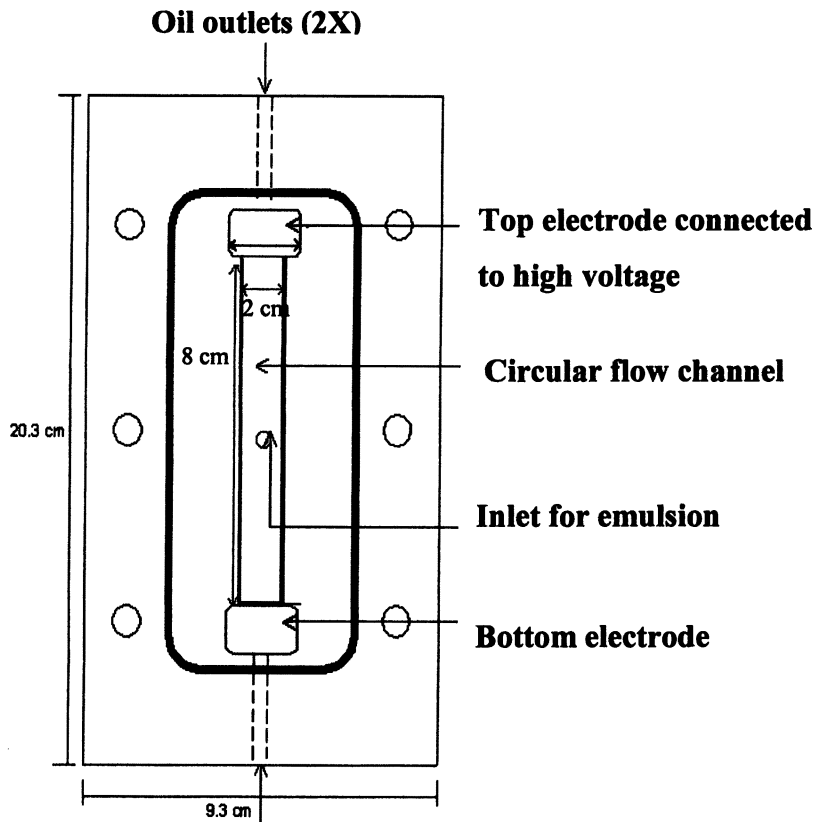


*Figure 1. Schematic diagram of the water-in-oil emulsion separation cell. The electrodes have two slits to allow fluid flow through two outlets located in each block of the separation cell.*

on the electrical equipment scaled to 15 mA. For safety reason, the power supply would automatically cut off when the current reaches 15 mA. Due to the current leakage at very high potentials, maximum level of applied potential was 5kV. Since this system is potentially hazardous, as a result of flammable oil and high voltage, after the unit that was turned off, it was left standing for at least ten minutes before further handling of the equipment to ensure there was no residual electrical charge. Samples from the top and bottom electrodes were collected in glass measuring cylinders and the emulsion was allowed to separate into oil and water phases and overall degree of separation was determined. The

degree of separation was determined immediately after collecting total of 400 ml sample (within ten minutes of separation) or alternatively after 1 hour or 24 hours.

The separation of the emulsion was conducted under constant electric field of 2.5kV (field strength of 312 V/cm) while varying the emulsion flow rate; or alternatively, at constant flow rate ( 60 mL/min) while varying the electric field strength. These experiments were repeated without the addition of any demulsifier adsorber in order to evaluate the effect of the polymer. At the end of the experiment, the demulsifier / adsorber was only present in the aqueous phase from where it was collected, dried and used in the Scanning Electron Microscopy (SEM) analysis.

#### *Scanning Electron Microscopy and EDAX*

The demulsifier / adsorber that have been used in the separation experiment was then analysed using Scanning Electron Microscope (SEM). Dried samples were mounted on aluminum specimen stubs, and coated with carbon and examined under SEM (Cambridge s240) with Energy Dispersive Analysis with X-rays (EDAX) facility. Scanning electron micrograph of the demulsifier / adsorber is shown in Figure 2.

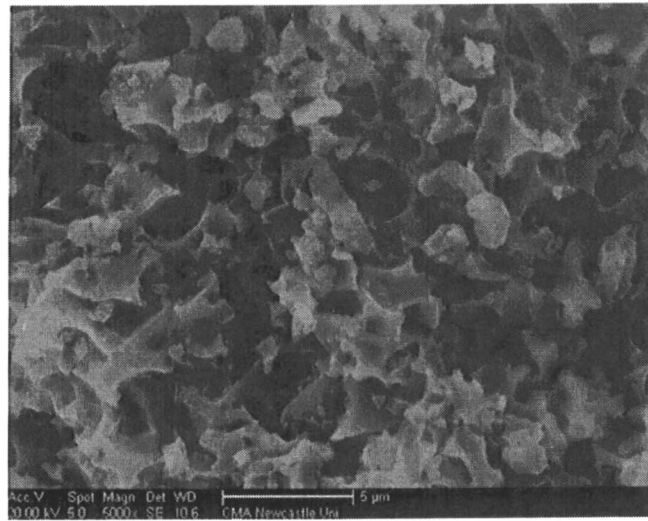


*Figure 2. Scanning electron micrograph of the demulsifier adsorber used in the experiments.*

## Results and Discussion

### Oil Water Separation Under Constant Electric Field Strength

The enhancement of electrical field separation by the use of PHP demulsifier was tested under two conditions: 1) varying flow rate of emulsion while voltage was held constant and; 2) varying voltage while flow rate of emulsion was held constant. This section described the result of the former condition. During this experiment, the voltage was held constant at 2.5 kV. In Figure 3, the variation of degree of separation immediately after the passage of the emulsion through the electric separator is shown as a function of flow rate. As shown in Figure 3, in the presence of PHP demulsifier, the separation efficiency is not reduced significantly with increasing flow rate where as, without PHP, there is no immediate separation when the flow rate is ca. 90 mL/min. However, at low flow rates, the effect of PHP is not as significant. Figures 4 and 5 illustrate the separation efficiency after 1 and 24 hours of standing respectively in the presence and absence of PHP demulsifier. As shown in these figures, as the standing time increases from 10 minutes to 24 hours, the effect of PHP demulsifier / adsorber decreases.

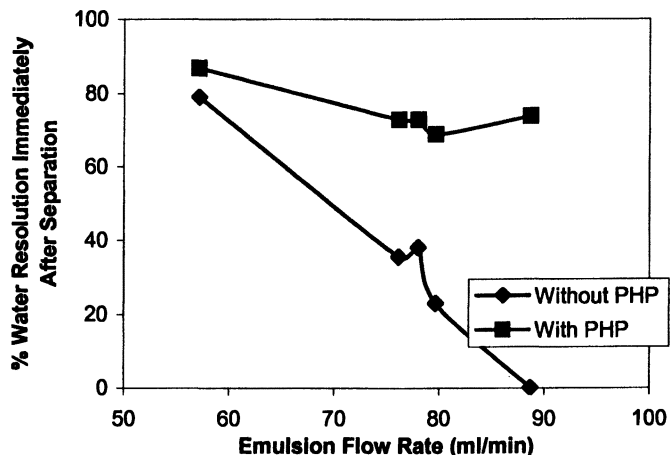


*Figure 3. Variation of percent phase separation with emulsion flow rate through the electro-static separator at 2.5 kV applied voltage immediately after emerging from the separator in the presence or absence of PHP demulsifier.*

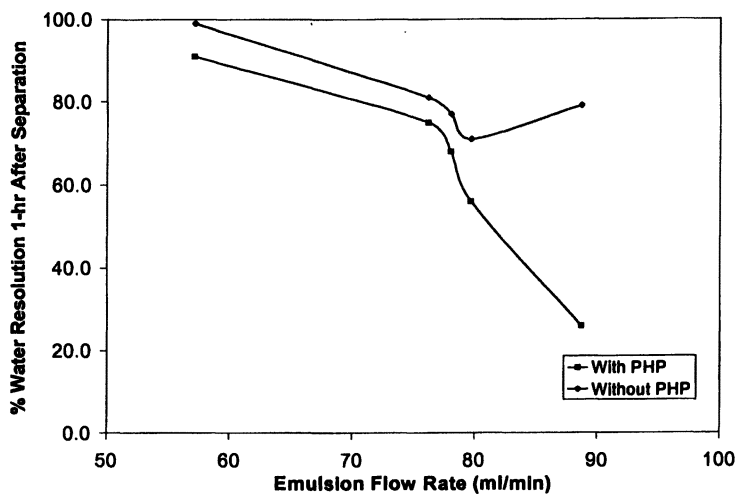


*Figure 4. Variation of percent phase separation with emulsion flow rate through the electro-static separator at 2.5 kV applied voltage after 1 hour of standing in the presence or absence of PHP demulsifier adsorber.*

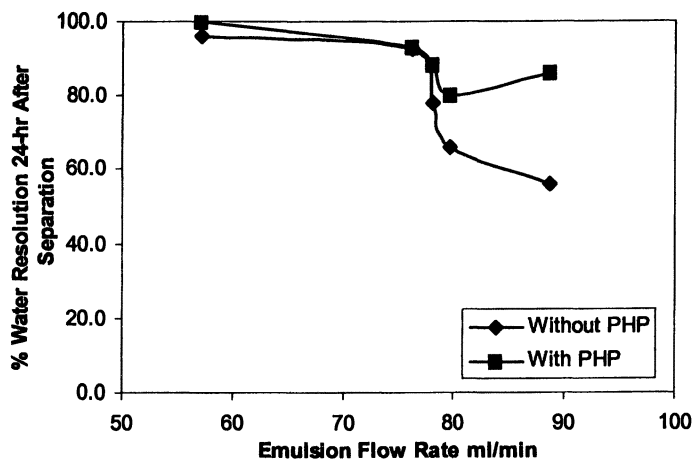


*Figure 5. Variation of percent phase separation with emulsion flow rate through the electro-static separator at 2.5 kV applied voltage after 24-hours of standing in the presence or absence of PHP demulsifier adsorber.*

### Oil/Water Separation Under Constant Flow Rate

The effect of electric field strength on the separation efficiency is shown in Figures 6 when the flow rate is kept constant at 60 mL/min. Similar to the previous case illustrated in Figures 3-5, at this emulsion flow rate 100% separation takes place within 10 minutes of leaving the electro-static separator even if the electric field strength is low (1kV) while no separation is observed without the PHP demulsifier / adsorber at this electric field strength. There is a slight improvement on the separation efficiency after an hour of standing without the polymer (data not shown).

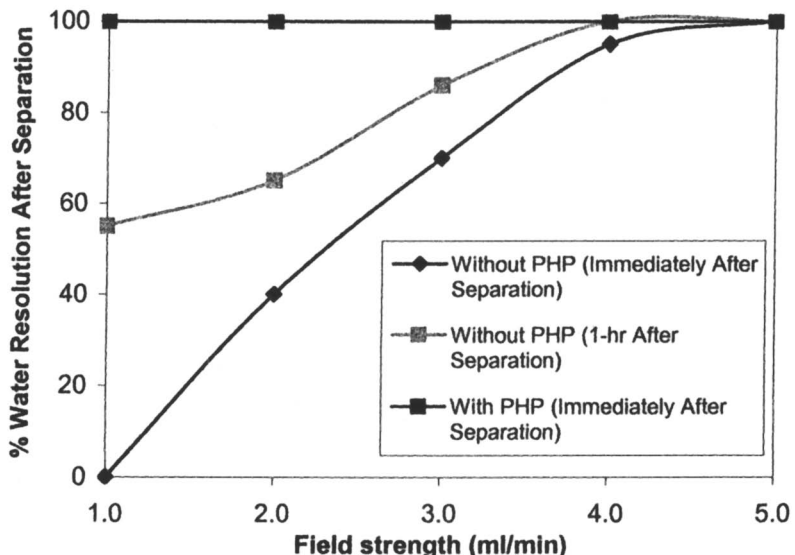


*Figure 6. Variation of percent phase separation with electric field strength at constant flow rate of 60 mL/min immediately after emerging from the separator in the presence or absence of PHP demulsifier adsorber.*

### SEM and EDAX Analysis

SEM micrograph in Figure 7 illustrates the appearance of spent demulsifier / adsorber, indicating the collapse of the porous structure due mechanical compression during the pumping of emulsion followed by drying. However,

when these dried samples are put into water, they swell again, recovering their original properties. Nevertheless, we only used fresh polymer in each experiment. Energy Dispersive Analysis with X-rays (EDAX) is summarised in Table 1 while the EDAX spectra of the carbon coated spent PolyHIPE Polymer demulsifier adsorber is shown in Figure 8 which indicates that the polymer contains several additional elements that were not present in the polymer and in aqueous phase. These additional elements are silica, aluminium, phosphorous which were removed from the crude oil. We conclude that the demulsifier adsorber is also able to remove several other compounds from the crude oil, and therefore PHP demulsifier adsorber is useful in reducing the metal loading of the crude oil.

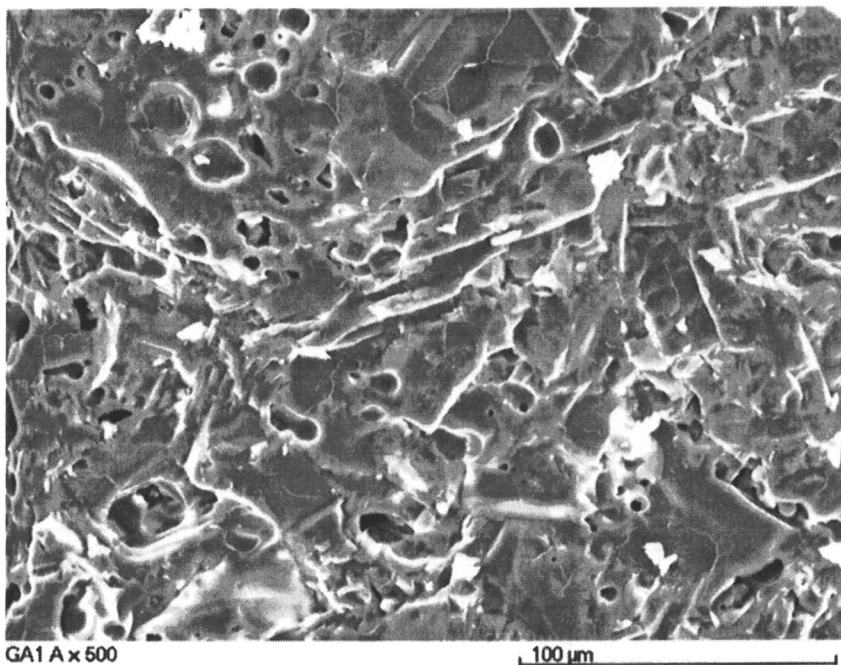


*Figure 7. Scanning Electron Microscopy of spent demulsifier adsorber indicating its collapsed structure after use and de-hydration.*

Table 1: Energy Dispersive Analysis with X-rays (EDAX) giving the molar concentration of metals adsorbed by the PolyHIPE Polymer during demulsification. Although carbon and oxygen appear in the X-ray spectrum (Figure 8 below) they were excluded from the analysis. Main elements adsorbed by the demulsifier are: Na, Mg, Al, P, S, Cl, and Ca.

*** EDAX Analysis ***					
elem/line	P/B	B	F	c(100%)	confid. h
Na K-ser	43.1	0.99937	1.00680	13.18	+ - 3.21
Mg K-ser	20.0	1.00255	1.01096	5.13	+ - 1.32
Al K-ser	11.5	1.00547	1.01852	2.65	+ - 0.8
P K-ser	22.4	1.01066	1.04885	4.05	+ - 1.13
S K-ser	150.8	1.01300	1.03648	24.61	+ - 4.13
Cl K-ser	233.9	1.01518	1.01085	37.84	+ - 5.61
Ca K-alpha	83.4	1.02104	1.01120	12.54	+ - 2.04
standardless				100.00	[2s]

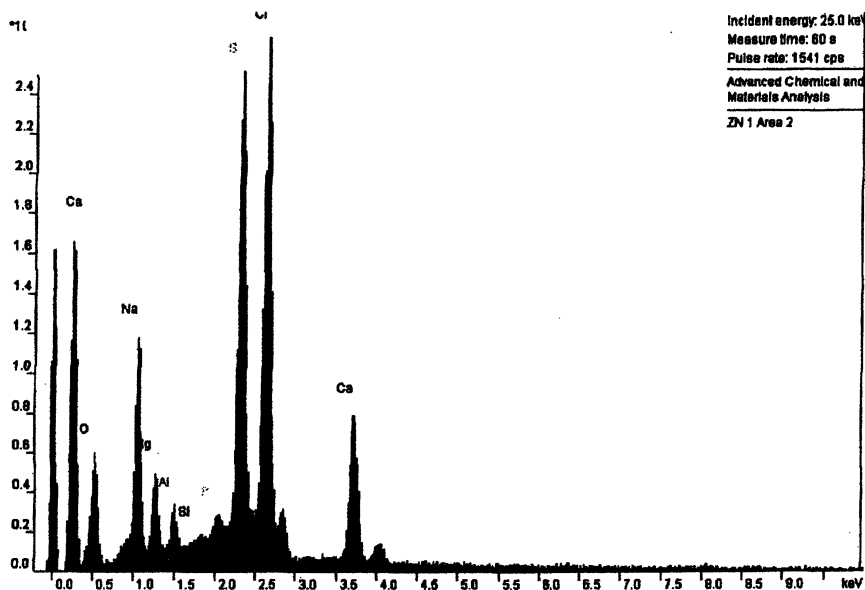


Figure 8. EDAX spectrum of spent demulsifier adsorber

## Discussion

Because of their unique ability to form well ordered molecular aggregates and structures, ranging from a few nanometers to several hundred microns, surfactants can be used in the intensification of separation processes such as the removal of organic and heavy metal ion contaminants from water. Surfactant mediated separations can be further enhanced by the orthogonal superimposition of crossflow separation field and an electric field (24-26). Furthermore, surfactants can be degraded electrochemically and therefore the emulsion separation can be achieved through this mechanism.

During the crossflow micro-filtration of dilute surfactant solutions, surfactants form highly stable gel-phases within micro-pores and they do not dissolve in water even though they are in contact with surfactant-free water flowing at shear rates in excess of  $5 \times 10^4 \text{ sec}^{-1}$  (24). Such stable-strong surfactant phases are expected to form at concentrations over 30 wt% in non-constraint environment. This phenomenon, first observed by one of us (GA), is utilized in cross-flow filtration and formed the bases of the demulsification of highly stable water-in-oil emulsions using micro-porous demulsifiers as well as the removal of tar/water from gases (14, 20). These observations indicate that microporous materials (with a varying degree of hydrophilicity) preferentially adsorb surface active species which forms the basis of oil-water separation using sulphonated PolyHIPE Polymers.

If the concentration of the demulsifier adsorber is high, it also starts adsorbing water and oil. The reason for the selective adsorption of the surface active species is that the molecular structure of the sulphonated PolyHIPE Polymer is 'surfactant like' with hydrophilic and hydrophobic moieties on the walls of the porous walls. This structure is ideal for the surfactants to associate with, thus eventually forming highly stable surfactant phases even in the presence of a strong surfactant concentration gradient. Thus these solid-state 'surfactant structures' act as template for the surfactants from the crude-oil to deposit on the walls of the PolyHIPE Polymer demulsifier which then results in the de-stabilisation of the water-in-crude oil emulsion. Under the combined effects of electric field and demulsifier, the emulsion separation is intensified.

## Conclusions

The efficiency of electro-coalescence of water-in-crude emulsion in the presence of PHP demulsifier was evaluated and compared to the demulsification using electric field only. The results indicate that the presence of PHP demulsifier has significantly improved the performance of oil/water separation in the presence of electric field, especially at high flow rates or when the electric

field strength is relatively low. From SEM results, it was also found that this demulsifier was able to adsorbed metal compounds present in the emulsion; both from the oil and aqueous phases. Hence the concentration of metal compounds in the separated water phase was lower (9). However, the demulsification mechanism is still not fully understood, thus further investigation is essential.

Since this demulsifier was only tested one type of emulsion, i.e. emulsion made from one type of crude oil, the results are exclusive. However, at this stage, we can conclude that the technique is likely to be applicable to other crude oil emulsions. Our own current studies involve both the modification of the demulsifier adsorber as well as the enhancement of the electric field and flow rates using a purpose built continuous demulsification equipment (14).

### Acknowledgements

We are grateful to the UK Engineering and Physical Sciences Research Council (EPSRC), UK Department of Trade and Industry, Avecia/Cytec, BLC Research, BP Amoco, Ecoprotech, Exxon Mobil, Intensified Technologies Incorporated (ITI), Morecroft Engineers Ltd., Safety Kleen Europe, Triton Chemical Systems, Willacy Oil Services Ltd., for their support. The PhD studentship for one of us (Z.Z.N.) from the University Technology of Malaysia and the Malaysian Department of Public Service is gratefully acknowledged.

### References

1. Eow, J. S. and Ghadiri, M., *Chem. Eng. J.*, **2001**, 85, 357.
2. Eow, J. S. and Ghadiri, M., *Chem. Eng. J.*, **2000**, 84, 173.
3. Lee, C. M., Sams, G. W. and Wagner, J. P. , *J. Electrostatic*, **2001**, 53, 1.
4. Winslow, J. D., *US Patent 4 040 535*, 1977.
5. Sams, G. W., Prestridge, F. L. and Inman, M. B., *US Patent 5 565 078*, 1996.
6. Bailes, P. J. and Watson, M. , *UK Patent 2,249,741*, 1992.
7. Edmonson, J. M., *US Patent 5 714 048*, 1998.
8. Bull, H. R., *US Patent 4 919 777*, 1990.
9. Akay, G., and Vickers, J., *European Patent, EP 1 307 402*, 2003 .
10. Pekdemir, T., Akay, G., Dogru, M., Merrells, R. E., and Schleicher, B., *Sep. Sci. Technol.*, **2003**, 38, 1161.
11. Akay, G., *Bioprocess and chemical process intensification; In Encyclopaedia of Chemical Processing*, Ed: S Lee, Marcel Dekker, NY., 2005.
12. Akay, G., Bhumgarra, Z., and Wakeman, R. J., *Chem. Eng. Res. Design*, **1995**, 73, 782.

13. Akay, G.; Dawnes, S.; Price, V.J., European Patent 1 183 328, 2002.
14. Akay, G., International Patent Application, WO 2004/004880, 2004.
15. Akay, G., Flow induced phase inversion in powder structuring by polymers. In *Polymer Powder Technology*, Eds: Narkis, M., Rozenzweig, N., NY, Wiley, 1995, pp. 541-587.
16. Bokhari, M., Birch, M., and Akay, G., *Adv. Experimental Medicine and Biology*, **2003**, 534, 247.
17. Akay, G., Birch, M.A., Bokhari, M.A., *Biomaterials*, **2004**, 25, 3991.
18. Erhan, E., Yer, E., Akay, G., Keskinler, B., Keskinler, D., *J. Chem. Technol. Biotech.*, **2004**, 79, 195.
19. Akay, G., Erhan, E., Keskinler, B., *Bioeng. Biotech.* **2004**. In press.
20. Dogru, M., Akay, G., International Patent Application, PCT / GB2004 / 004651, 2004.
21. Dalmazzzone, C., Bocard, C. and Ballerini, D., *Spill Sci. Technol. Bulletin*, **1995**, 2, 143.
22. Djuve, J., Yang, X., Fjellanger, I. J., Sjoblom, J. and Pelizzetti, E., *Colloid Polymer Sci.*, **2001**, 279, 232.
23. Jones, T. J., Nuestadter, E. L. and Whittingham, K. P., *J. Canadian Petroleum Technol.*, **1978**, 17, 100.
24. Akay, G. and Wakeman, R. J., *J. Membrane Sci.*, **1994**, 88, 177.
25. Akay, G. and Wakeman, R. J., *Chem. Eng. Res. Design*, **1996**, 74, 517.
26. Akay, G. and Wakeman, R. J., *J. Membrane Sci.*, **1997**, 131, 229.

## Chapter 24

### Intensification of Reaction and V-L Separation in Batch Systems

Jae W. Lee, Mudassir Ghufran, James Chin, and Zhe Guo

The Department of Chemical Engineering, The City College of New York,  
New York, NY 10031

This article addresses the feasibility requirement for producing pure products when intensifying reaction and V-L separation in batch systems. With one unstable node (UN) product in a residue curve map that is reachable from all distillation regions or a part of reaction equilibrium manifolds, a batch rectifier can produce pure products. The symmetric result is conserved for a batch stripper with one stable node (SN) product. With the UN and SN products that share a distillation region with a reaction equilibrium manifold, a middle vessel column (MVC) is feasible to produce those pure products. With all saddle (S) products, a batch reactive extractive (BRED) column can be used to produce pure products. In this case, we should use a suitable entrainer.

## 1. Introduction

The combination of reaction and distillation is not a recent idea. The earliest official record about reactive distillation dates back to Backhaus's patent on methyl acetate production in the 1920's (1). However, six decades had passed before Eastman Chemicals reported their commercially running process in the early eighties (2). This significant delay in commercializing the methyl acetate process reflects the lack of design methods for reactive separation. Since Eastman's methyl acetate production system came out, academia as well as industry has actively started to develop design methods for reactive separation. Representative design methods are static analysis (3, 4), the transformed space approach (5, 6, 7), the fixed-point method (8, 9), the mathematical programming approach (10, 11, 12), and the difference point method (13, 14, 15, 16). For more rigorous literature survey, refer to the recent two review articles (17, 18).

Despite the large volume of publications on reactive distillation, it's surprising that we cannot understand under what conditions we can combine reaction and V-L separation to produce pure products. This is the feasibility question of whether or not pure products can be produced with the integration of reaction and distillation. Producing pure products within their specifications is very important, otherwise, we still need additional separation units to purify products in addition to a reactive distillation column. In the past, to explore the feasibility of reactive distillation, a lot of time and money had to be spent to perform trial-and-error experiments and rigorous calculations.

In this work, we will present a feasibility guideline using the relatively simple information of reaction and phase equilibrium data. Here phase equilibrium is represented by residue curve maps (19, 20). In these maps, the reactants and products in the reaction will be categorized according to their dynamic properties as nodes and saddles. Then, reaction equilibrium manifolds will be superimposed onto these maps. Feasibility criteria for combining reaction and V-L separation will be developed for several batch configurations that are prevalent in specialty chemical and pharmaceutical processes. All of the feasibility criteria will be confirmed using dynamic simulations.

## 2. Motivation

To compare between one batch reactive distillation (BRD) unit and a conventional two-step process consisting of reaction followed by separation, we take the production of *tert*-amyl methyl ether as an example. A conventional batch process consists of a reactor followed by a separation column as shown in Figure 1. An intensified BRD column is given in Figure 2. The dynamic simulation results for producing TAME in these two flowsheets show the huge advantages of the intensified unit over the conventional unit: for the same TAME production purity (99.9 mol%), 1) the conventional process has an 80-tray

column with a reflux ratio of 40 while the BRD column with a reactive overhead drum has only 10 trays and a reflux ratio of 10, 2) the conventional process has a cycle time of 1.4 times the cycle time of the intensified process to recover an identical amount of TAME, and 3) the number of operation units reduces from 2 to 1 by integrating reaction and V-L separation in one column. In addition to these advantages, if we consider the time required for cleanup and transfer of process streams between the two units in the conventional flowsheet, the intensified unit has even more merit than the conventional process.

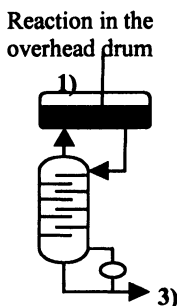


Figure 1. Conventional flowsheet for TAME production ( $MT + 2M2B \leftrightarrow TAME$ ).  
TAME: tert-amyl methyl ether, MT: methanol, 2M2B: 2-methyl-2-butene.

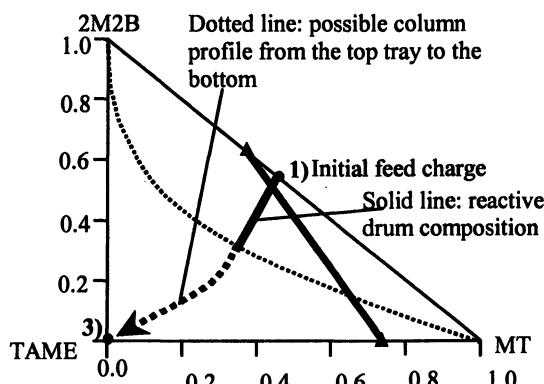


Figure 2. Intensified batch reactive distillation unit for TAME production.

Now, naturally, we can ask the following question: how can we combine reaction with V-L separation to produce pure products? In other words, we want to develop a systematic view to analyze the feasibility of BRD. In the TAME reaction system, there are two minimum boiling azeotropes and one distillation

boundary. If reaction equilibrium allows the reactive overhead drum composition to cross the distillation boundary as shown in Figure 2, then TAME can be produced at the bottom of the column since it is the least volatile in the residue curve map. Thus, using the simple information of reaction and phase equilibrium, it is possible to determine the feasibility of reactive separation systems before doing many experiments and rigorous simulations. To analyze the feasibility of BRD, we take three basic configurations: batch rectifier, batch stripper and middle vessel column (21) as shown in Figure 3. We allow reactions to occur in the charge drums, but not on the distillation trays, to simplify our analysis.

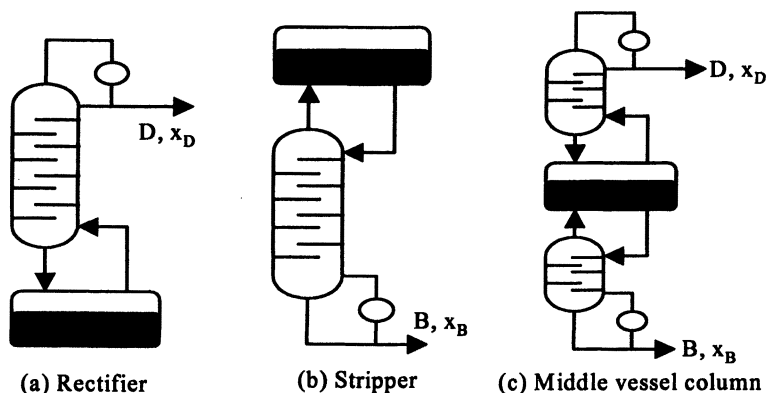


Figure 3. Three basic batch configurations with reactive charge drums (22). Reproduced with permission of the American Institute of Chemical Engineers. Copyright ©2003 AIChE.

### 3. Developing Feasibility Criteria for Basic Configurations

In this section, feasibility criteria will be developed with the decomposition reaction of  $2I \leftrightarrow L + H$  in the three basic BRD columns. Starting with this reaction, we will extend the feasibility criteria to any single reaction with arbitrary reaction stoichiometry. Constant molar overflow, absence of reaction, and V/L phase equilibrium are assumed on each stage. It is also assumed that the V/L holdups on each stage are negligible compared to the holdups of the feed charge drums, that the number of stages is very large, and that the columns operate with infinite reflux ratio ( $R$ ) or reboil ratio ( $s$ ).

### 3.1. Material balances

The following material balance equations are used to determine the dynamic composition trajectories of the reactive charge drums (or still pot) in the rectifier (23), the stripper, and the middle vessel (22).

$$\frac{dx_{S,i}}{d\xi} = (x_{S,i} - x_{D,i}) + Da(\nu_i - \nu_T x_{S,i})(x_{S,B}^2 - \frac{x_{S,A}x_{S,C}}{Keq}) \quad (1)$$

$$\frac{dx_{S,i}}{d\xi} = (x_{S,i} - x_{B,i}) + Da(\nu_i - \nu_T x_{S,i})(x_{S,B}^2 - \frac{x_{S,A}x_{S,C}}{Keq}) \quad (2)$$

$$\frac{dx_{S,i}}{d\xi} = (x_{S,i} - \frac{x_{D,i} + x_{B,i}}{2}) + Da(\nu_i - \nu_T x_{S,i})(x_{S,B}^2 - \frac{x_{S,A}x_{S,C}}{Keq}) \quad (3)$$

where Da is the Damköhler number and represents the reaction holdups in the reactive charge drum.

The calculations of composition profiles in the stages above or/and below the reactive charge drums are given as follows for the rectifying and stripping sections, respectively.

$$y_{n-1,i} = \frac{R}{R+1}x_{n,i} + \frac{1}{R+1}x_{D,i} \quad n=1, \dots, N \text{ stage}, \quad i=1, \dots, \text{components} \quad (4)$$

$$y_{n,i} = \frac{s+1}{s}x_{n+1,i} + \frac{1}{s}x_{B,i} \quad n=1, \dots, N \text{ stage}, \quad i=1, \dots, \text{components} \quad (5)$$

From the dynamic simulations using the above equations, we will develop and verify the feasibility criteria for the three batch configurations. During the simulations, equations (1) – (3) of reactive drums will be simultaneously solved with the equations of stages in equations (4) and (5).

### 3.2. Feasibility criteria for reactive batch rectifier and stripper

The V/L equilibrium data chosen for the ternary mixture in reaction  $2I \leftrightarrow L + H$  are given in residue curve map (RCM) 320, as shown in Figure 4(a). Here, reactant I is an intermediate bolier. It forms a minimum boiling azeotrope with heavy product H and a maximum boiling azeotrope with light product L. The details for the classification of residue curve maps can be found in previous literature (24, 25). In RCM 320, all of the liquid composition profiles leave the L vertex since it is the most volatile. So, vertex L is an unstable node (UN). All liquid composition profiles move into either the vertex H or the maximum boiling azeotrope. Therefore, these two singular points are stable nodes (SNs). At vertex I and the minimum boiling azeotrope, liquid compositions enter those

singular points from one direction and come out of them in a different direction. Those points are saddles (S). Two distillation regions are formed and are separated from each other by one distillation boundary that cannot be crossed by simple batch distillation.

The dynamic simulation results of RCM 320 with reaction  $2I \leftrightarrow L + H$  are shown in Figure 4(b). The still pot composition path starts from the initial feed point and ends at the H vertex. The most important point is that, from any location (distillation region I or II) of the still pot path, the UN product (L) is reachable by the non-reactive rectification of column trays above the still. Since product L is continuously removed from the still and withdrawn at the top, the reactive still path always lies in the forward reaction region. Consequently, reactant I is completely consumed and the still contains only H at the end of the reaction.

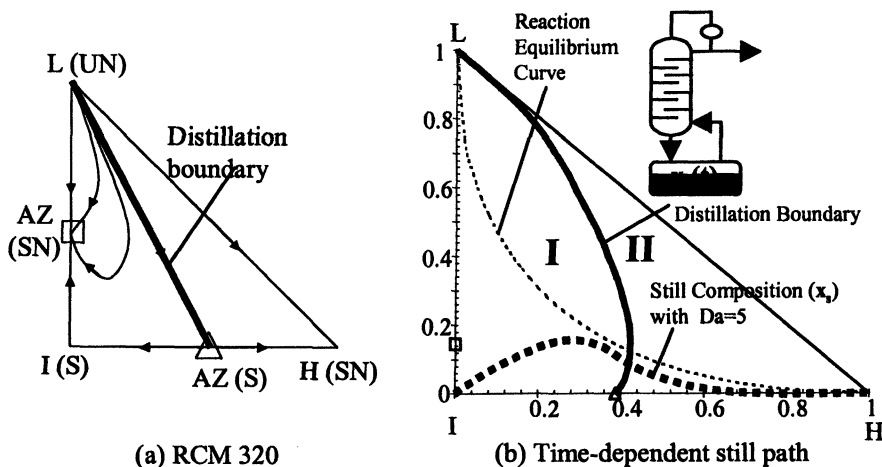


Figure 4. Dynamic simulation results of a batch reactive rectifier (22, Reproduced with permission of the American Institute of Chemical Engineers. Copyright ©2003 AIChE).

Here we can obtain one important feasibility criterion: *if one of the reaction products is a UN (the most volatile) that is reachable by non-reactive distillation from any distillation region, then the reactive batch rectifier can produce pure products.*

The second feasibility criterion for the batch rectifier is that *even if one of reaction products is a UN and is not reachable from both distillation regions, it can still produce pure products when reaction equilibrium allows the still path to cross the distillation boundary as shown in Figure 5. The reaction equilibrium*

curve lies within the same distillation region as the two products (L and H). Thus, the still path starting from the I vertex can move towards the reaction equilibrium curve and cross the distillation boundary. Once it reaches the distillation region from which the light product (L) is reachable using non-reactive distillation, then simultaneous distillation can begin and pure L can be produced. Again, the continuous removal of light product L forces the still path to lie in the forward reaction region and reactant I is completely converted, leaving only heavy product H in the still pot.

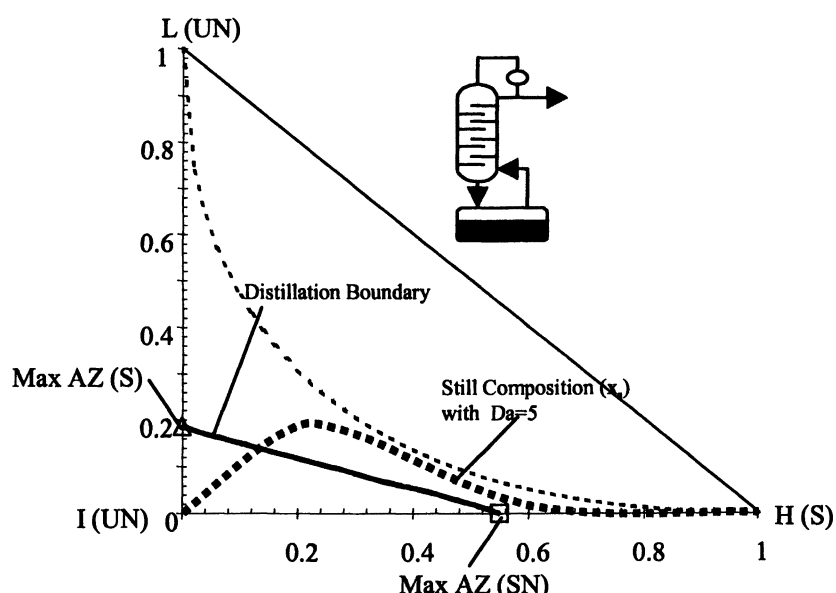


Figure 5. Dynamic simulation results of a rectifier with RCM 430 (22). Reproduced with permission of the American Institute of Chemical Engineers. Copyright ©2003 AIChE).

Similar arguments can be made for a batch reactive stripper: 1) If one of the products is an SN that is reachable from all distillation regions, then the batch stripper in Figure 3(b) can be used to produce pure products. 2) Even if the SN product is not reachable from all distillation regions, the batch stripper can still

produce pure products when the reaction equilibrium curve shares the same distillation region as the products. If the stable node product (H) is continuously removed at the bottom of a batch stripper, then the reactive overhead drum path lies within the forward reaction region. Then, the reactant (I) is completely consumed and, finally, the drum contains only light product L.

Figure 6 shows various RCMs whose V/L phase equilibrium can lead to the production of pure products using a batch rectifier with reaction  $2I \leftrightarrow L + H$ . Although they have different dynamic properties of singular points (pure vertices and azeotropes), they have one common feature: one of products is a UN and is reachable from the reaction equilibrium curve. The continuous removal of UN product L at the top forces the reactive still path to lie in the forward reaction region. Then, the reactant (I) is completely consumed and only the heavy product (H) remains in the still pot at the end of the reaction.

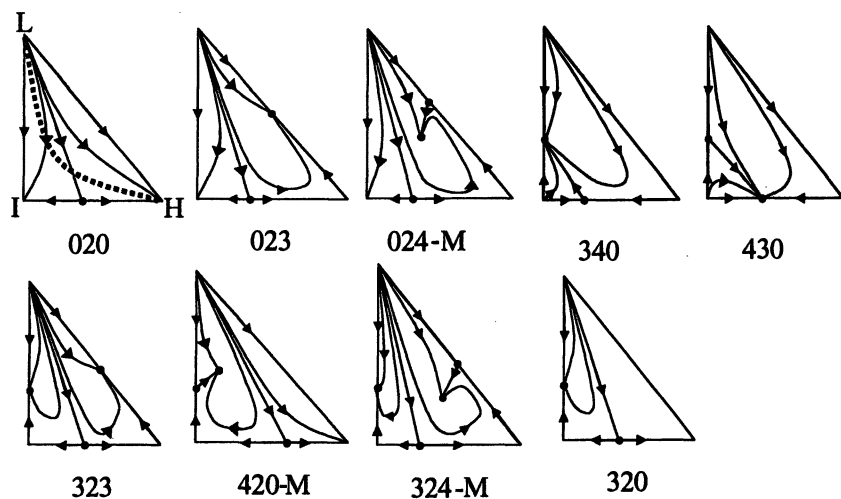


Figure 6. Various RCMs where pure products are obtained in a batch rectifier.

There is another set of RCMs where we can produce pure products using a batch stripper via reaction  $2I \leftrightarrow L + H$  as shown in Figure 7. The number of azeotropes and their dynamic properties are different in each RCM. But, the common characteristic is that one of products is an SN that is reachable from either any distillation region or the reaction equilibrium curve.

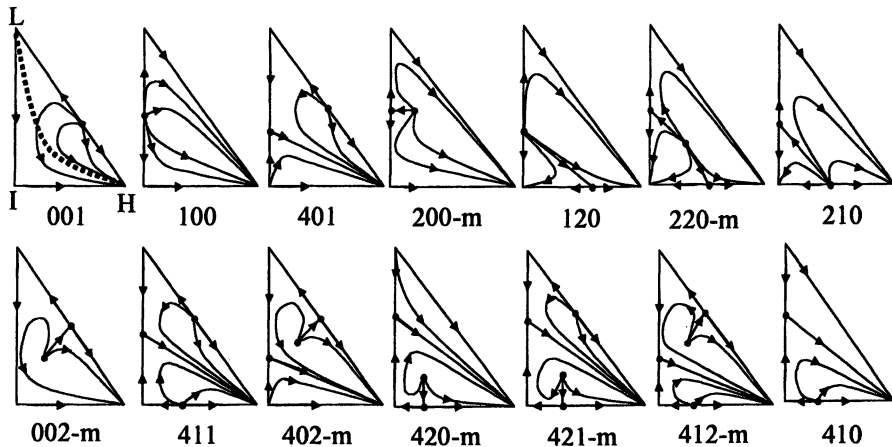


Figure 7. Various RCMs where pure products are obtained in a batch stripper.

### 3.2. Feasibility criteria for middle vessel column (MVC)

The middle vessel column (MVC) is a combination of a batch rectifier and a batch stripper and is shown in Figure 3(c). Figure 8 shows the dynamic simulation result of RCM 010-s with reaction  $2I \leftrightarrow L + H$ . This RCM in Figure 8(a) has four distillation regions (I, II, III, and IV) with one ternary azeotrope and a minimum boling azeotrope between I and H. The middle vessel still path in Figure 8(b) crosses the two distillation boundaries and settles down in distillation region IV where the desired products (L and H) can both be reached by simple distillation. Reaction equilibrium allows the still path to cross the distillation boundaries since its curve lies within distillation region IV. Then, the UN product (L) and the SN product (H) can be produced at the top and bottom of the column by using non-reactive rectifying and stripping sections. Thus, the final feasibility criterion is that pure UN and SN products can be produced in the MVC if they share the same distillation region with a part of a reaction equilibrium curve. As shown in Figure 8(b), to produce the UN and SN products at the same time, careful control should be made to hold the still path within distillation region 4 since the products are reachable only from this region. Besides RCM 010-s, a reactive MVC can also produce pure products in RCM 310-S.

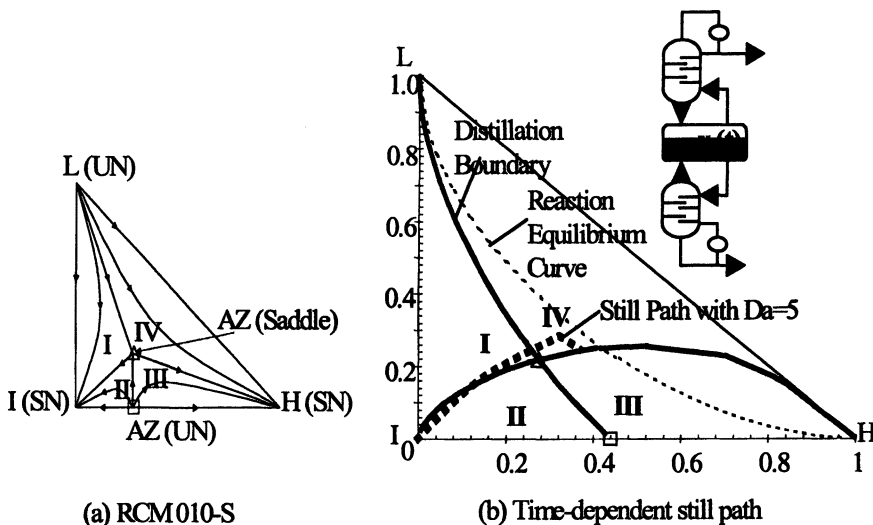


Figure 8. Dynamic simulation results of a batch MVC (22, Reproduced with permission of the American Institute of Chemical Engineers. Copyright ©2003 AIChE).

### 3.3. Extension of feasibility criteria to arbitrary stoichiometries

Until now, it seems that we have derived feasibility criteria only for the reaction  $2I \leftrightarrow L + H$ . However, these feasibility criteria can be extended to different reaction stoichiometries. For example, a reactive rectifier can produce pure products with any reaction stoichiometry of  $aI \leftrightarrow cL + dH$  as long as its feasibility criteria are satisfied. If the UN product (L) can be distilled from any distillation region or reaction equilibrium curve, we can continuously remove L at the top. The removal of product L at the top forces the still path to be located within the forward reaction region. Then, reactant I will be completely converted and only heavy product H will remain in the still. Even with quaternary reaction mixtures of  $aI + bB \leftrightarrow cL + dH$ , the feasibility criteria are still applicable as long as L is a UN product that can be distilled from any distillation region or the reaction equilibrium curve. Real examples include ethanol dehydration to diethyl ether and water (RCM 020), and the decomposition of tert-butyl alcohol to isobutene and water (RCM 020).

By using the same argument, we can use a reactive stripper to produce pure products in any reaction of the form  $aI \leftrightarrow cL + dH$  or  $aI + bB \leftrightarrow cL + dH$  if the SN product (H) can be distilled from all distillation regions or the reaction equilibrium manifolds. In addition to these types of reaction, the reactive stripper can produce a pure SN product in composition reactions of the form  $aL + bI \leftrightarrow cH$ . Pure ether production (TAME, ethyl tert-butyl ether (ETBE), and methyl tert-butyl ether (MTBE)) is possible in a batch stripper since all of these ethers are SNs that are reachable by simple distillation from their respective reaction equilibrium curves. Middle vessel columns can be used for producing pure products in any reaction of the form  $aI + bB \leftrightarrow cL + dH$  as long as UN and SN products (L and H) lie in the same distillation region as a part of reaction equilibrium manifolds.

### 3. Summary and Futher Work

We have derived several guidelines for evaluating the feasibility of three basic BRD columns with ternary and quaternary reaction systems. Reactive rectifiers can produce pure products with one UN product that is reachable from any distillation region or reaction equilibrium manifolds via distillation. Reactive strippers can lead to the production of pure products when one of products is an SN that is reachable from any distillation region or the reaction equilibrium manifold via distillation. With UN and SN products, reactive MVCs can produce those pure products if they share the same distillation region as part of the reaction equilibrium manifold.

With these three basic configurations, we can produce pure products only if at least one of products is a node. What happens if all of the products are saddles? In this case, we cannot reach saddle products by using simple distillation and we should use a third component (or heavy entrainer) to circumvent the non-ideal V/L equilibrium. Naturally, this results in a new configuration of BRD column, batch reactive extractive distillation (BRED). The BRED column is similar to the batch rectifier in Figure 3(a) but it has a side-feed stream for a heavy entrainer. The detailed scheme and feasibility analysis can be referred to the recent literature (26). The feasibility criteria developed for BRD systems can be the basis for establishing feasibility guidelines for continuous reactive distillation systems (27). Even if we do not enumerate many real reactions, we can apply these feasibility criteria to any single reaction system once their phase and reaction equilibrium data are available.

Two important tasks can be brought up as subjects of future research. One task is to develop feasibility criteria for combining multi-reaction (or multi-component) chemical systems into single columns. In combining multiple reactions with V/L separation in a single unit, increasing reaction selectivity for

desired products will be a main research goal. The other task is to extend our feasibility studies to L-L heterogeneous reactive distillation systems. In the heterogeneous reactive distillation system, the position of L-L splitting regions will influence the feasibility of each system. Thus, the relative positions of reaction equilibrium manifolds, L-L splitting regions, and the dynamic properties of reactants and products will determine whether or not we can produce pure products.

### Acknowledgement

J.W.L. is grateful for the partial support of the Professional Staff Congress City University of New York (PSC-CUNY) and the donors of the Petroleum Research Fund, administered by the American Chemical Society.

### References

1. Backhaus, A. A. US Patent 1,400,849, 1921.
2. Agreda, V. H.; Partin, L.R.; Heise, W. H. *Chem. Eng. Prog.* **1990**, *86*, 40-46.
3. Balashov, M. I.; Serafimov, *Theor. Found. Chem. Technol.* **1980**, *14*, 495-500.
4. Giessler, S.; Danilov, R. Y.; Pisarenko, Y. A.; Serafimov, L. A.; Hasabe, S.; Hashimoto, I. *Ind. Eng. Chem. Res.* **1998**, *37*, 4375-4382.
5. Barbosa, D.; Doherty, M.F. *Proc. R. Soc. London* **1987a**, *A413*, 443-458.
6. Barbosa, D.; Doherty, M.F. *Proc. R. Soc. London* **1987b**, *A413*, 459-464.
7. Pérez-Cisneros, E. S.; Gani, R.; Michelsen, M. L. *Chem Eng. Sci.* **1997**, *52*, 527-543.
8. Buzad, G.; Doherty, M. F. *Chem. Eng. Sci.* **1994**, *49*, 1947-1963.
9. Chadda, N.; Malone, M. F.; Doherty, M. F. *AIChE J.* **2000**, *46*, 923-936.
10. Ceric, A. R.; Gu, D. *AIChE J.* **1994**, *40*, 1479-1487.
11. Papalexandri, K. P.; Pistikopoulos, E. N. *AIChE J.* **1996**, *42*, 1010-1032.
12. Jackson, J. R.; Grossmann, I. E. *Comp. Chem. Eng.* **2001**, *25*, 1661-1673.
13. Hauan, S.; Westerberg, A. W.; Lien, K. M. *Chem. Eng. Sci.*, **2000**, *55*, 1053-1075.
14. Hauan, S.; Ceric, A. R.; Westerberg, A. W.; Lien, K. M. *Chem. Eng. Sci.* **2000**, *55*, 3145-3159.
15. Lee, J. W.; Hauan, S.; Lien, K. M.; Westerberg, A. W. *Chem. Eng. Sci.* **2000**, *55*, 3161-3174.
16. Lee, J. W.; Hauan, S.; Westerberg, A. W. *Ind. Eng. Chem. Res.* **2001**, *40*, 2714-2728.

17. Malone, M. F.; Doherty, M. F. *Ind. Eng. Chem. Res.* **2000**, *39*, 3953-3957.
18. Taylor, R.; Krishna, R. *Chem. Eng. Sci.* **2000**, *55*, 5183-5229.
19. Doherty, M. F.; Perkins, J. D. *Chem. Eng. Sci.* **1979**, *34*, 1401-1414.
20. Hoffman, E. J. *Azoetric and extractive distillation*; Wiley (Interscience); New York, 1964.
21. Robinson, C. S.; Gilliland, E. R. *Elements of fractional distillation*; Interscience Publisher; New York, 1961.
22. Guo, Z.; Ghufran, M.; Lee, J. W. *AICHE J.* **2003**, *49*, 3161-3172.
23. Venimadhavan, G.; Malone, M. F.; Doherty, M. F. *Ind. Eng. Chem. Res.* **1999**, *38*, 714 -722.
24. Matsuyama, H.; Nishimura, H. *J. Chem. Eng. Japan*, **1977**, *10*, 181-187.
25. Doherty, M. F.; Calderola, G. A. *Ind. Eng. Chem. Fundam.* **1985**, *24*, 474-485.
26. Guo, Z.; Lee, J. W. *AICHE J.* **2004**, *50*, 1484-1492.
27. Guo, Z.; Chin, J.; Lee, J. W. *Ind. Eng. Chem. Res.* **2004**, *43*, 3758- 3769.

## Chapter 25

# Microfibrous Entrapped ZnO-Support Sorbents for High Contacting Efficiency H<sub>2</sub>S Removal from Reformate Streams in PEMFC Applications

**Y. Lu, N. Sathitsuksanoh, H. Y. Yang, B. K. Chang, A. P. Queen,  
and B. J. Tatarchuk**

**Center for Microfibrous Materials Manufacturing, Department  
of Chemical Engineering, Auburn University, Auburn, AL 36849**

A sintered microfibrous carrier consisting of 2.0 - 3.0 vol% of 4 and 8  $\mu\text{m}$  (dia.) Ni fibers is utilized to entrap from 20 to 30 vol% of 150-250  $\mu\text{m}$  (dia.) carbon and SiO<sub>2</sub> support particulates. Zinc oxide is then placed onto the supports by impregnation at loadings ranging from 15 to 20 wt%. Two different sorbent recipes have been developed. ZnO/Carbon entrapped material for low temperature use is envisioned to operate as a last line of defense at stack temperatures. ZnO/SiO<sub>2</sub> entrapped material is employed for regenerable use in a continuous batch mode at ca. 400°C to scavenge bulk H<sub>2</sub>S. The nano-dispersed nature of ZnO combined with the use of small support particulates promotes high ZnO utilization, high contacting efficiency, and high accessibility of ZnO. At equivalent bed volumes, microfibrous entrapped sorbents provide 2- to 3-fold longer breakthrough time for H<sub>2</sub>S (with a 67% reduction in sorbent loading), compared to packed beds of commercial 1-2 mm extrudates. Five-log reductions in H<sub>2</sub>S concentration with up to 67% ZnO utilization at breakthrough are achieved. Hydrogen sulfide concentrations from 50 ppmv (up to 20,000 ppmv) can be reduced to as little as 0.1 ppmv (at R.T.) and 0.6 ppmv (at 400°C) in 30% H<sub>2</sub>O at face velocities of 1.2-1.7 cm/s for layers as thin as 1.0 mm. Regenerability in

air at 500-600°C is also facilitated by the nano-dispersed nature of the ZnO and the use of small support particulates. The recovery percentage of ZnO utilization using microfibrous entrapped sorbents is up to 5-fold higher than that for packed beds of 1-2 mm commercial extrudates. Furthermore, composite beds consisting of packed beds of large extrudates (ca. 1-2 mm dia.) followed by the above noted microfibrous entrapped sorbents as polishing layers has been demonstrated with a great extension in gas life. This approach synergistically combines the high volume loading of packed beds and the overall contacting efficiency of small particulates.

Proton-exchanged membrane fuel cells (PEMFC) for power systems have become the focus of significant interest. A recent challenge confronting these efforts is the development of on-board fuel processing technologies utilizing high energy density commercial-grade hydrocarbon fuels. The bed utilization efficiency as well as overall system weights and volumes are indeed very important fuel processor design considerations. Traditional approaches such as packed beds of 1-5 mm (dia.) catalysts and/or sorbents normally suffer from high intraparticle mass/heat transfer and low contacting efficiency. In those cases larger amount of catalysts and/or sorbents than necessary are needed for meeting the fuel cell requirements, which in turn result in low bed utilization efficiency while increasing overall system weight and volume. Sintered microfibrous media developed at Auburn University have substantial potential for enhanced heat/mass transfer, improved contacting efficiency and regenerability (1-9). This generic approach utilizes a high void volume and tailorable microfibrous carrier, with high contacting efficiency, to entrap micro-sized sorbent and/or catalyst particulates. Use of these materials allows reduction of both reactor weight and volume while permitting development of small and robust fuel processors. Microfibrous entrapped 16% Ni/Al<sub>2</sub>O<sub>3</sub> catalysts for toluene hydrogenation in a trickle bed reactor have demonstrated 2-6 times higher specific activities than conventional packed bed catalysts on a gravimetric basis, while volumetric activities of 40 vol% composite catalysts were 80% higher than conventional extrudates (8). Microfibrous entrapped 1% Pt-M/Al<sub>2</sub>O<sub>3</sub> for PrOx CO provided 3-fold higher or more bed utilization efficiency compared to packed beds of 2-3 mm (dia.) pellets (10, 11) at same CO conversion. Two-phase mass-transfer

testing indicated that microfibrous composite catalysts take advantage of both high gas-liquid contacting and bulk mixing at low pressure drop with the potential to provide enhanced catalyst utilization (12). Additionally, the microfibrous media can be made into thin sheets of large area and/or pleated to control pressure drop and contacting efficiency. The fabrication of the microfibrous media is based on reliable, proven, high-speed, roll-to-roll, papermaking and sintering processes, substantially reducing production costs while improving product quality.

Hydrogen sulfide removal is a key step in ensuring the activity maintenance of various fuel processing catalysts and high value membrane electrode assemblies. For achieving maximum useful life of the PEMFCs, it is crucial to reduce H<sub>2</sub>S concentration less than 0.1 ppmv (13, 14). Zinc oxide is well known as a highly efficient desulfurizer due to extremely low equilibrium H<sub>2</sub>S concentration and is widely used for sulfur removal from various gas streams. Normally, packed beds of large ZnO sorbent extrudates with high sorbent inventory, are employed to scavenge H<sub>2</sub>S from reformate streams for fuel cell applications (15). Large particles result in low ZnO utilization and poor regenerability because of low contacting efficiency, and intraparticle and lattice diffusion limits (16).

In this work, a microfibrous carrier consisting of 2.0-3.0 vol% of 4 and 8 $\mu$ m (dia.) Ni fibers was utilized to entrap 150-250  $\mu$ m ZnO/Carbon and ZnO/SiO<sub>2</sub> H<sub>2</sub>S sorbents. ZnO/Carbon for low temperature use is envisioned to operate as a last line of defense at stack temperatures. ZnO/SiO<sub>2</sub> for regenerable use is employed to scavenge bulk H<sub>2</sub>S from reformate streams in a continuous batch mode at ca. 400°C. Up to 30 vol% H<sub>2</sub>O in reformate streams is required to perform downstream WGSRs, and to keep membrane electrode assemblies from drying. Thermo-dynamic data indicates that H<sub>2</sub>S concentration in 30% H<sub>2</sub>O is 0.6ppmv at 400°C but can be reduced to less than 0.1 ppmv when temperature is below 200°C (16). That is why two different ZnO/support recipes were developed. Composite beds consisting of packed beds of 1-2 mm (dia.) commercial extrudates followed by high contacting efficiency microfibrous entrapped polishing sorbents were also demonstrated, providing a great extension of gas life.

## Experimental

### Preparation of Microfibrous Entrapped ZnO/Support Sorbents

Sintered microfibrous carrier was used to entrap 150-250  $\mu$ m diameter support particulates first by regular wet layer paper-making/sintering procedure (1-8), where SiO<sub>2</sub> (300 m<sup>2</sup>/g, Grace Davison), BPL activated carbon (560 m<sup>2</sup>/g, Calgon), and  $\gamma$ -Al<sub>2</sub>O<sub>3</sub> (220 m<sup>2</sup>/g, Alfa Aesar) were chosen as the supports. ZnO

was then placed onto the supports by incipient wetness impregnation. Detailed procedure is described in a sample preparation: 7.5 g of 8  $\mu\text{m}$  Ni fibers, 2.5 g of 4  $\mu\text{m}$  Ni fibers, and 2.5 g of cellulose were added into water and stirred vigorously to produce a uniform suspension. The produced suspension and 18 g of 150-250  $\mu\text{m}$   $\text{SiO}_2$  were added into the headbox of the 1.0  $\text{ft}^2$  M/K sheet former under aeration. 1.0  $\text{ft}^2$  preform was then formed by vacuum filtration followed by drying on a heated drum. Said preform was pre-oxidized in air flow for 2 h at 500°C followed by sintering in  $\text{H}_2$  flow for 1 h at 900°C. As-prepared microfibrous entrapped  $\text{SiO}_2$  was immersed into a  $\text{ZnO}$  sol for 10 min, and subsequently vacuum drained, calcined in air for 30 min at each temperature point of 80°C, 100°C, 120°C, 140°C, 160°C, 180°C. The  $\text{ZnO}$  sol was prepared by adding 70 ml  $\text{NH}_3\cdot\text{H}_2\text{O}$ , 42 g  $(\text{NH}_4)_2\text{CO}_3$ , and 66 g  $\text{Zn}(\text{Ac})_2\cdot 6\text{H}_2\text{O}$  in series into 56 ml water under vigorous stirring.

The composition and physico-chemical properties of as-prepared microfibrous entrapped  $\text{ZnO}$ /support sorbents are summarized in Table I. A commercial  $\text{ZnO}$  sorbent (3/16" pellet, 25  $\text{m}^2/\text{g}$ , 90 wt%  $\text{ZnO}$ ) from Sud Chemie and several carbon-based sorbents for respiratory cartridge use from the manufacturers of MSA, 3M, Scott, and Willson, were crushed and sieved into desired particle size for comparative study use.

It should be noted that by utilizing the wet layer paper-making/sintering process, the particulate sizes of 150-250  $\mu\text{m}$  can be entrapped and the uniform dispersion of the particulates within the fibrous matrix can be obtained. However, the different particulate sizes used result in different settling rate of the particulates during the wet layer paper-making process, which causes an ununiform dispersion of the particulates within the microfibrous structure. The well dispersed particulates throughout the microfibrous network is desired to avoid bypassing.

**Table I. Composition, physico-chemical properties of microfibrous entrapped  $\text{ZnO}$ /support sorbents**

<i>Microfibrous sorbent</i>	<i>ZnO</i>	<i>Support</i>		<i>Ni fiber</i>		<i>Voidage (%)</i>
	<i>wt%</i>	<i>wt%</i>	<i>vol%</i>	<i>wt%</i>	<i>vol%</i>	
$\text{ZnO}/\text{SiO}_2$	18 <sup>a</sup> /17.3 <sup>b</sup>	43	25	39	2	73
$\text{ZnO}/\text{Carbon}$	19 <sup>a</sup> /18.6 <sup>b</sup>	44	28	37	2	70
$\text{ZnO}/\gamma\text{-Al}_2\text{O}_3$	18 <sup>a</sup>	43	24	39	2	74

<sup>a</sup> By weighing; <sup>b</sup> ICP-AES analysis results, carried out on a Thermo Jarrell Ash ICAP 61 Simultaneous Spectrometer.

### Micro-Reactor Evaluation and Characterization

Hydrogen sulfide pulse reactions were carried out in a quartz tube reactor (i.d. 4 mm) system equipped with an online GC using a TCD. 0.11 g microfibrous entrapped ZnO/SiO<sub>2</sub> sorbent and 0.022 g Sud-Chemie extrudates were used with a constant ZnO loading (0.02 g), respectively. Hydrogen sulfide (50  $\mu$ L) was pulsed every 2 min using H<sub>2</sub> (30 mL) as carrier gas. Absorption with an H<sub>2</sub>S challenge of 50 ppmv in a model reformate (40% H<sub>2</sub>, 10% CO, 20% CO<sub>2</sub>, 30% N<sub>2</sub>, BOC GASES) was carried out at 400°C or stack temperatures (R.T.-100°C) at a face velocity of 1.7 cm/s. Sorbent loading was kept constant at 0.29 mL (11 mm dia.  $\times$  3 mm thick).

Absorption/regeneration cycle test and regenerability comparison were carried out using 2 vol% H<sub>2</sub>S in H<sub>2</sub> as feedgas. Sorbent loading was kept constant at 0.9 mL (7 mm dia.  $\times$  15 mm thick). Absorption was performed at 400°C at face velocity of 1.2 cm/s. Regeneration was performed at 500-600°C in an air flow (50 ml/min) for 1-3 h.

The composite bed consisting of a packed bed (7 mm dia.  $\times$  7 mm thick) of Sud-Chemie extrudates (1-2 mm) followed by a polishing sorbent layer (3 mm in thickness) was tested at face velocity of 1.2 cm/s using 2 vol% H<sub>2</sub>S in H<sub>2</sub> as feedgas at 400°C. The outlet H<sub>2</sub>S concentrations were determined by an online GC with TCD combined with lead acetate strip and a MultiRAE Plus multigas monitor (PMG-50/5P). One ppmv outlet H<sub>2</sub>S concentration was defined as breakthrough. H<sub>2</sub>S concentrations from 50 ppmv to 2.0 vol% were reduced to as little as thermodynamic equilibrium values (0.6 ppmv at 400°C and less than 0.1 ppmv at R.T. to 100°C in 30% H<sub>2</sub>O).

Powder XRD patterns were recorded on Rigaku instrument using a scanning speed of 4°/min and an accelerating voltage of 40 kV. SEM measurements were carried out using a Zeiss DSM 940 instrument.

## Results and Discussion

### Characteristics of Microfibrous Entrapped ZnO/SiO<sub>2</sub> and ZnO/Carbon

SEM micrographs in Figure 1 show microstructures of the thin microfibrous entrapped ZnO/SiO<sub>2</sub> and ZnO/Carbon sorbents for H<sub>2</sub>S absorption, respectively. ZnO/support particulates of 150-250  $\mu$ m were uniformly entrapped into a well sinter-locked 3-dimensional network of 8 and 4  $\mu$ m nickel fibers. Use of small particulate can significantly attenuate the intraparticle diffusion limit and allow high contacting efficiency with gas streams. XRD patterns in Figure 2 show that the mixtures of ZnO and supports with comparable composition with the corresponding ZnO/support sorbents afforded very strong and narrow peaks

assigned to large ZnO crystals. In comparison, both ZnO/Carbon and ZnO/SiO<sub>2</sub> entrapped materials afforded very weak and broad XRD peaks of ZnO. Zinc oxide crystal size for both SiO<sub>2</sub>- and Carbon-supported sorbents is determined to be <5 nm, 2-fold smaller than that for Sud-Chemie extrudates (ZnO crystal size: 15 nm). This reduction in ZnO crystal size can eliminate the lattice diffusion limit. Surface areas were determined to be 250 m<sup>2</sup>/g for ZnO/SiO<sub>2</sub> and 360 m<sup>2</sup>/g for ZnO/Carbon by N<sub>2</sub>-BET. The above results indicate that the 5 nm ZnO was highly dispersed on the entrapped SiO<sub>2</sub> and activated carbon supports, allowing for extremely high accessibility of ZnO. In contrast the N<sub>2</sub>-BET surface area is around 25 m<sup>2</sup>/g for Sud-Chemie ZnO sorbent extrudates. This suggests that most of ZnO crystals are buried inside the bulk, which in turn causes poor accessibility of ZnO.

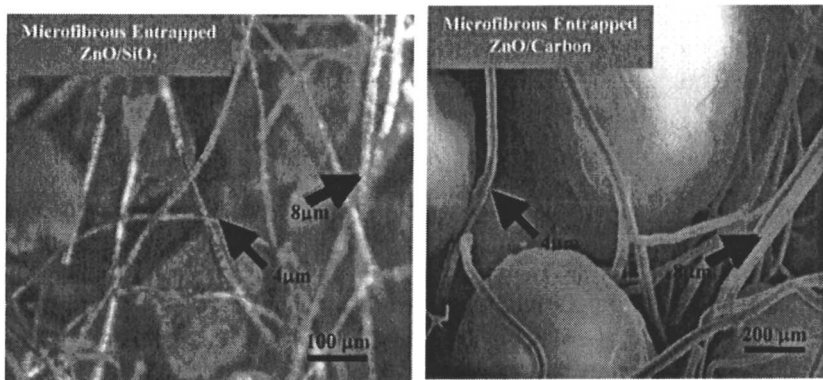


Figure 1. SEM micrographs of microfibrous entrapped ZnO/support sorbents.

#### Performance of Microfibrous Entrapped ZnO/SiO<sub>2</sub> for Regenerable Use

##### *H<sub>2</sub>S Pulse Reaction at 400°C*

Figure 3 shows H<sub>2</sub>S pulse reaction results over microfibrous entrapped ZnO/SiO<sub>2</sub> and Sud-Chemie ZnO sorbent extrudates at 400°C. At equivalent ZnO loading (0.02 g), 150-250 μm ZnO/SiO<sub>2</sub> entrapped materials and 150-250 μm Sud-Chemie ZnO sorbent extrudates provided higher ZnO utilization with sharp breakthrough curves, compared to ~1 mm Sud-Chemie ZnO sorbent extrudates. It is well known that H<sub>2</sub>S adsorption reaction is a mass transfer controlled process with both intraparticle and lattice diffusion limitations (16). As a result, the use of small sorbent particulates significantly attenuates the intraparticle diffusion limit while providing high contacting efficiency. For Sud-Chemie ZnO sorbent, reduction of particulate size from ~1 mm to 150-250 μm results in 2.5-

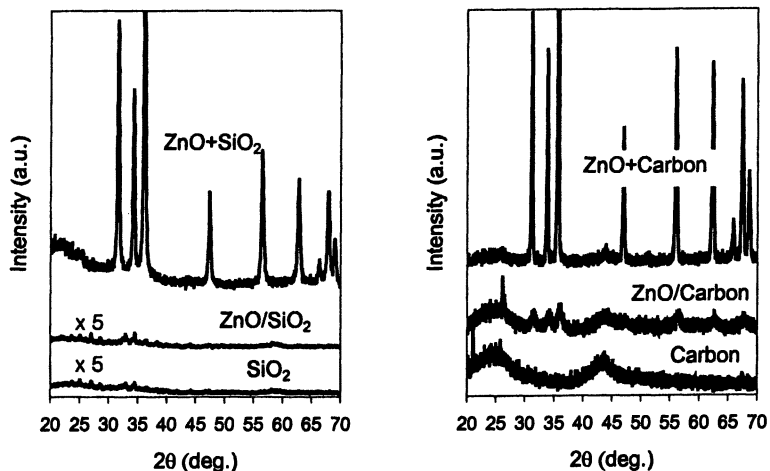


Figure 2. XRD patterns of microfibrous entrapped  $ZnO/SiO_2$  and  $ZnO/Carbon$ .

fold difference in  $ZnO$  utilization (Utl.) while making the breakthrough curve sharper. In comparison with 150-250  $\mu m$  Sud-Chemie extrudates, the nano-dispersed nature and high accessibility of the  $ZnO$  using microfibrous entrapped 150-250  $\mu m$   $ZnO/SiO_2$  sorbents results in another 22% increase in  $ZnO$  utilization with an even sharper breakthrough curve.

#### $H_2S$ Absorption in Continuous Batch Mode at 400°C in 30% $H_2O$

The size reduction of commercial  $ZnO$  sorbents does show the higher in removal capability and utilization efficiency. However, it should be noted that the size reduction of the commercial  $ZnO$  sorbents is not achievable in the fuel processing systems due to the issues of high pressure drop and potential fouling. These drawbacks can be overcome by utilizing the high-void nature of microfibrous carrier. Therefore, the comparison throughout will be made between microfibrous materials and packed beds of commercial 1-2 mm extrudates. Table II compares microfibrous entrapped  $ZnO/SiO_2$  with 1-2 mm Sud-Chemie  $ZnO$  extrudates for  $H_2S$  removal from model reformate at 400°C and face velocity of 1.7 cm/s in 30%  $H_2O$ . As expected, the nano-dispersed nature and high accessibility of the  $ZnO$  combined with high contacting efficiency using microfibrous entrapped  $ZnO/SiO_2$  promotes high  $ZnO$  utilization, compared to packed beds of 1-2 mm commercial extrudates. At equivalent bed volume (0.29 mL, 11 mm dia.  $\times$  3mm thick), microfibrous entrapped  $ZnO/SiO_2$  (150-250  $\mu m$ ) provided about 2-fold longer breakthrough times for  $H_2S$  at breakthrough with about 67% reduction of sorbent loading.  $ZnO$

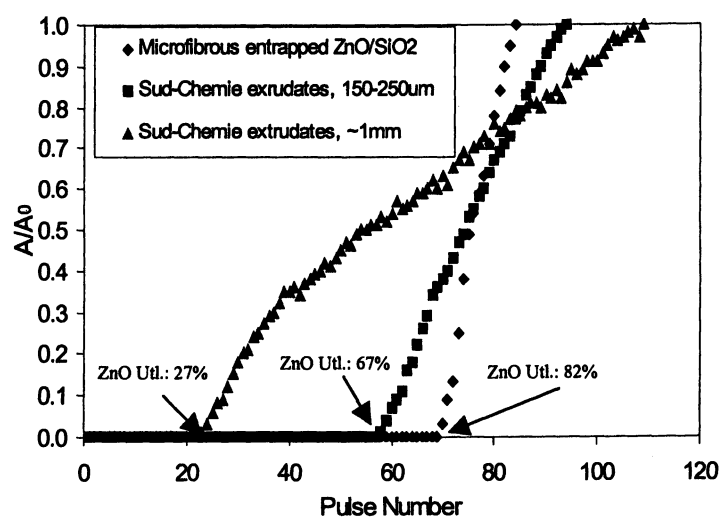


Figure 3.  $H_2S$  pulse reaction results of microfibrous entrapped  $ZnO/SiO_2$  and Sud-Chemie  $ZnO$  sorbent extrudates at 400°C.

utilization using microfibrous entrapped  $ZnO/SiO_2$  sorbents was 57%, 13-fold higher than that of 1-2 mm commercial extrudates.

**Table II. Comparison of microfibrous entrapped  $ZnO/SiO_2$  with Sud-Chemie  $ZnO$  sorbent extrudates for  $H_2S$  removal from model reformate at 400°C in the presence of 30%  $H_2O^*$**

<i>Sorbent</i>	<i>Microfibrous entrapped <math>ZnO/SiO_2</math></i>	<i>Sud-Chemie extrudates (1-2mm)</i>
Weight (g)	0.12	0.30
Volume (mL)	0.29	0.29
Bed thickness (mm)	3	3
Breakthrough time @1ppmv $H_2S$	12	4.5
detection limit ( h)		
$ZnO$ Utilization (%)	57	4

\* Face velocity: 1.7 cm/s @ 50 ppmv  $H_2S$  in model reformate (40%  $H_2$ , 10%  $CO$ , 20%  $CO_2$ , and 30%  $N_2$ ); dry gas flow rate: 100 mL/min (STP).

#### *Regenerability of Microfibrous Entrapped $ZnO/SiO_2$*

Table III compares the regenerability of microfibrous entrapped  $ZnO/SiO_2$  sorbents with 1-2 mm Sud-Chemie extrudates.  $H_2S$  absorption was carried out at 400°C and face velocity of 1.2 cm/s in the absence of  $H_2O$ . Clearly, the nano-dispersed nature of the  $ZnO$  combined with the use of small  $SiO_2$  particulates also facilitates the regeneration in air. At equivalent bed volume, after regenerating at 550-600°C for 1-3 h,  $ZnO$  utilization decreased from 67% to 32-60% for microfibrous entrapped  $ZnO/SiO_2$  and decreased from 33% to 4-20% for 1-2 mm Sud-Chemie extrudates, respectively. Under comparable regeneration conditions, the recovery percentage of  $ZnO$  utilization using microfibrous entrapped  $ZnO/SiO_2$  is up to 10-fold higher than that of 1-2 mm Sud-Chemie extrudates. Table III also shows that microfibrous entrapped  $ZnO/\gamma-Al_2O_3$  exhibited very poor regenerability compared to microfibrous entrapped  $ZnO/SiO_2$ . XRD results show that  $ZnO$  crystal size increased significantly on  $ZnO/\gamma-Al_2O_3$  entrapped materials during regeneration in air at 550-600°C. Furthermore, new XRD peaks assigned to  $ZnAl_2O_4$  spinel were clearly observed after regenerating at 600°C for 3 h. In comparison,  $ZnO$  crystal size increased slightly on  $ZnO/SiO_2$  entrapped materials even after regenerating at 600°C for 3 h, without any detectable new peaks. Rapid growth of  $ZnO$  crystal, strong metal support interaction even solid reaction during regeneration are possible reasons for the poor regenerability of  $ZnO/\gamma-Al_2O_3$  entrapped materials.

**Table III. Comparison of regenerability of microfibrous entrapped supported ZnO and Sud-Chemie ZnO sorbent extrudates<sup>a,\*</sup>**

Sorbent	ZnO Utilization, %		
	Microfibrous entrapped ZnO/SiO <sub>2</sub>	Microfibrous entrapped ZnO/γ-Al <sub>2</sub> O <sub>3</sub>	Sud-Chemie extrudates (1-2mm)
Fresh	67	65	31
3h@600°C in air**	60	8	21
1h@600°C in air**	57	12	13
3h@550°C in air**	44	15	4

<sup>a</sup> Bed configuration: 0.9 mL, 7mm (dia.) x 15 mm(thick).

\* H<sub>2</sub>S absorption was carried out at face velocity of 1.2 cm/s @ 2% H<sub>2</sub>S and 98% H<sub>2</sub> (dry gas flow rate: 30 mL(STP)/min) at 400°C; \*\* Regeneration conditions.

#### *Absorption/Regeneration Cycle Test*

Figure 4 shows the cycle test results over microfibrous entrapped ZnO/SiO<sub>2</sub> at 400°C and face velocity of 1.2 cm/s. The breakthrough times (@ 1 ppmv H<sub>2</sub>S detection limit) almost remained unchanged in 10 cycles at regeneration temperature of 600°C, and in 20 cycles at regeneration temperature of 500°C. The results suggest that ZnO/SiO<sub>2</sub> entrapped materials yield good thermal stability, even though they are regenerated many times. However, it is found that corrosion resistance of nickel fibers in air at higher temperature is a problem for regenerable use due to the oxidation of nickel fibers. The corrosion of nickel fibers during regeneration can be avoid by regenerating in hydrogen or other reducing environments. More recently, microfibrous carrier alternatives using corrosion resistant ceramic/glass fibers have been developed at Auburn University. The use of ceramic/glass fibers can extend the operating temperature range in oxidative environment up to 1200°C. This approach allows for continuous batch bulk H<sub>2</sub>S removal from reformatte streams while significantly increasing bed utilization efficiency and reducing overall system weight and volume. Figure 5 shows SEM micrographs of a typical sample of ceramic fiber entrapped 150-250 μm SiO<sub>2</sub> particulates.

#### **H<sub>2</sub>S Absorption of Microfibrous Entrapped ZnO/Carbon at Stack Temperature**

Table IV shows the performance of microfibrous entrapped ZnO/Carbon for trace H<sub>2</sub>S absorption from model reformatte at stack temperatures (R.T. to 100°C) and face velocity of 1.7 cm/s in the presence of different H<sub>2</sub>O content. Over 11 mm dia. x 3 mm thick) disc sorbent (0.29 mL), in 5% H<sub>2</sub>O

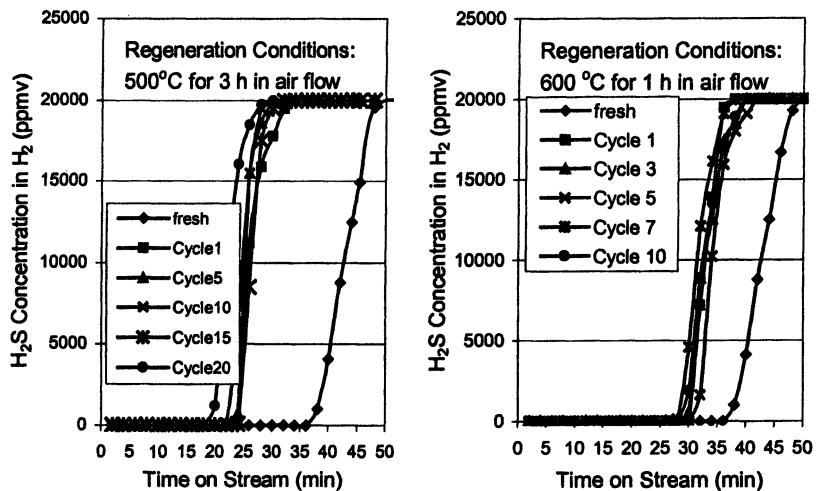


Figure 4. Absorption/regeneration cycle test results of microfibrous entrapped  $ZnO/SiO_2$  sorbent. Adsorption with  $H_2S$  was carried out at  $400^\circ C$  and face velocity of  $1.2 \text{ cm/s}$  @  $2\% H_2S$  and  $98\% H_2$  ( $30 \text{ mL/min}$  (STP)).

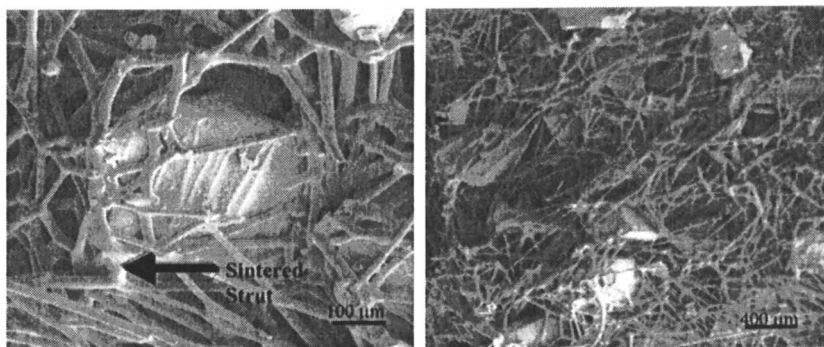


Figure 5. SEM micrographs of a typical sample of ceramic fiber entrapped  $SiO_2$ .

breakthrough time (@ 1ppmv H<sub>2</sub>S detection limit) was from 7.8 h at 25°C to 9.5 h at 100°C with ZnO utilization from 30% to 39%. In 30% H<sub>2</sub>O the disc sorbent provided breakthrough time of 8 h at 70°C and 32% of ZnO utilization.

**Table IV. Performance of microfibrous entrapped ZnO/Carbon for H<sub>2</sub>S absorption from model reformate at R.T. to 100°C in the presence of H<sub>2</sub>O\***

<i>Sorbent</i>	<i>Breakthrough Time (h)</i>	<i>ZnO Utilization (%)</i>
	9.5 @ 100°C in 5% H <sub>2</sub> O	39
Microfibrous entrapped ZnO/Carbon (11 mm dia. × 3 mm thick)	8.7 @ 70°C in 5% H <sub>2</sub> O	36
	7.8 @ 25°C in 5% H <sub>2</sub> O	30
	8.0 @ 70°C in 30% H <sub>2</sub> O	32

\* Face velocity: 1.7 cm/s @ 50 ppmv H<sub>2</sub>S in model reformate (40% H<sub>2</sub>, 10% CO, 20% CO<sub>2</sub>, and 30% N<sub>2</sub>); dry gas flow rate: 100 mL/min (STP).

This microfibrous entrapped ZnO/Carbon sorbent has been used as guard beds, for example, to protect PrOx CO catalyst at 150°C. In the presence of 50 ppmv H<sub>2</sub>S in the feed gas, guard bed layers as thin as 3 mm in thickness placed in the front of the PrOx CO catalyst bed could maintain the activity/selectivity of the PrOx CO catalyst until breakthrough for H<sub>2</sub>S occurred (17).

Figure 6 compares microfibrous entrapped ZnO/Carbon with several commercial sorbents for absorption with 50ppmv H<sub>2</sub>S challenge in a model reformate at 70°C in 30% H<sub>2</sub>O. At equivalent bed volume (0.29 mL, 11 mm dia. × 3 mm thick), 150-250 µm ZnO/Carbon entrapped materials provided 3-fold longer breakthrough times for H<sub>2</sub>S than the high-temperature sorbent which is Sud-Chemie extrudates (1-2 mm) with a 67% reduction of sorbent loading. Four carbon-based sorbents (2-3 mm) for respiratory cartridges taken from different manufacturers were also checked versus our low-temperature sorbent, because they made low temperature H<sub>2</sub>S absorption. In those cases, ZnO/Carbon entrapped materials provided about 3-fold longer breakthrough times for H<sub>2</sub>S compared to packed beds of those four carbon-based 2-3 mm sorbents, even though their bed thickness was doubled.

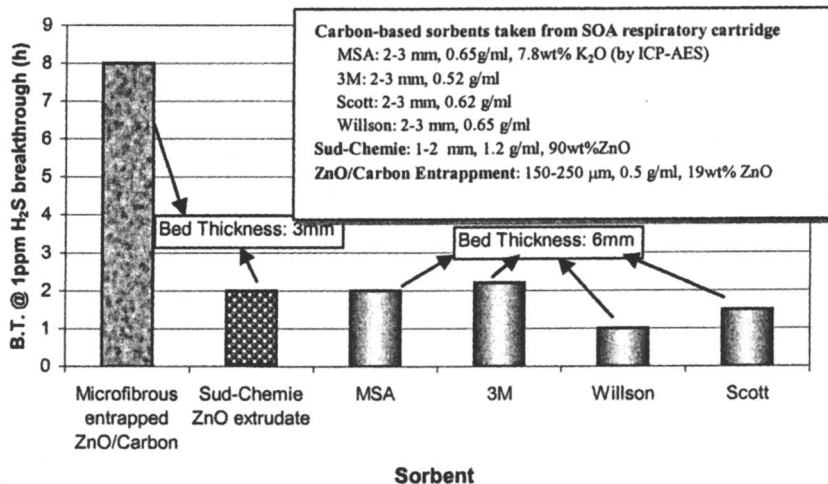


Figure 6. Comparison of microfibrous entrapped ZnO/Carbon with several commercially available sorbent particulates for absorption with 50 ppmv H<sub>2</sub>S challenge in a model reformate in 30% at 70°C and face velocity of 1.7 cm/s (100 mL/min, STP).

### Composite Bed: Optimization of Microfibrous Entrapped Particle Solid

The polishing sorbent concept allows opportunities for higher absorption capacity design by incorporating microfibrous sorbent composite as a polishing sorbent layer to back up a packed bed that suffers from high intraparticle mass transfer and low contacting efficiency.

A composite bed consisting of packed bed of 1-2 mm SudChemie ZnO extrudates followed by microfibrous entrapped ZnO/SiO<sub>2</sub> polishing sorbents has been demonstrated for H<sub>2</sub>S removal from a H<sub>2</sub> fuel stream. Figure 7 shows the breakthrough curves for a 2 vol% H<sub>2</sub>S challenge in H<sub>2</sub> in single and composite beds at 400°C and a face velocity of 1.2 cm/s. Two single beds, 7 mm (dia.)  $\times$  3 mm (thick) microfibrous entrapped ZnO/SiO<sub>2</sub> (A) and 7 mm (dia.)  $\times$  7 mm (high) packed bed of 1-2 mm Sud-Chemie ZnO sorbent extrudates (B), provided

breakthrough times (@1 ppmv H<sub>2</sub>S detection limit) of 5 min and 28 min, respectively. The breakthrough curve with small particulates (ZnO/SiO<sub>2</sub>) alone is very sharp. But the breakthrough curve in packed bed with large particulates (B) is very sigmoidal. When the polishing sorbent was placed behind the packed bed (B+A), the outlet from the packed bed B, where the H<sub>2</sub>S concentrations increased very slowly with time in stream after the breakthrough point in bed B, was encountered immediately with the high contacting efficiency polishing sorbent A. As a result of more efficient use of sorbent, breakthrough time of composite bed is extended to 52 min. The breakthrough with the sharpness of the curve is also indicative of the polishing sorbent. Similar absorption behavior for trace H<sub>2</sub>S removal from H<sub>2</sub> fuel stream has also been achieved at stack temperatures in a composite bed. The conjecture to explain this behavior might be due to the fact that the integral of the effluence from the first bed integrated to the total breakthrough time will be equal to the breakthrough time of the polishing sorbent multiplied by the challenge concentration (Area 1 as shown in Figure 7). This idea was early expressed as a "Bed Depth Service Time Equation" by Adams and Bohart (18). This equation is used to describe the packed beds of particles with strong physical adsorption; however, the equation does not take the residence time of the bed into account. Cahela and Tatarchuk (19) accounted for the residence time of the bed and obtained the concentration breakthrough equation to depict this conjecture. The concentration breakthrough equation was developed for a bed with a polishing filter under the assumption that a polishing filter will absorb the effluents from the front bed until the breakthrough time of the polishing filter and resulted in the equal areas behavior of a polishing sorbents.

## Conclusion

The growing demand in small, efficient, lightweight fuel processing systems utilizing commercial-grade liquid hydrocarbon fuels makes the microfibrous materials attractive for commercial applications. A highly void, tailororable sintered-nickel-fiber carrier can be fabricated via wet layer paper-making process. By entrapping and isolating ZnO/support with particulate size of 150-250  $\mu\text{m}$  into the microfibrous network, the low pressure drop can be maintained while withstand considerable shaking, and avoiding by-passing. A carrier consisting of 2 vol% Ni fibers was utilized to entrap 150-250  $\mu\text{m}$  ZnO/SiO<sub>2</sub> sorbents for H<sub>2</sub>S removal. The smaller size of ZnO sorbent enhances the intraparticle mass transfer and yields high-log removal, but in turn produces high pressure drop. The nano-dispersed nature of ZnO combined with the use of small support particulated not only promotes high ZnO utilization, high contacting efficiency, and high accessibility of ZnO, but also facilitates the regeneration in air at 500-600°C compared to that of the packed bed of 1-2 mm commercial extrudates. Moreover, the use of the microfibrous carrier allows a large number

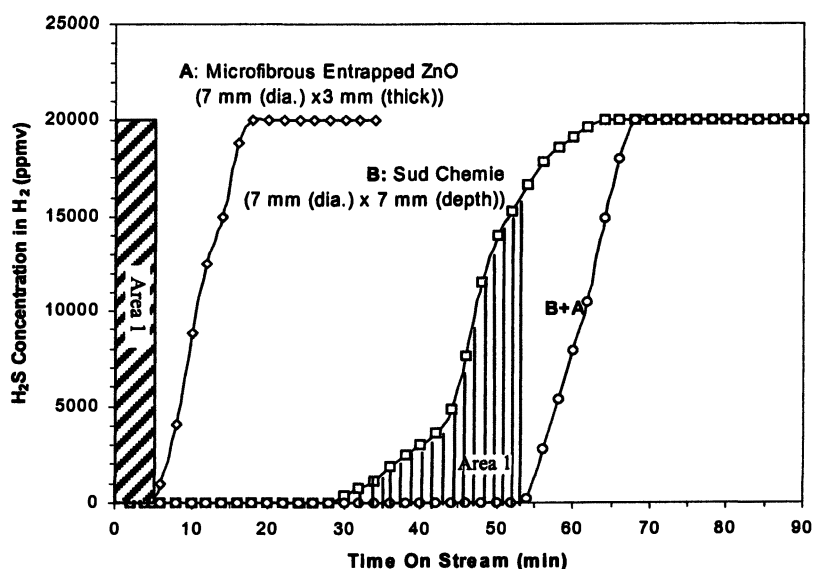


Figure 7. Performance of single and composite beds for  $H_2S$  absorption from 2%  $H_2S$  and 98%  $H_2$  at 400°C with a face velocity of 1.2 cm/s (30 mL/min, STP).

of absorption/regeneration cycles due to their high thermal stability. This approach synergistically combines the high volume loading of packed beds and the high contacting efficiency of small particulates, which allows a significant increase in bed utilization, contacting efficiency, and reduction in overall system weight and volume. This approach towards small-scale regenerable continuous batch fuel processing in PEMFC applications is commercially feasible by using microstructured particulate carriers.

### Acknowledgements

The authors are grateful to Dr. Thomas E. Albrecht-Schmitt for his assistance in performing the XRD. We also would like to acknowledge Drs. Wenhua Zhu, Don Cahela, B.K. Chang, and Mr. Dwight Cahela, all of the Center for Microfibrous Materials Manufacturing (CM<sup>3</sup>) at Auburn University, for their technical assistance and helpful discussions.

### References

1. Tatarchuk, B. J.; Rose, M. F.; Krishnagopalan, A.; Zabasajja, J.N.; Kohler, D. U.S. Patent 5,304,330, 1994; U.S. Patent 5,080,963, 1992.
2. Overbeek, R. A.; Khonsari, A. M.; Chang, Y.-F.; Murrell, L. L.; Tatarchuk, B. J.; Meffert, M. W. U.S. Patent 6,231,792, 2001.
3. Tatarchuk, B. J. U.S. Patent 5,096,663, 1992; U.S. Patent 5,102,745, 1992.
4. Cahela, D. R.; Tatarchuk, B. J. *Catal. Today* 2001, 69, 33-39.
5. Marrion, C. J.; Cahela, D. R.; Ahn, S.; Tatarchuk, B. J. *J. Power Sources* 1994, 47, 297-302.
6. Kohler, D. A.; Zabasajja, J. N.; Krishnagopalan, A.; Tatarchuk, B. J. *J. Electrochem. Soc.* 1990, 137(1), 136-141.
7. Ahn, S.; Tatarchuk, B. J. *J. Appl. Electrochem.* 1997, 27, 9-17.
8. Meffert; M. W. Ph.D. thesis, Auburn University, Auburn, AL, 1998.
9. Harris, D. K.; Cahela, D. R.; Tatarchuk, B. J. *Composites, Part A: Applied Science and Manufacturing* 2001, 32A(8), 1117-1126.
10. Chang, B. K.; Lu, Y.; Tatarchuk, B. J. Materials Solutions Conference and Exposition, Columbus, Ohio, USA, Oct. 18-21, 2004.
11. Karanjikar, M. R.; Lu, Yong; Chang, B. K.; Tatarchuk, B. J. Proceeding of the 41st Power Sources Conference, Philadelphia, Pennsylvania, United States, June 14-17, 2004, p 231-234
12. Trubac, R. E.; Dautzenberg, F. M.; Griffin, T. A.; Paikert, B.; Schmidt, V. R.; Overbeek, R. A. *Catal. Today* 2001, 69, 17-24.

13. Zawodzinski, T.; et. al. Proceedings of the Annual National Laboratory R&D Meeting, Oak Ridge, Tennessee, June 6-8, 2001.
14. Song, C. *Catal. Today* **2002**, 77(1-2), 17-49.
15. Cervi, M.; Hoffman, D. 2<sup>nd</sup> DOD Diesel Fuel Reforming Coordination Meeting, Fort Belvoir, Virginia, Dec. 2001.
16. Twigg, M. V. *Catalyst Handbook* (2<sup>nd</sup> ed.); Wolfe: London, 1989; pp.209.
17. Chang, B. K.; Tatarchuk, B. J. AIChE 2003 National meeting, San Francisco, CA, November 16-21, 2003, 170a.
18. Bohart, C. S.; Adams, E. Q. *J. Am. Chem. Soc.* **1920**, 42, 523-544.
19. Cahela D. R.; Tatarchuk B. J. AIChE 2003 National meeting, San Francisco, CA, November 16-21, 2003, 138c.

# Author Index

Aithal, K. R., 84  
Akay, G., 286, 378  
Akporiaye, D. E., 66  
Besser, R. S., 84, 129  
Brooks, K. P., 119, 238  
Buonomenna, M. G., 309  
Calkan, B., 286  
Calkan, O. F., 286  
Cao, Chunshe, 162, 273  
Cao, James, 102  
Chang, B. K., 406  
Chin, James, 393  
Chin, Ya-Huei, 102, 209  
Cominos, V., 194  
Dagle, Robert A., 162, 209  
Davis, J. M., 238  
Deshmukh, S. R., 179  
Dogru, M., 286, 378  
Drioli, E., 309  
Elliott, Douglas C., 273  
Fang, J., 84  
Fischer, C. M., 119, 238  
Gao, Yufei, 102  
Ghufran, Mudassir, 393  
Gillespie, Ralph, 66  
Guo, Zhe, 393  
Harrison, J., 224  
Hessel, Volker, 23, 194, 334  
Hofmann, C., 194  
Holladay, Jamie D., 162, 209  
Holmgren, J. S., 66  
Hu, Jianli, 84, 129, 273  
Irving, P., 224  
Jarosch, Kai T., 258  
Jensen, Klavs F., 2  
Johnson, Bradley R., 102  
Jones, E. O., 162  
Jones, Susanne B., 273  
Karlsson, A., 66  
King, D. L., 119, 238  
Kolb, G., 194  
Kuhlmann, David, 258  
Kuila, D., 84, 129  
Lee, A., 224  
Lee, Jae W., 393  
Li, X. Shari, 273  
Liang, Y., 84  
Licini, G., 309  
Löwe, Holger, 23, 334  
Lu, Y., 406  
Ming, Q., 224  
Nagineni, V. S., 84  
Nassar, R., 84, 129  
Noor, Z. Z., 378  
Norton, D. G., 179  
Palmer, J. D., 84, 129, 322  
Palo, Daniel R., 209  
Pederson, L. R., 119, 238  
Pennemann, H., 194  
Perry, Steven T., 258  
Plassen, M., 66  
Queen, A. P., 406  
Rawlings, G. C., 119, 238  
Rozmiarek, Robert T., 102  
Sathitsuksanoh, N., 406  
Scrimin, P., 309  
Seetala, N. V., 84  
Siriwardane, U., 84  
Stenkamp, V. Susie, 119, 238, 360  
Stevens, Don J., 273

Tatarchuk, B. J., 406  
TeGrotenhuis, W., 119, 238, 360  
Tonkovich, Anna Lee Y., 47,  
102, 258  
Twitchell, Alvin, 360  
Varahramyan, K., 84  
Veser, Götz, 145  
Vlachos, D. G., 179  
Wang, Yong, 47, 102, 162,  
258, 273  
Wegeng, R. S., 119, 238  
Wetzel, E. D., 179  
Whyatt, G. A., 119, 238  
Xia, G. G., 162  
Yang, H. Y., 406  
Zapf, R., 194  
Zeng, L., 322  
Zhao, S., 84, 129

# Subject Index

## A

Active micromixing  
air-bubble induced acoustic mixing, 337, 339  
chaotic electroosmotic stirring  
mixing, 335, 337, 338f  
electrokinetic instability mixing, 326–331, 335, 336f  
Air-bubble induced acoustic mixing, 337, 339  
Ammonia decomposition  
computational fluid dynamics (CFD)  
simulations for H<sub>2</sub> production, 187–191  
Damköhler numbers (Da), 188, 190f, 191  
parallel plate microreactor, 188, 190f, 191  
plug flow reactor (PFR) model, 188, 191  
post microreactor, 187–188, 189f  
pseudo-first-order reaction rate  
constant, 188  
reaction, 187  
ruthenium (Ru) catalyst, 187  
Aspect ratio, definition, 60  
Atomic efficiency, 160  
Attenuated Total Reflection (ATR)  
crystal, 7–8  
*See also* Multiple Internal Reflection  
(MIR) crystals

## B

Batch reactive distillation (BRD)  
advantages of intensified BRD  
column, 394–395  
background information, 393–394

batch reactive extractive distillation  
(BRED), 403  
batch reactive rectifiers  
configuration, 396f  
feasibility criteria, 397–399, 400, 403  
residue curve maps (RCM), 398f, 399f, 400f  
batch reactive strippers  
configuration, 396f  
feasibility criteria, 399–400, 403  
residue curve maps (RCM), 401f  
comparison to conventional batch  
process, 394–395  
feasibility criteria for batch  
configurations  
arbitrary reaction stoichiometries, 402–403  
batch rectifiers, 397–399, 400  
batch strippers, 399–400  
composition profiles, calculations, 397  
decomposition reaction, 396–402  
material balance equations, 397  
middle vessel column (MVC), 401, 403  
middle vessel column (MVC)  
configuration, 396f  
feasibility criteria, 401, 403  
residue curve maps (RCM), 402f  
residue curve map (RCM) terms, 394, 397–398  
*tert*-amyl methyl ether (TAME)  
production, 394–396, 395f  
V-L separation and, 394  
Battelle, Pacific Northwest Division  
breadboard fuel processor, 217–218  
fuel processing system development, 210–212

- integrated methanol fuel processor, 215, 218–222
- methanol reforming catalysts, 215–216, 217*f*, 241
- microchannel architecture and advanced catalysts, 214–215
- Bifurcation and interdigital multilamination mixing, 343–345
- Bimodal intersecting channel mixing, 352
- Biomass conversion to fuels and energy
  - advantages of microchannel reactors, 275–276, 281–283
  - catalyst preparation, 276–277
  - conventional GTL plant capital investment, 275*f*, 282
  - economic factors and analysis, 274–275, 281–283
  - effect of CO<sub>2</sub> on FT synthesis, 279–280
  - engineered catalyst tailored for microchannel reactor, 277*f*
  - Fischer-Tropsch (FT) synthesis in conventional processes, 274
  - Fischer-Tropsch process
    - intensification in microreactors, 278–279, 280–281
  - FT process intensification by catalyst in microreactor, 278–279
  - gasification for syngas production, 274
  - microreactor activity testing, 277–278
  - pyrolysis, 274
  - tailoring of FT product distribution, 280–281
  - thermal upgrading processes, 274*f*
- BMBF (Germany), 24, 35
- Bromination of 4-nitro toluene, 41*f*
- C**
- Cantilever-valve injection mixing, 353
- Capillary-force, self-filling bilaminating mixing, 342–343
- Casio, fuel cell development, 195–196, 197
- Catalyst foams, 50, 52, 58, 59*f*, 106, 122*f*
- Catalyst screening. *See* Parallel approaches to catalyst screening
- Catalysts
  - alkane steam reforming with precious metal catalysts, 123–125
  - Battelle steam reforming catalysts, 215–216, 217*f*, 241
  - catalyst ball milling and washcoating, 57, 58, 105, 106, 123, 124*f*
  - catalyst development stages, 48
  - catalyst foams, 50, 52, 58, 59*f*, 106, 122*f*
  - catalyst washcoating onto foams, 57, 58, 106
  - CO conversion over different catalysts, 202*f*, 204*f*
  - Co/Re-Al<sub>2</sub>O<sub>3</sub> catalyst for FT reaction, 266–267
  - conventional catalyst pellets, 103*f*
  - cyclohexene conversion with Fe and Co catalysts, 92, 94–96, 97*f*
  - Engelhard precious metal catalysts, 253, 254*f*
  - engineered catalysts
    - aerogels, 58
    - background information, 57
    - catalyst tailored for biomass microchannel reactor, 277*f*
    - felt catalysts, 58–60, 122*f*
    - foam catalysts, 50, 52, 58, 59*f*, 106, 122*f*
    - high temperature resistance alloy (HTRA) supporting materials, 231–234
    - rhodium (Rh)/Al<sub>2</sub>O<sub>3</sub> engineered catalyst for fuel reforming, 53–54, 55, 58
    - felt (metal fiber) catalysts
    - fecraloy (FeCrAlY) felts, 105–115, 121, 122*f*, 164

heat transfer and thermal characteristics, 58, 103  
structure, 59*f*, 60, 103*f*

homogeneous transition metal complexes, 310

methanol reforming catalysts, 215–216, 217*f*

methanol steam reforming results with Cu/ZnO/Al<sub>2</sub>O<sub>3</sub> catalyst, 199, 200*f*, 215

nano-structured catalysts, 292–293, 299, 301–305, 381

Ni-based catalysts for fuel reforming, 55–56, 164

palladium (Pd) catalyst for hydrogen combustion, 49

palladium (Pd) catalyst for hydrogen peroxide synthesis, 13, 14*f*

palladium zinc oxide (Pd/ZnO) catalyst, 165, 215–216, 217*f*

platinum-catalyzed cyclohexene conversion, 91–92, 93*f*

preferential CO oxidation (PROX), 131, 251, 253, 254*f*

rhodium (Rh)/Al<sub>2</sub>O<sub>3</sub> engineered catalyst for fuel reforming, 53–54, 55, 58

SudChemie nonprecious metal catalysts, 251, 253*f*, 410–415, 418–419

water gas shift reaction catalysts, 125

zeolite based catalysts for C5 isomerization of naphtha, 76–77, 77*f*, 78*f*

*See also* Metal-based structured supports; Microfibrous ZnO/support sorbents; Parallel approaches to catalyst screening; Sol-gel supports for catalysts

Catalytic fuel processing devices. *See* Fuel processing devices

Catalytic microburners

ceramic microburner fabrication, 183, 184*f*

critical external heat loss coefficient vs. wall thermal conductivity, 180–181, 182*f*

critical velocity vs. wall thermal conductivity, 181, 182*f*

design, 181–186

flame instability, causes of, 180, 181

fuel-lean limits, effect of device size, 185*f*, 186

gap size vs. ignition temperature and equivalence ratio, 183, 184*f*, 185*f*, 186

MiRTH-e catalytic burner, 205

Pt catalyst, 183

Swiss roll heating cycle, 186

*See also* Hydrogen, miniaturized hydrogen plant

Catalytic partial oxidation of methane (CPOM) to synthesis gas

background information, 146, 158–159

comparison between heat-integrated reactor concepts, 148–150, 159

heat exchange reactors (HXR)

characteristics, 146–148

effect of heat integration on syngas yields, 149*f*

effect of heat integration on upstream temperature profiles, 150*f*

schematic, 147*f*

intrinsic limitations on syngas yield, 146, 159

reverse-flow reactors (RFR)

catalyst stability, 154–156

characteristics, 146–148

effect of heat integration on syngas yields, 149*f*, 150–152, 151*f*

effect of heat integration on upstream temperature profiles, 150*f*, 151*f*, 152–154

efficiency ( $\eta$ ), 157–158

schematic, 147*f*

Catalytic polymeric membranes

background information, 309–310

- chemoselective oxidation of dibenzyl amine, 315*f*
- morphology of Ti(IV) complex in polymeric membrane, 312, 313*f*
- polyacrylonitrile (PAN) catalytic membrane, 312*f*, 313*f*
- polyetheretherketone (PEEKWC) catalytic membrane, 312*f*, 313*f*
- polyvinylidene difluoride (PVDF) catalytic membrane, 312*f*, 313*f*, 317–318, 319*t*
- process intensification, 310, 318
- stereoselective oxidation of benzyl phenyl sulfide, 314*f*, 315*t*
- sulfoxidation of alkyl aryl sulfides, 310–311
- synthesis of Ti(IV) complex in polymeric membrane, 311, 312*f*
- system recycling, 317–318, 319*t*
- titanium(IV) catalytic membrane reactivity, 314–318
- trialkanolamine complex synthesis, 310*f*
- Chaotic electroosmotic stirring mixing, 335, 337, 338*f*
- Chemical micro process engineering background information, 24–25
- brominations, 41
- catalytic filament reactors, 28
- definitions, 24
- Degussa large-capacity microstructured reactor, 30, 31*f*
- direct fluorination of organic reagents, 41
- docking platforms, bus concepts, and interfaces, 32–33, 34*f*
- dual-pipe reactor for titania particle production, 28, 29*f*
- emulsions, soap-free, 41
- FAMOS toolkit, 33, 34*f*
- generic and systemic evaluation, 26–27
- large-capacity microstructured apparatus, 30, 31*f*
- micro plant for allyl borane synthesis, 32
- micro plant with fluidic backbone, 32*f*
- microfluidic devices beyond microfabrication, 28–29
- microfluidics, 30
- multi-scale toolbox, 27–28
- need for information and benchmarking, 25–26, 42
- NeSSI backbone system, 33
- novel processes and routes, 40–41
- numbering-up, 33, 35
- phenyl boronic acid synthesis, 38–40, 41
- pigment production in CPC micoreactor and IMM caterpillar mixer, 27–28
- plant engineering, 35, 36*f*
- process development, 38–40
- pyrene butyric acid esterification, 41
- sensors and process control, 35, 37–38
- slug flow, merging and splitting, 30
- Suzuki coupling, base-free, 41
- trends at a device level, 25–30
- trends at a process level, 38–41
- trends at a system/plant level, 32–38
- Cinnamonic acid derivative, hydrogenation, 25*f*
- Clariant process development, 27–28, 37–38
- Coandra effect mixing, 352–353
- Combinatorial chemistry, 67
- See also* Parallel approaches to catalyst screening
- Combustion, 166–167, 181, 264
- Combustion reactors, 49, 264–266
- See also* Catalytic microburners; Homogeneous microcombustion
- Computational fluid dynamics (CFD) simulations
- ammonia decomposition reaction, 187

Damkhöler numbers (Da), 188, 190f, 191  
 flames, downsizing, 180  
 parallel plate microreactor, 188, 190f, 191  
 plug flow reactor (PFR) model, 188, 191  
 post microreactor, 187–188, 189f  
 pseudo-first-order reaction rate constant, 188  
 reaction, 187  
 ruthenium (Ru) catalyst, 187  
 Continuous processing technology, advantages, 3  
 Controlled deformation dynamic mixers (CDDM), 290  
 CPOM. *See* Catalytic partial oxidation of methane (CPOM) to synthesis gas  
 Cyclohexene conversion, 86f, 87, 88f, 91–92, 93f  
 Cyclone laminating mixing, 346

**D**

Damkhöler numbers (Da), 188, 190f, 191, 397  
 Darcy's equation, 362–363, 364  
 Deep reactive ion etch (DRIE) technology, 11  
 Degussa large-capacity microstructured reactor, 30, 31f  
 Demulsification applications, 379  
 definition, 379  
 electrostatic separation, 381, 382–391  
 oil-in-water emulsion separation cell, 382–384, 383f  
 polyHIPE polymers (PHPs) as demulsifier/absorber, 378, 380, 388–391  
 preparation of test emulsions, 382  
 surfactants, 379  
 techniques, 379–380  
 water-in-crude oil emulsions, demulsification, 378–391  
*See also* Emulsions  
 Design of microreactors. *See* Microreactor design and fabrication  
 Desulfuration, 163–164  
 Development of microchannel reactors. *See* Microchannel reactor development  
 Diesel fuel reformers adiabatic vs heat exchange reactors, 229–231  
 catalysts, 231–234  
 fuel injectors, 235, 236f  
 heat exchangers, 229–231, 234, 235–236  
 high temperature resistance alloy (HTRA) catalyst support, 231–234  
 microchannel steam reforming reactor, 227–229, 230–231  
 process diagram, 226f  
 steam reforming reactor designs, 226–229  
 system description, 225–226  
 tubular reactor, 225, 226–227, 228t  
 water gas shift reactor, 229–231, 234  
 Dimethoxypropane hydrolysis, 324–325  
 Direct fluorination of organic reagents, 13, 15f, 41  
 Distributive mixing with traditional static mixer designs, 347–348  
 DOE-EE/RE Freedom CAR Program preferred oxidation (PrOx) reactors for hydrogen purification, 240–241, 251–256  
 process flow diagram, 240f  
 program targets, 239–241  
 size of 50kWe fuel reforming system, 257t  
 steam reformer reactors, 241–246  
 water gas shift reactor, 240, 246–251

**E**

- Electrokinetic instability mixing, 326–331, 335, 336*f*
- Emulsions
  - electrostatic separation, 381, 382–391
  - high internal phase emulsions (HIPEs), 290, 293–294
  - interfacial crud, 379, 380
  - mixers for process intensification in emulsion preparation, 290
  - oil-in-water emulsion separation cell, 382–384, 383*f*
  - preparation of test emulsions, 382
  - soap-free, 41
  - surfactants, 379
  - water-in-crude oil emulsions, demulsification, 378–391
- See also* Demulsification; Flow induced phase inversion (FIPI)
- Energy density
  - formic acid fuel cell, 165
  - hydrocarbons, 163, 165*t*, 210–211
  - lithium-ion batteries, 163
  - methanol, 163, 165, 210*t*
  - various batteries and fuels, 210*t*
- Engelhard precious metal catalysts, 253, 254*f*
- Engineered catalysts
  - aerogels, 58
  - background information, 57
  - engineered catalyst tailored for microchannel reactor, 277*f*
  - felt catalysts, 58–60, 122*f*
  - foam catalysts, 50, 52, 58, 59*f*, 106, 122*f*
  - high temperature resistance alloy (HTRA) supporting materials, 231–234
  - Pacific Northwest National Laboratory (PNNL), 53–54, 57–60, 263–264

rhodium (Rh)/Al<sub>2</sub>O<sub>3</sub> engineered catalyst for fuel reforming, 53–54, 55, 58

*See also* Catalysts; Fecraloy (FeCrAlY) felts; Metal-based structured supports

**F**

- Fabrication of microreactors. *See* Microreactor design and fabrication
- FAMOS toolkit, 33, 34*f*
- Fecraloy (FeCrAlY) felts
  - catalyst ball milling and washcoating, 105, 106, 123, 124*f*
  - composition, 105
  - interfacial layer by chemical vapor deposition (CVD), 105, 111–112
  - methane steam reforming, 113–114, 115*f*, 164
  - native aluminum oxide scale formation, 105, 106, 107*t*, 108–111, 121, 122*f*
- See also* Metal-based structured supports
- Felt (metal fiber) catalysts, 58, 59*f*, 60, 103, 105–115
  - See also* Fecraloy (FeCrAlY) felts
- FIPI. *See* Flow induced phase inversion (FIPI)
- Fischer-Tropsch (FT) synthesis, 97*f*, 98
  - background information, 262
  - biomass conversion to fuels and energy
    - advantages of microchannel reactors, 275–276, 281–283
    - catalyst preparation, 276–277
    - conventional GTL plant capital investment, 275*f*, 282
    - economic factors and analysis, 274–275, 281–283
  - effect of CO<sub>2</sub> on FT synthesis, 279–280

- engineered catalyst tailored for microchannel reactor, 277*f*
- Fischer-Tropsch (FT) synthesis in conventional processes, 274
- FT process intensification by catalyst in microreactor, 278–279
- gasification for syngas production, 274
- microreactor activity testing, 277–278
- tailoring of FT product distribution, 280–281
- Co/Re-Al<sub>2</sub>O<sub>3</sub> catalyst for FT reaction, 266–267
- conventional, commercial FT processes, 263, 264
- cyclohexene conversion, 92, 94–96, 97*f*, 98
- Fe and Co catalysts, 92, 94–96, 97*f*
- FT reactor design, 266
- gas-to liquids (GTL) process, 263–264, 267, 269, 270*f*
- integrated steam reforming and combustion reactors, 264–266
- magnetization studies of sol-gel Fe/Co catalyst, 96, 97*f*
- microchannel FT reactor performance, 268–269
- microchannel processes for GTL conversion, 263–264
- Flames, downsizing
- computational fluid dynamics (CFD) simulations, 180
- critical external heat loss coefficient *vs.* wall thermal conductivity, 180–181, 182*f*
- critical velocity *vs.* wall thermal conductivity, 181, 182*f*
- instability, causes of, 180, 181
- quenching effect at walls, 166, 180
  - See also* Catalytic microburners
- Flow distribution, 13, 35, 36*f*, 89, 90*f*
- Flow induced phase inversion (FIPI) definition, 290
- effect of deformation state variables (DSVs), 290
- effect of thermodynamic state variables (TSVs), 289–290
- high internal phase emulsions (HIPEs), 290, 293–294
- paths for isothermal inversion of emulsions, 289
- process intensification (PI), 288–290
- uses, 288–289
- Fluorination. *See* Direct fluorination of organic reagents
- Focusing bi-laminating mixing, 343
- Fourier transform infrared spectroscopy (FTIR), 6–8, 37
- Fuel cells
- auxiliary power units (APU), 196–197, 198
- characteristics, 130
- direct methanol fuel cells (DMFC) comparison to PEMFCs, 197, 211*t*
- energy density, 165
- laptop computers and other applications, 195–196
- recreational vehicle applications, 197, 206
- Smart Fuel Cell AG, 197*f*
- formic acid fuel cell energy density, 165
- fuel cell conversion efficiency ( $\epsilon_{FC}$ ), 212
- fuel cell hydrogen utilization ( $\mu_{FC}$ ), 212
- fuel selection, 198
- gross electric power ( $P_{FC}$ ) from fuel cell, 212
- integration of devices, 204
- low power applications, 195–198, 206–207
- military uses, 210
- MiRTH-e (Micro reactor technology for hydrogen and electricity) catalyst test device, 199–200, 199*f*
- catalytic burners, 205

- catalytically coated plate reactor, 201
- integrated reformer-burner reactor, 199*f*
- integrated selective oxidation-heat exchange reactors, 203–205
- water gas shift reactors, 202
- polymer electrolyte fuel cells (PERF), 130–131
- portable systems, number of, 195
- proton exchange membrane fuel cells (PEMFC, PEM fuel cells)
  - advantages of liquid fuels, 212
  - comparison to DMFCs, 197, 211*t*
  - detrimental effect of CO, 131
  - fuel processing units, 198
  - laptop computers, 195–196
  - methanol reformation to hydrogen, 196
  - steps in fuel processing for fuel cells, 213–214
- See also* Fuel processing devices
- Fuel processing devices
  - 10-W fuel processor, 55, 56*f*
  - Battelle breadboard fuel processor, 217–218
  - Battelle integrated methanol fuel processors, 218–222
  - catalyst development stages, 48
  - commercial fuel processing
    - application development at PNNL, 61–62
    - development at Battelle, Pacific Northwest Division, 210–212
    - electric efficiency ( $\epsilon_e$ ), 212–213
    - fuel processing flow sheet, 199*f*
    - full-scale methanol reactor, 50–52
    - gasoline vaporization, 52–53
    - gross electric power ( $P_{FC}$ ) from fuel cell, 212
    - isooctane reformer, 53–54, 55*f*
    - isooctane steam reforming, 53–54, 55*f*
    - methanol vaporization, 49–52
  - microscale fuel processor design, 169–175
  - multi-fuel reforming in a microchannel reactor, 57*t*
  - Ni-based catalysts for fuel reforming, 55–56
  - process flow diagram of a fuel processor, 240*f*
  - steps in fuel processing for fuel cells, 213–214
  - synthesis gas formation from butane, 57–58
  - thermal efficiency ( $\epsilon_t$ ), 212–213
- See also* Fuel cells; Fuel reforming
- Fuel reforming
  - alkane steam reforming with precious metal catalysts, 123–125
  - catalyst challenges, 121
  - isooctane steam reforming, 53–54, 55*f*
  - methane steam reforming, 113–114, 115*f*
  - microchannel reactor advantages for onboard fuel processing by steam reforming, 120
  - microchannel reactor design for DOE-EE/RE's Freedom CAR Program
  - preferred oxidation (PrOx) reactors for hydrogen purification, 240–241, 251–256
  - process flow diagram, 240*f*
  - program targets, 239–241
  - steam reformer reactors, 241–246
  - water gas shift reactor, 240, 246–251
  - multi-fuel reforming in a microchannel reactor, 57*t*
  - Ni-based catalysts for fuel reforming, 55–56, 164
  - preferential CO oxidation (PROX) reaction, 125–126, 127*f*
  - preferred oxidation (PrOx) reactors for hydrogen purification, 167
  - process diagram, 226*f*

rhodium (Rh)/Al<sub>2</sub>O<sub>3</sub> engineered catalyst for fuel reforming, 53–54, 55, 58  
 single channel test reactor, 122*f*  
 size of 50kWe fuel reforming system, 257*t*  
 tubular reforming reactors, 225, 226–227, 228*t*  
 water gas shift reaction  
 catalyst requirements, 125  
 chemical reaction, 164, 229  
 in 10-W microchannel reactor, 55, 56*f*  
 MiRTH-e water gas shift reactors, 202

**G**

Gas-to-liquids (GTL) process  
 Co/Re-Al<sub>2</sub>O<sub>3</sub> catalyst for FT reaction, 266–267  
 conventional GTL plant capital investment, 275*f*  
 conventional processes for GTL conversion, 263  
 economic impact of microchannel process intensification, 269, 270*f*  
 experimental set-up, 267  
 FT reactor design, 266  
 integrated steam reforming and combustion reactors, 264–266  
 microchannel FT reactor performance, 268–269  
 microchannel processes for GTL conversion, 263–264  
*See also* Fischer-Tropsch (FT) synthesis

Gas–liquid processing in microchannels  
 background information, 360–361  
 breakthrough point, 364, 366–367, 370  
 Microwick technology, 361–362  
 partial condensation

heat exchangers, 367, 368*f*  
 heat fluxes, 370  
 heat transfer coefficient, 370, 371*f*  
 phase separation effectiveness, 370  
 schematic of microchannel partial condenser and phase separator, 368*f*  
 stacking of heat exchange and separation channels, 367–368  
 testing on NASA's KC-135 reduced gravity aircraft, 369–371, 372, 374

phase separation  
 hydrodynamic forces involved in liquid capture, 363, 366, 374  
 inertial forces involved in liquid capture, 363, 366, 374

microchannel partial condenser and phase separator, 368*f*, 369*f*  
 multi-channel phase separator, 372, 373*f*  
 pressure difference and, 364, 366–367, 370, 372, 374, 375*t*

Reynolds numbers, 366, 367*f*  
 schematic of microchannel phase separator, 362*f*  
 single-channel, microchannel phase separator test device, 363–367, 364*f*, 365*f*  
 Suratman criterion and Suratman numbers, 366, 367*f*  
 pore throat layer in wicks, 363  
 scaling up microchannel architectures, 367, 371–372, 373*f*  
 wicks and wicking, 362–363, 364, 366

Glass microreactors, 4

**H**

Heat exchange reactors (HXR)  
 characteristics, 146–148  
 diesel fuel reformers, 229–231, 234, 235–236

- effect of heat integration on syngas yields, 149*f*
- effect of heat integration on upstream temperature profiles, 150*f*
- schematic, 147*f*
- See also* Catalytic partial oxidation of methane (CPOM) to synthesis gas
- Heat-integrated reactors, 157–160
  - See also* Catalytic partial oxidation of methane (CPOM) to synthesis gas; Heat exchange reactors (HXR); Reverse-flow reactors (RFR)
- Heat transfer coefficients in microchannel reactors, 103, 180–181, 182*f*, 370–371
- Hexamethydisiloxane (HMDS), 132
- High internal phase emulsions (HIPEs), 290, 293–294
  - See also* PolyHIPE polymers (PHPs)
- High temperature resistant alloy (HTRA), 225, 231–234
- Homogeneous microcombustion
  - computational fluid dynamics (CFD) simulations, 180
  - critical external heat loss coefficient vs. wall thermal conductivity, 180–181, 182*f*
  - critical velocity vs. wall thermal conductivity, 181, 182*f*
  - instability, causes of, 166, 180, 181
  - quenching effect at walls, 166, 180
- See also* Catalytic microburners
- Hydrogen
  - ammonia decomposition, 187–191
  - energy density, 210*t*
  - hydrogen peroxide synthesis from H<sub>2</sub> and O<sub>2</sub>, 13, 14*f*
  - metal membrane purifiers, 167
  - methanation reactors for purification, 167, 173
  - miniaturized hydrogen plant
    - catalytic combustion, 166–167
    - combustor fuel and air feed, 170–171
- computational fluid dynamics
  - modeling, 180
- desulfurization, 163–164
- fabrication, 170, 171*f*
- flame instability, causes, 180
- heat loss, 164–165, 166
- microscale fuel processor design, 169–175
- overview, 162–163
- palladium zinc oxide (Pd/ZnO) catalyst, 165, 166*f*
- quenching effect at walls, 166, 180
- reactor system with methanation reactor, 173*f*
- reformer fuel, 171
- reforming reactor design, 170
- second-generation reactor
  - performance, 172–175
- temperature distribution, 172–173
- thermal efficiency ( $\eta$ ), 171–172
- water-gas shift reaction and, 164
- palladium (Pd) catalyst for hydrogen combustion, 49
- preferred oxidation (PrOx) reactors for purification, 167
- pressure swing adsorption (PSA), 167
- purification, 167
- See also* Catalytic microburners; Homogeneous microcombustion
- Hydrogen peroxide synthesis from H<sub>2</sub> and O<sub>2</sub>, 13, 14*f*
- Hydrogen sulfide removal. *See* Microfibrous ZnO/support sorbents

## I

- IMPULSE proposal and multiscale technology, 30
- Inductively Coupled Plasma (ICP) microreactor channel dry etching, 86*f*, 87, 132
- Innova Tek, diesel fuel reformer development, 224–236

Institut für Mikritechnik Mainz GmbH (IMM), 194–207

Institute of Micromanufacturing (IfM) of Louisiana Tech University, 85, 87, 93*f*, 99

*See also* Cyclohexene conversion; Microreactor design and fabrication; Synthesis gas (syngas)

**J**

Jet collision mixing, 356

**K**

KC-135 reduced gravity aircraft, 369–371, 372, 374

**L**

Lab-on-a-Chip sensors, 33, 85, 86*f*

Lamination width, effect on yield, 26–27

Laptop computers, 195–196

Liquid–gas processing in microchannels. *See* Gas–liquid processing in microchannels

Louisiana Tech University, Institute of Micromanufacturing (IfM), 85, 87, 99

Low-temperature co-fired ceramics (LTCC), 168

Lower heating values (LHV), 212–213

**M**

Manufacturing microchannel devices. *See* Microreactor design and fabrication

MEMS. *See* Microelectromechanical systems (MEMS)

Metal-based structured supports

- advantages, 103–104
- ceramic coatings, 105
- challenges and problems, 104–105
- fecraloy (FeCrAlY) felts
- catalyst washcoating, 105, 106, 123, 124*f*
- composition and structure, 105, 122*f*
- interfacial layer by chemical vapor deposition (CVD), 105, 111–112
- methane steam reforming, 113–114, 115*f*
- native aluminum oxide scale formation, 105, 106, 107*t*, 108–111, 121, 122*f*
- nickel foams, 50, 58, 106
- stainless steel foams, 58, 106
- structure, 103*f*, 122*f*
- thermal conductivity, 103, 104*t*

Methanation, 167, 173, 173*f*, 214

Methane

- combustion, 181
- steam reforming, 113–114, 115*f*, 164, 232–234
- See also* Catalytic partial oxidation of methane (CPOM) to synthesis gas

Methanol

- breadboard fuel processor, 217–218
- Cu/ZnO/Al<sub>2</sub>O<sub>3</sub> catalyst, steam reforming, 199, 200*f*, 215
- direct methanol fuel cells (DMFC)
- comparison to PEMFCs, 197, 211*t*
- energy density, 165
- laptop computers and other applications, 195–196
- recreational vehicle applications, 197, 206
- Smart Fuel Cell AG, 197*f*
- energy density, 163, 165, 210*t*
- full-scale methanol reactor, 50–52
- integrated methanol fuel processors, 215, 218–222
- methanol reforming catalysts, 215–216, 217*f*

- microchannel architecture and
  - advanced catalysts, 214–215
- proton exchange membrane fuel cells (PEMFC, PEM fuel cells)
  - advantages of liquid fuels, 212
  - comparison to DMFCs, 197, 211*t*
  - methanol reformation to hydrogen, 196
  - steam reforming, 164, 213–218
  - vaporization, 49–52
- Micro plume injection mixing, 349
- Micro reactor technology for
  - hydrogen and electricity (MiRTH-e). *See* MiRTH-e
- Micro Total Analysis systems (μTAS), 3
- Microburners, 181, 182*f*
  - See also* Catalytic microburners
- Microchannel reactor development
  - catalyst foams, 50, 52, 58, 59*f*, 106, 122*f*
  - catalyst washcoating, 57, 58
  - commercial development at PNNL, 61–62
  - diesel fuel microchannel steam reforming reactor, 227–229, 230–231
  - engineered catalysts, 53–54, 57–60
  - fabrication advances, 60–61
  - felt (metal fiber) catalysts, 58, 59*f*, 60
  - fuel processing applications
    - 10-W fuel processor, 55, 56*f*
    - catalyst development stages, 48
    - full-scale methanol reactor, 50–52
    - gasoline vaporization, 52–53
    - isoctane reformer, 53–54, 55*f*
    - isoctane steam reforming, 53–54, 55*f*
    - methanol vaporization, 49–52
    - multi-fuel reforming in a microchannel reactor, 57*t*
  - Ni-based catalysts for fuel reforming, 55–56
  - synthesis gas formation from butane, 57–58
- Institute of Micromanufacturing (IfM) of Louisiana Tech University, 85, 87, 93*f*, 99
- microchannel architecture and
  - advanced catalysts, 214–215
- Pacific Northwest National Laboratory (PNNL), 47–48
- palladium (Pd) catalyst for hydrogen combustion, 49
- rhodium (Rh)/Al<sub>2</sub>O<sub>3</sub> engineered catalyst for fuel reforming, 53–54, 55
- single channel test reactor, 122*f*
- stainless steel microreactor for partial oxidation reactions, 60, 61*f*
- See also* Microreactor design and fabrication
- Microelectromechanical systems (MEMS), 4
- Microfibrous ZnO/support sorbents absorption/regeneration cycle test, 410, 415, 416*f*
- comparison to packed beds of sorbents or catalysts, 407, 408, 411–412, 413*f*, 414*t*, 415*t*
- composite bed (use with packed bed sorbent), 410, 418–419, 420*f*
- composition and properties, 409
- contacting efficiency, 408
- fabrication, 408–409
- hydrogen sulfide removal, 408, 411–412, 413*f*, 415, 417–418, 420*f*
- regenerability, 414, 415*t*
- ZnO/carbon entrapped material
  - low (stack) temperature use, 408, 411–415, 417–418
- SEM micrograph, 410*f*
- XRD patterns, 412*f*
- ZnO/SiO<sub>2</sub> entrapped material
  - high-temperature use, 408, 411–412, 413*f*
- regeneration, 410, 414, 415*t*
- SEM micrographs, 410*f*, 416*f*
- XRD patterns, 412*f*

*See also* Proton exchange membrane fuel cells (PEMFC, PEM fuel cells)

**Micromixing**

- active mixing
- air-bubble induced acoustic mixing, 337, 339
- chaotic electroosmotic stirring mixing, 335, 337, 338*f*
- electrokinetic instability mixing, 326–331, 335, 336*f*
- background information, 323–324, 334–335, 356–357
- electrohydrodynamic mixing, 341
- membrane-actuated micropumping mixing, 340–341
- micro impeller mixing, 341
- mixing tees, experimental setup, 325–326, 327*f*, 328*f*
- moved-and shaked-droplet mixing, 339–340
- passive mixing
- bifurcation and interdigital multi-lamination mixing, 343–345
- bimodal intersecting channel mixing, 352
- cantilever-valve injection mixing, 353
- capillary-force, self-filling bi-laminating mixing, 342–343
- Coandă effect mixing, 352–353
- cyclone laminating mixing, 346
- distributive mixing with traditional static mixer designs, 347–348
- focusing bi-laminating mixing, 343
- jet collision mixing, 356
- micro plume injection mixing, 349
- passive chaotic mixing by posing grooves to viscous flows, 349–350
- passive chaotic mixing by twisted surfaces, 350
- rotation-and-break-up mixing, 347
- secondary flow mixing in zigzag micro channels, 348–349
- serial diffusion mixer for concentration gradients, 353
- split-and-recombine (SAR) mixing, 346–347, 348
- time pulsing mixing, 350, 351*f*, 352, 354*f*–355*f*
- vertical Y- and T-type configuration diffusive mixing, 342
- Reynolds Numbers, 322, 323, 326, 328*f*
- specific work effects, 329, 330*f*, 332*f*
- ultrasound enhancement of mixing, 323–324, 329, 330*f*, 339

**Microporous polymer applications**, 290–292, 299, 301–305

*See also* PolyHIPE polymers (PHPs)

**Microreactor design and fabrication**

- benefits and challenges of common materials, 168*t*
- bonding of layers, 261
- effect of channel geometry in straight and zigzag channels, 89, 90*f*
- full-scale reactor after bonding and machining, 262*f*

**Inductively Coupled Plasma (ICP)**

- dry etching, 86*f*, 87, 132

**Institute of Micromanufacturing (IfM) of Louisiana Tech University**, 85, 87, 93*f*, 99

lamination process, 259

machining process, 261

materials selection, 168

microscale fuel processor design, 169–175

overview, 86*f*, 87–89

parallel arrays, 99

peripheral equipment and setup, 89, 93*f*, 134

platinum-based PROX microreactor, 132, 133*f*

stacking process, 259, 261

steps in microchannel device fabrication, 259, 260*f*, 261

thermal conductivity and coefficient of thermal expansion of common materials, 169*t*

*See also* Microchannel reactor development; Silicon based microreactors

Microreactors, general information, 3, 85

MiRTH-e (Micro reactor technology for hydrogen and electricity) catalyst test device, 199–200, 199*f* catalytic burners, 205 catalytically coated plate reactor, 201 CO conversion over different catalysts, 202*f*, 204*f* goals, 198 integrated reformer-burner reactor, 199*f* integrated selective oxidation-heat exchange reactors, 203–205 methanol steam reforming results with Cu/ZnO/Al<sub>2</sub>O<sub>3</sub> catalyst, 199, 200*f* propane conversion at various temperatures and propane/oxygen ratios, 205 propane conversion at various temperatures and steam/carbon ratios, 201–202 water gas shift reactors, 202

Multifunctional reactors, 145

Multiple expansion contraction static mixers (MECSM), 290

Multiple Internal Reflection (MIR) crystals, 7–8 photograph of PDMS microreactor attached to MIR silicon crystal, 8*f* use in infrared spectroscopy, 7–8

*See also* Attenuated Total Reflection (ATR) crystal

## N

NASA's KC-135 reduced gravity aircraft, 369–371, 372, 374

NEC, fuel cell development, 195, 197

NeSSI backbone system, 33

Novel processes and routes, 40–41

Nuclear reprocessing, 379, 380

Numbering-up, 33, 35

## O

ODS (oxide dispersion strengthened) aluminum alloys, 108

Olefins, oxidation by ozone, 13

Oxide dispersion strengthened (ODS) aluminum alloys, 108

## P

Pacific Northwest National Laboratory (PNNL)

commercial fuel processing application development at PNNL, 61–62

DOE-EE/RE Freedom CAR Program preferred oxidation (PrOx) reactors for hydrogen purification, 240–241, 251–256

process flow diagram, 240*f*

program targets, 239–241

steam reformer reactors, 241–246

water gas shift reactor, 240, 246–251

engineered catalysts, 53–54, 57–60, 263–264

overview of development at PNNL, 47–48, 62

*See also* Microchannel reactor development

Palladium (Pd)

catalyst for hydrogen combustion, 49

cyclohexene conversion, 86*f*, 87, 88*f*

hydrogen peroxide synthesis from H<sub>2</sub> and O<sub>2</sub>, 13, 14*f*

hydrogen peroxide synthesis from H<sub>2</sub> and O<sub>2</sub> with palladium catalyst, 13

palladium zinc oxide (Pd/ZnO) catalyst, 165, 215–216, 217*f*

Parallel approaches to catalyst screening  
 advantages of parallelization, 67  
 catalyst library generation using different components and procedures, 76–77  
 compromises involved in levels of parallelization, 70–71  
 configurations of primary reactor units, 71, 72*t*, 73  
 configurations of secondary reactor units, 73, 74*f*, 75*t*, 76  
 goals, 67  
 integration of parallel screening with established workflow, 67, 68*f*  
 key sections of reactor systems, 69*f*, 70  
 parallel reactor system strategies, 69–73, 72*t*, 75*t*  
 parallel screening system interfacing with scale-up, 73, 74*f*, 76–79  
 workflow cycle in catalyst development, 68*f*, 69  
 zeolite based catalysts for C5 isomerization of naphtha, 76–77, 77*f*, 78*f*

Parallel plate microreactor, 188, 190*f*, 191

Passive chaotic mixing by posing grooves to viscous flows, 349–350

Passive chaotic mixing by twisted surfaces, 350

Passive micromixing  
 bifurcation and interdigital multi-lamination mixing, 343–345  
 bimodal intersecting channel mixing, 352  
 cantilever-valve injection mixing, 353  
 capillary-force, self-filling bi-laminating mixing, 342–343  
 Coandă effect mixing, 352–353  
 cyclone laminating mixing, 346  
 distributive mixing with traditional static mixer designs, 347–348

focusing bi-laminating mixing, 343  
 jet collision mixing, 356  
 micro plume injection mixing, 349  
 passive chaotic mixing by posing grooves to viscous flows, 349–350  
 passive chaotic mixing by twisted surfaces, 350  
 rotation-and-break-up mixing, 347  
 secondary flow mixing in zigzag micro channels, 348–349  
 serial diffusion mixer for concentration gradients, 353  
 split-and-recombine (SAR) mixing, 346–347, 348  
 time pulsing mixing, 350, 351*f*, 352, 354*f*–355*f*  
 vertical Y- and T-type configuration diffusive mixing, 342

PDMS. *See* Poly(dimethylsiloxane) (PDMS) microreactors

Pectel number, 5–6

PEMFCs. *See* Proton exchange membrane fuel cells (PEMFC, PEM fuel cells)

Phenomenon based process intensification, 286–306

Phenyl boronic acid synthesis, 38–40, 41

Photoacoustic spectroscopy (PAS), 8–9

PHPs. *See* PolyHIPE polymers (PHPs)

Platinum (Pt)  
 binding energy of Pt before and after reduction, 139*f*  
 cyclohexene conversion catalyst, 91–92, 93*f*  
 platinum-based PROX microreactor, 132, 133*f*  
 sol-gel supports for catalysts, 91–92, 93*f*, 130–131, 134  
*See also* Catalysts

Plug flow reactor (PFR) model, 188, 191

Poly(dimethylsiloxane) (PDMS) microreactors, 4, 8*f*

PolyHIPE polymers (PHPs)

- application in process intensification and microreactor technology, 290–292, 380–381
- cross-linked styrene-divinyl benzene PHP, 380
- demulsification effectiveness, 378, 380, 385–387, 390
- energy-dispersive analysis with X-rays (EDAX), 384, 388, 389*f*, 389*t*
- in electrostatic separation water-in-crude oil emulsions, 381, 382–391
- metallization, 294–295, 296*f*, 299, 301–305
- pore sizes, 291
- preparation, 293–294
- process intensification (PI), 290–292, 378–391
  - removal of metal ions by ion exchange mechanism, 378, 380, 388, 389*f*, 389*t*
  - scanning electron microscopy, 384*f*, 387–388
  - structure, 291*f*, 299, 300*f*
  - sulphonation, 294, 297, 298*f*
  - surfactant removal, 381, 390
- Polymer electrolyte fuel cells (PERF), 130–131
- Post microreactor, 187–188, 189*f*
- Preferential CO oxidation (PROX)

  - catalyst selection, 131, 251, 253, 254*f*
  - catalyst stability, 142
  - DOE-EE/RE Freedom CAR Program, 240–241, 251–256
  - Engelhard precious metal catalysts, 253, 254*f*
  - hydrogen purification, 167
  - microreactor design and fabrication, 132, 133*f*, 135, 136*f*–137*f*
  - O<sub>2</sub>:CO ratios, 255
  - peripheral equipment and setup, 134
  - reactions, 125–126, 127*f*, 131
  - reactor design, 251, 252*f*
  - residence time effects, 140*f*, 142
  - selectivity, need for, 131
  - steps in fuel processing for fuel cells, 214
  - SudChemie nonprecious metal catalysts, 251, 253*f*
  - temperature effects, 139*f*–140*f*, 141*f*, 142
  - temperature profile, 256

- Pressure swing adsorption (PSA), 167
- Process efficiency ( $\eta$ ), 145, 156–159
- Process intensification (PI)

  - background information, 3, 145–146, 287–288, 361
  - catalytic partial oxidation of methane (CPOM) to synthesis gas, 146–159
  - catalytic polymeric membranes, 310, 318
  - economic impact of gas-to liquids (GTL) process intensification, 269, 270*f*
  - Fischer-Tropsch (FT) synthesis, 258–270, 273–283
  - flow induced phase inversion (FIPI), 288–290
  - gas-to liquids (GTL) process, 258–270
  - inherently intensive processes, 288
  - microporous polymers, 290–292
  - mixers for process intensification in emulsion preparation, 290
  - multifunctional reactors, 145
  - nano-structured microporous materials, 292–293, 299, 301–305, 381
  - phenomenon based process intensification, 286–306, 287–288
  - physical process intensification, 288
  - PolyHIPE polymers (PHPs), 290–292, 378–391
  - process intensification and miniaturization (PIM), 288
  - process miniaturization (PM), 287
  - size dependent phenomena, 288
  - titanium(IV) catalysts, 310, 318

*See also* Batch reactive distillation (BRD); Gas–liquid processing in microchannels; Micromixing; Process efficiency ( $\eta$ )

Propane  
auxiliary power units (APU), 198  
combustion, 181  
conversion at various temperatures  
and propane/oxygen ratios, 205  
conversion at various temperatures  
and steam/carbon ratios, 201–202  
ignition/extinction behavior of  
propane/air mixtures, 183, 184<sup>f</sup>  
sulphur effect on propane  
conversion, 206  
Proton exchange membrane fuel cells  
(PEMFC, PEM fuel cells)  
advantages of liquid fuels, 212  
comparison to DMFCs, 197, 211<sup>t</sup>  
detrimental effect of CO, 131  
effect of CO, 131  
effect of hydrogen sulfide, 408  
fuel processing units, 198, 407  
laptop computers, 195–196  
methanol reformation to hydrogen,  
196  
*See also* Microfibrous ZnO/support  
sorbents  
PROX. *See* Preferential CO oxidation  
(PROX)  
Pyrene butyric acid esterification, 41

## Q

Quantum dots (QDs) of CdSe, 16–17

## R

Reactive distillation, history, 394  
*See also* Batch reactive distillation  
(BRD)  
Residence time distribution (RTD),  
measurement, 16

Reverse-flow reactors (RFR)  
catalyst stability, 154–156  
characteristics, 146–148  
effect of heat integration on syngas  
yields, 149<sup>f</sup>, 150–152, 151<sup>f</sup>  
effect of heat integration on upstream  
temperature profiles, 150<sup>f</sup>, 151<sup>f</sup>,  
152–154  
efficiency ( $\eta$ ), 157–158  
intrinsic limitations on syngas yield,  
146, 159  
schematic, 147<sup>f</sup>  
*See also* Catalytic partial oxidation of  
methane (CPOM) to synthesis gas  
Reynolds Number, 322, 323, 326, 328<sup>f</sup>  
Rhodium (Rh)/Al<sub>2</sub>O<sub>3</sub> engineered  
catalyst for fuel reforming, 53–54,  
55, 58  
Rotation-and-break-up mixing, 347

## S

Safety characteristics of  
microreactors, 3  
Scale-out technology, definition, 3  
Scale-up technology, comparison to  
scale-out, 3  
Screening of catalysts. *See* Parallel  
approaches to catalyst screening  
Secondary flow mixing in zigzag  
micro channels, 348–349  
Serial diffusion mixer for  
concentration gradients, 353  
Silica (colloidal) by Stöber method,  
15<sup>f</sup>, 16  
Silicon, characteristics, 4  
Silicon based microreactors  
advantages, 4, 6  
characteristics, 4, 85, 86<sup>f</sup>  
deep reactive ion etch (DRIE)  
technology, 11  
fabrication, 4  
high mass transfer rate gas  
multiphase reactors, 11, 12<sup>f</sup>

- high-temperature fuel conversion, 17–18
- high-temperature heterogeneous catalytic reactors, 5, 9, 10*f*, 11
- high throughput experimentation of homogeneous organic synthesis, 5–6
- hydrogenation of unsaturated hydrocarbons, 11
- integrated microreactor systems, 19
- integration of IR spectroscopy, 6–9
- microreactors for difficult to perform reactions
- direct fluorination of organic reagents, 13, 15*f*, 41
- flow distribution, 13
- hydrogen peroxide synthesis from H<sub>2</sub> and O<sub>2</sub> with palladium catalyst, 13, 14*f*
- microreactors for difficult to perform reactions, 14*f*, 15*f*
- numbered-up microreactors, 15*f*
- oxidation of olefins by ozone, 13
- post structures in multichannel reactors, 13, 14*f*
- optical (circuit boards), 19
- solid particles, synthesis of, 15*f*, 16–17
- suspended tube reactors, 17–18
- thermal losses, 17
- thermoelectric (TE) generators, 17
- thermophotovoltaic (TPV) generators, 17
- See also* Microreactor design and fabrication
- Sintered microfibrous ZnO/support sorbents. *See* Microfibrous ZnO/support sorbents
- Sodium borohydride (NaBH<sub>4</sub>), energy density, 210*t*
- Sol-gel supports for catalysts
- alumina sol-gel from aluminum tri-sec butoxide, 92, 94, 95*f*
- catalyst activity, 89, 91
- comparison to sputtered catalyst, 91–92, 93*f*
- magnetization studies of sol-gel Fe/Co catalyst, 96, 97*f*
- platinum catalyst, 91–92, 93*f*, 130–131, 134
- preparation, 91, 132–134
- ruthenium catalyst, 130–131
- silica sol-gel covering microchannels, 137*f*
- silica sol-gel from tetraethoxysilane (Si(OC<sub>2</sub>H<sub>5</sub>)<sub>4</sub>), 91, 92, 94, 95*f*, 132
- surface of coated silica sol-gel catalyst support, 138*f*
- See also* Catalysts
- Split-and-recombine (SAR) mixing, 346–347, 348
- Stainless steel microreactors, 3–4, 170, 171*f*
- Steam reforming (SR)
- advantages, 164
- alkane steam reforming with precious metal catalysts, 123–125
- cold start-up using isooctane fuel, 244–246
- diesel fuel microchannel steam reforming reactor, 227–229, 230–231
- DOE-EE/RE Freedom CAR Program, 241–246
- enthalpy, 264
- hydrocarbon reactions, 164
- integrated steam reforming and combustion reactors, 264–266
- isooctane steam reforming, 53–54, 55*f*
- issues for convention SR reactors, 164–165
- low pressure drop 500 We steam reformer, 241, 243–246
- low pressure drop 500 We steam reformer schematic, 244*f*
- methane steam reforming with fecraloy (FeCrAlY) felts, 113–114, 115*f*, 164

methanol steam reforming, 164, 213–218

methanol steam reforming results with Cu/ZnO/Al<sub>2</sub>O<sub>3</sub> catalyst, 199, 200*f*, 215

microchannel reactor advantages for onboard fuel processing by steam reforming, 120

MiRTH-e results with Cu/ZnO/Al<sub>2</sub>O<sub>3</sub> catalyst, 199, 200*f*

propane conversion at various temperatures and steam/carbon ratios, 201–202

reformate temperature effect on productivity, 241, 242*f*

tubular reforming reactors, 225, 226–227, 228*t*

SudChemie nonprecious metal catalysts, 251, 253*f*

Surfactants

- crossflow microfiltration, 390
- in water-in-crude oil emulsions, 379, 390
- removal by polyHIPE polymers (PHPs), 381, 390
- use in removal of metal ion contaminants, 390

Suzuki coupling, base-free, 41

Swiss roll burner design, 186

Synthesis gas (syngas)

- alkane formation (Fischer-Tropsch synthesis)
- CO conversion, 94, 96, 97*f*
- comparison to macroscale reactions, 97*f*
- empirical modeling and statistical analysis, 98
- Fe and Co catalysts, 92, 94–96, 97*f*
- magnetization studies of sol-gel Fe/Co catalyst, 96, 97*f*
- sol-gel preparation, 92, 94
- formation from butane in microchannel reactors, 57–58

*See also* Catalytic partial oxidation of methane (CPOM) to synthesis gas

**T**

Thermally grown oxide (TGO) formation, 107*t*, 108–111

Time pulsing mixing, 350, 351*f*, 352, 354*f*–355*f*

Titania particle production in dual-pipe reactor, 28, 29*f*

Titanium(IV) catalysts

- catalytic membrane reactivity, 314–318
- chemoselective oxidation of dibenzyl amine, 315*f*
- effect of substrate/catalyst ratio, 318, 319*t*
- morphology of Ti(IV) complex in polymeric membrane, 312, 313*f*
- nitrone formation by amine oxidation, 315–317
- polyacrylonitrile (PAN) catalytic membrane, 312*f*, 313*f*
- polyetheretherketone (PEEKWC) catalytic membrane, 312*f*, 313*f*
- polyvinylidene difluoride (PVDF) catalytic membrane, 312*f*, 313*f*, 317–318, 319*t*
- process intensification, 310, 318
- stereoselective oxidation of benzyl phenyl sulfide, 314*f*, 315*t*
- sulfoxidation of alkyl aryl sulfides, 310–311
- synthesis of Ti(IV) complex in polymeric membrane, 311, 312*f*
- system recycling, 317–318, 319*t*
- Ti(IV)(R,R,R)-tris-(2-phenylethanol)amine, structure, 310*f*

Toshiba, fuel cell development, 195, 196*f*, 197

Tubular reforming reactors, 225, 226–227, 228*t*

**V**

- V-L separation. *See* Batch reactive distillation (BRD)
- Vehicles, fuel cells and, 239, 257*t*
- See also* DOE-EE/RE Freedom CAR Program
- Vertical Y- and T-type configuration diffusive mixing, 342

**W**

- Water gas shift (WGS) reactors
- adiabatic vs heat exchange reactors, 229–231
- catalyst requirements, 125
- chemical reaction, 164
- CO conversion over different catalysts, 202*f*
- combined adiabatic/differential reactors, 246–251, 249*f*
- diesel fuel reactor, 229–231, 234

**DOE-EE/RE Freedom CAR**

- Program, 240, 246–251
- enthalpy of reaction, 164
- hydrogen production, 164
- in 10-W microchannel reactor, 55, 56*f*
- MiRTH-e water shift gas reactors, 202
- steps in fuel processing for fuel cells, 214
- temperature profiles, 246, 247*f*, 248*f*

**Y**

- Young–Laplace equation, 362, 366

**Z**

- Zeolite based catalysts for C5 isomerization of naphtha, 76–77, 77*f*, 78*f*



*Plate 6.1. a) Conventional catalyst pellets b) Scanning electron micrographs of FeCrAlY felt substrate used in microchannel reactor.*

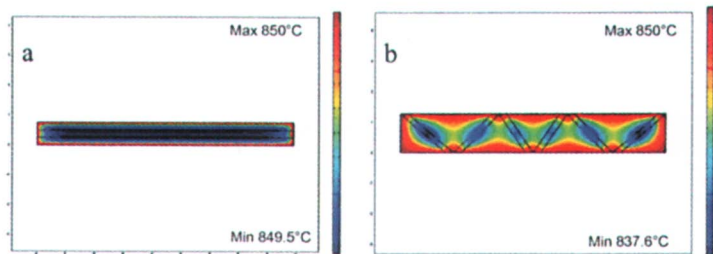


*Plate 6.7. Temperature distribution in a cross-section of methane steam reforming microchannel reactor ( $z=2.54\text{mm}$ , 13.8 msec contact time, 850°C, 20 atm, steam/C=2) for a) catalyst "DF", and b) catalyst "C".*

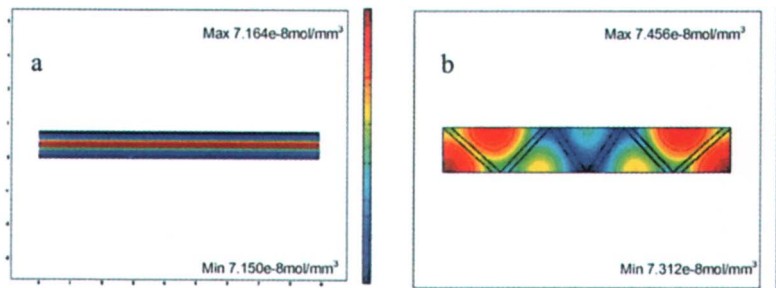


*Plate 6.8. Local methane concentration profile in a methane steam reforming microchannel reactor ( $z=2.54\text{ mm}$ , 13.8 msec contact time, 850°C, 20 atm, steam/C=2) for a) catalyst "DF", and b) catalyst "C".*

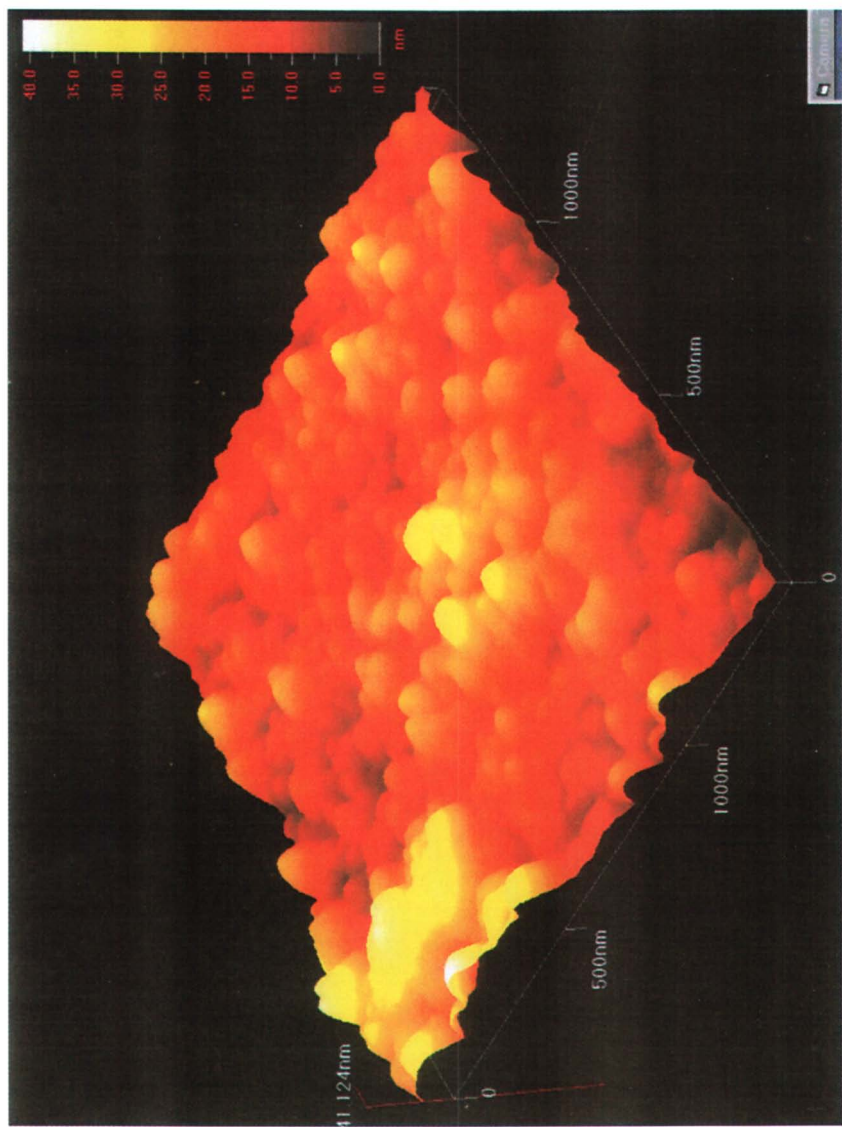
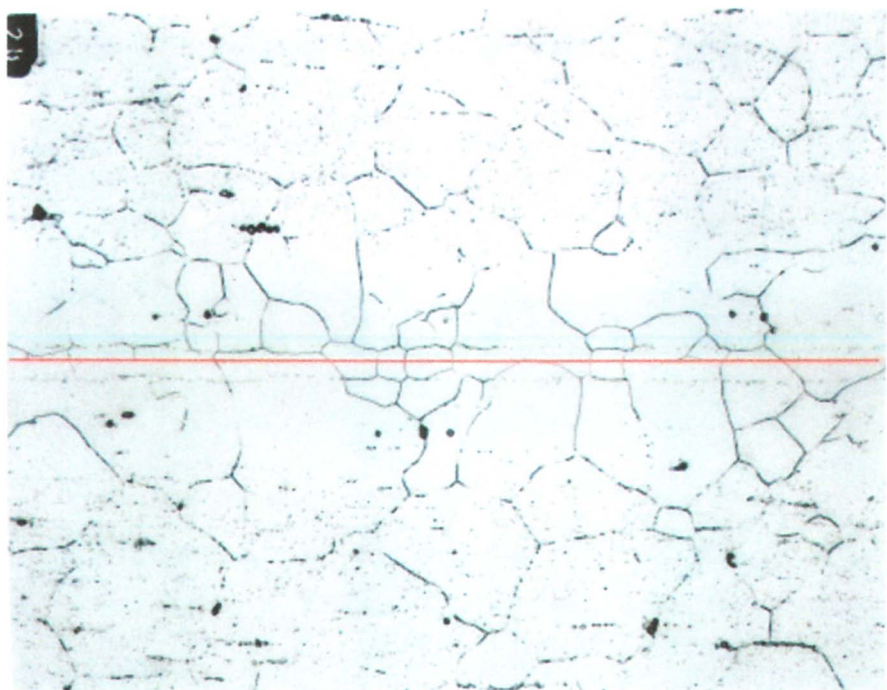


Plate 8.4. Surface of the coated silica sol-gel catalyst support



*Plate 16.2. 200X Photomicrograph of diffusion bonded microchannel layers.*



*Plate 20.1. Experimental setup*

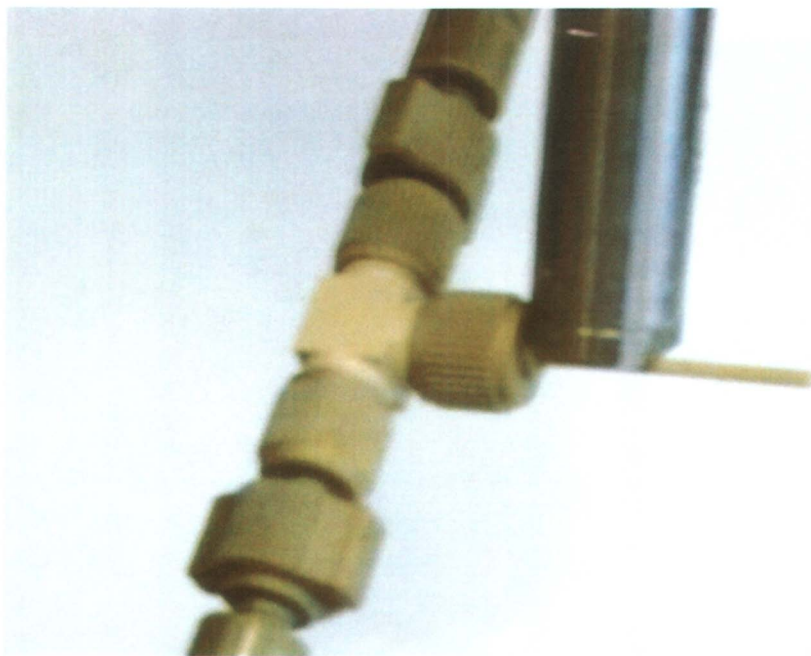


*Plate 20.2. Ultrasound generator touching 254  $\mu\text{m}$  mixing tee.*

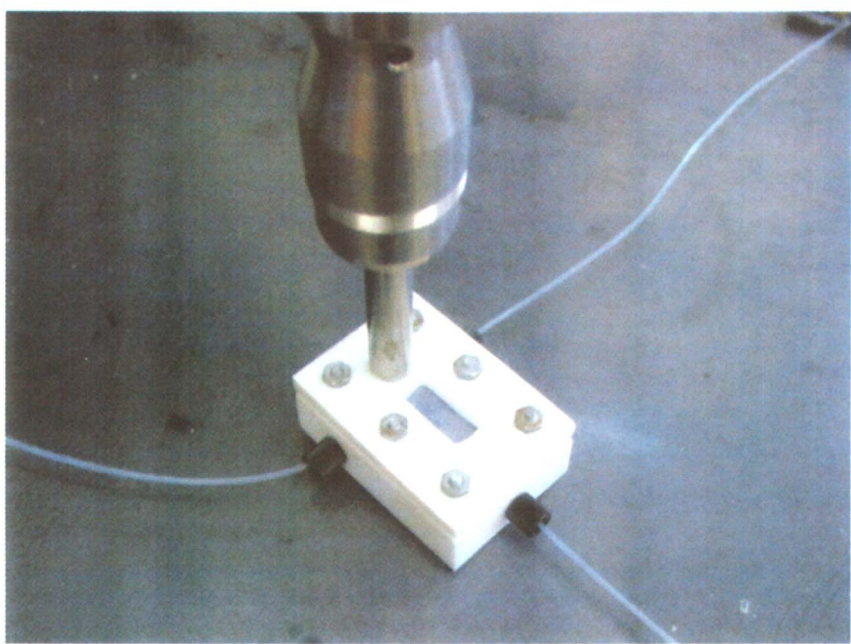


*Plate 20.3. Ultrasound generator touching 100  $\mu\text{m}$  mixing tee.*